National Defence | **Défense nationale**
Research and Development Branch | Bureau de recherche et développement

ABSTRACTS and SUMMARIES
of the
CANADIAN FORCES / CRAD MEETING
on

NAVAL APPLICATIONS
of
MATERIALS TECHNOLOGY

27 - 28 - 29 APRIL 1993

Defence
Research
Establishment
Atlantic

Centre de
Recherches pour la
Défense
Atlantique

Compiled by J. R. Matthews

Canada

CF/CRAD MEETING
on
NAVAL APPLICATIONS OF MATERIALS TECHNOLOGY

27th, 28th and 29th April 1993

AGENDA

Tuesday April 27th

Registration:

Welcome: Cdr R. H. Stillwell, NAO, NEUA

Opening Remarks: Mr. Rod Schmitke, Director,
Technology Division, DREA

Introduction: Dr. R.S. Hollingshead, Head,
Dockyard Laboratory

SESSION I:

Welding Processes
Chairman: Dr. R.S. Hollingshead

page

1. The DREA Welding Program 1980-1993, J. R. Matthews 1

COFFEE

2. Pulsed Welding of HY80/HY100 T.I.M.E.™ Process, R. Robichaud, Donelad Ltd and TIME Weld Canada 11

3. Evaluation of Heat Affected Zone Microstructure/Mechanical Properties of HY100 Grade Steels, J.T. Bowker, J.A. Gianetto and M.W. Letts, CANMET 35

4. Progress in Surface Engineering Research at DREA, C.V. Hyatt and J. Cunningham, DREA, K. Magee, Laser Institute, and T. Betancourt NSRFC 68

LUNCH

SESSION II: page

Fracture Toughness
Chairman: Mr. Ken KarisAllen

1. J-Resistance Curve of HY100, Dr. B. Faucher, CANMET, and K. KarisAllen, DREA 74
2. Fracture Toughness of Steel Weldments at High Loading Rates M.N. Bassim, University of Manitoba and J.R. Matthews, DREA 94

COFFEE

3. Application of Very Low Yield Strength Electrodes In The Root Pass of Weldments to Prevent Preheating, J. Vuik, J. C. van Wortel, TNO and Cees Van Sevenhoven, Royal Netherlands Navy 119
4. Application of J and CTOD Estimation Formulas to Naval Construction Steels, Dr. Jack Morrison and Zhenhua Zhai, DREP, and Ken KarisAllen, DREA 137
5. The Feasibility of Determining Percent Plate Strain in HY80 Structures Using X-Ray Diffraction Peak Analysis, J. Pineault, M. Brauss, Proto Manufacturing and J.F. Porter, DREA 153

Demonstrations of TIME Welding in SRU Welding Shop

RECEPTION
TUESDAY EVENING, 27th APRIL
TECHNICAL UNIVERSITY OF NOVA SCOTIA
FACULTY CLUB

1334 Barrington St

7:30 to 10:00 pm

Wednesday, 28th April

SESSION III:

Welding Processes
Chairman: Dr. R.S. Hollingshead

1. Long Range Reaction Stresses in Ship Structures, L. Malik and B. Cowper, Fleet and W.R. Tyson, CANMET 154

COFFEE

2. An Evaluation of Experimental Metal-Cored Electrodes For Submerged-Arc Welding of HSLA100 Steel, J.A. Gianetto, N.J.G. Smith and D.E. Dolan, CANMET 184

3. Laser Assisted Gas Metal Arc Welding of Thick Steel Plate, by Ken Magee, Alberta Laser Institute 211

4. Current Welding Consumables Research In The U.S. Navy, by J.J. DeLoach, Jr., G.L. Franke, M.G. Vassilaros, and R.J. Wong, presented by Paul Holsberg, Carderock Division, Naval Surface Warfare Center Welding Branch, Code 615, Annapolis, Maryland, USA 21402 212

LUNCH

SESSION IV:

Fracture Control
chairman: Mr. John Porter

1. The Influence of Weld Strength Mismatch on the Fitness-For Service of High Strength Steel Structures, Mark T. Kirk, Edison Welding Institute 240

2. Development of Computational Algorithms for Probabilistic Fracture Mechanics, I.R. Orisamolu, Q. Liu and M.W. Chernuka, Martec Ltd. 261

COFFEE

3. The Effect of Finite Crack Tip Radius on Initiation Fracture Toughness, Ken MacKay, TUNS, Ken KarisAllen, DREA, and G. Lee, TUNS 262

4. Buckling and Post-Buckling of Stiffened Shell Structures Using a Co-rotational Finite Element Formulation, L.Jiang and Dr M.W. Chernuka, Martec 280

5. Four PC-based Fracture Mechanics Packages Reviewed, G.V. Gorveatte and J.F. Porter 302

Demonstrations of TIME Welding in SRU Welding Shop

WEDNESDAY EVENING, 28th APRIL
BANQUET

Chateau Halifax
Bluenose Room

7:00 pm
(for 8:00 dinner)

Thursday, 29th April

SESSION V:

Non Destructive Research and Development
Chairman: C.V. Hyatt

page

1. Introduction to the APHIUS Development Project 323
   Gaetan Labbe, DSE 6, NDHQ, Ottawa
2. Background Research Leading to APHIUS Development Project, 341
   J.R. Matthews, DREA

COFFEE

3. Status of Current Development Project for APHIUS
   Bob Hay, Tektrend International
4. Advanced Flaw Sizing in Practice, Cees VanSevenhoven, Royal Netherlands Navy, and W.H. van Leeuwen, RTD 345
5. The Elastic Strain Field and Evidence for Plastic Deformation Near Cracks in Loaded Steel Bars, T.M. Holden, J.H. Root and J.F. Mecke, AECL and J.F. Porter, DREA 356

LUNCH

SESSION VI:

Steel and Welding Development Activities and the Future
Chairman: Mr Rod Schmitke

1. Introduction to Development Project for Canadian Steel and Welding Procedures For HY700WQT Steel, by Gaetan Labbe, DSE 6, NDHQ, Ottawa 383
2. Progress on Development Project for Canadian Steel and Welding Procedures For HY700WQT Steel, R. Rene and Charles Billard, Marine Industries Limited 396
3. Explosion Bulge Results for HY700WQT Steel, John Porter, DREA 422

COFFEE

SESSION VII:

Discussion and Tours
Chairman:

1. Open Discussion
2. Demonstrations i) TIME Welding
   ii) DREA Dockyard Lab

#510306 ①

The DREA Welding Program 1980-1993

by

J. R. Matthews

Defence Research Establishment Atlantic
FMO Halifax, Halifax Nova Scotia B3K 2X0

Abstract

From 1980 to 1993 DREA Dockyard Laboratory supported an extensive research program in welding processes for HY steels. This program was begun in long term anticipation of the Canadian Navy replacing the Oberon submarines and the need for extensive Canadian knowledge in fabrication and inspection with HY steels. In later years this program has found more immediate application in questions related to extension of Oberon life, ie cladding, mismatched steels, electrode substitution and certification etc. The welding program has included many types of welding, all position, numerous equipment and consumable types, different gases, a range of heat inputs etc. Several novel Canadian processes have been explored in addition to traditional welding methods. After considerable welding and evaluations, numerous procedures have been developed using different processes, and an optimized pulsed GMAW process has been identified that provides properties approaching those of HY steels.

Introduction

In the past twelve years DREA/DL has supported extensive research in welding processes for HY steels. We have examined SMAW (shielded metal arc welding), SAW (submerged arc welding), GMAW (gas metal arc welding), FCAW(flux cored arc welding), and laser assisted arc welding. Processes were examined to new specifications and requirements developed in parallel with the welding (ie dynamic tear and explosion bulge). Efforts were made to isolate those processes most suitable for shipyard work and most capable of routinely producing properties approaching HY steels. In addition to development of optimum procedures for standard processes, DREA isolated two Canadian welding processes that have proved outstanding. The first is frequency modulated pulsed GMAW and the second is TIME (transfer ionized molten energy) GMAW welding. In 1988 to 1990 these two processes were evaluated in a very complete 24 weldment series comparison. This resulted in identification of pulsed welding with Fronius equipment and TIME welding as the two most outstanding processes. In the past year four additional weldment series were made using a combination of these two processes. (Fronius developed special pulsed equipment for use with TIME.)

We will first give a brief background to welding of QT 28 and HY steels before outlining welding research conducted in the past twelve years in detail.

Background

In the late 1960's Canada purchased three Oberon submarines from the UK. Engineering and ship repair support had to come to full speed immediately in the areas of maintenance, repair, supply and alterations. This required immediate development of Canadian welding, inspection and supply of materials for the fabrication aspects of the job. The UK was the main source of supplies, in particular QT 28 steel and Fortrex B welding electrodes. The UK exchanged an engineering officer to work in NEU providing engineering support, on an ongoing basis from the late sixties scheduled to stop in the near future(1993/94). Specifications were provided for welding (DG Ships 240), inspection (DG Ships 9022) and acceptance (DG Ships 10000).

DREA/ Dockyard Laboratory's role in the early stages, late 60's to 1980, focused on engineering and technical support. Dockyard Lab provided early NDT including MPI, Ultrasonics and Radiography for the submarine work, and also technical support in establishing inspection requirements and actually providing for inspection and records (ie heat treat, root pass, back pass, temper bead, weld profile inspection, NDT coordination, production of records and certification). Dockyard Lab was involved in welder qualification, consumable qualification and procedure qualification, especially the acceptance and record keeping aspects.

In 1980, roles changed with creation of the Welding Inspector/Officer position at NEU aimed at taking over the inspection and record keeping aspects from DREA as well as responsibility for procedure qualification and welder qualification. Dockyard Lab retained responsibility for radiography (SRU established an NDT group to perform MPI/LPI, UT and all other forms of inspection around 1975), welding engineering consulting and certification of welders.

The main focus of DREA then switched to research of welding, inspection and weldment acceptance(explosion and fracture testing). To that point welding was still restricted to SMAW welding with Fortrex B electrodes. Acceptance of weld procedures and new consumables was believed to be possible with charpy and bend bar testing, and NDT was limited to standard industrial RT and UT. The weld acceptance criteria were very strict.

The main focus of this paper is to look at the research done in the past 12 years on welding processes that would give workmanship advantages over SMAW, but that would also provide properties approaching HY steels. In separate reports we explore the research work done to develop intelligent automated ultrasonic inspection. The intelligent automated inspection was required to permit identification and mapping of the various types of weld defects to allow condemnation criteria based on specific defect type. Finally, fracture research has focused on introduction of minimal testing requirements for procedure and consumable qualification. That work has established DT levels of 690 joules at -29C and 16 % strain in explosion bulge for HY80 and 12% for HY 100 as minimal acceptance levels. Fracture work has also focused on elastic plastic research and fracture control technology.

Welding research has been assisted greatly by contracts with many organizations, all of whom will be acknowledged and referenced in this report. The series of CF/CRAD Meetings on Research in Fabrication and Inspection of Submarine Pressure Hulls[1,2,3,4] has provided a forum for exchange of ideas between CF engineers, scientists, contractors and international welding specialists. International cooperation in this area has been fostered by two operating assignments in TTCP P(Materials) TP1(Metals); specifically an assignment on Welding HY80[5,6,7] and an assignment on Fracture Control for Naval Structures. Finally, NDHQ has started(1990/91) development work in producing a Canadian Steel and Welding Procedures for an HYW700QT steel.

We will continue this report by outlining the specific welding research that has been carried out.

Welding

Several overviews have been given over the years including those at the CF/CRAD Conferences[8,9,10] and the Defence Science Symposium[11]. The following overview will be divided according to welding process type. Table 1 gives a brief summary of the welding

Table 1. Welding Research at DREA 1980-1993

Shielded Metal Arc Welding (SMAW)

ELECTRODE	STEEL	
E7018	HY 80	SRUA
E9018M	HY 80	SRUA
Fortrex B	HY 80 and QT 28	SRUA
E11018M	HY 80	SRUA
E12018M2	HY 100	HDIL

Submerged Arc Welding (SAW)

HEAT INPUT	STEEL	
1.5kJ	HY 80	Versatile Vickers
2kJ	HY 80 HY 100 and HSLA 80	MTL (CANMET)
3kJ	HY 80 HY 100 and HSLA 80	MTL (CANMET)
4kJ	HY 80 HY 100 and HSLA 80	MTL (CANMET)

Gas Metal Arc Welding (GMAW)

a. T.I.M.E. (transfer ionized molten energy)

WIRE	JOINT	STEEL
LA 100	narrow gap	HY 80 Techno Sci
LA 100 Linde 95 Linde 120	double vee	HY 80 Weld Process/Techno Sci
LA 100 Linde 120	double vee	HY 80/100 Fleet/Weld Proc

b. Pulsed

MACHINE	STEEL	
Generac(Japan)	HY 80/100	WIC
Hobart(US)	HY 80/100	WIC
WIC/FM(Can)	HY 80/100	Fleet/WIC
TP Fronius(Austria)	HY 80/100	Fleet/WIC/Weld Proc

Flux Cored Arc Welding (FCAW)

HY 80/100	TUNS

Laser Assisted Gas Metal Arc Welding	Laser Institute

including the essential variables. In the early years the focus was HY 80 but in later years HY 100 was included in all work.

i. Shielded Metal Arc Welding (SMAW)

Welding for base line testing[12,13,14,15] in shielded metal arc welding was conducted at Ship Repair Unit Atlantic(SRUA) using procedures developed for work on Oberon submarines. The electrodes and steels evaluated are shown in Table 1. From this work electrodes available in North America suitable for replacement of Fortrex B were identified.

When interest in HY100 began we received advice from DTRC and DRA Dunfermline about the most promising stick electrodes and contracted HDIL to produce weldments for further base line testing.[16] The E12018-M2 electrodes were obtained from Alloy Rods in Hanover, Pa. Preheat and interpass temperatures were controlled in the usual way. Despite excellent quality welding the impact results (as predicted by DTRC and DRA Dunfermline) did not meet the required 690 joules at -29C. It was thus verified that any fabrication with HY 100 would require at least a semi-mechanical process.

ii. Submerged Arc Welding (SAW)

Research work in submerged arc welding was conducted at CANMET. Most welding was done in house but some was done in the ship yards at Versatile Vickers. Heat input was the major variable studied by CANMET. Values of 1.5 kJ, 2 kJ, 3 kJ and 4 kJ were evaluated for HY 80, HY 100 and HSLA 80 steels.[17,18] CANMET has a broad range of expertise in this area developed over a considerable period of time.

iii. Gas Metal Arc Welding (GMAW)

a. T.I.M.E. (transfer ionized molten energy)

In an effort to acquire all-position semi-mechanical welding for HY80 steel plate, several welding processes including those employing novel gas mixtures for gas metal arc welding have been studied. T.I.M.E.(transfer ionized molten energy) process from Weld Process International has been evaluated the most by DREA due to superb early results.[19,20,21]

The T.I.M.E. process[22,23] was developed in 1980 after many years of research and development of gas mixtures for shielding and metal transfer. The process is a gas metal arc welding process which employs a special gas, Table 2, and a specially designed nozzle.

Table 2. Composition of TIME Gas

gas	Ar	CO_2	He	O_2
T.I.M.E. 1	65	8	26.5	0.5

The process produces welds that are very clean with reduced sulfur and phosphorous levels and enhanced weldment toughness. It is believed that the reduced impurities are responsible for the improved toughness of the weldments. The transfer characteristic is effective in the short arc mode as well as the globular and spray modes. The welding in this work was all conducted in the spray arc mode.

In 1988, welding procedures were developed for the four positions of interest-flat, horizontal, vertical down and overhead, Table 3, using standard welding machines.[21,24]

Table 3. Welding Procedures for the Four Positions[21,24] (all spray transfer)

Welding Parameters	Flat	Horizontal	Vertical Down	Overhead
Wire Diameter (mm)	1.14	1.14	1.14	1.14
Tip Recess (mm)	2.5 - 3	2.5	2.5	2.5
Stick Out (mm)	12 - 16	12 - 16	12 - 16	12 - 16
Shield Gas	T.I.M.E.	T.I.M.E.	T.I.M.E.	T.I.M.E.
Gun Type (T.I.M.E.)	Watercooled	Watercooled	Watercooled	Watercooled
Angle of Gun	45	45	75	45
Plate Thickness (mm)	25	25	25	25
Gap (mm)	2.5	2.5	2.5	2.5
Included Angle	50	50	50	50
Wire Speed (m/min)	8.8	8.9	8.9	8.4
Amps	220	240	240-245	200-220
Volts Root Pass	29	26.5	26.5	29
Volts Subsequent Passes	30	27	29.5	27.5
Travel Speed Root Pass (mm/min)	337	450	450	337
Travel Speed Subsequent Passes	450	600	800	600
Heat Input Root Pass (kJ/mm)	1.14	.88	.85	1.1
Heat Input Subsequent Passes (kJ/mm)	.88	.65	.54	.61

At that time(1988), the welds were evaluated for impact and explosion resistance. 16 mm dynamic tear tests were carried out. These tests indicated the tearing resistance of the weldments for direct comparison to the performance of each other and the parent plate. Specimens were cut from weld metal and heat affected zones of the welded plates. The heat affected zone samples had the notches located in the space between the fusion line and 1 mm from the fusion line in the centre of the plate. The specimens were tested at -29°C. Shear index was determined for each DT sample. The dynamic tear results were in the normal range with a Linde 95 wire (650 J) but were much higher with a Lincoln LA 100 wire(1300 J). It was felt that the TIME gas had an enhancing effect on the toughness result for all welds while incomplete fusion defects had a detrimental effect for the Linde 95 Welds. Our net experience suggests that LA 100 wire should be utilized in the production welding of HY80 steel plate when weld toughness equal to the plate (T-L orientation) is required. All the samples passed the explosion bulge test.

Subsequent to the work completed in 1988 a weld study involving TIME and pulsed welding was carried out by Fleet Technology, TIME Weld Process, and WIC[25,26]. 24 weldments were prepared for HY80 and HY100 with a variety of machine gas combinations.

In 1992/93 a final weld series was carried out with the TIME process on HY80/100 using specially designed pulsed welding equipment from Fronius. This work has resulted in final recommendations for weld procedures using the TIME process.[27]

b. Pulsed GMAW

The earliest studies of pulsed welding supported by DREA were with WIC[28,29,30]. WIC had patented a frequency modulated pulsed welding system that relied on voltage feedback and frequency modulation of identical pulses, to compensate for required rate of metal transfer. This was different from synergic pulsed systems which used variable speed wire feed to compensate for rate of metal transfer requirements.

Studies involved comparisons of the WIC system to early commercial pulsed systems such as Generac[29] and Hobart[30], and later to TP Fronius[25,26], Table 4.

Table 4. Pulsed Welding Equipment Evaluated

MACHINE	STEEL	CONTRACTOR
Generac(Japan)	HY 80/100	WIC
Hobart(US)	HY 80/100	WIC
WIC/FM(Can)	HY 80/100	Fleet/WIC
TP Fronius(Austria)	HY 80/100	Fleet/WIC/Weld Proc

Unfortunately, despite early success in welding the HY steels[28,29,30], the commercial version of the WIC FM system was optimized around an .035 wire and was not suitable for the HY steels.[25,26]

Pulsed welding of HY80/100 with C5 gas and Fronius equipment remains one of the best performers to date.[25,26] This was a major contributing factor to TIME Weld Canada's having teamed up with Fronius to produce pulsed equipment optimized for the TIME gas.[27]

iv. Flux Cored Arc Welding (FCAW)

Work in Flux Cored Arc Welding for DREA was conducted by Keith Leewis, TUNS. Basic research in fluxes[33] was very successful but application of FCAW to HY80/100 was not.[34,35,36] The effort here was minimal.

v. Laser Assisted Gas Metal Arc Welding

Work in laser assisted GMAW at the Laser Institute has been progressing steadily for the last few years.[37] We hope to explosively test some of these welds in 1993.

Evaluations

In the welding section above general comments on the success of the various welding was summarized focusing on dynamic tear and explosion bulge highlights.

For more detailed information on these evaluations including information on fracture, fatigue and corrosion fatigue testing see the final references in this report.[38-50]

Conclusions

Semi mechanical welding for use on submarine pressure hulls have been successfully developed in the past twelve years under the DREA welding program.

Several welding procedures exhibit impact properties approaching those of HY Steels.

Optimum welding procedures for GMAW of HY80/100 using the TIME welding process have been determined.

References

General

1. J.R. Matthews, "Abstracts and Summaries of the lst Canadian Forces/CRAD Meeting on Research in Fabrication and Inspection of Submarine Pressure Hulls, Halifax, Nova Scotia, May 28-29, 1985.

2. J.R. Matthews, "Abstracts and Summaries of the 2nd Canadian Forces/CRAD Meeting on Research in Fabrication and Inspection of Submarine Pressure Hulls", Halifax, Nova Scotia, May 26-28, 1987.

3. J.R. Matthews, " Abstracts and Summaries of the 3rd CF/CRAD Meeting on Research in Fabrication and Inspection of Submarine Pressure Hulls", Halifax, Nova Scotia, June 6-8, 1989.

4. J.R. Matthews, " Abstracts and Summaries of the 4th CF/CRAD Meeting on Research in Fabrication and Inspection of Submarine Pressure Hulls", Halifax, Nova Scotia, June 4-6, 1991.

5. J.R. Matthews, "TTCP Operating Assignment - Welding of HY 80 Steel," TTCP P-TP1/CAN/2/86, January 1986.

6. J.R. Matthews, "1987 Progress Report on Welding of HY Steel", PTP1/CAN/2/88, March 1988.

7. J. Bird, J.R. Matthews et al, "Welding of HY 80 Steels", Technical Panel Assignment TTCP-P-TP1 Final Report, prepared by ARE(D) on behalf of NSRDC(Annapolis), DREA(Halifax) and MRL(Melbourne), PTP1/1/89, August 1989.

8. J.R. Matthews, "General Introduction to Shielded Metal Arc Welding (SMAW) on Oberon Class Submarines," Abstracts and Summaries of the CF/CRAD Meeting on Research in Fabrication and Inspection of Submarine Pressure Hulls, May 1985.

9. J.R. Matthews, "General Introduction to Shielded Metal Arc Welding (SMAW) on Oberon Class Submarines," Abstracts and Summaries of the 2nd CF/CRAD Meeting on Research in Fabrication and Inspection of Submarine Pressure Hulls, Halifax, N.S., May 26-28, 1987.

10. J.R. Matthews, "The DREA Submarine Welding Program 1980-1990", in abstracts and summaries of the 4th CF/CRAD Meeting on Research In Fabrication and Inspection of Submarine Pressure Hulls, Halifax, Nova Scotia, June 4-6, 1991.

11. J.R. Matthews, "Research on Fabrication and Inspection of Submarine Pressure Hulls," presented at Defence Science Symposium, Ottawa, April 1988.

Shielded Metal Arc

12. J.R. Matthews and K.J. Allen, "JId and Dynamic Tear of HY80 Weldments," presented at the 1st CF/CRAD Meeting on Research In Fabrication and Inspection of Submarine Pressure Hulls, May 1985.

13. J.F. Porter and J.R. Matthews, "Explosion Bulge Evaluation of SMAW and Narrow Gap Weldments,"presented at the 1st CF/CRAD Meeting on Research In Fabrication and Inspection of Submarine Pressure Hulls Ibid, May 1985.

14. J.F. Porter and J.R. Matthews, "Explosion Bulge Behavior of SMAW and Narrow Gap Weldments of HY 80," DREA RN/DL/85/6, September 1985.

15. J.R. Matthews and K.J. Allen, "Toughness of HY 80 SMAW and Narrow Gap Weldments Using J-Integral and Dynamic Tear," DREA RN/DL/85/3, April 1985.

16. R.M. Robichaud and I.M. Campbell, "Shielded Metal Arc Welding of HY100 Steel Plate with E12018M2 Electrodes", Halifax Dartmouth Industries Ltd., DREA CR/87/444, October 1987.

Submerged Arc

17. J.T. Bowker, M.W. Letts, J.A. Gianetto and R.F. Orr, "An Evaluation of the Notch Toughness of the Heat Affected Zone in HY and HSLA Steel", CANMET, DREA CR/87/451, October 1987.

18. J.T. McGrath, J.A. Gianetto and R.F. Orr, "A Comparison of the Microstructural and Mechanical Properties of Submerged Arc Welding in HY80 and HSLA80 Steels", CANMET, DREA CR/87/450, October 1987.

TIME

19. M.Macecek and J. Belbeck, "Narrow Gap Welding of HY80 Steels Using the TIME Process", Techno Scientific Inc., DREA Contractor Report, 1983.

20. M. Macecek and J. Belbeck, "Research in Narrow Gap Welding", Techno Scientific, DREA/CR/86/434, April 1986.

21. M.Macecek, "All Position Welding of HY80 Plate with the TIME Process", Techno Scientific Inc., DREA CR/88/419, 1988

22. Rodwell, M.H., "Evaluation of the T.I.M.E. MIG Welding System", Project Report LD22983/1/83, The Welding Institute, Cambridge U.K., October 1983

23. "Welding Characteristics of a new welding process, T.I.M.E. Process", prepared by the Aichi Sangyo Co. Ltd., Japan, July 1989

24. J.R. Matthews, J.F. Porter, J. Church, M. Macecek "An Evaluation of T.I.M.E. Welding of HY80 Plate," The Welding Journal,70, February 1991.

25. L. Malik, K.G. Morrison and L.N. Pussegoda, "All Position Gas Metal Arc Welding of HY80 and HY100 Steels, prepared by Fleet Technology Limited, contractor report, DREA CR/91/434, May 1991.

26. L. Malik, K.G. Morrison, L.N. Pussegoda and J.R. Matthews, "All Position GMAW Welding of HY80 and HY100 Steels", in abstracts and summaries of the 4th CF/CRAD Meeting on Research In Fabrication and Inspection of Submarine Pressure Hulls, Halifax, Nova Scotia, June 4-6, 1991.

27. R.M. Robichaud, "Evaluation of TIME Weld Procedures Optimized for HY80/100 Steels Using Specially Designed Fronius Welding Equipment", Donelad Ltd., DREA Contractor Report, 1993 (in edit)

Pulsed

28. A. Ditschun, "Application of Pulsed Current Techniques to Welding HY80 Steel", Welding Institute of Canada, DREA Contractor Report, 1984.

29. A. Ditschun, "Application of Pulsed Current Techniques to Welding HY80 Steel", Welding Institute of Canada, DREA Contractor Report, CR 85/421, September 1985.

30. E. Lassaline, "Application of Pulsed Current Techniques to Welding HY80 Steels", Welding Institute of Canada, DREA CR/887/405, 1987

31. J.R. Matthews, E.E. Lassaline, J.F. Porter, and K.G. Leewis, "Evaluating Frequency-Modulated GMA Welding for HY80 Steel", The Welding Journal, 71, September 1992.

32. J.R. Matthews, E.E. Lassaline, J.F. Porter, and K.G. Leewis, "An Evaluation of Pulsed Gas Metal Arc Welding for HY80 Steel," DREA RN/DL/93/1 , January 1993.

Flux Cored

33. K. Leewis, "Surface Tension Effects in the Flux Cored Arc Welding of HY80 Steels", TUNS, DREA CR/87/462, December 1987.

34. K.G. Leewis, "Flux Cored Welding for HY80/100 Steels", TUNS, DREA CR/89/432, Oct 1989.

35. K.G. Leewis and J.R. Matthews, "Qualification of a FCAW Consumable for HY 80 and HY 100 Steels", presented at the 3rd CF/CRAD Meeting on Research In Fabrication and Inspection of Submarine Pressure Hulls, June 1989.

36. M. Pineo, K.G. Leewis, and J.R. Matthews, "Flux Cored Welding of HY 80 and HY 100", presented at the 28th Annual Conference of Metallurgists, Halifax, August 1989.

Laser

37. K.H. Magee, V.E. Merchant and C.V. Hyatt, "Laser Assisted Gas Metal Arc Weld Characteristics", Laser Materials Processing, Vol. 71, 1991, 382-399.

Fracture, Fatigue and Corrosion Fatigue

38. T. Betancourt, "Corrosion Fatigue Crack Growth Behaviour of HY80 SMAW and Narrow Gap Weldments", NSRFC, DREA Contractor Report, CR/85/406, April 1985.
39. A. Kazi, "Effect of Welded Residual Stress on Fatigue Life of HY80 Plate", NSRFC, DREA Contractor Report, 1984.
40. T. Betancourt, "Corrosion Fatigue Crack Growth Behaviour of Shielded Metal Arc Weldments and Metal Inert Gas Weldments", NSRFC, DRREA CR/86/427, April, 1986.
41. A. Kazi, "Effect of Weld Stress on the Fatigue Life of HY80 Plate", NSRFC, DREA CR/87/417, March 1987.
42. T. Betancourt and M. Robichaud, "Study of Corrosion Fatigue Crack Growth Behaviour of Shielded Metal Arc Weldments and Metal Inert Gas Weldments", NSRFC, DREA CR/89/411, April 1989.
43. M.N. Bassim, "High Strain Rate Impact Study of Submarine Pressure Hull Weldments", University of Manitoba, DREA contractor Report, CR/86/404, March 1986.
44. M.N. Bassim, "High Strain Rate Impact Study of Submarine Pressure Hull Weldments", Univ of Manitoba, DREA CR/89/404, Feb 1989.
45. M. Nabil Bassim, "Determination of the Dynamic Fracture Toughness of Submarine Hull Weldments", DREA Contractor Report CR/92/423, April 1992
46. J.R. Matthews, K.J. Allen, and G.I. Dease, "Dynamic Tear of HY 80 Weldments," DREA RN/DL/86/1, January 1986.
47. J.R. Matthews and G.I. Dease, "Dynamic Tear of HY80, HSLA80 and HY100 Weldments," DREA Research Note DL/88/1, January 1988.
48. J.R. Matthews, G.I. Dease and R. LeTourneau, "Dynamic Tear and Shear Index for GMAW Weldments of HY 80 and HY 100", DREA Research Note, DL/91-1, Jan 1991.
49. J.F. Porter, D.O. Morehouse, J.R. Matthews, "Response of SMA and Narrow Gap HY80 Weldments to Explosive Shock Loading," DREA Technical Memorandum 88/206, March 1988.
50. J.R. Matthews, "On the Relationship Between Shear Index and Energy in Dynamic Tear Specimens," submitted to Engineering Fracture Mechanics.

#510307 ②

DONELAD LIMITED
ENGINEERING SERVICES

Pulsed Welding of HY80/HY100 Using the T.I.M.E.™ Process

by

R. Robicheau, P. Eng.

Donelad Limited
Bedford, N.S.
Canada

ABSTRACT

Over the past number of years, the Defence Research Establishment Atlantic has sponsored a number of projects aimed at evaluating welding processes suitable for the fabrication of submarines. The objective of these evaluations has been to maximize weldment toughness as determined by dynamic tear specimen testing. The Transferred Ionized Molten Energy **(T.I.M.E.™) Process** has emerged superior to other potential welding processes. The purpose of the present investigation was to optimize weldment properties employing the T.I.M.E.™ Process with state-of-the-art pulsing controllers and power sources.

The project involved preparing welding procedures for the pulse T.I.M.E.™ Process employing a T.I.M.E. 540 power source coupled with a TR-19 synergic pulsing unit, pre-programmed for use with the patented T.I.M.E.™ Process. These procedures were first proven on mild steel before they were applied each to HY100 and HY80 steels in both the 3G (vertical down) and 1G/4G (flat/overhead) positions.

A number of dynamic tear and explosion panels were prepared to evaluate the properties of the weldments.

Mechanical and non-destructive test results for both HY80 and HY100 are given.

SUITE 720, SUN TOWER, 1550 BEDFORD HIGHWAY
BEDFORD, NOVA SCOTIA, B4A 1E6
TEL. (902) 835-5777 FAX. (902) 835-6655

1.0 INTRODUCTION

Over the past number of years, the Defence Research Establishment Atlantic has sponsored several projects aimed at evaluating welding processes and procedures suitable for the fabrication of submarines. The objective of these evaluations has been to maximize weldment toughness as determined by dynamic tear specimen testing. The T.I.M.E.™ Process emerged with superior advantages over other potential welding processes. The purpose of the this investigation was to optimize weldment properties employing the T.I.M.E.™ Process with state-of-the-art pulsing controllers and power sources.

This investigation involved preparing welding procedures for pulse welding with the T.I.M.E.™ Process employing a T.I.M.E. 540 power source coupled with a TR-19 synergic pulsing unit, pre-programmed for use with T.I.M.E.™ gas. These procedures were first proven on mild steel, before they were applied each to HY100 and HY80 steels in both the 3G (vertical down) and 1G/4G (flat/overhead) positions.

A number of dynamic tear and explosion panels were prepared to evaluate the properties of the weldments. Hardness, chemical and macro examinations were also performed.

Results from explosion bulge testing were not available at the time this paper was written.

2.0 BACKGROUND

A great deal of work has been done over the last 25 years to establish the credibility of the gas shielded, solid wire GMAW Process. There are two challenges that face Industry with this process.

The first challenge is the ability to fuse weld metal from a small diameter solid wire into a prepared joint producing quality welds with sufficient penetration and dependable fusion. Lack of fusion, or cold lap, is a discontinuity in the weld deposit between fused faces that consist of weld to substrate or weld to weld. This condition in a welded joint is one of the major causes of failure in weldments which are subjected to load transfer and must be either prevented or removed and repaired by rewelding.

The second challenge is to deposit weld metal at a rate that is economically feasible. The process must compete with the shielded metal arc and submerged arc welding processes common to shipyard fabrication.

The penetration, fusion and deposit rates of the wire welding processes are controlled by the wire feed speed, voltage and arc speed. Therefore these variables can be classified as the quality controllers of all the welding procedures. The productivity and quality of the weld deposit is a direct result of the electrode's current density and its transferred condition across the arc.

The shielding gas's ability to transfer metal from the electrode across the arc into a satisfactorily fused geometric shape is the critical catalyst in the synergy of all the welding variables.

Each shielding gas mixture produces a primary event at the arc and triggers the consequences of the wire feed speed and current density at the arc. When wire feed speeds or current densities exceed the allowable limits of good fusion within the transfer capabilities of its shielding gas mixture, weld quality deterioration, poor appearance and repair costs increase dramatically.

Shielding gas chemistries control the weld metal transfer characteristics and is the single most important control factor for solid wire welding processes in achieving uniform quality and productivity reliability. Each shielding gas mixture ionizes into its own plasma size, shape, motion and structure. The shielding gas mixture determines the size of the metal droplets, their shapes, frequency, regularity and direction as they transfer across the arc. The droplets can be concentric or eccentric - they can drop in-line or off-line with the electrode. They can be micro droplets or macro globules. The droplets can transfer inside and/or outside the plasma and shielding gas. They can move in the direction of the rotational forces and the magnetic forces between the electrode and the plate. The droplets can absorb atmosphere or remain atmospherically inert in their journey from the electrode tip across the arc into the weld geometry design.

The T.I.M.E.™ gas mixture of argon, helium, carbon dioxide and oxygen has been designed to overcome many of the challenges associated with gas shielded, solid wire

GMAW and displays a stable, high frequency axial spray transfer resulting in a continuous, uniform droplet size transfer of weld metal in line with the direction of the electrode and totally within the arc cone. The result is a dramatic increase in both weld quality and productivity.

The T.I.M.E.™ Process

The Transferred Ionized Molten Energy (T.I.M.E.) Process is a modification of the gas metal arc welding (GMAW) technique consisting of a four component shielding gas and new types of welding equipment. The Patented T.I.M.E. gas is a mixture of argon, helium, carbon dioxide and oxygen. The gas creates a unique arc plasma that provides stability at wire feed speeds up to 2000 IPM with 0.045" diameter wire. This compares to less than 800 IPM for conventional GMAW welding processes. A specially designed wire feeder (T.I.M.E. 51) and inverter power source (T.I.M.E. 540) coupled with the new TR-19 pulse controller allows "one knob" synergic pulsing control of welding parameters.

The result is a process capable of depositing weld metal with high quality (i.e. higher toughness, no spatter, no undercut) at a very high deposition rate and welding speed (up to 8 times faster than SMAW).

Pulse Welding with T.I.M.E.™ Process

The pulsed gas metal arc welding process is a technique developed over 10 years ago to bridge the gap between short circuit and spray mass transfer of weld metal. In this process, a pulsating current is superimposed over the steady DC current causing brief inputs of energy. These current pulses produce a controlled droplet transfer which corresponds to the rhythm of the pulse frequency. The background current ensures that the tip of the electrode and the welding pool are kept molten. With each rise in current, a droplet is transferred to the workpiece due to the "pinch effect". In sophisticated pulsing systems, the size of the droplet can be controlled and adjusted to provide one droplet per pulse.

The background current is adjustable to suit the weld wire material and shielding gas composition. Since the critical level of current necessary to shed the droplets is a function of pulse current, the amount of heat produced is relatively low compared with conventional methods.

There are two features of P-GMAW that are of interest in welding HY80/HY100 steels. First, the critical level of current needed to achieve spray transfer is low enough to allow deposition rates in excess of that which can be easily controlled in normal GMAW for making out-of-position welds hence providing operational economy. Second, it has also been found that pulsing can actually enhance the quality and toughness of the deposited weld metal while maintaining acceptable levels of other mechanical properties. The reason for the increase in toughness is not clear. However, it is hypothesized that at similar heat inputs, the pulses cause changes in the solidification pattern resulting in a more desirable microstructure.

Pulsed welding introduces a number of new variables in addition to those normally controlled in the T.I.M.E.™ Process (i.e. WFS, tip recess, voltage, travel speed). These are:

I_p - pulse current
T_p - pulse duration
I_b - background current
T_b - background current duration
F_p - pulse frequency

Earlier work with the T.I.M.E.™ Process with and without pulsing (Ref. 6.1) reported unsurpassed toughness values approaching those of the base metal HY80/HY100. In the past two years, significant equipment improvements have evolved and now state-of-the-art synergic pulsing coupled with an ultra-responsive inverter power source is now commercially available and was used for this project.

3.0 EXPERIMENTAL PROCEDURE

Consumable Wires for the Program

Lincoln LA100 (ER 100S-G) wire was specified for welding of HY80 and L-Tec ER120 (ER 120S-1) was specified for welding HY100 panels. Both wires were 1.2 mm in diameter. The chemical analyses (typical) are given in Table 1.

Welding Equipment

The following equipments were used for this project:

(i) T.I.M.E. 540 Power Source
(ii) T.I.M.E. 51 Wire Feeder
(iii) T.I.M.E. Torch (750 amp water cooled)
(iv) T.I.M.E. Gas Diffuser/Tips
(v) Fronius TR-19 Synergic Pulsing Controller

Preparation of Steel Panels for Welding

Each of the HY80/HY100 steel panels was flame cut to rough dimensions (mechanical properties and chemical analyses are given in Tables 1 and 2). The final preparation was a balanced double vee groove with 60° included angles, (root face = 0 mm) prepared by machining. A total of 1.8 meters of weldment were required for each position/base material combination. This was achieved by welding the following panels for each combination:

(i) 1200 mm x 300 mm
(ii) 600 mm x 300 mm

Preheat Equipment

Preheat was provided by electric resistance heating. A Honeywell electronic chart recorder coupled with a 6 zone mini-controller and a 75 kw transformer were connected to the four heaters. Up to ten K-type thermocouples were spot welded to the 1200 mm panels and five to the 600 mm panels. The 100°C minimum preheat was controlled by the set-point on the mini-controller. Interpass and peak temperatures were closely monitored and welding was delayed until interpass temperatures reduced to acceptable values.

After all welding was completed on a panel, the temperature was allowed to stabilize for approximately 45 minutes before disconnecting the heaters. The panels were removed from the jig, wrapped with insulation and allowed to slow cool to room temperature. They were allowed to remain in this condition for 72 hours before non-destructive examination (NDE) was conducted.

Welding Method

Welding procedures in the development stage of the project were optimized on mild steel with each of the electrodes. The tolerance of each parameter was investigated in this manner and documented.

Joint design was specified to be a balanced double vee groove with 60° included angles and feather edge preparation (i.e. root face of 0 mm).

A similar technique was used for both materials in each position. A "push" angle of approximately 10°-20° was used in all but the root pass of side 2, vertical down (3G) plates where a "drag" angle of 10°-20° was used (layer R1). All passes were applied as stringer beads with little or no oscillation of the torch.

Backgrinding to sound metal of the root prior to welding side 2 was conducted on all panels. Magnetic particle inspection was used to verify that all suspect root material was removed before continuing the welding. Interpass grinding was only applied if visually the weld cap required dressing to allow proper blending with subsequent layers.

The number of passes varied with the fit-up of the panels and the Welding Procedure Data for each steel are given in Table 4 and 5. Average heat inputs varied from 0.67 - 0.76 kJ/mm for 1G/4G welds and from 0.47 - 0.55 kJ/mm for 3G.

Grounding at the workpiece was accomplished by clamping the ground cable in line of the weld groove on the weldment run-off tab. Welding progression was towards the ground.

The T.I.M.E.™ Process allows for variations in the tip recess causing marked changes in the welding characteristics through variations in electrode preheat from the tip to the arc. In the root passes, the tip was extended to 0 - 3 mm (+ve) to allow deeper penetration. Subsequent passes called for the tip to be recessed into the nozzle 0 - 6 mm (-ve).

The wire feed speeds, welding current and voltage settings used for the project were operated generally on the low end of the range for spray transfer and bordered on the transitional arc zone.

Torch travel speeds for the various positions ranged as follows:

Vertical (Down)	-	670 - 770 mm/min.
Flat/Overhead	-	420 - 430 mm/min.

These settings represented "manageable" ranges that an operator can achieve with a minimal amount of training.

Non-Destructive Examination

The ultrasonic examination was performed on the finished plates using a Krautkramer USK 7 and the following probes with Ultragel II used as the gel couplant:

(a) Longitudinal 2.25 MHz x 1.0"
(b) Shear Angle: 2.25 MHz x 0.625" x 0.625" x 70° AWS
(c) Shear Angle: 2.25 MHz x 0.75" x 0.75" x 60° AWS
(d) Shear Angle: 2.25 MHz x 0.75" x 0.625" x 45° AWS

Ultrasonics was employed to examine the completed weld in accordance with ASME Section V, Article 5. Twenty-five percent of reference was used as the record level.

Scanning from Face 1 (first side welded) detected the highest level of reflections in the first half skip. These reflectors are located on Face 2 in the root area. Some welds were scanned from Face 2 in addition to Face 1. In all cases, each weld was scanned from both sides of the weld on the same face.

Macroexamination, Hardness Testing and Chemical Analysis

Four welds were prepared for macroexamination, hardness testing and chemical analysis.

A metallographic cross-section was prepared from each weld, and ground to 600 Grit finish. The sections were then etched with 10% nital and photographed.

Hardness readings were obtained from each section using a Vickers machine and 10 kg load. Generally, eight or more identations were placed uniformly along the thickness of the specimen, at the weld centreline. The range and average of these readings is shown in Table 3. As well, three additional identations were placed in the weld metal at the half thickness location, and four in the heat affected zone of the capping passes, next to the fusion boundary on the second side. These data are also shown in Table 3.

After hardness testing, weld metal chemical analysis was obtained using optical emission spectroscopy. For oxygen and nitrogen analysis, ≈ 1 mm thick slice of weld metal at the weld centre line (≈15 mm along weld length) was removed, and divided into three 5 mm long pieces for triplicate analysis. The middle 10 mm was then removed from each piece for oxygen and nitrogen analysis.

The chemical analysis results are reported in Table 1, noting that Oxygen and Nitrogen values are in ppm and represent the average of three specimens for each weld.

4.0 DISCUSSION

The purpose of this project, as previously mentioned, was to optimize weldment properties (i.e notch toughness) using the T.I.M.E. Process and synergic pulsing equipment pre-programmed for T.I.M.E. Gas.

The experience gained during the development of procedures on mild steel was invaluable and a number of factors contributing to welding performance were improved upon before striking an arc on HY steel. However, with the objective to maximize high notch toughness, the low heat inputs increased the risk of fusion defects in the root pass of Face 2 (layer R1). The sophisticated TR-19 pulsing controller allowed heat inputs to be lowered to 0.32 kJ/mm while still achieving stable arc characteristics.

One observation of interest was made during the welding of the 1.2 m long plates. It was discovered that the power cables were neatly coiled resulting in the formation of inductance which limited the pulse current peak. Further testing revealed that the peak current was reduced as much as 30% and caused arc characteristics in a transition zone between non-free flight and free flight mass transfer. This condition was corrected for the 0.6 m plates and the arc displayed stable, spatterless, free flight mass transfer.

Although defect free weldments were not the primary objective of this Project, the smaller plates revealed only minor amounts of discontinuities and were acceptable to current DND inspection standards as well as to ASME IX.

Throughout the course of this work, the difference in the operating characteristics of the weld wires was very pronounced. The Lincoln LA100, used for joining HY80 has excellent characteristics and has a much lower tendancy to cause discontinuities when compared to L-Tec ER120-S1 (used for joining HY100). The operator appeal of LA100, coupled with overlapping chemistries and mechanical properties with ER120 S-1, makes LA100 wire a potential and the preferred consumable for joining HY100.

The equipment used performed flawlessly and the TR-19 synergic controller is very easy to program and operate. There were no operational problems with the power source or the wire feeder.

With the pursuit of notch toughness, it was unfortunate that the weld groove was positioned in line with the rolling direction of the plate instead of transverse as was the case in previous projects. For example, HY80 exhibits a dynamic tear energy of 1960 J@-29° (L-T orientation, i.e. notch transverse to rolling direction) and only 1140 J@ -29° C. (T-L orientation, i.e. notch parallel to rolling direction). The effect this has on the resultant weld metal and HAZ properties is not clear.

The Dynamic Tear Results for both steels and positions are given in Table 6. The standard 16 mm size samples were tested at -29°C and all specimens were notched in the T-L orientation. Heat affected zone results were excellent with dynamic tear energy as high as 1757 J@ -29°C. Weld metal results although not as good as the HAZ more than met military requirements for this application.

The quality of the final weld deposits are visually far superior to that of comparable Shielded Metal Arc Welding with no undercut or spatter. Ultrasonic examination revealed some fusion defects in the larger plates due to inductance in the welding circuit but with the welding parameter adjustments made on the smaller plates, defect free welds were deposited.

5.0 CONCLUSIONS

5.1 All position welding of HY80 and HY100 was successful using pulsed welding and the T.I.M.E. Process. The welding procedures developed will pass DND non-destructive examination acceptance criteria and dynamic tear toughness requirements.

5.2 Lincoln LA 100 has superior operating characteristics to the L-Tec ER 120S-1 and may be suitable as a filler metal for both HY80 and HY100.

5.3 The T.I.M.E. equipment performed flawlessly throughout this project and was able to maintain free flight transfer with heat inputs as low as 0.32 kJ/mm.

5.4 Travel speeds employed with the T.I.M.E. Process ranged from 670 mm/min. to 770 mm/min. (26-30 IPM) in the 3G position and 420 mm/min. to 430 mm/min. (16 - 17 IPM) in the 1G/4G positions. These speeds are very manageable, although 3-5 times faster than SMAW and are representative of the torch speeds associated with aluminum welding.

5.5 Vertical down (3G) weldments require less manual skill than welding vertically up and with the T.I.M.E. Process, fusion and penetration were found to be excellent.

5.6 The T.I.M.E. welding equipment is easy to operate, durable and dependable making it an ideal candidate for shipyard use.

6.0 REFERENCES

6.1 Malik, L.; Morrison, K.; Pussegoda, L.; "All Position Gas Metal Arc Welding of HY80 and HY100 Steels", DREA CR/91/434. Defence Research Establishment Atlantic.

TABLE 1

COMPARISON OF CHEMICAL ANALYSIS

MATERIAL	C	Si	Mn	S	P	Al	Cr	Ni	Mo	Cu	O	N
HY80	.145	.19	.26	.007	.008	-	1.4	2.23	.34	.11	-	-
LINCOLN LA100	.07	.34	1.47	.007	.007	-	.05	1.81	.34	.11	-	-
WELD 3G	.71	.36	1.4	<0.008	.012	<.005	.14	1.8	.44	.10	308	128
1G/4G	.80	.33	1.2	<.008	.012	.01	.35	1.8	.43	.10	298	110
HY100	.140	.20	.25	.004	.007	.30	1.41	2.67	.34	.12	-	-
L-TEC 120S-1	.06	.38	1.63	.005	.006	.012	.31	2.37	.50	.01	-	-
WELD 3G	.059	.27	1.3	.0089	.008	<.005	.39	<2.1	.50	.02	553	117
1G/4G	.066	.24	1.2	.0082	.008	<0.005	.46	>2.1	.46	.03	422	129

NOTE: OXYGEN AND NITROGEN IN PPM

TABLE 2

MECHANICAL PROPERTIES OF
THE STEELS USED IN THE PROGRAM

Property	HY80	HY100
Yield Strength (MPa)	638	724
UTS (MPa)	741	805
Hardness (BHN)	229	245
CVN @ - 18°C (J)	200	191
CVN @ - 84°C (J)	184	125

TABLE 3

HARDNESS RESULTS

HARDNESS HV_0			
STEEL		WELD CENTRE	HAZ
HY80	3G	293-332	370
HY80	1G/4G	288-293	384
HY100	3G	308-349	392
HY100	1G/4G	289-291	370

TABLE 4

EXPERIMENTAL PROCEDURE

WELDING PROCEDURES:

- HY80 3G POSITION

AMPS	197-290	AVG. 220
TRAVEL SPEED	460-1110 mm/min (18-44 IPM)	AVG. 770 mm/min (30.5 IPM)
HEAT INPUT	0.32-1.04 kJ/min	AVG. 0.47 kJ/min
NUMBER OF PASSES	22	

- HY80 1G/4G POSITION

AMPS	175-230	AVG. 192
TRAVEL SPEED	310-560 mm/min (12-22 IPM)	AVG. 430 mm/min (17 IPM)
HEAT INPUT	0.5-0.95 kJ/mm	AVG. 0.67 kJ/mm
NUMBER OF PASSES	15	

TABLE 5

EXPERIMENTAL PROCEDURE

WELDING PROCEDURES:

- HY100 3G POSITION

AMPS	195-270	AVG. 217
TRAVEL SPEED	320-1010 mm/min (13-40 IPM)	AVG. 670 mm/min (26.5 IPM)
HEAT INPUT	0.35-1.00 kJ/min	AVG. 0.55 kJ/min
NUMBER OF PASSES	21	

- HY100 1G/4G POSITION

AMPS	160-230	AVG. 190
TRAVEL SPEED	275-600 mm/min (11-24 IPM)	AVG. 420 mm/min (16.5 IPM)
HEAT INPUT	0.46-1.40 kJ/mm	AVG. 0.76 kJ/mm
NUMBER OF PASSES	14	

TABLE 6

DYNAMIC TEAR RESULTS

			DYNAMIC TEAR ENERGY J@ - 29°C	
MATERIALS	POSITION	HEAT INPUT (kJ/mm)	WELD METAL (# OF DATA POINTS)	HAZ (# OF DATA POINTS)
HY80	3G	0.32-1.04 X = 0.47	916 (4)	1436 (2)
HY80	1G/4G	0.55-0.95 X = 0.67	1101 (2)	1395 (2)
HY100	3G	0.35-1.00 X = 0.56	670 (1)	1757 (1)
HY100	1G/4G	0.46-1.40 X = 0.76	689 (2)	1368 (2)

* ALL SPECIMENS TAKEN IN T-L ORIENTATION

#510308 ③

EVALUATION OF HEAT AFFECTED ZONE MICROSTRUCTURE/MECHANICAL PROPERTIES OF HY100 GRADE STEELS

By

J.T. Bowker, J.A. Gianetto and M.W. Letts

Metals Technology Laboratories-CANMET
Ottawa, Ontario, Canada, K1A 0G1

ABSTRACT

A joint agreement project between MTL and DREA was initiated to evaluate the HAZ structure and properties of candidate HY100 grade steels for submarine fabrication. In this investigation Gleeble simulation is being employed to identify the microstructural constituents, hardness and resultant notch toughness of a range of HAZ regions which may act as local brittle zone in multipass weldments. The steels under investigation which have a nominal yield strength of 700 MPa are a highly alloyed HRS 650 M steel made in France and a conventional HY100 grade steel produced in the United States.

The experimental program included evaluation of both single and double cycled HAZ regions with two cooling times representing welding energy inputs of 2 and 4 kJ/mm. A series of single thermal cycles were developed to represent the grain coarsened (GC) HAZ with a peak temperature Tp = 1350°C, grain refined (GR) HAZ with Tp = 1000°C, intercritical (IC) HAZ with Tp = 800°C and subcritical (SC) HAZ with Tp = 650°C. Second thermal cycles with Tp2 = 1000°C, Tp2 = 800°C and Tp2 = 650°C were used to establish the effects of reheating on the GCHAZ.

The results showed that superior notch toughness properties were obtained for all the simulated HAZ regions of the French HRS-650M steel compared with the corresponding regions of the US HY100 grade steel. For the French HRS-650M steel a trend of decreasing notch toughness and increasing hardness was observed with an increase in peak temperature Tp = 650°C to 1350°C. A deterioration in notch toughness occurred after imposing second thermal cycles on the original GCHAZ with TP2 = 1000°C or Tp2 = 800°C. These results will be explained based on the change in microstructure and hardness. An improvement in notch toughness observed for a Tp2 = 650°C occurred as a result of tempering effects caused by subcritical reheating which produced a significant decrease in hardness. In the case of the HY100 steel the results show that increasing Tp from 650°C to 1350°C produced a marked decrease in notch toughness. This was essentially attributed to transformation to a high percentage of hard lath martensite independent of cooling time. An overall improvement in notch toughness occurred as a result of reheating the GCHAZ to Tp = 1000°C, 800°C or 650°C.

EVALUATION OF HEAT AFFECTED ZONE MICROSTRUCTURE / MECHANICAL PROPERTIES IN HY100 GRADE STEELS

by

J.T. Bowker, J.A. Gianetto and M.W. Letts

CANMET-Metals Technology Laboratories
Ottawa, Ontario,
Canada,
K1A-0G1

OBJECTIVE

- To identify the microstructural constituents, hardness and resultant notch toughness of a range of HAZ regions which may act as local brittle zones in multipass high-strength weldments using Gleeble simulation.

Steel	Element wt %										
	C	Mn	Si	S	P	Al	Ni	Cr	Mo	Cu	Nb
HRS 650M	0.13	0.39	0.15	0.007	0.007	0.02	4.26	0.39	0.33	0.04	< 0.010
HY100	0.17	0.33	0.23	0.008	0.010	0.02	2.62	1.52	0.48	0.04	0.012

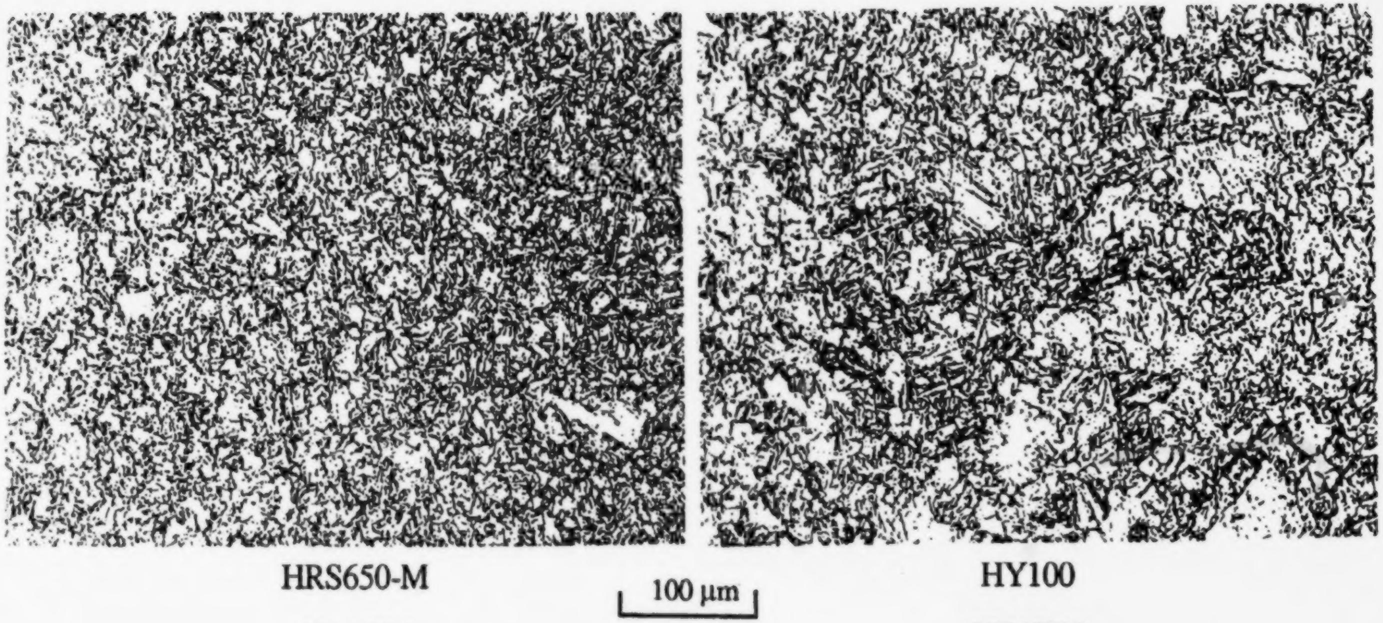

HRS650-M

271 VHN
195 J at -40°C

HY100

257 VHN
135 J at -40°C

Base Materials

Thermal Cycle Conditions

Single Cycle

GCHAZ	$T_p = 1350°C$
GRHAZ	$T_p = 1000°C$
ICHAZ	$T_p = 800°C$
SCHAZ	$T_p = 650°C$

Cooling Times $\Delta t_{800-500} = 11$ and 45 s corresponding to energy inputs of 2 and 4 kJ/mm.

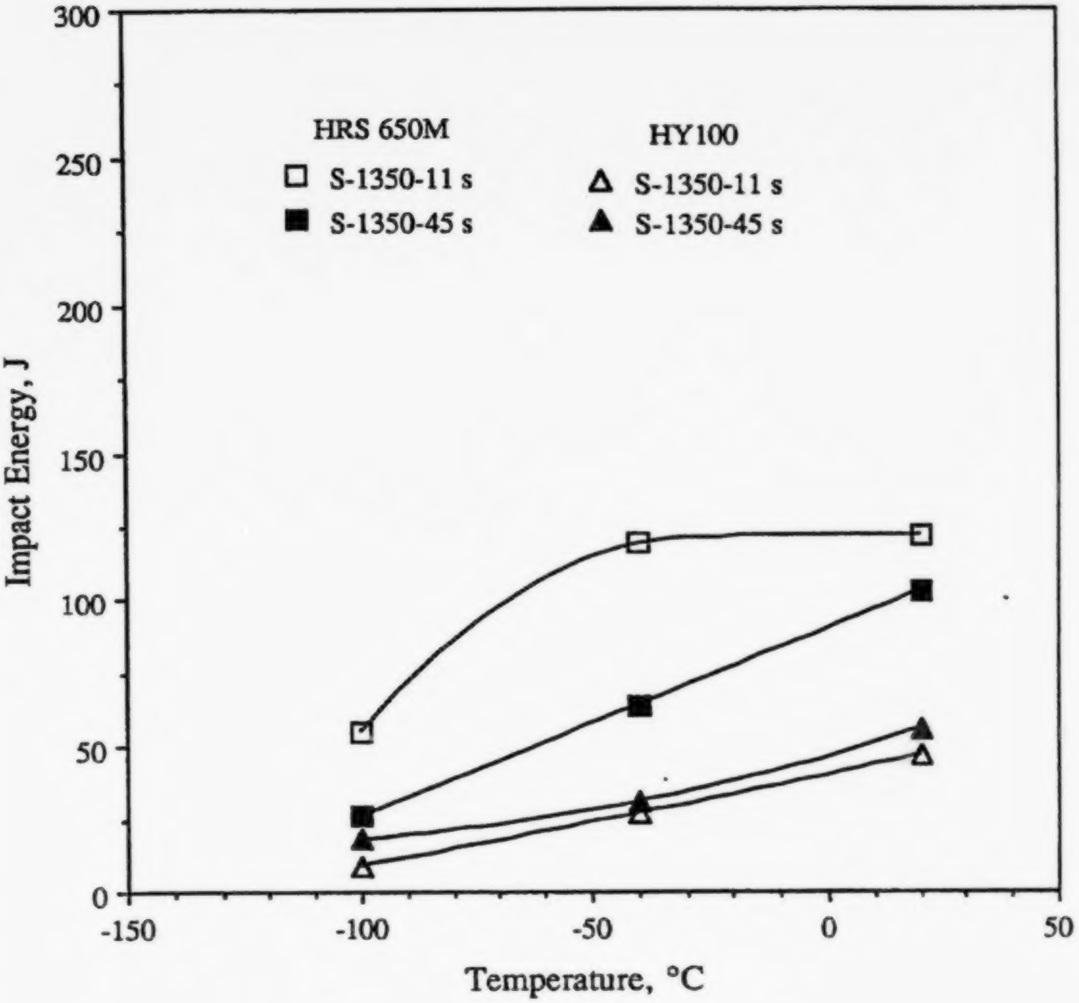
300
250
200
150
100
50
0
Impact Energy, J
-150
-100
-50
0
50
Temperature, °C
HRS 650M
□ S-1350-11 s
■ S-1350-45 s
HY100
△ S-1350-11 s
▲ S-1350-45 s

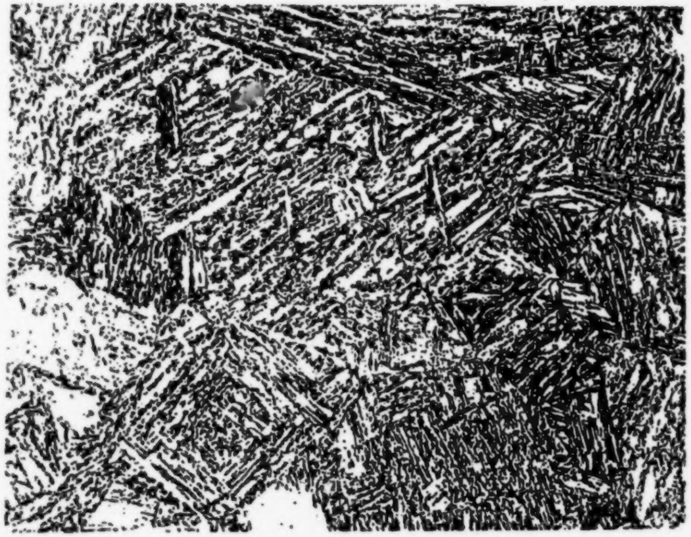

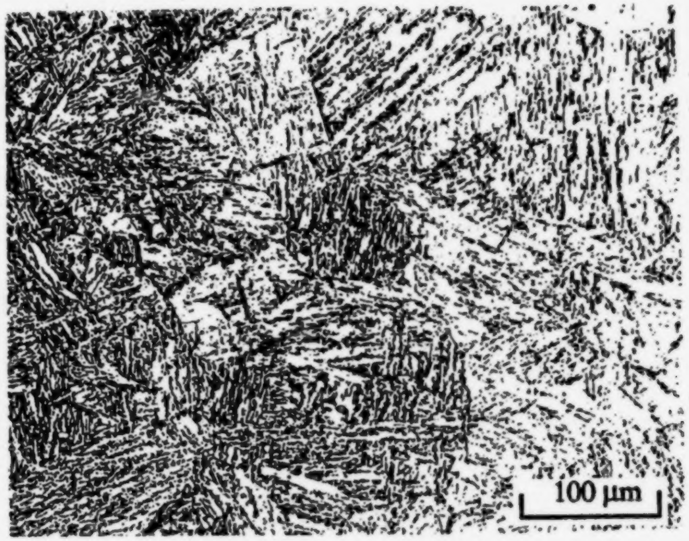

S1350-11 s (421 VHN) HRS 650M S1350-45 s (363 VHN)

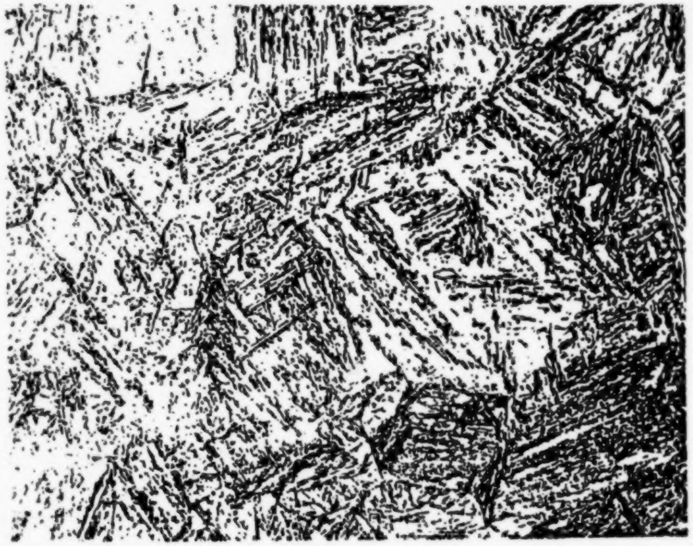

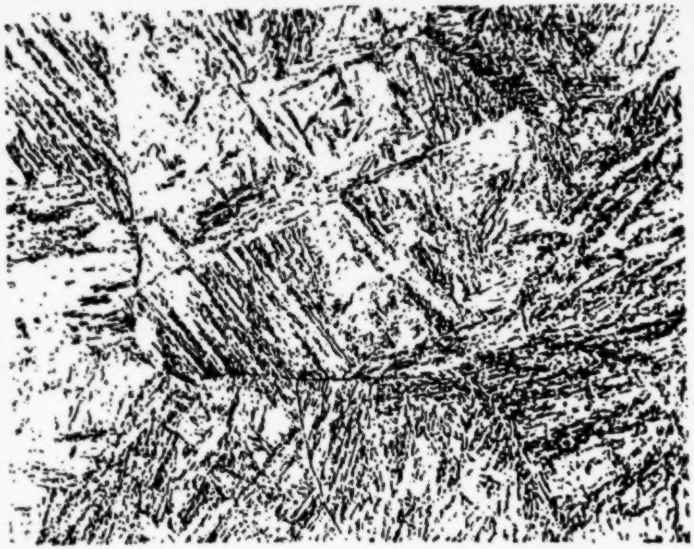

S1350-11 s (427 VHN) HY100 S1350-45 s (427 VHN)

HRS 650M Peak Temperature = 1350°C		
$\Delta t_{800-500}$ (s)	Transformation Temperature °C	Proportion of Constituents %
11	Bs ~ 430 Ms ~410	~95 - M
45	Bs ~ 430 Ms ~410	~30 - B ~70 - M

HY100 Peak Temperature = 1350°C		
$\Delta t_{800-500}$ (s)	Transformation Temperature °C	Proportion of Constituents %
11	Bs ~ 430 Ms ~405	~95 - M
45	Bs ~ 430 Ms ~405	~95 - M

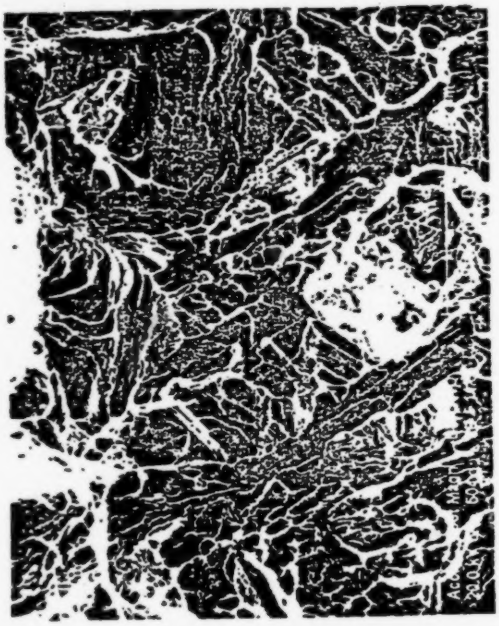

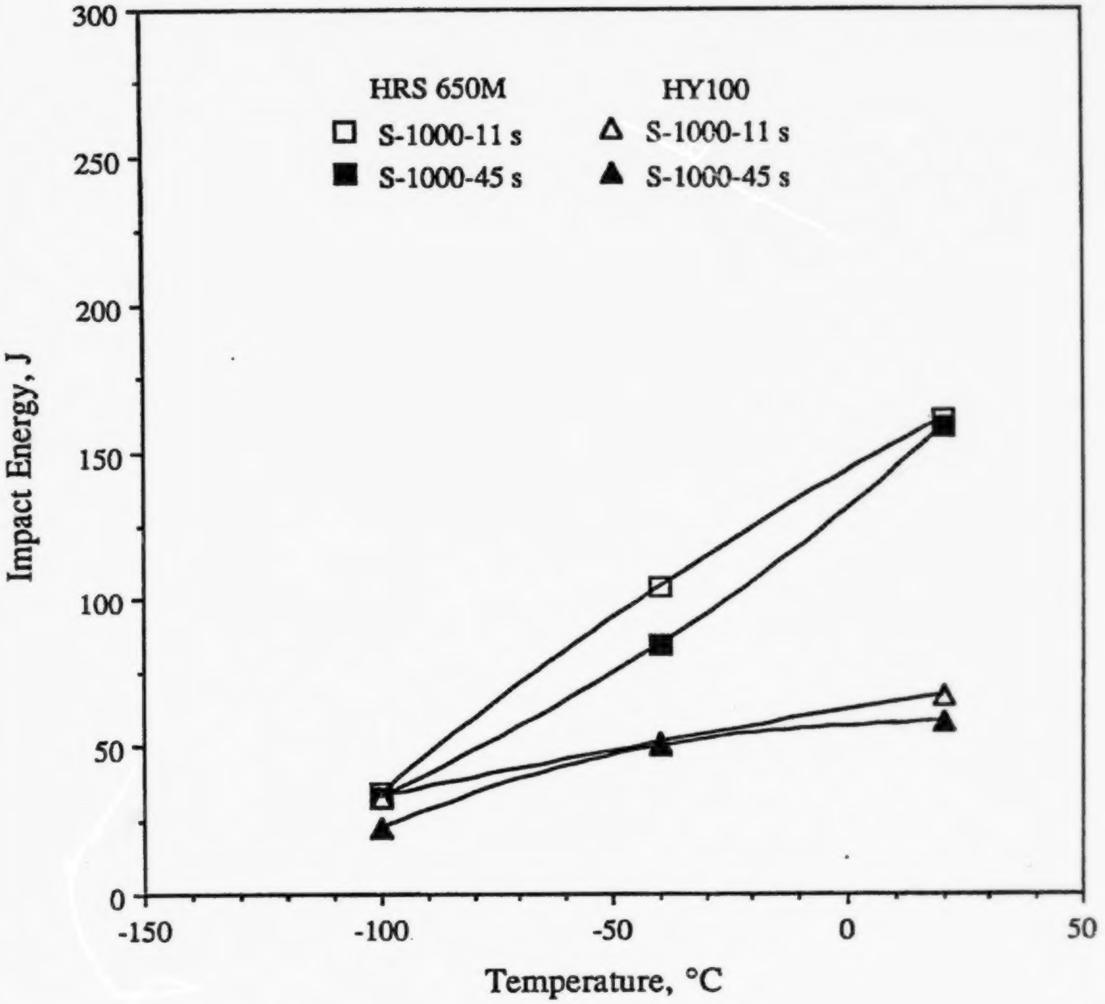
HRS 650M
□ S-1000-11 s
■ S-1000-45 s
HY100
△ S-1000-11 s
▲ S-1000-45 s
Impact Energy, J
Temperature, °C
0
50
100
150
200
250
300
-150
-100
-50
0
50

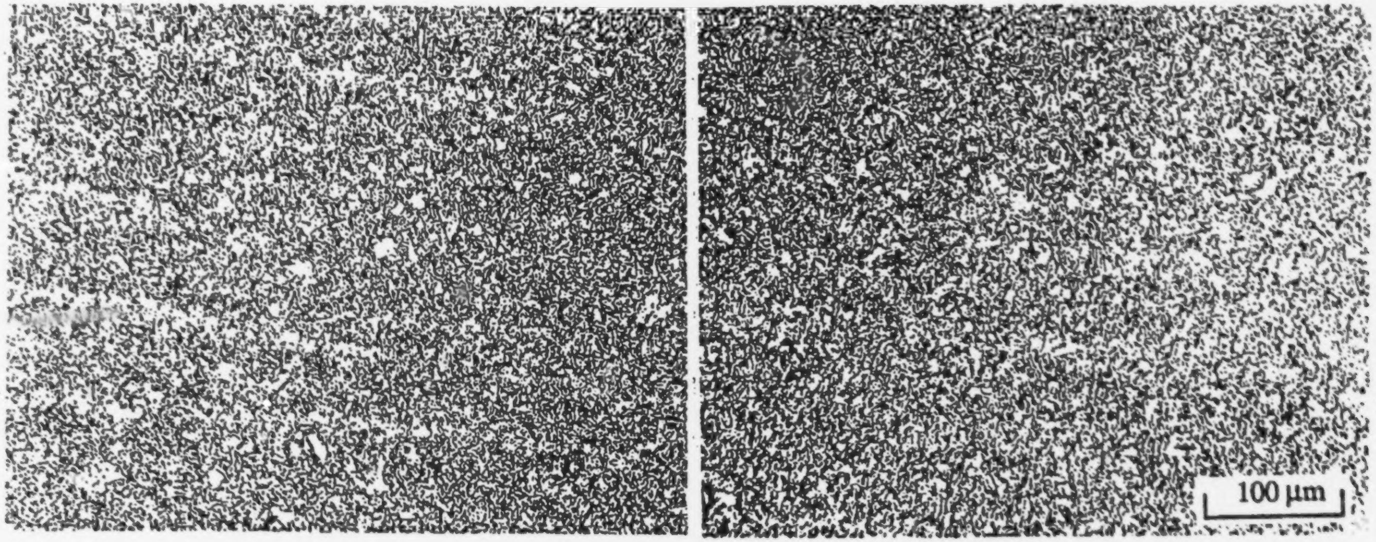

S1000-11 s (338 VHN) HRS650 M S1000-45 s (334 VHN)

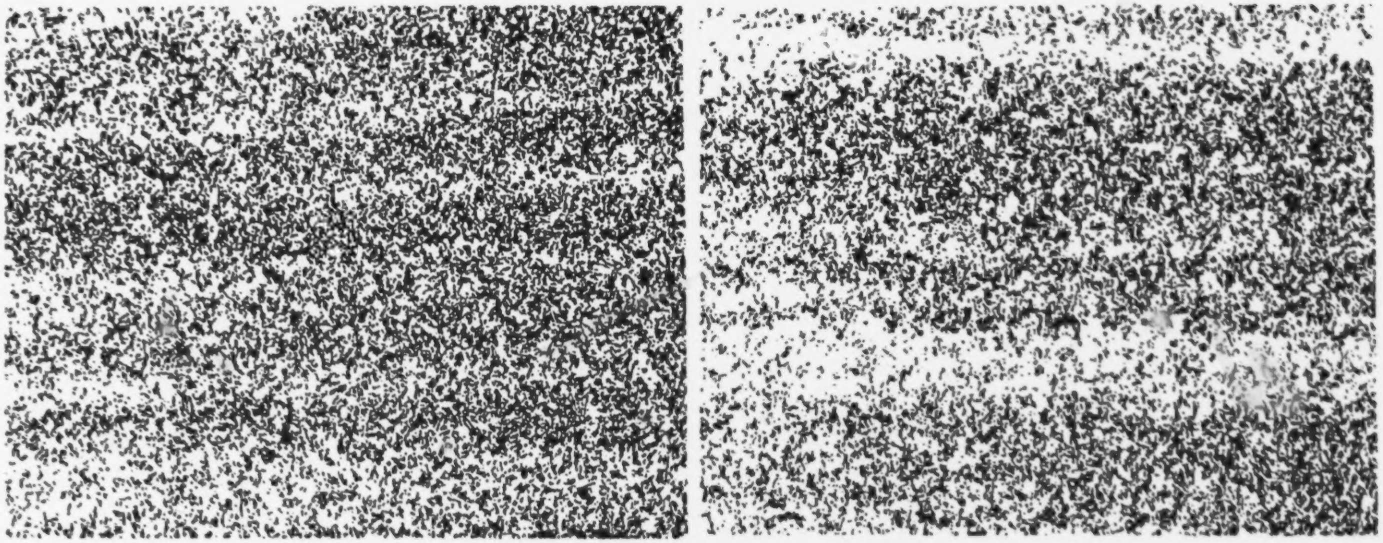

S1000-11 s (438 VHN) HY100 S1000-45 s (424 VHN)

HRS 650M Peak Temperature = 1000°C		
$\Delta t_{800\text{-}500}$ (s)	Transformation Temperature °C	Proportion of Constituents %
11	Bs ~ 570	~65 - B
	Ms ~410	~35 - M
45	Bs ~ 570	~80 - B
	Ms ~410	~20 - M

HY100 Peak Temperature = 1000°C		
$\Delta t_{800\text{-}500}$ (s)	Transformation Temperature °C	Proportion of Constituents %
11	Bs ~ 495	~30 - B
	Ms ~405	~70 - M
45	Bs ~ 500	~35 - B
	Ms ~405	~65 - M

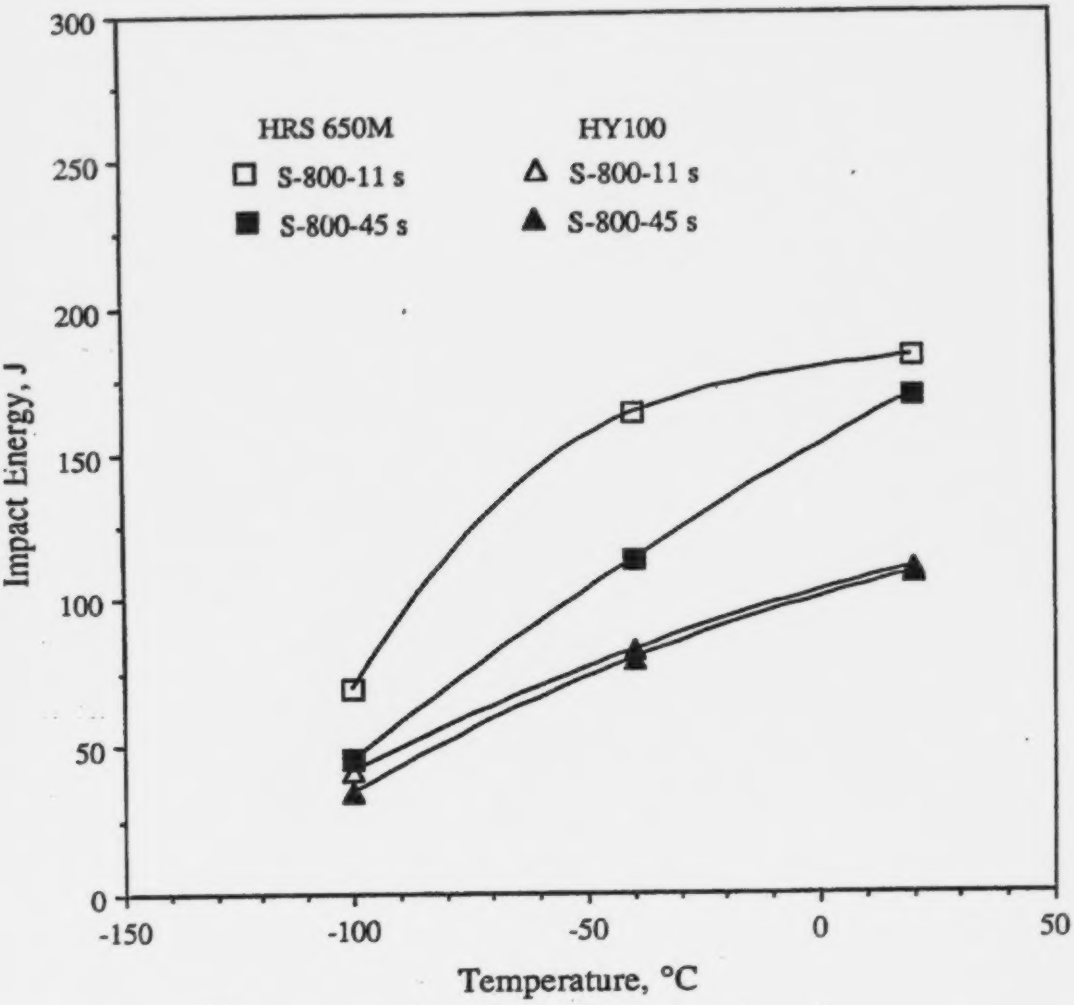
HRS 650M
□ S-800-11 s
■ S-800-45 s
HY100
△ S-800-11 s
▲ S-800-45 s
Impact Energy, J
Temperature, °C
300
250
200
150
100
50
0
-150
-100
-50
0
50

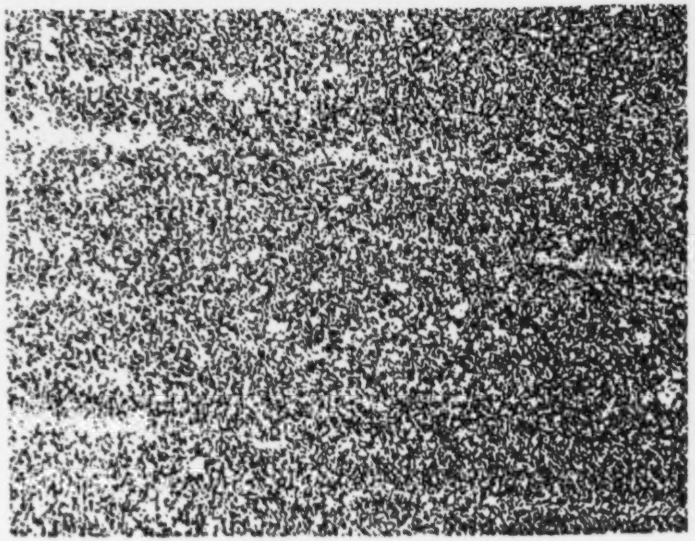

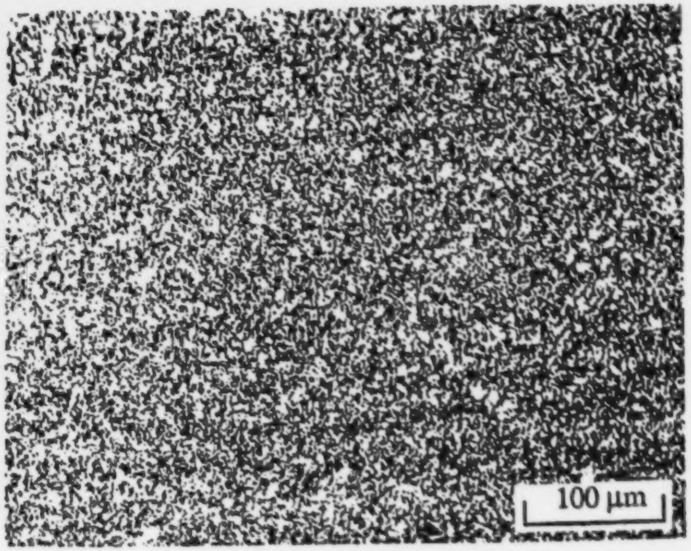

S800-11 s (351 VHN) HRS650 M S800-45 s (353 VHN)

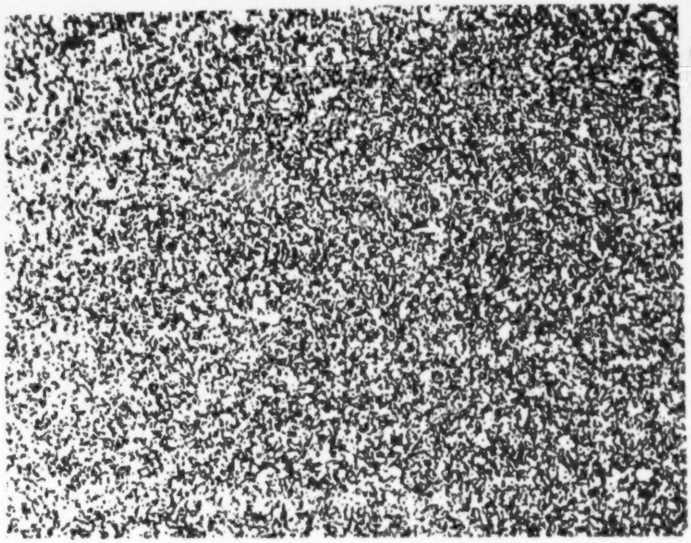

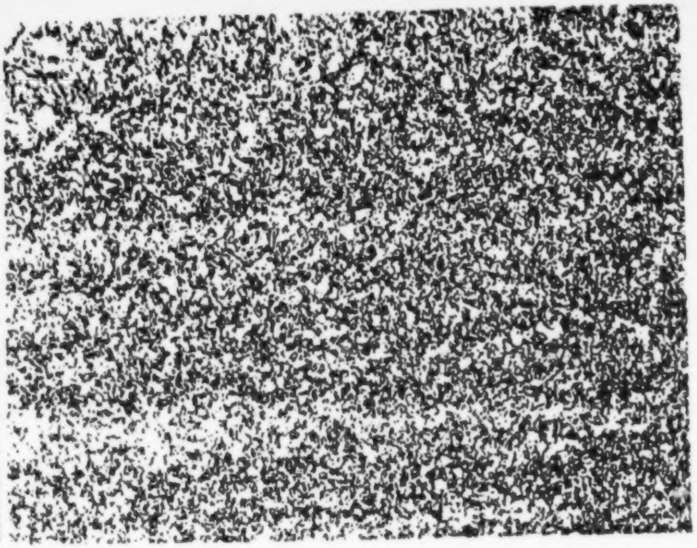

S800-11 s (365 VHN) HY100 S800-45 s (387 VHN)

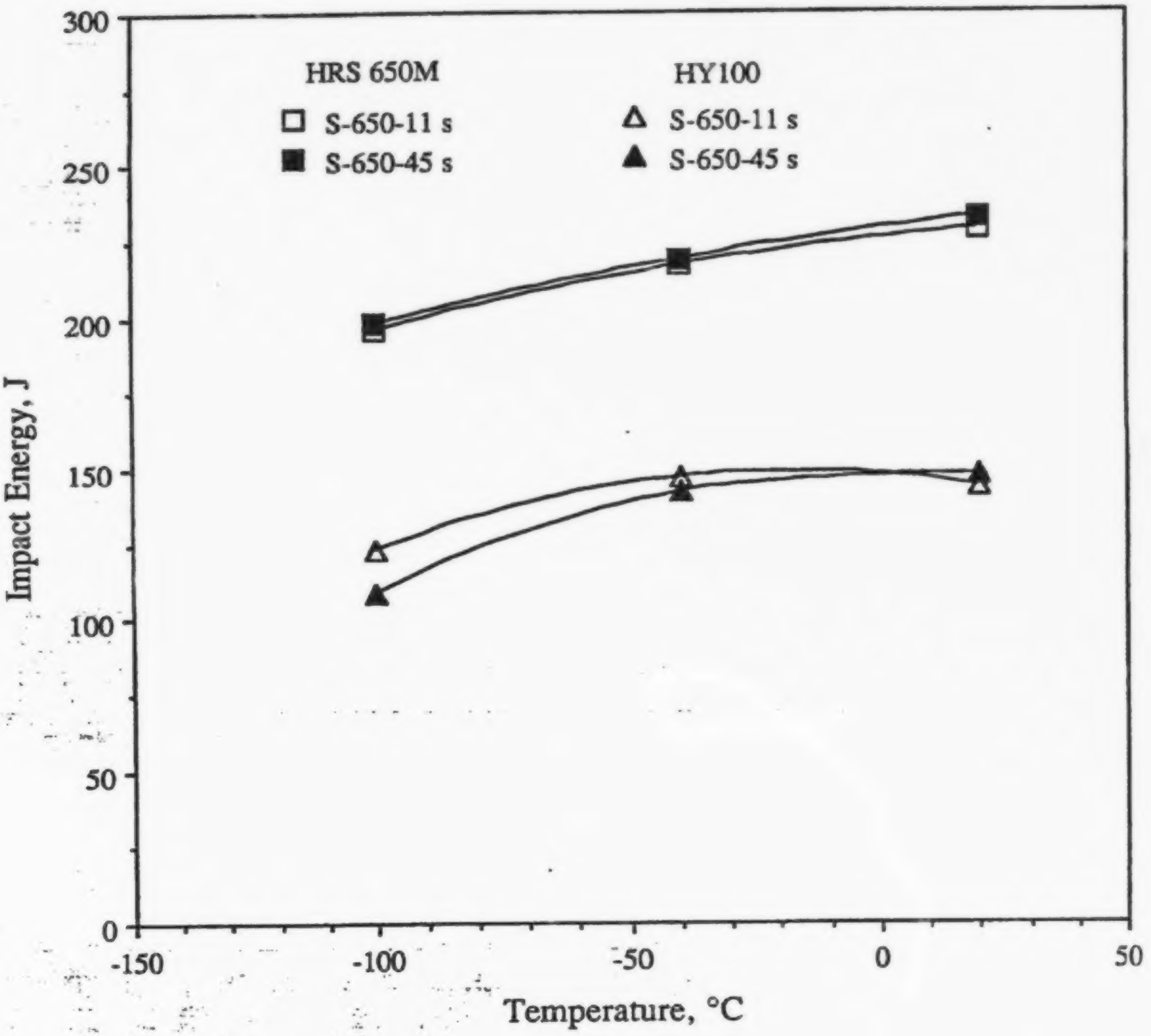
HRS 650M
□ S-650-11 s
■ S-650-45 s
HY100
△ S-650-11 s
▲ S-650-45 s
Impact Energy, J
0
50
100
150
200
250
300
-150
-100
-50
0
50
Temperature, °C

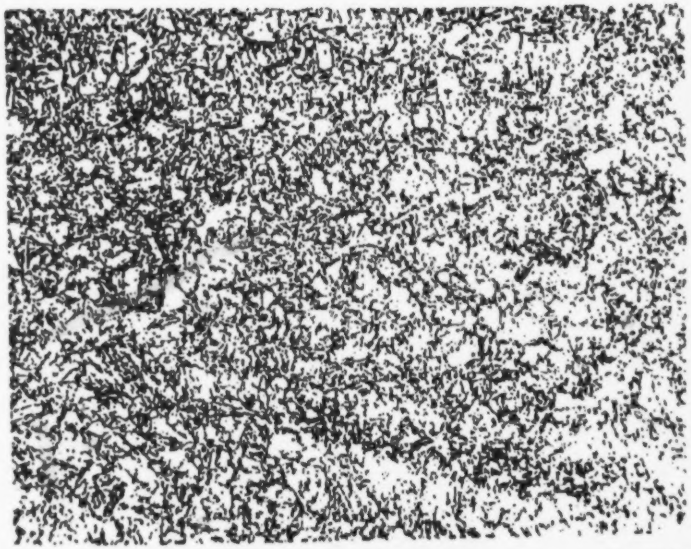

S650-11 s (291 VHN)

HRS650 M

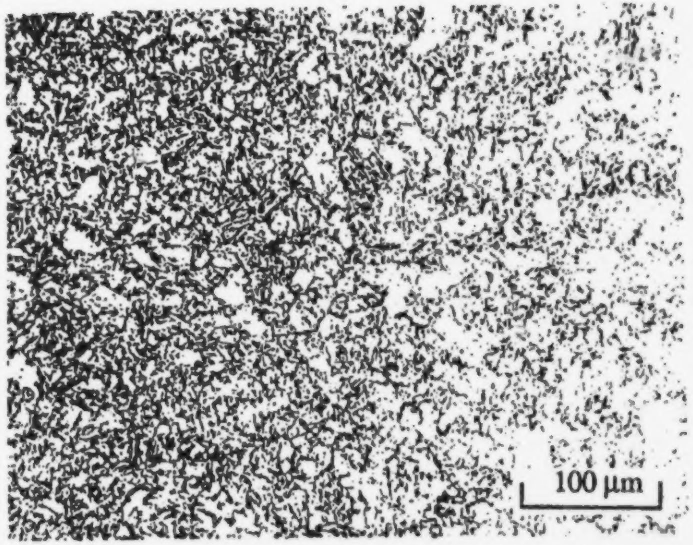

S650-45 s (285 VHN)

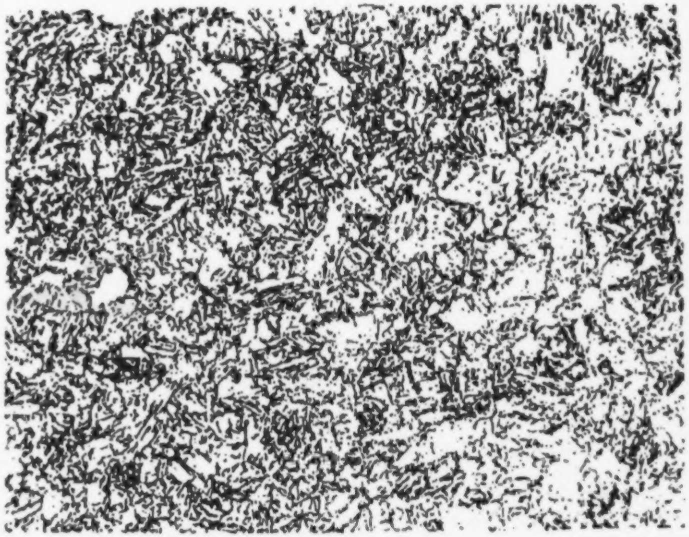

S650-11 s (271 VHN)

HY100

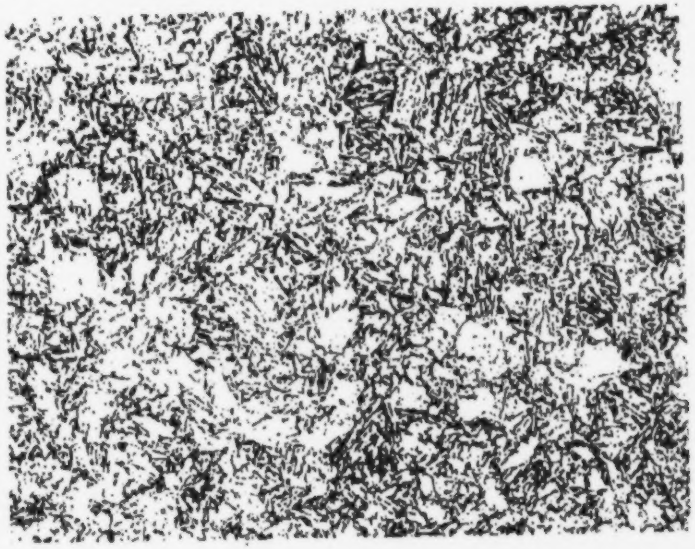

S650-45 s (274 VHN)

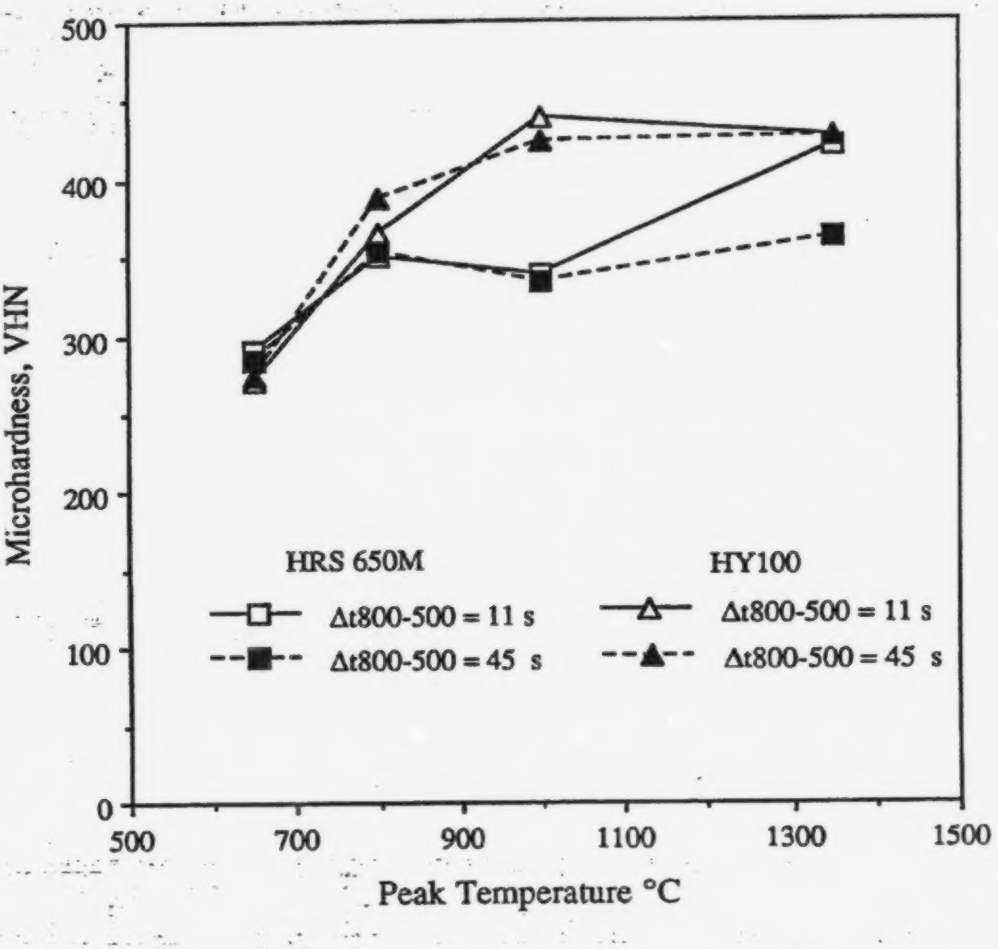
500
400
300
200
100
0
500
700
900
1100
1300
1500
Microhardness, VHN
Peak Temperature °C
HRS 650M
Δt800-500 = 11 s
Δt800-500 = 45 s
HY100
Δt800-500 = 11 s
Δt800-500 = 45 s

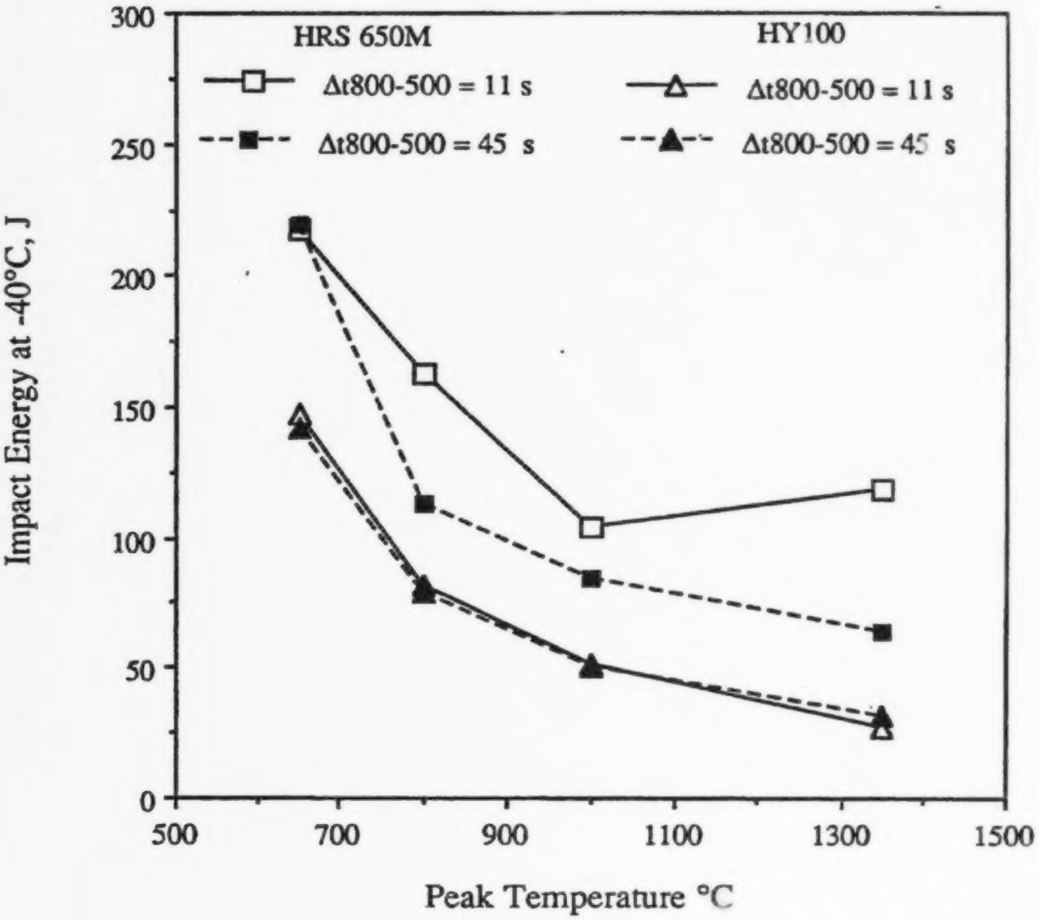
HRS 650M
HY100
Δt800-500 = 11 s
Δt800-500 = 45 s
Δt800-500 = 11 s
Δt800-500 = 45 s
300
250
200
150
100
50
0
500
700
900
1100
1300
1500
Impact Energy at -40°C, J
Peak Temperature °C

Thermal Cycle Conditions

Double Cycle

$(T_{p1} + T_{p2})$
where $T_{p1} = 1350°C$

GRGCHAZ	$T_{p2} = 1000°C$
ICGCHAZ	$T_{p2} = 800°C$
SCGCHAZ	$T_{p2} = 650°C$

Cooling Times $\Delta t_{800\text{-}500} = 11$ and 45 s corresponding to energy inputs of 2 and 4 kJ/mm.

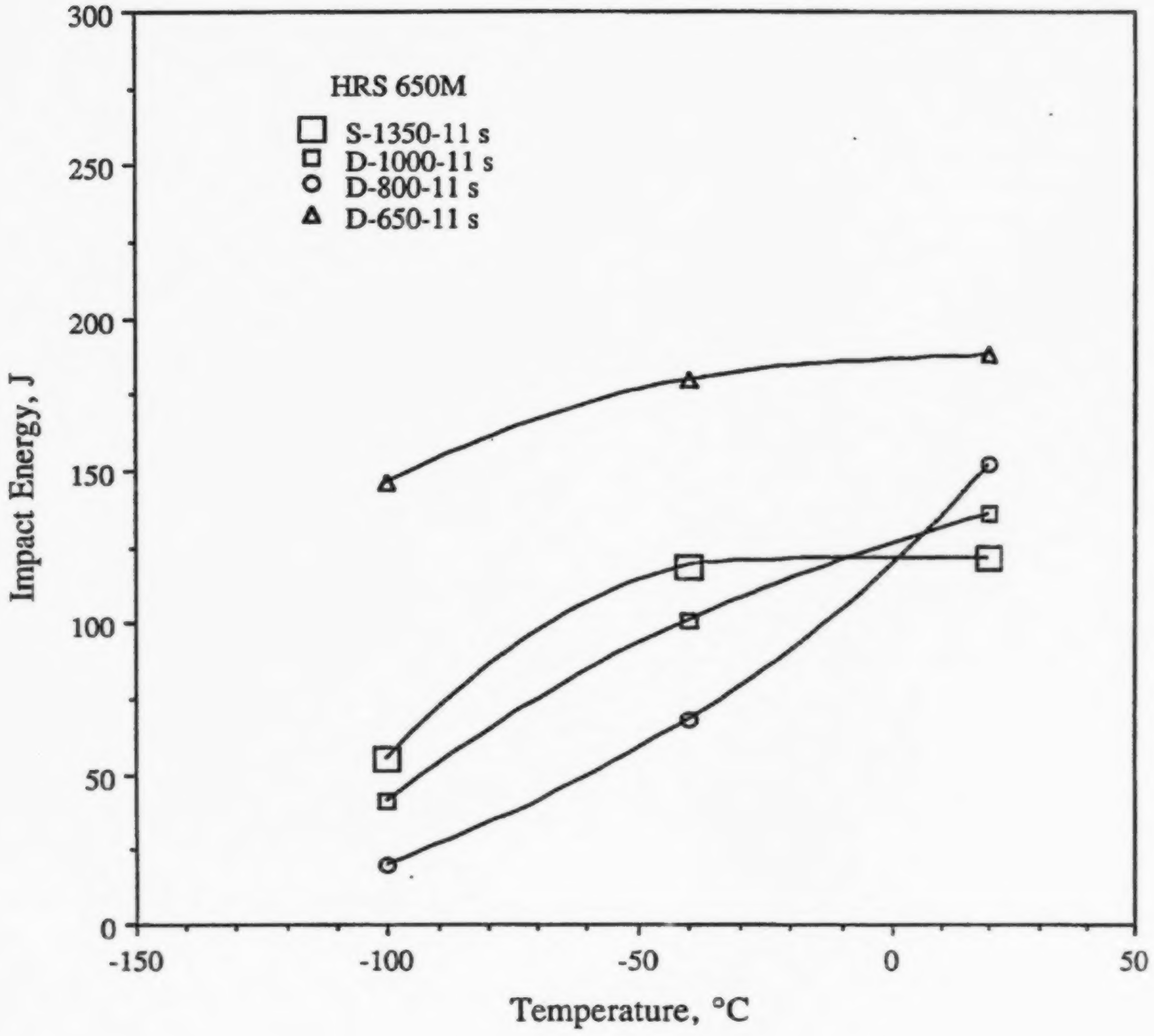
HRS 650M
S-1350-11 s
D-1000-11 s
D-800-11 s
D-650-11 s
Impact Energy, J
Temperature, °C
300
250
200
150
100
50
0
-150
-100
-50
0
50

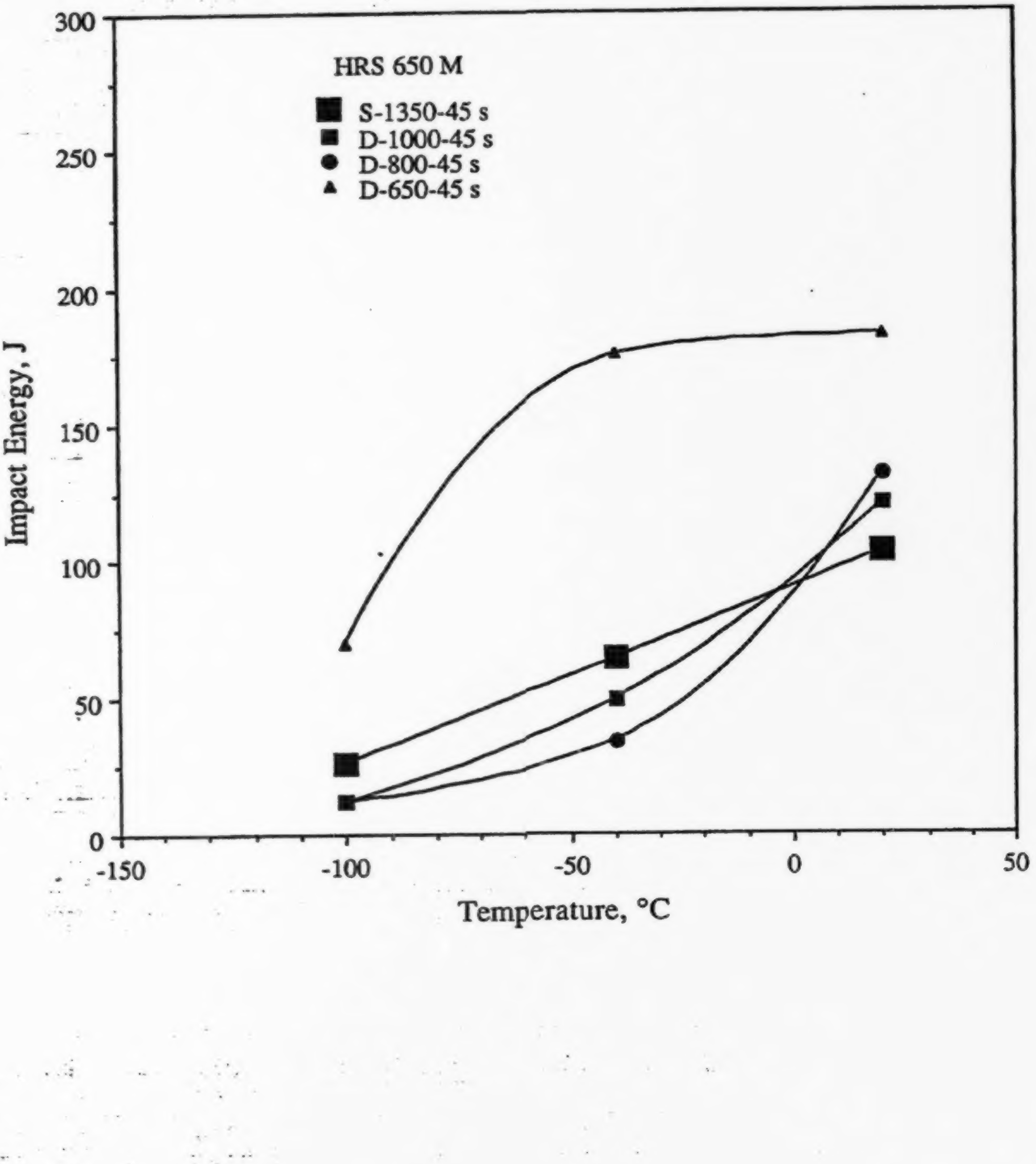
HRS 650 M
■ S-1350-45 s
■ D-1000-45 s
● D-800-45 s
▲ D-650-45 s
Impact Energy, J
Temperature, °C
300
250
200
150
100
50
0
-150
-100
-50
0
50

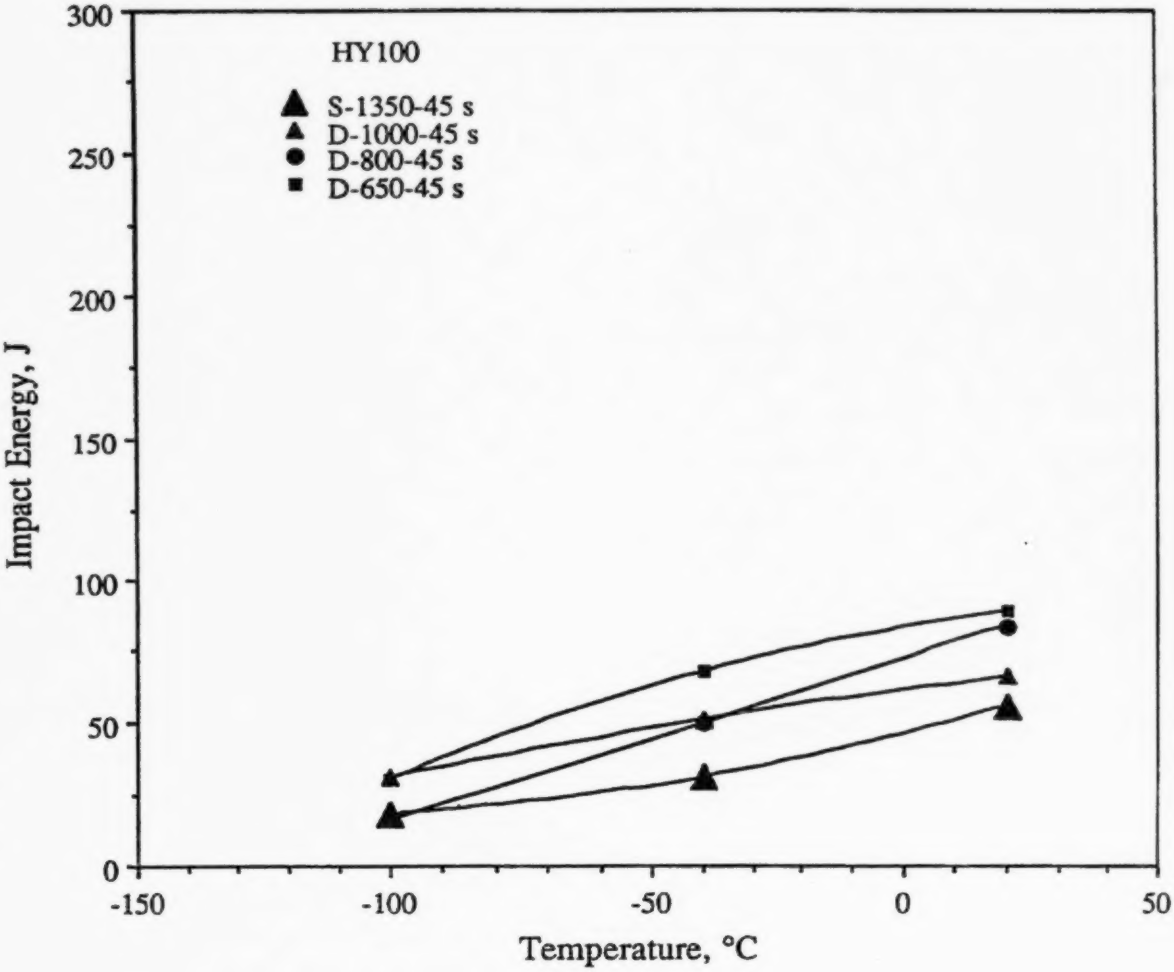

HY100
▲ S-1350-45 s
▲ D-1000-45 s
● D-800-45 s
■ D-650-45 s
Impact Energy, J
0
50
100
150
200
250
300
-150
-100
-50
0
50
Temperature, °C

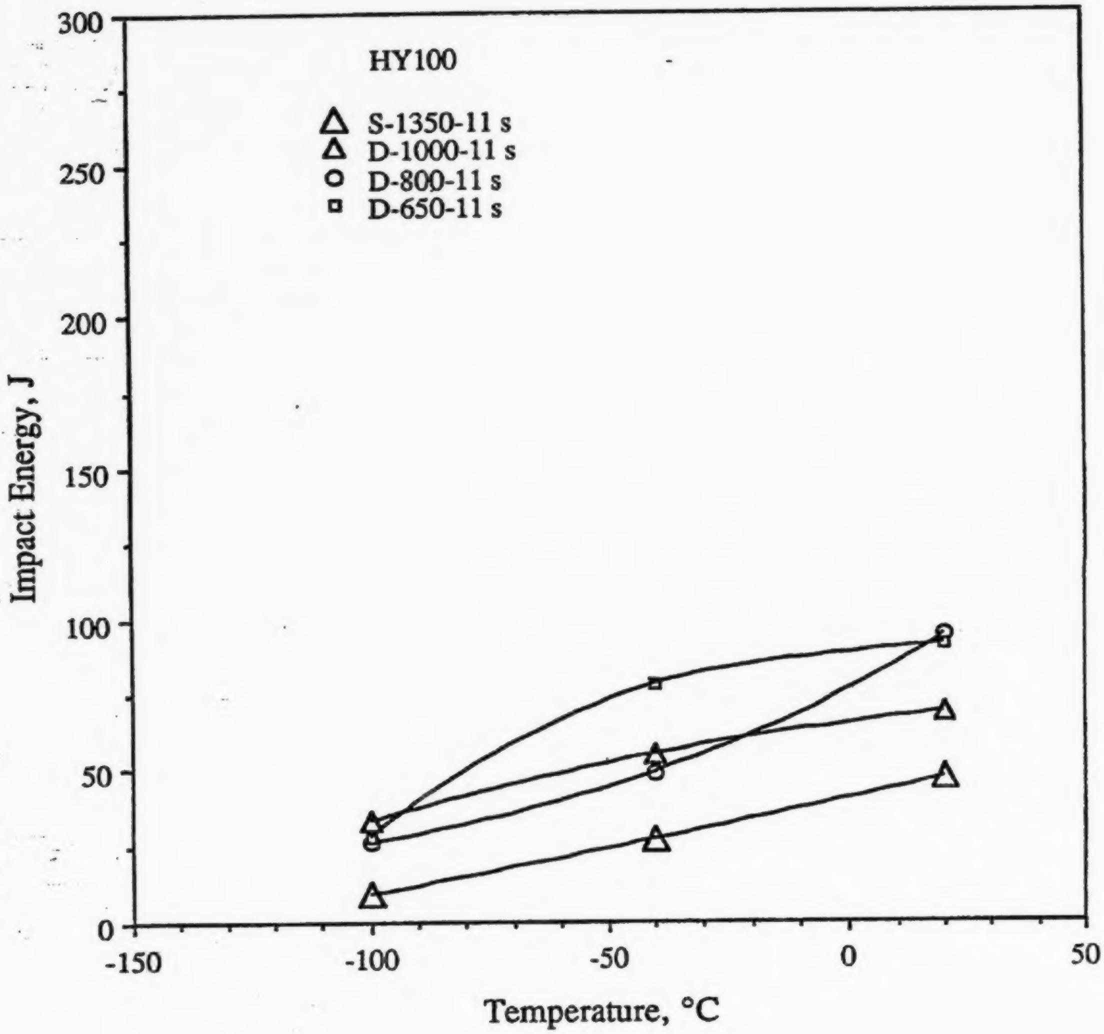
HY100
△ S-1350-11 s
△ D-1000-11 s
○ D-800-11 s
□ D-650-11 s
Impact Energy, J
Temperature, °C
0
50
100
150
200
250
300
-150
-100
-50
0
50

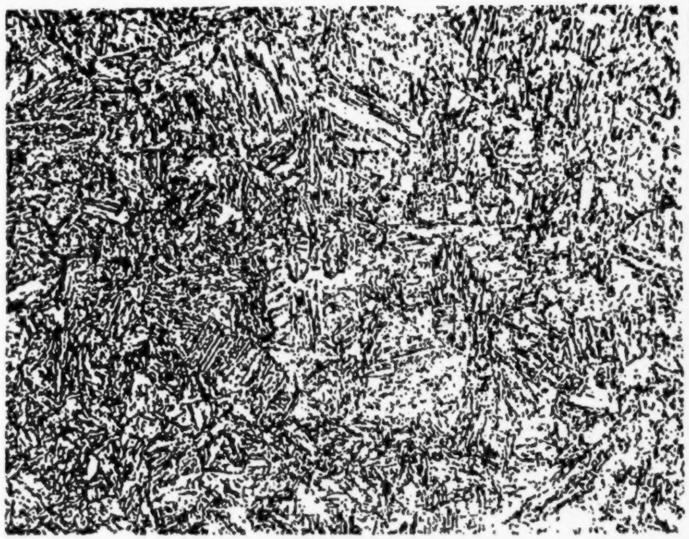

D1000-11 s (404 VHN)

HRS 650M

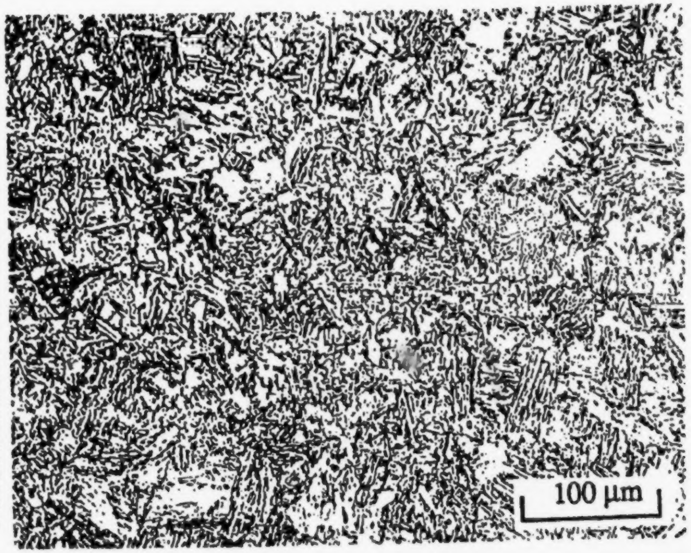

D1000-45 s (354 VHN)

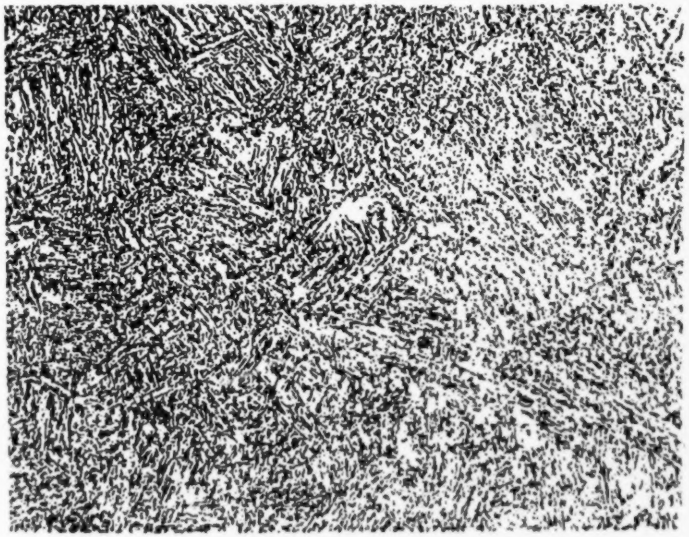

D800-11 s (379 VHN)

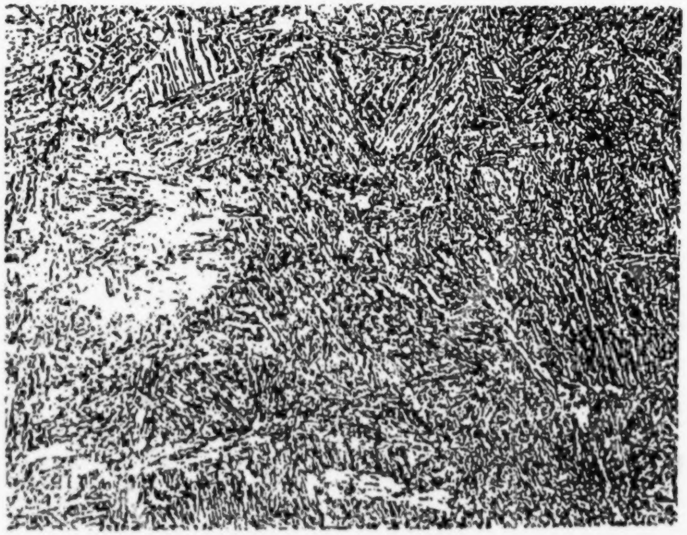

D800-45 s (337 VHN)

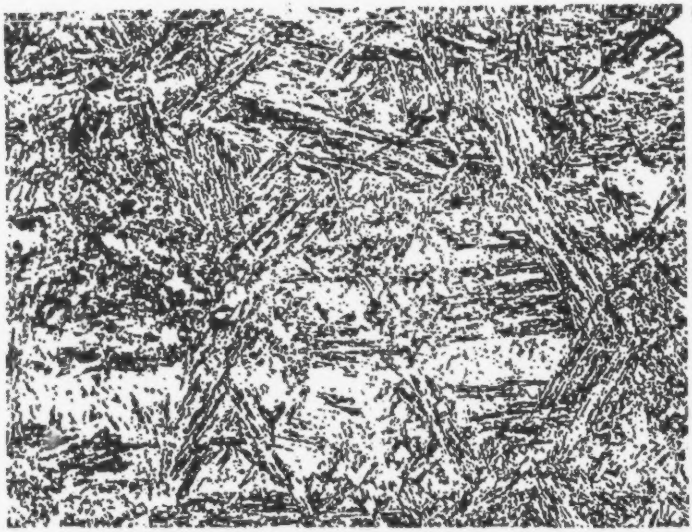

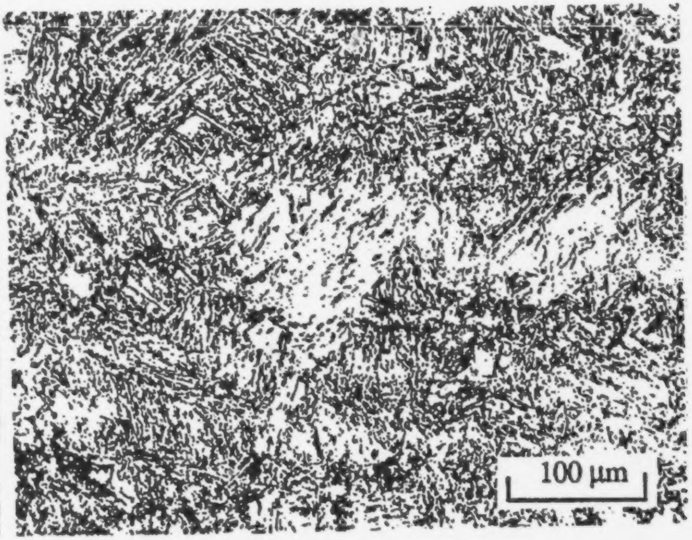

D1000-11 s (460 VHN)

HY100

D1000-45 s (463 VHN)

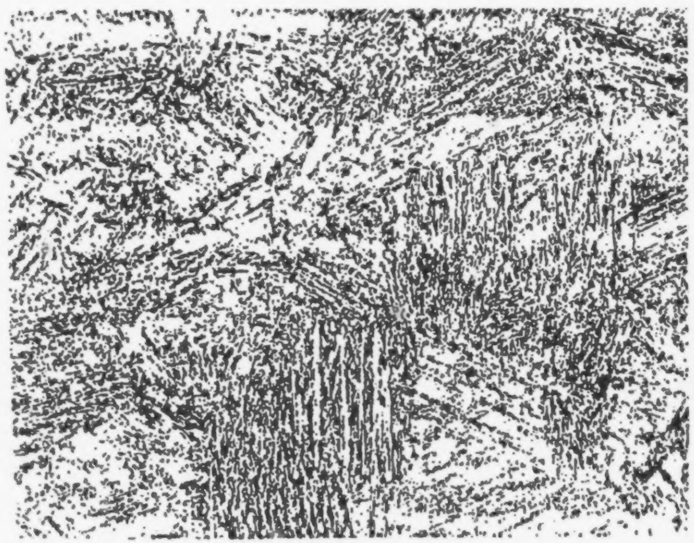

D800-11 s (429 VHN)

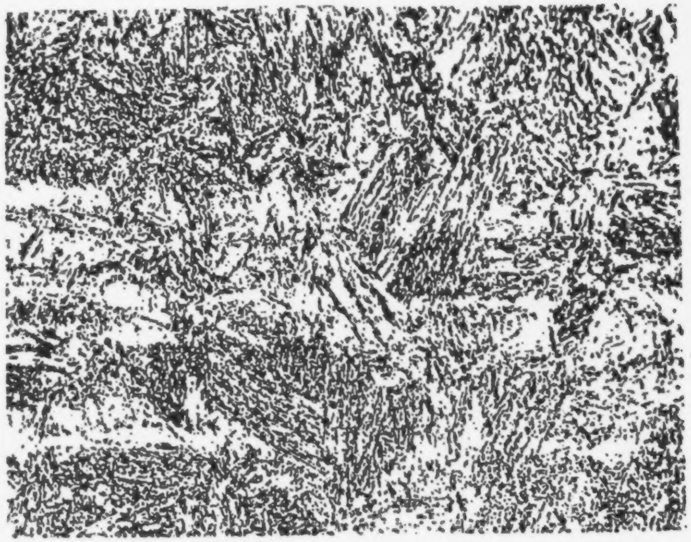

D800-45 s (407 VHN)

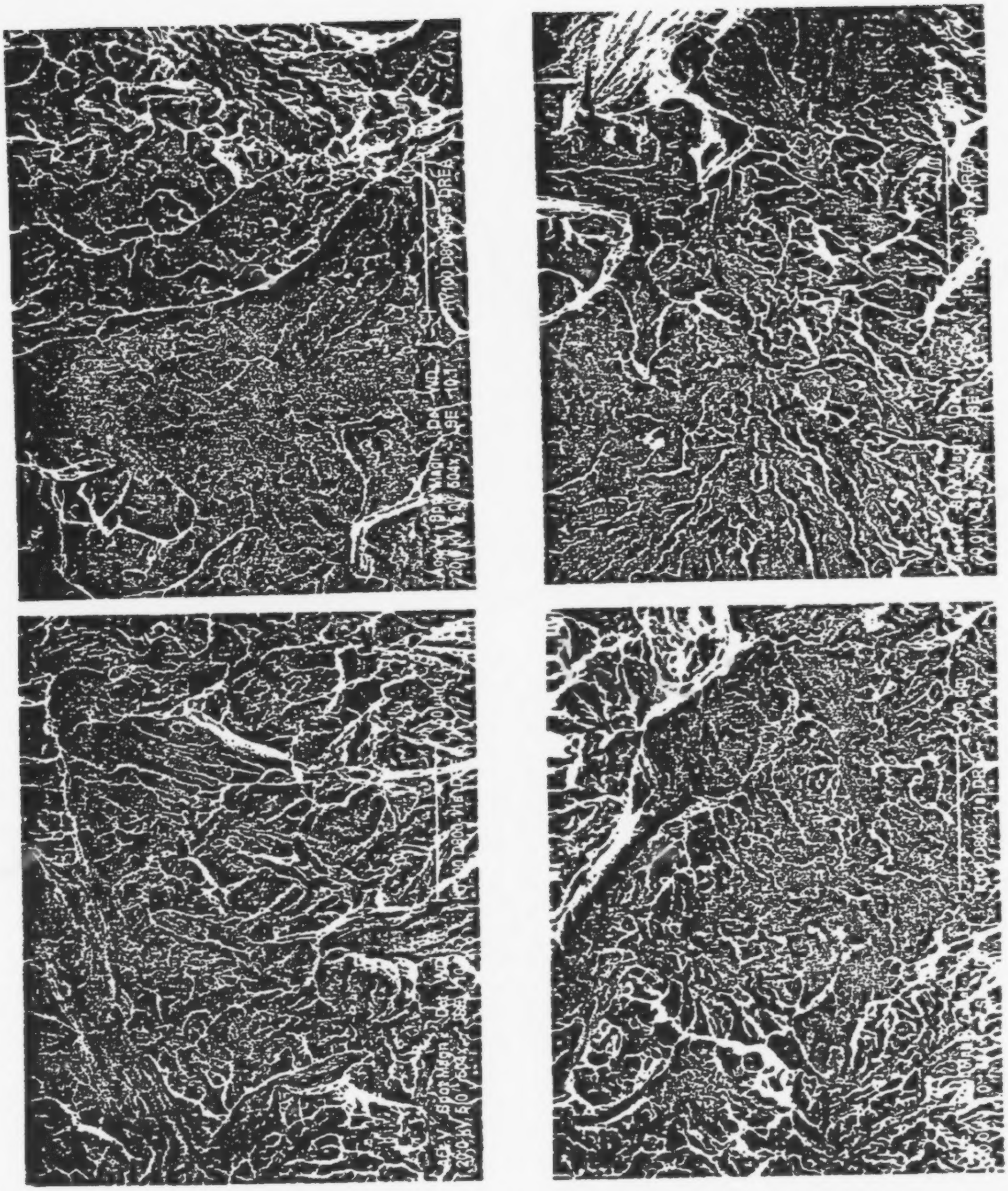

HRS 650M

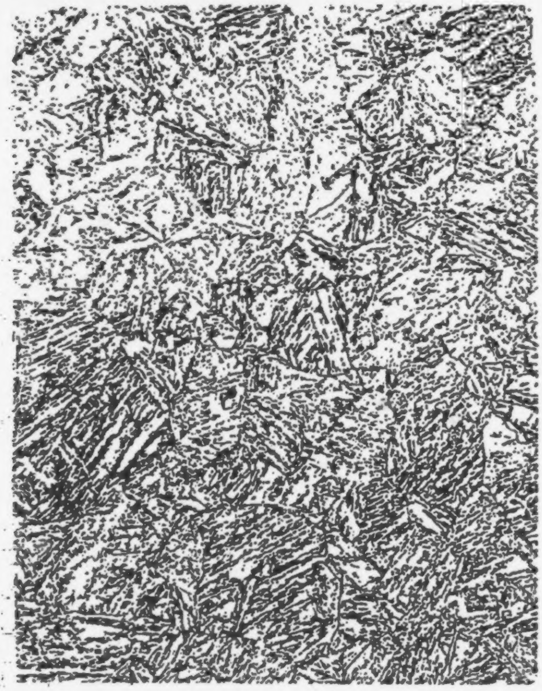

D650-11 s (319 VHN)

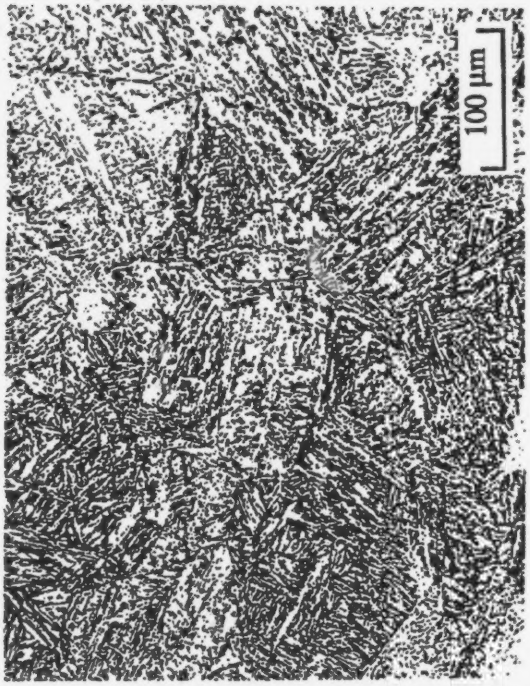

D650-45 s (318 VHN)

HY100

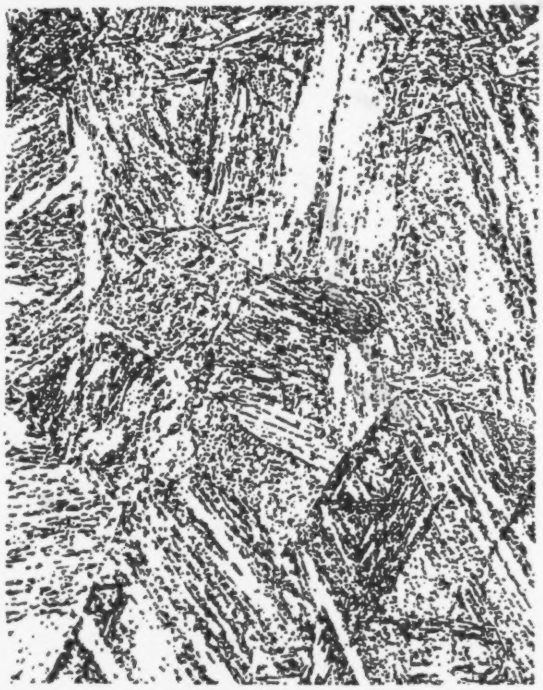

D650-11 s (379 VHN)

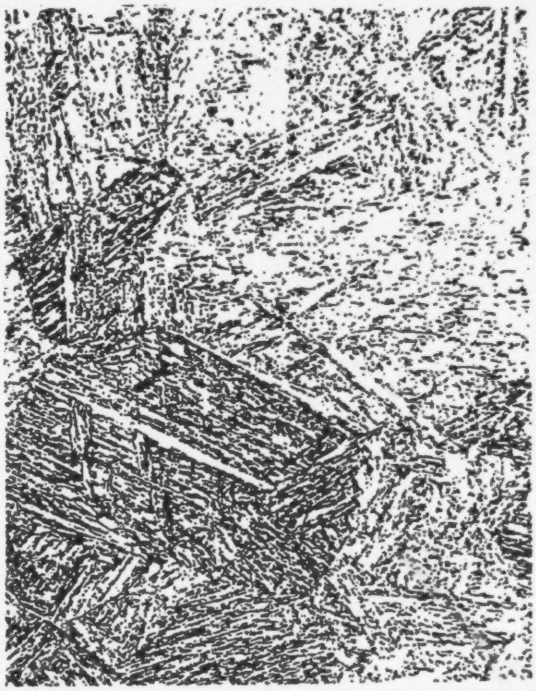

D650-45 s (358 VHN)

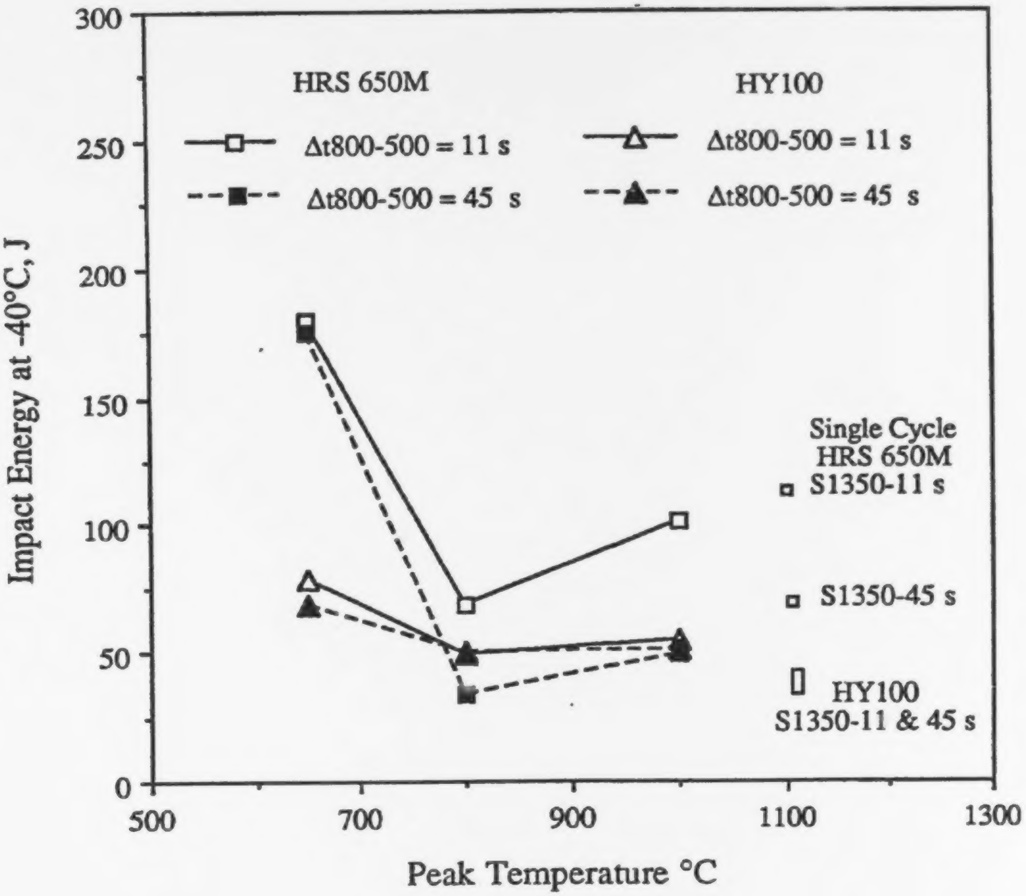
HRS 650M
HY100
Δt800-500 = 11 s
Δt800-500 = 45 s
Δt800-500 = 11 s
Δt800-500 = 45 s
Single Cycle
HRS 650M
S1350-11 s
S1350-45 s
HY100
S1350-11 & 45 s
Impact Energy at -40°C, J
Peak Temperature °C
0
50
100
150
200
250
300
500
700
900
1100
1300

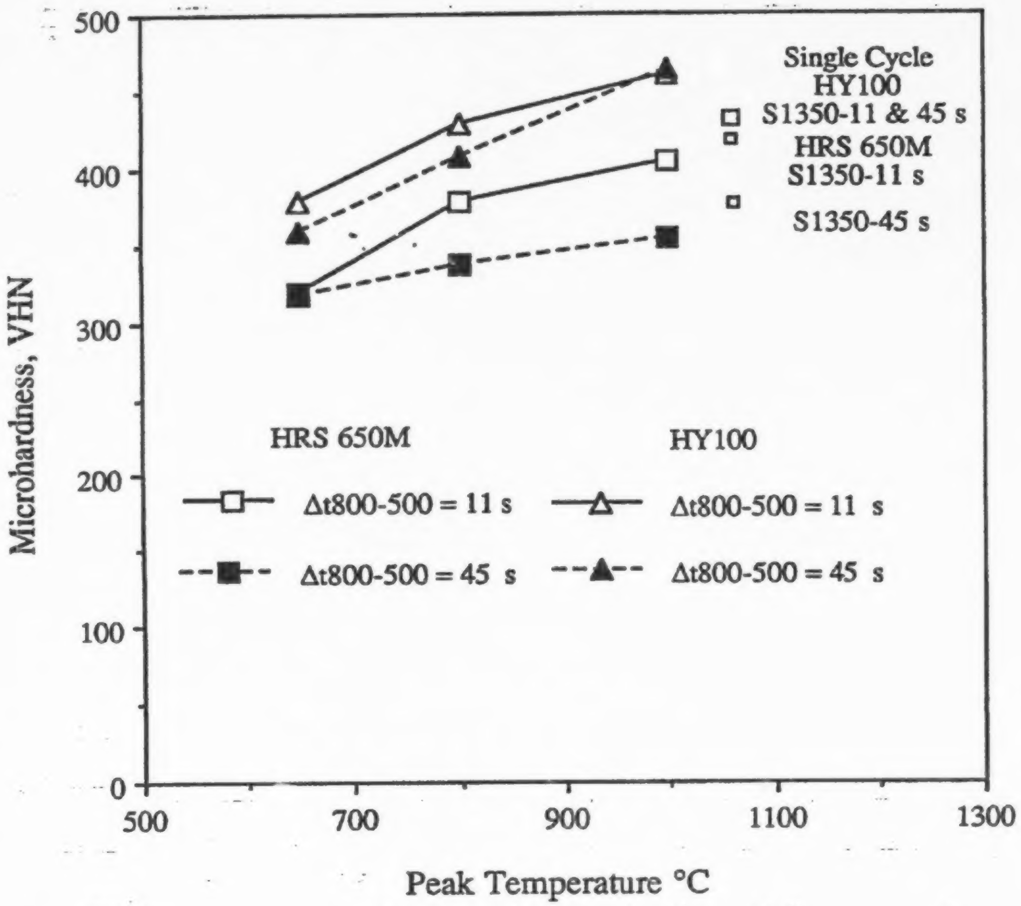
Single Cycle
HY100
S1350-11 & 45 s
HRS 650M
S1350-11 s
S1350-45 s
HRS 650M
HY100
Δt800-500 = 11 s
Δt800-500 = 45 s
Δt800-500 = 11 s
Δt800-500 = 45 s
Microhardness, VHN
0
100
200
300
400
500
500
700
900
1100
1300
Peak Temperature °C

SUMMARY & CONCLUSIONS

Single Cycle HAZ

- Notch toughness of single cycle HAZ regions decreased with increasing Tp.
  SCHAZ > ICHAZ > GRHAZ > GCHAZ

- There was a corresponding increase in hardness with increasing Tp.

- For HRS 650M steel there was lower GCHAZ toughness with increase in cooling time.

- For HY100 steel poor toughness existed in the GCHAZ independent of cooling time.

- For all HAZ regions investigated superior toughness properties occurred for the HRS 650M steel compared with HY100 steel

Double Cycle HAZ

- For HRS 650M steel a decrease in toughness occurred for the GCHAZ reheated to $T_{p2} = 1000$ and 800°C, while improvement occurred for subcritical reheating $T_{p2} = 650$°C.

- For HY100 steel the notch toughness of the GCHAZ was progressively improved with reheating peak temperatures of 1000, 800 and 650°C.

MTL - R&D Activities Related to High Strength Steels

- Simulation studies have been performed on the following commercial and experimental high strength steels

    -HY80/100

    -HSLA80

    -HSLA80/100 1.7 Ni

    -HSLA100 3.5 Ni

    -Experimental HSLA80 & HSLA100 (Effect of TI-B, Mn and Ni)

- Real weld HAZ evaluations have been carried out using CVN and DT tests

- Future work will focus on client sponsored R&D related to the development and HAZ evaluation of high strength steels.

#510309 ④

PROGRESS IN SURFACE ENGINEERING RESEARCH AT DREA

by

C.V. Hyatt
Defence Research Establishment Atlantic
P.O. Box 1012, Dartmouth, Nova Scotia, B2Y-3Z7,

K. Magee
The Laser Institute
9924-45 Avenue, Edmonton, Alberta, T6E 5J1,

J. M. Cunningham
Defence Research Establishment Atlantic
P.O. Box 1012, Dartmouth, Nova Scotia, B2Y-3Z7,

and

T. Betancourt
Nova Scotia Research Foundation,
P.O. Box 790, Dartmouth, Nova Scotia, B2Y-3Z7.

ABSTRACT

DREA's progress in laser surface engineering research in the past year included determining the optimum process window for laser surface melting nickel aluminum bronze alloys, determining how laser treatment conditions affect laser induced surface topography, developing and applying a laboratory scale method of laser cladding and developing a method to assess preferential dissolution of α in the heat-affected zone of laser treated or laser clad nickel aluminum bronze. In addition the characteristics of electrostatic discharge machined surfaces of TERFENOL-D were examined.

1. INTRODUCTION

For the past three years the Defence Research Establishment Atlantic has been investigating surface engineering processes and laser surface engineering processes in particular. The first two years of work is summarized in a number of reports which cover process window development [1,2], corrosion and fatigue behavior [3,4], corrosion and stress corrosion evaluation [5-7], material characterization [7-9] and laser cladding [10]. The current document summarizes this years work. It deals mostly on the development and verification of cladding procedures for nickel aluminum bronze and a bit of new work on the surface characteristics of EDM machined TERFENOL-D. As well, our future plans are briefly discussed.

2. LASER SURFACE ENGINEERING OF NICKEL ALUMINUM BRONZE

One of the short term goals of our laser surface engineering research is to develop the knowledge and understanding required to confidently apply laser surface engineering to marine copper alloys and to practically demonstrate this technology. The technology has a number of potential applications in surface texturing, component reclamation, and surface modification for wear, corrosion and erosion resistance. It may also be useful for the deposition of metastable alloys with novel properties such as high damping capacity. Though our studies have focused on copper nickel alloys and nickel aluminum bronzes, qualitatively, the results and conclusions should be applicable to most copper alloys with a sufficiently low reflectivity and a fairly narrow, albeit as yet undefined, melting temperature range.

2.1 Laser Surface Melting of Nickel Aluminum Bronze.

Laser surface melting of marine copper alloys has some practical value. However, the most immediate benefit of laser melting experiments on nickel aluminum bronze alloys was to provide information useful in designing and assessing laser cladding experiments. This information, which is considered in detail in [11], includes information about surface character, gas shield effects, and microstructure as a function of processing conditions. Most useful was the determination that a single phase martensitic structure could be produced under a wide range of conduction limited laser treatment conditions, but that above a critical laser energy (500 J/cm at 8.5 mm/s laser scan speed) what appears to be Widmanstätten α forms in the heat affected zone.

Comparing the laser surface melting experiments on nickel aluminum bronze with previous work on Cu-Ni alloys[1] we noted the behavior of nickel aluminum bronze was quite similar to that of Cu-30Ni alloys. One important difference between these alloys is an increased tendency to what appears to be surface breaking gas micro-porosity in the nickel aluminum bronze alloys. One possibility is that this may be a result of differences in inclusion number density and type between the alloys. More work on the possible role of prior inclusions on laser induced defects and characterization of the base materials is needed however.

One final observation we have made in these experiments is that laser surface melting offers an excellent method of controlling surface roughness and waviness. It can be used to produce a uniform waviness with wavelength of 0.25 to 3 mm and amplitude of up to 50 μm–perhaps more.

2.2 Laser Cladding of Nickel Aluminum Bronze.

Laser cladding experiments on nickel aluminum bronze have been quite successful. In contrast to other workers, we have used matching clad material and concentrated on developing a process which could be implemented commercially. We considered both powder and wire feeds to provide clad material, but selected a wire feed despite conventional wisdom which suggests that this would produce a slightly rougher deposit. We did this because commercial powders in appropriate compositions are not available and special batches are prohibitively expensive, especially if one wishes to adapt the technology to other alloys. Our first experiments were performed with a wire feeder from a GMAW torch, using the smallest commercially available wire diameter (0.89 mm) at the slowest feed rate possible with this device (0.8 cm/s). A high heat input, about four times that observed to produce no α in the interpass heat affected zones, was used. These clad layers may ultimately, through erosion and corrosion assessment, prove acceptable. However, concern about the nature of material in the heat affected zone led us to use a smaller custom drawn wire with diameter 0.25 mm so that the heat input could be reduced. Using this small wire and reduced heat input and a custom built small wire feeder, we were able to produce an essentially single phase deposit, with minimal transformation in the heat affected zone. Remaining problems with the cladding procedure are mostly feeder design problems that should be worked out in the coming year.

To demonstrate the (near) commercial viability of the procedure, we laser clad part of a submarine pressure hull valve which had been rejected and partially destroyed during a failure analysis. Fig. 1 shows one area of the clad surface.

2.3 Evaluation of Laser Clad and Laser Surface Modified Material.

We have only just begun detailed investigations of the laser surface melted and laser clad nickel aluminum bronze. Erosion tests on untreated material as a baseline against which to compare the treated material are now in progress and a rapid metallographic method to assess preferential phase dissolution has been developed. Applying this method to clad specimens produced at very high power levels revealed that some preferential dissolution–probably of grain boundary and Widmänstatten α–occured under the most severe high P.H. test conditions.

2.4 Future Work

Our plans for future work on this topic include basic metallographic characterization of the specimens generated to date—much fundamental work is needed here—additional rapid dissolution tests, some long term exposure tests, mechanical tests on clad and treated specimens, and possibly some stress corrosion experiments and erosion-corrosion studies. As well, we intend to refine the design of our cladding system, especially the wire feeder, so that its operation is more consistent.

3. MICROSTRUCTURE AND TOPOGRAPHY OF TERFENOL-D AFTER ELECTROSTATIC DISCHARGE MACHINING

Giant magnetostrictive materials such as TERFENOL-D have many potential military applications; sonar transducers, smart structures and active noise suppression for example. One problem with this material, which is a brittle Laves phase, is that it is difficult to machine with conventional methods. Recently, in collaboration with DREA's Transducer Group we have investigated the effect of electrostatic discharge machining on this material. So far we have characterized surface and subsurface flaw densities and assessed the effect of various parameters on susceptibility to cracking during machining [12]. One conclusion is that significant reductions in machining damage are possible by heating the specimen during machining. This work is ongoing.

4. REFERENCES

1. K.H. Magee, *Surface Modification of Copper Nickel Alloys by Continuous Carbon Dioxide Laser Melting*, DREA CR/92/427, Defence Research Establishment Atlantic, Halifax, 1992.

2. K.H. Magee and C.V. Hyatt, *Laser Surface Melting of Copper Nickel Alloys*, to be published.

3. T. Betancourt, *Effect of High Energy Beam Surface Modifications on the Fatigue and Corrosion Behavior of Metals*, DREA CR/91/418, Defence Research Establishment Atlantic, Halifax, 1991.

4. S.J. Clarke, *Corrosion of Surface Modified Metals*, DREA CR/91/411, Defence Research Establishment Atlantic, Halifax, 1991.

5. C.V. Hyatt, K. Mackay, and T. Betancourt, *Evaluation of Laser Treated Copper Alloys*, to be published.

6. T. Betancourt, *Stress Corrosion Cracking Resistance of Laser Surface Modified Copper Alloy* UNS C36000 in Seawater, DREA/CR/91/463, Defence Research Establishment Atlantic, Halifax, 1991.

7. T. Betancourt, *Stress Corrosion Cracking Resistance of Laser Surface Modified Copper* Nickel Alloys, DREA/CR/91/477, Defence Research Establishment Atlantic, Halifax, 1991.

8. C. V. Hyatt and K. D. Mackay, *Defects in Laser Treated Copper Alloys.* in Proceedings of the International Conference on Beam Processing of Advanced Materials, Chicago, November 1992.

9. K. Mackay and C. V. Hyatt, *Laser Surface Treatment of Copper Alloy UNS C36000*, Informal report, DREA Research Note DL/90/2, 1990.

10. K.H. Magee, T*he Applications and Technology of Laser Weld Overlaying*, DREA/CR/92/419, Defence Research Establishment Atlantic, Halifax, 1992.

11. K.H. Magee, *Laser Surface Modification and Laser Cladding of Nickel Aluminum Bronze*, DREA/CR/93/421.

12. K. D. Mackay and C. V. Hyatt, *Optical and Scanning Electron Microscope Study of EDM Machined TERFENOL-D*, Research Note DL/92/3, June, 1992.

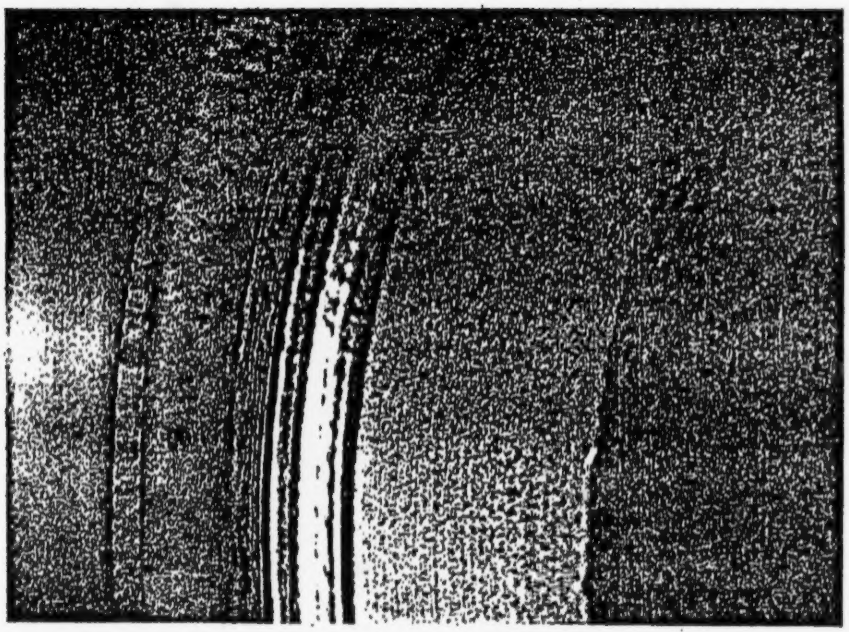

Figure 1. Laser clad Nickel Aluminum bronze valve.

#510310 ⑤

J-Resistance Curve of HY100

by Dr. B. Faucher and Dr. K. Karis Allen

Metals Technology Laboratories, CANMET, Energy Mines & Resources
Canada, 568 Booth, Ottawa, K1A 0G1
and
Defence Research Establishment Atlantic, Dockyard Laboratory
FMO Halifax, Halifax, Nova Scotia, B3K 2X0

ABSTRACT

A precise knowledge of toughness of materials is needed to evaluate the fitness-for-purpose of structures with defects. For brittle materials as steels at low temperatures, the toughness is measured with the stress intensity factor, K. Steels at high temperature are tough and their toughness is then measured either with the CTOD (Crack tip opening displacement) or the J-integral. These quantities are related as:

$$J = K^2/E = \sigma_y \ (CTOD)$$

where E and σ_y are material's Young's modulus and yield strength, respectively. Increasing resistance of material to crack advance during tearing is taken into account by the J-resistance curve. It is a graph of J as a function of crack extension. J is obtained from experimental load-deformation curve, and crack extension from different techniques to monitor crack length during the test; the most common one, standardized by ASTM, is the unloading technique which requires to stop the test for a short period of time to measure the compliance of the specimen at regular intervals. This technique is delicate of application, time consuming and, of course, not applicable to impact testing.

An alternative method to obtain the crack length is by comparing the experimental load-displacement curve to a reference curve, the "key-curve", obtained for a specimen with no crack extension. In this method, the crack extension is obtained by numerical calculations from the difference between the two load-displacement curves. The key-curve may be either measured from experiment with sub-size or blunt-notch specimens, calculated from the tensile properties of the material, or obtained directly from the test with the growing crack. The aim of these approaches is to derive a simplified method to measure experimentally the J-resistance curve, and contribute to increasing the use of J_{Ic} as a convenient toughness parameter

Preliminary results on the effectiveness of the key-curve will be presented by comparing key-curves of HY100, calculated with the standardized unloading compliance method and the key-curve approach.

J-RESISTANCE CURVE OF HY 100

B. Faucher[1] and K. KarisAllen[2]

[1]Metals Technology Laboratories, CANMET
Energy Mines & Resources Canada, 568 Booth, Ottawa, K1A 0G1
and
[2]Defence Research Establishment Atlantic, Dockyard Laboratory
FMO Halifax, Halifax, Nova Scotia, B3K 2X0

Presented at the Canadian Forces CRAD meeting on "Naval Applications of Materials Technology", Halifax, April 1993.

The J-resistance curve of HY 100 has been obtained for several specimen geometries with the standardized unloading compliance technique and the key-curve method.

EXPERIMENTAL

The specimens were all taken from a one inch thick armour plate of HY100 MIL-S-16216J, austenitized at 905°C for 70 minutes, water-quenched and then tempered at 660°C for 70 minutes. A typical microstructure is shown in Fig.1. The average yield and tensile strength measured with three standard tensile specimens are 818 and 937 MPa, respectively. Compact C(T), and three-point-bend SE(B), specimens were prepared according to ASTM E-813 Standard for J_{Ic} Testing. The thickness was 25 mm, large enough to ensure valid J_{Ic} values. Three different values of crack length, a/W = 0.25, 0.5, and 0.75, were used for SE(B) and the two larger values for C(T) specimens. Specimens were made with 20% side-grooves (SG) and without side-grooves (Fig.2). The standardized (E813) unloading technique was used to obtain J-resistance curves. Experimental key-curves were determined using specimens without fatigue precracks.

The tests were carried out in a servo-hydraulic universal testing machine at a displacement rate of 0.01 mm/s. Test control and data acquisition were performed with an Instron 8500 controller, using dedicated software for machine control and data acquisition developed and implemented on an IBM compatible PC. A typical graph of the load as a function of load-line displacement is shown with the unloading cycles in Fig.3. The extraneous displacement for the bend specimens was fitted with a fourth degree polynomial and subtracted from the measured overall load-line displacement. After testing, the specimens were heat-tinted at 375°C for 15 minutes, cooled at liquid nitrogen temperature, and broken open to measure the initial and final crack lengths. Typical fracture surfaces show the fatigue precrack and the crack advance.

UNLOADING COMPLIANCE

Typical J-resistance curves are shown for the various geometries in Figs.4 and 5. Side-grooves promote a state of plane strain , i.e. increase the out-of-plane constraint. The effect is obvious on the tearing resistance (the slope of the J-resistance curve), which is much smaller for SG specimens. The critical value of J, J_{Ic}, defined by the intersection of the J-resistance curve with the 0.2 mm offset blunting line, is not affected significantly neither by the crack length, nor by the side-grooves, except for bend specimens with the shallowest initial crack lengths which have also the highest values of the tearing resistance. This effect may be quantified by an in-plane constraint parameter such as the T-stress (Fig.6). The results show that the toughness may be significantly larger for negative values of the T-stress, that is for shallow cracks loaded in bending. Tension loading, which is characterized by large negative T values, could also exhibit high toughness.

KEY-CURVE

The key-curve method is based on the assumption that the load, P, can be expressed as separable multiplicative functions of crack length, a, and plastic component of load line displacement, Δ_p:

$$P = G\left(\frac{a}{W}\right) H\left(\frac{\Delta_p}{W}\right)$$

where W is the specimen width. For deeply cracked bend type specimens in the fully plastic range, the function G(a/W) is proportional to b^2, the square of the remaining ligament (b=W-a). The load varies also with the specimen net section thickness, B_N, and the material flow stress, σ_f, the average between yield and tensile strengths, so that we may write:

$$H(\frac{\Delta_{pl}}{W}) = \frac{P}{G(a/W)} = \frac{4PW}{B_N\, b^2\, \sigma_f}$$

Defining the normalized load as:

$$P_N = \frac{4PW}{B_N\, b_o^2\, \sigma_f}$$

the crack length is obtained as:

$$\Delta a = b_o\left(1 - \sqrt{H/P_N}\right).$$

For compact, C(T), specimens:

$$H(\frac{\Delta_{pl}}{W}) = \frac{P}{G(a/W)} = \frac{4PW}{B_N\, b^2\, \sigma_f \exp(0.522\, b/W)}$$

and we define the normalized load as:

$$P_N = \frac{4PW}{B_N b_o^2 \sigma_f \exp(0.522 b_o/W)}.$$

Hence, for small increments of crack extension:

$$\Delta a \approx \frac{b_o\left(1-\sqrt{H/P_N}\right)}{1+0.261 b_o\sqrt{H/P_N}/W}$$

The key curve (the function H) can be determined from the crack length obtained from the unloading compliance. It is compared to the load normalized with the initial crack length in Fig.7. Alternatively, crack extension is easily determined, if the key-curve is known. An "experimental" key-curve can be obtained with specimens with blunt notches for which crack extension starts at larger values of deformation than for specimens with sharp cracks. It is also possible to use a functional relationship for the key curve (or "calibration" curve). Two possibilities are the power law:

$$H = H_o\ (\Delta_p/W)^n$$

and the so-called "LMN" function:

$$H = \frac{L + M\Delta_{pl}/W}{N + \Delta_{pl}/W}\ \Delta_{pl}/W$$

In this work, the parameters H_o and n, and L,M, and N have been obtained from the last data point (where the crack length is known) and by fitting the key curve to the normalized experimental curve in the largest possible region just before maximum load. The calibration curves are compared with the normalized experimental curves for each of the methods in Figs.8, 10, and 12, and the resulting J-resistance curves are compared to the unloading compliance curve for one specimen in Figs. 9, 11, and 13. The calibration curves for all bend specimens are also shown in Fig.14 in terms of the crack-mouth-opening rather than load-line displacement.

CONCLUSIONS

The critical value of J is not affected significantly by the out-of-plane constraint (side-grooves); it changes with the in-plane constraint, i.e., it increases at large negative values of the T-stress. The tearing resistance (slope of the J-resistance curve) is affected significantly by the out-of-plane constraint.

Key-curve methods give reasonable values of the J-resistance curve; values of J_{Ic} seem to be somewhat larger than the value obtained by the unloading compliance method which is the most conservative.

ACKNOWLEDGEMENTS

Helpful discussions with Dr. W.R. Tyson are gratefully acknowledged.

BIBLIOGRAPHY

Ernst, Hugo, Paris, P.C., Rossow, Mark, and Hutchinson, J.W., **"Analysis of Load-Displacement Relationships to Determine J-R Curve and Tearing Instability Material Properties"**, in *Fracture Mechanics, ASTM STP 677*, C.W. Smith Ed., American Society for Testing and Materials, 1979, pp.581-599.

Joyce, J.A., Ernst, Hugo, and Paris, P.C., **"Direct Evaluation of J-Resistance Curves from Load Displacement Records"**, in *Fracture Mechanics: Twelfth Conference, ASTM STP 700*, American Society for Testing and Materials, 1980, pp.222-236.

Ernst, H. A., Paris, P.C., Landes, J.D., **"Estimations on J-Integral and Tearing Modulus T from a Single Specimen Test Record"**, in *Fracture Mechanics: Thirteenth Conference, ASTM STP 743*, Richard Roberts, Ed., American Society for Testing and Materials, 1981, pp. 476-502.

Landes, J.D., Zhou. Z., Lee, K., and Herrera, R., **"Normalization Method for Developing J-R Curves with the LMN Function"**, J. of Testing and Evaluation, 19, 4, 1991, pp. 305-311.

"Constraint Effects in Fracture",ASTM STP 1171, E. M. Hackett, R.-H. Schawlbe, and R. H. Dodds, Eds., American Society for Testing and Materials, Philadelphia, 1993.

"Shallow Crack Fracture Mechanics Toughness Tests and Applications", TWI, Cambridge, UK, 1992, Proceedings of an international conference, in press.

FIGURE CAPTIONS

Figure 1: Typical microstructure of the HY100 steel.

Figure 2: Fracture surfaces of bend specimens showing machined notch, fatigue pre-cracking, and ductile tearing for six different geometries.

Figure 3: Load as a function of the load-line displacement with unloadings to measure the compliances.

Figure 4: J-resistance curves for C(T) specimens.

Figure 5: J-resistance curves for bend specimens.

Figure 6: Critical values of J as a function of the constraint. Side-grooved (SG) specimens represent a lower bound for toughness; only some J_Q from SG specimens qualifies as J_{Ic}.

Figure 7: Comparison of the key-curve obtained from the unloading compliances with the normalized load. The displacement is normalized by the specimen width.

Figure 8: Comparison of the experimental key-curve with the normalized load.

Figure 9: Comparison of the J-resistance curves obtained with the experimental key-curve and with the unloading compliance (dots).

Figure 10: Comparison of the power law key-curve with the normalized load.

Figure 11: Comparison of the J-resistance curves obtained with the power law key-curve and with the unloading compliance (dots).

Figure 12: Comparison of the "LMN" key-curve with the normalized load.

Figure 13: Comparison of the J-resistance curves obtained with the "LMN" key-curve and with the unloading compliance (dots).

Figure 14: Comparison of the H-values obtained with the various key-curve methods as a function of the plastic CMOD.

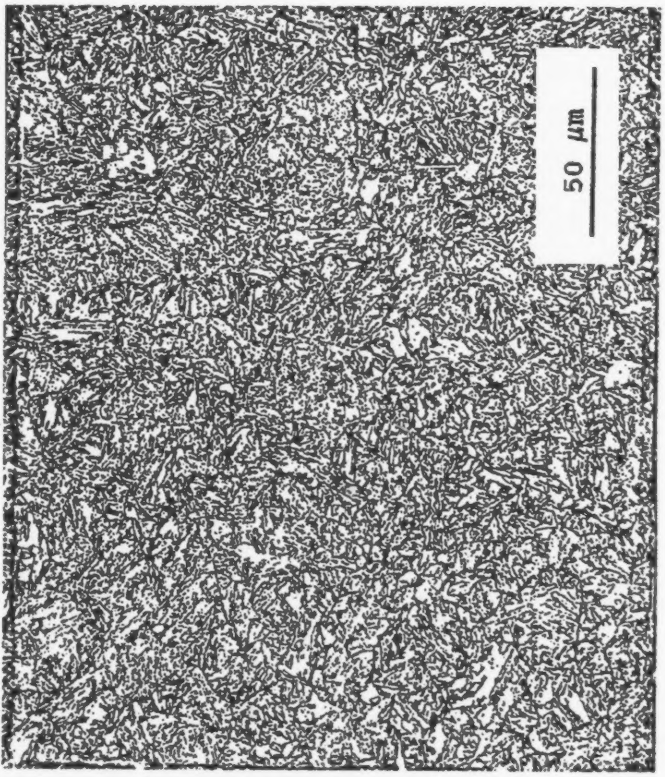

Figure 1

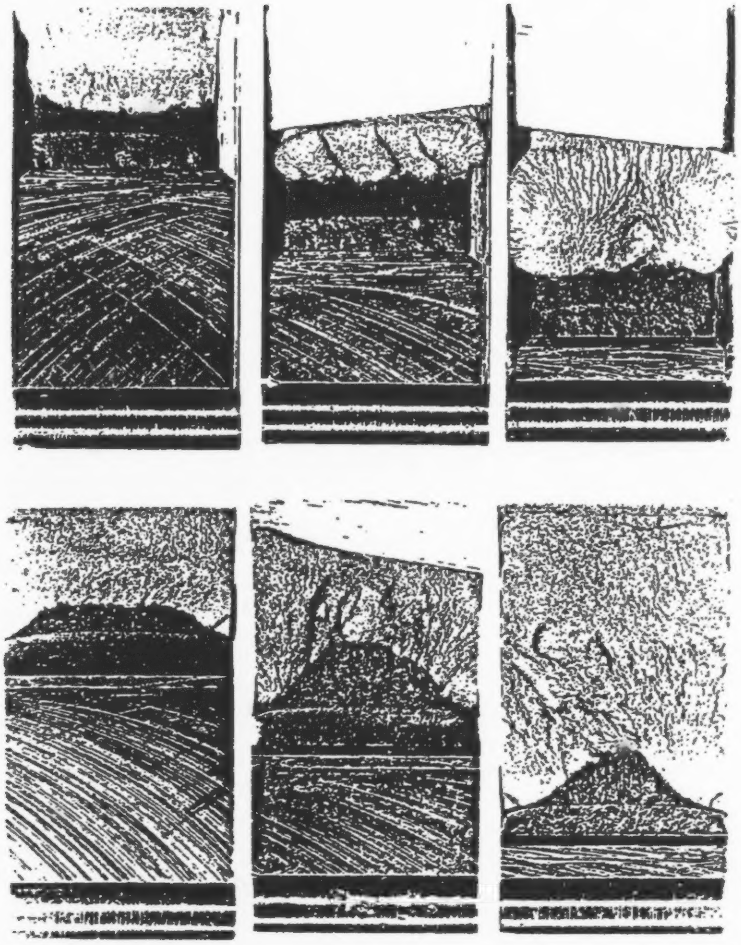

Figure 2

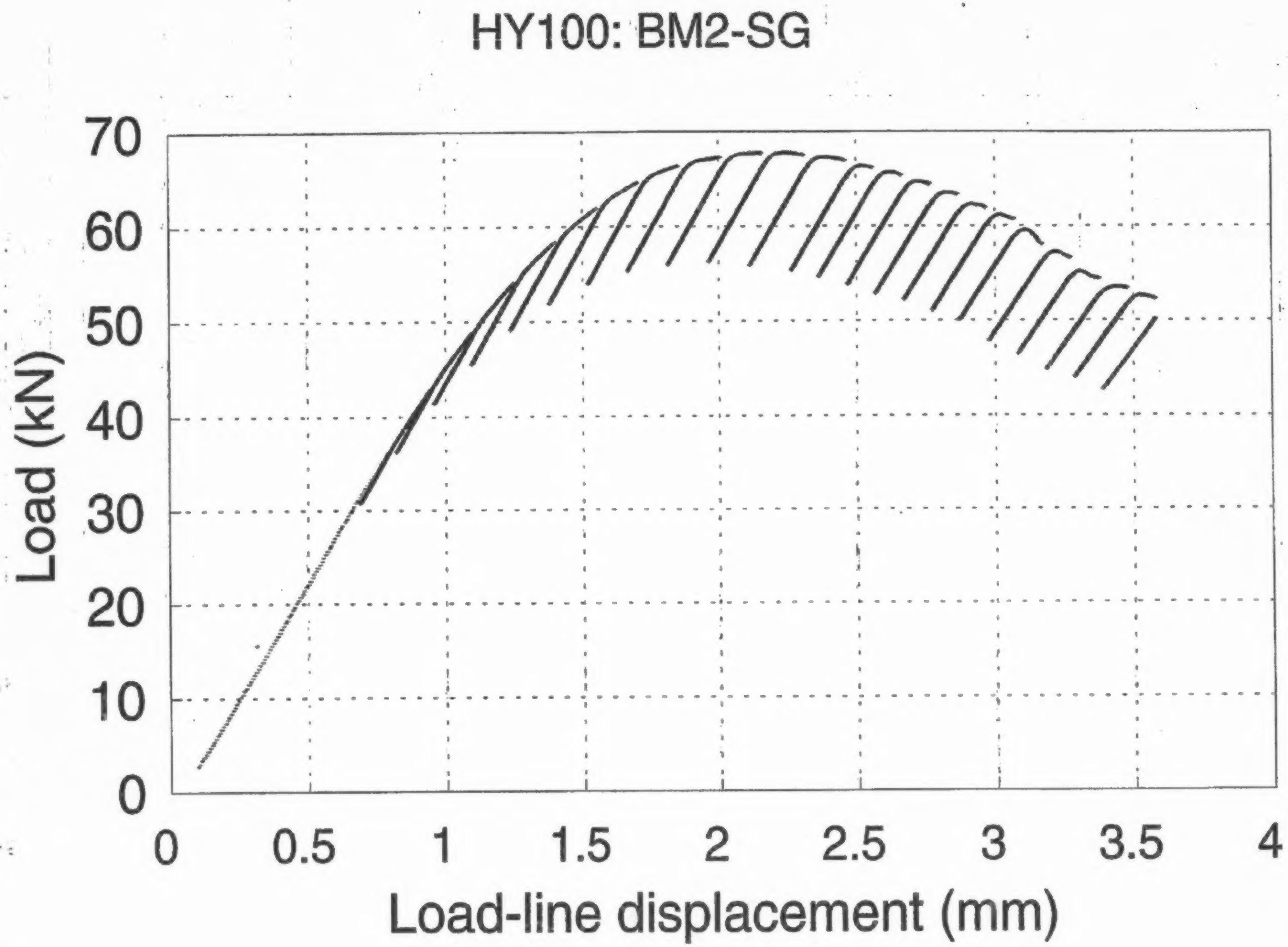
HY100: BM2-SG
Load (kN)
0
10
20
30
40
50
60
70
Load-line displacement (mm)
0
0.5
1
1.5
2
2.5
3
3.5
4

Figure 3

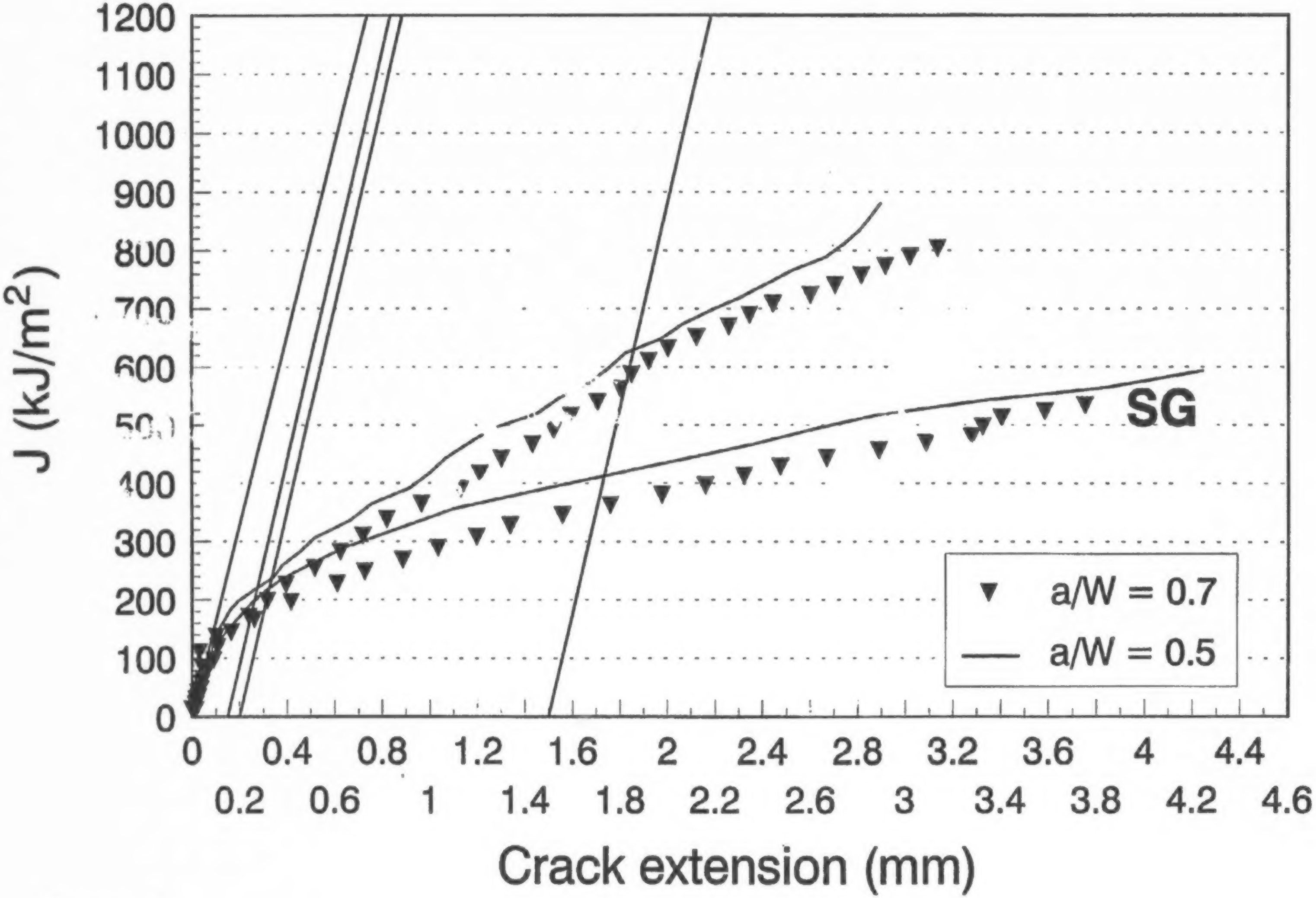
J (kJ/m²)
1200
1100
1000
900
800
700
600
500
400
300
200
100
0
0
0.2
0.4
0.6
0.8
1
1.2
1.4
1.6
1.8
2
2.2
2.4
2.6
2.8
3
3.2
3.4
3.6
3.8
4
4.2
4.4
4.6
Crack extension (mm)
SG
▼ a/W = 0.7
— a/W = 0.5

Figure 4

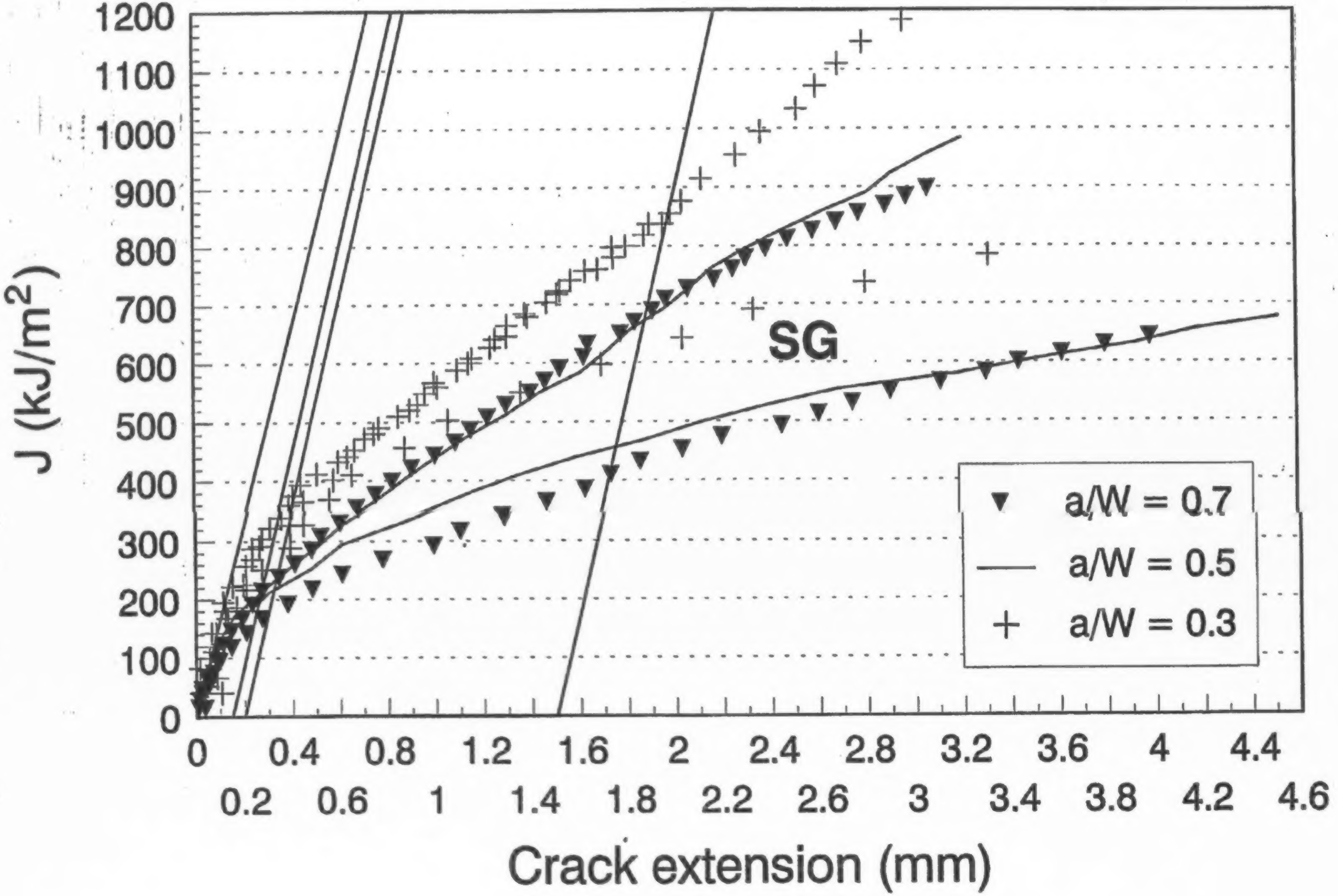
J (kJ/m²)
1200
1100
1000
900
800
700
600
500
400
300
200
100
0
0
0.2
0.4
0.6
0.8
1
1.2
1.4
1.6
1.8
2
2.2
2.4
2.6
2.8
3
3.2
3.4
3.6
3.8
4
4.2
4.4
4.6
Crack extension (mm)
SG
▼ a/W = 0.7
— a/W = 0.5
+ a/W = 0.3

Figure 5

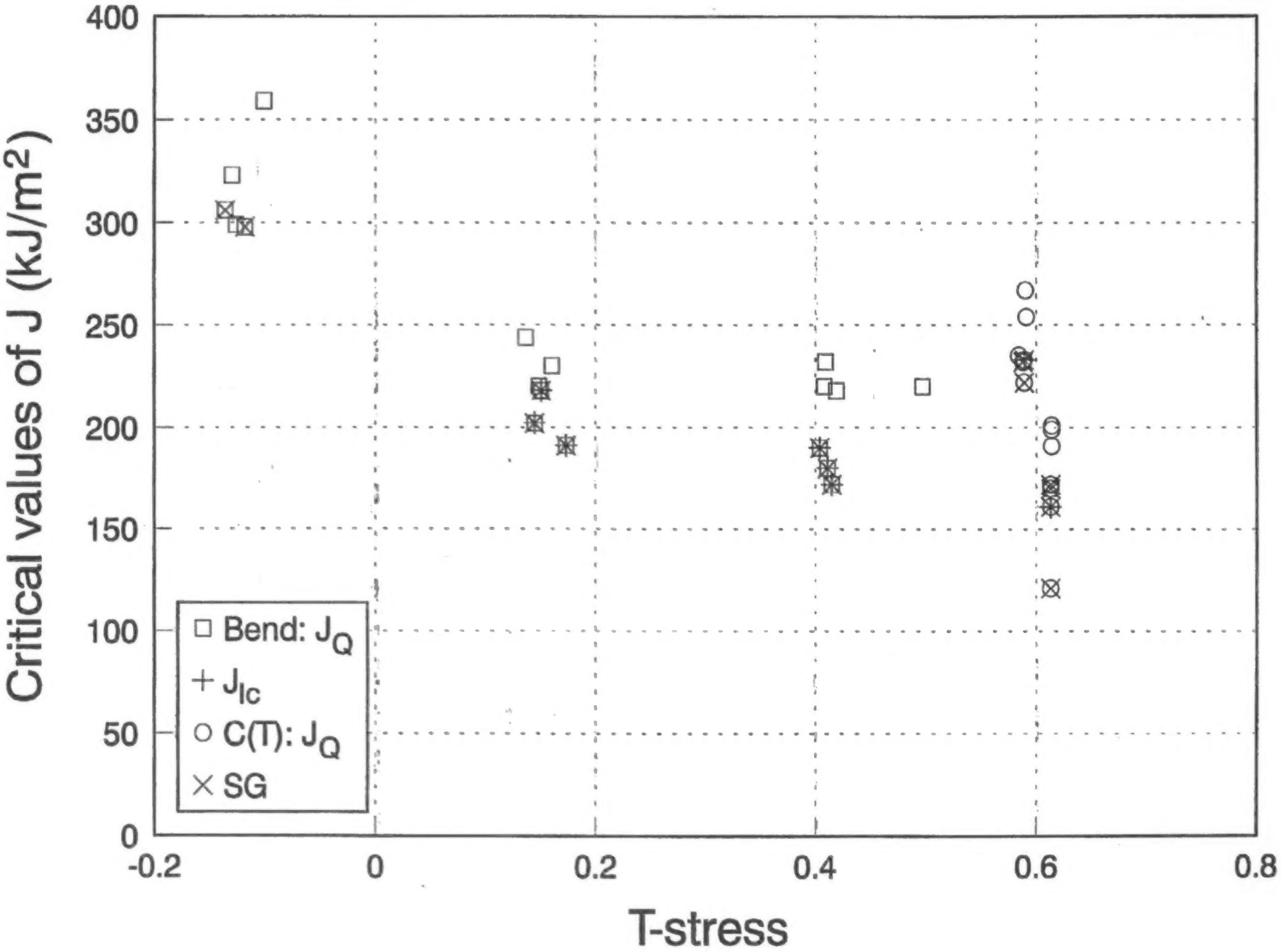
Critical values of J (kJ/m²)
400
350
300
250
200
150
100
50
0
-0.2
0
0.2
0.4
0.6
0.8
T-stress
□ Bend: J_Q
+ J_{Ic}
○ C(T): J_Q
× SG

Figure 6

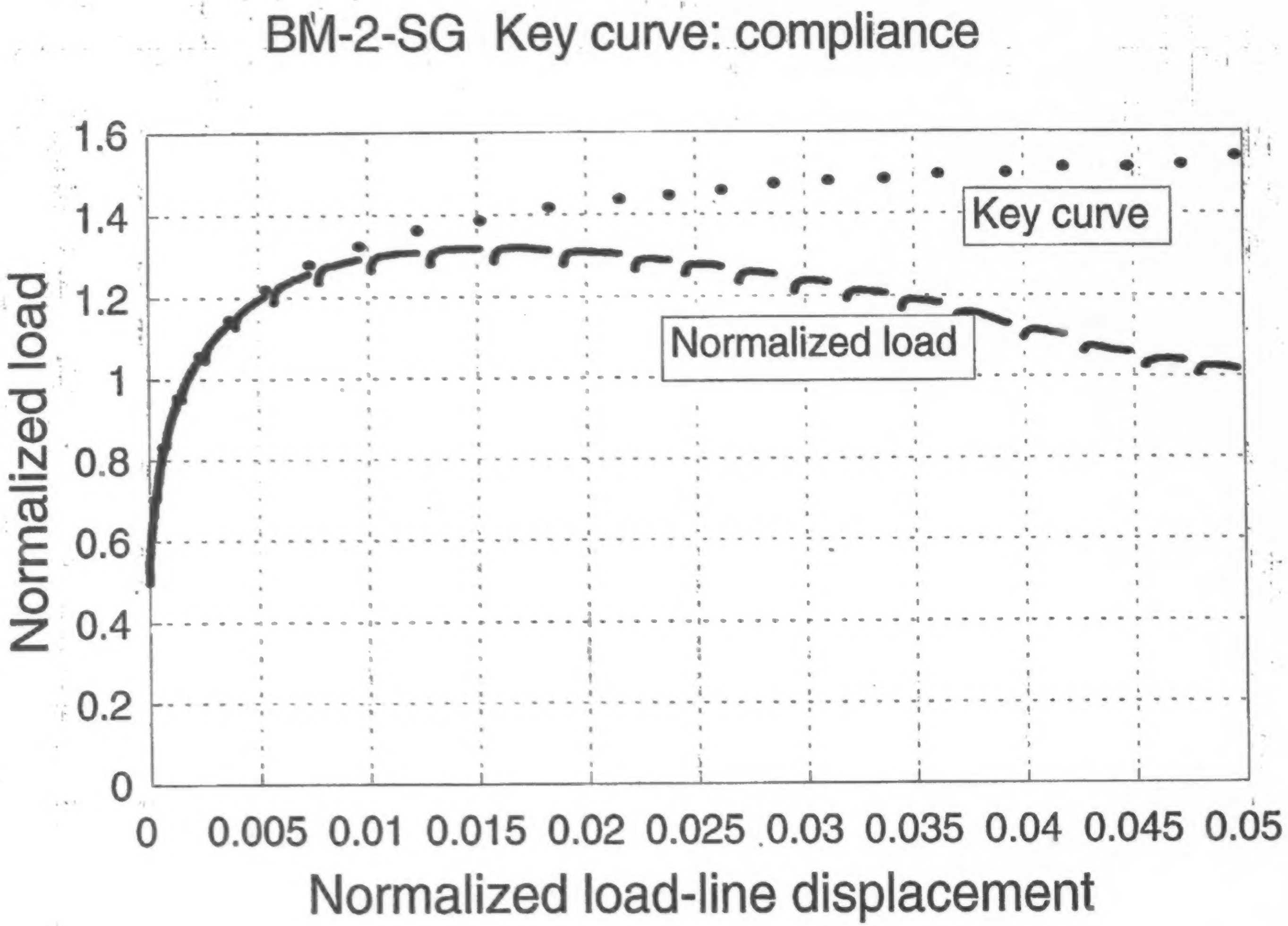

BM-2-SG Key curve: compliance

Figure 7

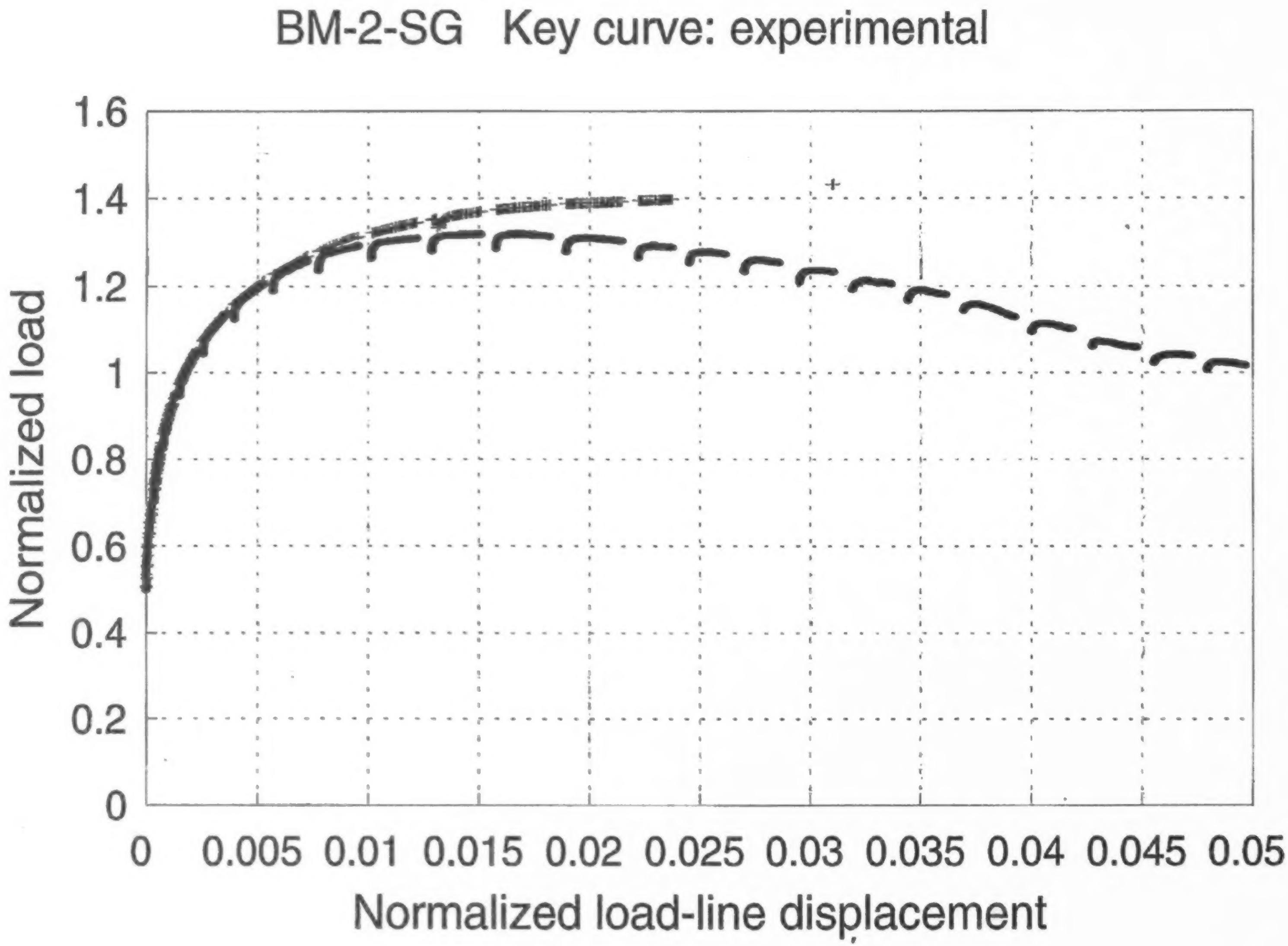
BM-2-SG Key curve: experimental
Normalized load
1.6
1.4
1.2
1
0.8
0.6
0.4
0.2
0
0
0.005
0.01
0.015
0.02
0.025
0.03
0.035
0.04
0.045
0.05
Normalized load-line displacement

Figure 8

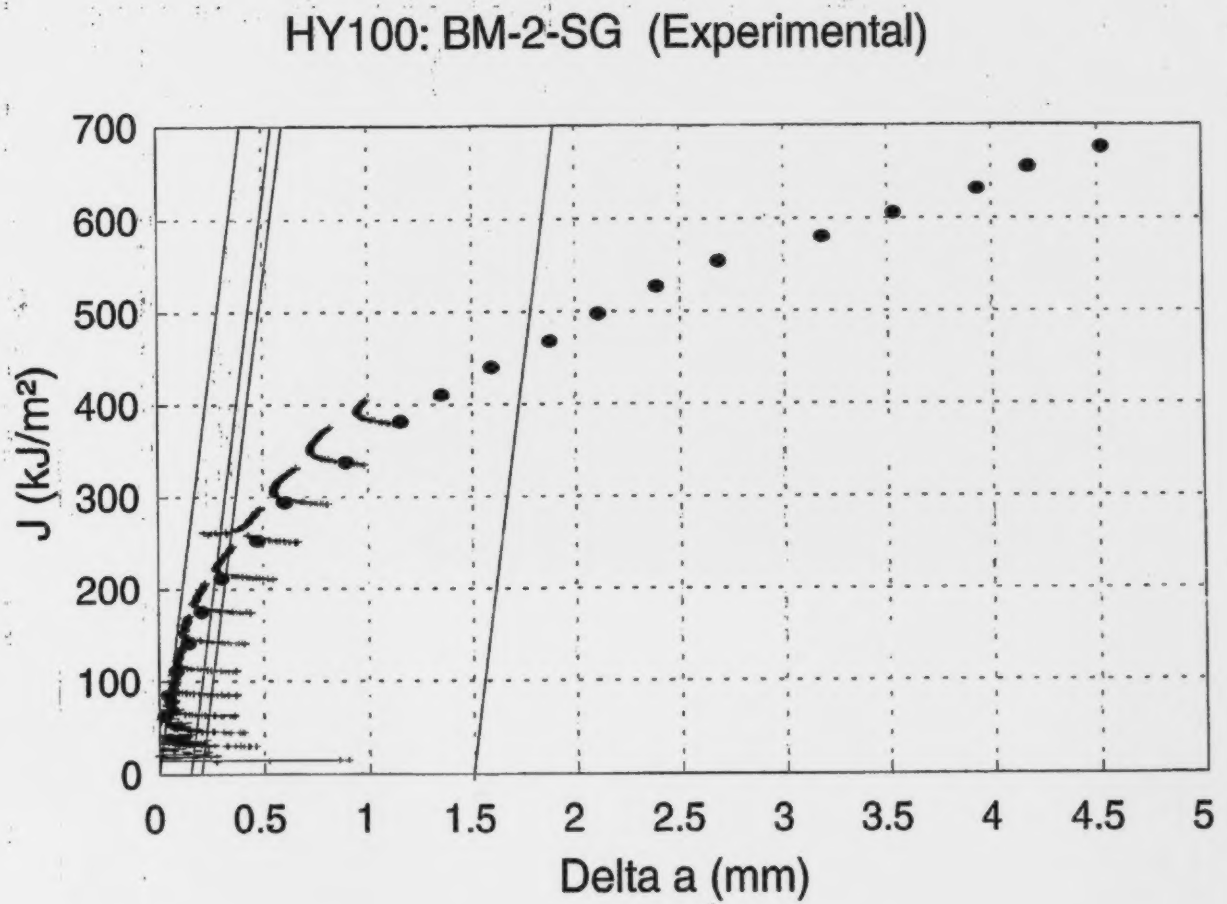
HY100: BM-2-SG (Experimental)
J (kJ/m²)
700
600
500
400
300
200
100
0
0
0.5
1
1.5
2
2.5
3
3.5
4
4.5
5
Delta a (mm)

Figure 9

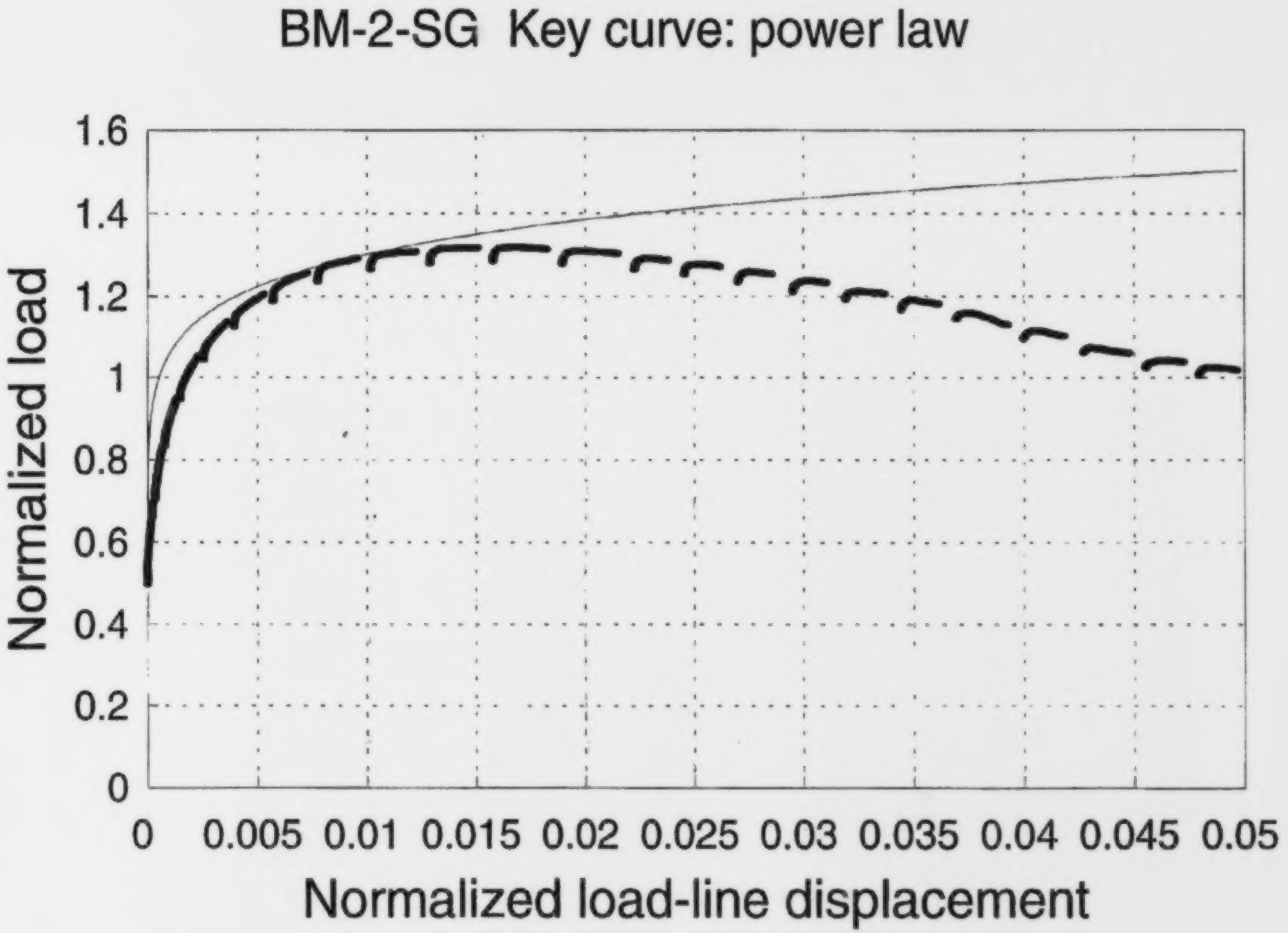
BM-2-SG Key curve: power law
Normalized load
1.6
1.4
1.2
1
0.8
0.6
0.4
0.2
0
0
0.005
0.01
0.015
0.02
0.025
0.03
0.035
0.04
0.045
0.05
Normalized load-line displacement

Figure 10

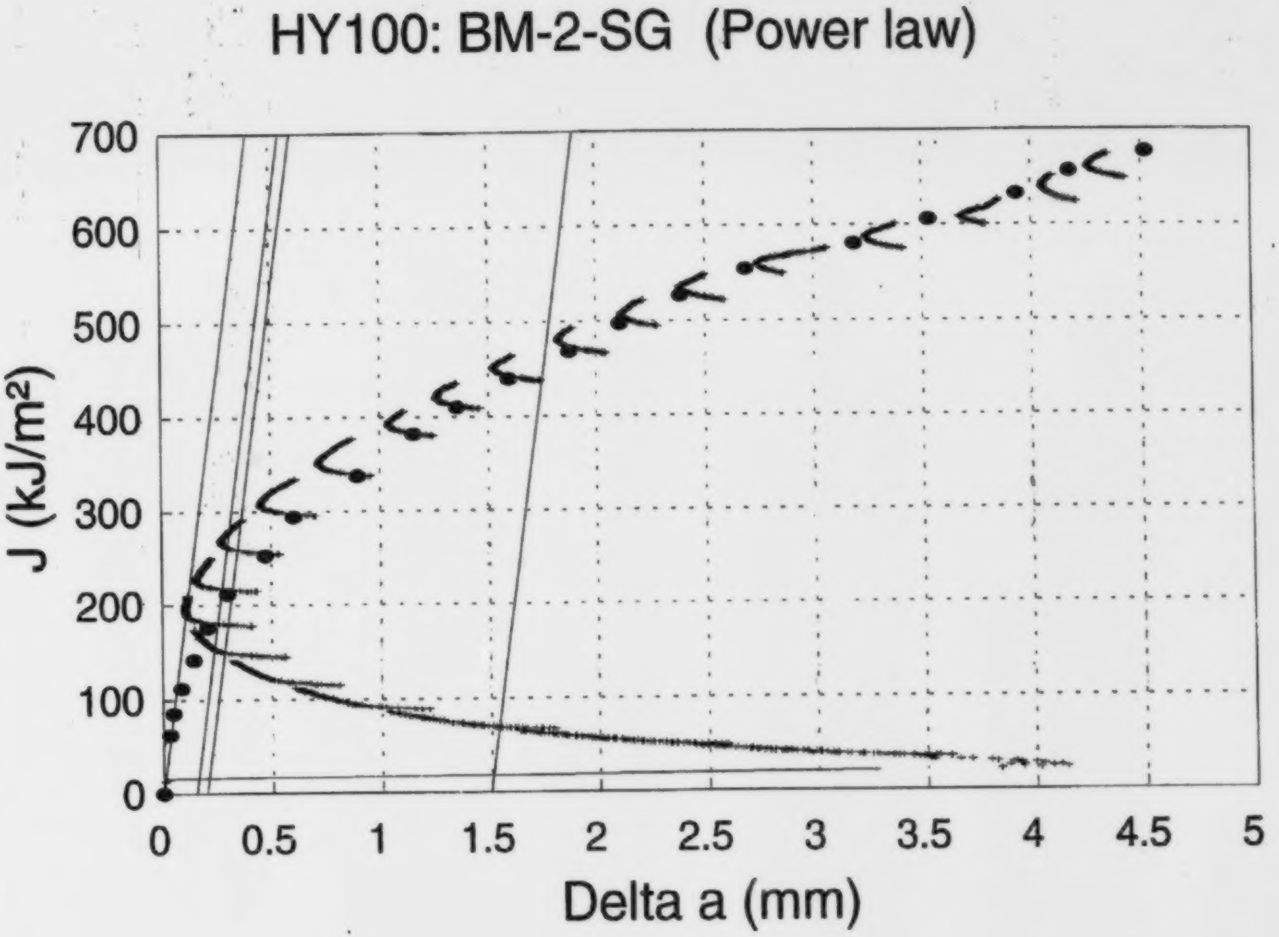
HY100: BM-2-SG (Power law)
J (kJ/m²)
700
600
500
400
300
200
100
0
0
0.5
1
1.5
2
2.5
3
3.5
4
4.5
5
Delta a (mm)

Figure 11

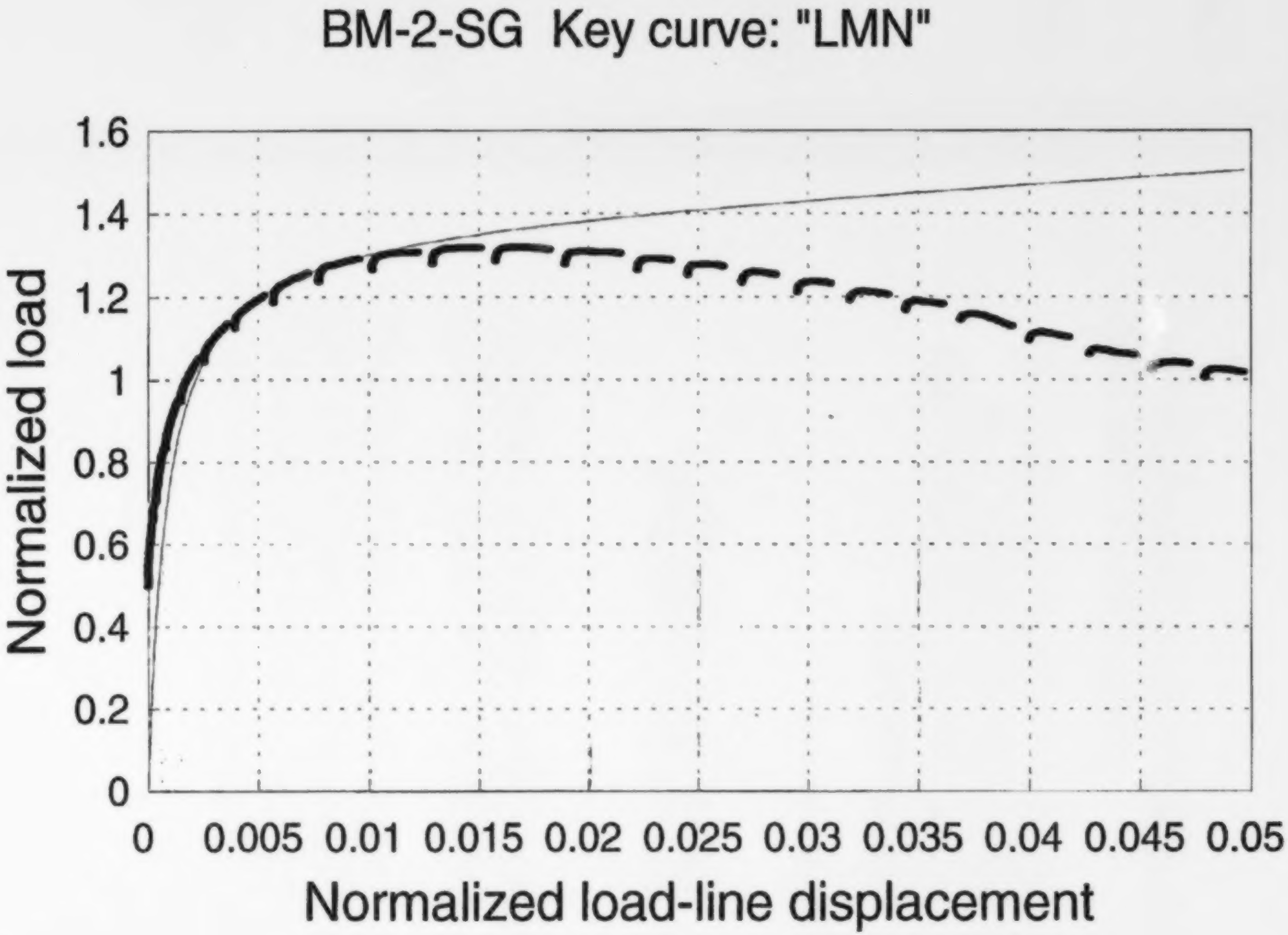
BM-2-SG Key curve: "LMN"
Normalized load
1.6
1.4
1.2
1
0.8
0.6
0.4
0.2
0
0
0.005
0.01
0.015
0.02
0.025
0.03
0.035
0.04
0.045
0.05
Normalized load-line displacement

Figure 12

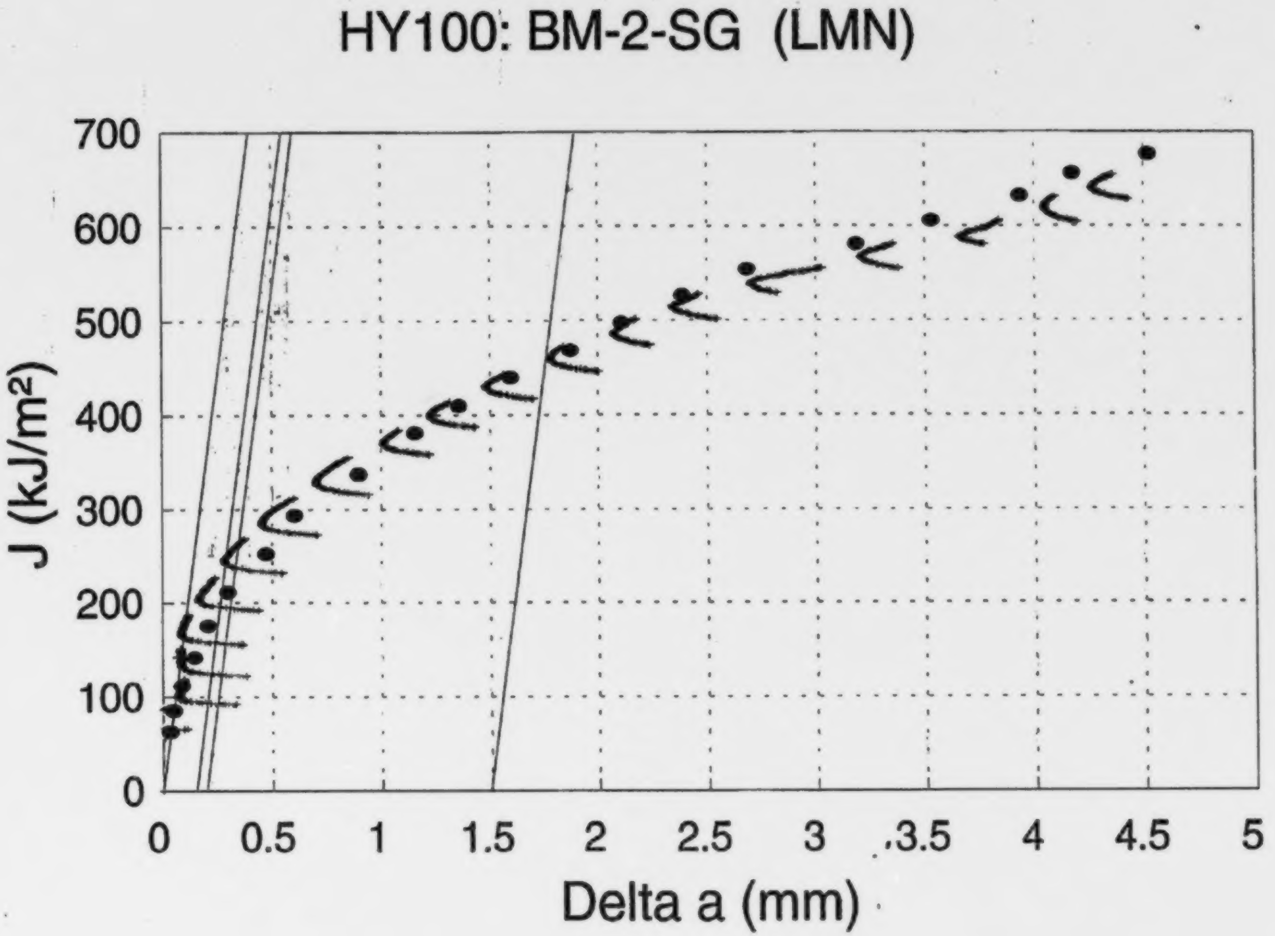
HY100: BM-2-SG (LMN)
J (kJ/m²)
700
600
500
400
300
200
100
0
0
0.5
1
1.5
2
2.5
3
.3.5
4
4.5
5
Delta a (mm)

Figure 13

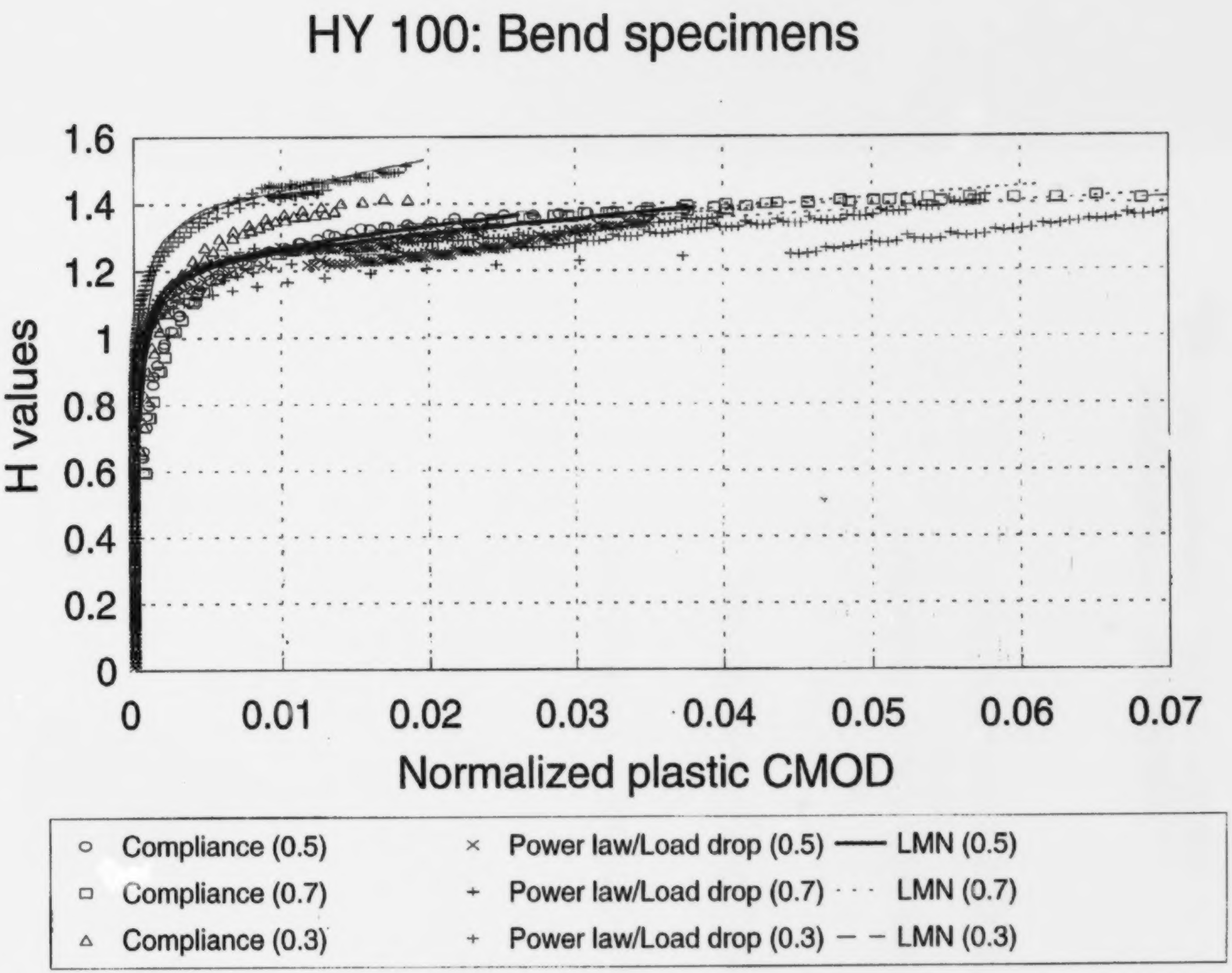
HY 100: Bend specimens
H values
1.6
1.4
1.2
1
0.8
0.6
0.4
0.2
0
0
0.01
0.02
0.03
0.04
0.05
0.06
0.07
Normalized plastic CMOD
○ Compliance (0.5)
□ Compliance (0.7)
△ Compliance (0.3)
× Power law/Load drop (0.5)
+ Power law/Load drop (0.7)
+ Power law/Load drop (0.3)
LMN (0.5)
LMN (0.7)
LMN (0.3)

Figure 14

#510311 ⑥

FRACTURE TOUGHNESS OF STEEL WELDMENTS AT HIGH LOADING RATES

by

M.N. Bassim* and J.R. Matthews**

* Department of Mechanical and Industrial Engineering, University of Manitoba, Winnipeg, Manitoba, Canada R3T 2N2

** Defence Research Establishment Atlantic, Dockyard Laboratory, FMO Halifax, Nova Scotia, Canada B3K 2XO

ABSTRACT

Fracture toughness for a number of submarine hull steels and steel weldments was determined at very high rates of loading, in excess of strain rates of 10^3 s^{-1}, corresponding to loading rates of $\dot{K}$ larger than 10^6 MPa $m^{1/2}$ s^{-1} using a modified version of a Split Hopkinson pressure bar equipped with a swing arm mechanism. The parameter J_{IC} was determined from measurement of the stretch zone width (SZW) using scanning electron microscopy on the fractured specimens. The impact tests were performed on compact tension specimens at -30°C. Concurrently, two studies, one involving impact testing at slower velocities using a drop-weight tester and the other relating the measured SZW to the fatigue prestraining, were conducted. It was found that, while prestraining has a significant effect on the SZW, there are no significant differences in the SZW between using a nine-point approach, (ASTM) and a three point approach for very high strain rates.

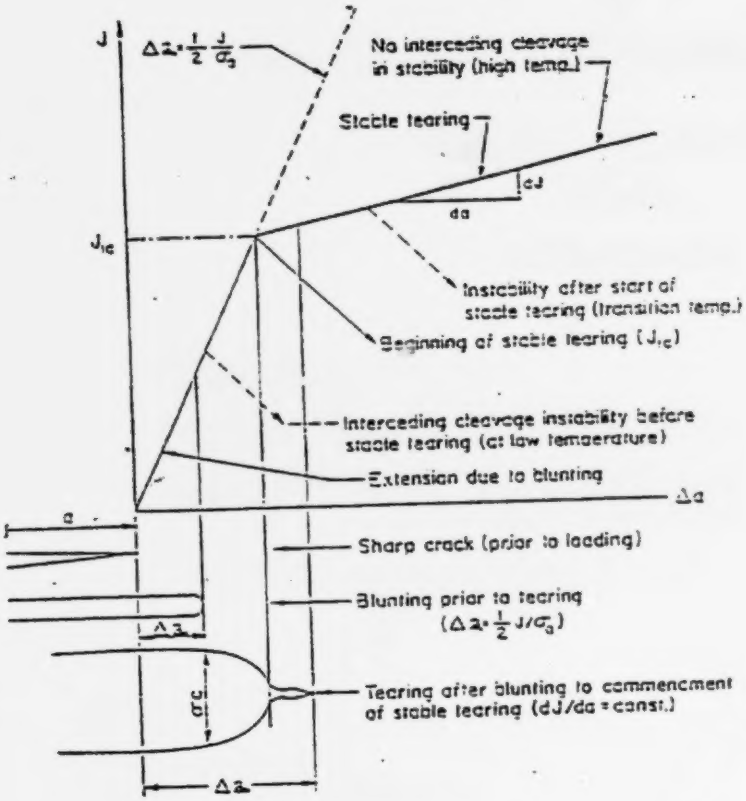
J
Δa = 1/2 J/σy
No interceding cleavage in stability (high temp.)
Stable tearing
dJ
da
J_Ic
Instability after start of stable tearing (transition temp.)
Beginning of stable tearing (J_Ic)
Interceding cleavage instability before stable tearing (at low temperature)
Extension due to blunting
Δa
a
Sharp crack (prior to loading)
Blunting prior to tearing
(Δa = 1/2 J/σy)
Δa
Tearing after blunting to commencment of stable tearing (dJ/da = const.)
Δa

Figure 1: The relationship between J integral and Δa.

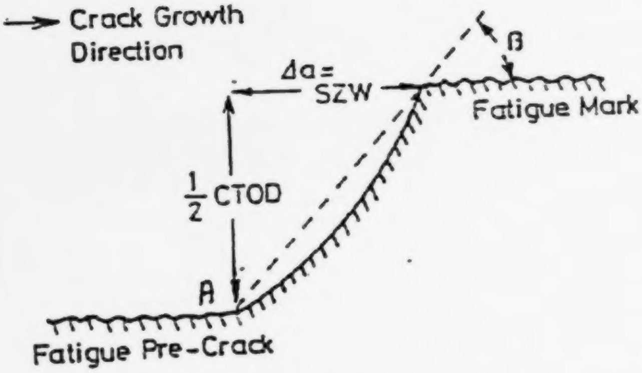
Crack Growth Direction
Δa = SZW
B
Fatigue Mark
1/2 CTOD
A
Fatigue Pre-Crack

Figure 2: Schematic section profile of stretch zone.

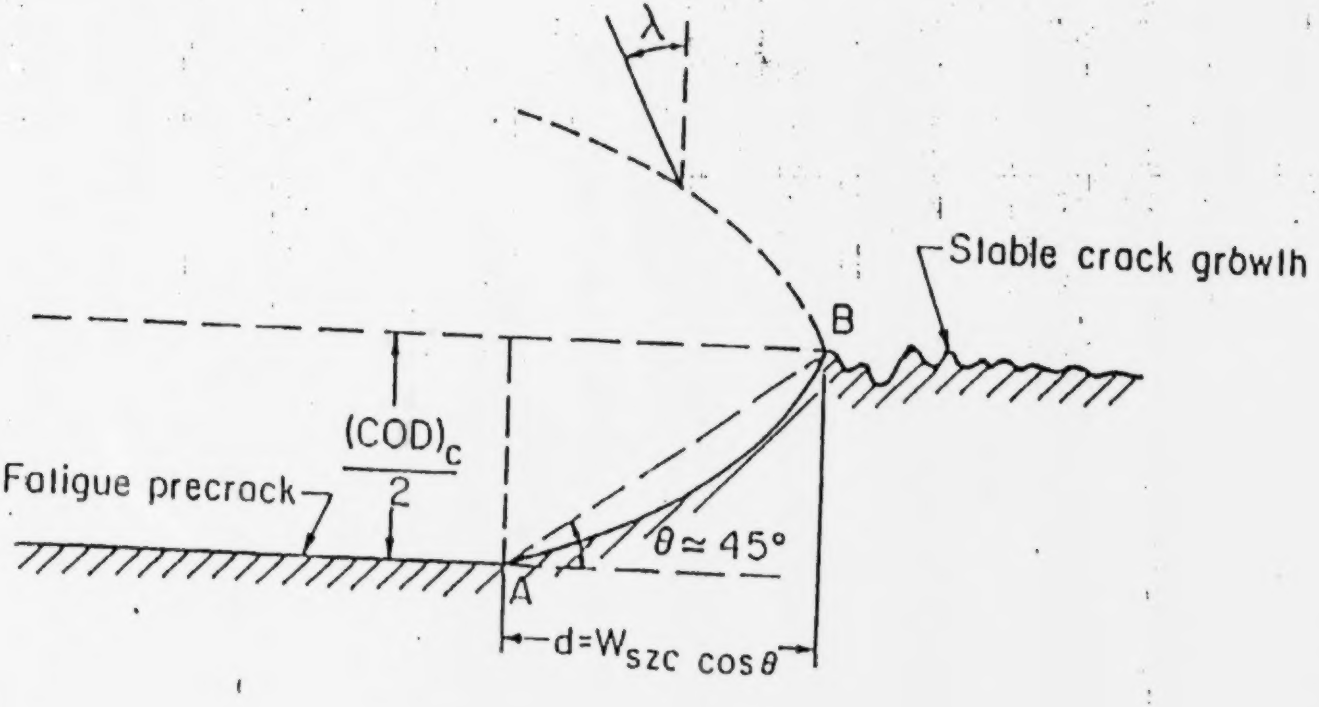
λ
B
Stable crack growth
$\frac{(COD)_c}{2}$
Fatigue precrack
$\theta \simeq 45°$
A
$d = W_{szc} \cos\theta$

FIG 1. CONCEPT OF THE STRETCH ZONE APPROACH

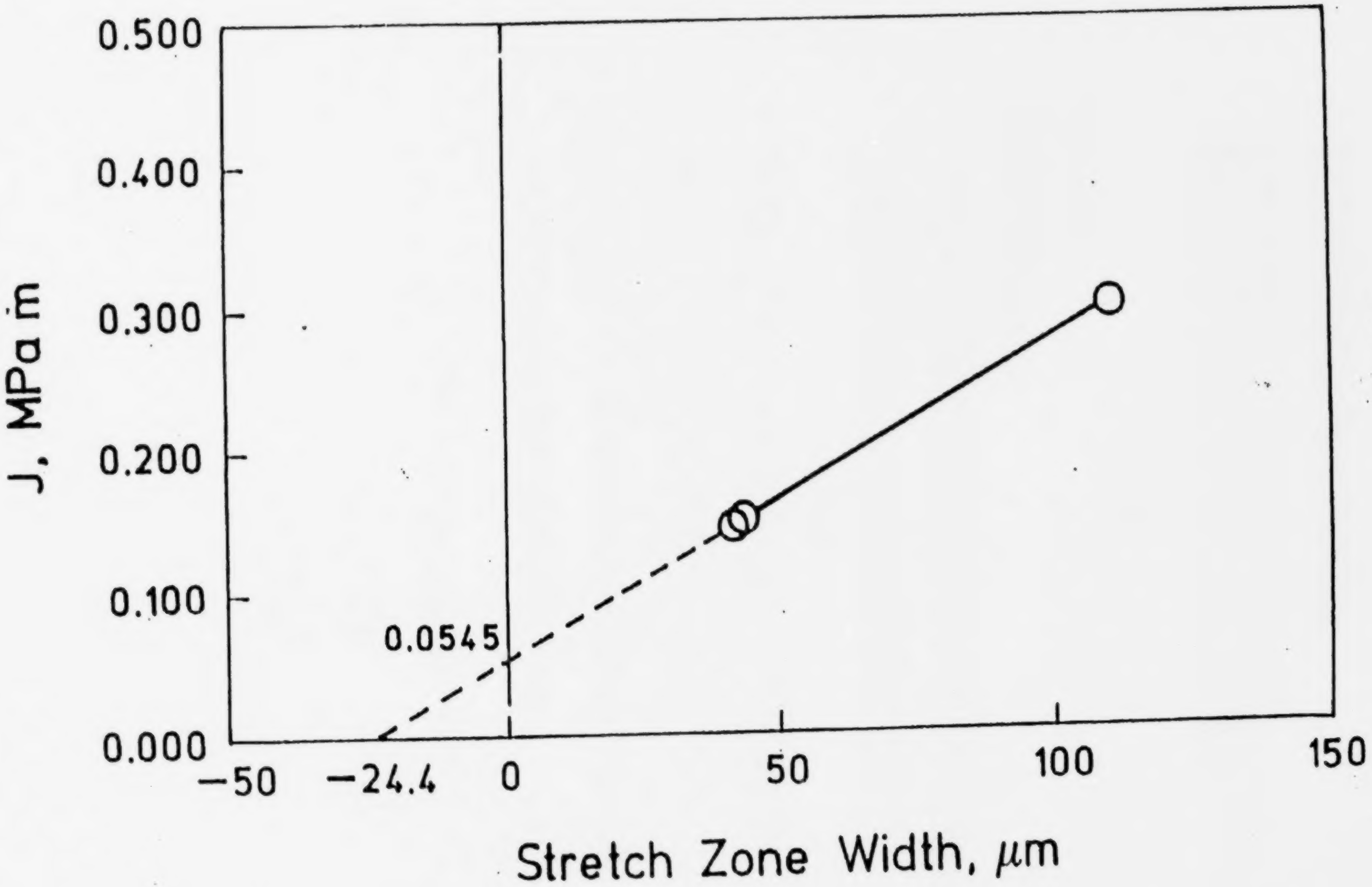
0.500
0.400
0.300
0.200
0.100
0.000
J, MPa m
0.0545
−50
−24.4
0
50
100
150
Stretch Zone Width, μm

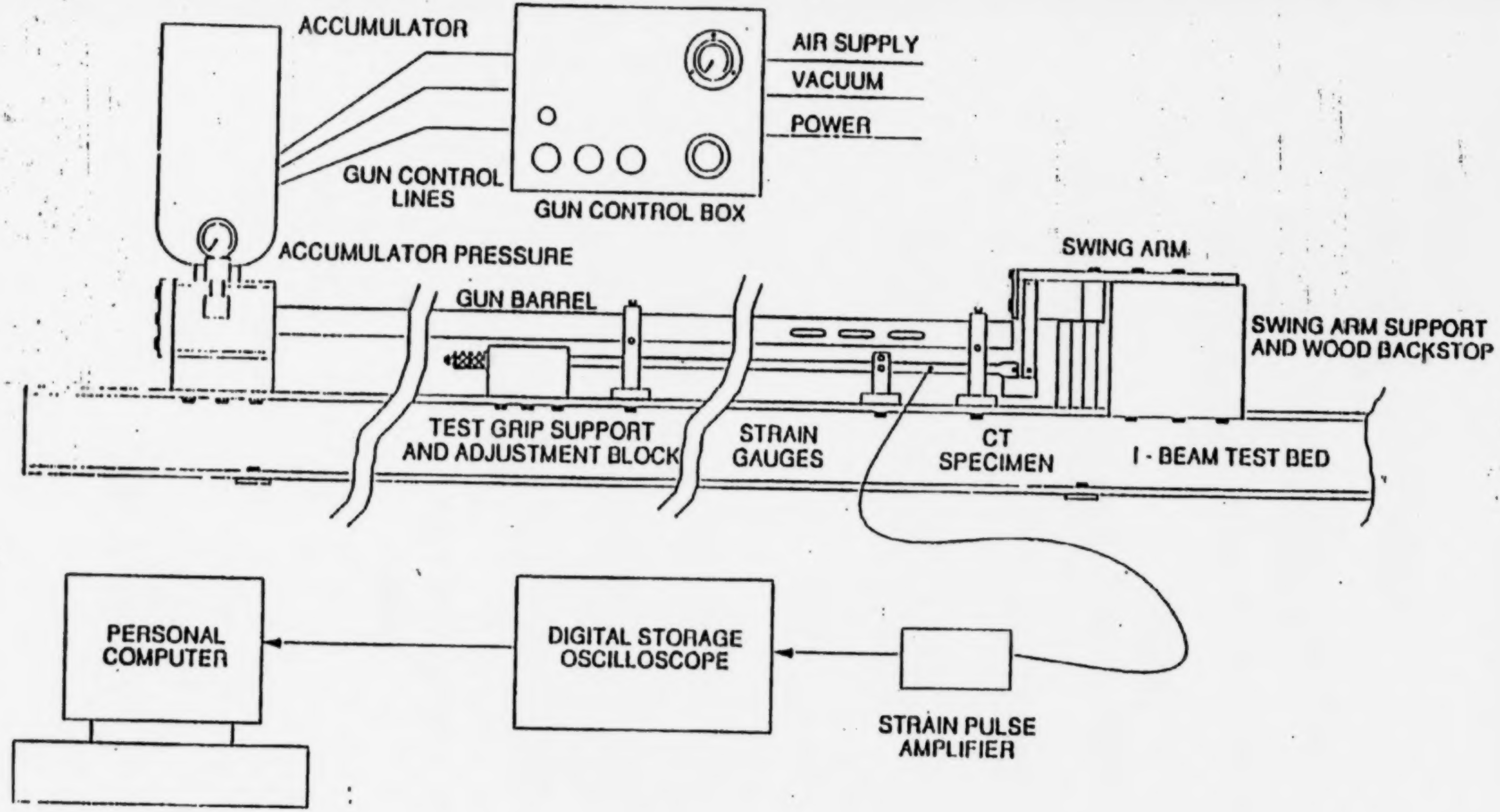
ACCUMULATOR
AIR SUPPLY
VACUUM
POWER
GUN CONTROL LINES
GUN CONTROL BOX
ACCUMULATOR PRESSURE
SWING ARM
GUN BARREL
SWING ARM SUPPORT AND WOOD BACKSTOP
TEST GRIP SUPPORT AND ADJUSTMENT BLOCK
STRAIN GAUGES
CT SPECIMEN
I - BEAM TEST BED
PERSONAL COMPUTER
DIGITAL STORAGE OSCILLOSCOPE
STRAIN PULSE AMPLIFIER

Fig 2

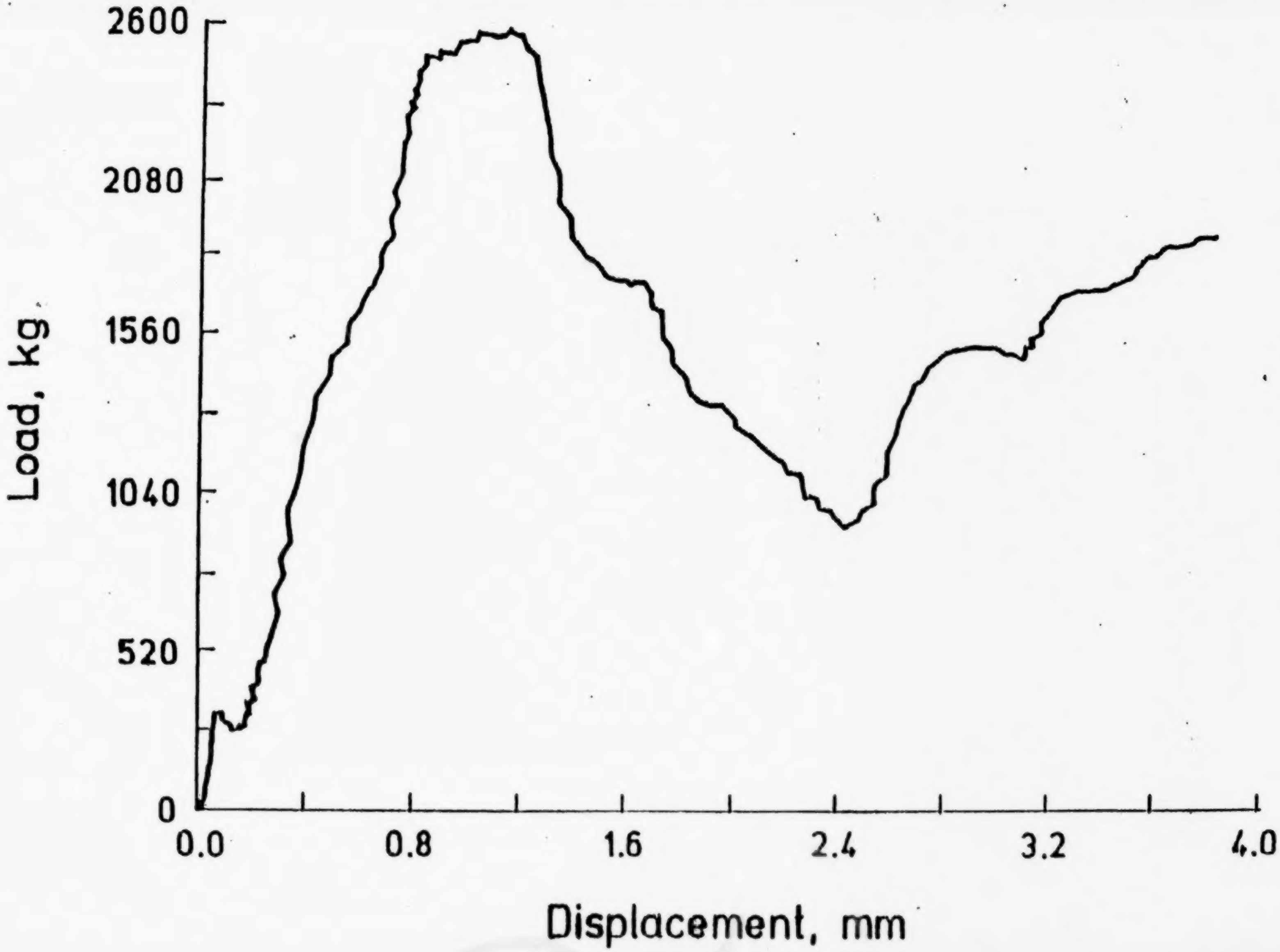
2600
2080
1560
1040
520
0
Load, kg
0.0
0.8
1.6
2.4
3.2
4.0
Displacement, mm

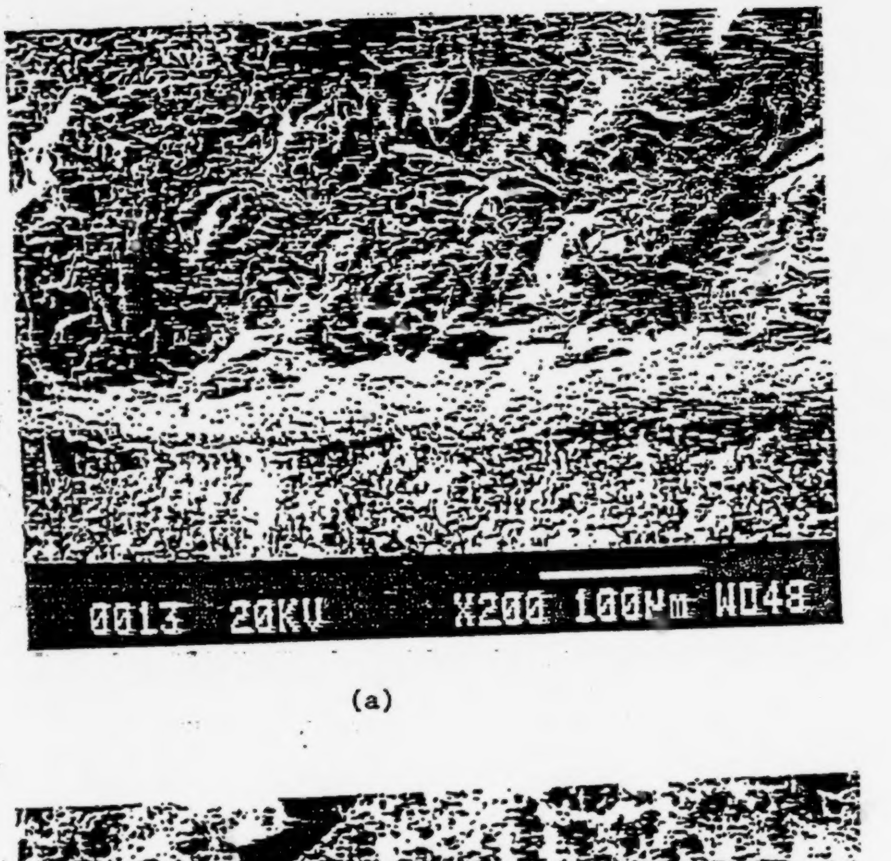
0013 20KV X200 100µm WD48
0026 20KV X50 100µm WD39

(a)

(b)

FIG.17: Stretch zone width micrographs of (a) QS1 and (b) SHB5 specimen

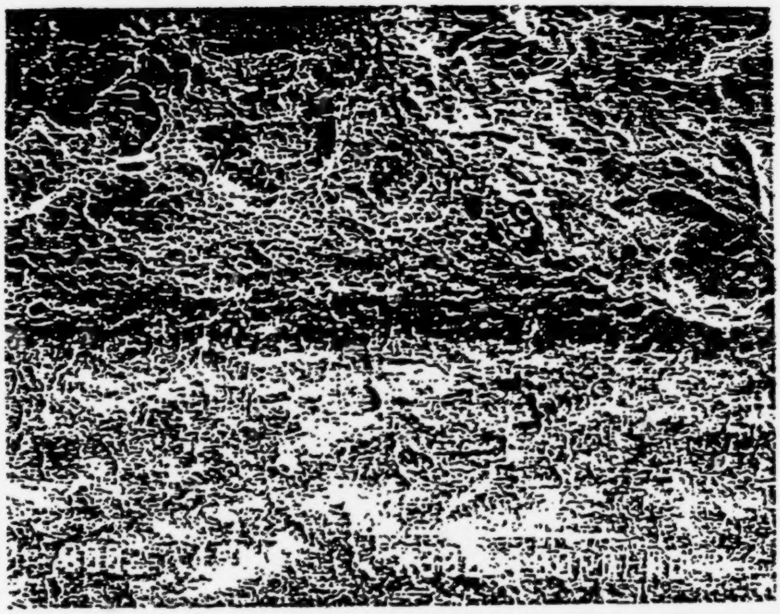

(a)

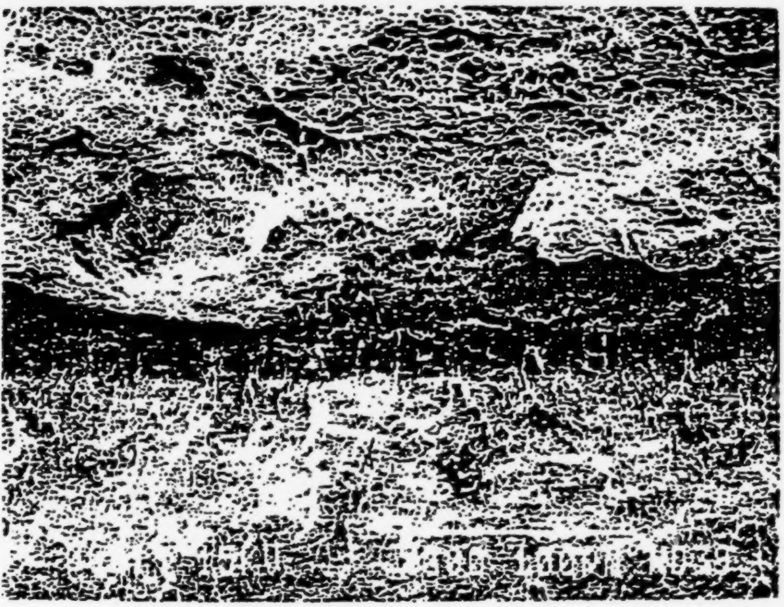

(b)

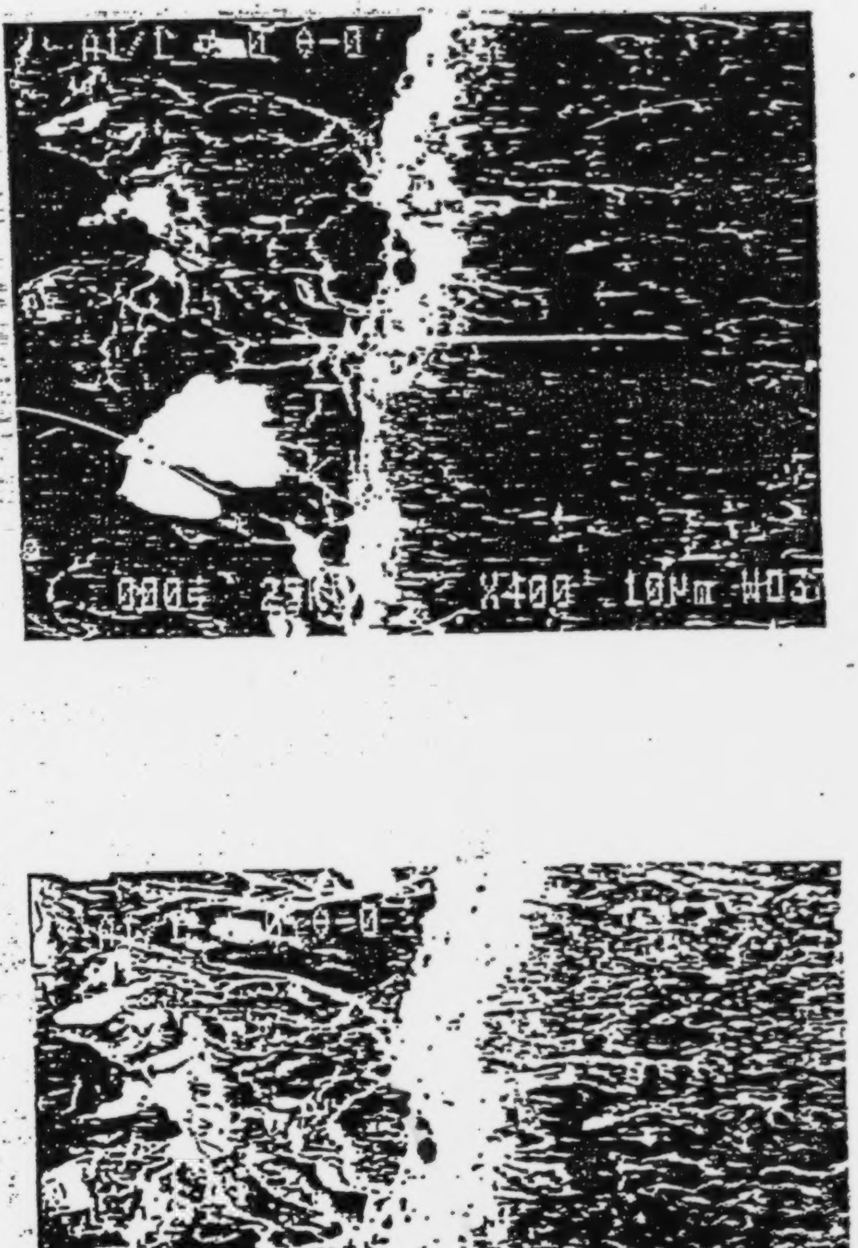

FIG. 16: Typical stretch zone micrographs.

Table 1

Average Stretch Zone Width
Using 9-point and 3-point Averaging Techniques

	Samples			
Positions	**SHB1**	**SHB2**	**SHB4**	**SHB6**
1	108	100	105	36
2	109	64	103	35
3	99	104	102	48
4	103	91	101	59
5	95	79	105	60
6	97	96	104	66
7	96	93	111	90
8	82	78	120	95
9	98	95	104	106
9-point average	98	88	106	66
3-point average	98	89	103	62

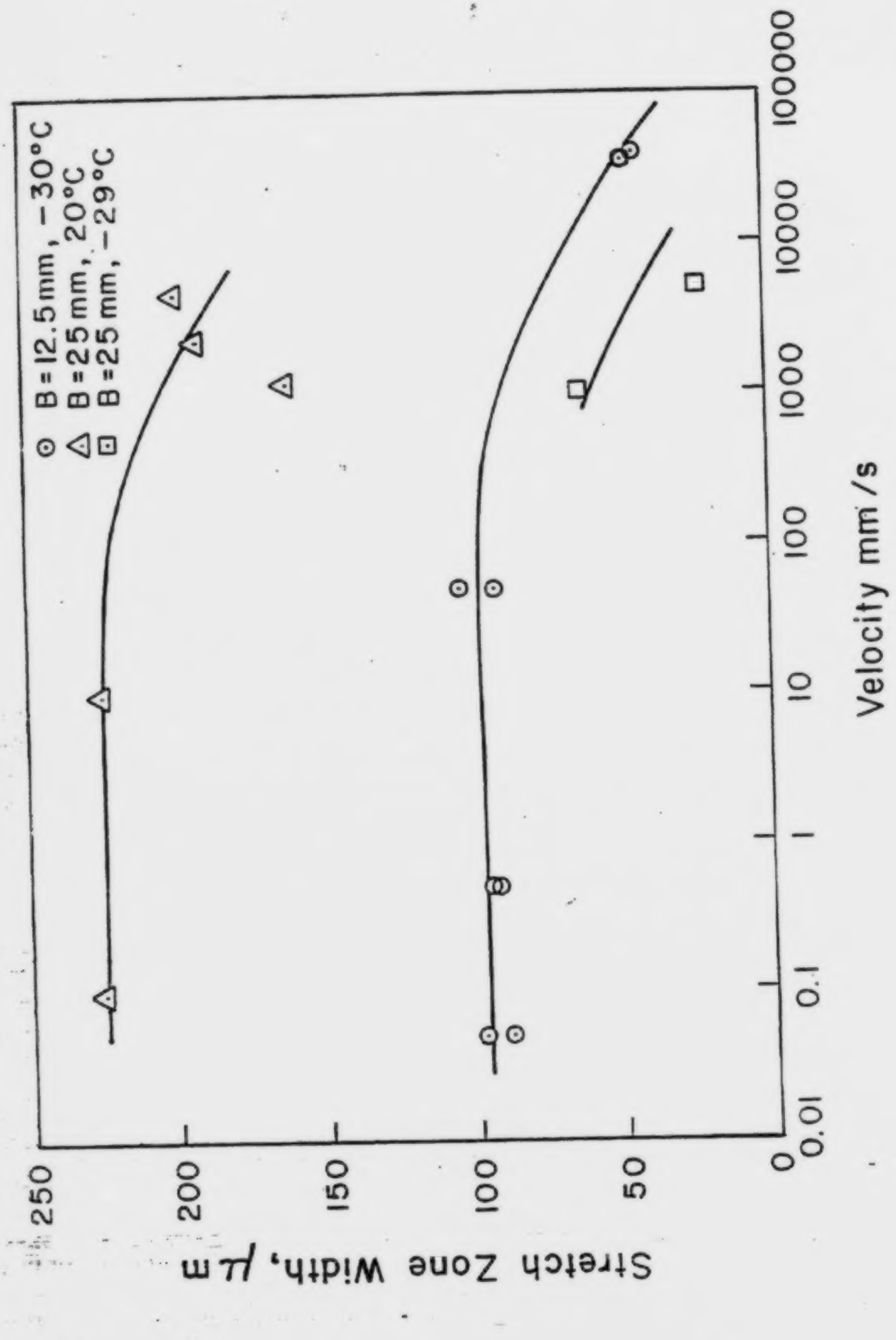
⊙ B = 12.5 mm, −30°C
△ B = 25 mm, 20°C
⊡ B = 25 mm, −29°C
Stretch Zone Width, μm
0
50
100
150
200
250
0.01
0.1
1
10
100
1000
10000
100000
Velocity mm/s

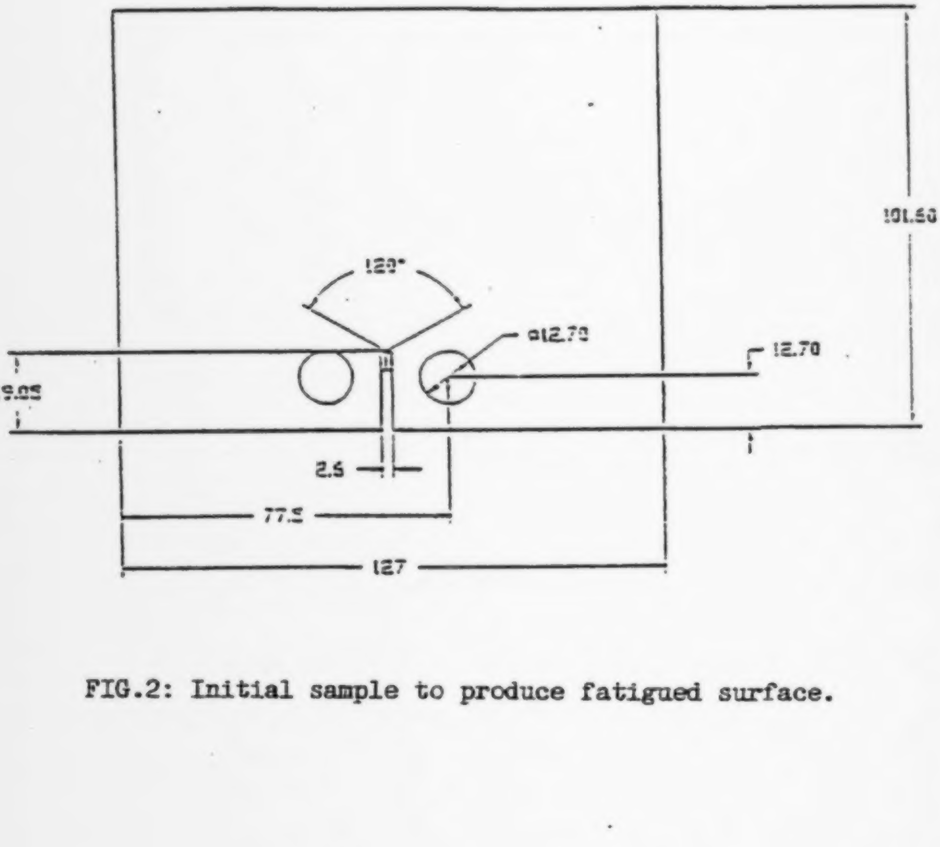
120°
⌀12.70
12.70
101.60
19.05
2.5
77.5
127

FIG.2: Initial sample to produce fatigued surface.

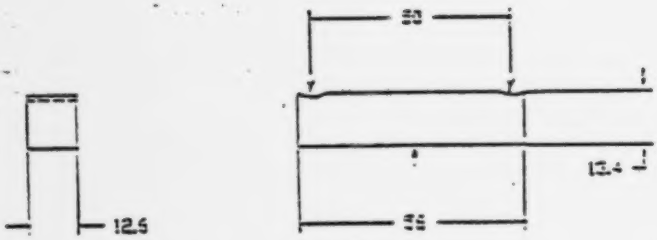

FIG.3: Final sample for bending test.

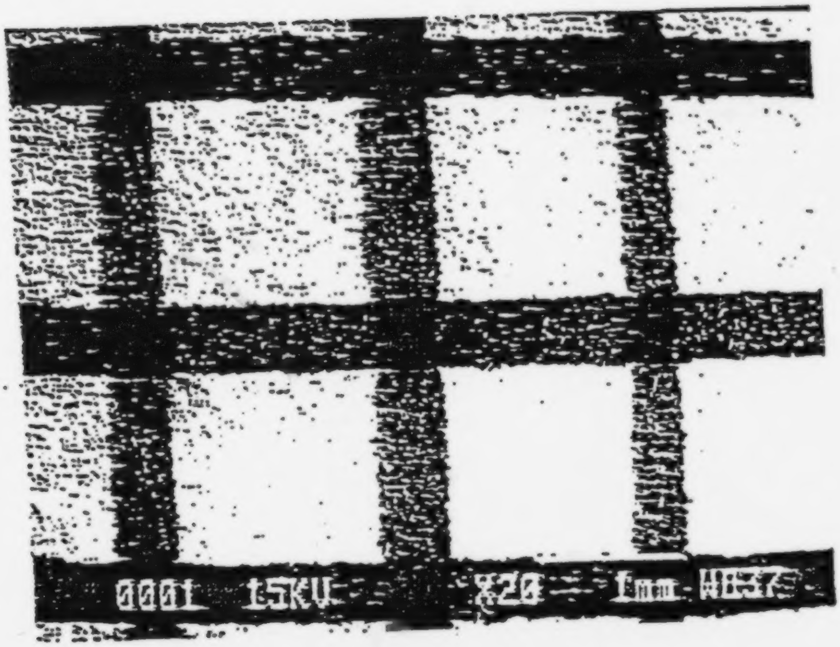
0001 15KV X20 1mm W037

FIG.4: Grids of the fatigued surface of the specimen.

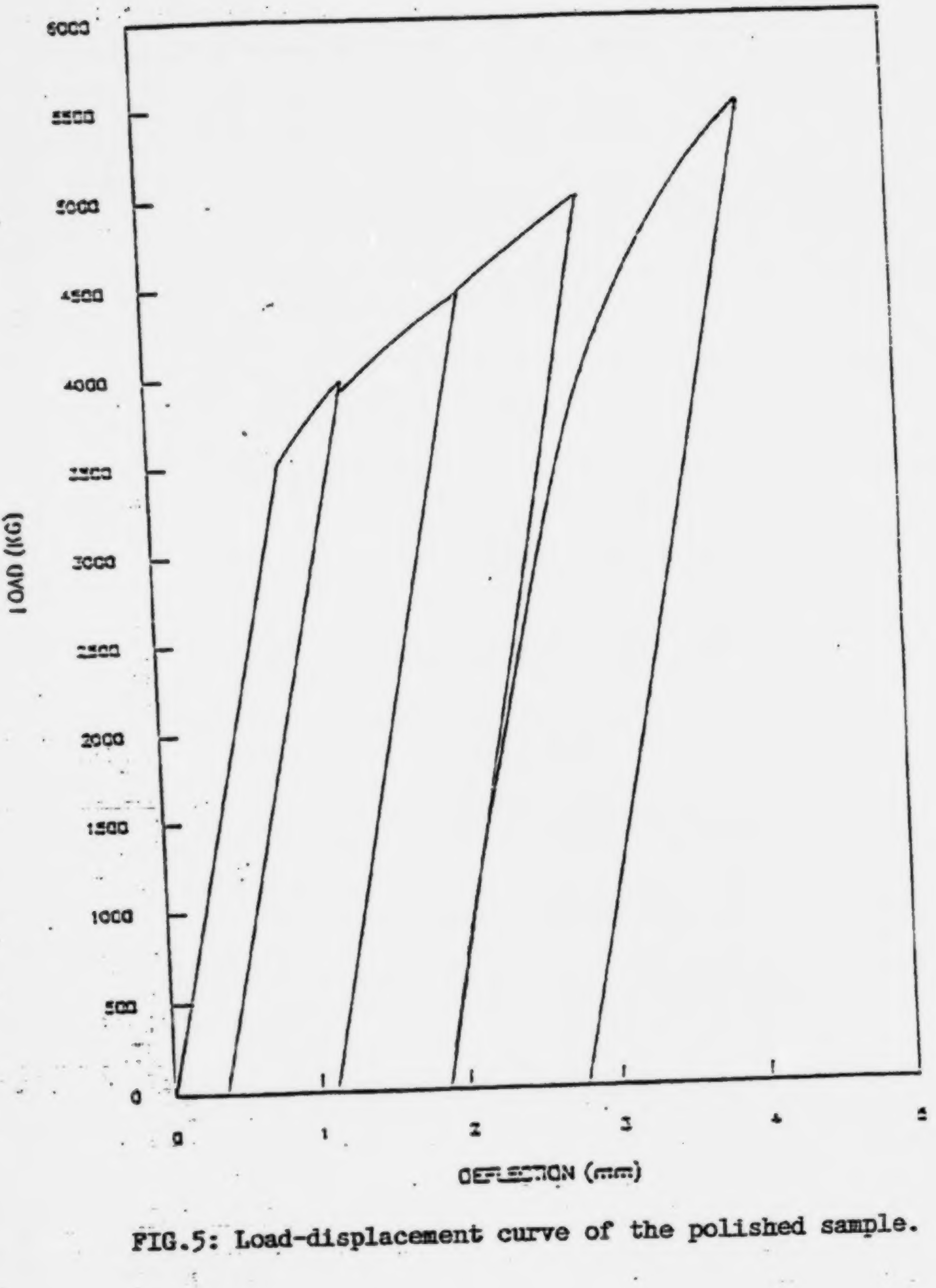

FIG.5: Load-displacement curve of the polished sample.

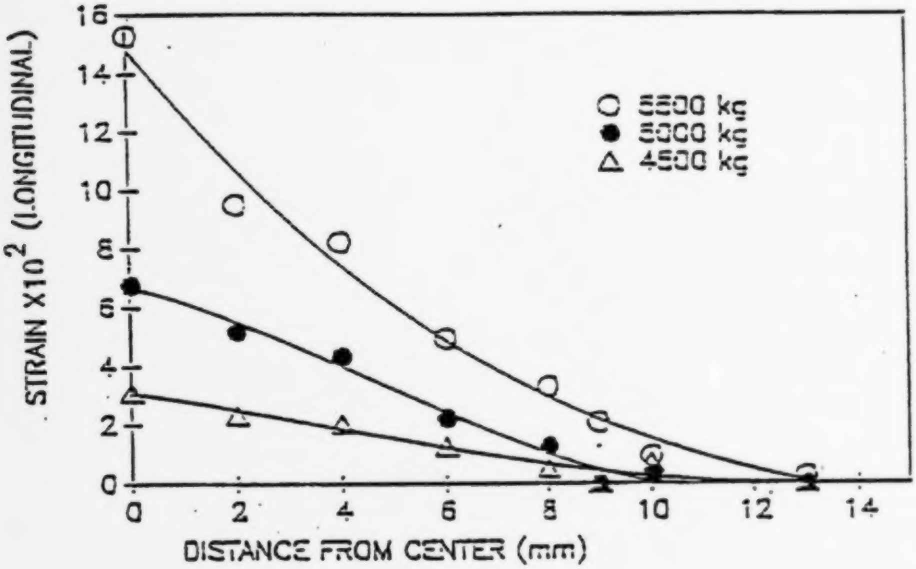

FIG.7: Longitudinal strain of the fatigued fractured sample.

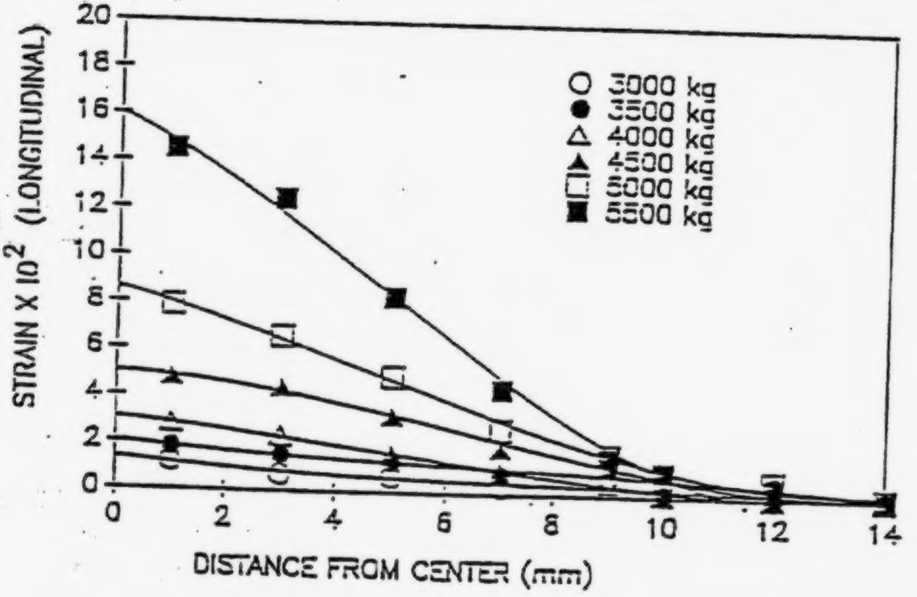

FIG.8: Longitudinal strain of the polished surface sample.

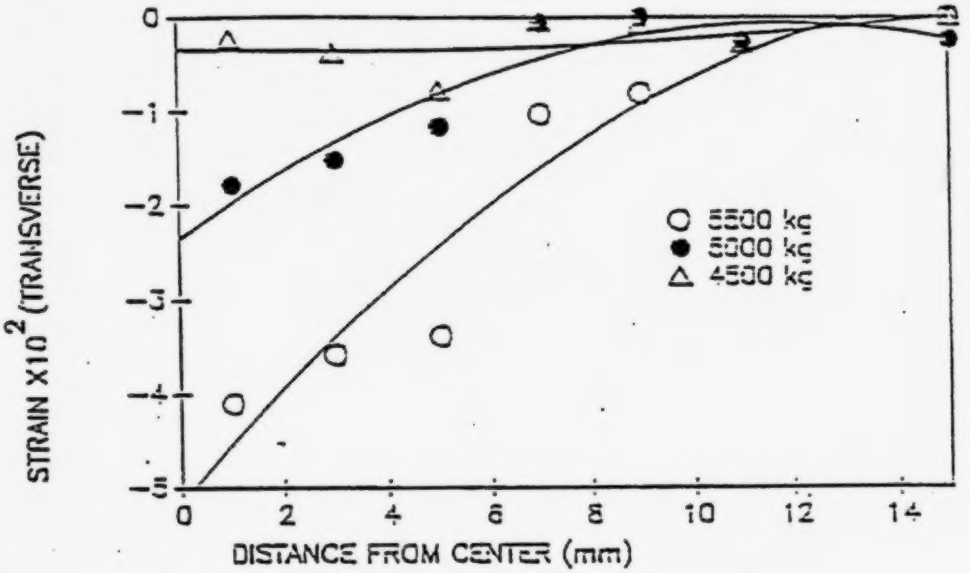

FIG.9: Transverse strain across the fatigue fractured surface.

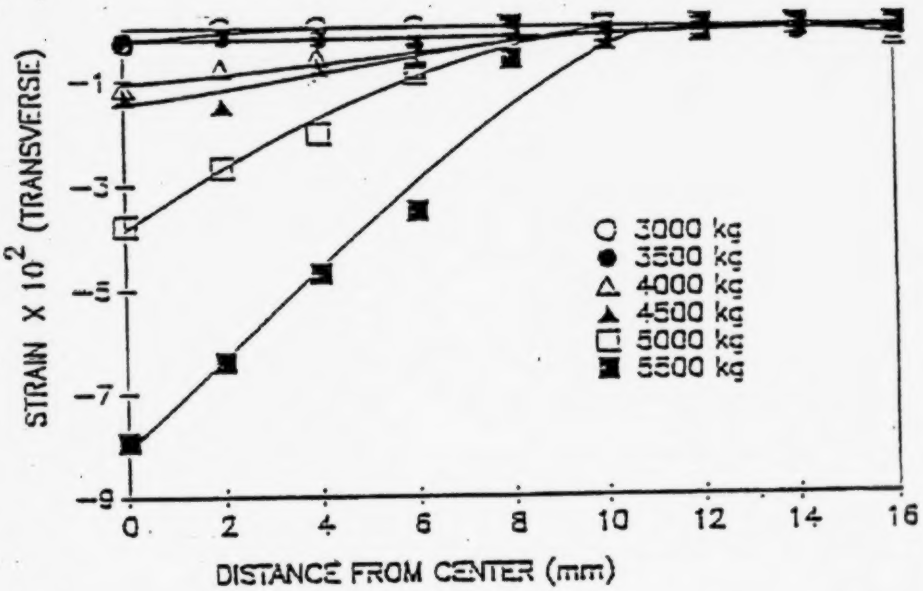

FIG.10: Transverse strain across the polished surface sample

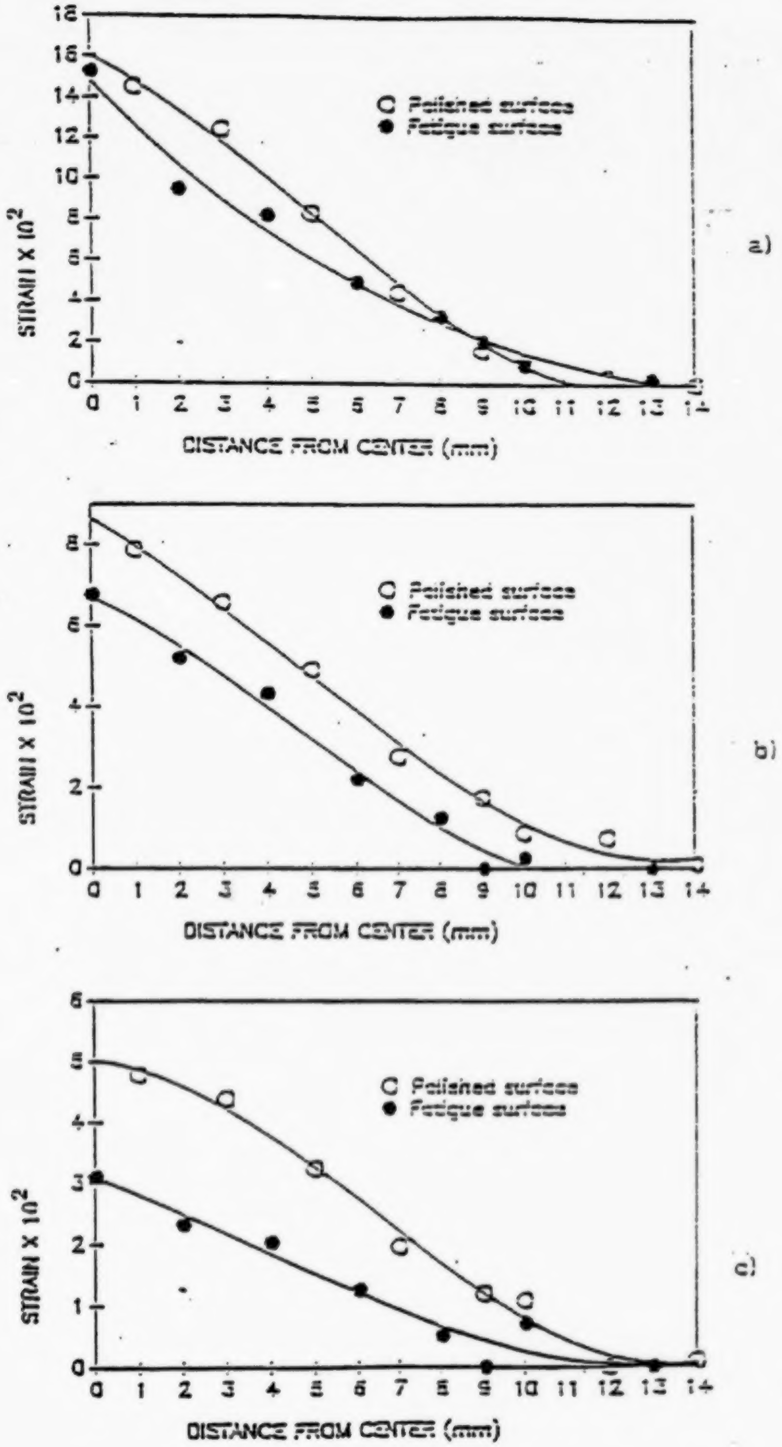

FIG.11: Comparison of the strains along the samples for two fatigue fractured and polished specimens for a) 4500 kg, b) 5000 kg and c) 5500 kg.

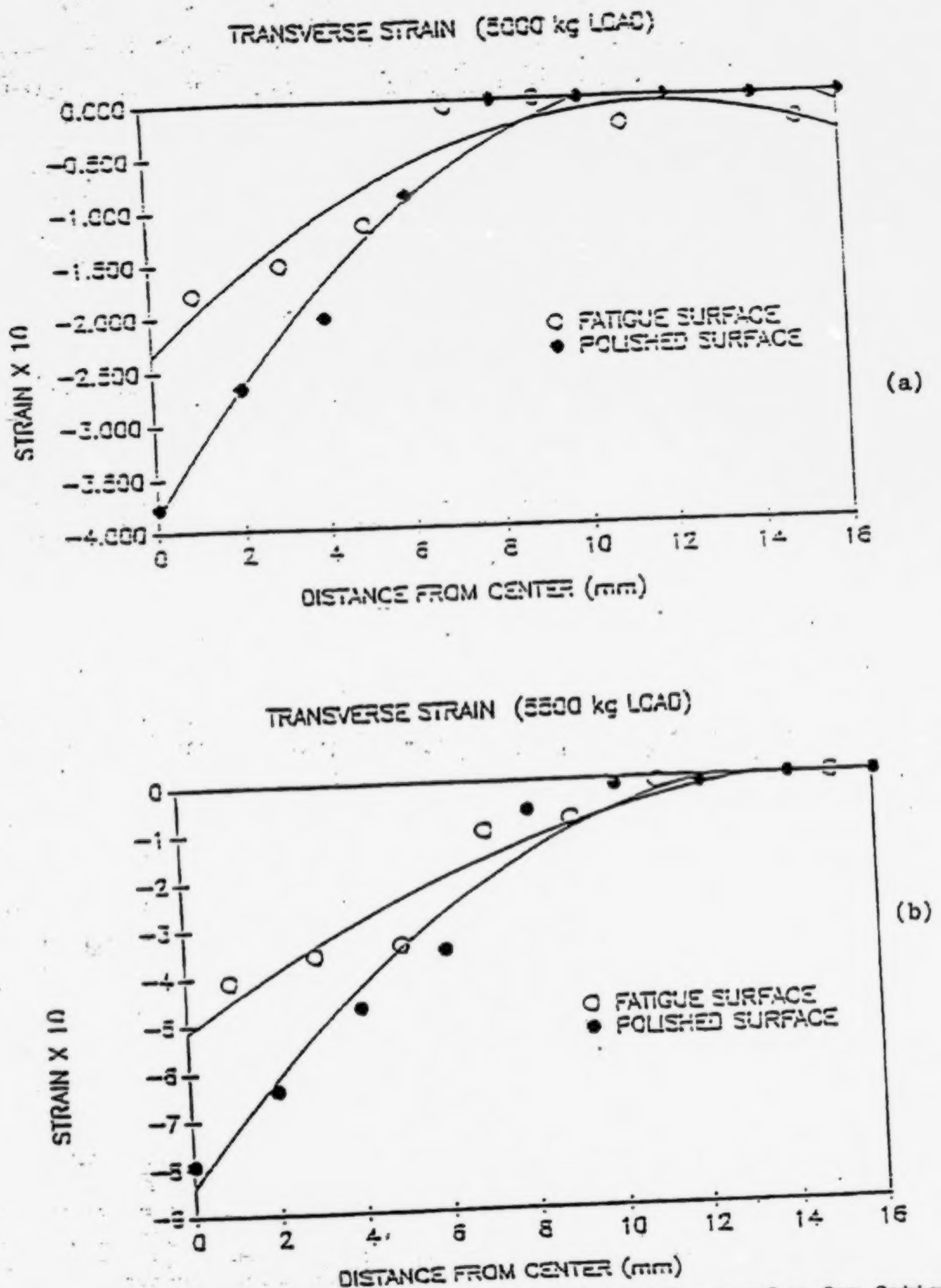

FIG.12: Comparison of the strains across the samples for fatigue fractured and polished surface specimens for a) 5000 kg. and b) 5500 kg.

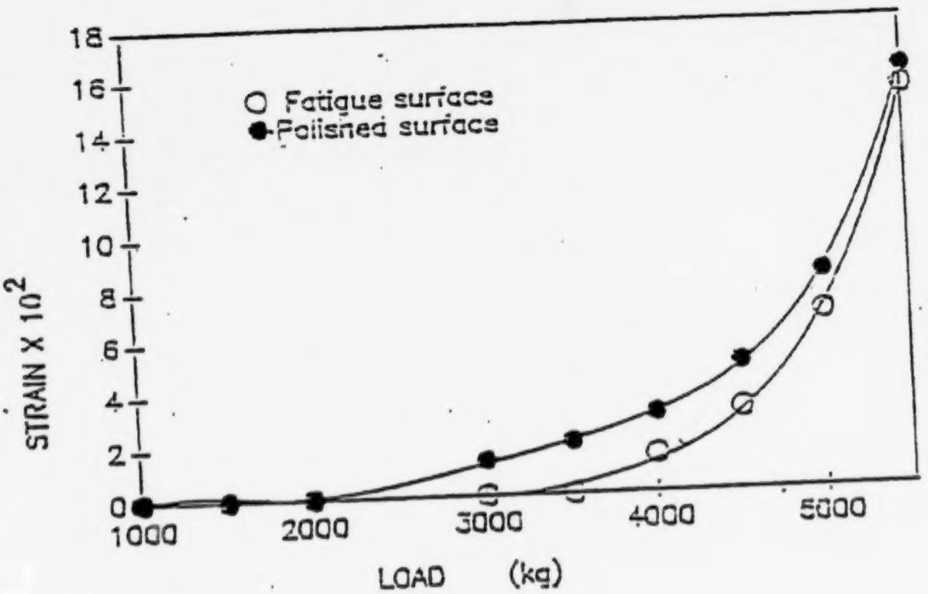

FIG. 13: Maximum longitudinal strain at the middle of the sample versus applied load.

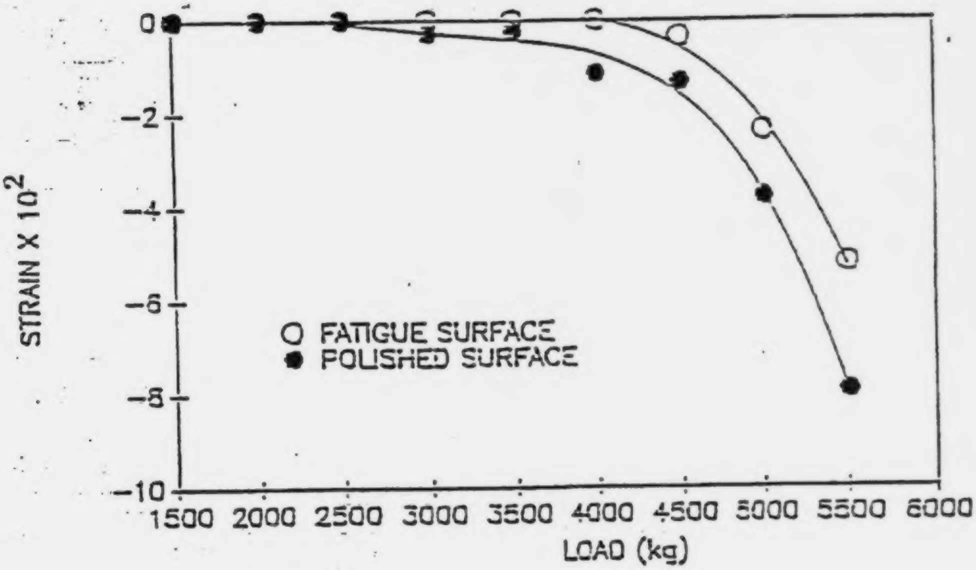

FIG. 14: Maximun transverse strain at the middle of the sample versus applied load.

Where k is the strength coefficient and n is the strain hardening coefficient. Assuming that the stresses are the same for both fatigue surfaced and polished surfaced specimens and combining the experimental results for strains with calculated stresses, the bending tensile stress versus strain for both specimens is given in Figure 8. From this graph, σ_{y2} i.e. the yield point on the fatigue fractured surface, can be estimated. Since the stretch zone deformation is also a fatigue surface, the starting stress for deformation of this zone should also be the same. In other words, the stretch zone starting point occurs when the stress reaches σ_{y2}.

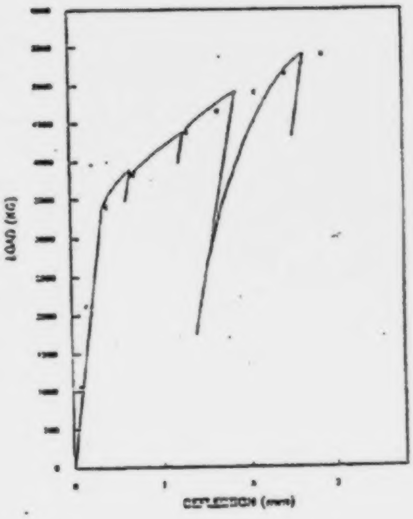

Fig. 6: Load- displacement curve of the polished specimen.

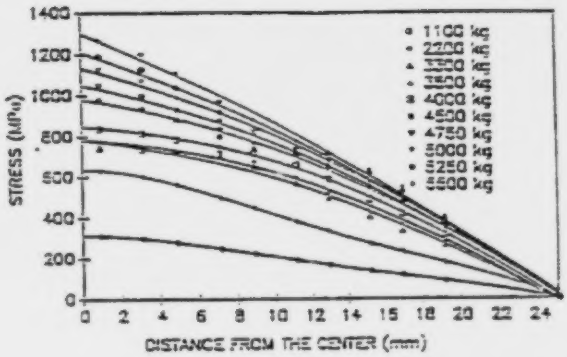

Fig. 7: Calculated Stress along the specimen by Finite element program.

In high strain rate experiments by Hyatt and Matthews (1990) the stretch zone width was measured for the J values below the critical value required for stable cracking. Figure 9 shows the linear function of the stretch zone width with J value below J_{IC}. The crack blunting theory assumes no deformation around the crack prior to loading the specimen. However Figure 9 shows that J is not zero at zero stretch zone width and the area around the crack tip is strain hardened prior to loading. The results agree that about 15% higher stress is required to start the deformation on a fatigue surface as shown in Figure 8.

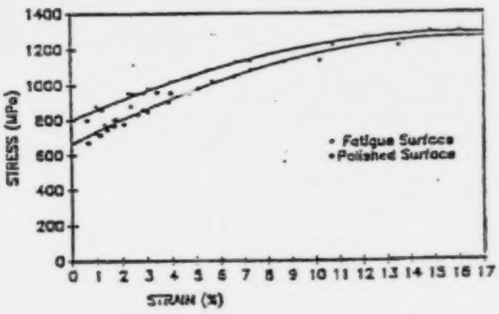

Fig. 8: Stress-Strain Curves for two fatigue surfaced and polished specimens resulted from bending test.

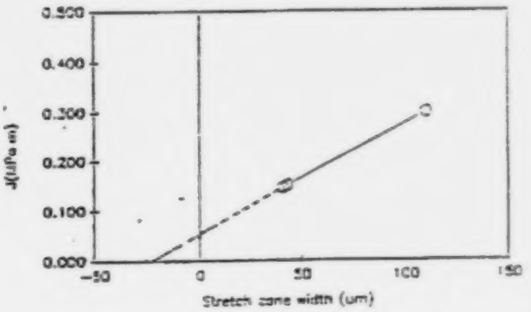

Fig. 9: Variation of stretch zone width with J.

Conclusions

The program showed that there is considerable merit in using the stretch zone width measurement as a procedure for evaluation of the fracture toughness of ductile submarine hull steels particularly at high loading rates where it is not feasible to perform compliance measurements. A better understanding of the Stretch Zone was obtained by studying its deformation characteristics and the role of fatigue predeformation on its development.

#510312 ⑦

APPLICATION OF VERY LOW YIELD STRENGTH CONSUMABLES IN THE ROOT PASS OF WELDMENTS TO PREVENT PREHEATING

J. Vuik[1]), J.C. van Wortel[1]), C. van Sevenhoven[2])

[1]) TNO Institute of Production and Logistics Research
P.O. Box 541, 7300 AM APELDOORN, The NETHERLANDS.
[2]) Royal Netherlands Navy
P.O. Box 20702, 2500 ES The HAGUE, The NETHERLANDS.

ABSTRACT

One of the problems that arise when welding structural steels, with a yield strength of 355 N/mm^2 and above, is the possible occurrance of cold cracking.
The development of modern steel types has reduced this risk of cold cracking, and the availability of very low hydrogen electrodes reduced it even further. Hydrogen levels in the deposited weld metal of ≤3 ml/100 g are possible nowadays. When packed in vacuum packages, or sealed tins, the hydrogen content of these electrodes can be guaranteed up to the moment the welding operation is to be carried out.

These developments give the contractors the option to weld structural steels without preheating up to a thickness and chemical composition that would have been impossible ten years ago.
Still, despite all those developments, increasing thickness (restraint) or yield strength of the materials to be welded, makes preheating necessary again. This is also the case for repair welding of older constructional steels, with the corresponding higher carbon contents and/or carbon equivalents.

For the situations where preheating still can't be omitted, the Dutch TNO Institute of Production and Logistics Research has initiated the development of low hydrogen SMAW electrodes with a very low yield strength. By using these electrodes for the penetration bead, where the risk for cold cracking is the most severe, welds without cold cracks can be obtained without preheating where otherwise preheat temperatures up to 100°C would have been required.
In order to obtain a weld that (as a whole) overmatches the base material, the low yield strength electrode should only be used in the root layer. Filling of the bevel takes place with consumables designed for the strength level of the base material that is welded.

In this paper, the results will be discussed of a research programme in which the limits of welding without preheating have been studied. In the first part, information will be given on experiments in which the influence of chemical composition of the base material and the weld metal hydrogen content on cold cracking is established. In the second part, the application of very low yield strength electrodes in the root run is discussed.

INFLUENCE OF CHEMICAL COMPOSITION OF THE BASE MATERIAL AND THE WELD METAL HYDROGEN CONTENT ON COLD CRACKING

In order to establish the effect of the chemical composition of the base material and the weld metal hydrogen content on the susceptibility for cold cracking, standard Tekken tests have been performed on seven commercially available FeE355 steels (*Ref. 1*).
These steels vary in chemical composition, and are representative for the steels that are available on the market nowadays. The relevant data for these steels are given in Table 1 (Steels nr. 1 - 7).

The Tekken tests (sloped-Y, 2 mm slit, 60° opening angle, see Figure 1) have been welded with a 3.2 mm E7018 SMAW electrode, welded with a heat-input of 11 kJ/cm. This E7018 electrode is delivered in a vacuum package, as is quite normal nowadays in the Netherlands. A number of these vacuum packages/sealed tins are shown in Figure 2.
By using this vacuum package (some manufacturers have sealed tins instead of vacuum packages) the electrodes are protected against moisture absorption from the atmosphere. In this way, the manufacturer can guarantee the condition of the electrodes (= the hydrogen content of the weld metal) up to the moment they are used. This guarantee is of course only valid in a restricted range of atmospheric conditions, as in literature (*Ref. 1, 2 and 3*) it has been proven that the moisture content of the atmosphere during welding influences the hydrogen content of the deposited weld metal quite considerably.
Ref. 4 shows that the hydrogen content of the weld metal increases by 1 ml/100 g per 10 g/m^3 moisture in the atmosphere. As in Europe, the climate is such that the moisture content in the atmosphere can vary between 1 and 20 g/m^3, this means that, in principle, the hydrogen content during production welding can be 1 - 2 ml/100 g higher than during testing of the electrodes in a laboratory.

In order to vary the hydrogen content of the electrodes used for performing the cold cracking tests, part of the vacuum packed electrodes are exposed to humid air. In this way, it has been possible to create one batch of electrodes with an increasing hydrogen content: 2.5 - 3 ml/100 g, 5 - 5.5 ml/100 g and 9.5 - 11 ml/100 g.

The minimum required preheat temperatures of the standard Tekken tests have been plotted versus the CEN value in Figure 3. This CEN value is calculated from the chemical composition, and indicates the susceptibility to cold cracking. The CEN value is calculated by:

$$\text{CEN} = C + A(C)*(Si/24 + Mn/6 + Cu/15 + Ni/20 + (Cr + Mo + Nb + V)/5 + 5*B)$$

$$A(C) = 0.75 + 0.25*\tanh(20*(C - 0.12))$$

The results have been plotted versus the Pcm factor (Pcm = C + Si/30 + Mn/20 + Cu/20 + Ni/60 + Cr/20 + Mo/15 + V/10 + 5B) and the carbon equivalent (CE (Si) = C + Mn/6 + (Cr + Mo + V)/5 + (Ni + Cu)/15 + Si/24) as well: the Pcm factor gives more or less the same correlation as the CEN value, but the correlation between the preheat temperature and the CE is less good. This is in accordance with the fact that the Pcm factor and the CEN value are based on cold cracking tests (*Ref. 5 and 6*), whereas the CE is a characterization of the hardenability of the steel rather than its susceptibility for cold cracking (*Ref. 7*). The CE can be used to characterize the cold cracking susceptibility of constructional steels with a rather high carbon content: 0.15 - 0.25%.

The effect of reducing the hydrogen level from 5 to 3 ml/100 g proves to be rather pronounced. A hydrogen level of 3 ml/100 g enables the fabricator to weld 50 mm FeE355 steel without preheating as long as the CEN value is less than 0.31 (Pcm less than 0.20, %C less than 0.11). In the range from CEN = 0.31 to 0.36 (Pcm = 0.20 to 0.23) the difference in preheat temperature for a level of 5 and 3 ml/100 g amounts to approximately 50 - 75°C.

Recent literature supports the fact that a decrease in preheat temperature can be achieved by using very low hydrogen consumables (*Ref. 8*). However, the decrease in preheat temperature that has been reported in this document was less than was found in *Ref. 1*. A possible explanation for this difference is that *Ref. 8* takes into account a wider range of steel types.

In practice, a lot of K- and double V-beveled joints are used for welding materials with a thickness of 40 - 50 mm. In order to determine whether such bevels require preheat levels that systematically differ from the results obtained with standard Tekken tests, Tekken tests have been performed with an adapted bevel. Both K- and double V-bevels have been tested in a Tekken specimen, the root gap of both non-standard Tekken tests amounted to 4 mm. These non-standard Tekken tests have been welded at a heat-input of approx. 22 kJ/cm, which is quite normal for welding the penetration bead in a K- or double V-bevel.

The results of Tekken tests with a standard sloped-Y, a K- and a double V-bevel, performed on one specific steel (Steel nr. 7 in table 1), are shown in Figure 4.
From the results it appears that there is quite a difference between the behaviour of a sloped-Y Tekken test, and the K- or double V-bevel Tekken tests.

The K-bevel welded in the 1G position, is known to be very sensitive to poor wetting on the straight side of the bevel. It appeared that not only the K-bevel, but the double V-bevel as well suffered from this poor wetting. This poor wetting acts as a stress raiser, and attributes to the increase of the susceptibility to cold cracking. This effect of a stress raiser on cold cracking susceptibility is mentioned in *Ref. 9*, too.

These measured preheat temperatures with the K- and double V-bevel Tekken tests are not in agreement with the claim of Yurioka (*Ref. 10*), who says that the preheat temperatures that are found in sloped-Y Tekken tests should be decreased by 75°C in order to find the preheat temperature to be used in practice.

The main conclusion from these experiments is that for steels with a low carbon content and Pcm or CEN value, the reduction of the hydrogen content of the weld metal from 5 to 3 ml/100 g has a very large influence on the required preheat temperatures. At a hydrogen level of 3 ml/100 g, 50 mm thick FeE355 steels up to a CEN = 0.31 (Pcm = 0.20) can be welded without preheating, even in very high restraint conditions. However, Tekken tests with K- and double-V bevels revealed that these joint types are more susceptible to cold cracking than would be predicted from the standard Tekken tests.

APPLICATION OF VERY LOW YIELD STRENGTH CONSUMABLES IN THE ROOT PASS

Cold cracking susceptibility

From the results with the standard Tekken tests, and the K- and double V-bevel Tekken tests, it appears that in practice there are several situations where preheating cannot be avoided. The reason for this preheating can either be the composition of the base material, the hydrogen content of the weld metal, or the fact that the K- or double V-joints, that are applied very often in practice, have been shown to be more susceptible to cold cracking than would be predicted from the standard Tekken tests.

In order to create the maximum opportunities for welding without preheating, in *Ref. 1* the possibility of using specially developed very low yield strength electrodes for the penetration bead has been studied. These very low yield strength electrodes (low yield electrodes in the remaining part of this paper) lead to a less high stress level in the weld metal and the HAZ, and hence could contribute to a decrease of the risk of cold cracking.

The basic idea behind the application of these low yield electrodes (Re of the undiluted weld metal amounts to approx. 380 - 400 N/mm²) is that these electrodes are used for the penetration bead, where the risk for cold cracking is the highest. Matching electrodes are used to fill the bevel, so that the weldment as a whole overmatches the base material.

Preliminary results of K-bevel Tekken tests welded with these low strength electrodes show that a very large reduction of the required preheat temperature can be achieved. Figure 5 shows that in comparison with the standard E7018 electrode, one type of low yield electrodes decreases the preheat temperature with approx. 75 - 100°C, whereas another type of low yield electrodes allows for welding without preheating at all.
Although it is recognized that a K-bevel Tekken test is a very severe test, which leads to higher preheat temperatures than would be necessary for the majority of the joints to be welded in practice, the observed decrease in preheat temperature, when using the very low yield strength electrodes for the penetration bead, indicates the large reduction of the susceptibility to cold cracking.

In order to determine whether these low yield/very low hydrogen electrodes in the penetration bead of thick walled structures could be used to avoid preheating, a series of experiments have been performed in a research project for the Royal Netherlands Navy (*Ref. 11*).

The low yield electrodes have been tested in two steels: FeE355 with a very high carbon content (0.19 %) and FeE690. The data of these steels are given in Table 1 (Steels nr. 8 and 9).

The K-bevel Tekken tests revealed that the cold cracking susceptibility of the high carbon FeE355 was higher than of this specific FeE690, when both steels were welded with matching electrodes (140°C versus 95°C). The FeE355 and FeE690 steel were welded with respectively an E7018 and an E11018 electrode. Both electrodes had a hydrogen content less than 3 ml/100 g.
In Table 2 the minimum preheat temperatures are given for Tekken tests with several low yield electrodes. These results confirm the results presented in Figure 5, including the different susceptibility to cold cracking when different types of low yield electrodes were used for welding the penetration bead.

The yield strength of the low yield electrodes was approximately 380 - 400 N/mm^2 in the undiluted condition (DIN 1913 test, *Ref. 12*). The yield strength of the undiluted weld metal is clearly less than the yield strength of FeE690, but of the same order of magnitude as for FeE355.

Measurement of the actual yield strength of the weld metal of the penetration bead revealed that due to dilution with the parent plate metal, the yield strength has increased to a level of approximately 430 - 550 N/mm^2. These measurements have been performed on 2.5 mm diameter tensile specimens, taken from the test weld in K-bevel Tekken tests. The actual yield and tensile strength of the different Tekken test welds are incorporated in Table 2, together with the actual values of CE, Pcm and CEN values for the weld metals. The average chemical composition of the undiluted very low yield strength weld metal is: 0.02 - 0.03%C, 0.2 - 0.4%Mn, 0.15 - 0.35%Si, ≤ 0.5%Ni (not mentioned in the table).

From these results it can be seen that an increased level of alloying elements in the weld metal of the penetration bead, leads to both a higher yield strength and preheat temperature. For both FeE355 and FeE690, the relation between the CEN value and the tensile properties is given in Figure 6 and 7. The relation between the CEN value and the required preheat temperatures is shown in Figure 8 (Pcm and CE give more or less comparable figures).
A striking detail is that when welded in FeE690, the matching E11018 electrode required a preheat temperature 15°C less than the E7018 electrode.

Mechanical properties

In both steels, two test welds have been produced: one weld with a low yield penetreation bead and first filling bead on the reverse side, and another weld with matching electrodes in the entire weld. It must be emphasized that the low yield electrodes were only used for the penetration bead (and the first filling bead on the reverse side). Due to the requirement of overmatching of the weld as a whole, compared to the base material, matching/overmatching electrodes have been used for filling the bevel. The characteristic parameters of the applied welding procedures are given in Table 3.

The test welds have been preheated at the temperatures that were determined in the K-bevel Tekken tests. From these welds, tensile, side bend, Charpy-V and CTOD specimens have been machined and tested. All transverse tensile tests fractured in the base material, and the side bend tests (D = 4d) did not show any unacceptable defects.

The results of the Charpy-V and CTOD tests are given in Figure 9 and Table 4. A macrograph of both test welds in FeE355 (with matching and with low yield penetration bead) is shown in Figure 10.

Figure 9 shows that the Charpy-V notch toughness properties of the low yield penetration bead are better than of the undiluted weld metal (characteristic transition temperatures at 40J for undiluted low yield strength weld metal amount to approx. -20 - -30°C, according to producers data sheets). This is caused by the fact that the low yield weld metal in the test weld has a thickness of only two layers, which is less than the thickness of the Charpy-V specimen, and by the dilution of the low yield weld metal with the parent plate. This dilution amounts to approx. 30 - 40%, and leads to an increased carbon and manganese level. These elements strongly influence the microstructure

(*Ref. 13 and 14*), which is important for obtaining good Charpy-V notch toughness properties.

The microstructures that are characteristic for matching weld metal, undiluted low yield weld metal and diluted low yield weld metal are shown in Figure 11. The main difference between the matching weld metal and the diluted low yield weld metal is the percentage of Primary Ferrite (PF) and Ferrite with Second Phase (FS) (*Ref. 15*). Numerous investigations have shown that an increasing percentage PF and FS (and hence a decreasing percentage acicular ferrite) leads to less favourable Charpy-V notch toughness properties, and a less high yield and tensile strength. These results are in line with what has been found in this investigation.

Although the Charpy-V properties of the low yield penetration bead weld metal have improved compared to the undiluted low yield strength weld metal, Figure 9 shows that for FeE355 the Charpy-V notch toughness properties of the matching penetration bead are better than of the low yield penetration bead. For the low yield procedure in FeE690, no degradation of Charpy-V notch toughness properties was noticed.

These results are in line with the results of the CTOD tests. For the low yield FeE355 procedure, a pop-in was measured, at a level which was clearly below the minimum CTOD value of the matching procedure (0.05 vs 0.39 mm). Examination of the fracture appearance revealed that this pop-in initiated in the low yield penetration bead. This phenomenon is observed as well in another research programme, currently being executed (*Ref. 16*).
Although the measured CTOD levels of both FeE690 procedures were less favourable than of the 355-M procedure, no effect of the low yield strength penetration bead was visible.

Apparantly the dilution of the low yield weld metal with the FeE690 parent plate upgraded the toughness level of the penetration bead to the values that have been measured for the matching weld metal. This absence of a difference in notch toughness properties is not in line with the rather unfavourable microstructure that is present in the low yield penetration bead.

The measured pop-in in the FeE355-LY weld metal is considered to be of limited importance for the behaviour of a structure welded according to this principle. The pop-in is restricted to the low yield penetration bead, and the first (low yield) filling bead on the reverse side of the bevel. This means that a surface breaking defect, which is the most common defect in industry, can have a depth of approx. half the plate thickness before it reaches the low yield area. In practice, one would detect such a defect during inspection, and repair it.

However, in a recently started ECSC project (*Ref. 17*) the yield and fracture behaviour of weldments with and without a low yield penetration bead will be studied extensively. This project concentrates on FeE460 and FeE690.

GENERAL DISCUSSION

The results of the experiments with consumables with a very low hydrogen content, and/or a very low yield strength show that a very large reduction of the required preheat temperature can be achieved when welding either thick constructional steels of the type FeE355 or high yield strength steels. These base materials should otherwise be preheated at a temperature of approx. 75 - 125°C.

This welding without preheating leads to a remarkable reduction in production cost, not only by a reduction of the cost directly related to preheating, but by reduced preparation and control time as well. Furthermore, it improves the working conditions of the welders, and hence the quality of the welded joint.
Figures that have been mentioned by Grootint BV, the contractor that applied vacuum packed electrodes for welding the second "Van Brienenoord" bridge near Rotterdam, claim a reduction of production cost of approx. 5%.

The use of very low hydrogen consumables in combination with very low yield strength electrodes in the penetration bead can lead to savings of this order of magnitude for steels that cannot be welded without preheating by using the very low hydrogen consumables alone.

Another area where the techniques described in this paper can have very large advantages is in repair welding. In repair welding, most of the time the restraint conditions are severe, and the steels can originate from a period when the chemical composition was less favourable with respect to cold cracking.
Combined with the fact that during repair welding, preheating is often either very difficult, or not possible at all, the application of very low yield strength/very low hydrogen electrodes for repair welding gives considerable advantages.

The mechanical properties of weldments with and without low yield penetration beads will be studied in more detail in a large ECSC project. However, the results of the experiments described in this paper indicate that the mechanical properties meet the relevant requirements.
This system of applying low yield consumables for the root run, will therefore be applied in the fabrication (without preheating!) of the storm surge barrier in the "Nieuwe Waterweg", the entrance to Rotterdam harbour. This construction, with plate thicknesses up to 200 mm, would otherwise have required preheating temperatures of approx. 100°C.

CONCLUSIONS

From the experiments that have been described in this paper, the folowing conclusions can be drawn:

1 With electrodes having a hydrogen content less than 3 ml/100 g, 50 mm FeE355 can be welded without preheating (based on standard Tekken tests) up to a CEN value of 0.31 (Pcm ≤ 0.20, %C ≤ 0.11).

2 Compared to electrodes with a hydrogen content of 5 ml/100 g, the application of electrodes with a hydrogen content less than 3 ml/100g in FeE355 leads to a decrease of the preheat temperature required in standard Tekken tests of approx. 50 - 75°C in the compositional range CEN = 0.31 - 0.36 (Pcm = 0.20 - 0.23).

3 Tekken tests with adapted bevels revealed that the standard sloped-Y Tekken tests can give unsafe predictions for the preheat temperature when welding K- and double-V joints in a high restraint condition in practice.

4 Application of very low yield strength electrodes in the penetration bead leads to a very large decrease of the required preheat temperature of both FeE355 and FeE690 steels. In a number of cases, no preheat at all is needed, not even in K- or double V-joints.

5 The susceptibility to cold cracking (preheat temperature) of the penetration bead can be correlated with the CEN and Pcm value of the penetration bead weld metal, diluted with the parent plate. This holds for both the low yield and the matching electrodes.

6 The mechanical properties of test welds with low yield electrodes in the penetration bead in FeE355 and FeE690 were acceptable.

7 Application of electrodes with a hydrogen content less than 3 ml/100 g, and the use of very low yield strength/very low hydrogen electrodes for the penetration bead, lead to a considerable reduction of the production cost.

ACKNOWLEDGMENTS

The authors whish to expres their gratitude to the Ministry of Defence, Royal Netherlands Navy, and to the Innovation Oriented Projects "Metals" for supporting the experimental work, and for their permission to publish the results.

REFERENCES

1 Vuik, J., and Wortel, J.C. van. "Reducing the preheat temperature during welding of constructional steels", IOP-Metals research project, 1992 (in Dutch).

2 Ruge, J., and Dickehut, G. "Method for predicting the content of diffusible hydrogen in the weld metal under the influence of atmospheric moisture", Schweissen und Schneiden, Vol 40 (1988), pp 238 - 241.

3 Wortel, J.C. van, "Influence of the atmospheric conditions on the hydrogen content of weld metal", TNO-IPL research report, 1991 (in Dutch).

4 Wortel, J.C. and Martijn, S.C. "Reliability of hydrogen measurements in weld metal, at a level of approx. 3 ml/100 g", IPL-TNO report of a IOP-Metals research project, 1992 (in Dutch).

5 Ito, Y, and Bessyo, K. "Weldability formula of high strength steels". IIW doc IX-576-68.

6 Yurioka, N., Suzuki, H., Ohshita, S. and Saito, S. "Determination of necessary preheating temperatures in steel welding", Welding Journal, Vol 62 (1983), pp 147s - 153s.

7 Dearden, J. and O'Neill, H. "A guide to the selection and welding of low alloy structural steels", Institute of Welding Transactions, Vol 3 (1940), pp 203 - 214

8 Uwer, D., and Höhne, H. "Minimum preheat temperature for the cold-crack-free welding of steels", IIW doc IX-1631-91.

9 Yurioka, N. and Suzuki, H. "Hydrogen assisted cracking in C-Mn and low alloy steel weldments", International Materials Reviews, Vol. 34 (1990) No.4, pp 217 - 249)

10 Yurioka, N. "Carbon equivalents for hardenability and cold cracking susceptibility of steels", Conference "Hardenability of Steels", Derby, UK, May 1990.

11 Wortel, J.C. van. "Investigation towards the applicability of very low yield strength electrodes for the penetration bead in FeE355 and FeE690", TNO-IPL research report, 1991/1992 (in Dutch).

12 DIN 1913. "Stabelektroden für das Verbindungsschweissen von Stahl, unlegiert und niedriglegiert", 1984.

13 Evans, G.M. "The effect of carbon on the microstructure and properties of C-Mn all-weld metal deposits", Welding Journal, Vol 62 (1983), pp 313s - 320s.

14 Evans, G.M. "The effect of manganese on the microstructure and properties of C-Mn all-weld metal deposits", Welding Journal, Vol 59 (1980), pp 67s - 75s.

15 "Guide to examination of ferritic steel weld metals", IIW document IXJ-123-87.

16 Wortel, J.C. and Vuik, J. "Applicability of very low yield strength electrodes in the penetration bead of weldments in FeE355", TNO-IPL research report, 1993 (in Dutch)

17 ECSC research contract 7210-KA/609 92-F1.01b. "The effect of application of electrodes with a very low yield strength on the fabrication procedures and the yield and fracture behaviour of welded joints", in progress at RWTH-Aachen, Institut für Eisenhüttenkunde and TNO Institute of Production and Logistics Research.

Table 1 Data concerning the base materials

		Steel								
		1 50 mm AcC	2 50 mm N	3 50 mm N	4 40 mm N	5 40 mm N	6 50 mm N	7 50 mm N	8 45 mm N	9 38 mm QT
Chemical compo-sition [weight%]	C	0.07	0.086	0.11	0.12	0.13	0.17	0.13	0.19	0.12
	Mn	1.44	1.47	1.50	1.49	1.56	1.44	1.33	1.49	0.41
	Si	0.21	0.41	0.48	0.43	0.47	0.42	0.43	0.17	0.22
	P	0.006	0.012	0.019	0.014		0.019	0.015	0.001	0.012
	S	0.002	0.003	0.007	0.001	0.004	0.015	0.001	0.017	0.005
	Al		0.027	0.06	0.047	0.047	0.029	0.039	0.036	0.025
	Ni	0.38	0.26	0.027	0.47	0.037	0.05			4
	Cr	0.02	0.076	0.03	0.043	0.013				0.45
	Cu	0.11	0.25	0.02	0.044	0.085	0.04			
	Mo		0.022	0.002	0.003	0.004				0.33
	Ti	0.01			0.003	0.002				
	Nb		0.027	0.031	0.041	0.042	0.025	0.029		
	V				0.005	0.003				
	N	0.0023	0.0078		0.008	0.008				
	CE	0.35	0.38	0.37	0.41	0.40	0.42	0.35	0.44	0.64
	CE (+Si)	0.36	0.40	0.39	0.43	0.42	0.43	0.37	0.45	0.65
	Pcm	0.16	0.19	0.20	0.22	0.23	0.26	0.21	0.27	0.27
	CEN	0.23	0.26	0.31	0.35	0.36	0.42	0.33	0.44	0.47
Mecanical properties	Re [N/mm²]	424	384	368	404	387	367	360	380	698
	Rm [N/mm²]	518	484	525	535	523	546	515	553	786
	A5 [%]	29	33	31	30	31	28	31	27	21

AcC = Accelerated cooled, N = Normalized, QT = Quenched and Tempered.

Table 2 Minimum required preheat temperatures, tensile properties and characteristic values of the chemical composition for K-bevel Tekken tests for steels 8 and 9 from table 1 for several electrodes (matching and low yield)

Steeltype	Electrode	Preheat temperature [°C]	Ro [N/mm²]	Rm [N/mm²]	CE	Pcm	CEN
FeE355 t = 45 mm	E7018	140	542	635	0.4	0.22	0.35
	LY 1	50	432	549	0.18	0.12	0.14
	LY 2	110	447	552	0.25	0.16	0.2
	LY 3	110	523	618	0.32	0.2	0.27
	LY 4	125	495	579	0.29	0.17	0.25
	LY 5	80			0.25	0.16	0.2
	LY 6	125			0.27	0.16	0.22
	LY 7	80			0.26	0.14	0.19
	LY 8	95			0.27	0.16	0.21
FeE690 t = 38 mm	E11018	80	718	914	0.7	0.28	0.44
	LY 1	20	447	542	0.19	0.1	0.12
	LY 2	20	458	541	0.29	0.13	0.17
	LY 3	65	548	629	0.34	0.18	0.24
	LY 4	80			0.23	0.14	0.17
	7018	95	578	701	0.45	0.24	0.36

Table 3 Characteristic parameters of the test welds. The preheat temperature that is mentioned was applied for the penetration bead, and the first filling bead.

Weld	355-M	355-LY	690-M	690-LY
Base material	FeE355 t = 45 mm	FeE355 t = 45 mm	FeE690 t = 38 mm	FeE690 t = 38mm
Welding consumables	E7018	Root: Low yield Filling: E7018	E11018	Root: Low yield Filling: E11018
Preheat temp. [°C]	140	50	80	20
Max. Interpass temp. [°C]	150	120	120	120
Heat input [kJ/cm]: Penetration bead Filling beads	 22 11 - 15	 24 12 - 15	 28 11 - 14	 26 12 - 14
Waiting time after penetration bead	1h	3 days	1h	3 days

Table 4 CTOD values of procedures 355-M, 355-LY, 690-M and 690-LY from table 3. Test temperature: -10°C, BxB specimens.

Procedure	CTOD values [mm]		
	1	2	3
355-M	0.60, δ_c	0.39, δ_c	0.65, δ_c
355-LY	0.47, δ_c	0.79, δ_c	0.05 pop-in 0.49, δ_c
690-M	0.18, δ_c	0.23, δ_c	0.23, δ_c
690-LY	0.19, δ_c	0.23, δ_c	0.30, δ_c

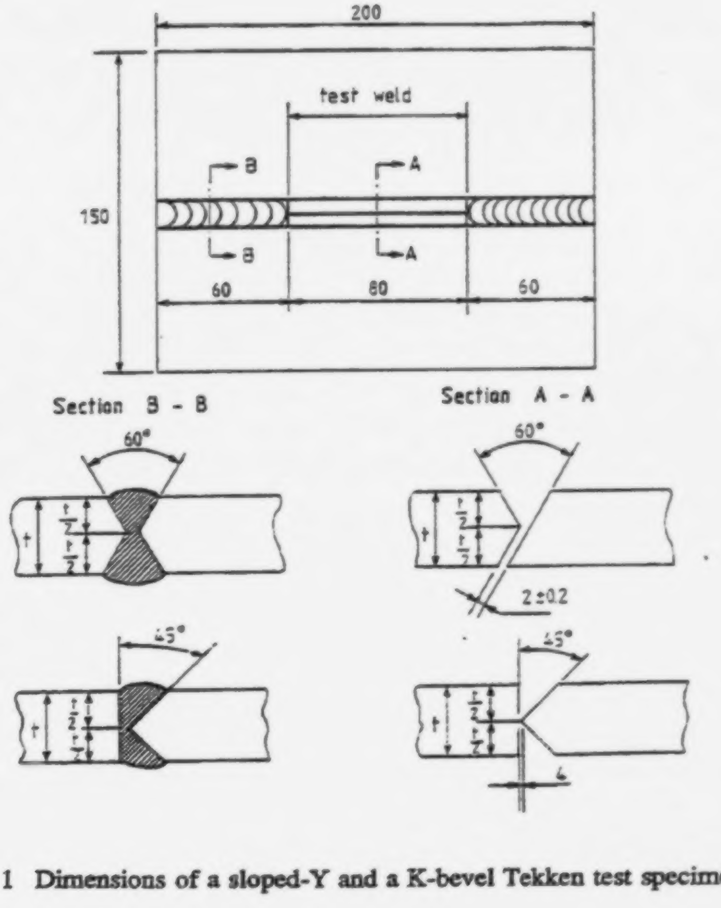
200
test weld
B
A
150
B
A
60
80
60
Section B - B
Section A - A
60°
60°
t
t/2
t/2
2±0.2
45°
45°
4

Figure 1 Dimensions of a sloped-Y and a K-bevel Tekken test specimen.

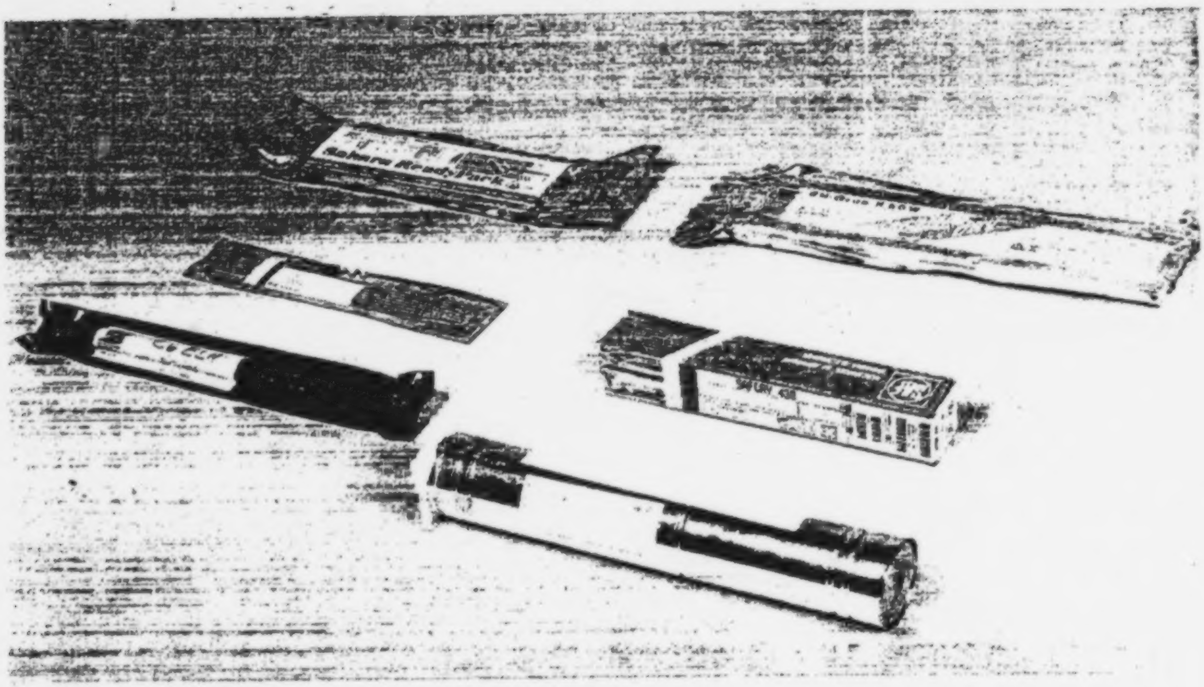

Figure 2 Photograph of several vacuum packed very low hydrogen electrodes. In one case the electrodes are packed in a sealed tin.

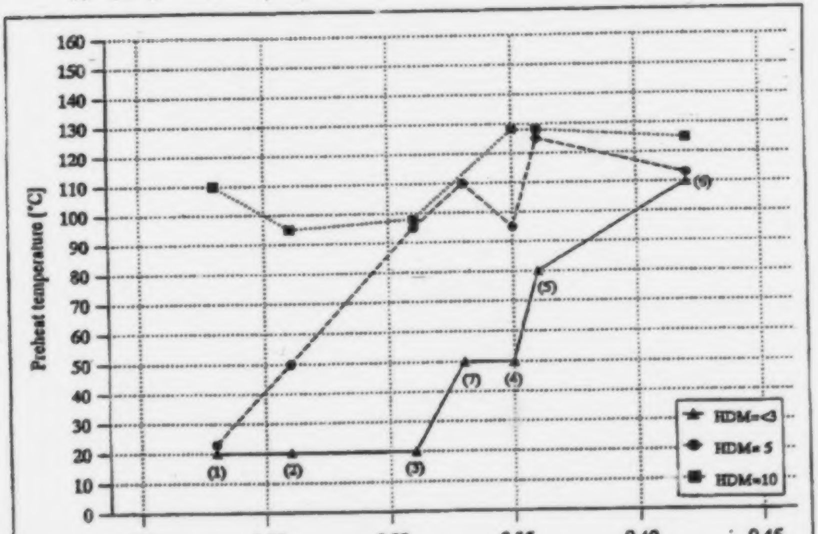

Figure 3 Minium required preheat temperature (determined with standard Tekken tests) for the steels from table 1 as a function of CEN.

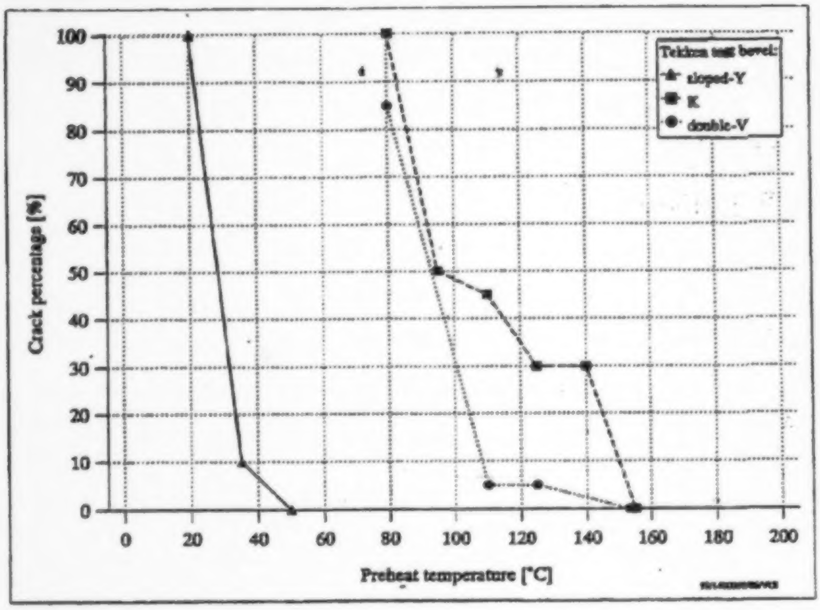

Figure 4 Influence of the type of bevel of a Tekken test on the minium required preheat temperature (Steel nr. 7 from table 1).

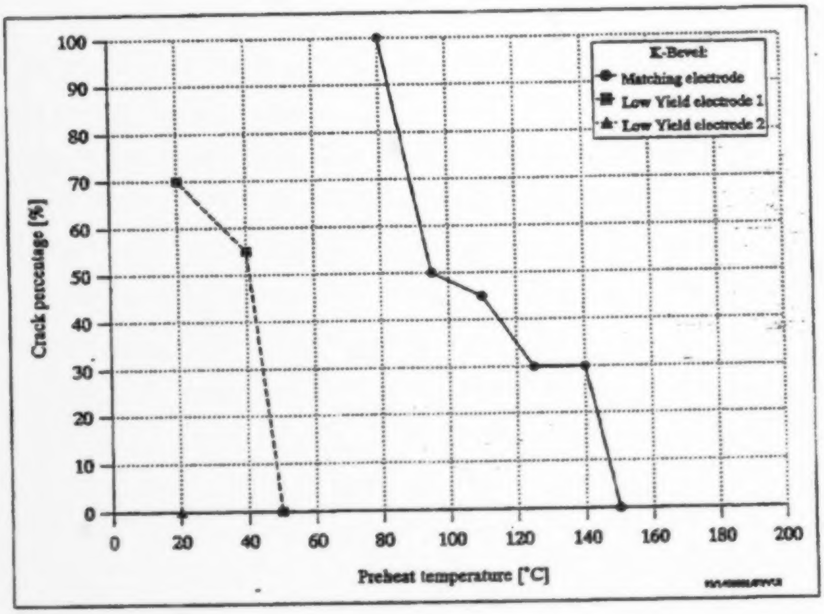

Figure 5 Effect of very low yield strength electrodes on minimum required preheat temperature (K-bevel Tekken test, Steel nr. 7 from table 1)

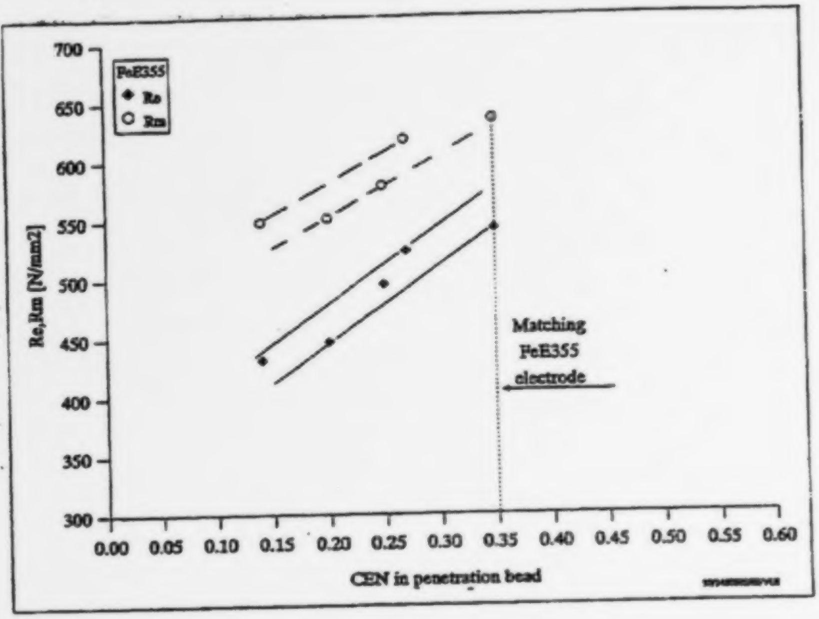

Figure 6 Relation between tensile properties of the FeE355 penetration bead and the CEN value.

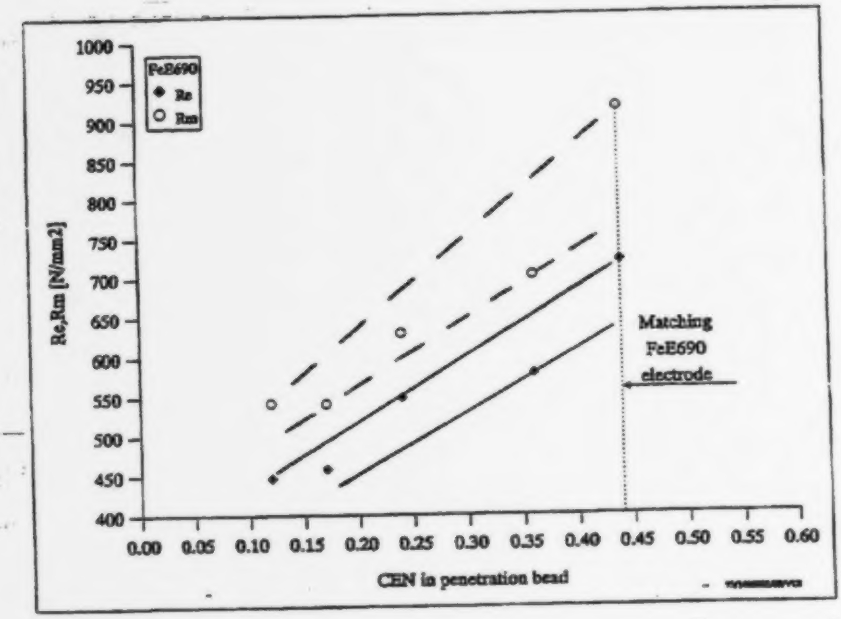

Figure 7 Relation between tensile properties of the FeE690 penetration bead and the CEN value.

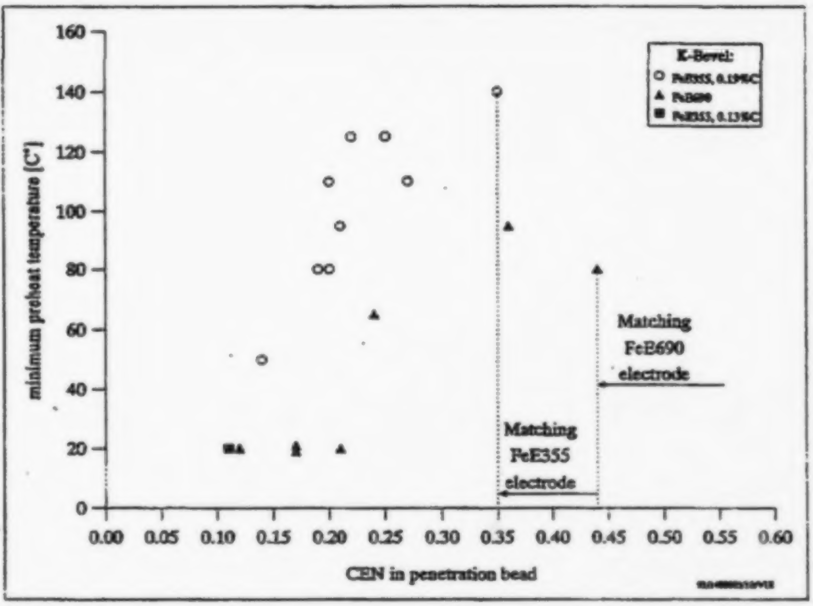

Figure 8 Relation between the minimum required preheat temperatures and the CEN value of the penetration bead.

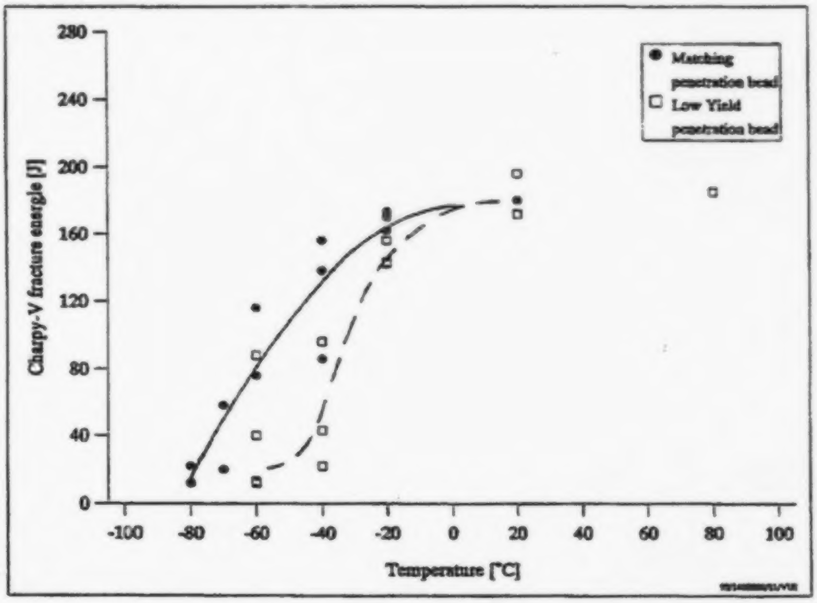

Figure 9 Charpy-V transition curve of welds 355-M and 355-LY, specimens taken from the root position.

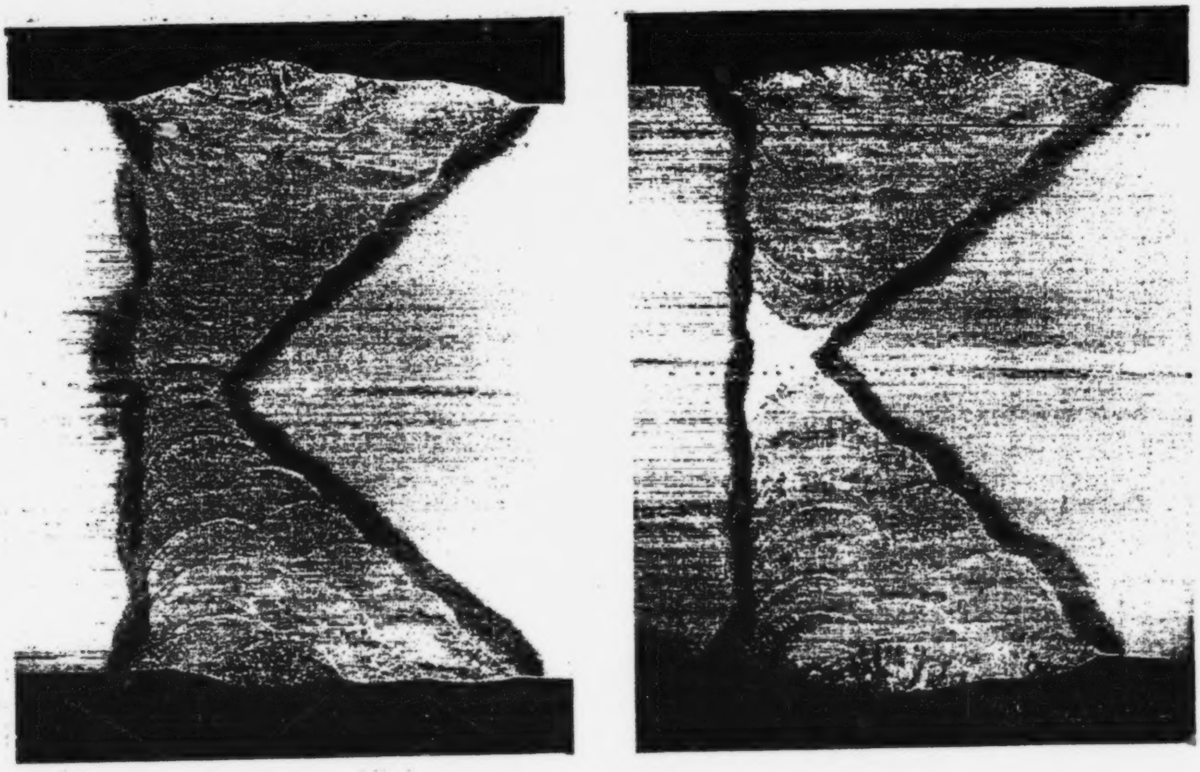

a b

Figure 10 Macrographs of the welds 355-M (a) and 355-LY (b).

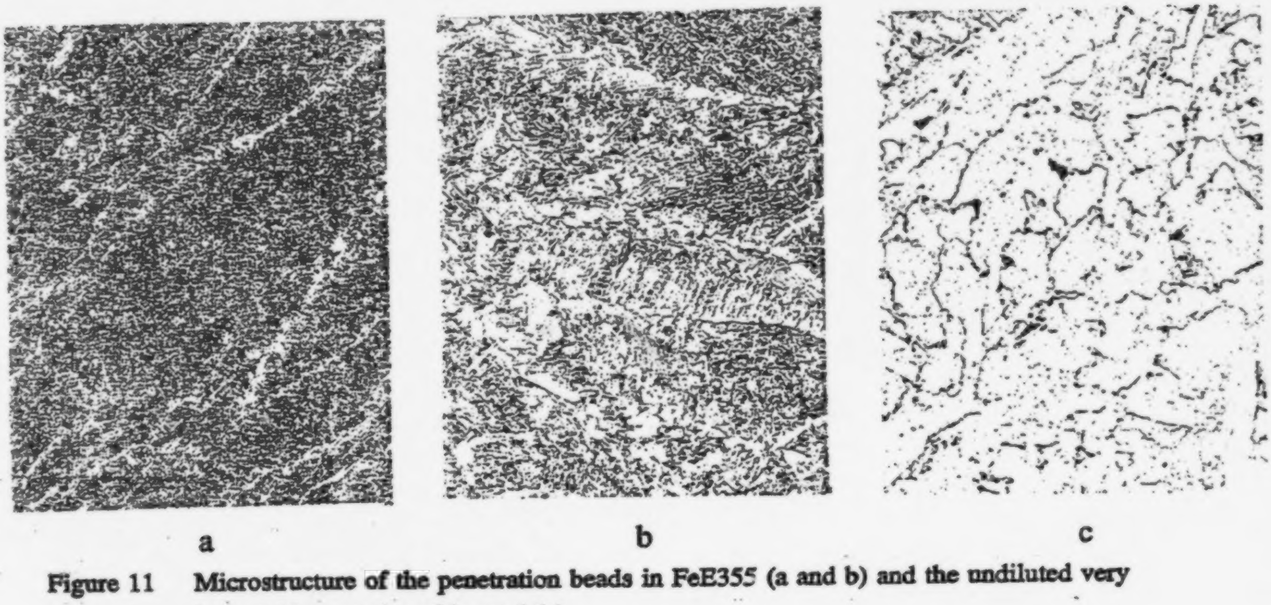

a b c

Figure 11 Microstructure of the penetration beads in FeE355 (a and b) and the undiluted very low yield strength weld metal (c).
a: Matching electrode, b: Low yield electrode. M = 120 X.
c: Undiluted very low yield strength weld metal. M = 300 X.

#510313

⑧

APPLICATION OF J AND CTOD ESTIMATION FORMULAS TO NAVAL CONSTRUCTION STEELS

Jack Morrison and Zhenhua Zhai
Defence Research Establishment Pacific

K.J. KarisAllen
Defence Research Establishment Atlantic

INTRODUCTION

Over the past two decades standardized experimental procedures for laboratory elastic-plastic toughness determination using J_{Ic}, J-R Curves, and Crack Tip Opening Displacement have all been developed and widely employed (e.g. ASTM Standards E813, E1152, and E1290, and British Standard BS 5762). These standards include the most commonly used specimen types, namely compact and three point bend geometries. Depending on the parameter being measured, for example J, there may be a requirement for measurement during the test of both specimen crack mouth opening and load-line displacement. If required, compact fracture specimens can fairly easily be modified to make the two suitably coincident. When single edge notched bend specimens are employed, however, the required instrumentation tends to become more complex, and in the case of small specimens, difficult to accommodate. It would therefore be useful if estimates of J and CTOD could be made from either mouth opening or load line displacement. At the same time estimation formulas applicable to wider ranges of crack length would also be useful, particularly for evaluating specimens containing shorter cracks than are currently permitted in the standard procedures (1, 2). Recently Kirk and Dodds (3) provided a series of estimation formulas allowing for both J and CTOD calculation from either load-load-line displacement, or load-crack mouth opening, based on a finite element analysis. This paper describes an investigation of how well these formulas apply to three point bend specimen fracture tests on both 25 mm HSLA80 steel plate and the fusion zone of a 50 mm Q1(N) steel weldment .

In general the estimation formulas show excellent agreement.

SUMMARY

The following summary provides additional comments on the pages which follow.

Page 4. CTOD Estimation Formulas. Refer to reference (3) for nomenclature. Equation (1) is from the ASTM procedure E1290, using CMOD. Equation (2) uses the area under the load-CMOD curve. Equation (3) uses the area under the load-load line displacement curve. Note that the elastic first term is the same in each case. The η values are tabulated in reference (3) as a function of a/W and work hardening coefficients derived from tensile tests using a Ramberg-Osgood fit.

Page 5. J estimation formulas. These relationships corresponding to equations (2) and (3). Equation (5) is the formula found in the standards

HSLA80

Pages 8 and 9. Typical load-CMOD and load-LLD curves for the HSLA80 plate using unloading compliance for crack length determination. Specimens were 25x50 mm with a/W=0.5.

Page 10. Effect of rate and temperature on the onset of unstable fracture. The estimation formulas were applied to specimens which cleaved only after maximum load.

Page 11. Comparison of CTOD formulas for HSLA80. Some error is expected at high Δa because the formulas do not correct for crack extension.

Page 12. Comparison of J formulas for HSLA80.

Q1(N) WELD

Pages 13 and 14. Typical load-CMOD and load-LPD curves. In this case LPD was determined indirectly using machine displacement and known machine compliance. The test was carried out at -5°C with a displacement rate of 2 mm/s.

Pages 15 and 16. Comparison of CTOD and J estimation formulas for Q1(N) weld. Note the very large final crack extension. Over the first 2 mm of crack extension the agreement is reasonably good, and even at long crack lengths and after encountering instabilities, the area base calculations are in excellent agreement.

OUTLINE

- Introduction
- J and CTOD Estimation formulas
- Materials
    - chemical composition
    - tensile properties
    - impact properties
- Test Procedures
    - tensile
    - fracture toughness
- Results
    - load-displacement curves
    - temperature/rate sensitivity of HSLA80 steel
    - variation of toughness with crack length in Q1(N) weld

    - CTOD and J R-curves from estimation formulas

    - Conclusions

J ESTIMATION FORMULAS

4. Using the area under the load-crack mouth opening displacement curve:

$$J = \frac{K^2(1-\upsilon^2)}{E} + \frac{\eta_{J\text{-}C}A_{pl(CMOD)}}{Bb} \qquad (4)$$

5. Using the area under the load-load line displacement curve:

$$J = \frac{K^2(1-\upsilon^2)}{E} + \frac{\eta_{pl}A_{pl(LLD)}}{Bb} \qquad (5)$$

CTOD ESTIMATION FORMULAS

1. Using the plastic component of crack mouth opening displacement:

$$\mathrm{CTOD} = \frac{K^2(1-\upsilon^2)}{m\sigma_f E} + \frac{r_{pl} b \mathrm{CMOD}_{pl}}{r_{pl} b + a} \tag{1}$$

2. Using the area under the load-crack mouth opening displacement curve:

$$\mathrm{CTOD} = \frac{K^2(1-\upsilon^2)}{m\sigma_f E} + \frac{\eta_{C\text{-}C} A_{pl}(\mathrm{CMOD})}{Bb\sigma_f} \tag{2}$$

3. Using the area under the load-load line displacement curve:

$$\mathrm{CTOD} = \frac{K^2(1-\upsilon^2)}{m\sigma_f E} + \frac{\eta_{C\text{-}L} A_{pl}(\mathrm{LLD})}{Bb\sigma} \tag{3}$$

Chemical composition wt %.

	HSLA plate	Q1(N) plate	sample Q1(N) weld	Q(1)N HAZ
C	0.06	0.15	0.06	0.14
Mn	0.61	0.38	1.42	0.38
Si	0.30	0.26	0.55	0.43
Ni	0.81	2.77	1.83	2.86
Cr	0.74	1.41	0.13	1.43
Cu	1.01	0.02	0.01	0.02
Mo	0.22	0.4	0.04	0.41
V	-	-	0.02	-
Ti	-	0.005	0.06	0.04
Co	-	-	0.02	0.01
S	0.006	0.007	0.009	0.008
P	0.02	0.03	0.03	0.03
Al	0.07	0.1	0.03	0.1

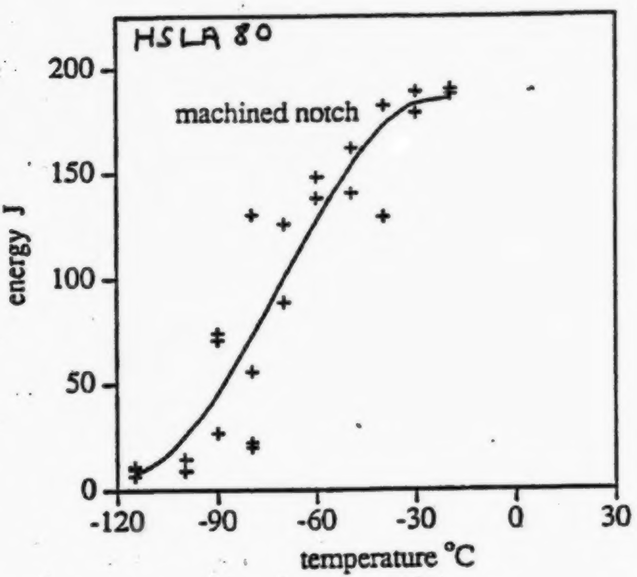

Charpy transition curve

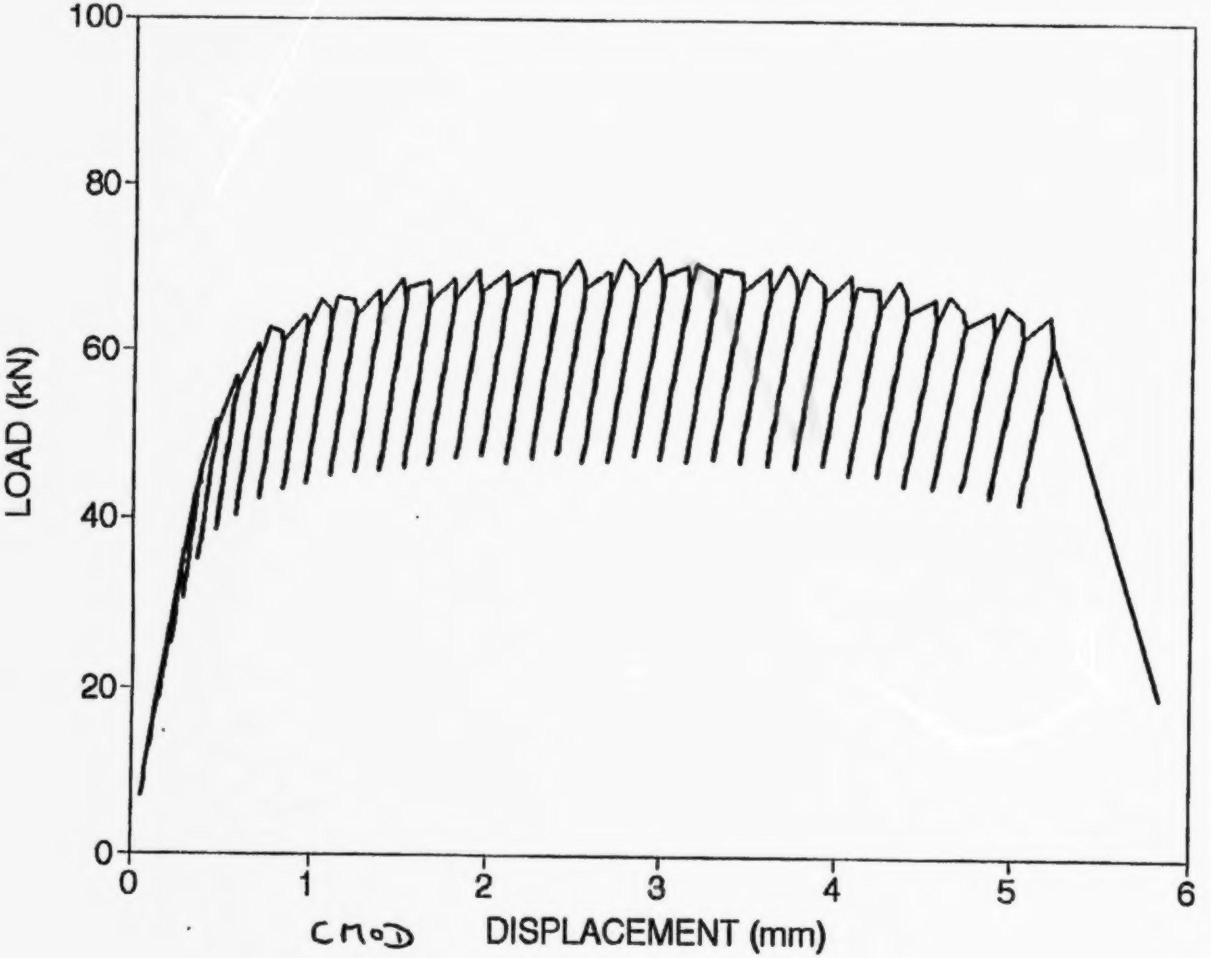

HSLA PLATE

sample 4 - 0.2 mm/sec, -20 C

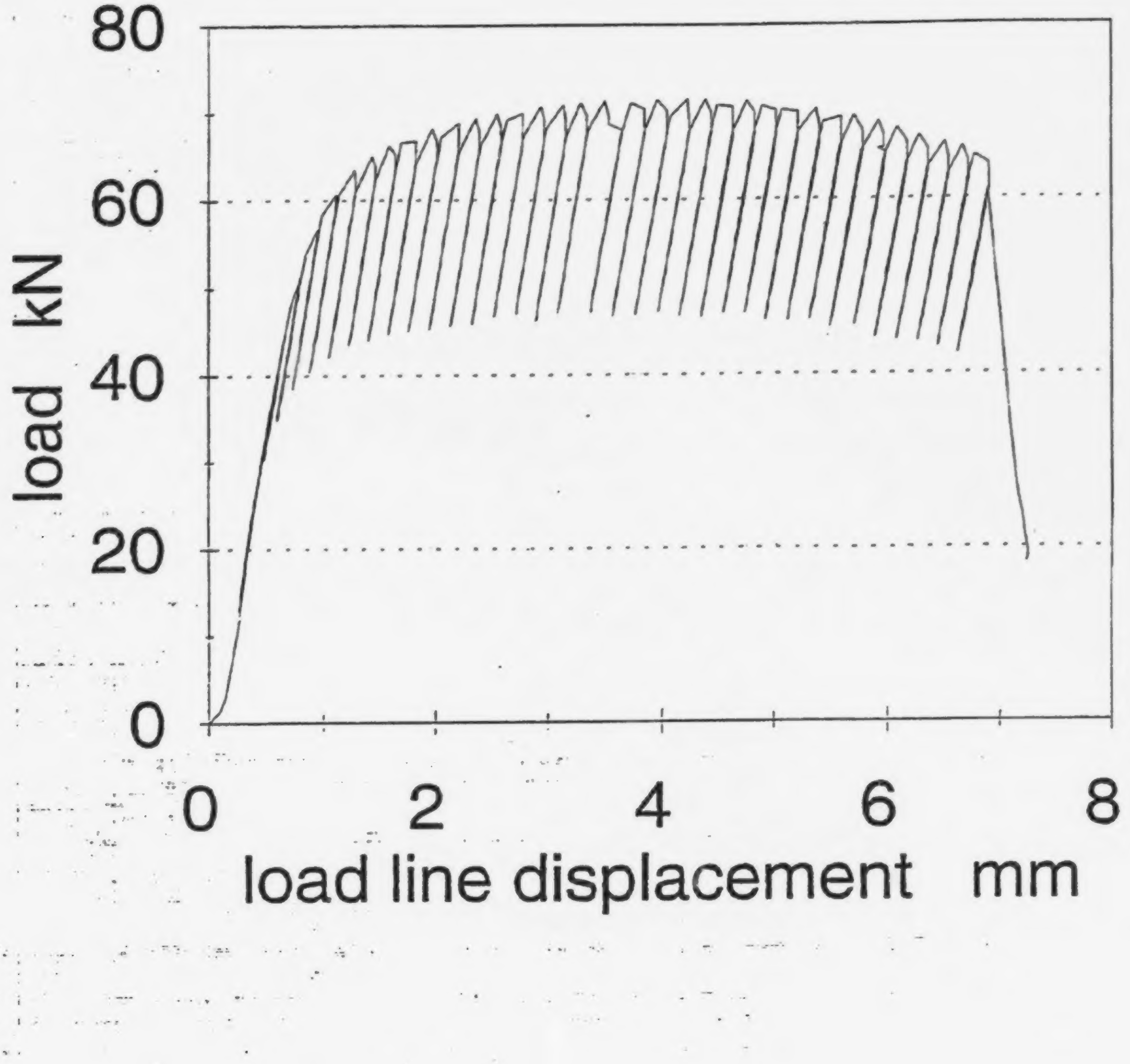

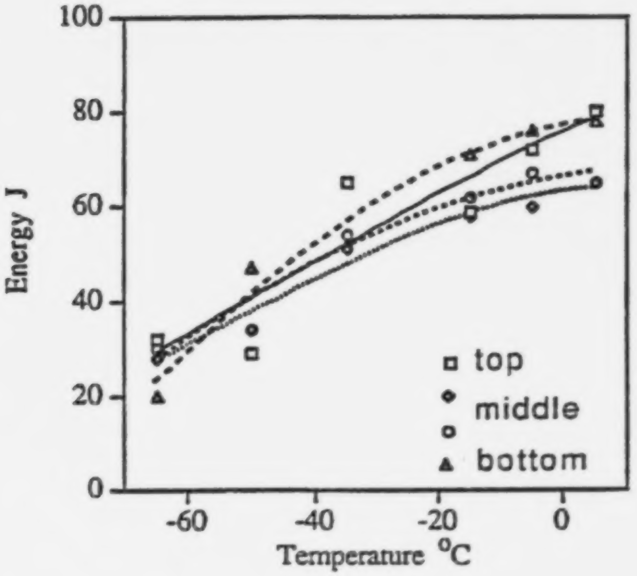

T-S orientation

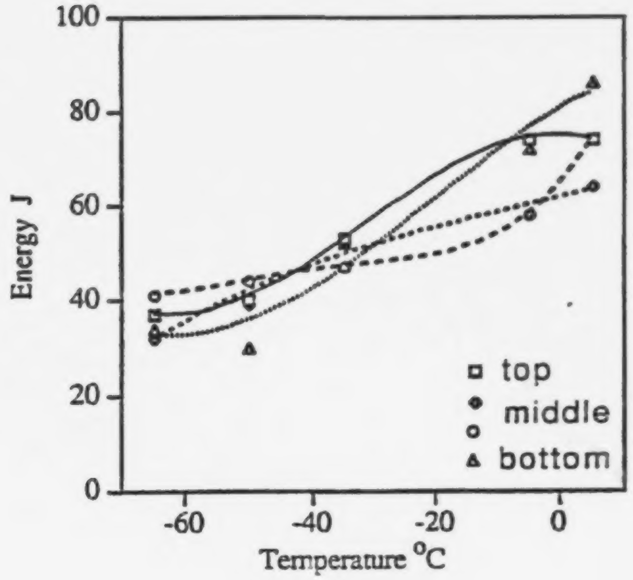

T-L orientation

Charpy impact test results for Q1(N) steel weld

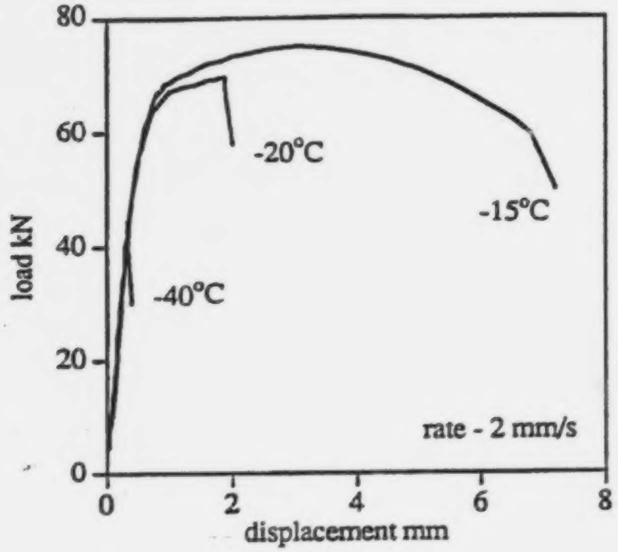

Effect of temperature

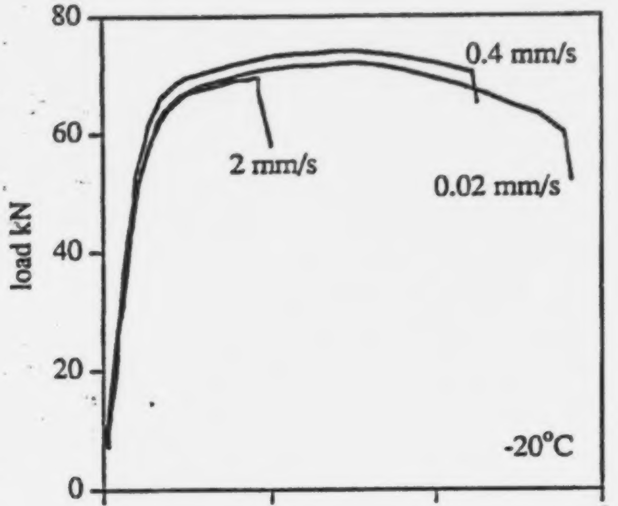

Effect of displacement rate

Load-displacement curves for HSLA steel

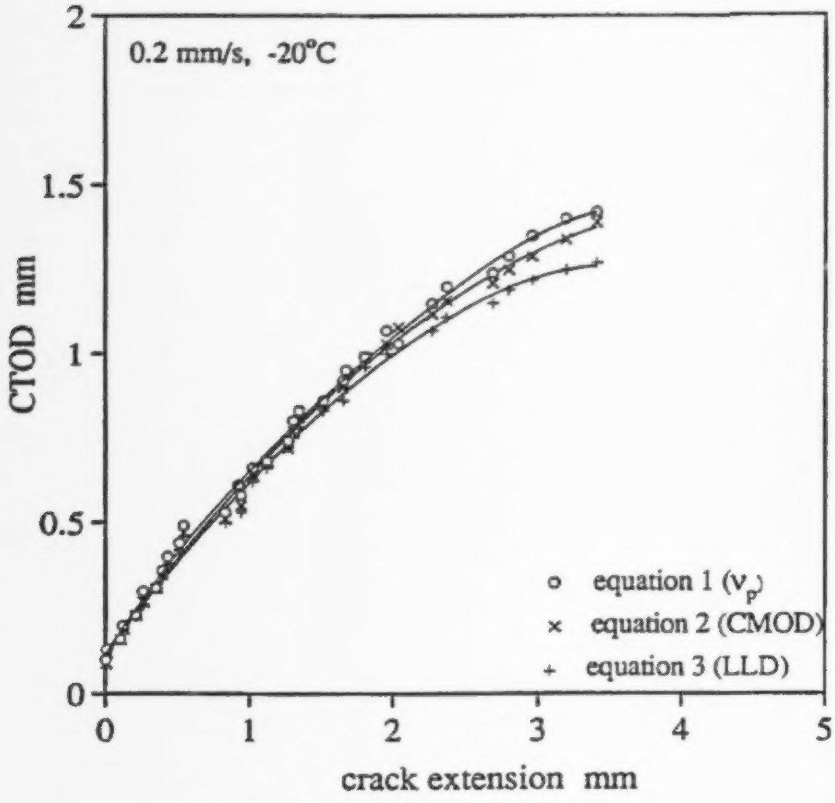

HSLA-80 CTOD Comparisons

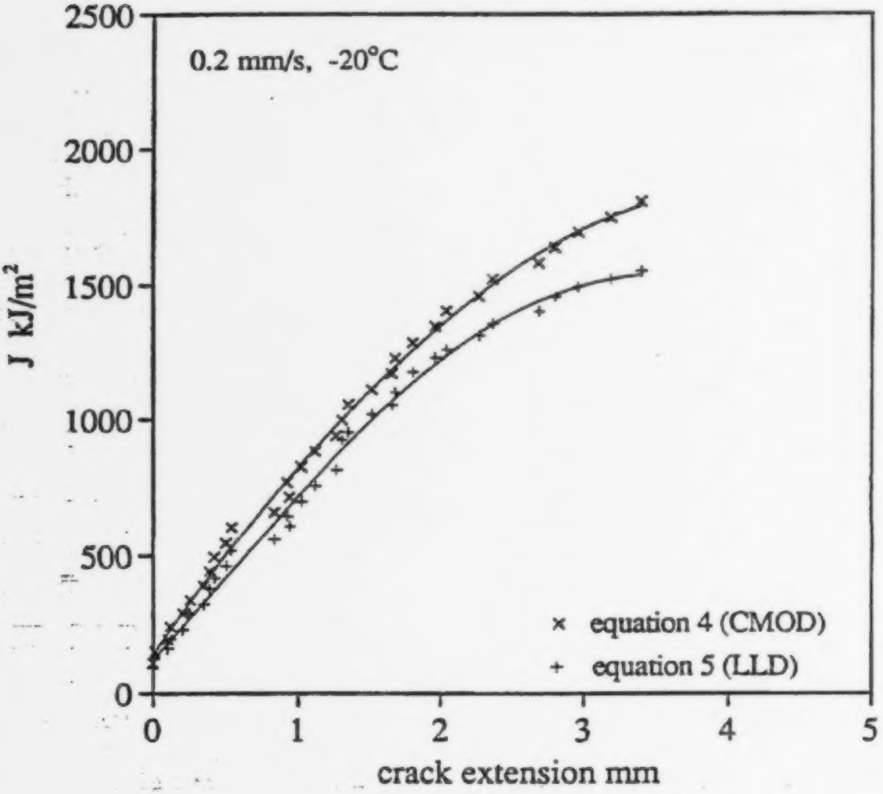

HSLA-80 J Comparisons

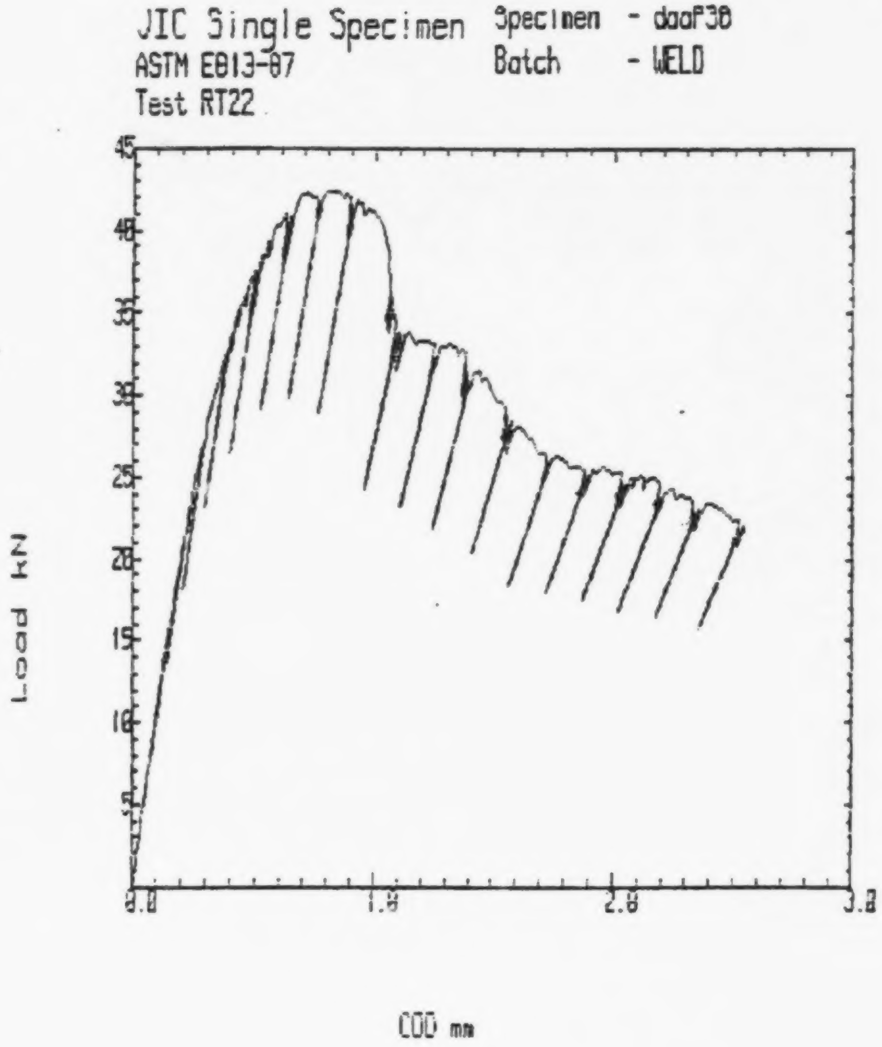
JIC Single Specimen
ASTM E813-87
Test RT22
Specimen - daaf38
Batch - WELD
45
40
35
30
25
20
15
10
5
0.0
1.0
2.0
3.0
Load kN
COD mm

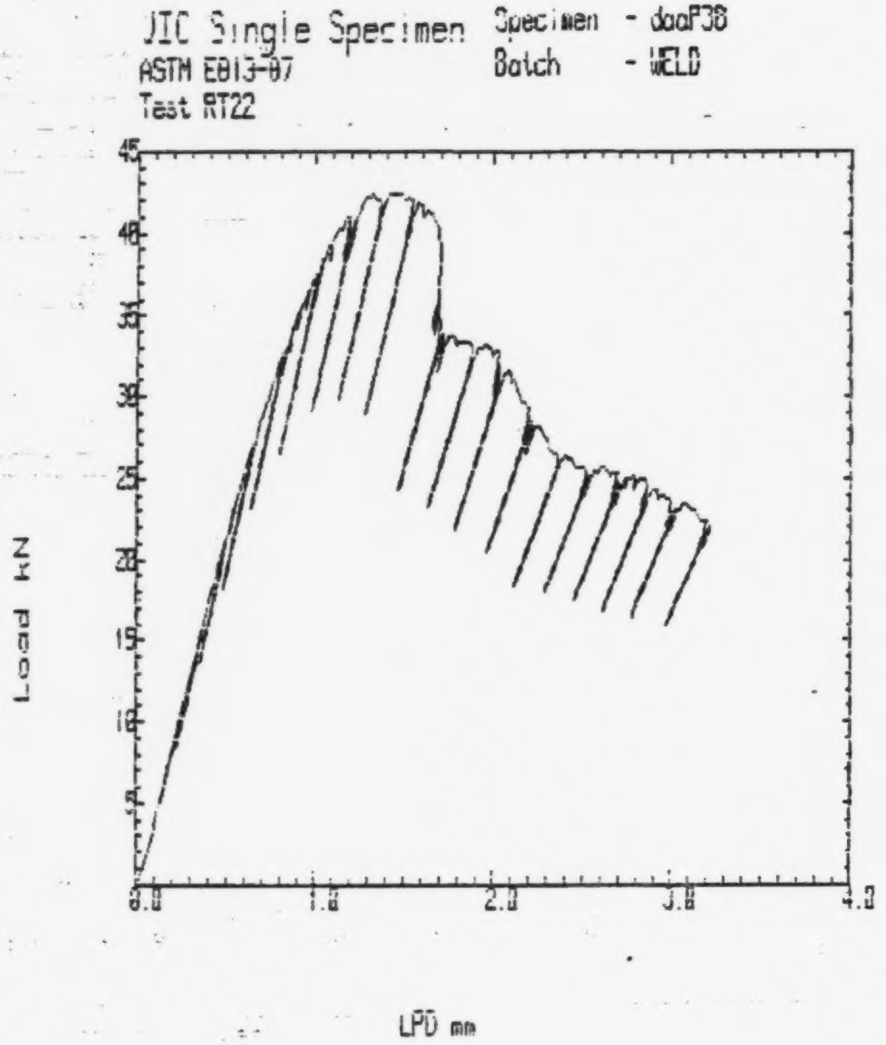
JIC Single Specimen
ASTM E813-87
Test RT22
Specimen - doaP38
Batch - WELD
45
40
35
30
25
20
15
10
5
0.0
1.0
2.0
3.0
4.0
Load kN
LPD mm

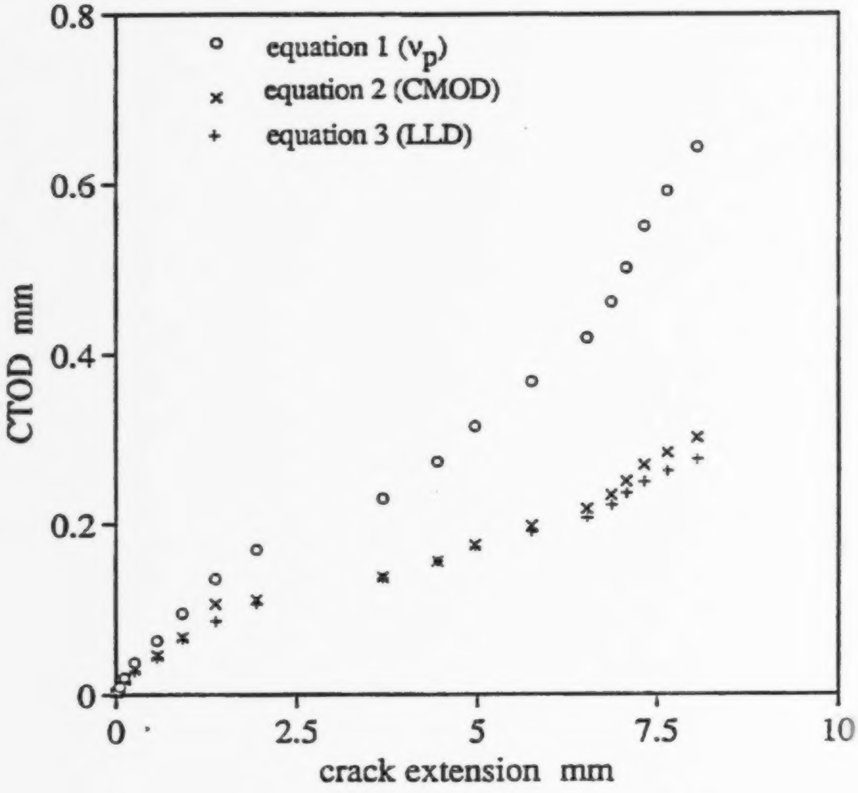

Q1(N) Weld CTOD Comparisons

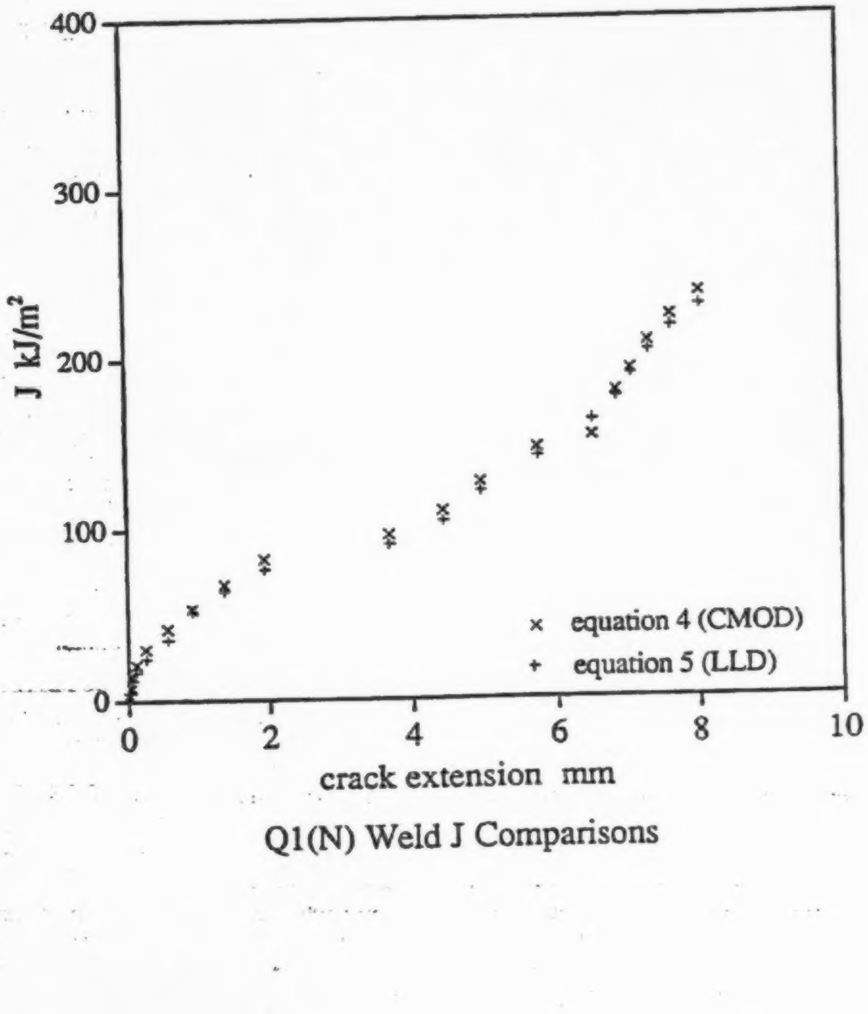

Q1(N) Weld J Comparisons

#510314

(9)

The Feasibility of Determining Percent Plastic Strain in HY80 Structures Using X-Ray Diffraction Peak Analysis

by

J. Pineault*, M. Brauss* and J. Porter**

* Proto Manufacturing Ltd., Oldcastle, Ontario
** Defence Research Establishment Atlantic, Dockyard Lab,
FMO Halifax, Halifax, Nova Scotia

ABSTRACT

This paper describes the approach and summarises the results of an investigation on the feasibility of employing non-destructive X-ray diffraction techniques to determine percent plastic strain in marine platforms fabricated with HY80. The study began by creating a series of dog bone samples machined from HY80 stock. The sample surfaces were electro-etched with a regular pattern of circles and plastically deformed to various levels. The ellipsometry of the etched circles, now deformed, were analysed using the FAMOSS system to characterise the degree of plastic deformation on each sample.

The samples were then analysed using x-ray diffraction techniques. The integral peak breadth and full width half maximum (FWHM) of several samples were measured and the results correlated to the optical strain data. It was hoped that a calibration of the integral breadths versus the optically determined strains would permit the determination of plasticity in other blind specimens. This was not possible as several different phenomena occur simultaneously when a material undergoes plastic deformation. These various phenomena affect the baseline necessary for a reliable calibration of percent plastic strain.

The necessity of segregating effects on peak broadening due to instrumental optics, domain size and microstrain distributions became apparent. Several different techniques exist to conduct this type of analysis. Various different approaches were used and their respective results compared and correlated with the optical data.

#510315 (10)

Long Range Reaction Stresses in Ship Structures

by

L. Malik*, B. Cowper*, and W.R. Tyson**

(* Fleet Technology Limited, Ottawa)
(** Metals Technology Laboratories (CANMET), Ottawa)

ABSTRACT

It is now recognized that in complex welded structures such as ships, long range reaction stresses develop due to assembly, fit-up, and structural restraint against the weld zone shrinkage. The long range reaction stresses are different from the short range weld residual stresses, the latter being always present in the weld zone, even if the weld is deposited on a small plate, free to move and contract.

Such stresses can be ignored in fatigue design as yield level residual stresses are usually assumed to be present. However, in fracture assessment (for initiation or crack arrest), this could lead to unsafe predictions.

Literature was, therefore, reviewed to assess the magnitude of such long range reaction stresses in ships. Early studies suggested it to be 25 to 30% of the steel's yield strength. However, due to the increasing use of higher strength steels, and the absence of any recent studies on this subject, a small investigation was undertaken to measure long range reaction stresses during the fabrication of a Super Ferry. The presentation will describe the results obtained which indicated that long range reaction stresses could exceed 75% of the yield strength.

1. Long Range Reaction Stresses?

- Different from ‘short range’ weld thermal residual stresses.
- Caused by assembly and fit-up requirements and by the resistance/structural restraint to weld zone contraction.

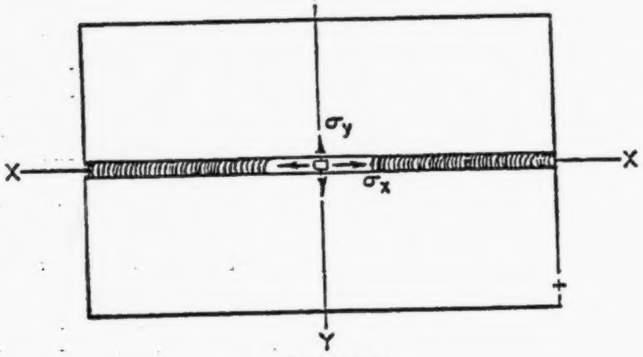
Y
σ_y
X
X
σ_x
Y

a. Butt Weld

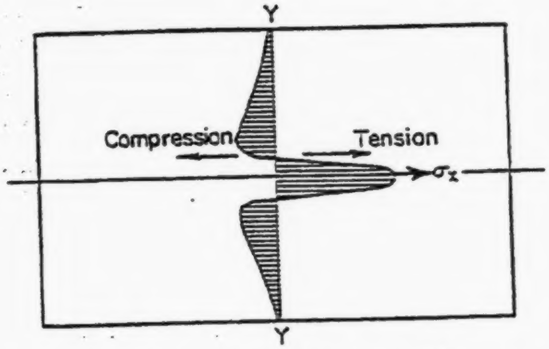
Y
Compression
Tension
σ_x
Y

b. Distribution of σ_x Along YY

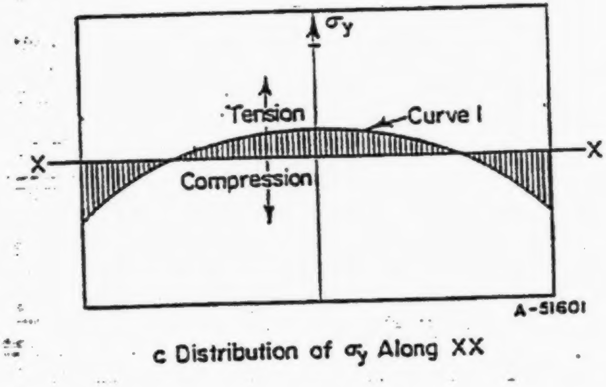
σ_y
Tension
Curve I
X
X
Compression
A-51601

c Distribution of σ_y Along XX

Figure 1: Typical distributions of residual stresses in butt weld

$$K = E.t / \ell$$

$$\sigma_R = m.K.$$

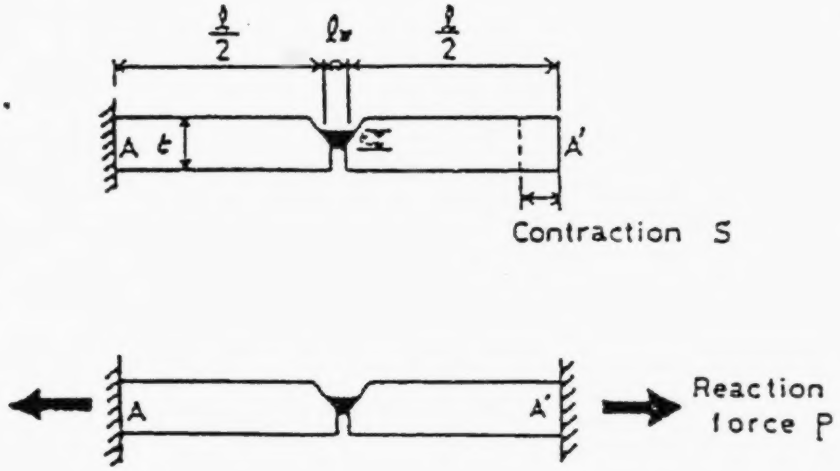

$\frac{\ell}{2}$
ℓ_w
$\frac{\ell}{2}$
A
t
A'
Contraction S
A
A'
Reaction force P

Figure 16: Simple butt joint showing concept of restraint

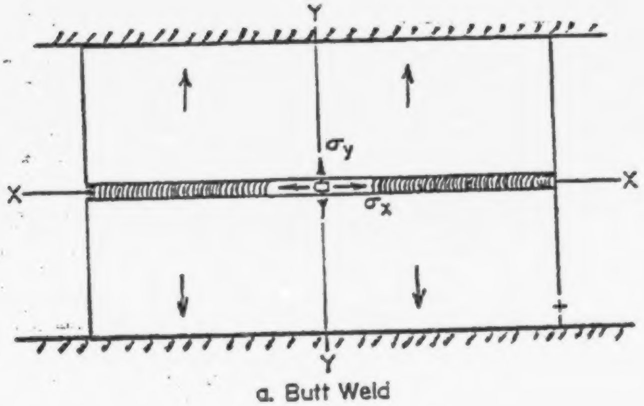

a. Butt Weld

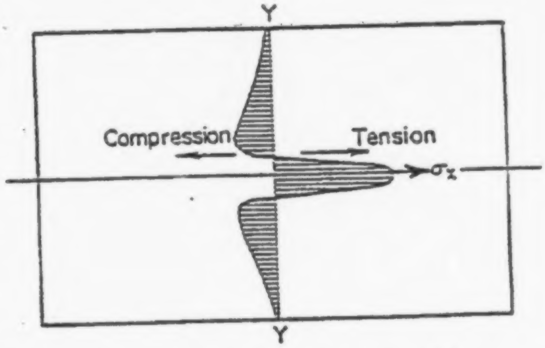
Y
Compression
Tension
σx
Y

b. Distribution of σ_x Along YY

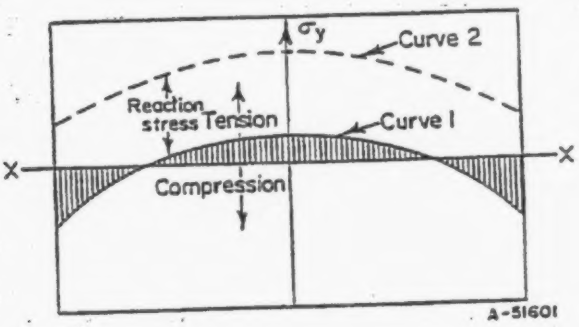
σy
Curve 2
Reaction stress
Tension
Curve I
X
X
Compression
A-51601

c Distribution of σ_y Along XX

Figure 1: Typical distributions of residual stresses in butt weld

TABLE I: Measured and Calculated Restraint Intensities for Ship Structures (from Reference 14)

Structure	Weld joint	Plate thickness (mm)	Restraint intensity (kg/mm.mm)	Restraint coeff. (kg/mm².mm)	Estimation method	Remarks
Ship	Deck longi.	25-30	av. 400	16	measurement & calculation	weld deferment Δ = 200mm
	Trans. web	16	av. 500	31	measurement	
	Collar plate at the slot	20	av. 500	25	〃	
	Butt joint (trans. bulkhead)	16	av. 1638	102	〃	after tack weld* (its pitch 80mm)
	(longi. bulkhead)	13.5	av. 1258	93	〃	
	(side shell)	20	av. 886	44	〃	
	(bottom shell)	28	av. 784	28	〃	
	(upper deck)	32	av. 1277	40	〃	
		32	av. 1222	38	〃	
Ship	Bottom longi.face	32	av. 573	18	calculation	
	Bottom trans.face	30	av. 158	5	〃	
	Strut face	25	av. 85	3	〃	
	Side longi. web	12.5	av. 118	9	〃	
	Butt joint (upper deck)	22.5	av. 158	7	measurement	
	(lower deck)	22.5	av. 131	6	〃	

2. Reason For The Study

- Fracture toughness requirements implicitly assume:
    - a peak service stress;
    - a 'critical' flaw size.

- For small flaws in the weld region, yield level residual stresses also assumed.

- For larger flaws, with flaw tips outside the zone of short range weld residual stresses, these can be ignored.

But What About Long Range Reaction Stresses in Ships?

Sumpter (1980's):

Reaction stresses can be ignored for long cracks (meter long).

Pellini (1970's):

Tensile reaction stresses about 50% of yield strength in new ships; 20% in in-service ships.
(20% also assumed in CASPPR)

Ignoring long range reaction stress may be nonconservative since fracture toughness requirements, to prevent crack initiation, would increase.

$$K_{app} = y \cdot \sigma \sqrt{a}$$

Also, the crack arrest performance of the steel would be adversely affected.

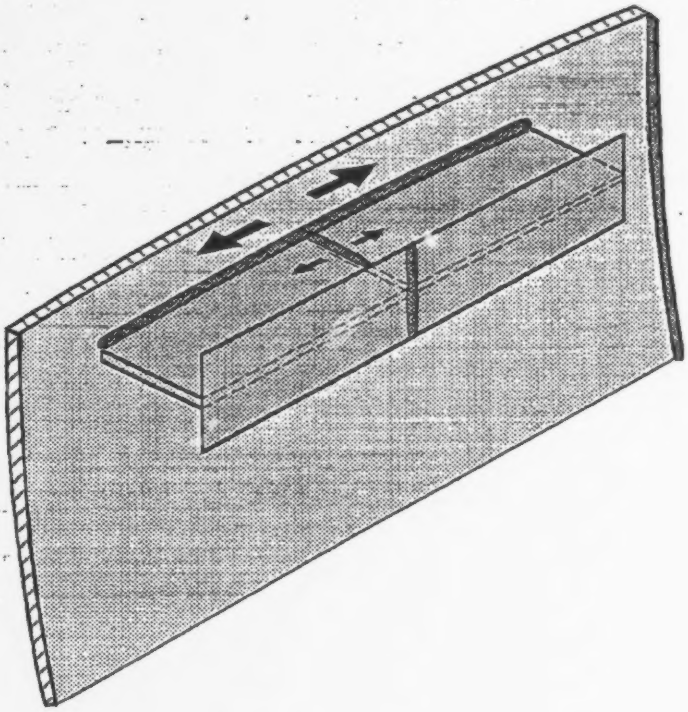

Therefore, it is considered important to assess the magnitude of the long range reaction stresses in ships.

Literature Search:

- Leide (1977)
- DeGarmo (1946)
- Ffield (1946)

Leide (1977)

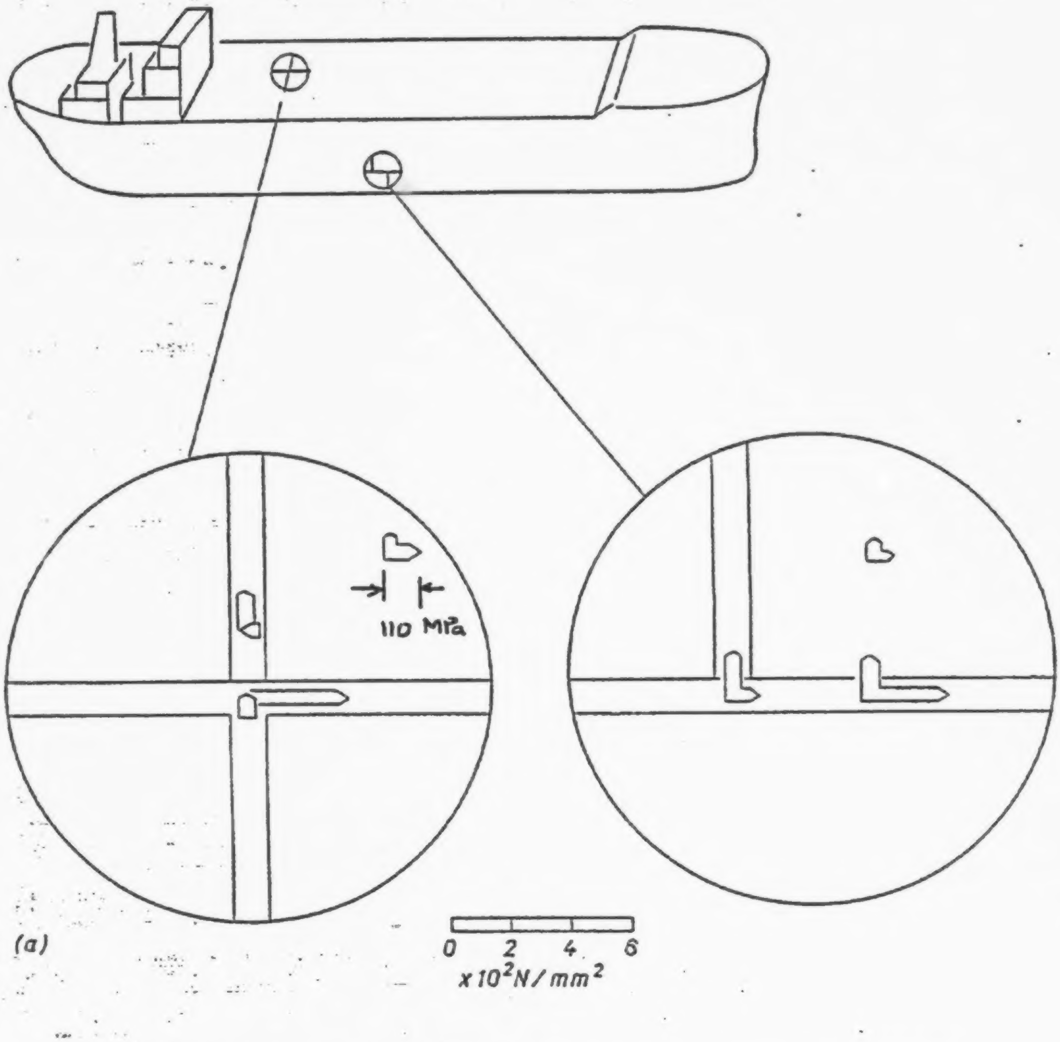
110 MPa
(a)
0 2 4 6
$x\,10^2 N/mm^2$

Figure 2: Weld residual and reaction stresses in a newly constructed 25,500 ton tanker (from Reference 3)

- Degarmo (1946)
- 17m x 8m welded panel
- Vertical weld made last

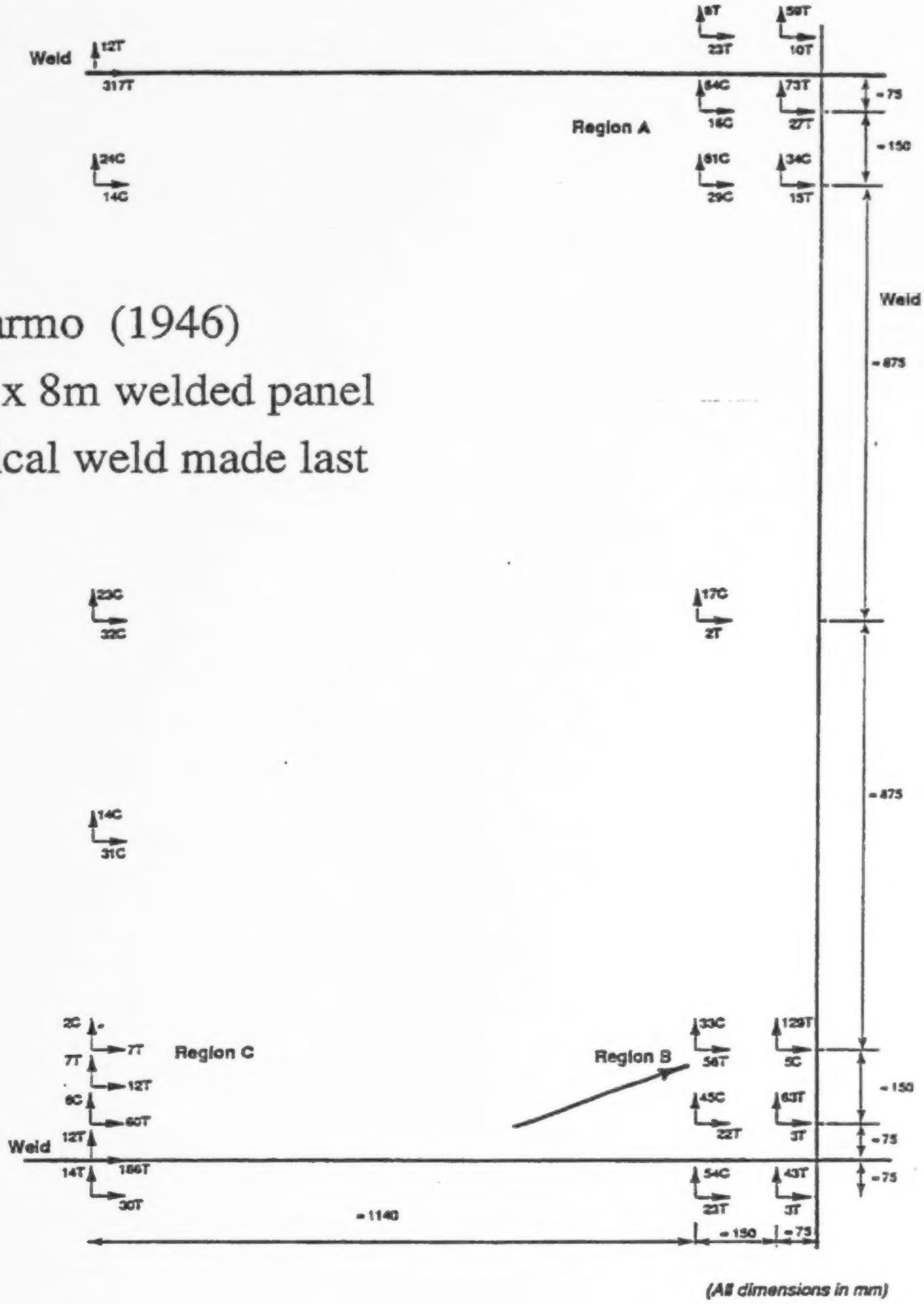
9T
23T
59T
10T
Weld
12T
317T
64C
16C
73T
27T
≈ 75
Region A
24C
14C
61C
29C
34C
15T
≈ 150
Weld
≈ 875
23C
32C
17C
2T
≈ 875
14C
31C
2C
7T
7T
Region C
12T
6C
60T
12T
Weld
14T
186T
30T
Region B
33C
56T
129T
5C
≈ 150
45C
22T
63T
3T
≈ 75
54C
23T
43T
3T
≈ 75
≈ 1140
≈ 150
≈ 75
(All dimensions in mm)

Figure 5(b): 'Reaction stresses (MPa) at some of the locations in Figure 5(a)

Ffield (1946)

- Reaction stress up to 10 ksi tensile
- One value as high as 15 ksi

} *6" from weld*

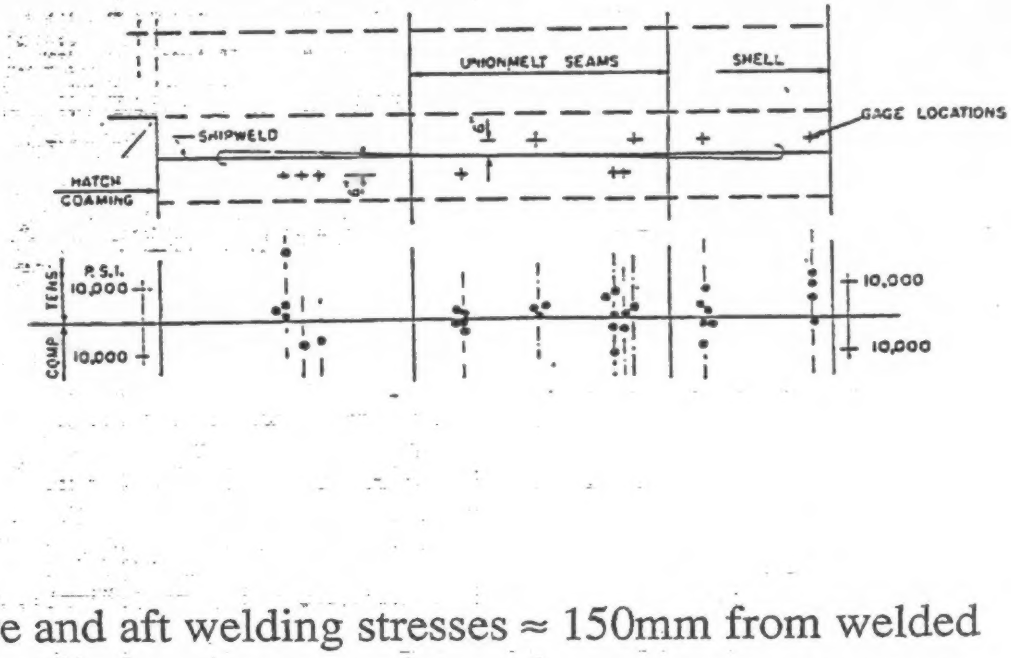
UNIONMELT SEAMS
SHELL
GAGE LOCATIONS
SHIPWELD
HATCH COAMING
6"
P.S.I.
TENS.
10,000
COMP.
10,000
10,000
10,000

Fore and aft welding stresses ≈ 150mm from welded butts in upper deck of 7 Beth Fairfield Liberty Ships (from reference 10).

Ffield (1946)

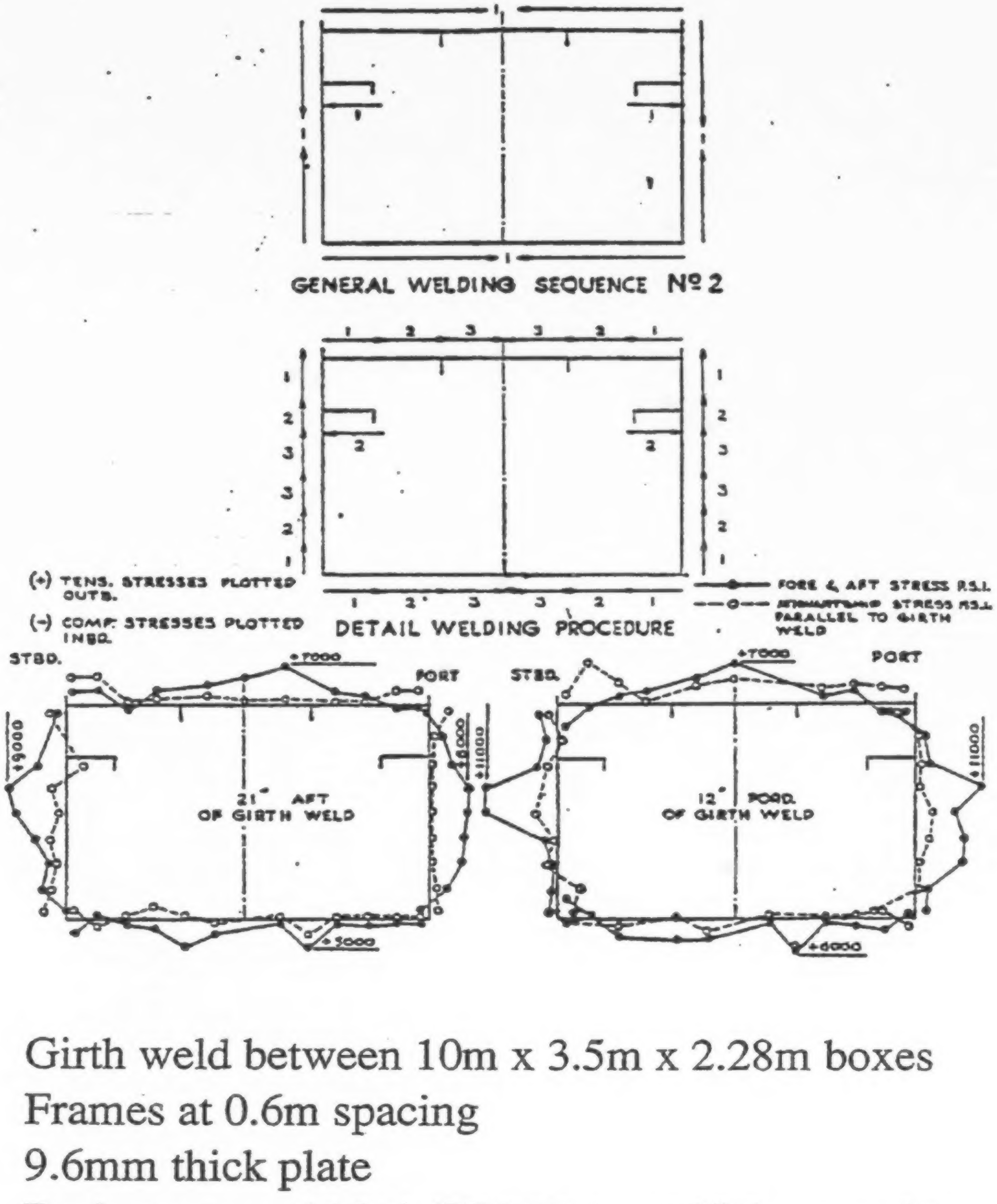
GENERAL WELDING SEQUENCE Nº 2
DETAIL WELDING PROCEDURE
(+) TENS. STRESSES PLOTTED OUTB.
(-) COMP. STRESSES PLOTTED INBD.
FORE & AFT STRESS P.S.I.
ATHWARTSHIP STRESS P.S.I. PARALLEL TO GIRTH WELD
STBD.
PORT
+7000
+9000
+10000
+11000
21" AFT OF GIRTH WELD
12" FORD. OF GIRTH WELD
+5000
+6000

- Girth weld between 10m x 3.5m x 2.28m boxes
- Frames at 0.6m spacing
- 9.6mm thick plate
- Peak stress 11 ksi (77 MPa) 12" from weld
  9 ksi (63 MPa) 21" from weld
- Peak stress at neutral axis.

Ffield (1946)

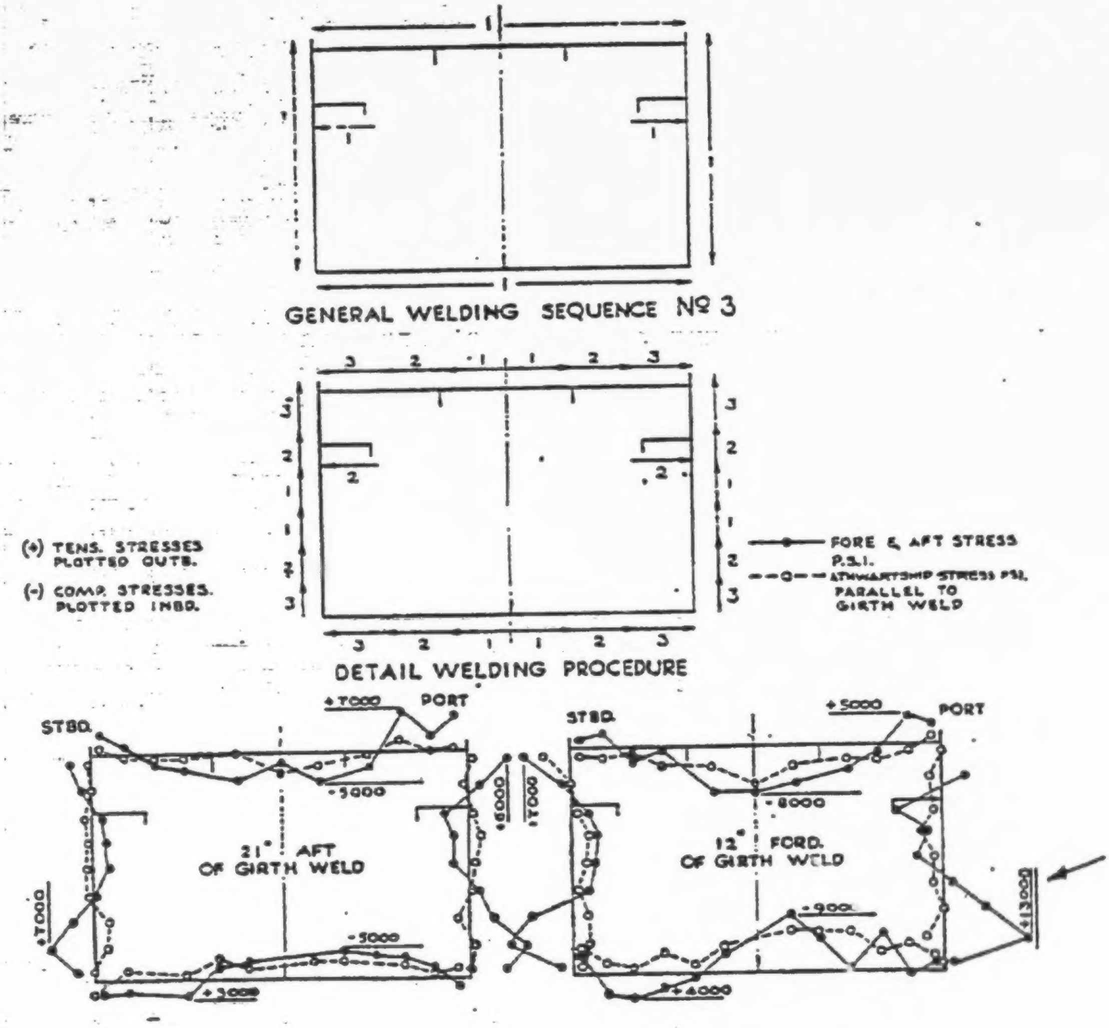
GENERAL WELDING SEQUENCE Nº 3
DETAIL WELDING PROCEDURE
(+) TENS. STRESSES PLOTTED OUTB.
(-) COMP. STRESSES. PLOTTED INBD.
FORE & AFT STRESS P.S.I.
ATHWARTSHIP STRESS PSI. PARALLEL TO GIRTH WELD
STBD.
PORT
21" AFT OF GIRTH WELD
12" FORD. OF GIRTH WELD
+7000
-5000
+3000
+5000
-8000
-9000
+4000
+13000

- Peak stress 13 ksi (91 MPa) 12" from weld
  7 ksi (49 MPa) 21" from weld
- Peak stress at corners.

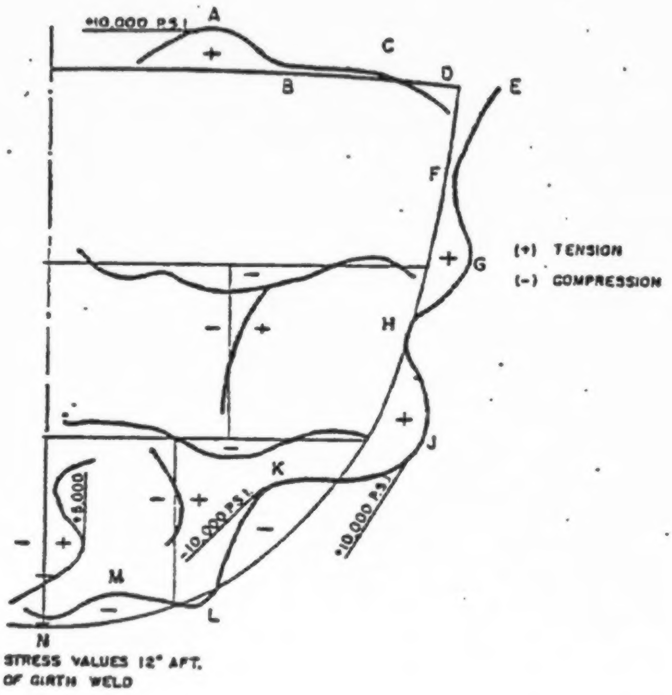
+10,000 P.S.I.
A
+
C
B
D
E
F
+
G
(+) TENSION
(-) COMPRESSION
-
-
+
H
+
J
-
K
+5,000
-
+
-
+
-10,000 P.S.I.
-
+10,000 P.S.I.
M
-
L
N
STRESS VALUES 12" AFT.
OF GIRTH WELD

Figure 15: Fore and aft stress plot (ksi) on DE girth weld, Sum of Steps 1, 2 and 3 (from Reference 10)

- Peak stress at completion of fabrication:
  10 ksi (70 MPa) 12" from weld.

Summary – Literature Search

Tensile Reaction Stress (MPa)	Location	Distance From Weld	Reference
120	Deck; Weld Intersection	≈5 weld widths (100 to 125mm)	3
17	Laboratory Size Plate	100mm	9
56	Ship Subassembly	225mm	9
70 to 105	Liberty Ships	150mm	10
77 to 91	Girth Weld Model	305mm	10
70	Destroyer Escort Girth Weld (Deck & Hull Plating)	305mm	10

- Reaction stress at locations 300mm (12") from the weld can be as high as 91 MPa (13 ksi) It could be higher at locations closer (say 150mm away) to the weld; and conversely lower at locations further away from the weld.

4. Reaction Stress Measurements in a Super Ferry

Objective: Strain gauge two plates and monitor the changes in strain as they are welded into the structure. (The plates were identically located, one on the port side and one on the starboard side).

- Plate thickness: 15mm
- Yield strength: 350 MPa
- $\sigma_1 = [E/(1 - \nu^2)] (\varepsilon_1 + \nu \varepsilon_2)$

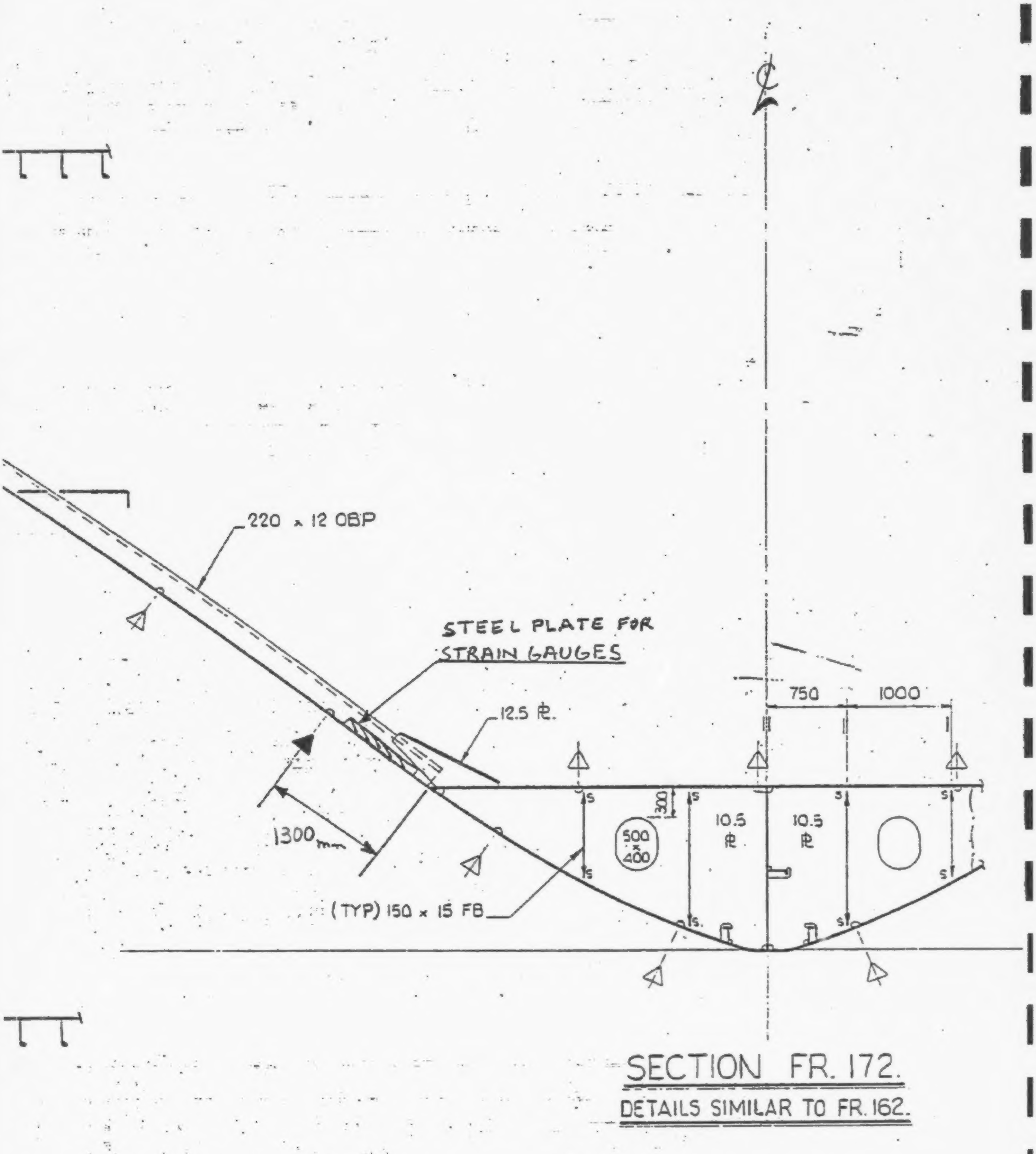
℄
220 x 12 OBP
STEEL PLATE FOR STRAIN GAUGES
12.5 ℞.
1300mm
750
1000
300
S
500 x 400
10.5 ℞
10.5 ℞
(TYP) 150 x 15 FB
SECTION FR. 172.
DETAILS SIMILAR TO FR. 162.

Figure 3 Location of Steel Plates for Instrumentation: Section View Frame 172

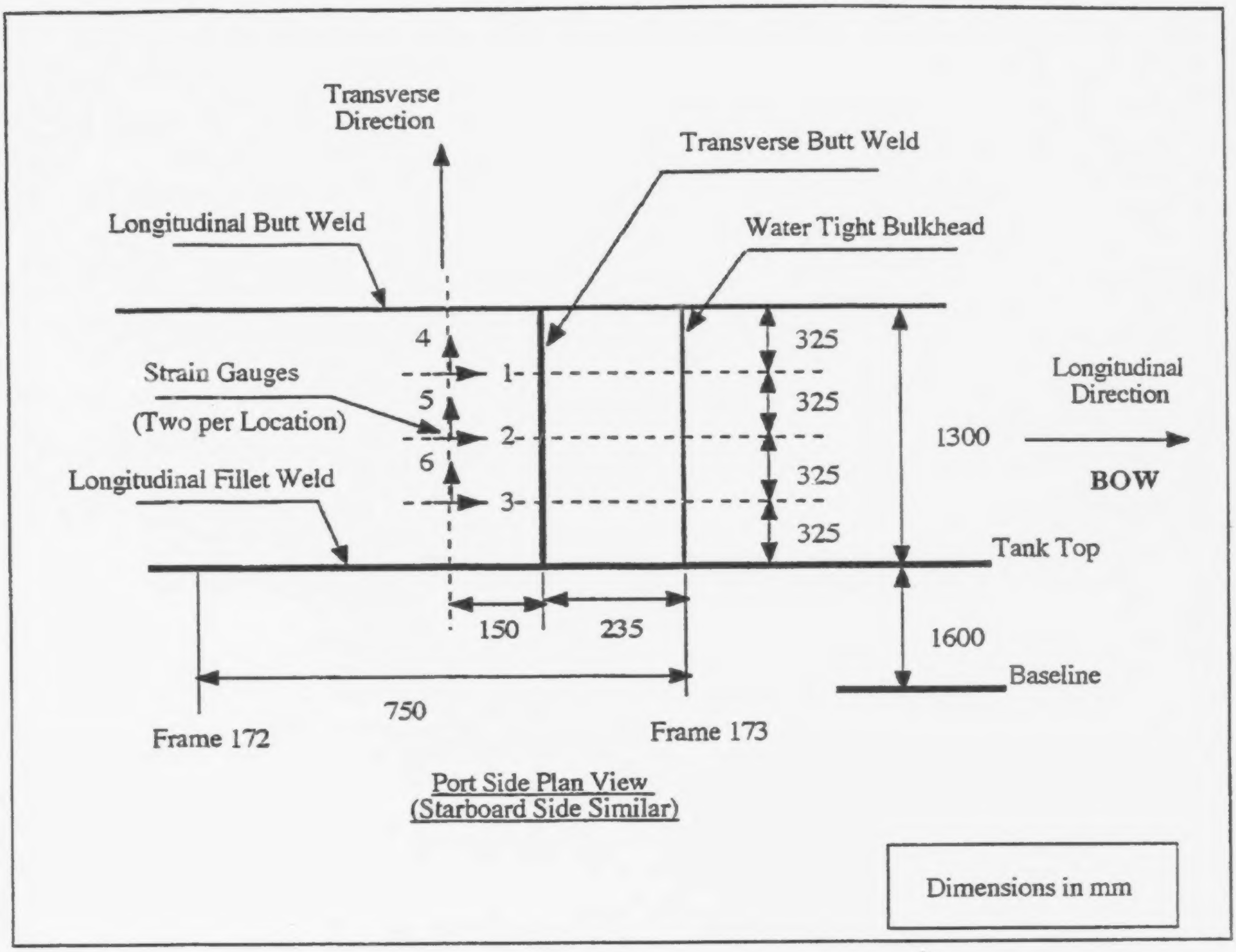
Transverse Direction
Transverse Butt Weld
Longitudinal Butt Weld
Water Tight Bulkhead
4
1-
5
2-
6
3-
Strain Gauges
(Two per Location)
Longitudinal Fillet Weld
325
325
325
325
1300
Longitudinal Direction
BOW
Tank Top
150
235
1600
Baseline
750
Frame 172
Frame 173
Port Side Plan View
(Starboard Side Similar)
Dimensions in mm

Figure 4: Location of Strain Gauges

Figure 11 Measured Strain Change on Port Side Plate - Transverse Direction

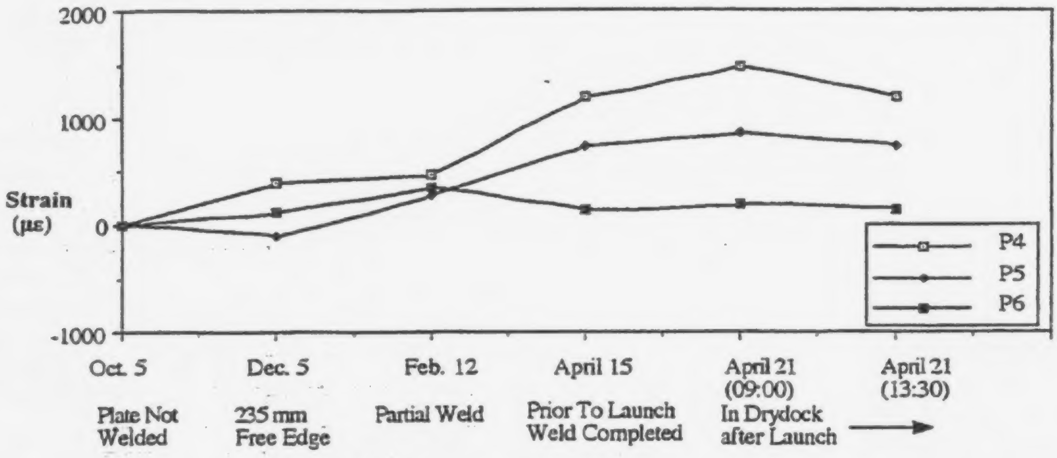

Measurement Date and Construction Phase

Figure 10 Measured Strain Change on Starboard Plate - Transverse Direction

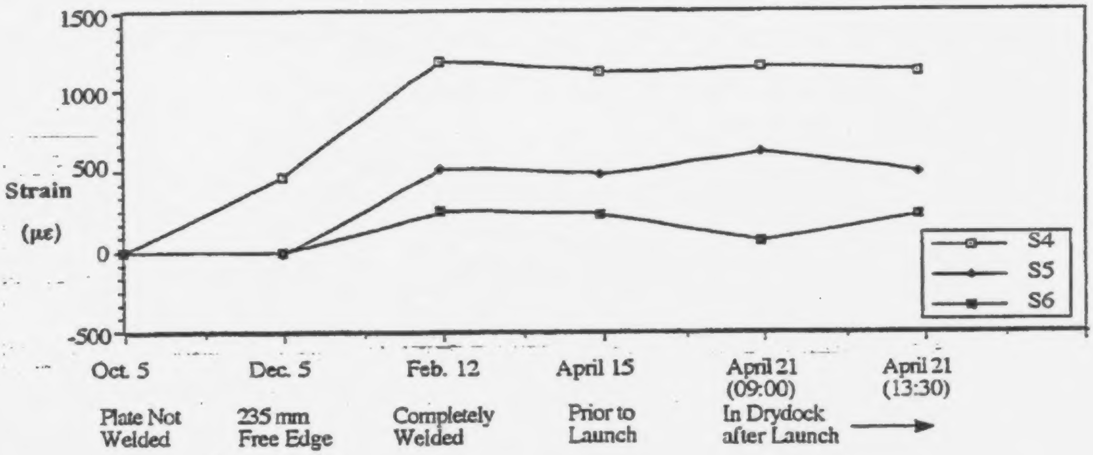

Measurement Date and Construction Phase

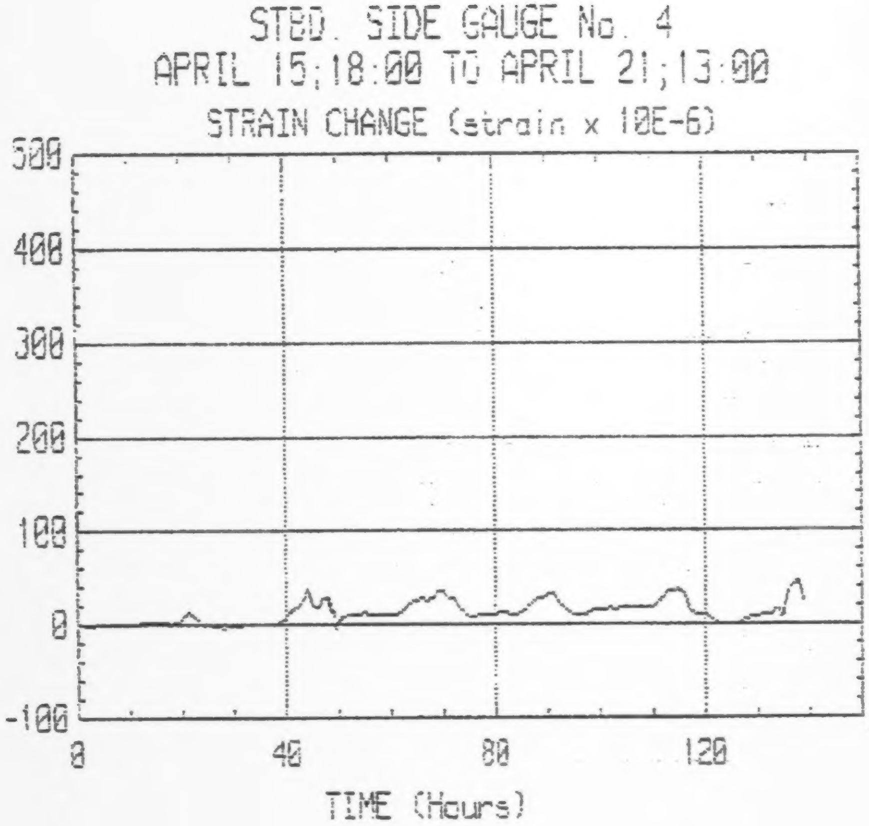
STBD. SIDE GAUGE No. 4
APRIL 15;18:00 TO APRIL 21;13:00
STRAIN CHANGE (strain x 10E-6)
500
400
300
200
100
0
-100
0
40
80
120
TIME (Hours)

PORT SIDE GAUGE No. 4
APRIL 15;18.00 TO APRIL 21;13:00

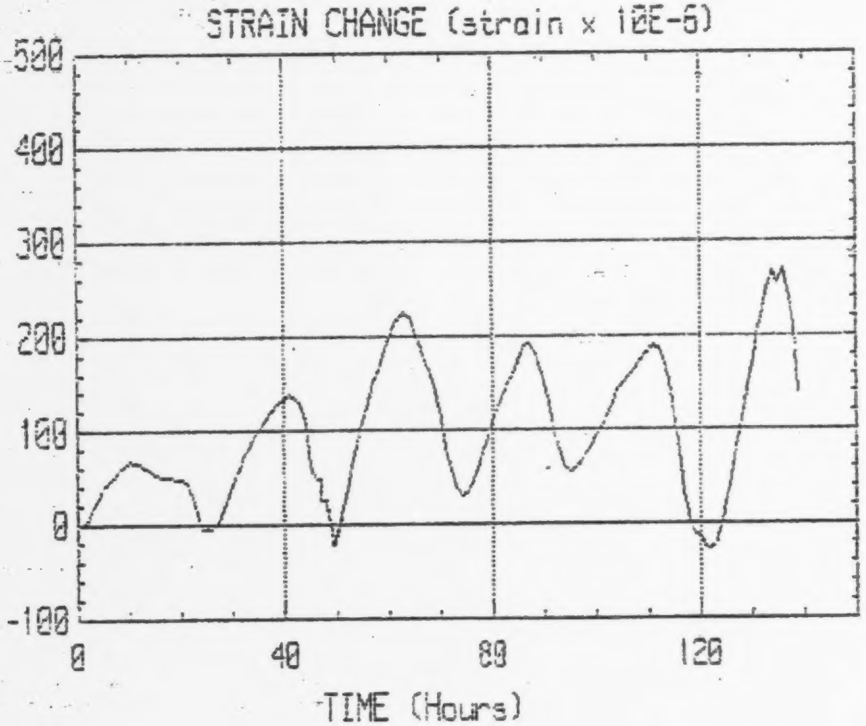

PORT SIDE GAUGE No. 3
APRIL 15;18:00 TO APRIL 21;13:00

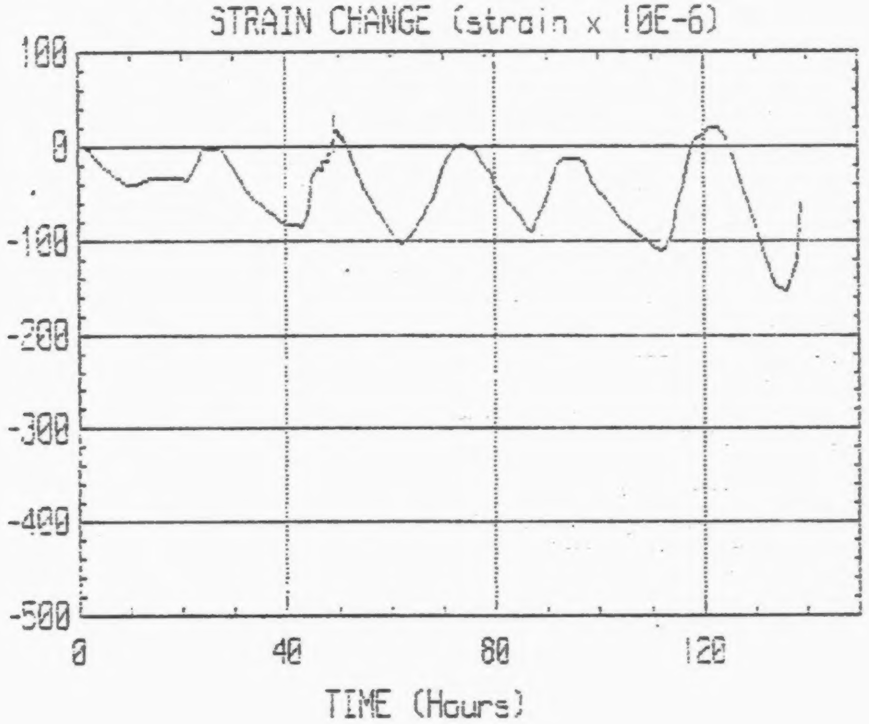

Table 3 Maximum Change in Measured Strain Levels From April 15 to April 21: Launching/Towing/Dry Docking

	Strain	(με)	Stress	(MPa)
Gauge #	L	T	L	T
Port				
1	120		46	
4		270		70
2	-190		-34	
5		130		17
3	-150		-30	
6		60		3
Stbd.				
1	-30		-4	
4		43		8
2	130		39	
5		140		41
3	-40		-20	
6		-160		-39

Notes

L - Longitudinal Direction
T - Transverse Direction
Base Line Strain Level Defined on April 15: 18:00

The changes in the strain during the April 15 - April 21 time span are periodic in nature, the period being exactly 24 hours. This suggests that periodicity is related to exposure to sun and that the resulting changes in stress can be as high as 70MPa.

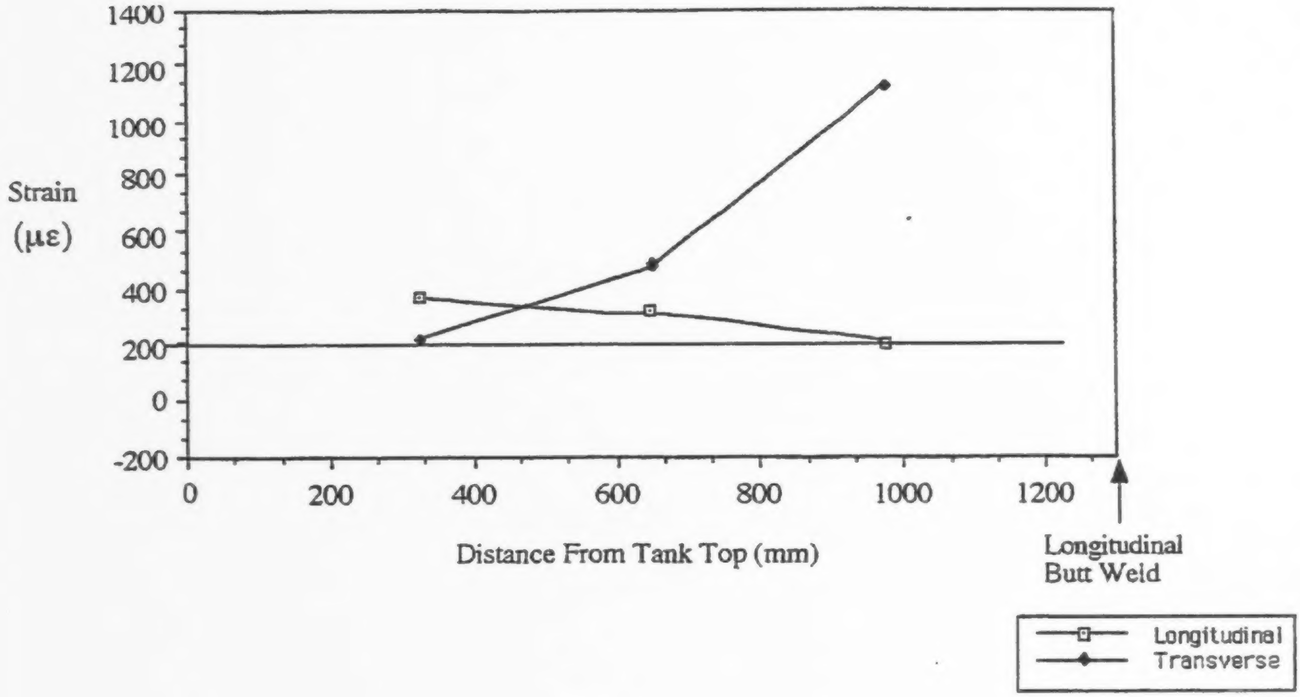

Port Side Shell Plate

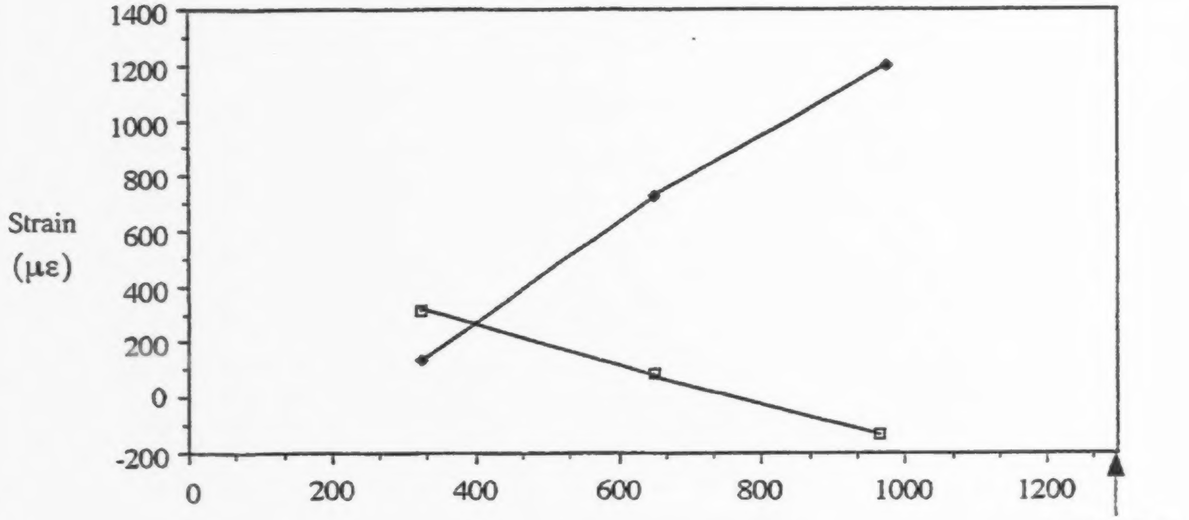

Figure 6 Reaction Strain Distributions on Welded Plate: April 21

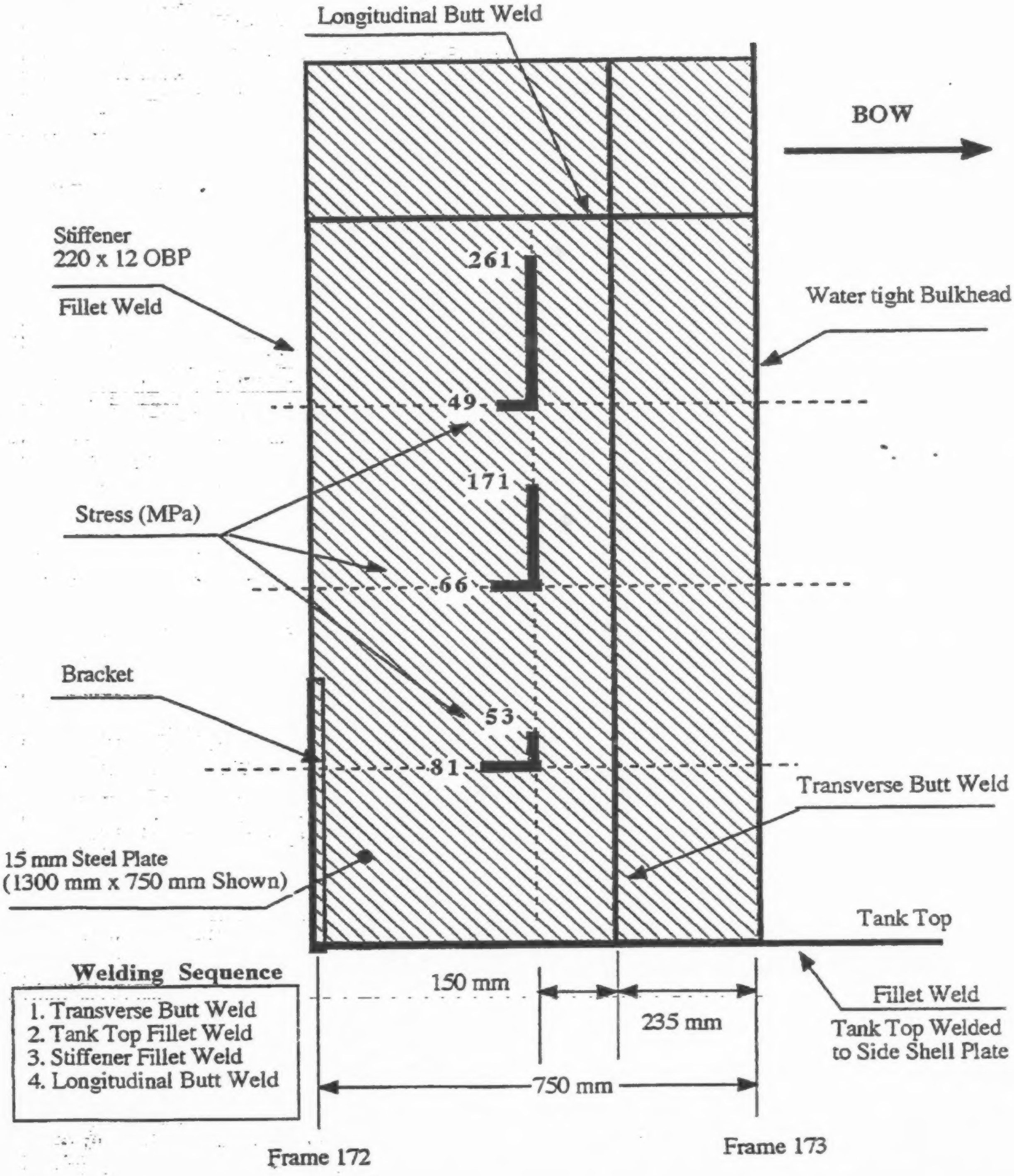
Longitudinal Butt Weld
BOW
Stiffener
220 x 12 OBP
Fillet Weld
Water tight Bulkhead
261
49
171
66
53
81
Stress (MPa)
Bracket
Transverse Butt Weld
15 mm Steel Plate
(1300 mm x 750 mm Shown)
Tank Top
Fillet Weld
Tank Top Welded
to Side Shell Plate
150 mm
235 mm
750 mm
Frame 172
Frame 173

Welding Sequence

1. Transverse Butt Weld
2. Tank Top Fillet Weld
3. Stiffener Fillet Weld
4. Longitudinal Butt Weld

Figure 8 Reaction Stress Distribution on Port Side Shell Plate: April 21

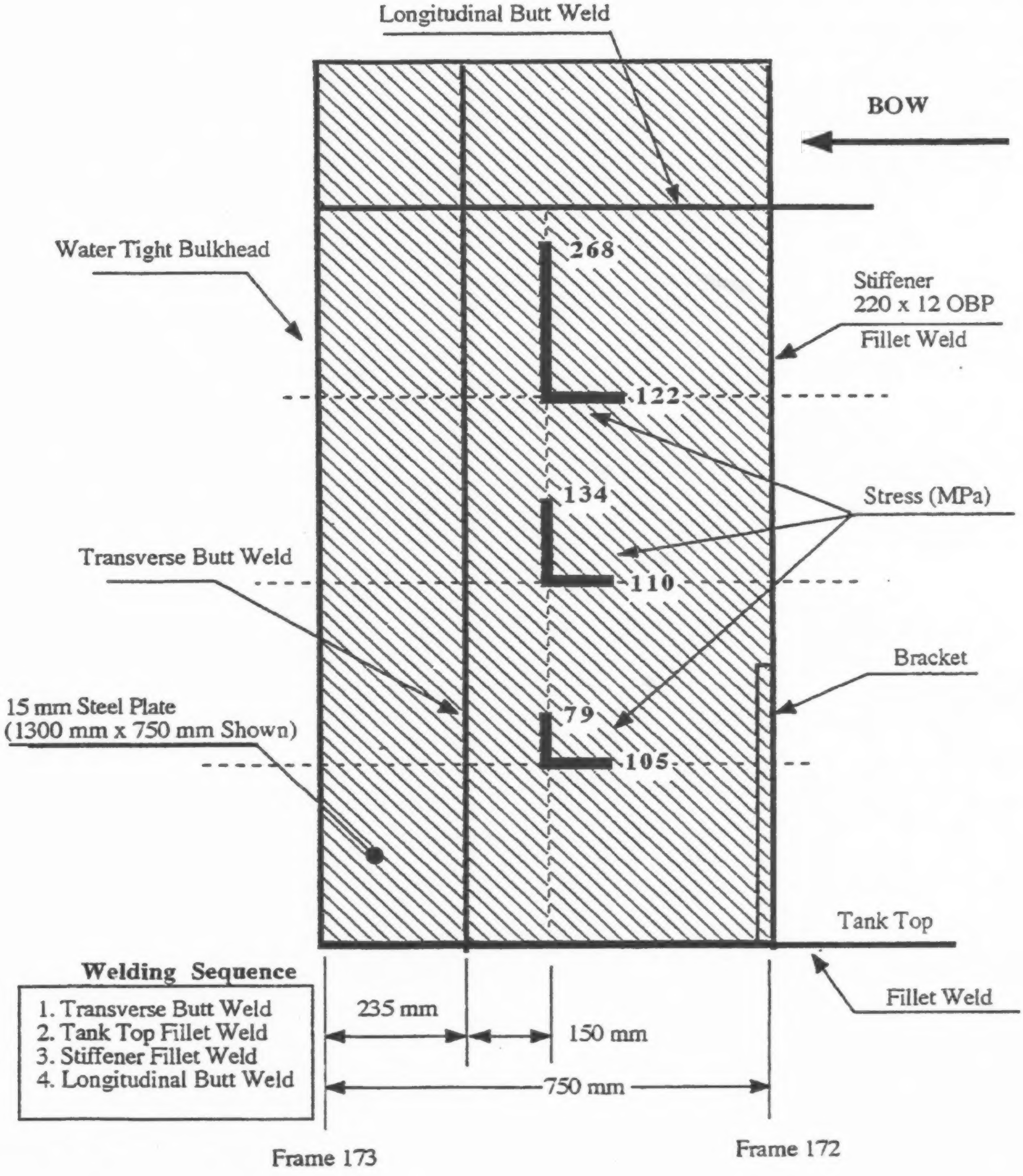
Longitudinal Butt Weld
BOW
Water Tight Bulkhead
268
Stiffener
220 x 12 OBP
Fillet Weld
122
134
Stress (MPa)
Transverse Butt Weld
110
Bracket
15 mm Steel Plate
(1300 mm x 750 mm Shown)
79
105
Tank Top
Welding Sequence
1. Transverse Butt Weld
2. Tank Top Fillet Weld
3. Stiffener Fillet Weld
4. Longitudinal Butt Weld
235 mm
150 mm
750 mm
Fillet Weld
Frame 173
Frame 172

Figure 7 Reaction Stress Distribution on Starboard Side Shell Plate: April 21

Conclusions

1. Based on experimental data in literature, the long range tensile reaction stresses, perpendicular to the weld and at locations ≈ 300 mm (12") from it, can be as high as 91 MPa (13 ksi). At locations closer to the weld, they are expected to be higher.

2. In measurements made during the construction of a large ferry, the reaction stress perpendicular to a longitudinal butt weld, at a location 325 mm (13") from the weld was 268 MPa (≈ 38 ksi), though the transient reaction stress reached 330 MPa (47 ksi), about 95% of the steels yield strength.

Conclusions

3. Parallel to the hull girder longitudinal bending stresses, the peak reaction stress, 150 mm (6") from the transverse weld was 122 MPa (18 ksi), and the peak transient value was 149 MPa (21 ksi)

4. Reaction stresses should not be ignored in developing material specifications for fracture toughness or in fitness for purpose evaluation.

5. Further work is needed to quantify the magnitude of the reaction stresses, and their possible‘shakedown’ in service.

#510316

(11)

AN EVALUATION OF EXPERIMENTAL METAL-CORED ELECTRODES FOR SUBMERGED-ARC WELDING OF HSLA100 STEEL

By

J.A. Gianetto, N.J.G. Smith and D.E. Dolan

Metals Technology Laboratories-CANMET
Ottawa, Ontario, Canada, K1A 0G1

ABSTRACT

The object of this investigation was to develop and evaluate experimental electrode wires for joining HSLA100 steel with particular emphasis on improvement of weld metal toughness properties. The work focused on the development of metal-cored wires with varying C and Mo contents for submerged-arc (SA) welding.

The series of SA welds produced with the metal-cored wires, in combination with a highly basic flux, provided better toughness than achieved using the reference 120S-1 electrode. Optimum toughness was achieved with the intermediate C and Mo contents. In general, the results were attributed to the influence of weld metal chemistry on the final weld microstructure, specifically the formation of a relatively fine bainitic structure with some lath martensite and limited grain boundary ferrite in both the as-deposited and reheated weld metal regions. For increasing weld metal C (0.040-0.090%) and Mo (0.45-0.70%) there was an increase in yield strength, hardness and tensile strength. With increasing C there was refinement of the microstructure, increased evidence of lath martensite, almost no grain boundary ferrite, and greater carbide precipitation. Changes in microstructure were much less pronounced with variation in Mo. In addition, increasing C was found to reduce the upper shelf energy, attributed to high weld metal yield strength and increase in carbide precipitation (enhanced microvoid coalescence).

OBJECTIVES

- to develop and evaluate experimental electrode wires for joining HSLA100 steel with particular emphasis on improvement of weld metal toughness properties.

- to establish the effect of small variations in C and Mo contents.

Chemical composition of HSLA100 base material.

Element wt %										
C	Mn	Si	S	P	Cr	Ni	Mo	Cu	Nb	C.E
0.05	1.00	0.34	0.003	0.009	0.61	1.77	0.51	1.23	0.037	0.64

Note: Plate Thickness = 25.4 mm

$$CE = C + Mn/6 + (Cu + Ni)/5 + (Cr + Mo + V)/15$$

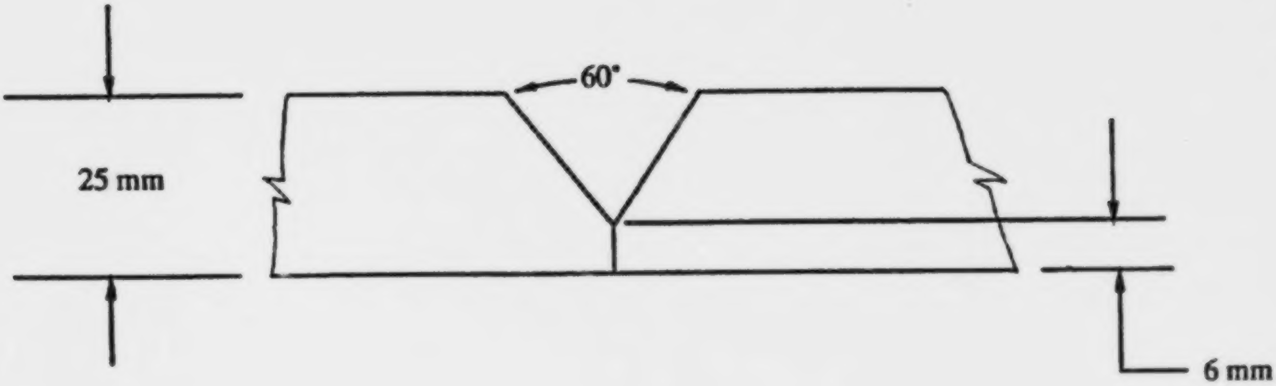

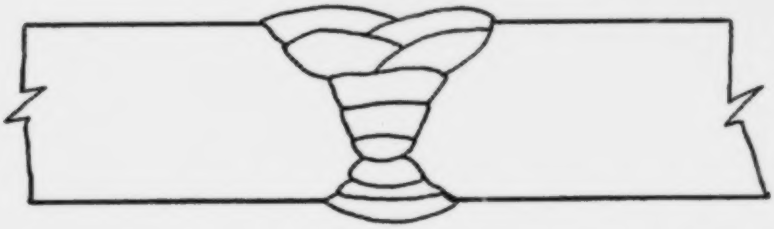

Wire	LTEC 120S1
Flux	Oerlikon OP121TT
Current	470 A
Voltage	35 V
Travel Speed	7.8 mm/s
Energy Input	2 kJ/mm
Preheat Temperature	93°C
Interpass Temperature	150°C
Post Weld Hydrogen Removal	250°C - 2 h

Chemical composition of reference solid electrode wire (120S-1).

Wire	Element wt %										
No	C	Mn	Si	S	P	Al	Cr	Ni	Mo	Cu	Nb
MIL 120-S1	0.056	1.58	0.35	0.006	0.011	0.02	0.29	2.36	0.53	0.02	-

Targeted weld metal chemical compositions for experimental metal-cored wires.

	Element wt %										
	C	Mn	Si	S	P	Al	Cr	Ni	Mo	Cu	Ti
MC1	0.04	1.50	0.30	0.010	0.015	0.005	0.35	2.50	0.40	<0.20	0.007
MC2	0.07	"	"	"	"	"	"	"	0.40	"	"
MC3	0.11	"	"	"	"	"	"	"	0.40	"	"
MC4	0.07	"	"	"	"	"	"	"	0.60	"	"
MC5	0.07	"	"	"	"	"	"	"	0.80	"	"

Chemical composition of SA welds.

Weld	Element wt %													
No.	C	Mn	Si	S	P	Cr	Ni	Mo	Cu	Nb	O	N	CE	Pcm
HS12-1	0.047	1.30	0.45	0.008	0.017	0.40	2.3	0.47	0.32	0.01	0.0283	0.0129	0.61	0.23
HS12-4	0.040	1.40	0.37	0.012	0.010	0.45	2.3	0.45	0.42	0.02	0.0375	0.0078	0.63	0.23
HS12-5	0.060	1.40	0.40	0.011	0.011	0.46	2.2	0.45	0.38	0.02	0.0325	0.0075	0.65	0.25
HS12-7	0.090	1.40	0.36	0.011	0.012	0.43	2.6	0.42	0.40	0.02	0.0217	0.0072	0.69	0.28
HS12-8	0.054	1.40	0.34	0.012	0.010	0.46	2.4	0.54	0.37	0.01	0.0317	0.0061	0.67	0.25
HS12-9	0.051	1.40	0.36	0.012	0.010	0.44	2.4	0.70	0.35	0.01	0.0336	0.0058	0.70	0.26

Note: $CE(IIW) = C + Mn/6 + (Cr + Mo + V)/5 + (Ni + Cu)/15$

$Pcm = C + Si/30 + (Mn + Cu + Cr)/20 + Ni/60 + Mo/15 + V/10 + 5\,B$

Mechanical property requirements for submerged-arc welds deposited in HSLA100 steel (MIL 23765/2D).

Yield Strength (MPa)	703
Elongation (%)	20
Reduction of Area (%)	50
Charpy Impact Energy	81 J at -18°C 61 J at -51°C
Dynamic Tear	540 J at -29°C

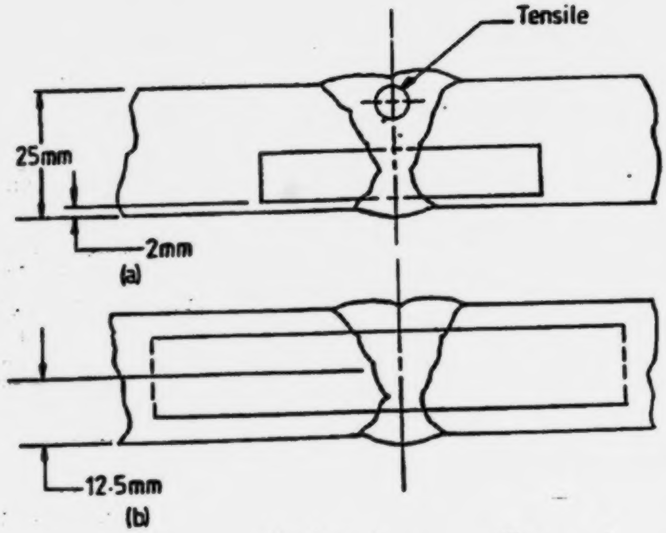
Tensile
25mm
2mm
(a)
12·5mm
(b)

Location and orientation of mechanical test specimens in SA welds (a) tensile and CVN specimens and (b) dynamic tear specimen.

Tensile properties of full-thickness SA welds deposited in HSLA100 steel.

Weld No.	Yield Strength MPa	Ultimate Strength MPa	Elongation %	Reduction of Area %
HS12-1	717	863	23	70
HS12-4	668	829	21	65
HS12-5	695	846	20	69
HS12-7	800	975	20	62
HS12-8	721	868	22	66
HS12-9	743	891	21	65

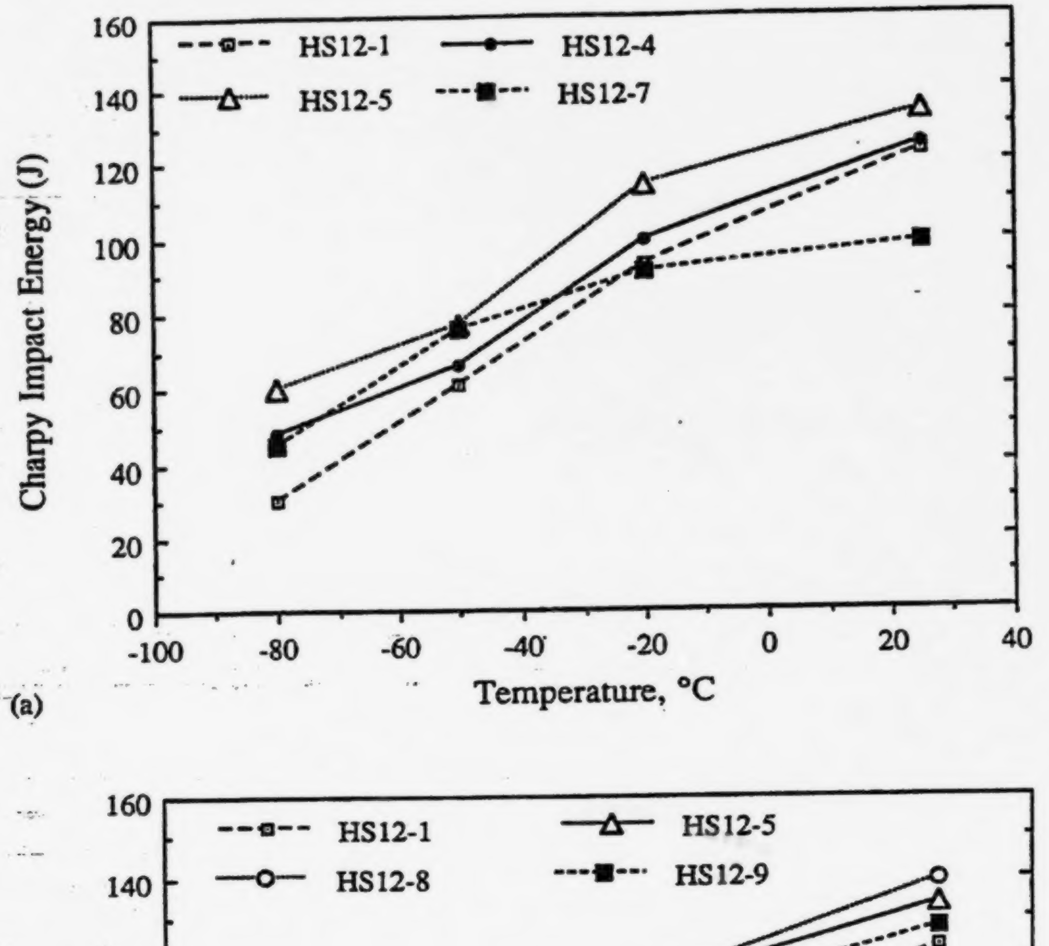

Charpy impact transition curves for the series of SA welds.

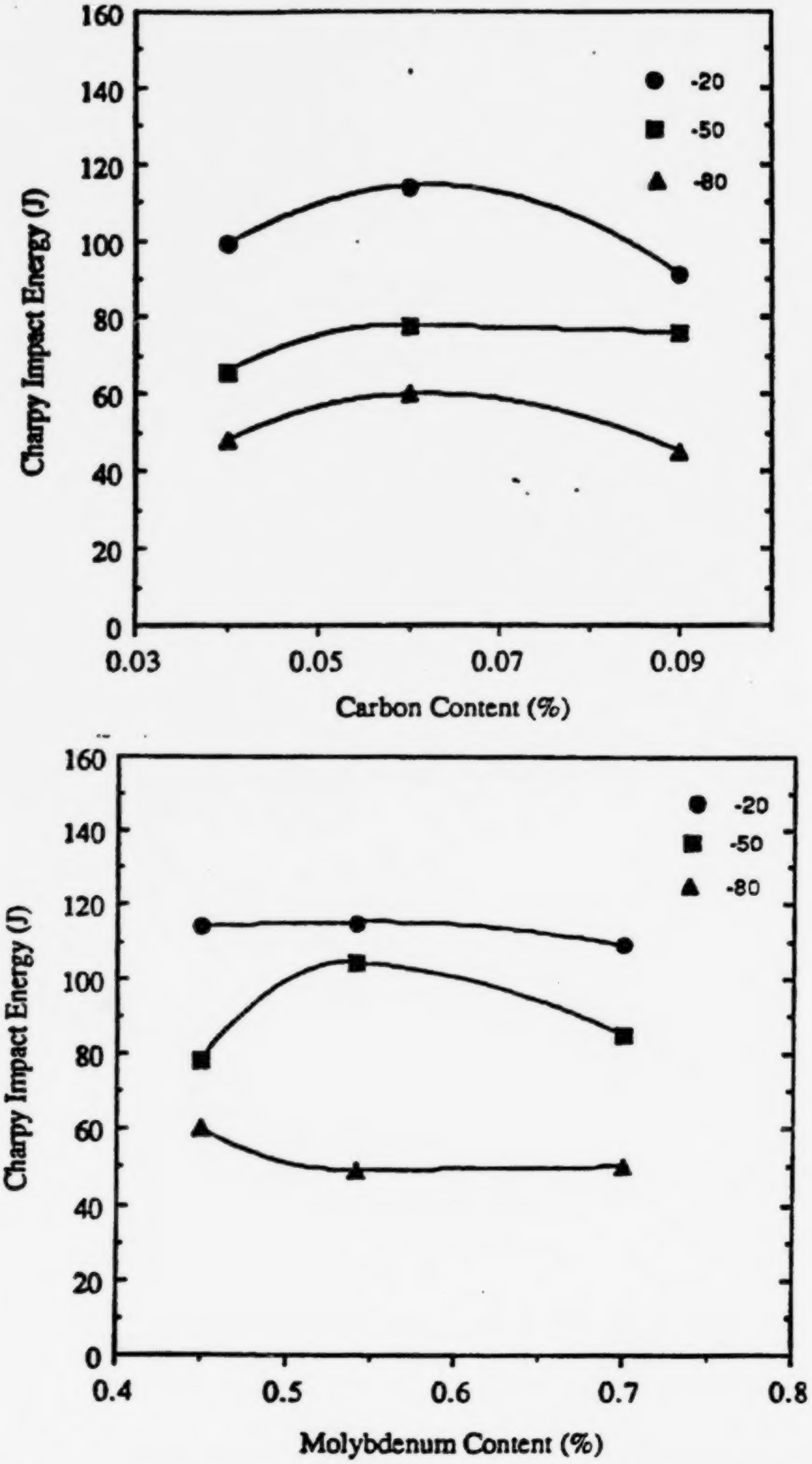

Charpy impact energy versus (a) % carbon and (b) % molybdenum for the welds produced with the experimental metal-cored electrode wires.

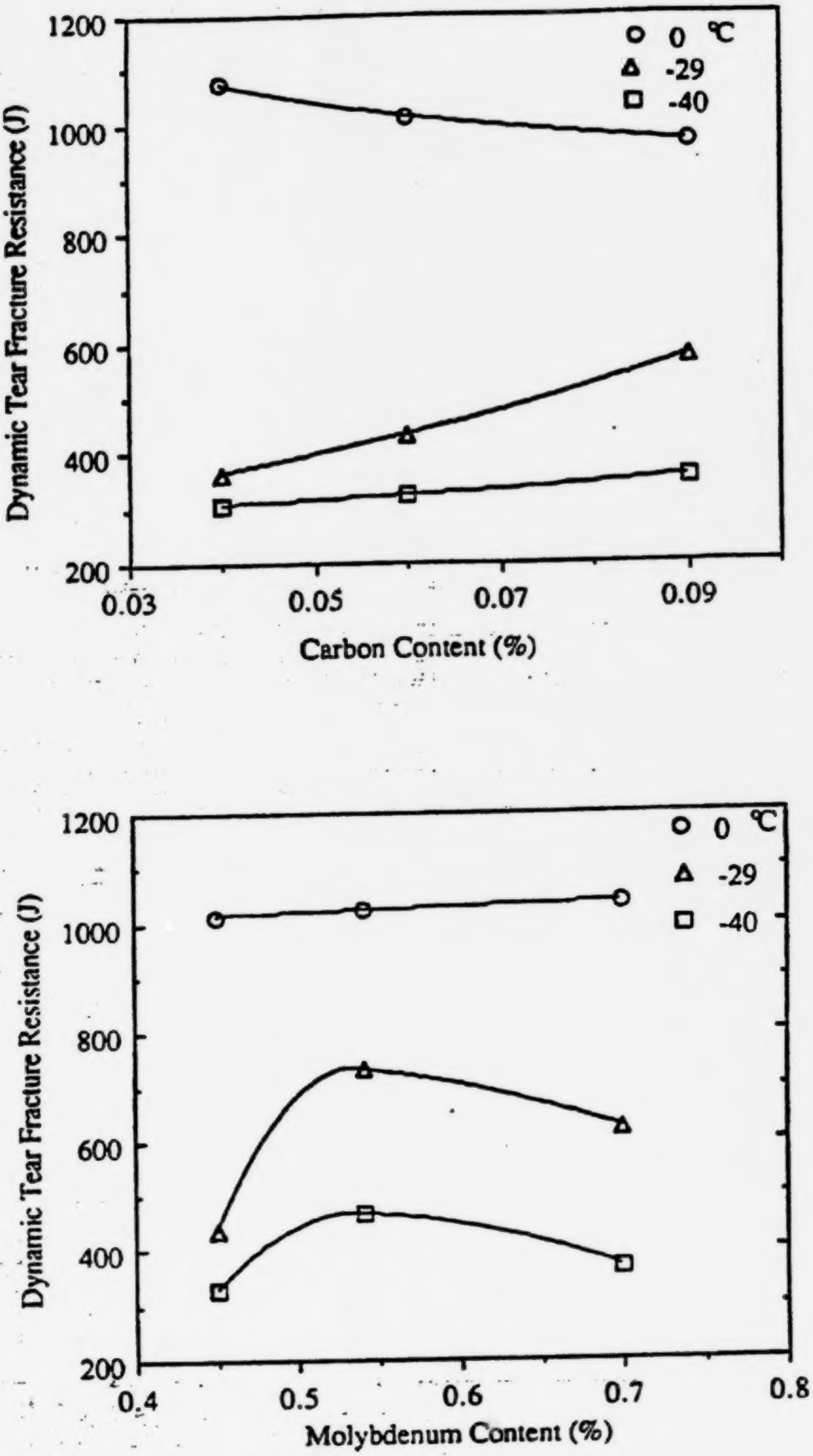

Dynamic tear impact energy versus (a) % carbon and (b) % molybdenum for the welds produced with the experimental metal-cored electrode wires.

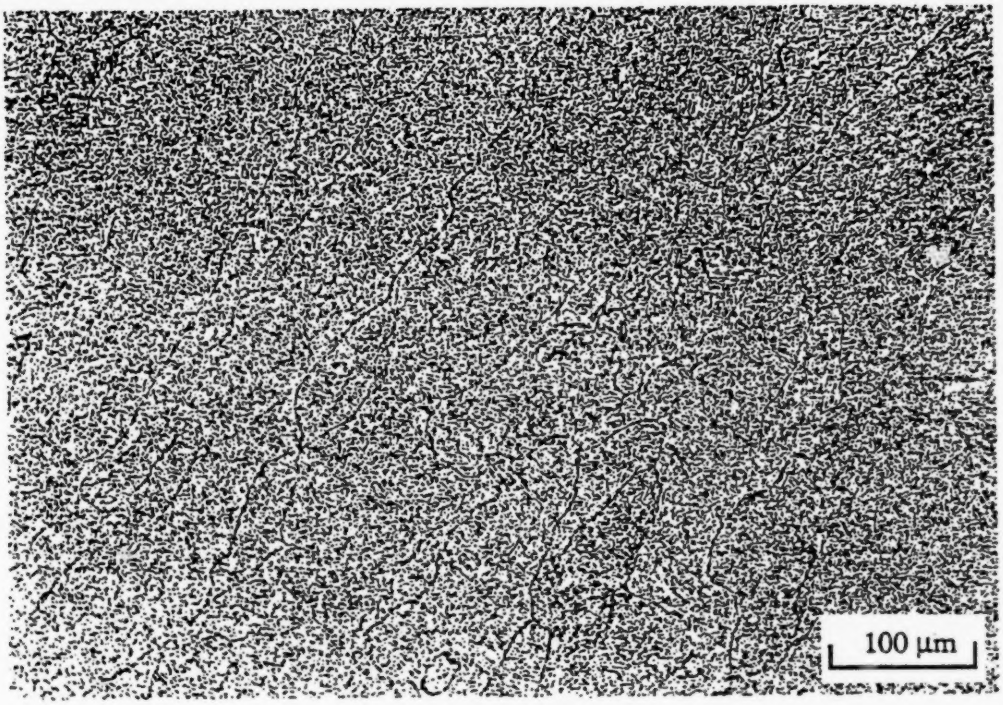

(a) columnar structure

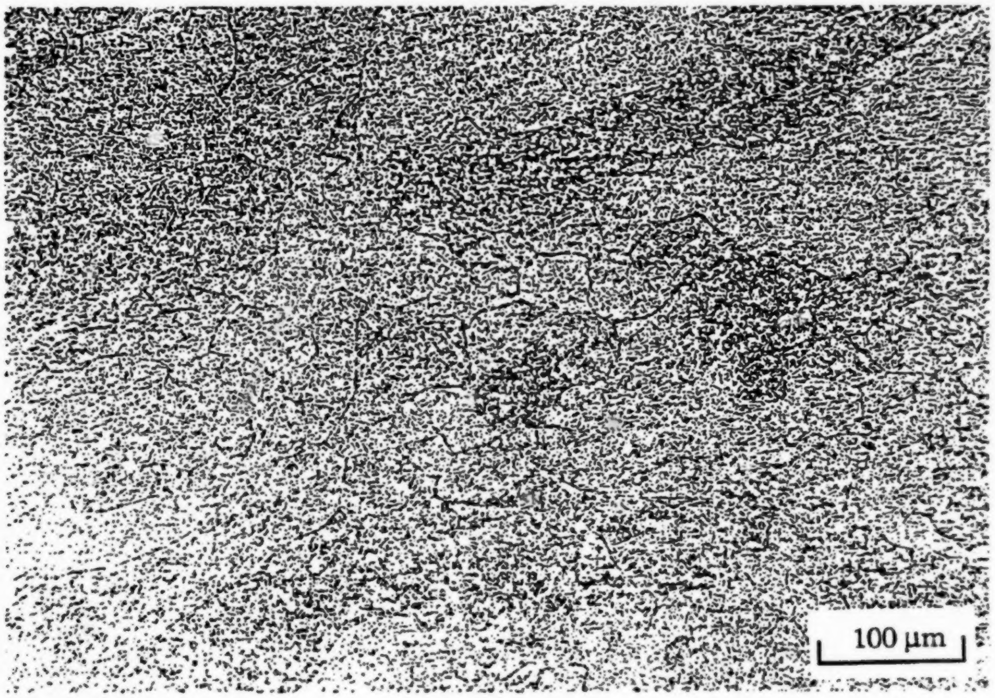

(b) reheated region

Representative micrographs of the as-deposited and reheated weld metal regions for the reference SA weld HS12-1 showing delineation of boundaries. Etched in a solution containing 4 g picric acid in alcohol with 1 ml of HCL.

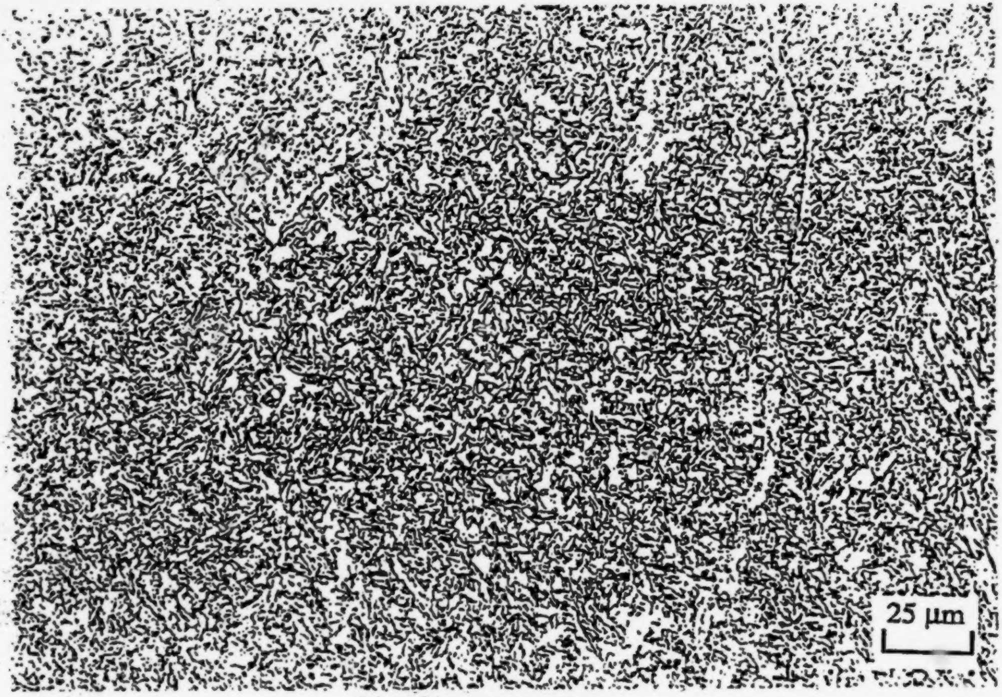

(a) columnar structure

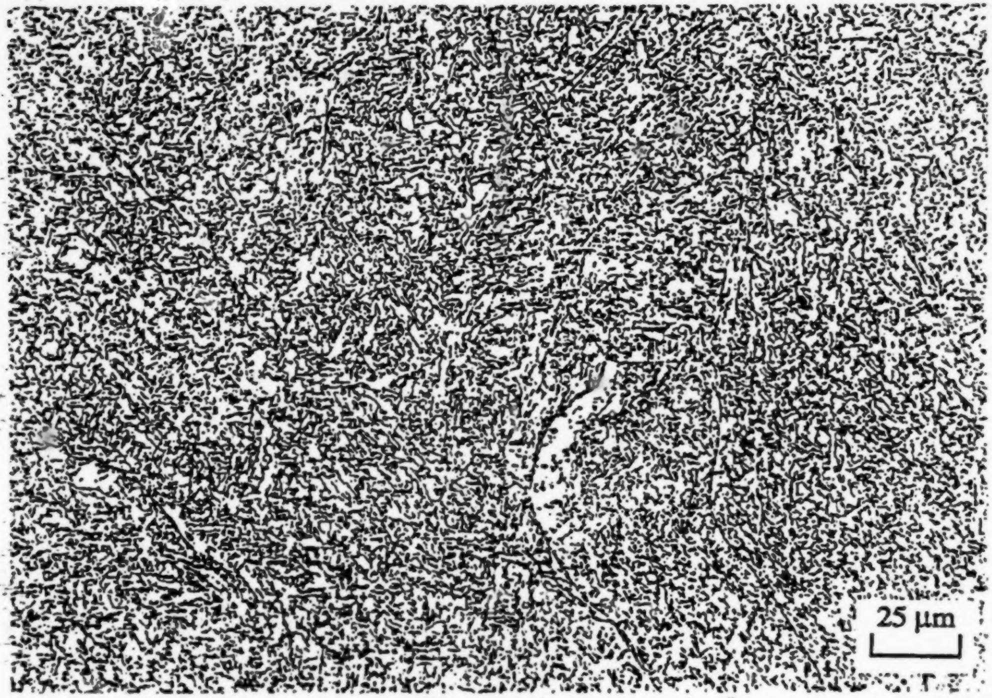

(b) reheated region

Represenative microstructure of (a) the as-deposited and (b) reheated region of SA weld HS12-4.

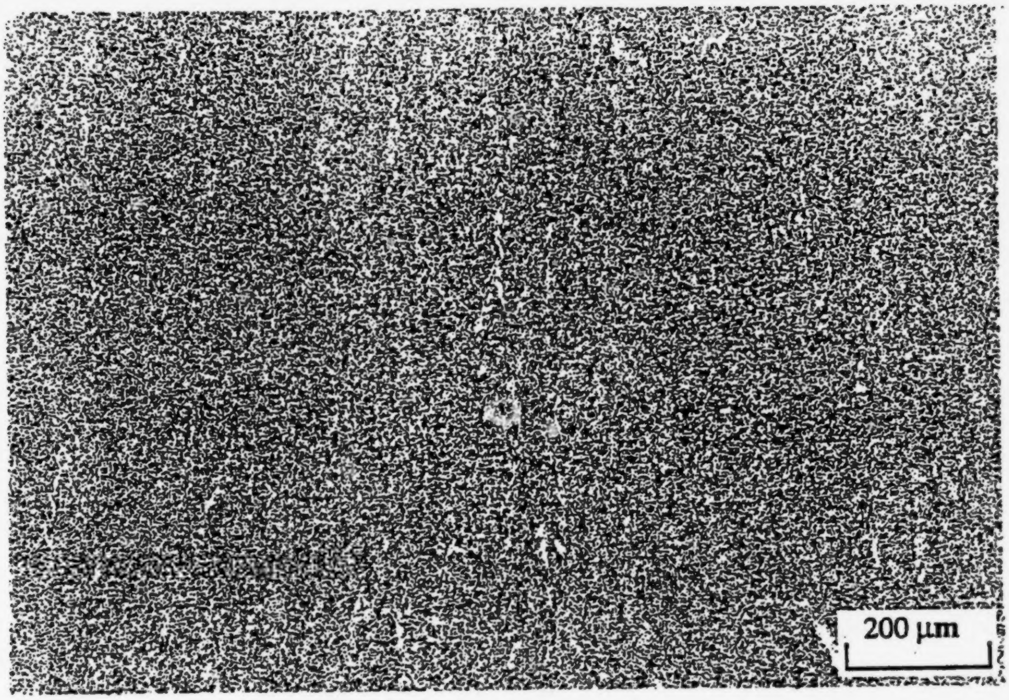

(a) columnar structure

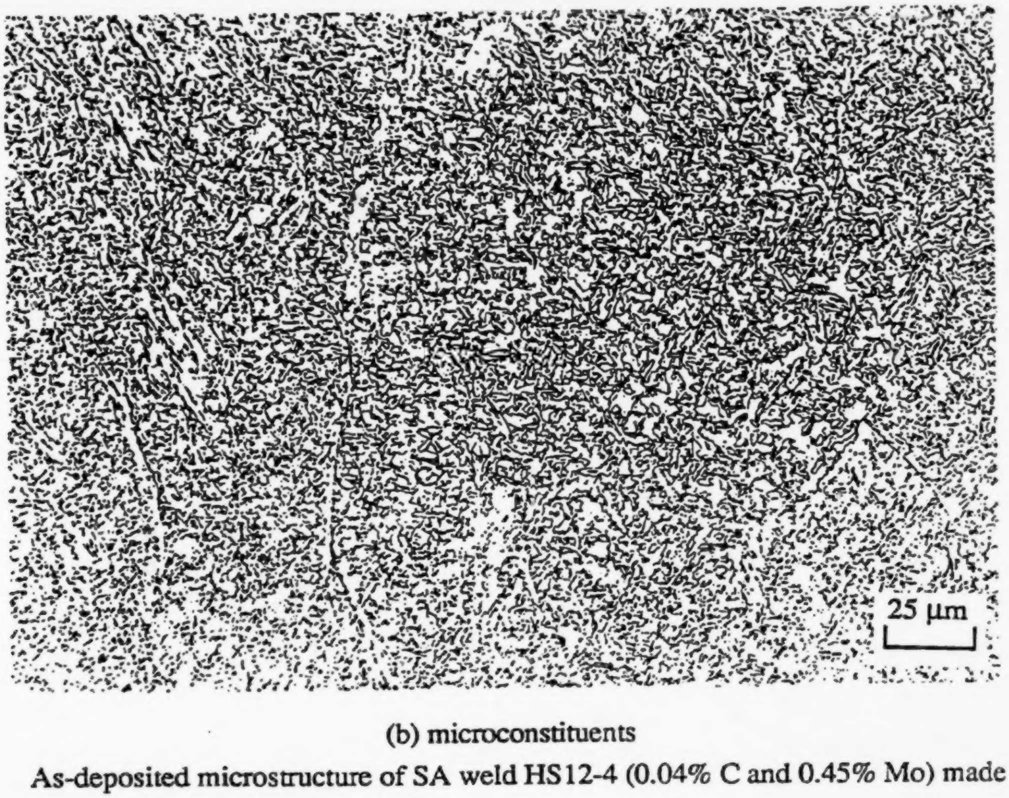

(b) microconstituents

As-deposited microstructure of SA weld HS12-4 (0.04% C and 0.45% Mo) made with experimental metal-cored electrode wire MC1.

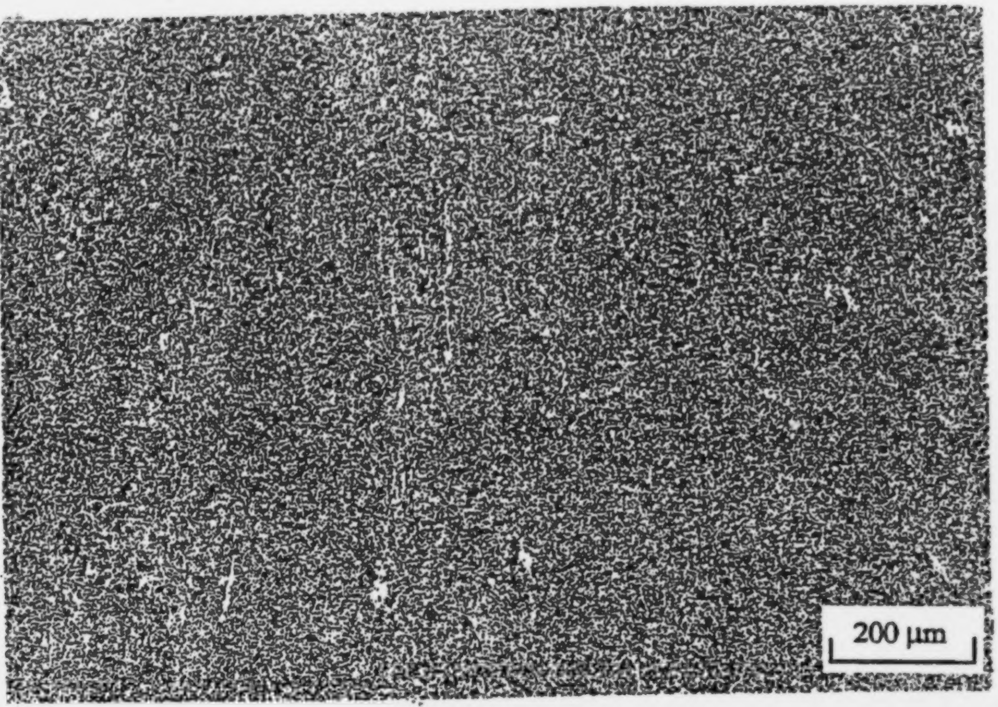

(a) columnar structure

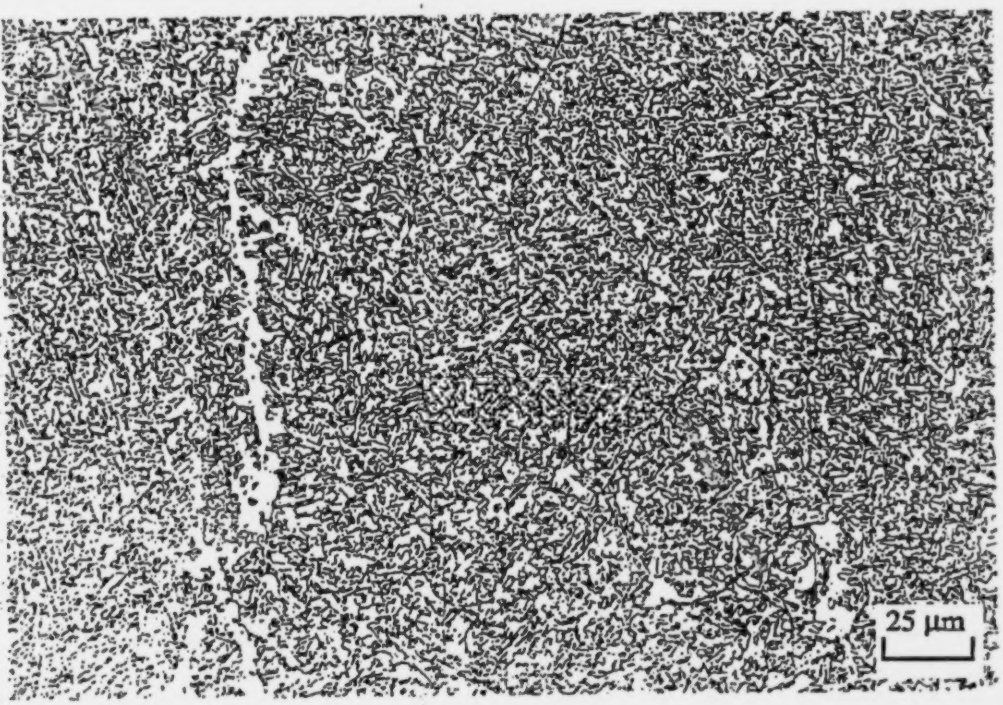

(b) microconstituents

As-deposited microstructure of SA weld HS12-5 (0.060 %C and 0.45 %Mo) made with experimental metal-cored electrode wire MC2.

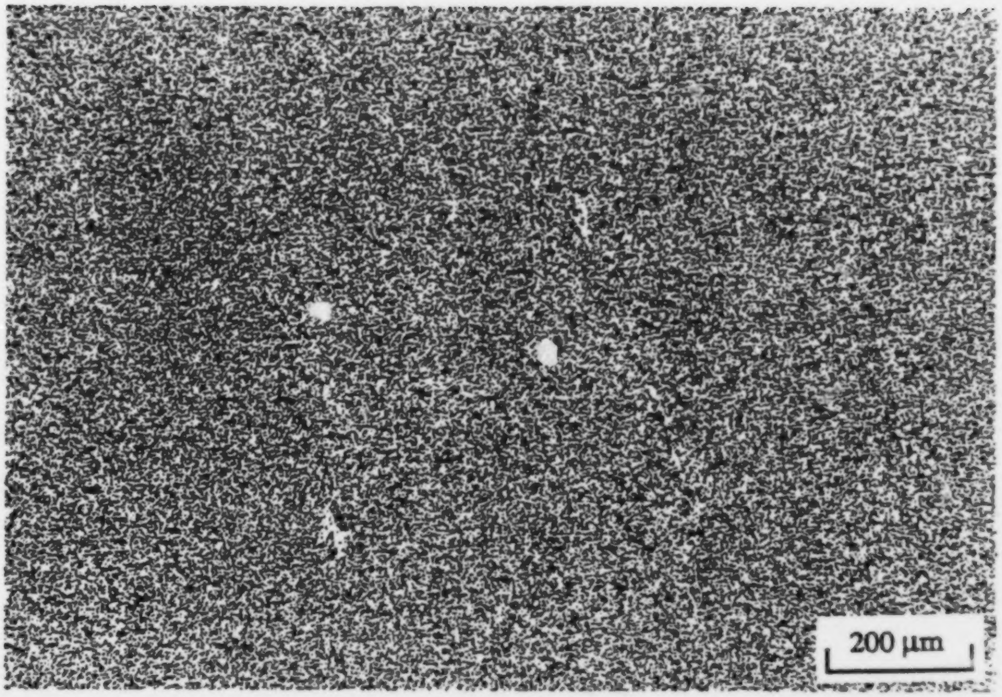

(a) columnar structure

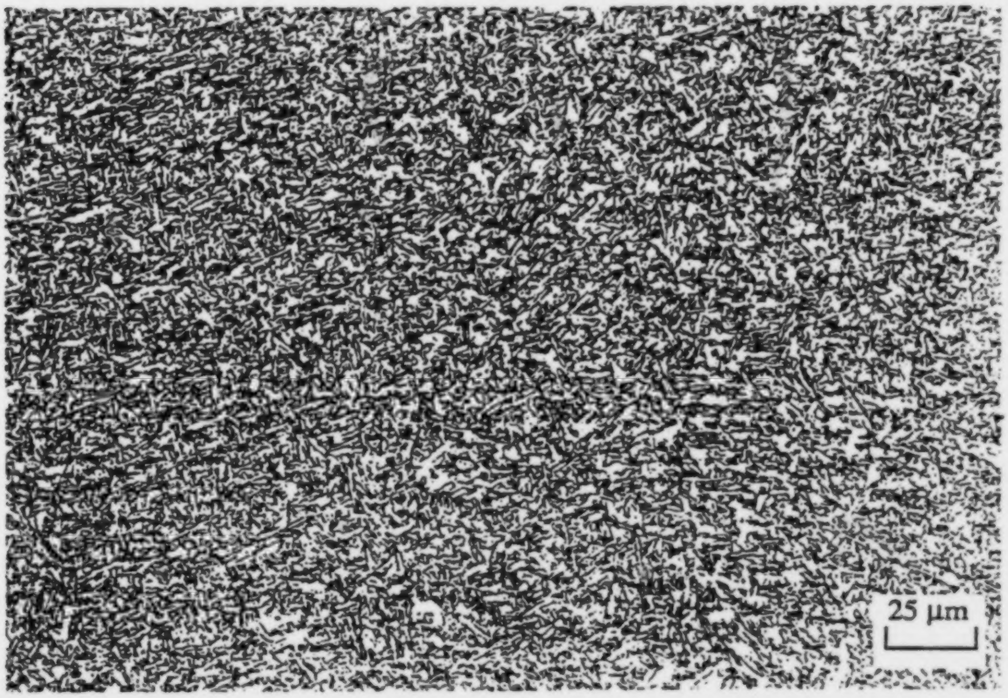

(b) microconstituents

As-deposited microstructure of SA weld HS12-7 (0.090 %C and 0.42 %Mo) made with experimental metal-cored electrode wire MC3.

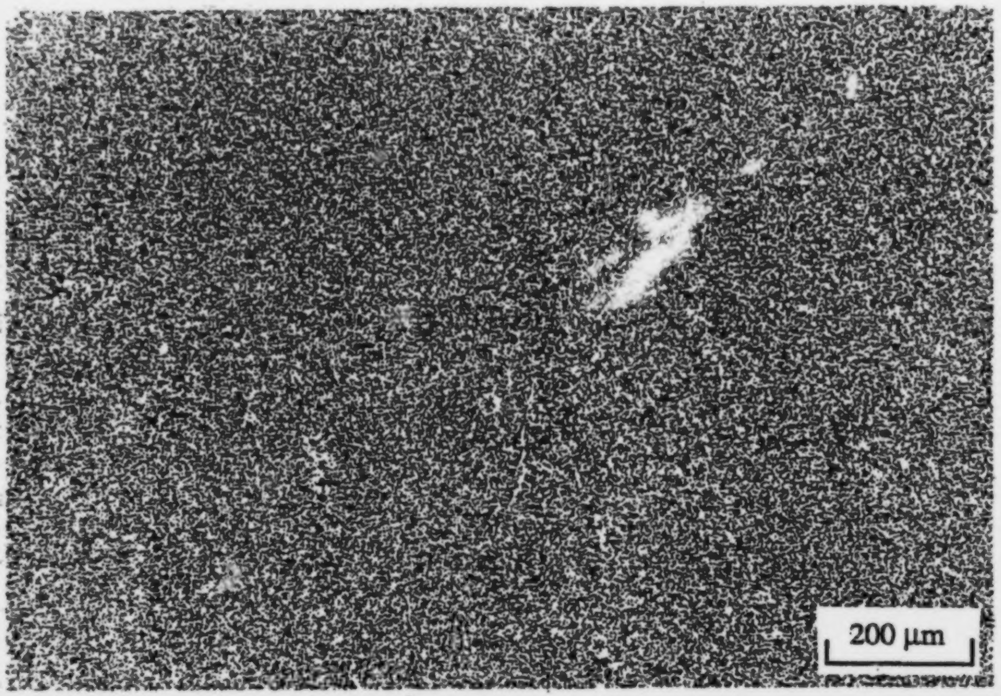

(a) columnar structure

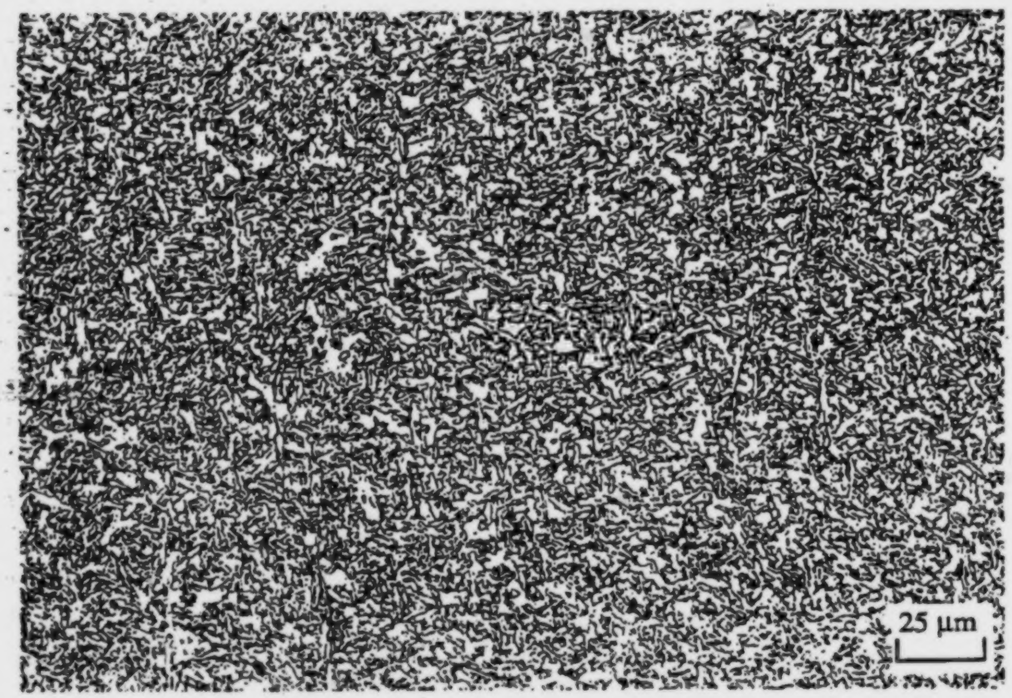

(b) microconstituents

As-deposited microstructure of SA weld HS12-8 (0.054 %C and 0.54 %Mo) made with experimental metal-cored electrode wire MC4.

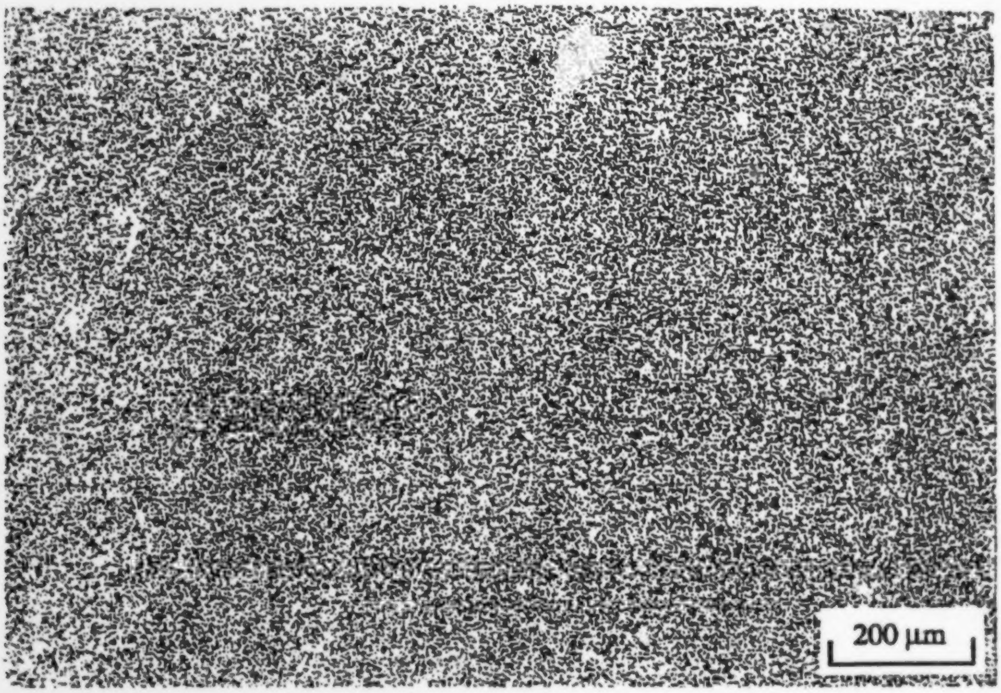

(a) columnar structure

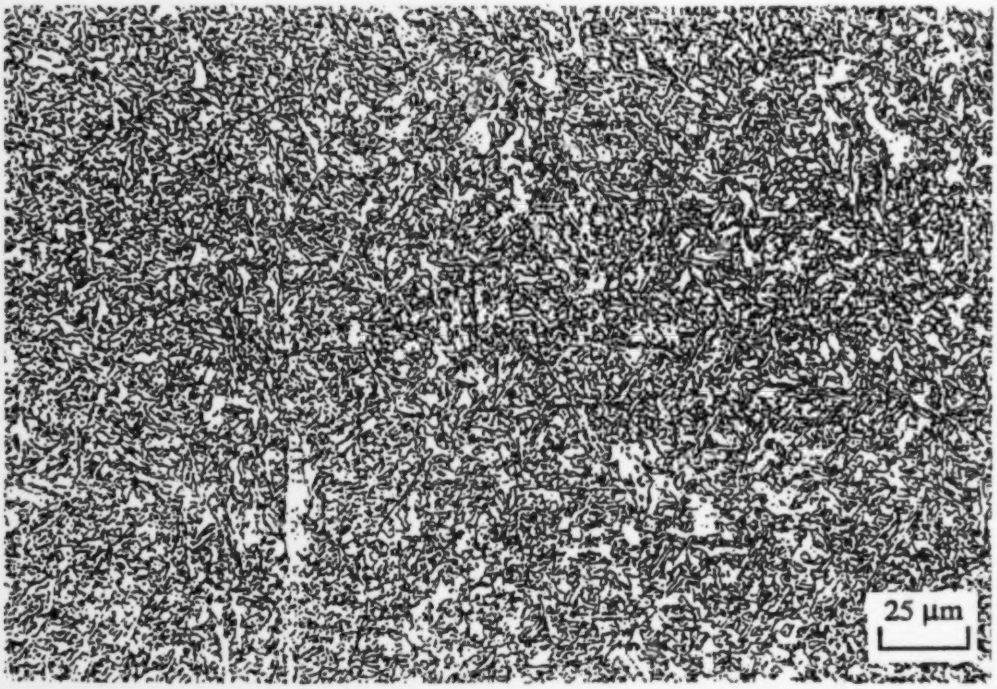

(b) microconstituents

As-deposited microstructure of SA weld HS12-9 (0.051 %C and 0.70 %Mo) made with experimental metal-cored electrode wire MC5.

Hardness results for full-thickness SA welds deposited in HSLA100 steel.

Weld No.	Macrohardness, Rc	Microhardness, VHN	
		as-deposited	reheated
HS12-1	27	290	282
HS12-4	25	281	280
HS12-5	27	288	278
HS12-7	32	316	299
HS12-8	27	290	281
HS12-9	29	296	283

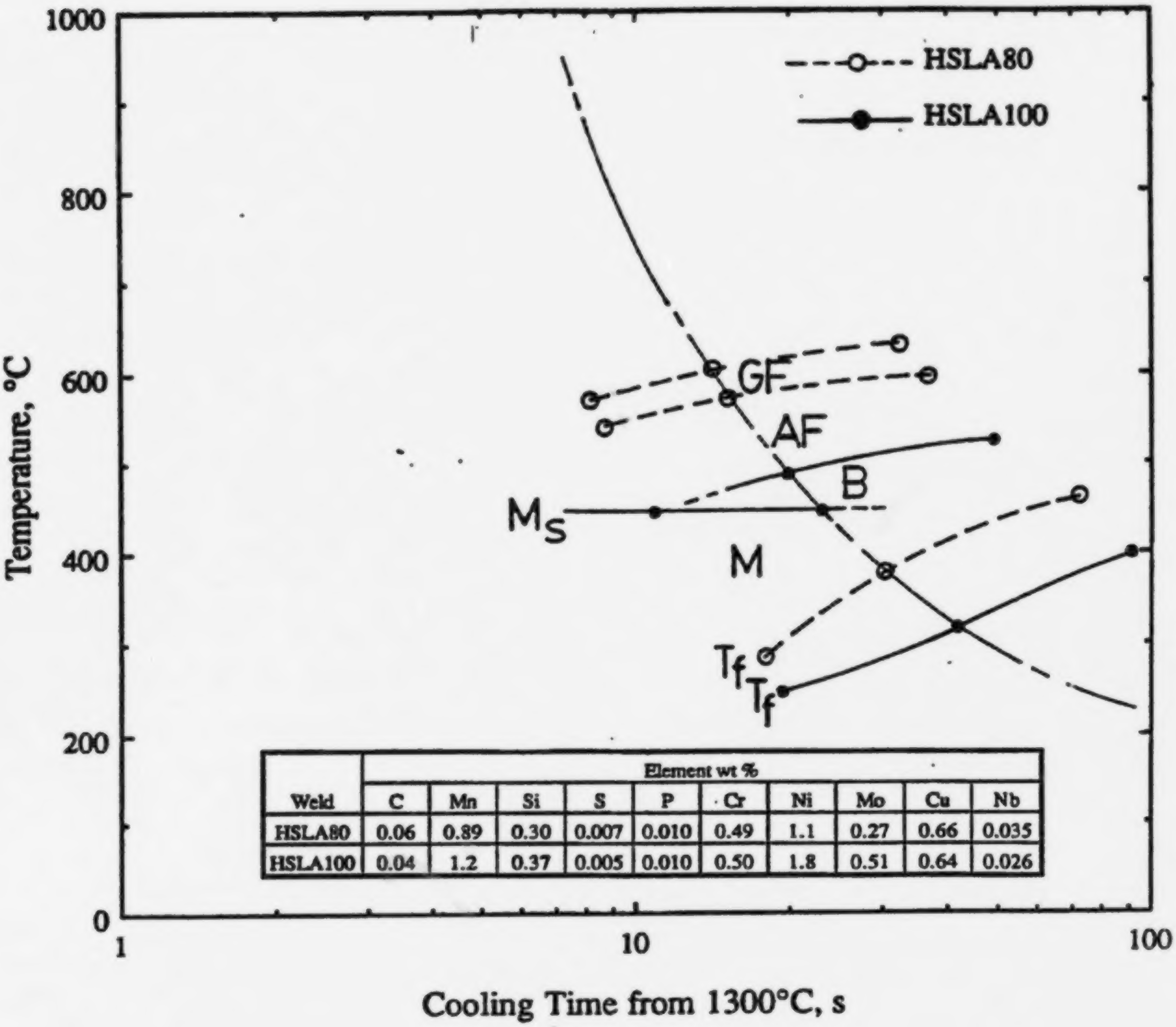

Weld	Element wt %									
	C	Mn	Si	S	P	Cr	Ni	Mo	Cu	Nb
HSLA80	0.06	0.89	0.30	0.007	0.010	0.49	1.1	0.27	0.66	0.035
HSLA100	0.04	1.2	0.37	0.005	0.010	0.50	1.8	0.51	0.64	0.026

CCT diagram showing transformation for 2 kJ/mm HSLA80 and HSLA100 weld metals. Based on peak temperature of 1300°C and cooling time Δt800-500 of 11 s.

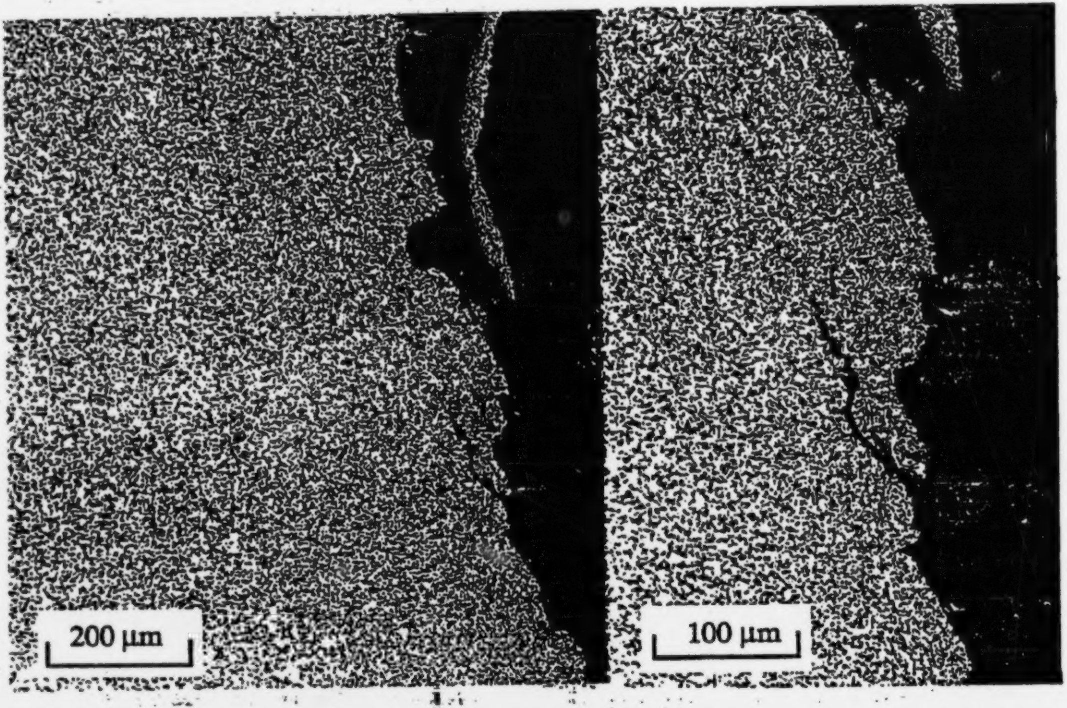

(a) Note crack propagation is both parallel as well as across columnar grain boundaries.

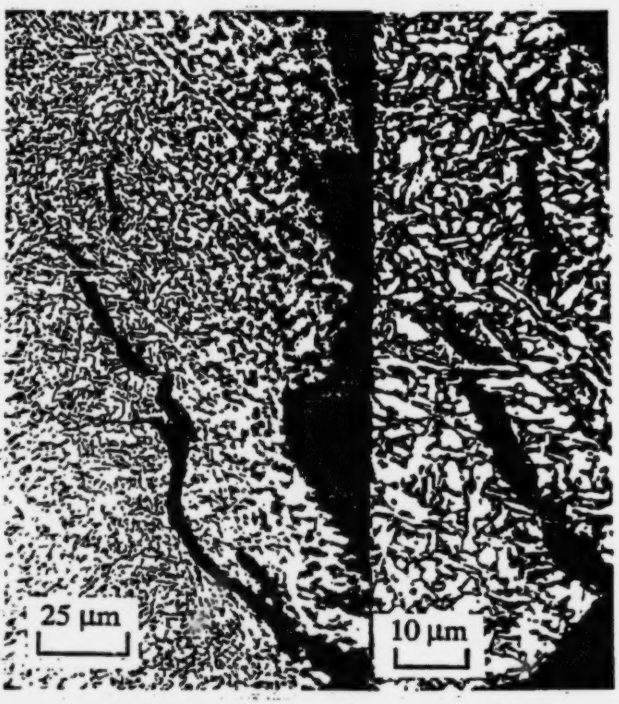

(b) Details of microcracking at columar grain boundaries

Micrographs showing through-thickness crack front in a CVN specimen tested at -50°C. Weld HS12-1.

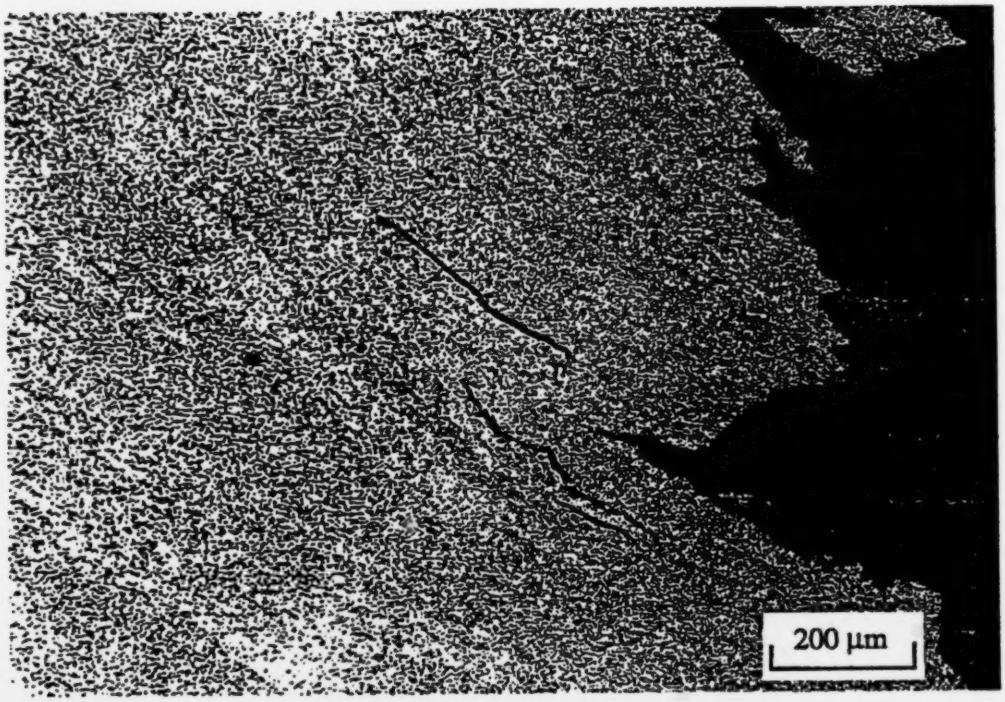

(a) Note crack propagation is mainly across columnar grain boundaries.

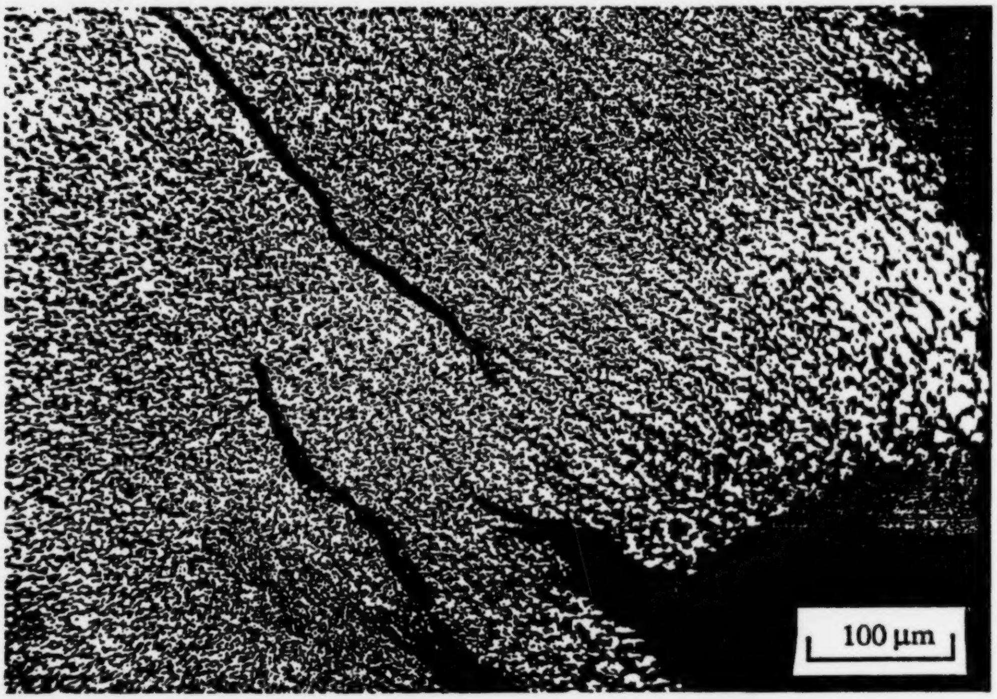

(b) Microcracking along columar grain boundaries.

Micrographs showing through-thickness crack front in a DT specimen tested at -29°C.

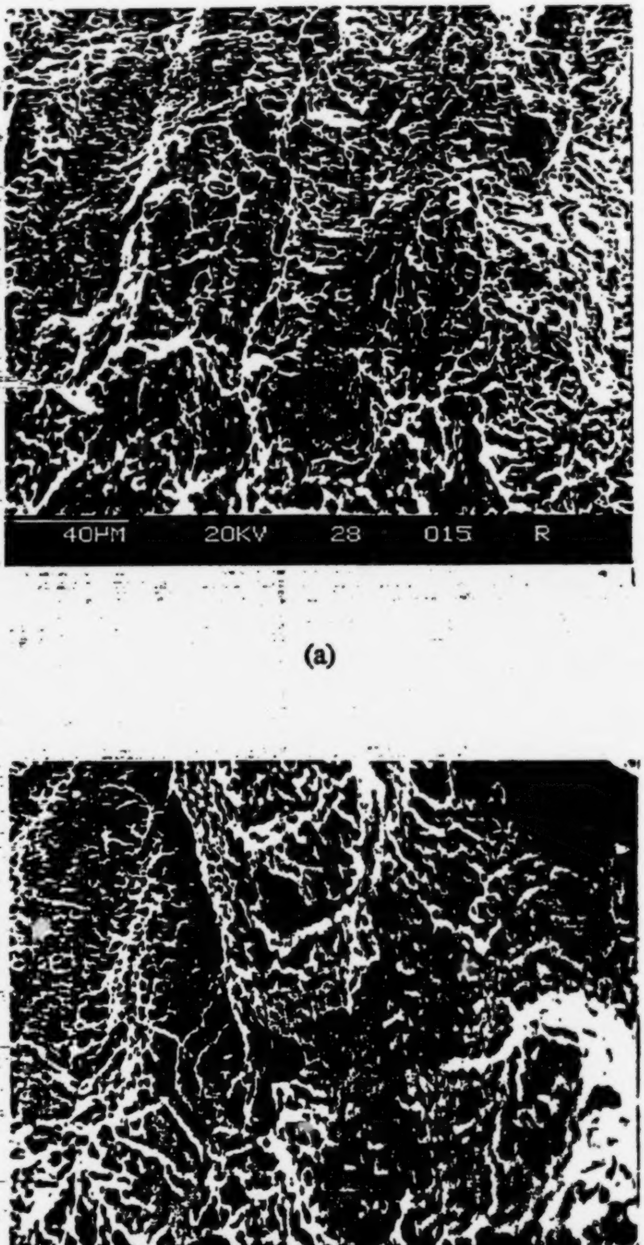
40HM 20KV 28 015 R
20HM 20KV 28 017 R

(a)

(b)

Fractographs showing elongated facets associated with intergranular failure along columnar prior austenite grain boundaries in as-deposited weld metal.

SUMMARY & CONCLUSIONS

- Strength and toughness depended on weld metal composition and its influence on final weld microstructure.

- Properties were related to the formation of a relatively fine bainitic structure with some lath martensite.

- Welds produced with the experimental metal-cored electrodes provided improved notch toughness over the weld produced with the solid reference electrode.

- With increasing C and Mo there was an increase in yield strength, hardness and tensile strength; more pronounced for the change in %C.

- Optimum toughness was obtained with intermediate C and Mo contents.

- Varying %C produced overall refinement, almost complete elimination of GBF and an increase in lath martensite and carbide precipitation.

R&D Activities Related to Welding of High Strength Steels

- Detailed evaluations of the influence of chemical composition and energy input have been carried out on welds prepared in HY80/100 and HSLA80/100.

- Current weld evaluation studies are focused on GMAW and SAW.

- Future work will focus on client sponsored R&D related to the development and evaluation of welding consumables for joining high-strength steels.

#510317 ⑫

Laser Assisted Gas Metal Arc Welding of Thick Steel Plate

by K. H. Magee

The Laser Institute
9924 - 45 Avenue, Edmonton, Alberta, T6E 5J1

ABSTRACT

High power lasers can be used to produce high quality, distortion free, single pass welds in thick steel plate. However, lasers with sufficient power to produce deep penetrating welds can be expensive. The capital cost can be reduced by employing laser assisted arc welding; a hybrid process which combines inexpensive arc welding energy with more costly, but highly controllable laser energy.

The process parameters have been investigated using bead on plate welding trials, and by producing welds in a variety of V-groove designs. The investigation has resulted in the development of a four pass welding procedure that can successfully weld 25 mm thick steel plate using approximately 5 kW of continuous wave carbon dioxide laser energy combined with sufficient GMAW arc energy to produce a LAGMAW heat input of 1.6 kJ/mm for each pass. The process has been applied to HY80 plate typically used in submarine hull construction.

#510318 (13)

CURRENT WELDING CONSUMABLES RESEARCH IN THE U.S. NAVY

by J.J. DeLoach, Jr., G.L. Franke, M.G. Vassilaros, and R.J. Wong

presented by P.W. Holsberg

Carderock Division, Naval Surface Warfare Center
Welding Branch, Code 615, Annapolis, Maryland, USA 21402

ABSTRACT

One of the thrusts of U.S. Navy research is directed toward providing new and advanced material systems with improved properties, and developing methods and materials to construct current and future generation naval vessels more economically. It focuses on materials of construction, fabrication methods and consumables, and methods to ensure and enhance structural integrity. One specific area in this thrust is that of welding the Navy's high strength steels. Toward this end, work is being conducted on a number of topics pertaining to welding Navy steels with yield strengths exceeding 100 ksi.

Four tasks are discussed in this presentation. HSLA-100 Welding Consumables Development addresses evaluation of experimental compositions, data analysis, and identification of optimum compositions. Low-Carbon Bainitic Weld Metals discusses the effects of alloying on weld metal strength and cooling rate sensitivity, and the effect of titanium-bearing inclusions on weld toughness. Weldability Methodology addresses transformation expansion, Weldability tests, diffusible hydrogen, and cracking models. Welding Fluxes discusses determination of flux composition and correlations with weld performance. Future research for each task is also described.

Paper to be presented at OMAE-93, Glasgow, Scotland, June, 1993

CURRENT WELDING CONSUMABLE RESEARCH IN THE U S NAVY

by

J DELOACH, G FRANKE, M VASSILAROS & R WONG

PAUL W HOLSBERG
Carderock Division
Naval Surface Warfare Center

NAVAL APPLICATIONS OF MATERIALS TECHNOLOGY
FMO, Halifax, N.S.
28 April 1993

WELDING CONSUMABLES
THRUST AREAS

* GMAW Filler Metals for HSLA-100
* Low-Carbon Bainitic Filler Metals
* Weldability Methodology
* Welding Fluxes

HSLA-100 CONSUMABLE WELDMENTS
WELDING VARIABLES

Single V, 60 degree included angle

1/2 inch root, 1/2 inch backing bar

Flat position

GMAW with Ar-5%CO2 gas (C-5)

Nominally 50 KJ/in

Preheat/interpass 225-275F

Weld metal compositions and mechanical properties from Phase 1.

Formulation	C	Ni	Mo	Ti	Mn	Si	O	N	Yield Strength (ksi)	CVN at 0°F (ft-lb)	CVN at -60°F (ft-lb)
1	0.040	2.18	0.42	0.011	1.53	0.19	0.041	0.014	90	88	50
2	0.036	2.14	0.44	0.018	1.41	0.14	0.041	0.010	83	57	45
3	0.040	2.31	0.64	0.012	1.49	0.21	0.043	0.008	94	63	41
4	0.035	2.20	0.64	0.017	1.42	0.14	0.068	0.013	90	66	34
5	0.040	3.26	0.44	0.011	1.54	0.20	0.042	0.008	102	65	51
6	0.037	3.12	0.45	0.017	1.49	0.14	0.041	0.012	93	79	47
7	0.040	3.23	0.63	0.011	1.50	0.21	0.050	0.011	104	69	43
8	0.035	3.18	0.63	0.022	1.53	0.18	0.042	0.013	101	69	49
9	0.050	2.13	0.44	0.012	1.52	0.19	0.041	0.008	98	55	33
10	0.059	2.25	0.46	0.013	1.36	0.09	0.053	0.011	87	50	29
11	0.060	2.35	0.65	0.012	1.55	0.20	0.042	0.007	105	45	17
12	0.060	2.21	0.65	0.023	1.53	0.18	0.033	0.011	102	67	40
13	0.060	3.15	0.44	0.014	1.50	0.20	0.041	0.009	107	55	43
14	0.060	3.12	0.45	0.022	1.57	0.18	0.029	0.010	103	62	54
15	0.060	3.15	0.63	0.014	1.52	0.20	0.041	0.008	111	64	53
16	0.066	3.11	0.63	0.018	1.40	0.15	0.034	0.010	106	60	50
Target Properties									102-122	60 min	45 min

Weld metal compositions and mechanical properties from Phase 2.

Formulation	C	Ni	Mo	Ti	Mn	Ti/N	Si	O	Yield Strength (ksi)	CVN at 0°F (ft-lb)	CVN at -60°F (ft-lb)
17	0.048	2.57	0.50	0.018	1.52	2.25	0.23	0.042	99	51	38
18	0.044	2.68	0.51	0.015	1.27	1.25	0.22	0.039	99	38	25
19	0.049	2.50	0.49	0.021	1.70	2.10	0.23	0.020	108	60	47
20	0.057	3.90	0.62	0.016	1.50	1.78	0.22	0.042	122	33	27
21	0.064	3.15	0.61	0.023	1.57	2.55	0.25	0.036	118	48	39
22	0.058	3.06	0.61	0.022	1.52	3.14	0.24	0.038	110	46	39
23	0.057	2.99	0.59	0.023	1.48	2.30	0.23	0.043	111	48	36
24	0.065	3.30	0.46	0.015	1.39	1.67	0.25	0.023	112	48	40
25	0.033	6.90	0.58	0.018	1.46	2.57	0.24	0.049	129	24	21
Target Properties									102-122	60 min	45 min

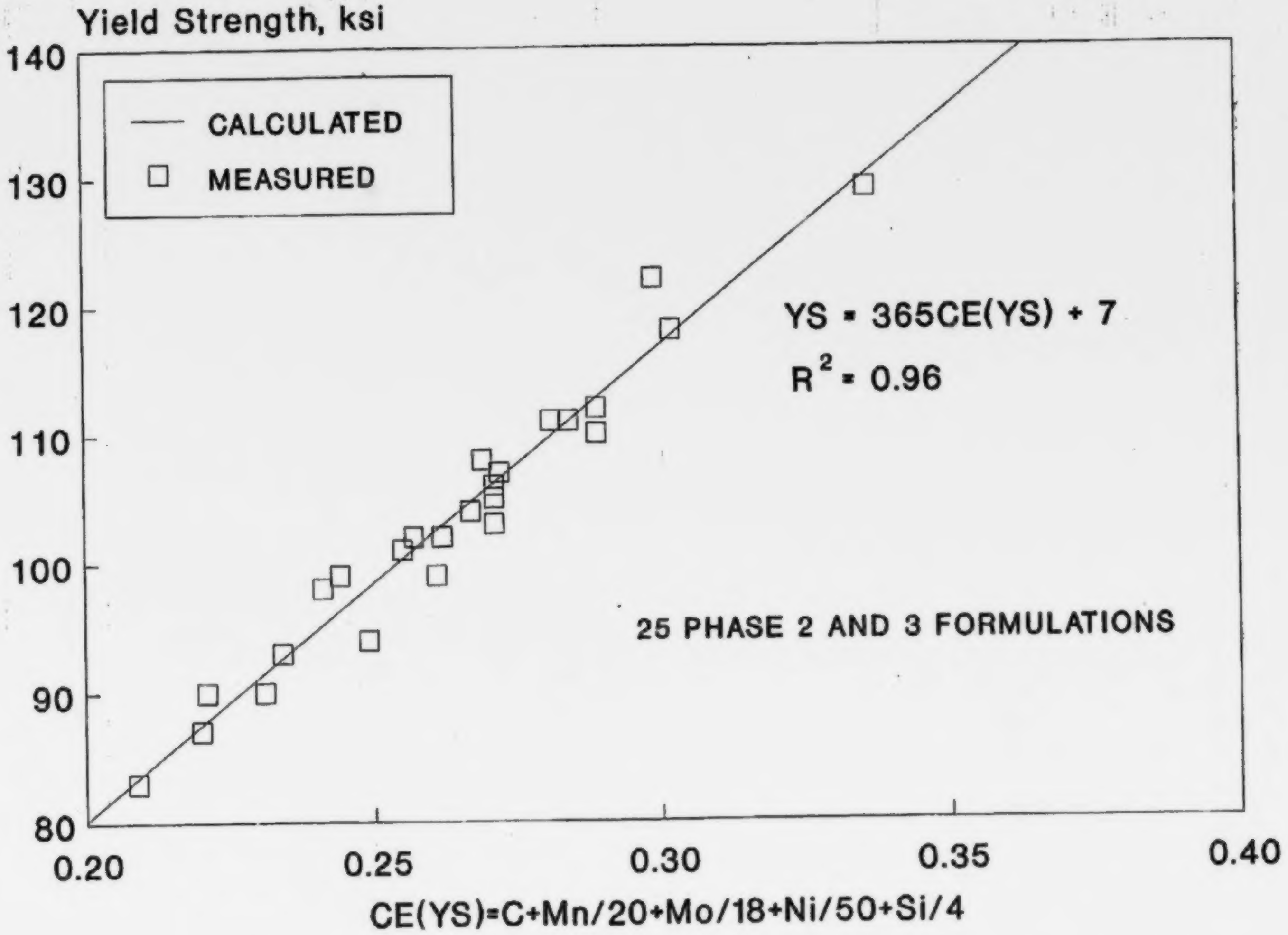

Effect of composition on yield strength.

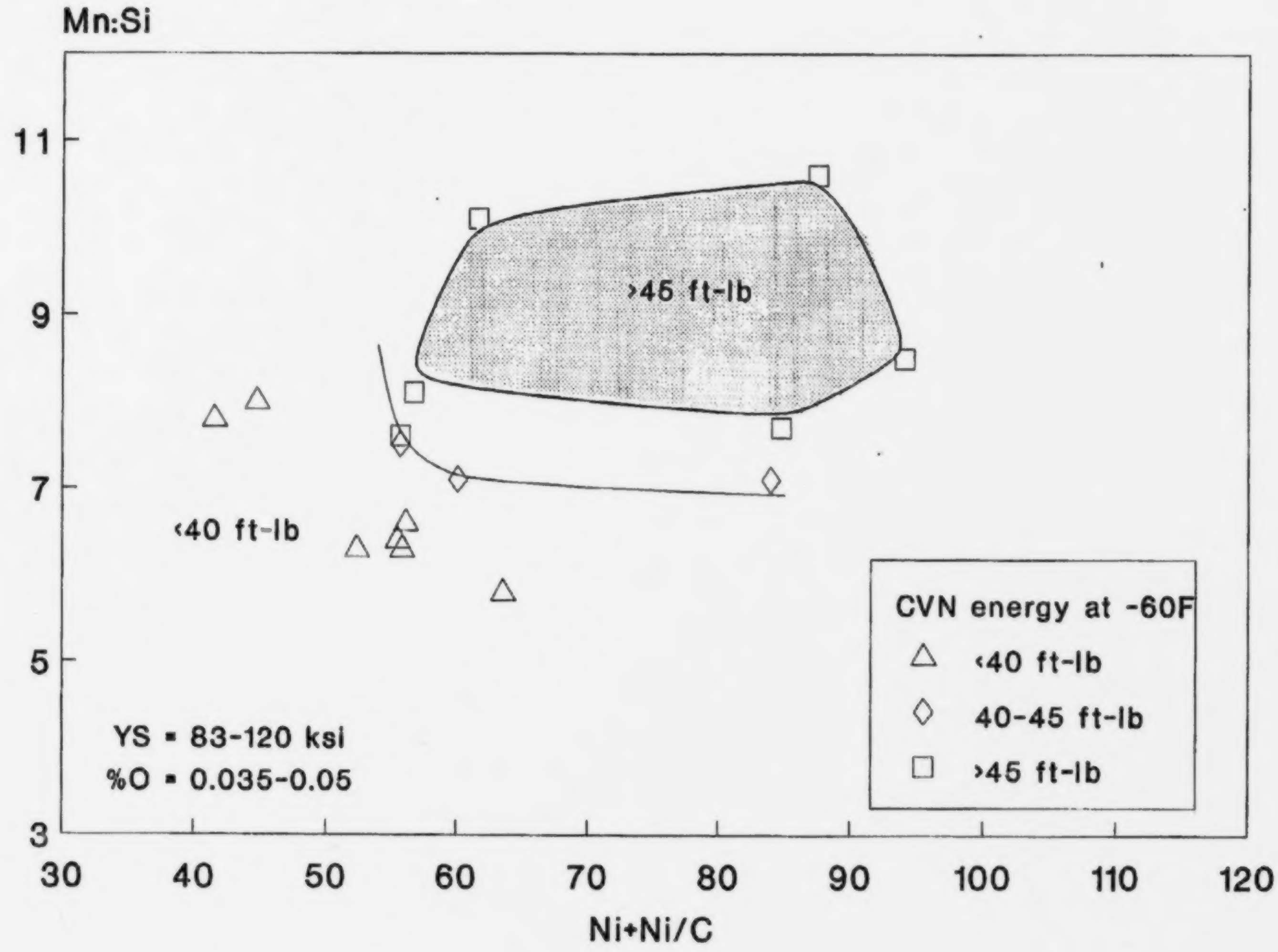

Effect of composition on CVN energy at -60°F.

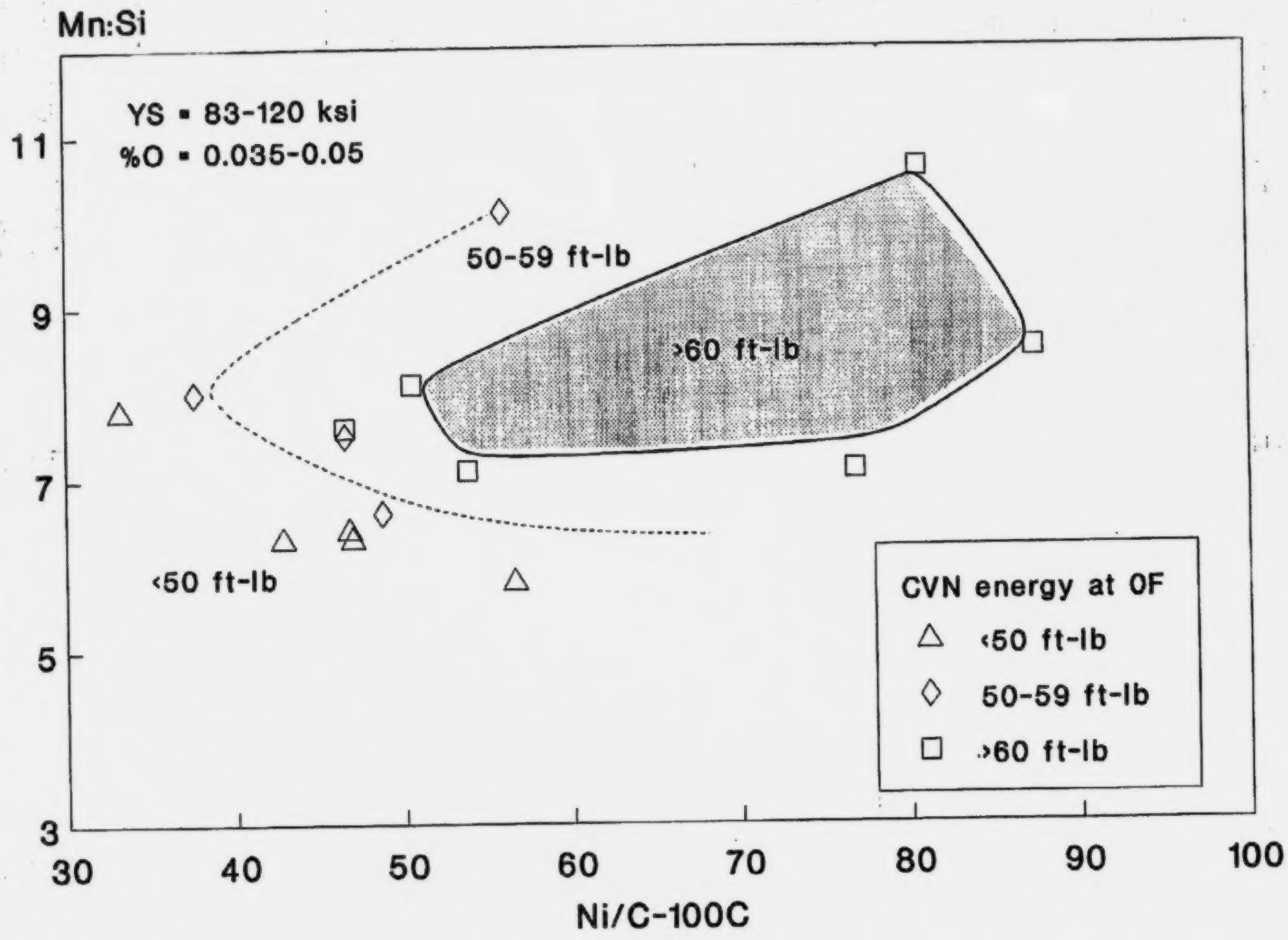

Effect of composition on CVN energy at 0°F.

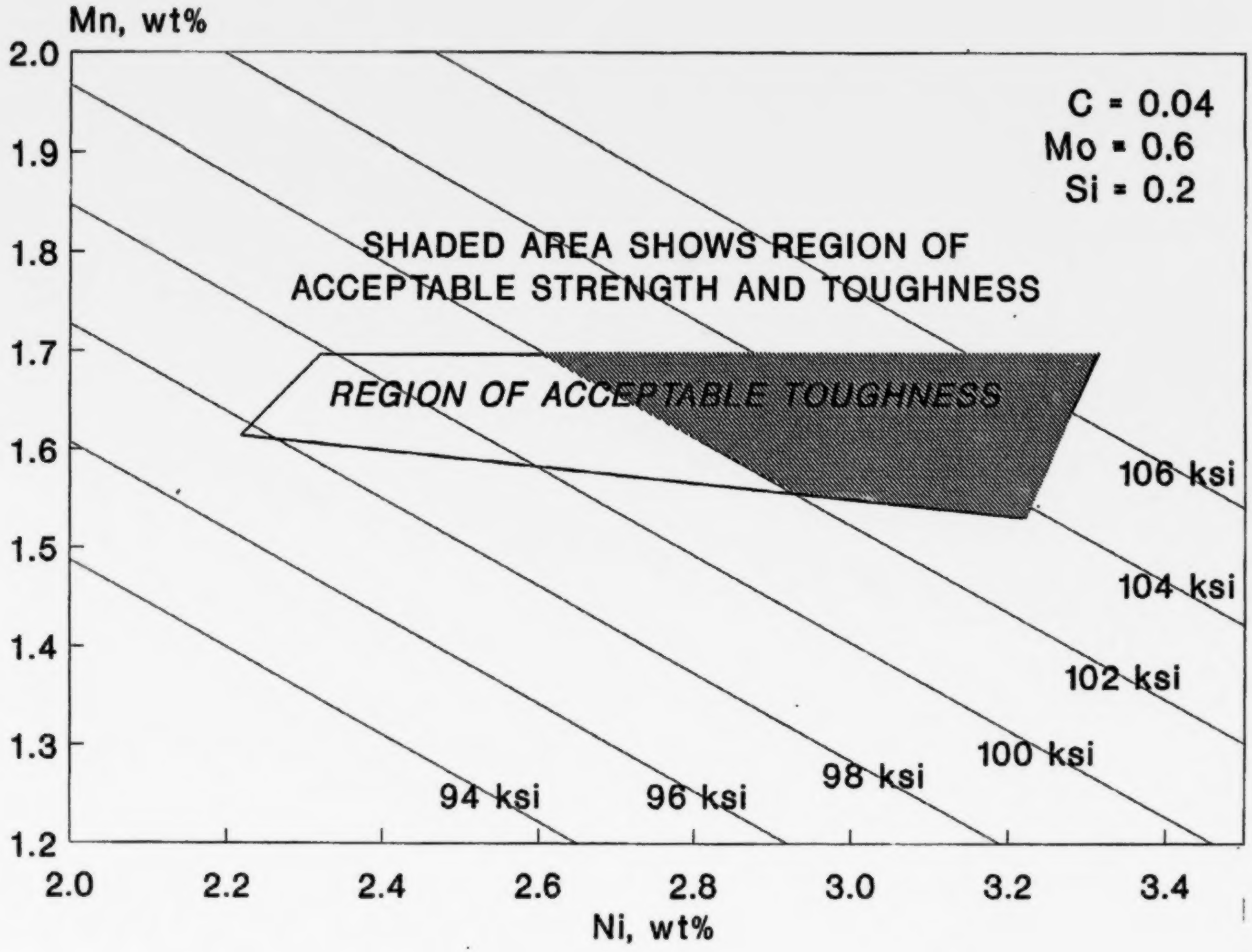

Example of graphical method of identifying the compositional range that provides acceptable mechanical properties.

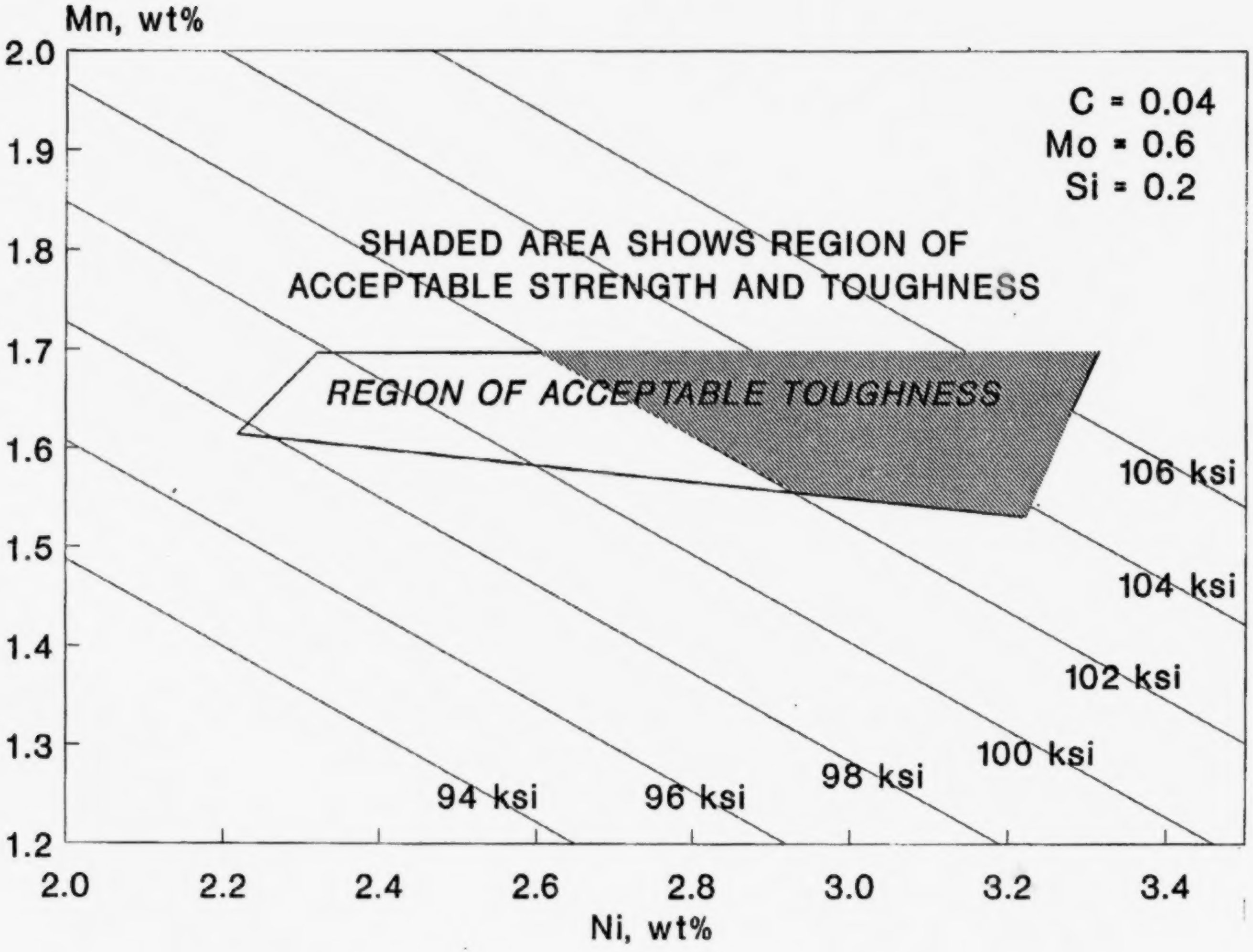

Example of graphical method of identifying the compositional range that provides acceptable mechanical properties.

LOW CARBON BAINITIC WELD METAL

- * Is high strength (>100ksi) low carbon (<0.02C) weld metal possible?
- * Is the strength of such a weld metal less cooling rate sensitive than conventional (martensitic) types?
- * Can necessary toughness be developed?

LOW CARBON BAINITIC WELD METAL

COMPOSITION RANGES

C	<0.02
Mn	1.0 - 2.0
Mo	1.5 - 5.0
Ni	2.5 - 5.0
Ti	0.10 - 0.25
Nb	<0.10

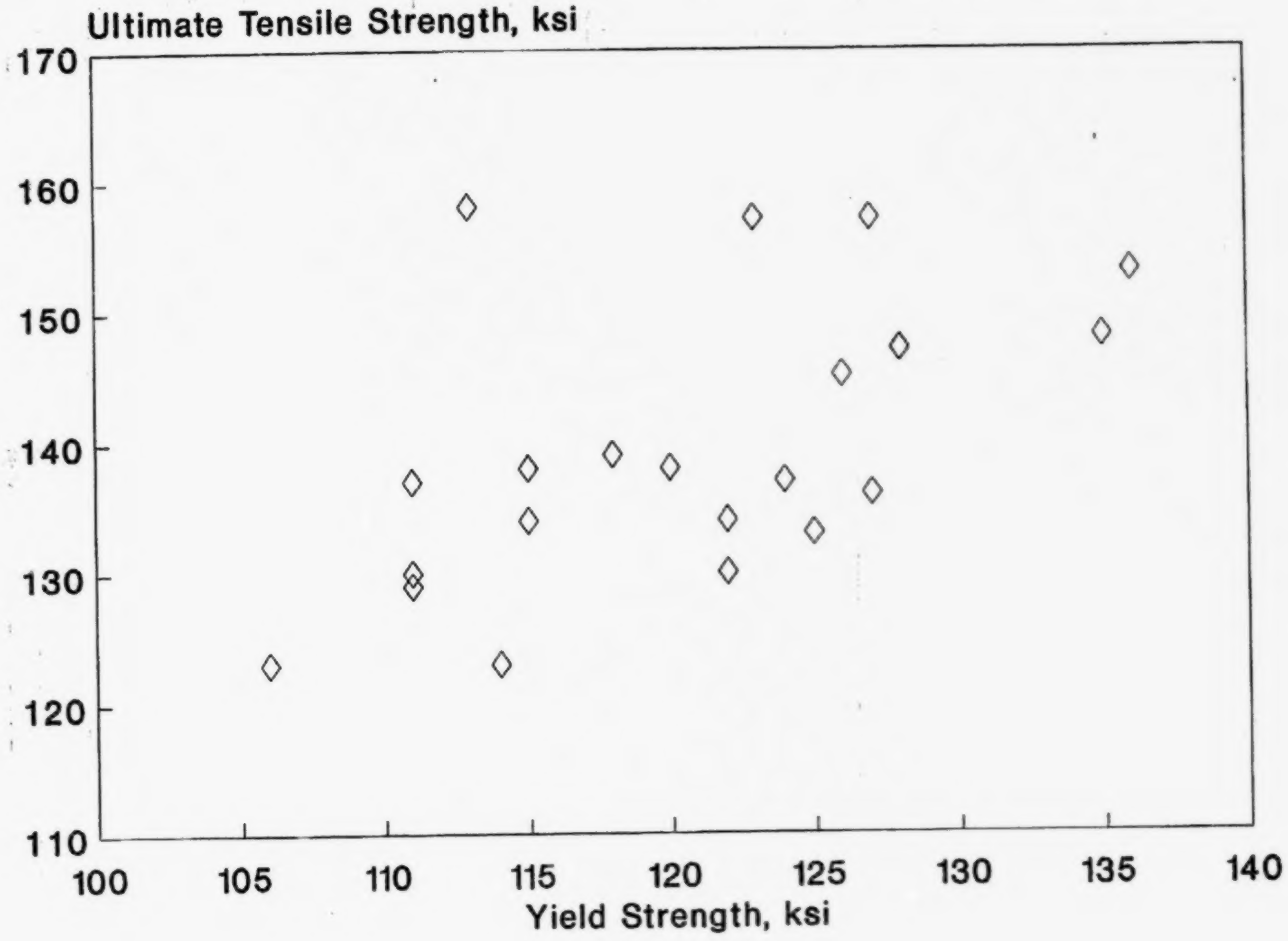

Tensile test results for LCB weld metals.

Change in weld metal yield strength (ksi) per % alloying

	Element Addition															
	<3.5% Ni		>3.5% Ni		Mo		C		<1.5% Mn		>1.5% Mn		<0.045% Nb		>0.045% Nb	
Heat Input (kJ/in)	60	120	60	120	60	120	60	120	60	120	60	120	60	120	60	120
at low Mo (2.5%)	6.25	4.17	-2.3	-1.1	---	---	76.9	230	22.5	18.4			261	130		
at high Mo (3.5%)	4.52	9.03	4.52	9.03	---	---	875	625	30.6	21.3	1.3	-1.3	267	133	467	333
at low Ni (2.5%)	---	---	---	---	4.72	4.72										
at high Ni (3.5%)	---	---	---	---	-1	2							140	70		
at high Mn (2.0%)					-3.1	-2.1			---	---	---	---				
Heuschkel [22]	3.9	3.9	3.9	3.9	17.6	17.6	115	115	15.3	15.3	15.3	15.3	---	---	---	---
Pickering [23]	1.1	1.1	1.1	1.1	17.4	17.4	247	247	12	12	12	12	168	168	168	168

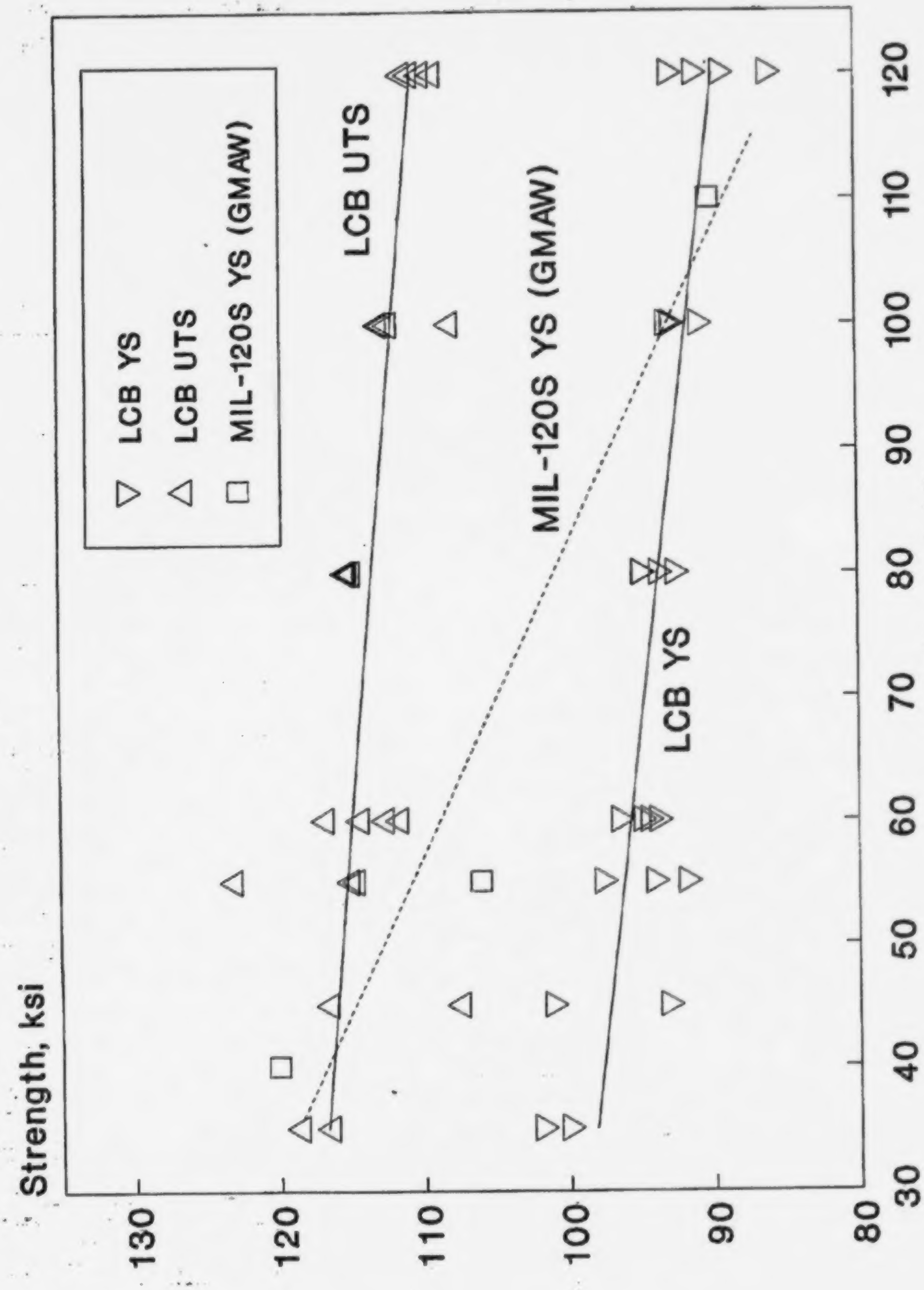

Effect of welding heat input on LCB weld metal strength.

LOW CARBON BAINITIC WELD METAL
COOLING RATE SENSITIVITY

* Reduced with low carbon

* Ni & Mo produced best strength with least cooling rate sensitivity

* Mn, Nb & C increased strength but also cooling rate sensitivity

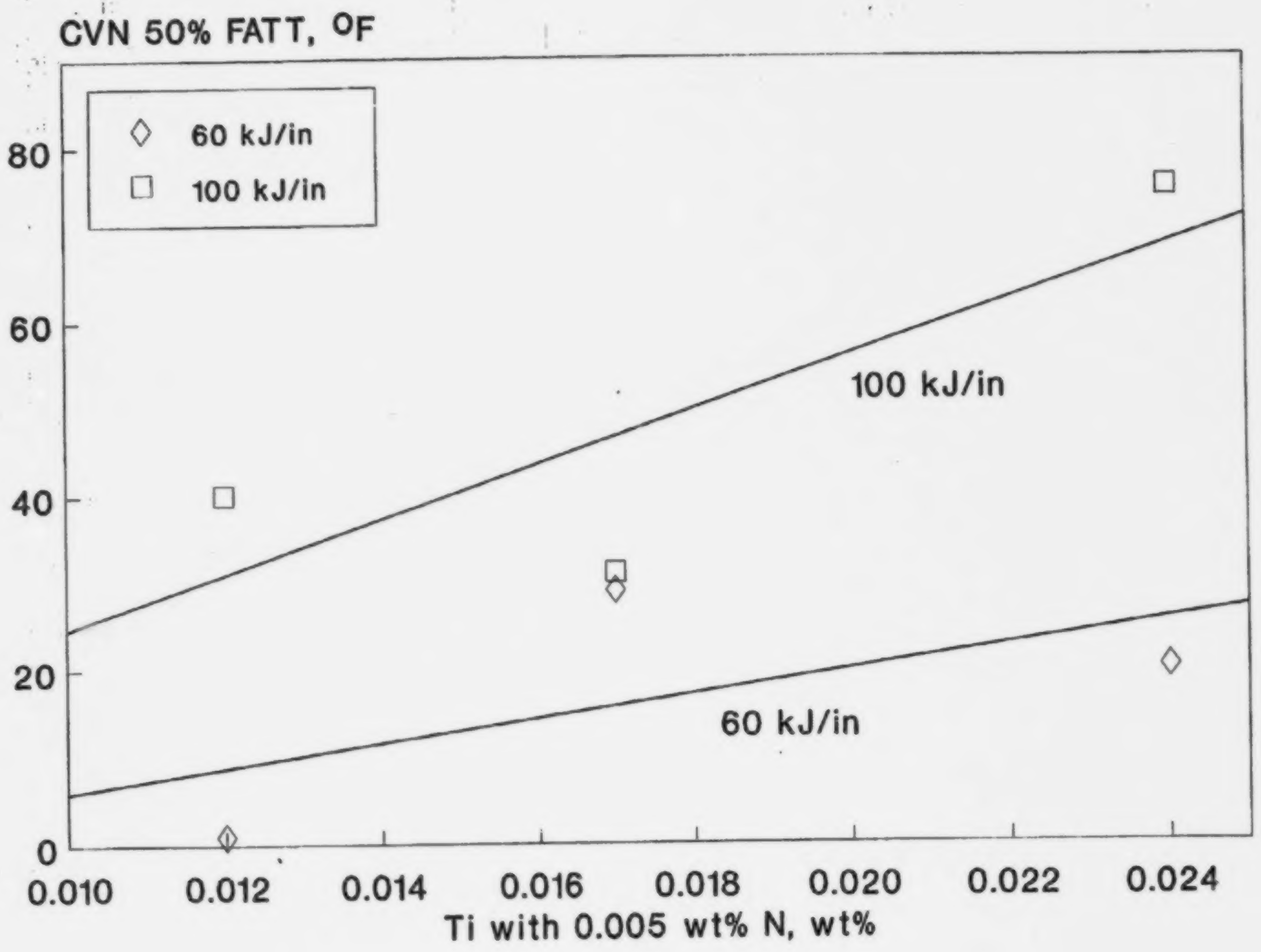

Effect of TiN on LCB weld metal impact performance.

WELD METAL CRACKING TESTS

WELDING INSTITUTE OF CANADA HIGH RESTRAINT CRACKING TEST (WIC)

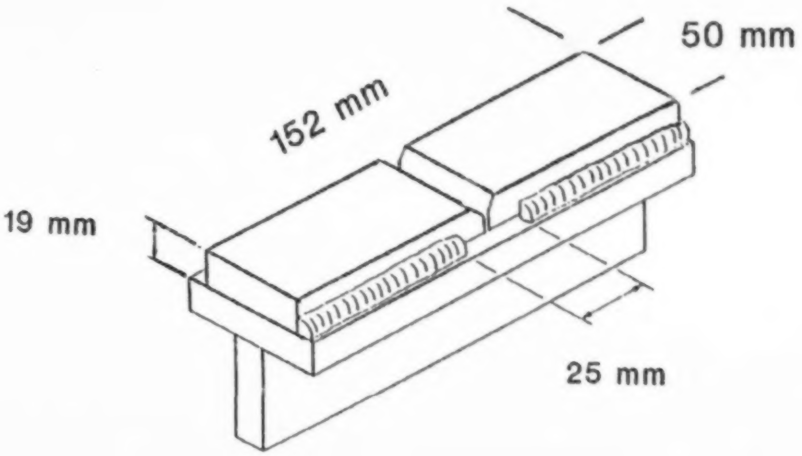
50 mm
152 mm
19 mm
25 mm

GAPPED BEAD ON PLATE TEST (GBoP)

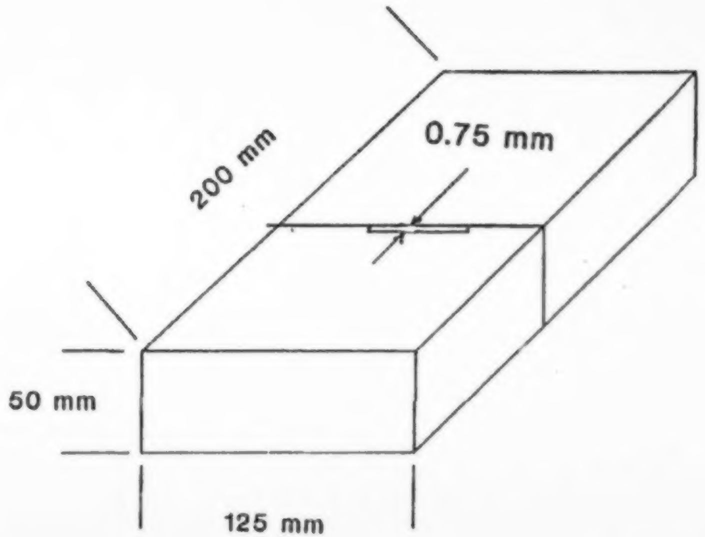
200 mm
0.75 mm
50 mm
125 mm

WELDABILITY METHODOLOGY
COOLING TIME PARAMETER (SUZUKI)

$t_{100}cr = (1.145)*(P_{HA}^2) + (864)*(P_{HA}) - 171$

where: $P_{HA} = \log(\lambda * H_D) + (11.9)*(P_{CM}) + (0.000089)*(R_{FY}) - 2.55$

λ = 0.6 for low hydrogen electrodes

H_D = weld metal diffusible hydrogen

R_{FY} = intensity of restraint.

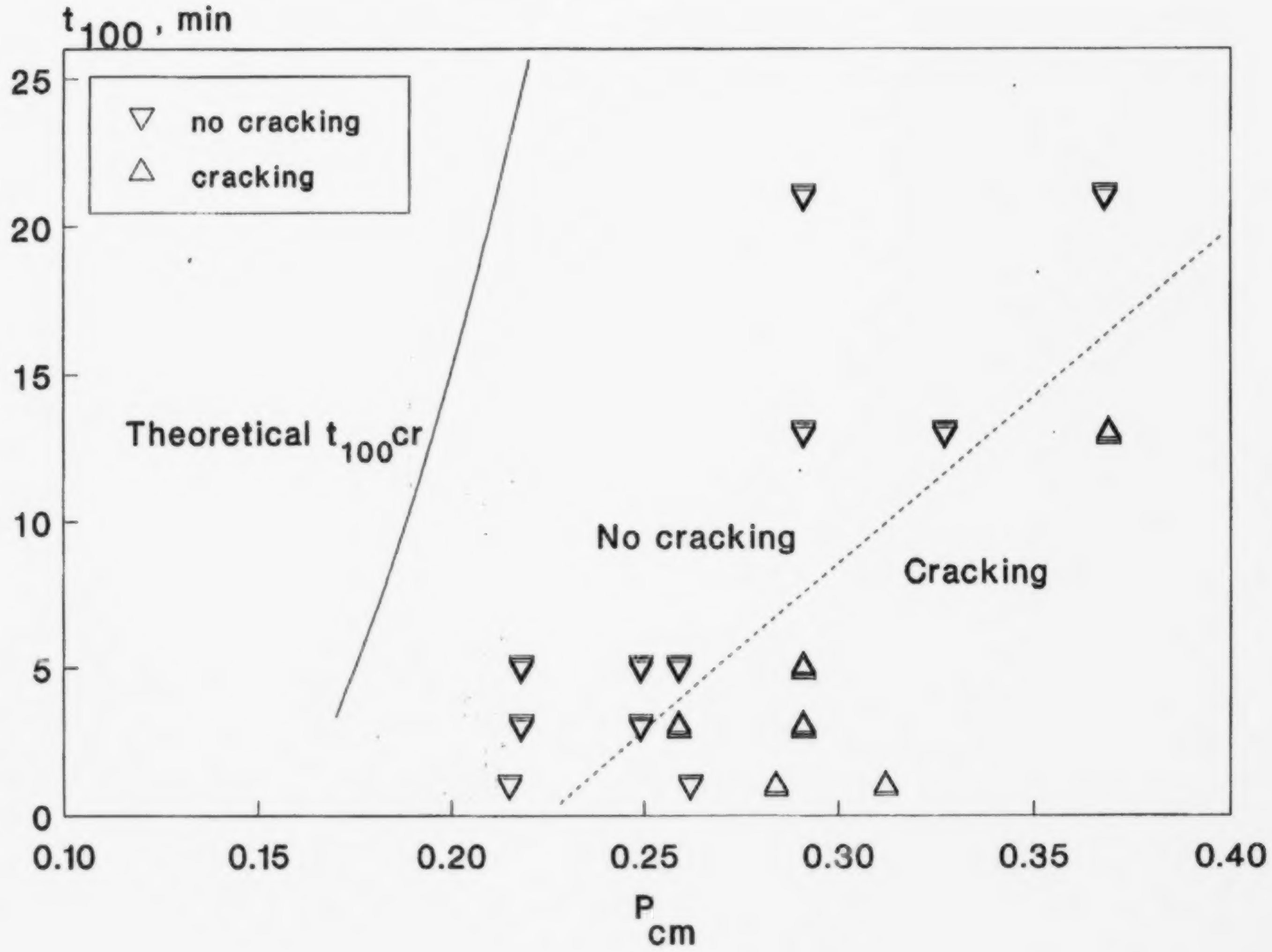

Results of WIC and GBoP weldability tests using SMAW consumables

Results of WIC weldability tests performed at ambient temperature for HSLA-100 steel and a MIL-100S welding consumable.

Hydrogen in Shielding Gas, %	H_D ml/100g	P_{CM}	Extent of Cracking, %
0	4.7	0.23	0
0.3	7.5	0.22	0
0.6	10.0	0.25	96
0.9	14.7	0.25	100

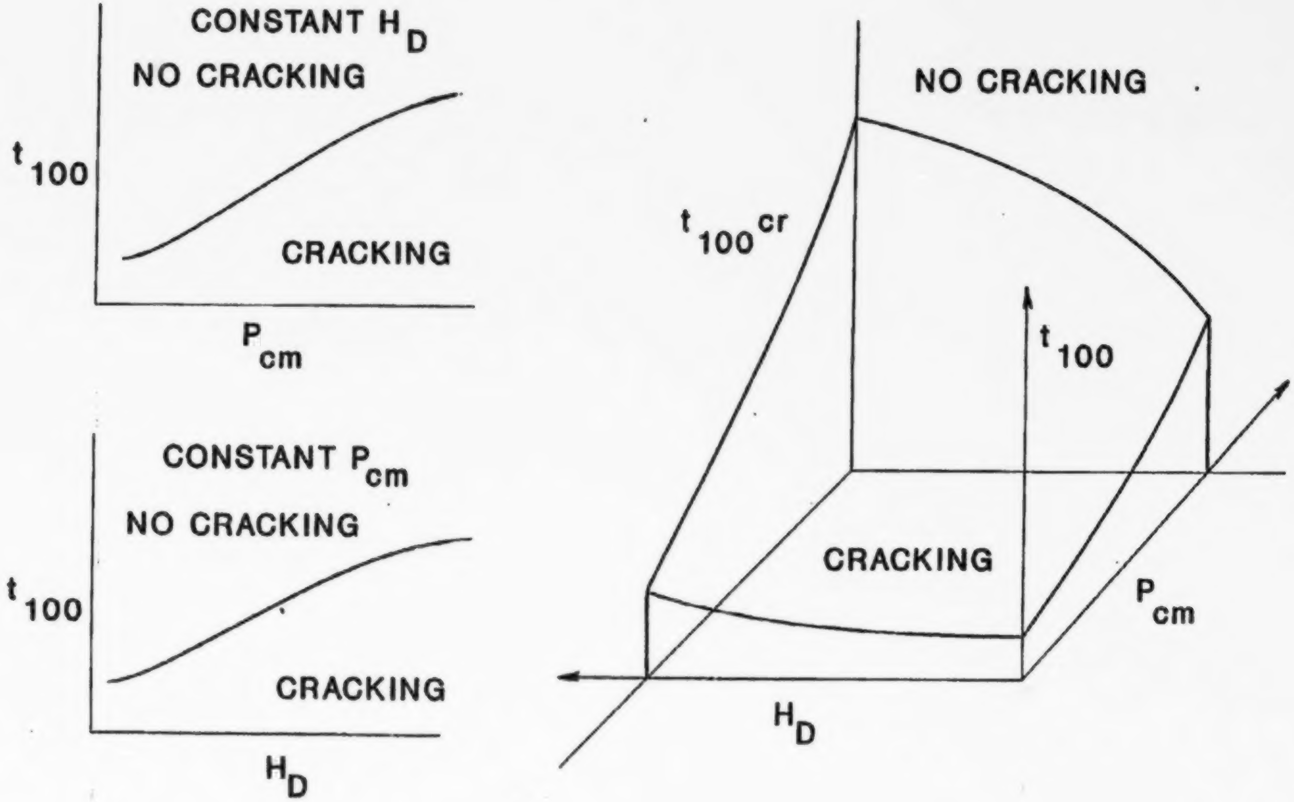
CONSTANT H_D
NO CRACKING
t_{100}
CRACKING
P_{cm}
CONSTANT P_{cm}
NO CRACKING
t_{100}
CRACKING
H_D
NO CRACKING
t_{100}^{cr}
t_{100}
CRACKING
P_{cm}
H_D

Schematic response surface for hydrogen cracking resistance.

WELDING FLUXES
COMPOSITION DETERMINATION

Optical Emission Spectroscopy (OES) - 35 elements

X-Ray Fluorescence (XRF) - 10 elements

Inductively Coupled Plasma - 44 elements

Selective Ion Electrode Technique - Fluorine

Submerged arc welding flux composition.

Compound	FLUX AA7	FLUX EC2	FLUX CB2	Flux FC2	Flux HD2
SiO_2	14.7	13.3	16.5	14.5	15.6
MgO	28.9	32.5	28.3	32.1	35.0
CaO	10.2	11.6	17.3	9.9	8.1
CaF_2	22.2	22.2	14.0	20.9	17.2
Al_2O_3	18.2	14.1	13.1	15.4	16.9
Fe_2O_3	1.09	1.09	1.19	1.05	2.00
TiO_2	0.72	-	-	0.52	0.68
MnO	0.89	0.45	0.05	1.60	2.52
K_2O	0.99	1.08	1.24	1.34	0.39
Na_2O	0.94	1.01	1.99	1.20	1.23
BaO	0.050	0.017	0.027	0.009	0.035
SrO	0.009	0.013	0.014	0.006	0.025
CeO_2	0.004	-	0.326	0.006	0.014
La_2O_3	0.006	0.002	0.269	0.007	0.009
Nd_2O_3	-	-	0.093	-	0.007
ZrO_2	0.04	0.03	-	0.08	0.04
B.I. [40]	2.66	3.40	2.75	2.97	2.63

Chemistry of welding consumable and submerged arc weld metal.

Element	Wire	FLUX AA7	FLUX EC2	FLUX CB2	Flux FC2	Flux HD2
C	0.081	0.062	0.063	0.056	0.064	0.064
Mn	1.50	1.45	1.33	1.28	1.54	1.51
Si	0.40	0.38	0.28	0.42	0.34	0.28
Ni	2.25	2.33	2.33	2.51	2.34	2.34
Mo	0.42	0.46	0.45	0.47	0.49	0.47
Cr	0.28	0.25	0.41	0.40	0.50	0.47
Ti	0.014	0.006	0.004	0.004	0.006	0.005
Cu	0.011	0.020	0.020	0.017	0.026	0.021
Al	0.012	0.013	0.012	0.011	0.014	0.011
V	0.001	0.003	0.002	0.002	0.003	0.004
B	0.004	0.004	0.004	0.004	0.001	0.004
O	0.003	0.030	0.032	0.034	0.032	0.035
P_{CM}	0.269	0.250	0.249	0.248	0.256	0.264

Properties for submerged arc weld metals.

Property	FLUX AA7	FLUX EC2	FLUX CB2	Flux FC2	Flux HD2
YS (ksi)	101	100	100	120	102
CVN (avg, ft-lb)					
@ -60°F	71	73	49	66	44
@ 0°F	91	101	86	87	63
Upper Shelf	106	130	120	92	94
50% FATT (°F)	-65	-75	-49	-99	-52

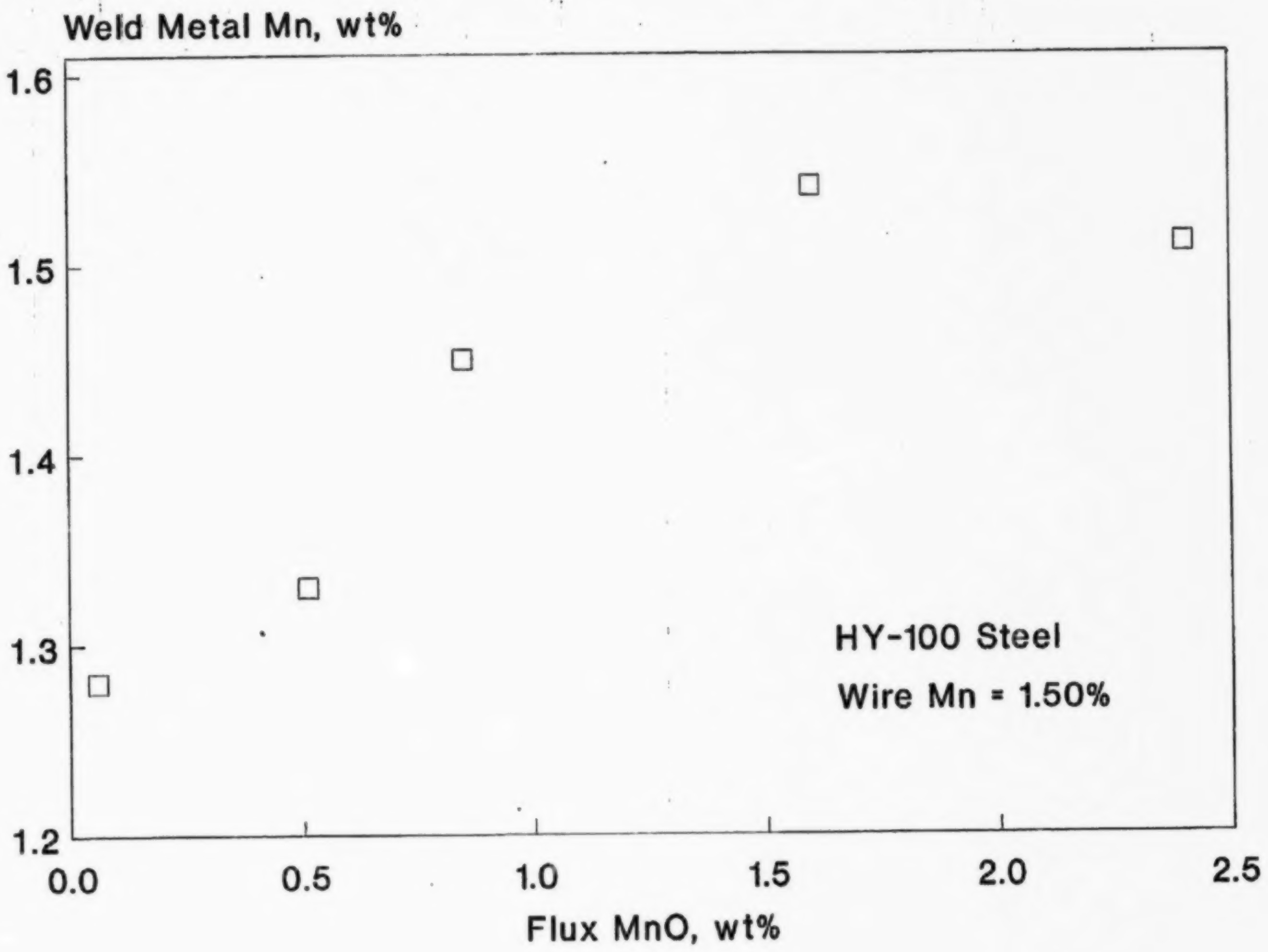

Effect of flux MnO content on weld metal manganese content.

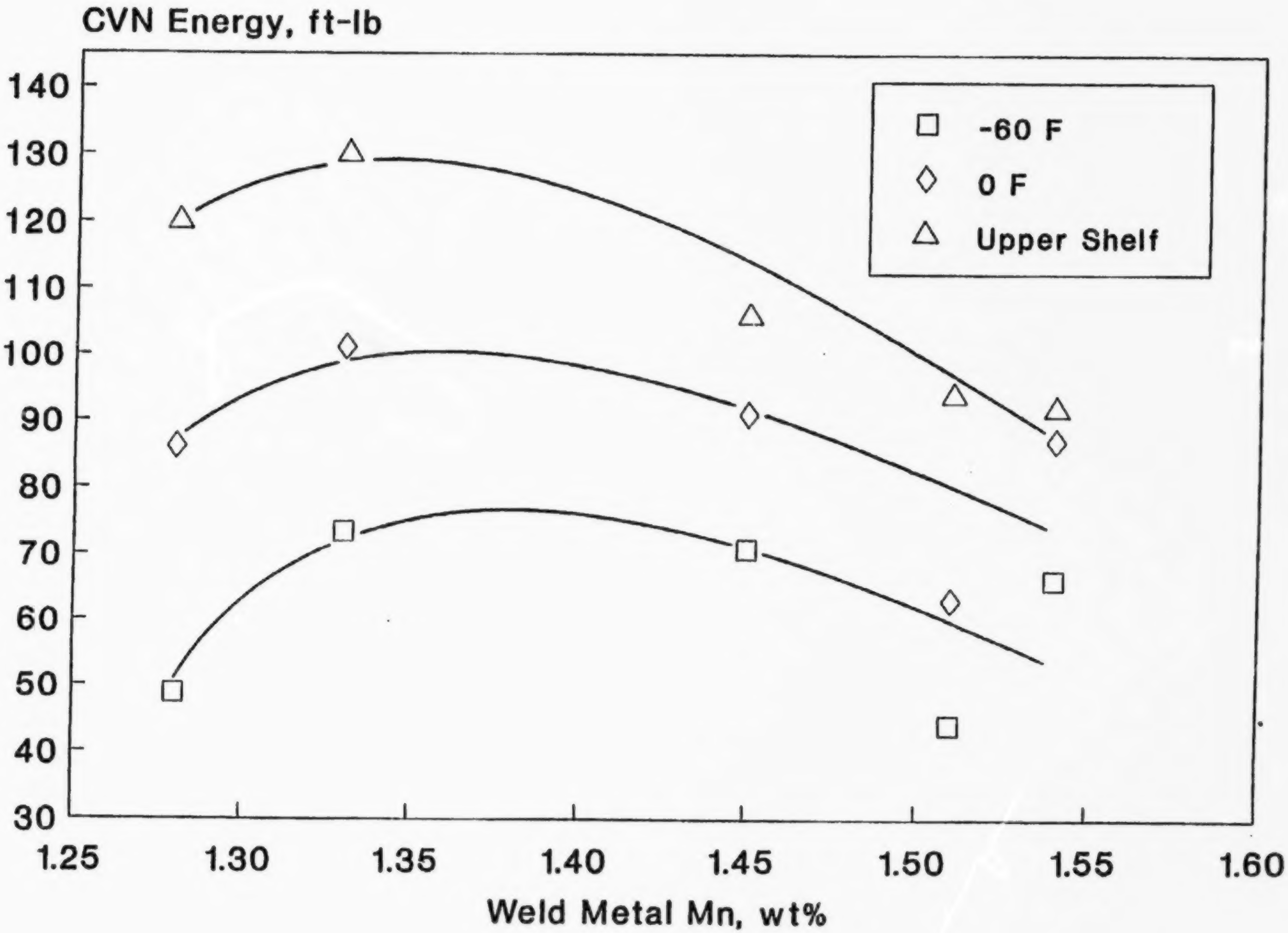

Effect of weld metal manganese content on CVN performance.

510319 (14)

The Influence of Weld Strength Mismatch on the Fitness–for–Service of High Strength Steel Structures

Mark T Kirk

Edison Welding Institute, 1100 Kinnear Rd., Columbus, Ohio, 43212, USA

In welded construction, the solidified metal and surrounding region (heat affected zone, or HAZ) have fracture toughness that is characteristically lower and less well controlled than that of the base material joined due to inferior metallurgical quality of the metal in the weld region [Kerr, 1976]. Further, welding produces defects which must be considered to insure structural integrity against fracture. Taken together, the low fracture toughness and high defect probability characteristic of weldments provide incentive to prevent large deformations in welded regions. For this reason, many codes require use of weld metals whose strength exceeds that of the plates joined [ASME, 1980; AWS, 1980; USDOT, 1979]; a practice referred to as *overmatching*. Overmatched welds generally force plastic deformation into the lower strength plate [Denys, 1990] where better fracture resistance and fewer defects are expected.

Unfortunately, overmatching weld metal strength has economic and technical disadvantages which undermatched (weld metal yield strength less than plate yield strength) construction might alleviate. For example, welding of high strength steels requires preheat to prevent hydrogen cracking. Satoh and co–workers [1978] demonstrated that preheat requirements could be halved by switching to undermatched construction. This change produced a significant energy savings and increased productivity because the lower preheat temperature permitted extension of the welder's duty cycle. Howden, et al. [1983] found that, for welding the HY steels commonly used in Naval construction (80 to 130 ksi nominal yield strength), the use of undermatched welds increases weld metal deposition rate relative to overmatched practice. Undermatching also reduces the need to hold electrodes at an elevated temperature prior to use, reduces the lack of fusion / lack of penetration defect rate (higher heat inputs improve arc penetration), reduces restraint stresses, and increases weld metal toughness.

The forgoing information suggests that overmatched welds, while used effectively in low strength steel construction, may not be as advantageous for structures fabricated from higher strength grades. However, relative to overmatching, undermatching significantly increases the strain carried by the weld, and thereby the applied driving force for fracture in the weld region. Therefore, current practice generally prohibits undermatching. Limited experimental data indicates that undermatched welds may have slightly higher toughness than overmatched welds to resist the increased driving force for fracture [Cunha and Pope, 1986]. However, experimental and finite element investigations demonstrate that weld strength mismatch affects significantly the relationship between remotely applied loading and crack–tip driving force [Read and Petrovski, 1990; Cray, et al., 1989]. Consequently, studies on the effects of strength matching on fracture toughness are regarded as inconclusive because the formulas used to calculate fracture toughness values from experimentally measured quantities neglect the presence of a weld in the testpiece [ASTM E813, 1989; ASTM E1290, 1989]. Commonly used techniques for assessing structural defects [PD6493, 1991; Milne, et al., 1986] also neglect the effect of weld strength mismatch. Therefore, these techniques cannot quantify the effect of weld strength mismatch on structural defect tolerance. Before undermatching is accepted as an alternative to conventional overmatched practice, techniques that address weld strength mismatch are needed to measure fracture toughness and to assess structural defects.

Acceptance of undermatched weld metal systems as a more economical alternative to conventional overmatched welds for high strength steel construction is impeded by an inability to relate applied loading to crack driving force (i.e. J or CTOD) for both fracture test specimens and structures containing welds. Previous studies have quantified the effects of weld strength mismatch on the formulas used to relate measurable quantities to J and CTOD in fracture toughness tests [Kirk and Dodds, 1992; Leggatt and Gordon, 1992]. In this investigation, two–dimensional, plane–strain finite element analyses of M(T) specimens containing welds are described for a wide range of strain hardening coefficients, weld sizes, and strength mismatch levels to quantify the influence of weld strength mismatch on fitness–for–service assessment procedures. Table 1 describes the configurations considered. This study focuses on cracks that are small compared to the panel width as these represent most closely the conditions encountered in structures. All cracks are located on the weld centerline parallel to the weld axis. Loading is applied transverse to the weld axis, which generates nominally equal stresses in both weld and plate material. Weld strength mismatch exerts a greater influence for this configuration than for equal–strain loading (weld axis parallel to the loading axis). Moreover, welds stressed transverse to their axis are common in critical members of many engineering structures.

Table 1: M(T) specimens modelled.

a/W	Weld Metal Strain Hardening Coefficient (n)	Percent Mismatch		
		20% Under	20% Over	75% Over
0.025	13	0.5 to 15	0.5 to 15	0.5 to 15
	6	0.5 to 10	0.5 to 10	0.5 to 10
0.050	13	0.5 to 10	0.5 to 10	0.5 to 10
	6	0.5 to 10	0.5 to 10	0.5 to 10

Notes:
1. Table entries indicate range of weld height to crack length (h/a) values analyzed.
2. Constitutive properties used in these models are detailed below.
3. Throughout this chapter, analyses having a weld metal strain hardening coefficient of 13 are referred to as "low" strain hardening whereas analyses having a weld metal strain hardening coefficient of 6 are referred to as "high" strain hardening.

Percent Mismatch	Weld Metal		Plate	
	n	σ_y [ksi]	n	σ_y [ksi]
20% Under	13	104	18	130
20% Over			10	86
75% Over			6	60
20% Under	6	60	9	75
20% Over			5	50
75% Over			4	34.5

#510320 (15

DEVELOPMENT OF COMPUTATIONAL ALGORITHMS FOR PROBABILISTIC FRACTURE MECHANICS

By

I.R. Orisamolu, Q. Liu and M.W. Chernuka

Computational Mechanics Group
Martec Limited
Suite 400, 1888 Brunswick Street
Halifax, Nova Scotia, Canada, B3J 3J8

ABSTRACT

Probabilistic fracture mechanics is increasingly gaining recognition and acceptance as the most realistic framework for assessing the integrity of engineering structures that are susceptible to fatigue crack growth and fracture. This is due to the fact that the presence of aleatory uncertainties in material properties, geometry and loads and the epistemic uncertainties associated with modelling and application of fatigue damage and fracture strength formulations are best accounted for using stochastic models. The merit of this approach has long been recognized by the nuclear and aerospace industries where fatigue/fracture failures could be of catastrophic proportions. It is not surprising, therefore, that most of the existing computer programs for probabilistic fracture mechanics were developed by these industries. However, the programs are mostly proprietary and are generally not available in the public domain. Furthermore, most of the programs are based on simulation schemes which are prohibitively expensive especially for application to large-scale structures such as submarines or ships.

A corporate research and development effort was recently initiated at Martec to develop generic and specialized computer programs that could be routinely utilized for probabilistic reliability analysis of structures prone to a variety of failures. A software package COMPASS (acronym for Computer Methods for Probabilistic Analysis of Structures and Systems) has been developed to meet the needs of affordability and accessibility of a practical computational tool that can be applied for risk assessment. Algorithms for efficiently calculating the reliability indices and failure probabilities corresponding to defined limit state conditions were implemented. These include accurate approximate methods such as first-order reliability methods (FORM) and second-order reliability methods (SORM) for single defect problems and probability bounding techniques and the PNET procedure for multiple-site defect/damage problems. Also implemented in COMPASS are facilities for computing various probabilistic sensitivity measures which are useful for identifying the parameters which have the most significant influences on structural reliability. In this paper, some of these features are briefly reviewed and verification problems on fatigue damage and crack growth reliability are presented to illustrate the capabilities of COMPASS.

#510321 ⑯

THE EFFECT OF CRACK TIP RADIUS ON INITIATION FRACTURE TOUGHNESS

Ken MacKay[1], Ken KarisAllen[2], G.M.C. Lee[1]

[1]Department of Mining and Metallurgy
Technical University of Nova Scotia
P.O. Box 1000, Halifax, Nova Scotia
Canada, B3J 2X4

[2] Dockyard Laboratory
Defence Research Establishment Atlantic
P.O. Box 1012, Dartmouth, Nova Scotia
Canada, B2Y 3Z7

Abstract

Fracture standards maximize crack tip constraint by including a mandatory fatigue precracking procedure prior to determining initiation fracture toughness. This procedure is time consuming and may introduce considerable scatter and uncertainty in the determined toughness values. A mechanical or electrical means of manufacturing defects would provide a significant economic benefit as well as a more reproducible initial crack tip profile. The objective of this research is to evaluate various alternative methods of producing defects by determining the relationship between lower bound initiation fracture toughness and crack tip radius. A review of the literature indicates that a critical crack tip radius exists below which the apparent fracture toughness becomes independent of any further decrease in radius. Preliminary tests using low alloy steel fatigue precracked specimens ($a/W = 0.60$) and electric discharge machining (EDM) notched specimens ($a/W = 0.45$, with crack tip radii 60 -75 mm) generate average apparent toughness values of 232 kJ/m^2 and 400 kJ/m^2, respectively. EDM notched specimens provide greater reproducibility of the apparent toughness values compared to the fatigue precracked specimens. From the limited data obtained to date, it is uncertain whether the increase in toughness for the $a/W = 0.45$ specimens results from the decrease in crack depth or from the increase in crack tip radius.

Introduction

Current ASTM fracture standards [1] maximize crack tip constraint by including a mandatory fatigue precracking procedure prior to determining initiation fracture toughness. In general, the apparent toughness increases as the crack tip radius increases. Therefore, a fatigue crack gives a conservative value of the J-integral since the crack tip radius for a fatigue crack approaches zero. This procedure is time consuming and may introduce considerable scatter and uncertainty in the determined toughness value. Much of the uncertainty is due to the lack of reproducibility in the crack tip profile owing to slight differences in applied loading and material variation across the crack front (a particular problem with welded specimens) during the fatigue precracking. A reproducible mechanical or electrical means of creating defects with finite crack tip radii could replace fatigue precracking if a relationship between the lower bound initiation fracture toughness and crack tip radius existed.

Background

For linear-elastic material, the stresses near a sharp crack (r→0) in an infinite plate subjected to a tensile stress σ are [2, 3, 4]:

$$\sigma_x = \sigma\sqrt{\frac{\pi a}{2\pi r}} \cdot \cos\frac{\theta}{2}\left[1-\sin\frac{\theta}{2}\sin\frac{3\theta}{2}\right] \tag{1}$$

$$\sigma_y = \sigma\sqrt{\frac{\pi a}{2\pi r}} \cdot \cos\frac{\theta}{2}\left[1+\sin\frac{\theta}{2}\sin 3\frac{\theta}{2}\right] \tag{2}$$

$$\tau_{xy} = \sigma\sqrt{\frac{\pi a}{2\pi r}} \cdot \sin\frac{\theta}{2}\cos\frac{\theta}{2}\cos\frac{3\theta}{2} \tag{3}$$

where the stress components and the polar coordinates are depicted in Figure 1. The above equations are only valid for r<<a. For plane stress conditions, $\sigma_z = 0$, and for plane strain conditions, $\sigma_z = \nu(\sigma_x + \sigma_y)$, where ν is Poisson's ratio. Equations 1, 2, and 3 show that the stresses near the crack tip are a function of position ($f(\theta) / (2\pi r)^{1/2}$) and a function of the remote stress and crack length ($\sigma(\pi a)^{1/2}$). The $\sigma(\pi a)^{1/2}$ term in Equations 1, 2, and 3 is defined as the stress intensity factor, K_I, for Mode I loadings.

Creager and Paris [5] developed a similar set of equations for a crack with a finite tip radius:

$$\sigma_x = \frac{K_I}{\sqrt{2\pi r}} \cdot \cos\frac{\theta}{2}\left[1-\sin\frac{\theta}{2}\sin 3\frac{\theta}{2}\right] - \frac{K_I}{\sqrt{2\pi r}} \cdot \frac{\rho}{2r}\cos\frac{3\theta}{2} \tag{4}$$

$$\sigma_y = \frac{K_I}{\sqrt{2\pi r}} \cdot \cos\frac{\theta}{2}\left[1+\sin\frac{\theta}{2}\sin 3\frac{\theta}{2}\right] + \frac{K_I}{\sqrt{2\pi r}} \cdot \frac{\rho}{2r}\cos\frac{3\theta}{2} \tag{5}$$

$$\tau_{xy} = \frac{K_I}{\sqrt{2\pi r}} \cdot \sin\frac{\theta}{2}\cos\frac{\theta}{2}\cos\frac{3\theta}{2} - \frac{K_I}{\sqrt{2\pi r}} \cdot \frac{\rho}{2r}\cos\frac{3\theta}{2} \tag{6}$$

The origin of the polar coordinate system for Equations 4, 5, and 6 is half the root radius away from the crack tip, as shown in Figure 2. For a blunted crack the stress at the crack tip is finite, whereas the stresses at the tip of a sharp crack approach infinity (i.e. there is no crack tip singularity in the case of the blunted crack). For ρ = 0, Equations 4, 5, and 6 reduce to Equations 1, 2, and 3 for the stress fields for sharp crack.

Equations 4 through 6 show that the stress distribution ahead of a crack is affected by the crack tip radius. For plane strain conditions, an increase in crack tip radius decreases the maximum value of σ_y and moves the position of the maximum towards the elastic-plastic boundary as shown in Figure 3 [2, 6, 7]. This change in the stress distribution is due to a reduction in the triaxiality at the crack tip brought about by the increased free surface at the blunted crack tip. For perfectly elastic-plastic materials, the stress in the plastic zone is given by [7, 8]:

$$\sigma_y = \sigma_{ys}\left(1+\ln\left(1+\frac{X}{\rho}\right)\right) \tag{7}$$

using Tresca yield criterion and taking the origin at the crack tip (see Figure 3). The maximum value of σ_y, given by Equation 7, occurs at the elastic-plastic interface.

Several studies have been conducted on the relationship between root radius and apparent fracture toughness [6, 9, 10, 11 - 17]. These studies conclude that, in general, the apparent fracture toughness, J_{IA}, decreases as the crack tip radius decreases until a limiting value of $\rho = \rho_c$ is reached. Below this limiting value, the apparent fracture toughness becomes independent of crack tip radius.

Xiulin [18] derived equations for the elastic and elastic-plastic fracture toughness based on notch strain analysis and strain fracture criterion for ductile materials under plane strain conditions as:

$$K_{IA} = 0.32\sqrt{\pi E \sigma_f \varepsilon_f \rho} \tag{8}$$

and

$$J_{IA} = 0.1(1-\nu^2)\pi \sigma_f \varepsilon_f \rho \tag{9}$$

where σ_f is the critical fracture stress and ε_f is the fracture strain. When the crack tip radius decreases to the critical value ρ_c, the fracture toughness is described by:

$$J_{IC} = 0.1(1-\nu^2)\pi \sigma_f \varepsilon_f \rho_c \tag{10}$$

The value of ρ_c was determined to be a constant which depended on the microstructure of the material. For low alloy high strength steels, ρ_c is approximately equal to the spacing between inclusions [12, 16, 18]. Xiulin discovered that for steel with a martensitic microstructure, the value of ρ_c depended upon the type of martensite present. For high strength steels of lath martensite, and also for aluminum alloys, the value of ρ_c was equal to the strain hardening exponent, n, in mm. For high strength steels with a mixed martensite microstructure, ρ_c was equal to the uniform elongation, δ_b, in mm, or the prior austenite grain diameter, or 9 times the diameter of the dimples found on the ductile fracture surface [18]. For AISI 4340 steel with a martensite microstructure, the value of ρ_c was found to be the grain diameter of prior austenite [18]. Xiulin compared experimental toughness values found in the literature with those calculated using Equation 9. For twelve alloy steels, each tempered to different levels of toughness, and for four aluminum alloys, the difference between the experimental values and the calculated values was less than 10%. Since the dimple size and uniform elongation increase with toughness, ρ_c is also expected to increase with fracture toughness. The increase in ρ_c with fracture toughness has already been implied by Equations 9 and 10.

The results of Xiulin are based on ductile fracture. However, similar models have been proposed for brittle fracture in low alloy steels. Ritchie and Horn [6] proposed that the apparent fracture toughness for stress controlled fracture (intergranular cleavage and quasicleavage) is:

$$K_{IA} \approx 2.9\sigma_{ys}\sqrt{\rho\left[\exp\left(\frac{\sigma_f}{\sigma_{ys}}-1\right)-1\right]} \tag{11}$$

$$J_{IA} \approx 8.4\sigma_{ys}^2\rho\left[\exp\left(\frac{\sigma_f}{\sigma_{ys}}-1\right)-1\right] \tag{12}$$

Using the critical crack tip radius ρ_c, the fracture toughness is given by:

$$K_{IC} \approx 2.9\sigma_{ys}\sqrt{\rho_c\left[\exp\left(\frac{\sigma_f}{\sigma_{ys}}-1\right)-1\right]} \tag{13}$$

$$J_{IC} \approx 8.4\sigma_{ys}^2\rho_c\left[\exp\left(\frac{\sigma_f}{\sigma_{ys}}-1\right)-1\right] \tag{14}$$

Equations 13 and 14 again indicate that the critical root radius increases as fracture toughness increases. Experimental results show that an increase in ρ_c is accompanied by an increase in toughness for as-quenched AISI 4340 steel austenitized at different temperatures where fracture occurred by quasicleavage [10]. Similar results have been observed for a mild steel and for an HSLA steel where fracture occurred by cleavage [13].

This report describes an experimental investigation into the relationship between lower bound initiation fracture toughness and crack tip radius. The objective is to determine the initiation fracture toughness where the toughness determined using specimens with finite crack tip radius deviates from the toughness determined in accordance with ASTM standard E813-89 [1]. The hypothesis is that the initiation fracture toughness decreases as the limiting crack tip radius decreases. Thus, for a given finite crack tip radius, a lower bound initiation fracture toughness should exist above which the apparent fracture toughness equals the initiation fracture toughness.

Experimental Program

Two sets of single edge notched three-point-bend specimens were machined from a 25 mm plate of HLES 80 in the T-L orientation. Detailed specimen dimensions are given in Table 1. The first set of specimens (a/W = 0.60) were fatigue precracked in accordance with ASTM E813-89. In the second set of specimens (a/W = 0.45), precracking was replaced by electric discharge machining slots. The crack tip radius for this manufactured defect is approximately 60-75 μm (0.0025 - 0.003 in.). All specimens were side grooved 10 percent on each side to promote uniform crack extension across the crack front.

Quasi-static fracture tests were conducted on a computer controlled servo-hydraulic materials testing system. Periodic unloading compliance measurements were carried out to measure crack length in accordance with ASTM E-813. Initial and final 9 point average crack extension measurements were optically determined from the fracture surfaces subsequent to testing. Load and CMOD displacement data were collected and bussed to a microprocessor for storage and analysis.

For each specimen J-resistance curves were generated using the procedure outlined in ASTM E-813. The J-Δa data pairs were fitted to a power law function. J_{IC} was defined as the intersection of the 0.20 mm offset blunting line and fitted resistance data. Triplicate tests were performed for each specimen configuration.

Results and Discussion

Figures 4 and 5 show typical load displacement curves for each type of specimen. Figures 6 and 7 show plots of applied J vs Δa for a fatigue precracked specimen and an EDM notched specimen respectively. Both resistance curve data sets fit well to a power law function. The results of the tests are shown in Figure 8. The average apparent toughness value for the fatigue precracked specimens is 232 kJ/m^2. The two lower values for the fatigue precracked specimens are valid J_{IC} toughness values . The third toughness value is not valid due to insufficient crack extension. The average apparent toughness value for the EDM notched specimens is 400 kJ/m^2. This is significantly higher than the average apparent toughness determined from the fatigue precracked specimens. There are two possible explanations for this difference in the average apparent toughness values. The first possibility is that the crack tip radius of the EDM notched bars is greater than the limiting crack tip radius. The second factor is that there is a difference in crack depth between the fatigue cracked and EDM notched specimens. The shorter crack depths in the EDM notched specimens may be responsible for the difference in the apparent toughness values between the two specimen types.

There is less scatter in the apparent toughness values obtained from the EDM notched specimens. The range between the two valid toughness values obtained from the fatigue precracked specimens is 70 kJ/m^2. The range between the highest and lowest apparent toughness values obtained from the EDM notched specimens is 25 kJ/m^2. Thus, the use of the EDM notch improves the reproducibility of the determined toughness values compared to fatigue precracking. This improved reproducibility can be partially accounted for by the more uniform crack tip profiles produced using an EDM notch. Figure 9 compares the crack profiles of the fatigue precracked and EDM notched specimens. The fatigue precracked specimens extend a curved crack front with the leading edge near the surface of the side groove root. The EDM notched specimens start with a straight crack front which remains essentially straight during extension.

Conclusions

1) From a review of the literature, ρ_c was generally found to increase as the fracture toughness increased. While the value of ρ_c could be estimated from a number of material properties (e.g. inclusion spacing, uniform elongation, the prior austenite grain diameter, the strain hardening exponent, or the average dimple size on the ductile fracture surface), in each case the value of ρ_c increased as fracture toughness increased for low alloy steels in both the as-quenched and tempered conditions.

2) A significant difference exists between the apparent initiation fracture toughness determined using EDM notched specimens with $a/W = 0.45$ and using fatigue precracked specimens with $a/W = 0.60$. From the limited data obtained to date, it is uncertain whether the increase in toughness for the $a/W = 0.45$ specimens results from the decrease in crack depth or from the increase in crack tip radius.

3) Preliminary tests show that a machined notch of finite root radius provides improved reproducibility of the determined fracture toughness value, compared to fatigue precracking.

References

[1] "E813 Test Method for J_{IC}, A Measure of Fracture Toughness", Annual Book of ASTM Standards, Vol. 3.01, ASTM, Philadelphia, 1992.

[2] Ewalds, H.L., Wanhill, R.J.H., Fracture Mechanics, Edward Arnold, New York, 1989.

[3] Barsom, J.M., and McNicol, R.C., in "Fracture Toughness and Slow Stable Cracking", ASTM STP 559, American Society for Testing and Materials, Philadelphia, 1974, pp. 183-204.

[4] Irwin, G.R., "Analysis of Stresses and Strains Near the End of a Crack Traversing a Plate", Journal of Applied Mechanics, Vol. 24, 1957, pp. 361-364.

[5] Creager, M., and Paris, P.C., "Elastic Field Equations for Blunt Cracks with Reference to Stress Corrosion Cracking", International Journal of Fracture Mechanics, Vol. 3, 1967, pp. 247-252.

[6] Ritchie, R.O., and Horn, R.M., "Further Considerations on the Inconsistency in Toughness Evaluation of AISI 4340 Steel Austenitized at Increasing Temperatures", Metallurgical Transactions, Vol. 9A, 1978, pp. 331-341.

[7] Tetelman, A.S., Wilshaw, T.R., Rau, C.A., Jr., "The Critical Stress Criterion for Cleavage", International Journal of Fracture Mechanics, Vol. 4, 1968, pp. 147-156.

[8] Knott, J.F., "Macroscopic Aspects of Crack Extension", Advances in Elastic-Plastic Fracture Mechanics, Larsson, L.H., Ed., Applied Science Publishers, London, 1979, pp. 1 - 20

[9] Faucher, B., Tyson, W.R., Hong, Y., and Boutin, J., "Dependence of Ductile Fracture Toughness of a Weld Metal on Notch Root Radius and Inclusion Content", International Journal of Fracture, Vol. 46, 1990, pp. 173-184.

[10] Ritchie, R.O., Francis, B., and Server, W.L., "Evaluation of Toughness in AISI 4340 Alloy Steel Austenitized at Low and High Temperatures", Metallurgical Transactions, Vol. 7A, 1976, pp. 831-338.

[11] Mulherin, J.H., Armiento, D.F., and Markus, H., "The Relationship Between Fracture Toughness and Stress Concentrations Factors for Several High Strength Aluminum Alloys", Journal of Basic Engineering, Dec., 1964, pp. 709, 717.

[12] Yoda, M., "The Effect of Notch Root Radius on the J-Integral Fracture Toughness Under Modes I, II, and III Loadings", Engineering Fracture Mechanics, Vol 26, No.3, 1987, pp. 425- 431.

[13] Pandey, R.K., "Significance of Limiting (Equivalent) Tip Radius and Crack Tip Deformation for Cleavage Induced Fracture in Structural Steels", Journal of Materials Science, Vol. 19, 1984, pp. 607-614.

[14] Pratap, C.R., and Pandey, R.K., "Effect of Geometry and Finite Root Radius on Plastic Zone and Tip Opening Displacement", Engineering Fracture Mechanics, Vol. 19, No. 5, 1984, pp. 849-861.

[15] Swanson, R.E., Thompson, A.W., and Bernstein, I.M., "Effect of Notch Root Radius on Stress Intensity in Mode I and Mode III Loading", Metallurgical Transactions, Vol. 17A, 1986, pp. 1633-1637.

[16] Firrao D., Begley, J.A., De Benedetti, B., Roberti, R., and Silva, G., "Fracture Initiation and Propagation at the Root of the Notch in As-Quenched AISI 4340 Steel Charpy Type Bars with Varying Notch Root Radii", Scripta Metallurgica, Vol. 14, 1980, pp. 519-524.

[17] Zeman, J., Rolc, S., Buchar, J., and Pokluda, J., in "Fracture Mechanics: Twenty-First Symposium", ASTM STP 1074, ASTM, Philadelphia, 1990, pp. 396-418.

[18] Xiulin, Z., "On a Unified Model for Predicting Notch Strength and Fracture Toughness of Metals", Engineering Fracture Mechanics, Vol. 33, No. 5, pp. 685-695.

Table 1. Dimensions of three point bend bars (SENB) used for preliminary tests.

	Fatigue Precrack	EDM Notch
ρ	≈ 0	60 - 75 mm (0.0025 -0.003 in.)
W	50.8 mm (2.00 in.)	50.8 mm (2.00 in.)
B	24.3 mm (0.955 in.)	24.3 mm (0.955 in.)
B_{net}	20.3 mm (0.80 in.)	20.3 mm (0.80 in.)
a_o	30.1-30.5 mm (1.18-1.20 in.)	23.0 mm (0.906 in.)
a_o/W	0.59 - 0.60	0.45
Material:	Low alloy steel (0.15 %C, 0.37 %Mn, 0.56 %Cr, 4.29 %Ni, 0.29% Mo)	

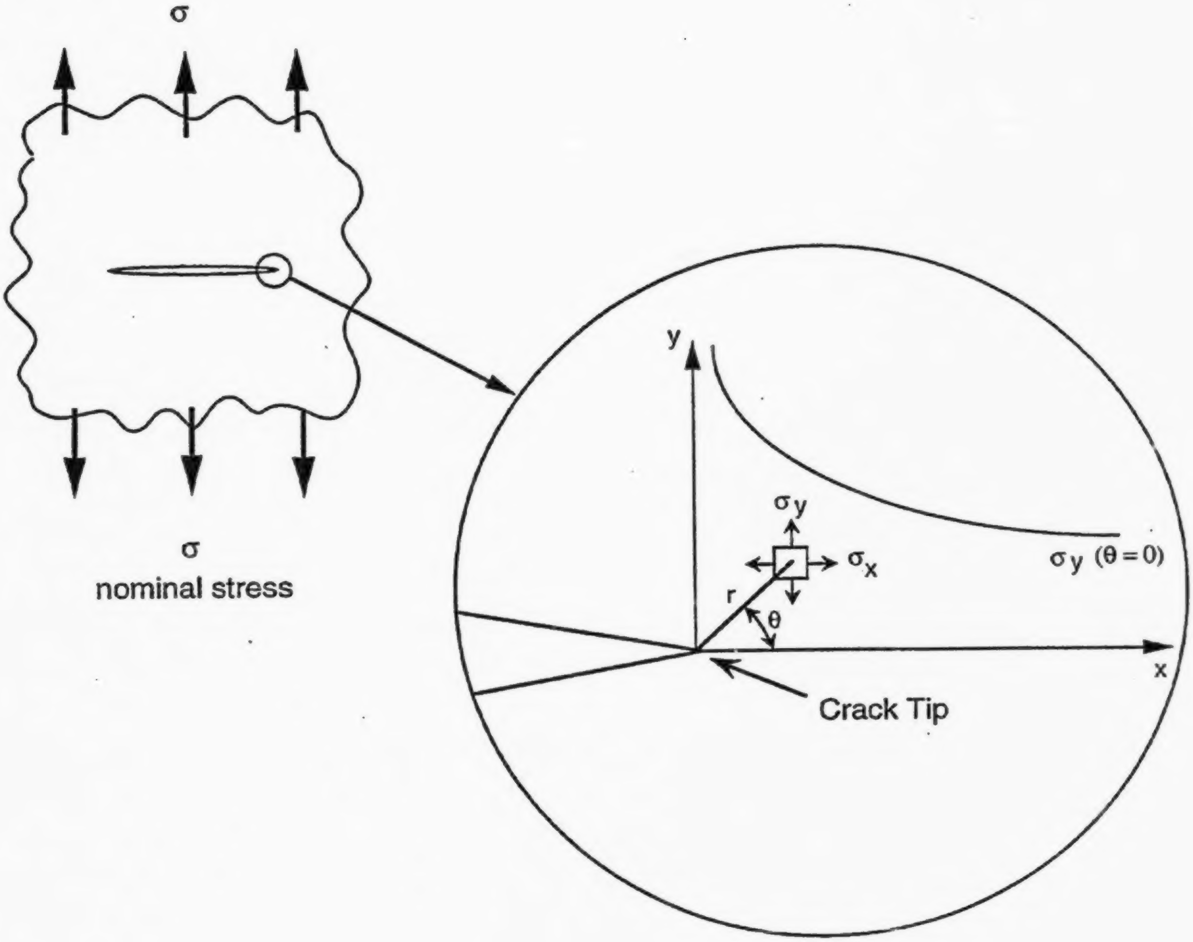
σ
σ
nominal stress
y
x
σy
σx
σy (θ=0)
r
θ
Crack Tip

Figure 1. Illustration of the elastic stresses ahead of a fatigue crack.

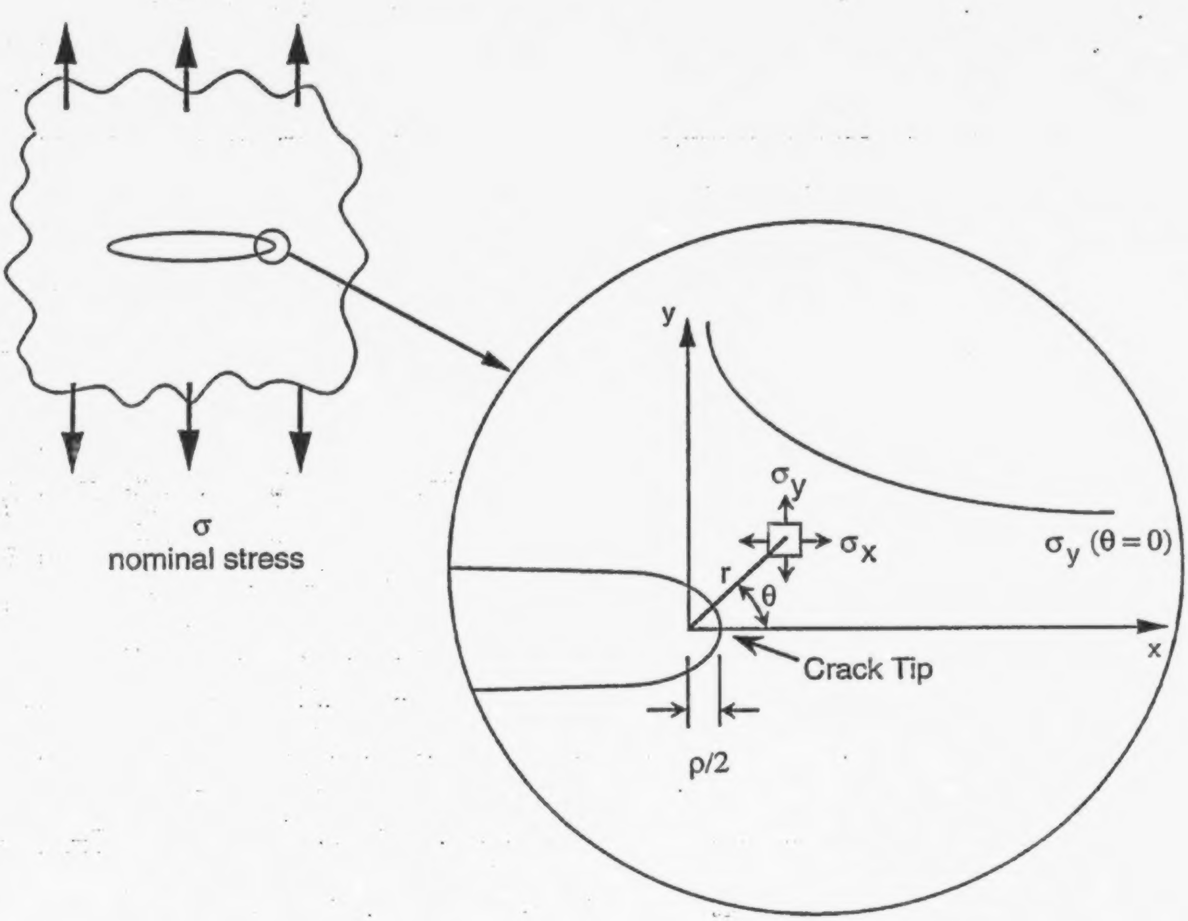
σ
σ
nominal stress
y
σ_y
σ_x
σ_y (θ = 0)
r
θ
x
Crack Tip
ρ/2

Figure 2. Illustration of the elastic stress distribution ahead of an elliptical notch with crack tip radius ρ.

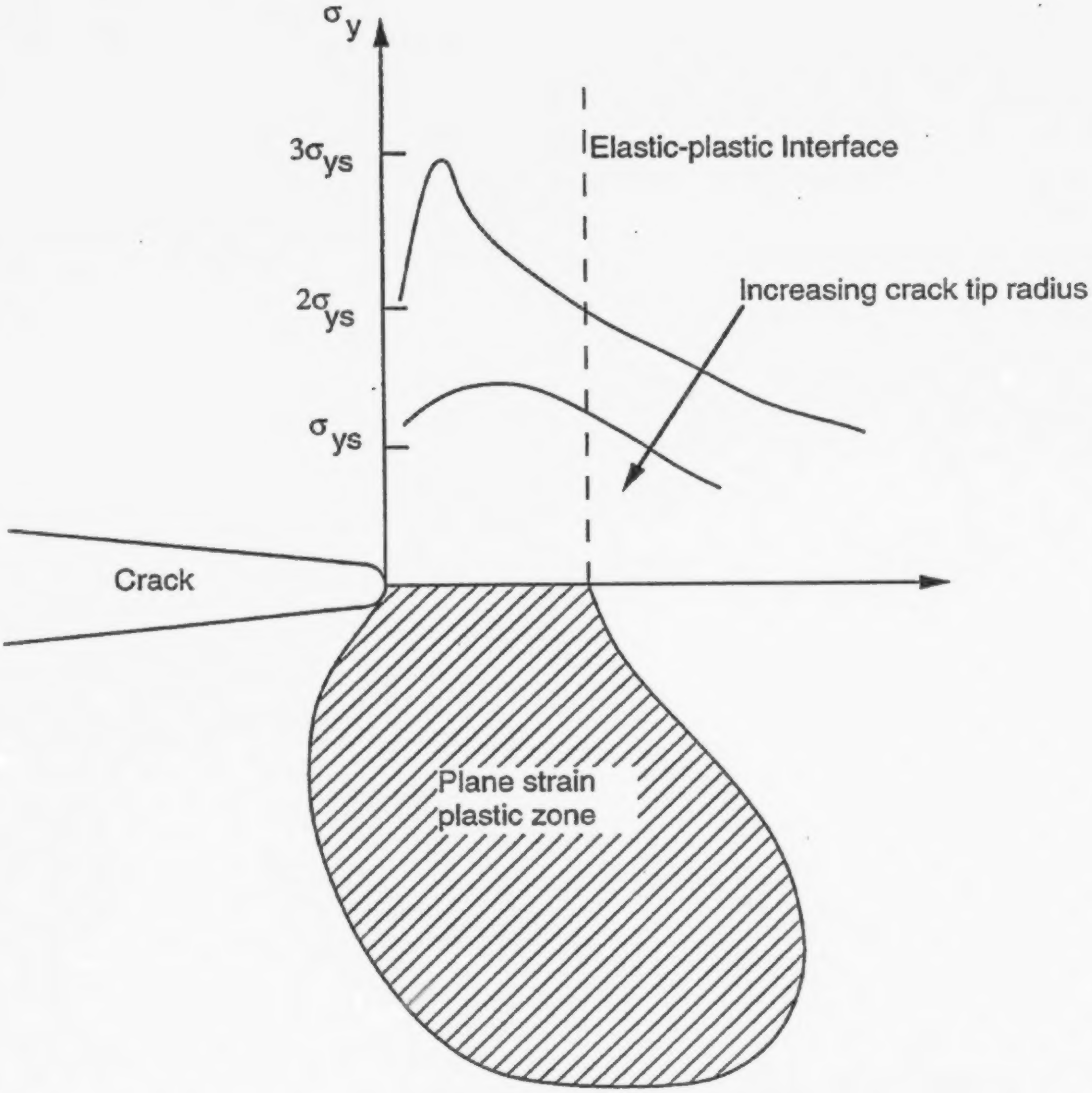
σ_y
$3\sigma_{ys}$
$2\sigma_{ys}$
σ_{ys}
Elastic-plastic Interface
Increasing crack tip radius
Crack
Plane strain plastic zone

Figure 3. Illustration of the effect of increasing crack tip radius on the stress (σ_y) distribution ahead of the crack for a perfectly elastic-plastic material under plane strain conditions.

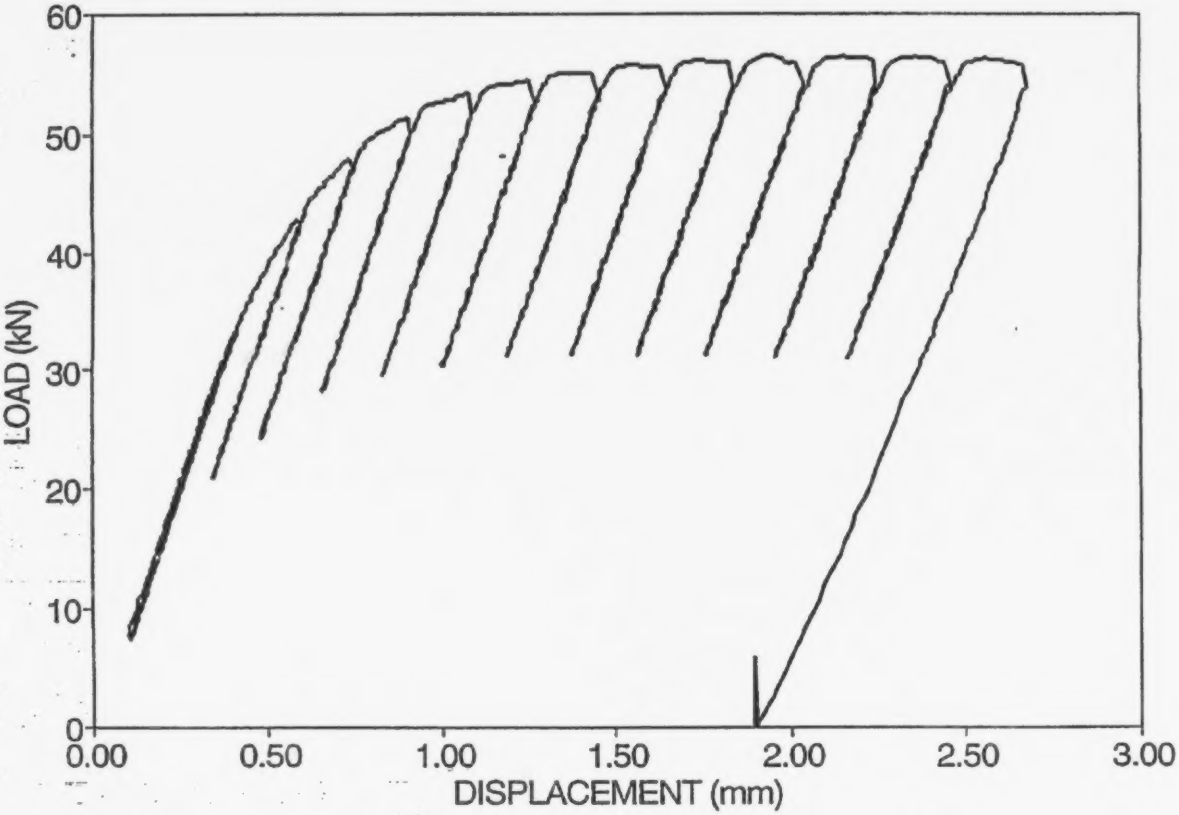

Figure 4. Typical load-displacement curve for a fatigue precracked specimen.

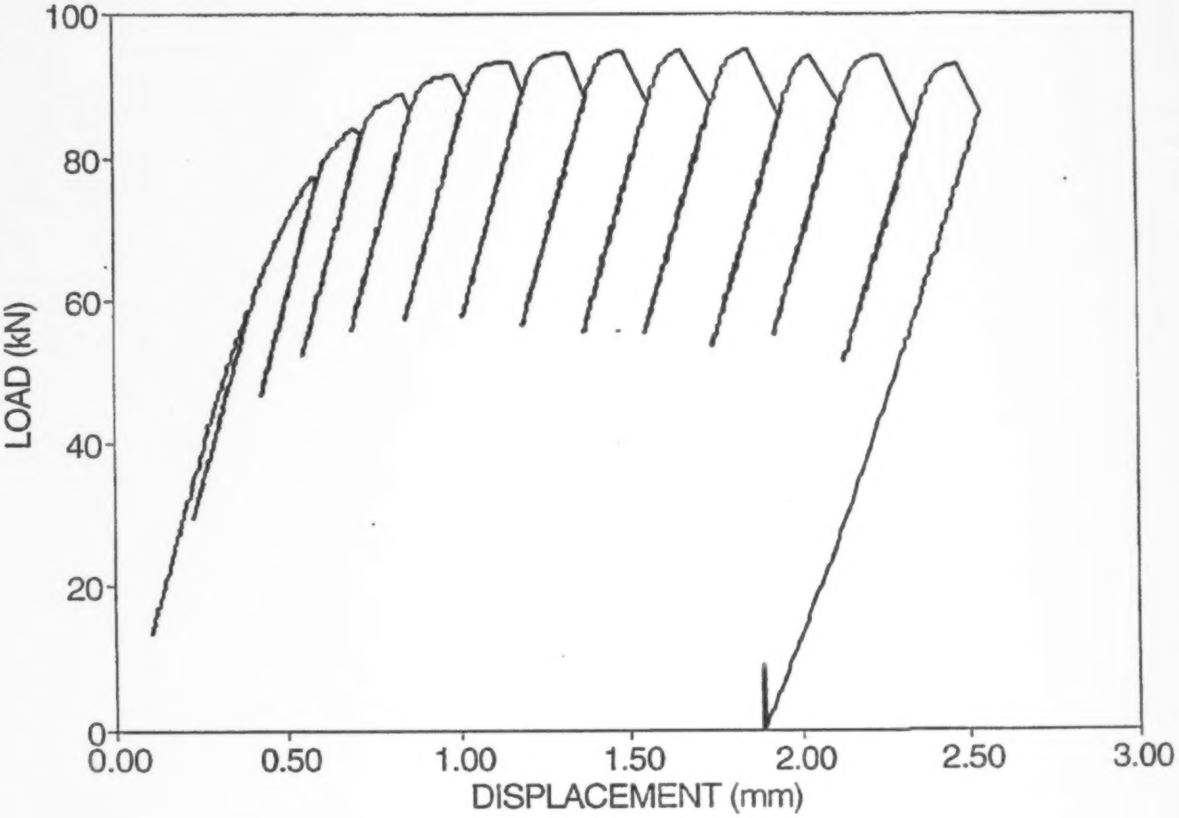

Figure 5. Typical load-displacement curve for an EDM notched specimen.

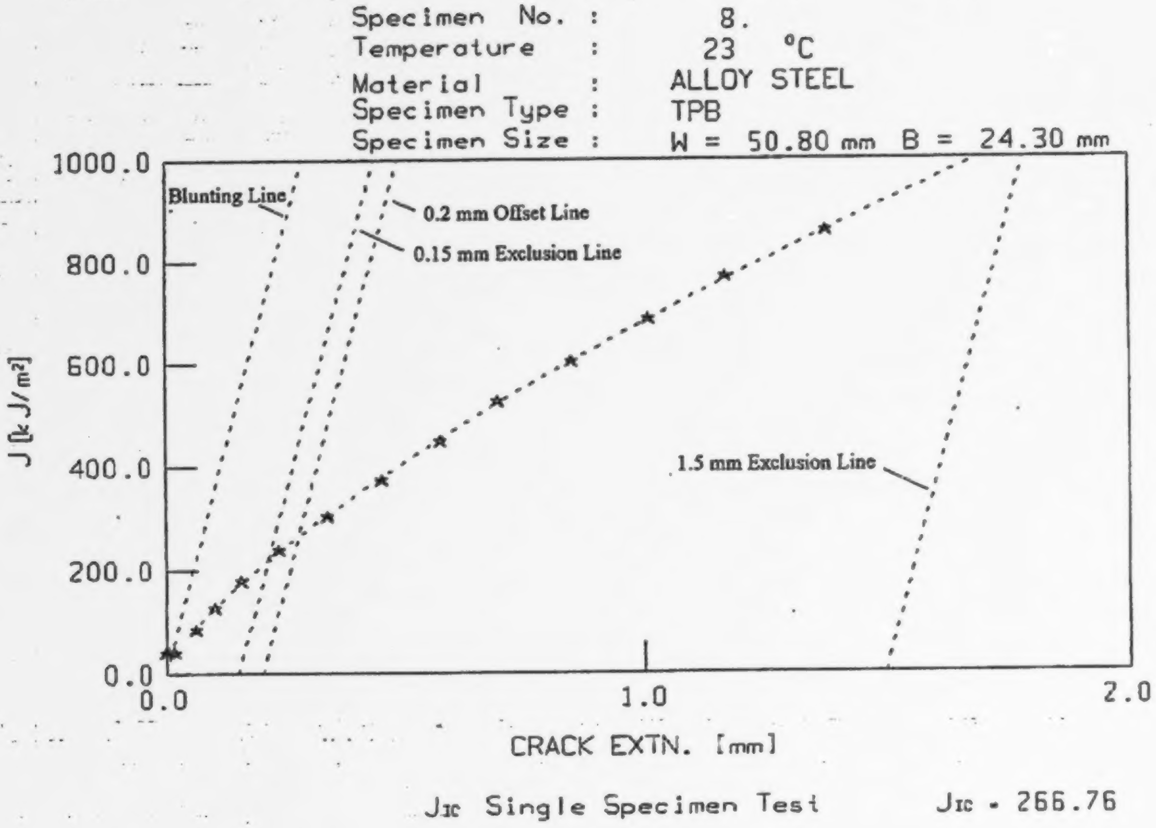

Figure 6. Typical J vs Δa curve for a fatigue precracked specimen.

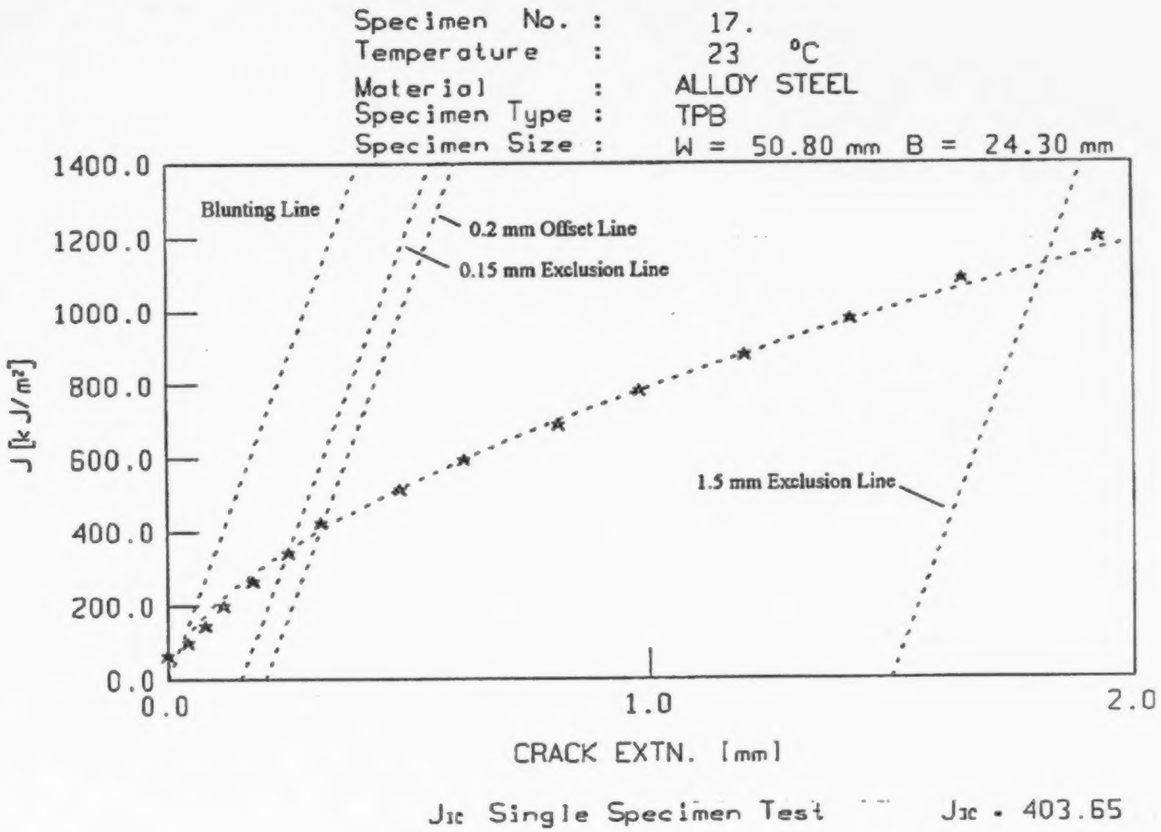

Figure 7. Typical J vs Δa curve for an EDM notched specimen.

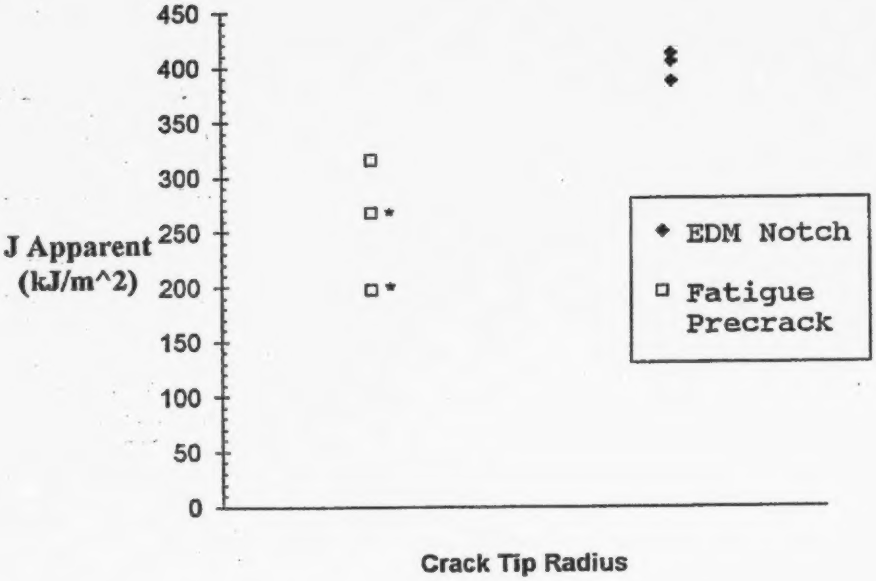

Figure 8. Apparent fracture toughness for the fatigue precracked and EDM notched specimens. (* valid J_{IC}).

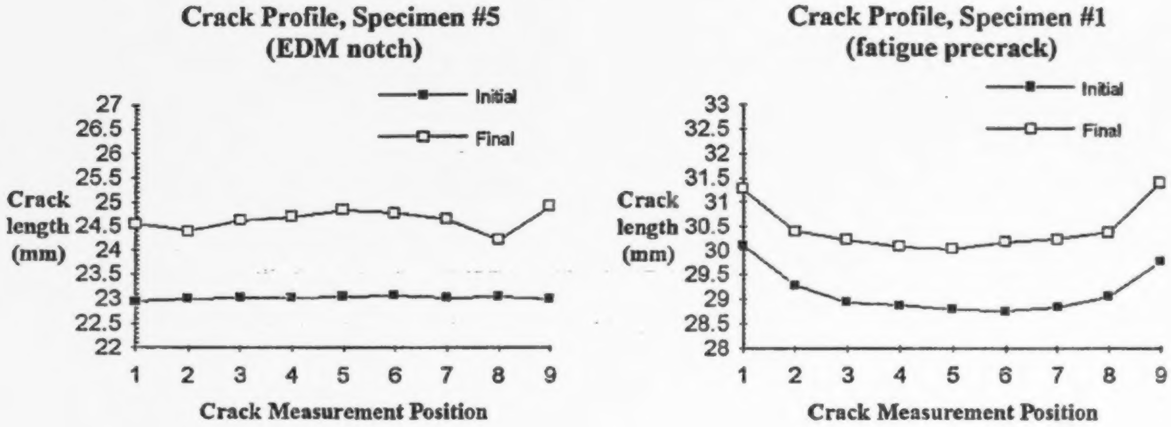
Crack Profile, Specimen #5 (EDM notch)

Crack Profile, Specimen #1 (fatigue precrack)

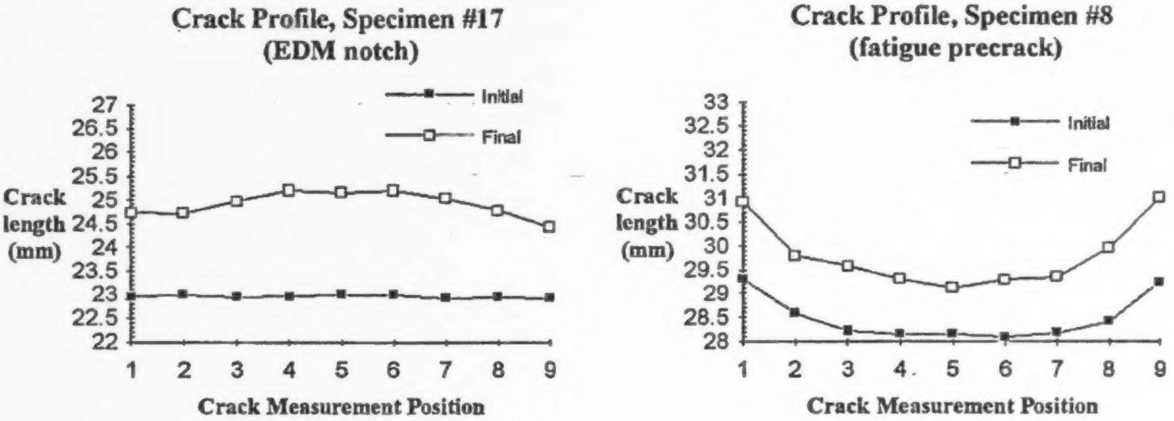
Crack Profile, Specimen #17 (EDM notch)

Crack Profile, Specimen #8 (fatigue precrack)

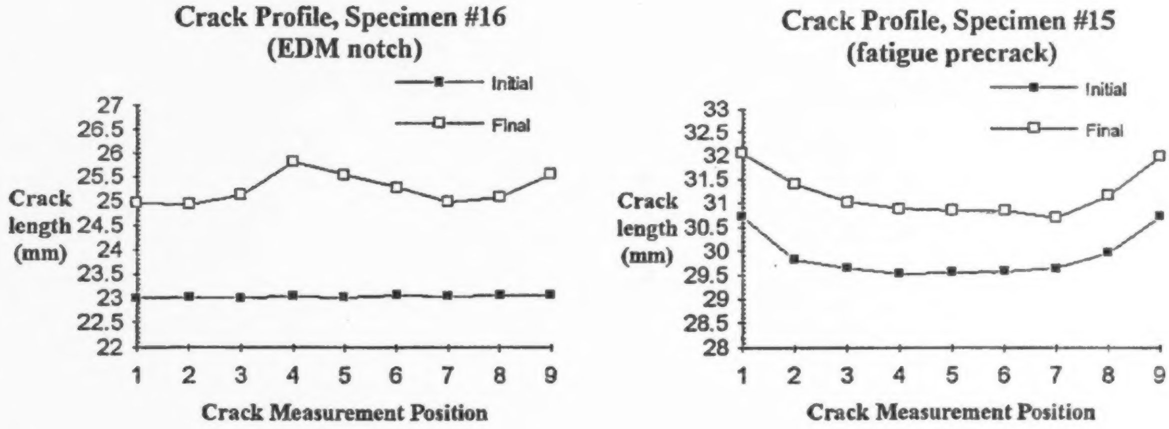
Crack Profile, Specimen #16 (EDM notch)

Crack Profile, Specimen #15 (fatigue precrack)

Figure 9. Initial and final crack profiles for the EDM notched and fatigue precracked specimens.

#510322 (17)

Buckling and Post-buckling of Stiffened Shell Structures Using a Co-rotational Finite Element Formulation

L. Jiang and M.W. Chernuka

Martec Limited, Suite 400, 1888 Brunswick Street
Halifax, Nova Scotia, B3J 3J8

Accurate predictions of the buckling loads and the post-buckling responses of stiffened shell structures are of particular interest in submarine design. In this paper, a co-rotational, updated Lagrangian finite element formulation is presented for geometrically nonlinear structural analysis. This formulation has been incorporated into all the plate/shell and beam elements in the general purpose finite element program VAST along with a group of advanced solution techniques including the displacement control and Crisfield's arc-length methods. In finite element analyses using VAST, stiffened shells can be modelled by either combining compatible shell and beam elements or employing the newly developed stiffened shell element. In the former, beam elements must coincide with shell element edges, whereas in the latter, beam stiffeners are permitted to be located anywhere inside the shell element. Both finite element models have been used to investigate the buckling and post-buckling behaviour of various ring stiffened cylindrical shells under hydrostatic loading. Special emphasis is placed on the sensitivity of geometric imperfections. Excellent numerical solutions have been obtained in the present study.

BUCKLING AND POST-BUCKLING OF STIFFENED SHELL STRUCTURES USING A COROTATIONAL FINITE ELEMENT FORMULATION

Lei JIANG and Michael W. CHERNUKA
Martec Limited, Suite 400, 1888 Brunswick Street, Halifax, Nova Scotia,
Canada B3J 3J8

Introduction

Accurate predictions of the buckling loads and post-buckling responses of stiffened shell structures are of particular interest in submarine design. Although the critical load levels can be obtained by using linearized buckling analyses, some deficiencies should be noted. In particular, critical loads may be significantly overestimated if the structure has a highly nonlinear pre-buckling deformation and the sensitivity of the structural collapse to geometric imperfections cannot be studied properly. To obtain post-buckling responses, which are normally characterized by large displacements and rotations, a fully nonlinear finite element formulation has to be employed.

Among the approaches proposed for nonlinear finite element analysis, the most commonly used are the total and updated Lagrangian formulations [1,2]. However, for a special class of nonlinear problems, in which displacements and rotations could be arbitrarily large, but strains are of moderate magnitude, the Lagrangian formulations can be further simplified without significant loss in accuracy. Theoretically, the motion of a continuous medium can always be decomposed into a rigid body motion followed by a pure deformation. The rigid body motion is not involved in the constitutive equation, whereas the pure deformation is not involved with geometric nonlinearities. For problems with arbitrarily large displacements and rotations but small strains, the pure deformation part extracted from the total displacement field is always a small quantity compared with the element dimensions. As a result, the linear finite element theory can be used in element local coordinate systems. Direct separation of the total displacements into its rigid body motion and pure relative deformation components can be accomplished by using a corotational formulation.

The corotational concept has been adopted by several authors in the development of efficient algorithms for geometrically nonlinear analysis of shell structures [3-8]. In the present study, a corotational, updated Lagrangian procedure is developed, in which the element tangent stiffness matrices are generated as in the standard updated Lagrangian formulation [2]; whereas the corotational approach is employed to update element strains, stresses and internal force vectors in the incremental-iterative solution procedure [9-14]. One of the major difficulties in geometrically nonlinear analysis of shells is associated with the non-vectorial characteristic of finite rotations [15].

Several methods have been proposed for updating element geometry and calculating the deformational rotations [6,8]. In our work, the procedure proposed by Rankin and Brogan [8] is followed.

The present corotational procedure is very simple and ideally suited for implementation in existing general purpose linear finite element programs, like VAST [16]. Its effectiveness, robustness and reliability have been demonstrated by a large number of highly nonlinear test problems. In this paper, we will focus on nonlinear analysis of stiffened and unstiffened cylindrical shells, which are often used as simplified test models of submarine pressure hulls.

Nonlinear Finite Element Formulation

Using the principle of virtual work and in the finite element context, the discretized equilibrium equation can be expressed as [1,2]:

$$F({}^{t}U) - {}^{t}\lambda P = 0 \tag{1}$$

where U indicates the generalized nodal displacement vector. For shell elements, **U** contains both nodal translational displacements, **u**, and rotational variables, θ. **F** is the internal force vector which is a nonlinear function of the generalized nodal displacements. **P** denotes a reference external load vector and λ is a load parameter which controls the actual magnitude of external load. In eqn (1), a proportional conservative loading condition is assumed. In case of nonconservative loading, **P** is also a nonlinear function of the generalized nodal displacements. The left superscript (t) denotes a typical load level.

Incremental-iterative solution algorithms are normally employed to solve the nonlinear equilibrium equations (1). For a typical iteration, (k), in the load step from $(t-\Delta t)$ to (t), the nonlinear equations can be linearized using the Newton-Raphson method as:

$$K_T({}^{t}U^{(k-1)})\ \Delta U = ({}^{t}\lambda^{(k-1)} + \Delta\lambda)P - F({}^{t}U^{(k-1)}) \tag{2}$$

where K_T is the tangent stiffness matrix. ${}^{t}U^{(k-1)}$ and ${}^{t}\lambda^{(k-1)}$ indicate the total generalized nodal displacements and load parameter obtained at the end of the previous iteration, whereas ΔU and $\Delta\lambda$ are the incremental displacements and load parameter for the current iteration.

To solve eqn (2) for ΔU and $\Delta\lambda$, an additional constraint equation has to be specified in the solution space. The commonly used constraint equations include the constant load incrementation [1,2], the displacement control [17] and the arc-length method [18]. In the constant load incrementation method, a load increment, which is indicated by a left subscript 't', is specified at the beginning of a load step as:

$$ {}_t\lambda = {}^t\lambda - {}^{t-\Delta t}\lambda \tag{3} $$

and kept as constant during the Newton-Raphson iterations as shown in Fig. 1(a). Although this constraint equation is adequate for a wide range of nonlinear engineering problems, convergence difficulties may occur in the vicinity of load limit points. This numerical difficulty can be overcome by employing the constant arc-length constraint, defined as:

$$ \left({}_t\mathbf{U}^{(k-1)} + \Delta \boldsymbol{U}\right)^T \left({}_t\boldsymbol{U}^{(k-1)} + \Delta \boldsymbol{U}\right) + \left({}_t\lambda^{(k-1)} + \Delta\lambda\right)^2 = \Delta\ell^2 \, , \tag{4} $$

by which the equilibrium state $({}^t\mathbf{U}, {}^t\lambda)$ is approached on a cylindrical surface in the solution space and the load limit points can then be passed easily as shown in Fig. 1(b).

After each iteration, the accumulated load parameter and translational displacement increments in the current load step can be updated as:

$$ {}_t\lambda^{(k)} = {}_t\lambda^{(k-1)} + \Delta\lambda \quad \text{and} \quad {}_t u^{(k)} = {}_t u^{(k-1)} + \Delta u \tag{5} $$

and the total load parameter and nodal translations updated as:

$$ {}^t\lambda^{(k)} = {}^{t-\Delta t}\lambda + {}_t\lambda^{(k)} \quad \text{and} \quad {}^t u^{(k)} = {}^{t-\Delta t}u + {}_t u^{(k)} \tag{6} $$

where ${}^{t-\Delta t}\lambda$ and ${}^{t-\Delta t}u$ indicate the converged solution obtained for the previous load step. Sophisticated large rotation theory [15] is required when updating the nodal rotational variables.

Corotational Procedure

In order to describe the corotational procedure, three Cartesian coordinate systems have to be defined. They are:

i) The global coordinate system, **G**;

ii) The element corotational coordinate system, **E**, which is associated with each element and undergoes rigid body rotations and translations with the element; and

iii) The shell surface coordinate system, $\mathbf{V}_i$, which is the nodal triad associated with node i in a shell or beam element.

As previously mentioned, in the present study, the corotational approach is only employed in the internal force calculation. In order for the linear finite element theory to generate sufficiently accurate results, the pure deformational displacements and rotations employed in internal force calculations must be small quantities relative to the element dimensions. For this reason, it is appropriate to update the reference configuration after each new converged solution has been obtained. By doing this, we are dealing with the increments of the deformational displacements and rotations in the current load step instead of the accumulated ones in the whole deformation process as was done by other investigators [4-7].

Transforming both the internal force vector and the Cauchy stress tensor into the element corotational framework, the linear strain-displacement matrix in the element co-rotational coordinate system can be expressed as:

$$ {}^{t}\tilde{B}_{L} = \Phi({}^{t}E)\ {}^{t}B_{L}\ {}^{t}E \tag{7}$$

where the tilde '$\sim$' indicates quantities measured in the corotational coordinate system and Φ is the standard strain transformation matrix, which is a function of **E**.

If the incremental strains are small quantities in each load step, the quadratic terms in the incremental Green-Lagrange strain tensor can be neglected in the element corotational coordinate system and the second Piola-Kirchhoff and the Cauchy stress tensors also become indistinguishable. As a result, the corotational Cauchy stress can be updated approximately using a piece-wise linear strain-displacement relation as:

$$ {}^{t+\Delta t}\tilde{\tau} \approx \tilde{C}\ {}^{t}\tilde{B}_{L}\ \tilde{U}_{def} + {}^{t}\tilde{\tau} \tag{8}$$

where $\tilde{C}$ indicates the incremental constitutive matrix and $\tilde{U}_{def}$ is the increment of the deformational displacements and rotations in the current load step.

The element internal force vector for the current (t+Δt) configuration can now be evaluated in the global coordinate system as:

$$ {}^{t+\Delta t}f = \int_{{}^{t+\Delta t}v} {}^{t+\Delta t}B_{L}^{T}\ \Phi({}^{t+\Delta t}E)\ {}^{t+\Delta t}\tilde{\tau}\ d\,{}^{t+\Delta t}V \tag{9}$$

The integral in (9) is evaluated using numerical integration. The approximate Cauchy stress tensor given in (8) is also employed to calculate the geometric stiffness matrix.

The element-independent corotational approach proposed by Rankin and Brogan [8] is adopted in the present study to extract the deformational part of displacements and rotations. Assuming that the local co-rotational coordinate system in the latest obtained configuration associated with a typical element rotates to ${}^{t+\Delta t}\mathbf{E}$ from ${}^{t}\mathbf{E}$ in the reference configuration, the deformational translations, $\tilde{\mathbf{u}}_{def}$, and rotation matrix, $\tilde{\mathbf{D}}_i$, can be expressed as:

$$\tilde{u}_{def} = {}^{t+\Delta t}E^T\,({}^{t}X + {}_{t}u) - {}^{t}E^T\,{}^{t}X \tag{10}$$

and

$$\tilde{D}_i = {}^{t+\Delta t}E^T({}^{t+\Delta t}V_i\,{}^{t}V_i^T)\,{}^{t}E. \tag{11}$$

Based on large rotation theory, the pseudo-vector corresponding to the deformational rotations can be obtained through a skew-symmetric matrix defined as:

$$\Omega_i = \frac{2(\tilde{D}_i - \tilde{D}_i^T)}{1+trace\ (\tilde{D}_i)} \tag{12}$$

and used as a part of $\tilde{U}_{def}$ in (8).

Computer Implementation

The present corotational procedure has been implemented for eight elements in our general purpose finite element program, VAST [9-14, 16]. These elements include 8-noded degenerate, isoparametric thick/thin shell (IEC=1); 4-noded quadrilateral shell (IEC=5); 3-noded triangular plate/shell (IEC=4); 3-noded curved beam (IEC=7); 2-noded general beam (IEC=3); 8-noded stiffened shell (IEC=25); 20-noded 3D solid (IEC=2) and 13-noded transition (IEC=6) elements, which are shown graphically in Fig. 2. To alleviate the shear and membrane "locking" problem in isoparametric structural elements, uniformly reduced numerical integration technique is employed in 8-noded thick/thin shell, 8-noded stiffened shell, 3-noded curved beam and 13-noded transition elements and the mixed interpolation formulation of tensorial transverse shear components, initially proposed by Bathe and Dvorkin [19,20], is adopted in 4-noded quadrilateral shell element. Element corotational coordinate systems are calculated using the corner nodes for higher-order finite elements.

Numerical Examples

Example 1: Pre- and Post-buckling of a Cylindrical Shell

In this example, we considered a cylindrical shell with diaphragm ends under uniform pressure as shown in Fig. 3. In order to initiate buckling, a geometric imperfection corresponding to the third buckling mode is imposed on the undeformed configuration according to:

$$\Delta R = \delta \cos(3\psi)\cos\left(\frac{\pi X}{2L}\right) \tag{13}$$

where R is the radius of the cylinder and δ indicates the maximum imperfection. In this example, we took $\delta = 0.005$m. L denotes half length of the cylinder and ψ is measured counterclockwise from the positive Y direction. Due to the symmetry, only a quarter of the whole cylinder was included in our finite element model and discretized into meshes of the 8-noded, 4-noded and 3-noded shell elements, respectively, as shown in Fig. 4. The deformed configurations obtained by using different shell elements are displayed in Figs. 5-7 and the load-deflection curves are compared in Fig. 8, where node A (see Fig. 4) is the one having maximum total deflection in the symmetric plane X=0. The nonconservative characteristic of hydrostatic pressure was taken into account. Both the critical load levels and the post-buckling responses predicted by these three shell elements are in good agreement.

Example 2: Pre- and Post-buckling of a Stiffened Cylindrical Shell

In the second example, we considered two simplified test models of a submarine pressure hull, which are cylindrical shells reinforced by four ring stiffeners, as shown in Fig. 9. These test models have diaphragms at both ends and are subjected to uniform hydrostatic pressure. When the stiffeners are weak compared with the shell and the nonlinear pre- and post-buckling response is dominated by the shell stiffness, an overall buckling mode is produced. On the other hand, when the stiffeners are stiff compared with the shell, the lowest buckling load is associated with a interframe buckling mode.

For the overall buckling model, we imposed the same geometric imperfection on the undeformed configuration as in the previous example. Making use of the symmetry condition, a quarter of the shell was discretized into 8x10 and 12x10 finite element meshes as shown in Fig. 10, where the shell was modelled by 8-noded thick/thin shell elements and the stiffeners by 3-noded curved beam elements. Deformed configurations obtained using the finer finite element model are shown in Fig. 11 and the load-deflection curves obtained by VAST are compared with the ADINA solution [21] in Fig. 12. Good agreement between VAST and ADINA solutions are observed.

To initiate buckling in the interframe buckling model, a geometric imperfection corresponding to the seventh buckling mode was imposed and a very coarse 7x10 finite element mesh was employed to model a quarter of the structure (see Fig. 13). The final deformed configuration is shown in Fig. 14, where the "interframe buckling" deformations are clearly demonstrated. The load-deflection curve is compared to ADINA solution in Fig. 15 with good agreement.

Example 3: Structure's Sensitivity to Geometric Imperfections

In the last example, we considered another stiffened cylindrical shell as shown in Fig. 16. It is similar to the one in the previous example. However, the primary focus for this example is the effect of geometric imperfections on the critical load and the nonlinear pre- and post-buckling responses of the structure. Using our newly developed 8-noded stiffened shell element (see Fig. 2(f)), in which stiffeners are permitted to locate arbitrarily, three finite element models were generated containing one-eighth of the shell, as shown in Fig. 17, where the solid lines indicate the boundaries of the stiffened shell elements and the dashed lines indicate the locations of the stiffeners.

Geometric imperfections corresponding to the fourth buckling mode and having maximum magnitudes of 10%, 30% and 50% of the shell thickness were imposed on each of these three finite element models. A group of linearized buckling analyses were carried out and the first critical loads obtained for each case are summarized in Table 1. However, the effect of geometric imperfections were not apparent . This is due to the limitation of the linearized buckling analysis method for problems with highly nonlinear pre-buckling deformation. Using the corotational, updated Lagrangian formulation presented in this paper, the sensitivity of the structure to geometric imperfections can be directly observed from the load-deflection curves in Fig. 18, where the good agreement between the results obtained using different meshes indicates the convergence of the nonlinear solution. The final deformed configuration obtained using the finest mesh and the smallest geometric imperfection is displayed in Fig. 19.

Conclusion

A simple corotational, updated Lagrangian formulation has been presented for geometrically nonlinear analysis with arbitrarily large displacements and rotations. In this formulation, the element strain, stress and internal force vectors are updated using a corotational approach, whereas the tangent stiffness matrices are evaluated using a standard updated Lagrangian formulation. The use of a piece-wise linear strain-displacement relation permits the element strains to be in moderate range. The non-vectorial characteristic of large rotations was taken into account when updating total deformation and extracting the pure deformational rotations. The current nonlinear formulation is ideally suited for implementation in existing linear finite element programs and has been incorporated in eight most commonly used elements of VAST. In this paper, the effectiveness and robustness of the nonlinear capability in VAST have been demonstrated through a set of buckling analyses of geometrically imperfect, stiffened and unstiffened, cylindrical shells, for which the linearized buckling analysis is normally inadequate.

References

1. O.C. Zienkiewicz, *The Finite Element Method*, 3rd Edn. McGraw-Hill, London (1977).
2. K.J. Bathe, *Finite Element Procedures in Engineering Analysis*, Prentice-Hall, New Jersey (1982).
3. T. Belytschko and B.J. Hsieh, Nonlinear Transient Finite Element Analysis with Convected Coordinates. *Int. J. Numer. Meth. Engng.* **7**, 255-271 (1973).
4. G. Horrigmoe and P.G. Bergan, Nonlinear Analysis of Free-form Shells by Flat Finite Elements. *Comput. Meth. Appl. Mech. Engng.* **16**, 11-35 (1978).
5. S. Oral and A. Barut, A Shear-flexible Facet Shell Element for Large Deflection and Instability Analysis. *Comput. Meth. Appl. Mech. Engng.* **93**, 415-431 (1991).
6. K.M. Hsiao, Nonlinear Analysis of General Shell Structures by Flat Triangular Shell Element. *Comput. Struct.* **25**, 665-675 (1987).
7. K.M. Hsiao and H.C. Hung, Large-deflection Analysis of Shell Structure by Using Corotational Total lagrangian Formulation. *Comput. Meth. Appl. Mech. Engng.* **73**, 209-225 (1989).
8. C.C. Rankin and F.A. Brogan, An Element Independent Corotational Procedure for the Treatment of Large Rotations. *J. Press. Vessel Technol. ASME* **108**, 165-174 (1986).

9. L. Jiang and M.W. Chernuka, *Implementation of a Large Displacement Capability for VAST - Phase I.* Martec Technical Report TR-91-28, Martec Limited, Halifax, Nova Scotia (1991).
10. L. Jiang and M.W. Chernuka, *Implementation of a Large Displacement Capability for VAST - Phase II.* Martec Technical Report (under preparation), Martec Limited, Halifax, Nova Scotia (1993).
11. L. Jiang, M.W. Chernuka and N.G. Pegg, A Corotational Updated Lagrangian Formulation for Geometrically Nonlinear Finite Element Analysis. *Finite Elements in Analysis and Design* (in press) (1993).
12. L. Jiang and M.W. Chernuka, A Corotational Formulation for Geometrically Nonlinear Finite Element Analysis of Spatial Beams. *Tran. CSME* (submitted) (1993).
13. L. Jiang and M.W. Chernuka, A Simple Four-noded Corotational Shell Element for Arbitrarily Large Rotations. *Comput. Struct.* (submitted) (1993).
14. L. Jiang and M.W. Chernuka, An Eight-noded Stiffened Shell Element with Geometrically Nonlinear Capability. *Eng. Comput.* (under preparation) (1993).
15. J.H. Argyris, An Excursion into Large Rotations. *Comput. Meth. Appl. Mech. Engng.* **32**, 85-155 (1982).
16. *VAST User's Manual*, Version 6.0, Martec Limited, Halifax, Nova Scotia, Canada (1992).
17. J.L. Batoz and G. Dhatt, Incremental Displacement Algorithms for Nonlinear Problems. *Int. J. Numer. Meth. Engng.* **14**, 1262-1266 (1979).
18. M.A. Crisfield, A Fast Incremental/iterative Solution Procedure that Handles "Snap-through". *Comput. Struct.* **13**, 55-62 (1981).
19. E.N. Dvorkin and K.J. Bathe, A Continuum Mechanics Based Four-node Shell Element for General Nonlinear Analysis. *Eng. Comput.* **1**, 77-88 (1984).
20. K.J. Bathe and E.N. Dvorkin, A Formulation of General Shell Elements — the Use of Mixed Interpolation of Tensorial Components. *Int. J. Numer. Meth. Engng.* **22**, 697-722 (1986).
21. S.C. Burrell and M.W. Chernuka, *Submarine Pressure Hull Buckling Models*, Martec Technical Report TR-89/90-06G, Martec Limited, Halifax, Nova Scotia (1990).

Mesh	Geometric Imperfection			
	0%	10%	30%	50%
4x5	38.725	38.812	38.949	39.017
5x6	39.213	39.319	39.478	39.564
7x8	39.185	39.296	39.458	39.548

(Reference pressure load = 10^5 N/m^2)

Table 1 First critical load predicted by the linearized buckling analysis for different meshes and geometric imperfections.

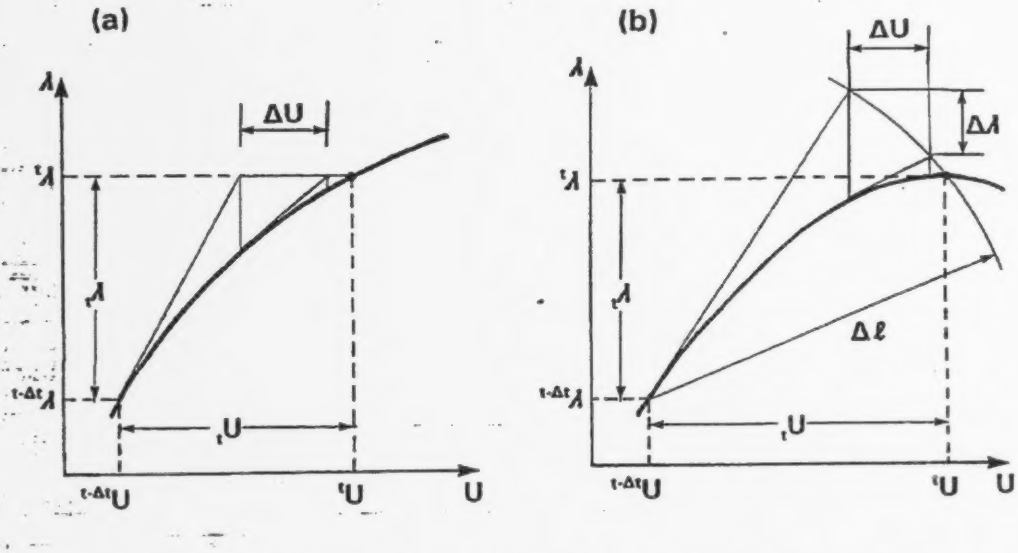
(a)
λ
ΔU
${}^{t}\lambda$
${}_{t}\lambda$
${}^{t-\Delta t}\lambda$
${}_{t}U$
${}^{t-\Delta t}U$
${}^{t}U$
U
(b)
ΔU
λ
$\Delta\lambda$
${}^{t}\lambda$
${}_{t}\lambda$
$\Delta \ell$
${}^{t-\Delta t}\lambda$
${}_{t}U$
${}^{t-\Delta t}U$
${}^{t}U$
U

Fig. 1 Incremental-iterative solution procedure for nonlinear finite element equations.

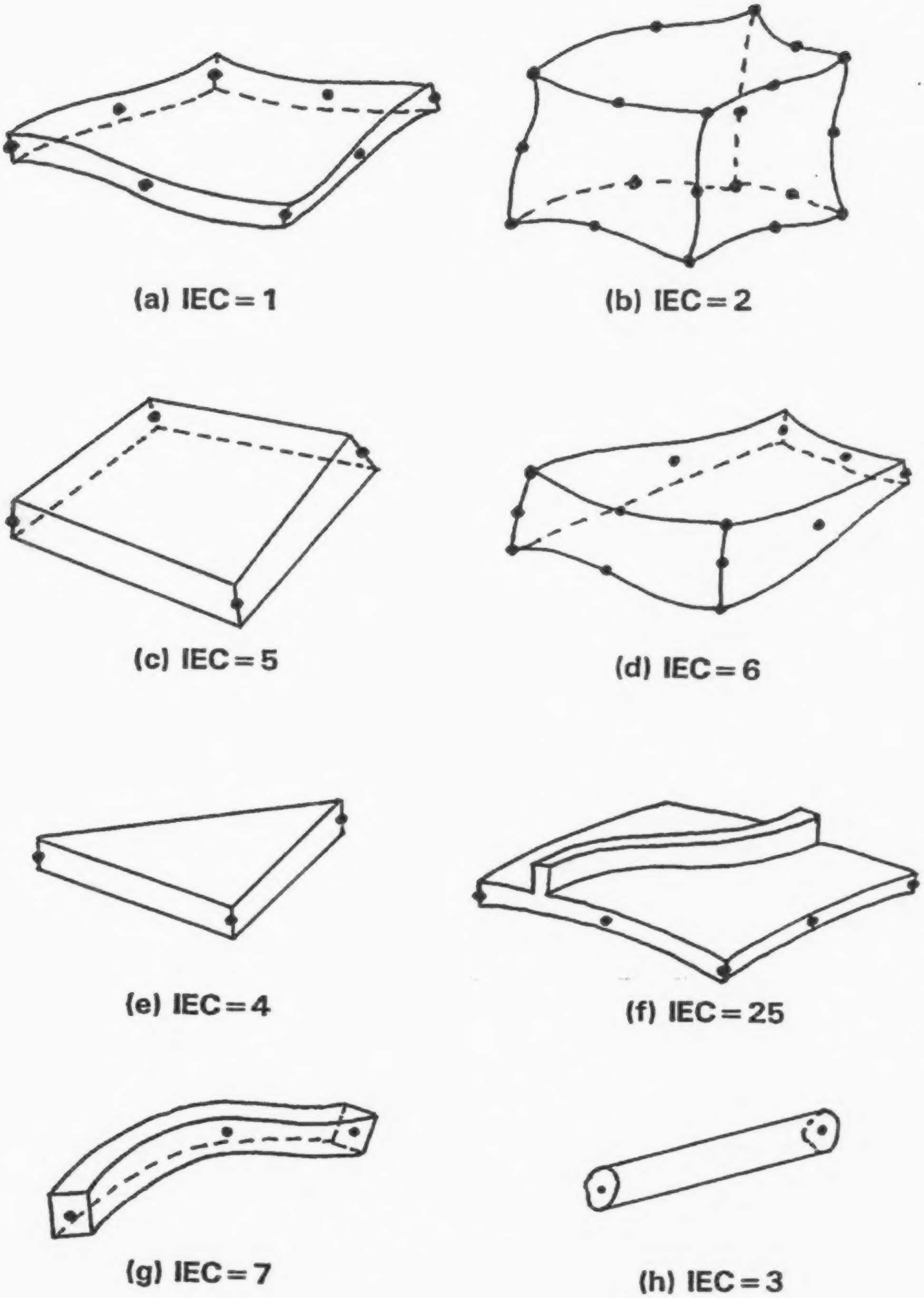

(a) IEC = 1

(b) IEC = 2

(c) IEC = 5

(d) IEC = 6

(e) IEC = 4

(f) IEC = 25

(g) IEC = 7

(h) IEC = 3

Fig. 2 Nonlinear element library of VAST 7.0.

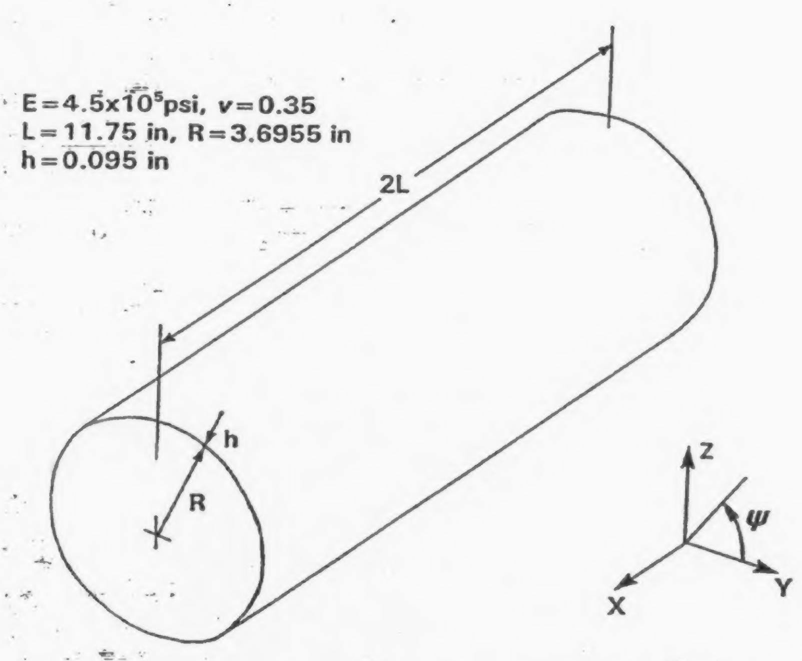
E=4.5x10⁵psi, v=0.35
L=11.75 in, R=3.6955 in
h=0.095 in
2L
h
R
Z
ψ
Y
X

Fig. 3 Problem geometry and material properties of a diaphragmed cylindrical shell.

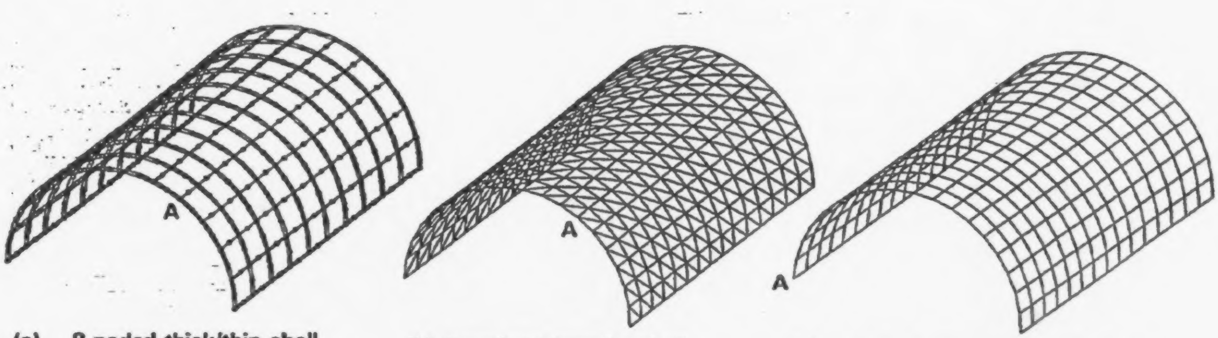

(a) 8-noded thick/thin shell **(b) 3-noded triangular shell** **(c) 4-noded quadrilateral shell**

Fig. 4 Finite element models for buckling analysis of the cylindrical shell.

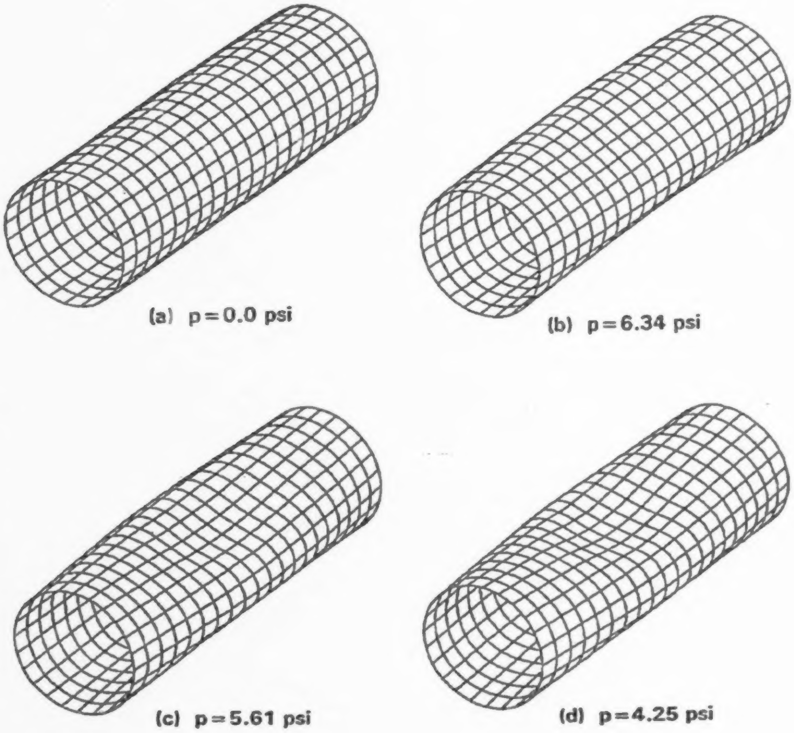

(a) p=0.0 psi

(b) p=6.34 psi

(c) p=5.61 psi

(d) p=4.25 psi

Fig. 5 Deformed configurations of the cylindrical shell obtained using 8-noded shell elements.

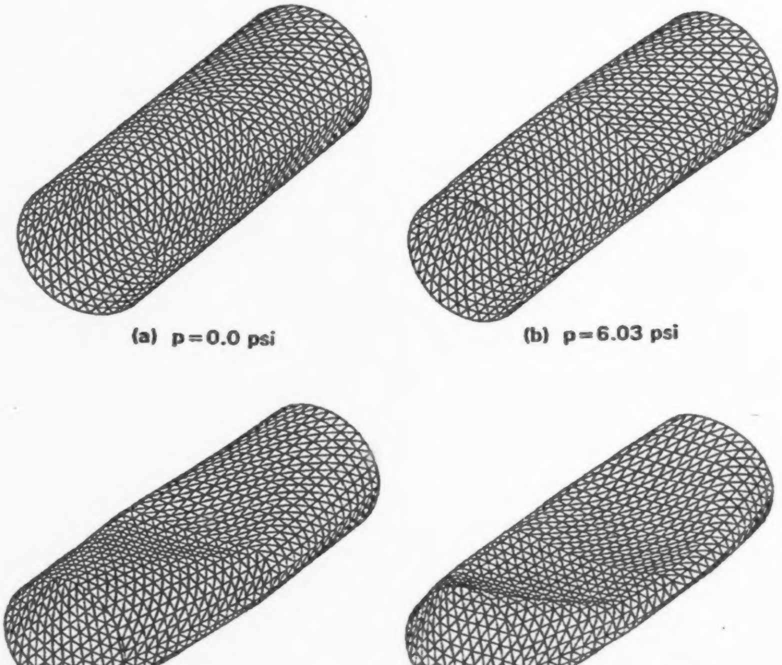

(a) p=0.0 psi

(b) p=6.03 psi

(c) p=2.83 psi

(d) p=7.24 psi

Fig. 6 Deformed configurations of the cylindrical shell obtained using 3-noded shell elements.

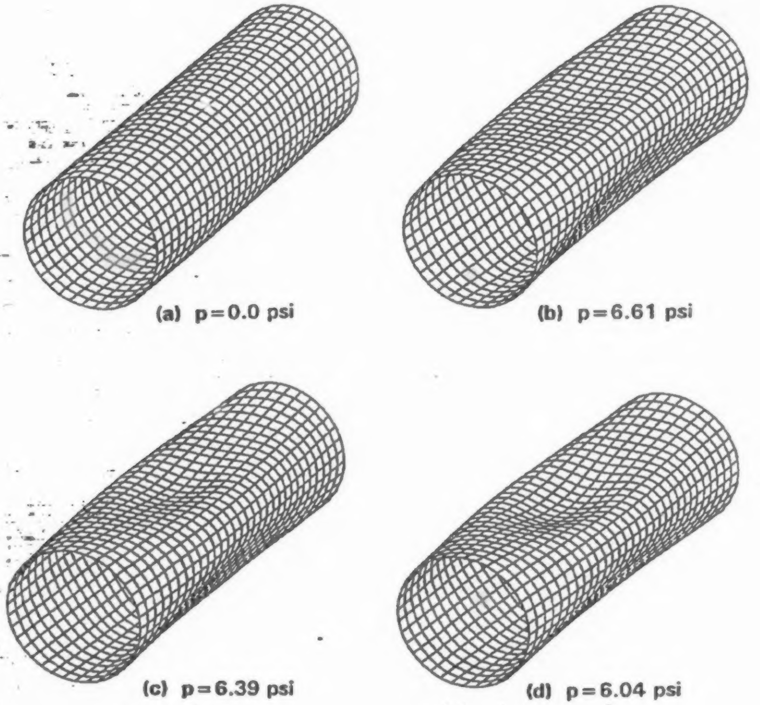
(a) p=0.0 psi
(b) p=6.61 psi
(c) p=6.39 psi
(d) p=6.04 psi

Fig. 7 Deformed configurations of the cylindrical shell obtained using 4-noded shell elements.

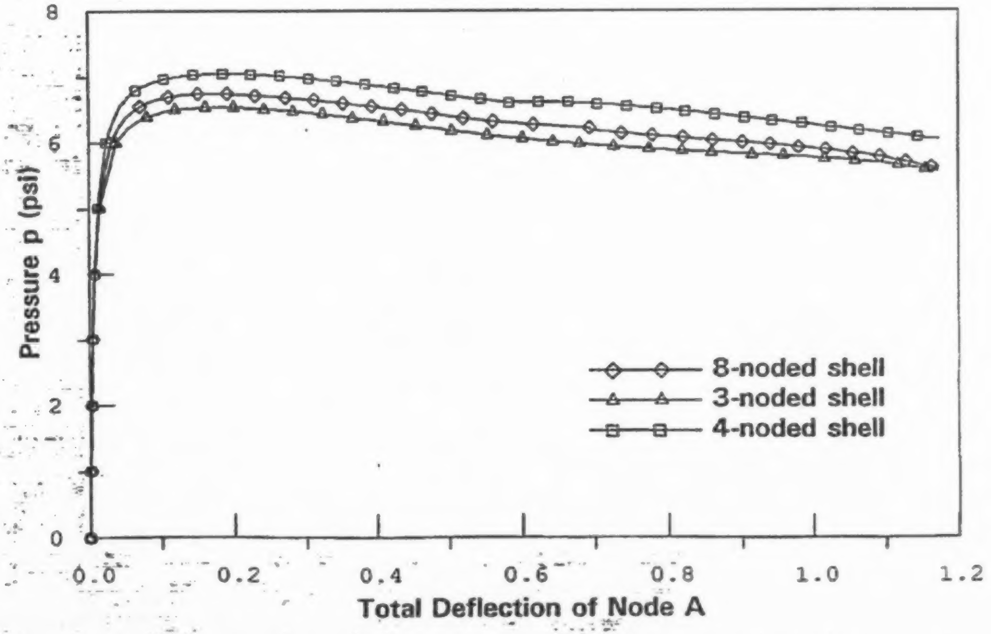

Fig. 8 Comparison of load-deflection curves obtained using different shell element models.

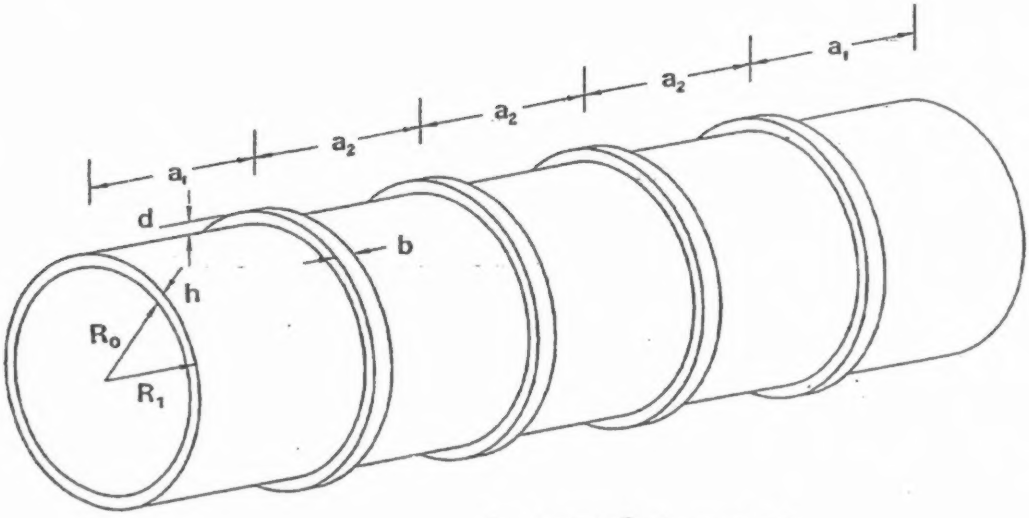

$E=4.5\times10^{5}$psi, $\nu=0.35$
$a_1=5.0$ in, $a_2=4.5$ in, $R_0=3.648$ in

For overall buckling model:

$R_1=3.743$ in, $h=0.095$ in
$b=d=0.1$ in

For interframe buckling model:

$R_1=3.7$ in, $h=0.052$ in
$b=0.25$ in, $d=0.4$ in

Fig. 9 Problem geometry and material properties of diaphragmed stiffened cylindrical shells.

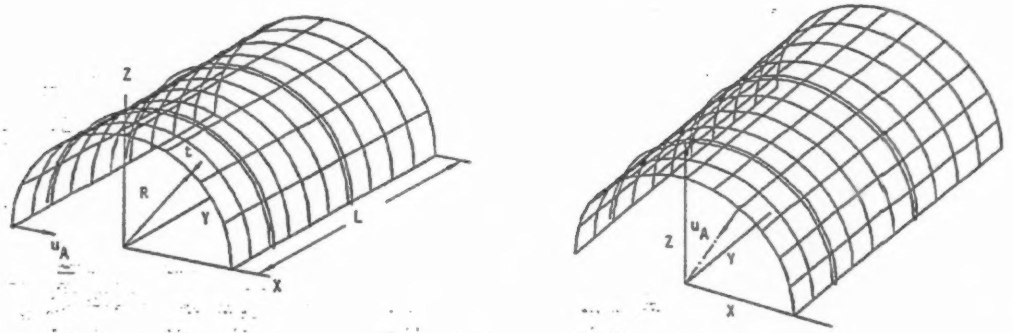

(a) 8x10 mesh **(b) 12x10 mesh**

Fig.10 Finite element meshes of buckling analysis of the overall buckling model.

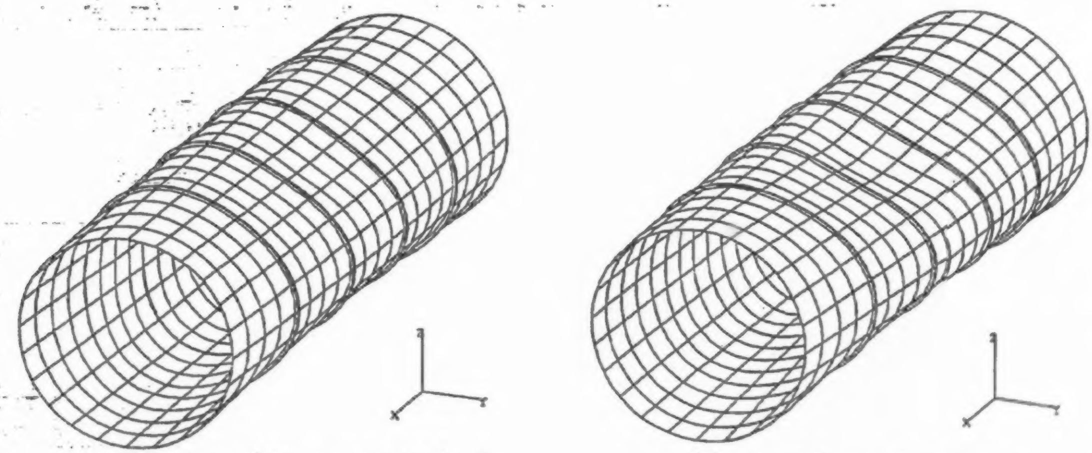

(a) p=8.98 psi **(b) p=8.14 psi**

Fig.11 Deformed configurations of the overall buckling model obtained using the finer mesh.

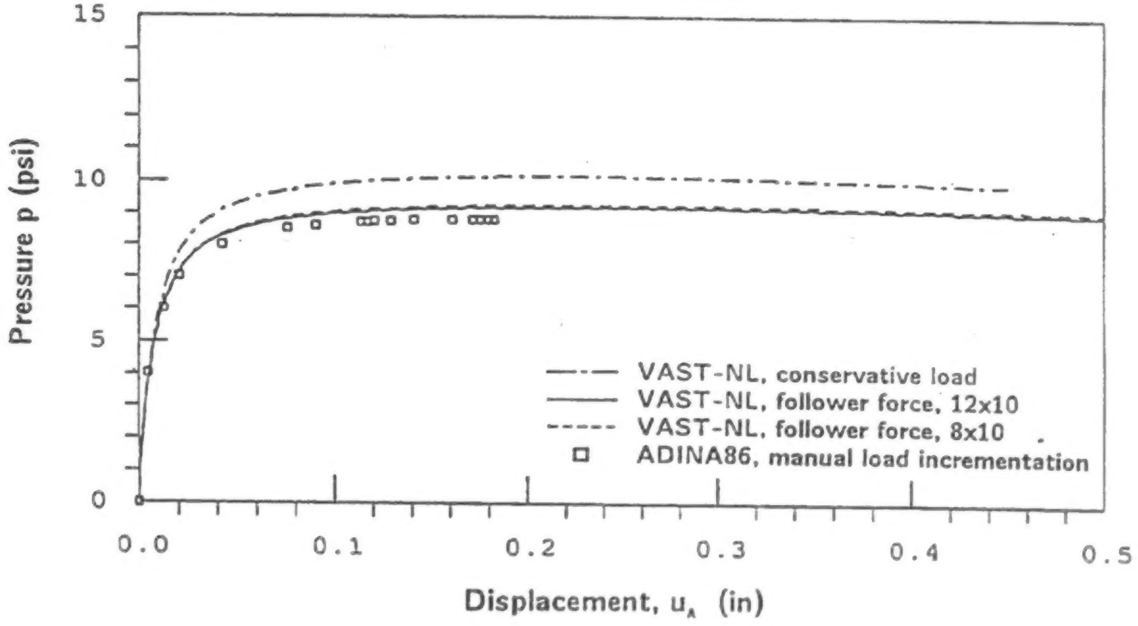

Fig.12 Comparison of load-deflection curves obtained by VAST 7.0 and ADINA for the overall bucking model.

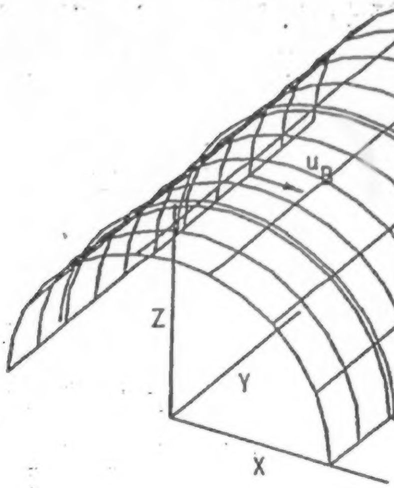

Fig. 13 Finite element mesh for the interframe buckling model.

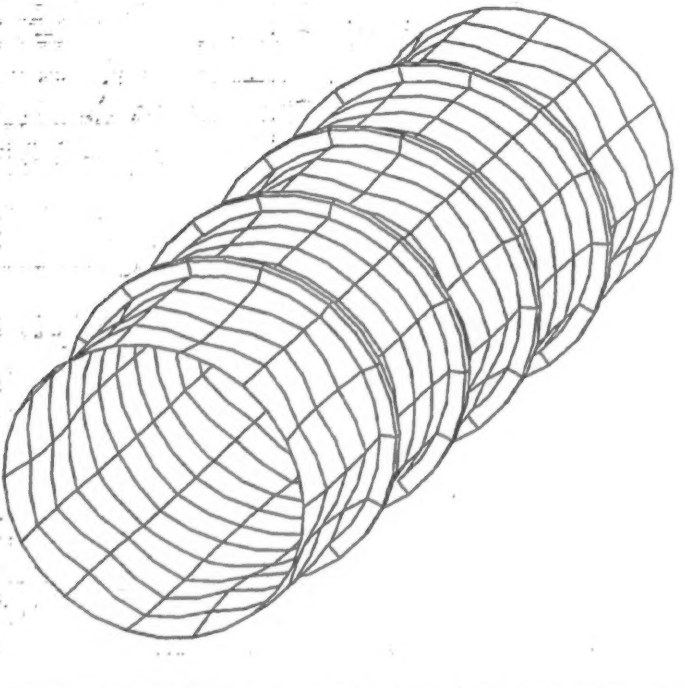

Fig. 14 Final deformed configuration (p=10.44 psi) of the interframe buckling model.

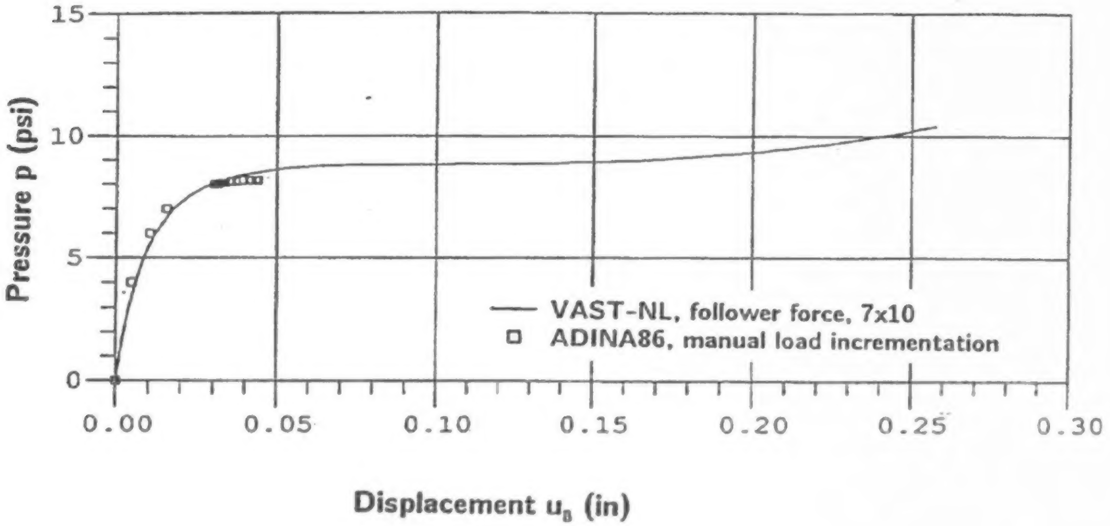

Fig.15 Comparison of load-deflection curves obtained by VAST 7.0 and ADINA for the interframe bucking model.

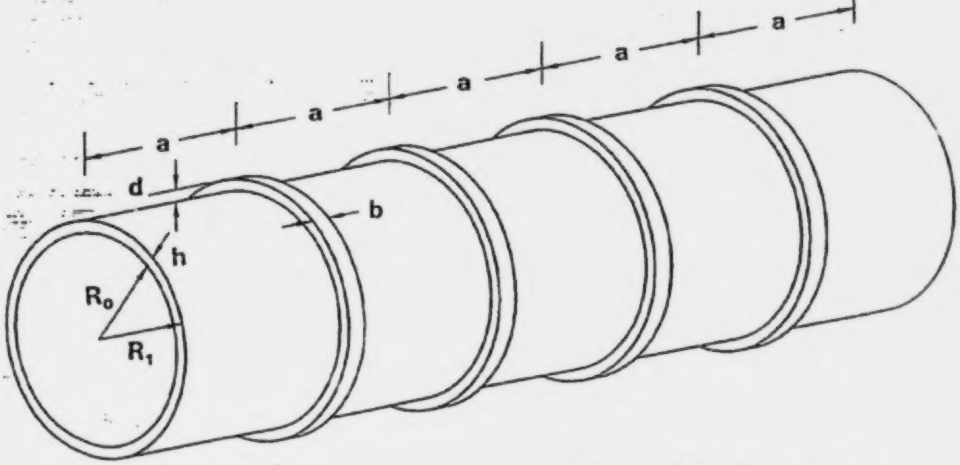

$E=2.07\times10^{11}N/m^2$, $\nu=0.3$
$R_o=0.495m$, $R_1=0.505m$
$h=0.01m$, $b=d=0.01m$

Fig.16 Problem geometry and material properties of a stiffened cylindrical shell used for investigating structure's sensitivity to geometric imperfections.

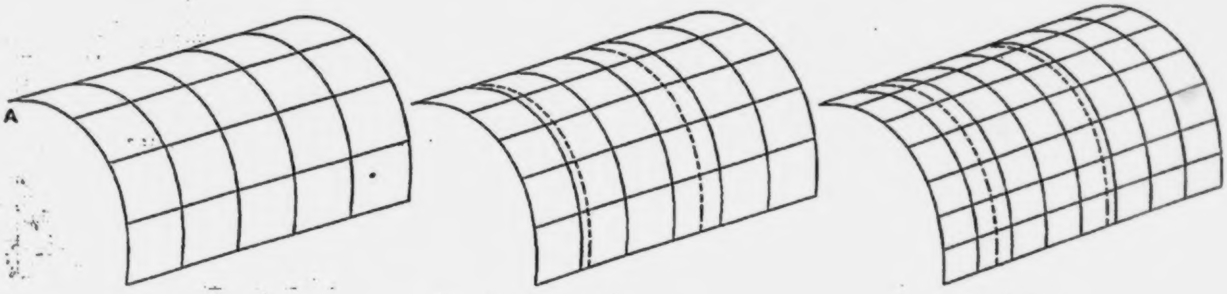

(a) (b) (c)

Fig.17 Finite element models of the stiffened shell elements. (a) 4x5, (b) 5x6, (c) 7x8.

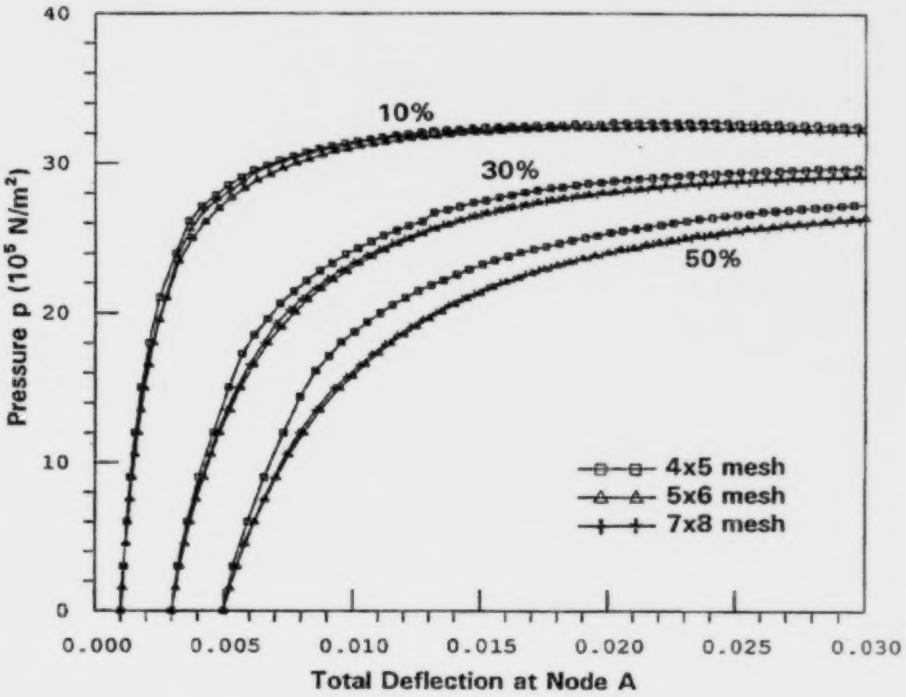

Fig.18 Comparison of load-deflection curves obtained by using different finite element meshes and amount of geometric imperfections.

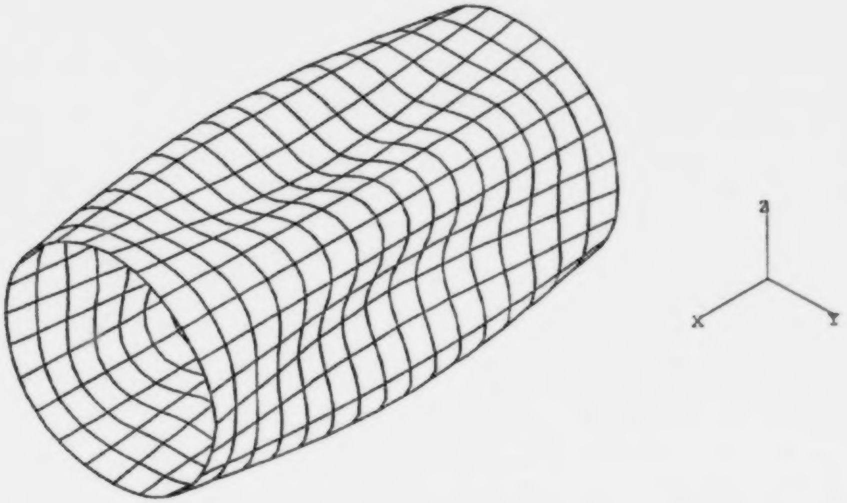

Fig.19 Final deformed configuration ($p=3.21x10^6$ N/m^2) obtained by using the finest mesh and 10 percent of geometric imperfection.

#516323 ⑱

Four PC-Based Fracture Mechanics Packages Reviewed

by

G. V. Gorveatte and J. F. Porter

Defence Research Establishment Atlantic, Dockyard Laboratory
FMO Halifax, Halifax, Nova Scotia, Canada, B3K 2X0

ABSTRACT

The proliferation of powerful personal computing systems has made viable the creation of software programs to determine the fracture mechanics characteristics of engineering materials in various configurations, replacing bulky and time consuming handbooks. This report compares four such programs; NASCRAC, pc-CRACK, Fracture Mechanics and Damage Tolerance Analysis Software (FM&DT) and PC-Failure Assessment Diagram (PC-FAD).

A brief description of each package and a review of their respective features is presented. Each package was rated in terms of their various capabilities and functionality. Comparisons were made based on items such as number and types of geometries, materials libraries, analysis methods, fatigue crack growth capabilities, user interface, user manuals and system requirements. Several representative test problems were attempted with each code to verify accuracy and to highlight limitations.

The code NASCRAC proved superior in many categories with pc-CRACK as a close second. FM&DT suffered from a very poor user interface and PC-FAD was limited in its functionality.

1.0 INTRODUCTION

When studying fracture mechanics an engineer has at his disposal many tools, the premier one being fracture mechanics handbooks. These large texts contain a large quantity of data, such as crack growth rates for various loadings and geometries or material properties, and stress intensity factors for different geometries. This data may be represented in either tabular or plot form. Due to the proliferation of desktop computers, this information has been incorporated into a variety of software packages. Four such computerized packages are evaluated here:

NASCRAC (NASA CRack Analysis Code), by Failure Analysis Associates [1]
PC-FAD (PC-Failure Assessment Diagram), by Babcock & Wilcox [2]
Fracture Mechanics and Damage Tolerance Analysis Software (to be referred to as **F.M. & D.T.**), by FractuREsearch [3]
pc-CRACK, by Structural Integrity Associates [4]

These packages are evaluated and compared with respect to their capabilities and general ease of use. Their capabilities were demonstrated by running several of the respective sample problems included with the software, and by running a common set of test problems on each package.

2.0 SOFTWARE FEATURES

Three of the four packages; NASCRAC, pc-CRACK, and F.M. & D.T. are all similar in scope. These are all multi-purpose packages that allow the user to do a comprehensive fracture mechanics analysis. They fill the role of the handbooks most commonly used in today`s engineering office. PC-FAD is a single purpose, failure assessment diagram package. Since PC-FAD lacks the comprehensive abilities of the other packages it cannot be directly compared with the other software.

The comparison consists of separate sections for some features available to the user. For example the number and types of geometries available in each package were looked at. Other points of interest were the types of analysis each package was able to perform, the growth laws it used to perform calculations and the loading forms possible.

2.1 Available Geometries

Flexibility is very important to a software package that is to meet the requirements of a user that may be studying various types of problems. This flexibility is based partially on the number of geometries present and whether they are sufficient for his purpose. If they are not suitable it is important that the software is able to accept input for user definable geometries.

Each package has a set of crack geometries that it uses for analysis. pc-CRACK has two sets of geometric models. There are nineteen geometries available for linear elastic fracture mechanics (LEFM) analysis, and nine geometries for creep and elastic plastic fracture mechanics (EPFM) analysis. NASCRAC has thirty three geometries, while PC-FAD has fifteen and F.M. & D.T. has twelve. Table 1 shows the geometries available in each package. NASCRAC and pc-CRACK also allow the user to input 'a' (crack size) versus 'K' (stress intensity factor) tables. This allows the user a great amount of flexibility in the problems which may be analyzed. F.M. & D.T. allow the user to include a table of Beta factors (stress intensity correction factors) instead of selecting a geometry. This Beta table may be generated in a separate module (GEOFAC) or may be created by the user. PC-FAD does not allow the user to input his own data.

2.2 Material Libraries

The inclusion of materials data in a software package is an option which, while not essential, is very beneficial, as it frees the user from the time consuming task of looking up the required data from a text. NASCRAC and F.M. &D.T. contain materials data libraries, while pc-CRACK and PC-FAD do not.

NASCRAC's data comes in ten separate data libraries: six aluminum, stainless steel, carbon and alloy steel, titanium, and nickel alloys. Each library contains between one and ten materials records, the constants for the Modified Forman Equation and K_{IC} (critical stress intensity factor). When a material is selected, its data is transferred to the materials' menu in the program where the user may edit it. NASCRAC will only select the data it needs to perform the calculation. The user may input all the data available, then run the model allowing NASCRAC to do the selection of data.

F.M. &D.T.'s data is available through a separate module (MATDAT), but unlike NASCRAC it does not output the raw data. Instead it uses its libraries to output a table (or plot) of ΔK versas $\frac{da}{dN}$ (crack growth rate). This setup is cumbersome since the user must exit MATDAT and then start the module in which the data is to be employed. There are seven libraries: structural steel, austenitic and precipitation hardened stainless steel, general steel, high strength steel, aluminum alloys, titanium alloys, and nickel alloys. Each of these libraries contains individual metals and the instructions needed to create the table (or plot).

Similar in both packages is the ability to use this data in whatever calculation the user might be executing, or the ability to input his own data from another source. The list of materials contained in the NASCRAC and F.M. & D.T. libraries are shown in Table 2.

2.3 Fatigue Crack Growth Analysis

Fatigue crack growth laws are a basic element of fracture mechanics analysis. All the software packages reviewed have options for fatigue crack growth analysis, except PC-FAD. They model the relationship between the rate of crack growth, $\frac{da}{dN}$, and the change in the stress intensity factor, ΔK. Some of the more common crack laws are:

PARIS: $\frac{da}{dN} = C(\Delta K)^m$ where $\Delta K = K_{max} - K_{min}$

C and m are material constants

WALKER: $\frac{da}{dN} = C\left(\frac{\Delta K}{(1-R)^{1-m}}\right)^n$ where $\Delta K = K_{max} - K_{min}$

C, n, and m are material constants

$R = \frac{K_{min}}{K_{max}}$

MODIFIED FORMAN: $\frac{da}{dN} = C(1-R)^m \Delta K^n \frac{\left(\Delta K - (1 - C_O R)^d \Delta K_O\right)^p}{((1-R)K_c - \Delta K)^q}$

where $\Delta K = K_{max} - K_{min}$

C, n, m,p,q,d, and C_0 are material constants

$R = \frac{K_{min}}{K_{max}}$

$\Delta K_O = \Delta K$ threshold

K_c is the critical stress intensity factor

All the software packages except PC-FAD have menu selections where the user may choose the fatigue crack growth law to be used. Pc-CRACK has seven selections, F.M. & D.T. has five and NASCRAC has six. F.M. & D.T. has four laws: Paris, Walker, Forman, and Threshold. It also has a tabular input so the user may use custom data for rate of change in stress intensity. pc-CRACK uses the Paris, Walker, Bilinear, Modified Forman, Collipriest, ASME Section XI Bilinear, and Hyperbolic correction fatigue laws. NASCRAC uses the following laws: Paris, Walker, Modified Forman, Collipriest, and Hop-Rau. NASCRAC also permits the option of inputting tabulated data as an alternative to using a predefined crack growth law.

Each package has a menu or module for performing fatigue crack growth analysis and its specific options. An important option in a fatigue crack analysis is the ability to model efficiently the load or stress applied to the test specimen. This means being able to handle random, semi-random, and cyclic (constant) loads. NASCRAC, pc-CRACK, and F.M. & D.T. all have this attribute. Another important feature is the ability to include the effects of peak loads on the growth rate, or retardation. Only NASCRAC and F.M. & D.T. can manage retardation models.

2.4 Stress Corrosion Crack Growth

Stress corrosion crack growth is similar to fatigue crack analysis, but it is the relation between time, 'K', 'a', rate $\frac{da}{dt}$ and the interaction of the material with its environment. Two of the four packages have specific menu or module options related to this.

F.M. & D.T. and pc-CRACK both have specific options affiliated to stress corrosion crack growth. F.M. & D.T. is able to input variable or constant amplitude stresses, while pc-CRACK only needs the maximum applied stress intensity factor, K_{max}. While NASCRAC does not have a specific menu or module for stress corrosion crack growth, it can handle such analysis through its fatigue crack growth option. This involves substituting the rate $\frac{da}{dN}$ and load blocks with the rate $\frac{da}{dt}$ and time.

2.5 Additional Features

Creep analysis is the study of materials at elevated temperatures and under static stress. Creep analysis is only available in pc-CRACK. Only nine predefined geometries are available for this analysis. NASCRAC allows the user to do creep life calculations by using creep crack growth laws.

F.M. & D.T. allows the user to study the probability of crack detection based on such things as crack location and inspection method.

Some other features and outputs are available to the user of these software packages; 'a' versus 'K' plots are available in NASCRAC and pc-CRACK, while only the former offers 'a' versus 'J' output. However, pc-CRACK and NASCRAC both do a number of other J calculations . NASCRAC also offers Crack Opening Area (COA) and life after proof test calculations. All except PC-FAD have options for critical crack size calculations. Only PC-FAD calculates a safety factor for the given data.

2.6 Documentation

With any complicated software, complete documentation is very important. NASCRAC and pc-CRACK both have excellent manuals, full of examples, description and theory. The NASCRAC manual has the bulk of its theory in a separate section, whereas pc-CRACK and F.M. & D.T. have theory combined with the instructions. Unlike the pc-CRACK manual, the F.M. & D.T. documentation is hard to read. The PC-FAD manual provides a good description of the program's operation, but very little theory.

3.0 OPERATION AND EASE OF USE

Each piece of software studied has a menu driven interface, while NASCRAC also gives the user the ability to run it in batch mode, with no user input. All the software support dot matrix printers and plotters, but unfortunately none support laser printers. NASCRAC, pc-CRACK, and PC-FAD give the user the ability to view their plots on the CRT of the computer. All output their plots to a plotter. None of the packages allow the user to output the plots to a printer except through a screen dump, which only applies to the software that displayed the plots on the CRT. pc-CRACK gives the user a file management routine, allowing him to perform various tasks on the stored files. None of the packages allow for mixed units, except where their internal data is in a different unit (pc-CRACK). All but F.M. & D.T. allow the user to save and then restart a session. NASCRAC has an on-line help feature, that the other software lacks. All the software can save files containing their plots and output the data as an ASCII file, allowing the user to plot the data on a separate software package. pc-CRACK has black and white menus, while NASCRAC, F.M. & D.T. and PC-FAD have color menus.

Installation is easy for all; however, NASCRAC uses files backed up on disk, and restores them to the harddrive, which is a cumbersome way to store the software. None of the software except NASCRAC has copy protected software. NASCRAC uses a hardware form of copy protection that protrudes from the parallel port of the computer.

While each program is straightforward and easy to use, some are better than others. NASCRAC, PC-FAD and pc-CRACK are simple in their set ups. Their menu systems allow for the sequencial input of data and finally the output of the answer. Their menu systems lead the user through, with very little reference to the manual. F.M. & D.T. is also menu driven, but the fact that the user has to exit each module and start up another is cumbersome, and impedes the flow of the problem. This is a poor feature, especially for the novice user, as he finds himself constantly referring to the manual to see what each module does. For the user this switching from one program to another becomes very inconvenient.

4.0 SAMPLE PROBLEMS

4.1 Find K For Specific Data

For a flat plate of width W equal to 101.6 mm (4.0 in), containing a centrally positioned internal crack of length 2a equal to 25.4 mm (1.0 in) and under tensile loading, determine the minimum plane strain fracture toughness necessary to ensure fracture will not occur for a design stress of 60000 psi (415 MPa). An exact solution was derived using the following equation [5].

$$Y=\left(\frac{W}{\pi a}\tan\frac{\pi a}{W}\right)^{\frac{1}{2}}$$

The question was also attempted using each software package. pc-CRACK and NASCRAC solved the problem simply and quickly. F.M. & D.T. could not perform the required task with the data given; however, it could calculate Beta (BETA = Y in this example) and this was used to calculate K. PC-FAD could not perform this task at all. The results are as follows:

exact solution	K=85.13
pc-CRACK	K=86.12

NASCRAC	K=86.25
F.M. & D.T.	K=86.24

4.2 Compact Tension Specimen

This example deals with the fatigue crack growth of a compact tension specimen. The specimen was 2.5 in (63.5 mm) wide, 1.25 in (31.75 mm) thick, and had an initial crack size of 0.625 in (15.875 mm). The cyclic load was between zero and 10 ksi (0→68.94 MPa). The specimen was 7075-T6 AL, L-T, 75F. Since PC-FAD doesn't output equivalent data, only NASCRAC, F.M. & D.T. and pc-CRACK were used for this example. The modified Forman equation was used for the NASCRAC and pc-CRACK analysis, with the constants for both coming from the NASCRAC materials library. In F.M. & D.T., since there was no compact specimen geometry in the LICAFF module (used for unretarded fatigue crack growth), a table of crack size and Beta was calculated using the GEOFAC module. Also, since F.M. & D.T. has a material data library, it was used to create a table of growth rates versus the change in stress intensity factors, which was subsequently used in the growth analysis. A summary of the Modified Forman constants is included in Table 3. For the initial crack size, the results for NASCRAC and pc-CRACK are very similar:

pc-CRACK	NASCRAC	F.M. & D.T.
a=0.6254	a=0.6250	R-RATIO=0.1
ΔK=24.92	ΔK=24.57	ΔK=24
da/dN=2.2e-4	da/dN=2.057e-4	da/dN=1.9726e-4

Plots of crack size, a versus growth rate, da/dN may be found in Figure 1 and Figure 2 for pc-CRACK and NASCRAC respectively. These two programs also output K_{max}, K_{min}, and all three can output blocks until failure. Plots of crack length versus K are included in Figures 3 and 4, while plots of K versus da/dN for the three packages may be found in Figures 5 through 7. For interest a plot from PC-FAD for the same data may be found in Figure 8.

4.3 Center Cracked Panel

In this example a plot of stress intensity factor versus crack size is developed so that it can be directly compared with a handbook solution [6]. While F.M. & D.T. was the only package that could output the data in the same fashion as the handbook, with a little manipulation the output from NASCRAC and pc-CRACK could be plotted in the same manner. The handbook represented its stress intensity as a ratio of K_I/K_o and its crack size as the ratio of a/b where a is the half crack length and b is the half panel width. The input width was taken as unity in this problem. K_o is defined as $\sigma\sqrt{\pi a}$.

When the results from the software (Figure 9), and the handbook (Figure 10) are compared, it can be seen that NASCRAC and pc-CRACK are in excellent agreement with the ∞ line, which is the expected result. The results from F.M. & D.T. are less satisfying, however, as they quickly deviate form the handbook`s curve.

4.4 Circumferential Crack in a Cylinder

The purpose of this example is to compare the solutions of the packages using a circumferentially cracked cylinder in tension. Again, a plot of the stress intensity ratio, K_I/K_o is used, but this time its horizontal axis is crack size 'a'. K_o is defined as $\sigma\sqrt{\pi a}$. NASCRAC and pc-CRACK both had resultant curves that were smooth, although they were separated by an almost uniform distance. F.M. & D.T.'s results agreed with the higher results from NASCRAC for half the plot, then agreed with the lower results from pc-CRACK for the remainder of the plot.

5.0 CONCLUSION

Four computerized handbooks containing a variety of features were compared based on capabilities and user friendliness. NASCRAC, pc-CRACK, and F.M. & D.T. are similar in that they are multifunction fracture mechanics analysis tools. PC-FAD is a single purpose analysis tool. It gives the user access to a quick safety reference, based on fracture mechanics. A summary of the various features and characteristics are presented in Table 4. The software package NASCRAC appears to be the most comprehensive, flexible and user friendly.

REFERENCES

1. Failure Analysis Associates, Engineering and Scientific Services, "NASCRAC; NASA CRack Analysis Code Version 2.2", 2225 East Bayshore Road, P.O. Box 51470, Palo Alto, California 94303.

2. Babcock & Wilcox, Alliance Research Center, "PC-Failure Assessment Diagram Revision 4", Alliance, Ohio 44601, April 1990

3. FractuREsearch, "Fracture Mechanics and Damage Tolerance Analysis Software 2nd Edition", 9049 Cupstone Drive, Galena, Ohio, 43021, June 1989

4. Structural Integrity Associates, "pc-CRACK Version 2.0", 3150 Almaden Expressway, Suite 226, San Jose, California 95118.

5. William D. Callister, Jr., Materials Science and Engineering: An Introduction, John Wiley & Sons, Toronto, Ontario, 1991.

6. D.P. Rooke and D.J. Cartwright, Compendium of Stress Intensity Factors, Procurement Executive, Ministry of Defence, Her Majesty`s Stationary Office, London, 1976.

Geometry	F.M. &D.T.	pc-CRACK	PC-FAD	NASCRAC
compact tension	YES, EPFM	YES	YES	YES
disk-shaped compact tension	NO	NO	NO	YES
arc-shaped compact tension	NO	NO	NO	YES
3 point bend	YES, EPFM	NO	NO	YES
center cracked finite plate	YES	YES	YES	YES
cracked infinite plate	NO, USE ABOVE	NO, USE ABOVE	NO, USE ABOVE	YES
single-edge cracked plate	YES	YES	YES	YES
double-edge cracked plate	NO	NO	NO	YES
axial cracked cylinder (ID)	YES	YES	YES	YES
edge cracked solid disk	NO	NO	NO	YES
axial cracked cylinder (OD)	NO	NO	NO	YES
plate through cracked from a hole	YES	INFINITE PLATE	NO	YES
through crack from a hole in a lug	NO	NO	NO	YES
through cracked sphere	NO	NO	NO	YES
axial through cracked cylinder	NO	NO	NO	YES
through cracked cylinder	YES	NO	YES	YES
ID cracked cylinder (circumferential)	YES	YES	YES	YES
OD cracked cylinder (solid) (circumferential)	NO	NO	NO	YES
OD cracked cylinder (circumferential)	NO	NO	NO	YES
edge cracked circular bar	NO	NO	NO	YES
subsurface elliptical cracked plate	NO	YES	NO	YES & USER DEFINED
quarter elliptical cracked plate at a hole	NO	NO		YES
quarter elliptical cracked plate at a lug	NO	NO	NO	YES
corner, quarter elliptical cracked plate	NO	NO, BUT CIRCULAR	NO	YES + USER DEFINED
semi-elliptical surface cracked plate	NO	YES, AND CIRCULAR	NO	YES
semi-elliptical circumferential surface cracked cylinder	NO	NO	NO	YES
semi-elliptical axial surface cracked cylinder	NO	YES	YES	YES
semi-elliptical surface cracked sphere	NO	NO	NO	YES
continuous surface crack in half space	NO	YES	NO	NO
nozzle corner crack	NO	YES	NO	NO
corner crack at hole	YES	NO, USE ABOVE	NO	NO, USE ABOVE
two corner cracks at hole	YES	NO	NO	NO
two through cracks at hole	YES	NO	NO	NO

Table 1. Geometries Available

NASCRAC	F.M. & D.T.
2024-T3 AL, L-T & T-L, 75F	AL 2024 T3 SHEET, LT TL, LAB AIR ,70F
2024-T351 AL, L-T & T-L, 75F	AL 2024 T3 SHEET, LT TL, WET AIR, 70F
2024-T351 AL, L-T & T-L, 300-400F	AL 2024 T3 SHEET, LT TL, SUMP TANK, 70F
2024-T62 AL, L-T & T-L, 75F	AL 2024 T3 SHEET, LT TL, 3.5% NaCl, 70F
2024-T81 AL, L-T & T-L, 75F	AL 2024 T3 SHEET, LT TL, AIR, -65F
2024-T81 AL, L-T & T-L, 350F	AL 2024 T3 SHEET, LT TL, JET FUEL, 70F
2024-T851 AL, L-T, 75F	AL 2024 T351 SHEET, LT TL, LAB AIR, 70F
2024-T851 AL, T-L, 75F	AL 2024 T351 SHEET, LT TL, WET AIR, 70F
2024-T851 AL, T-L, 350F	AL 2024 T351 SHEET, LT TL, SUMP TANK, 70F
2024-T851 AL, L-T & T-L, 75F	AL 2024 T351 SHEET, LT TL, 3.5% NaCl, 70F
2124-T851 AL, L-T, 75F	AL 2024 T351 SHEET, LT TL, AIR, -65F
2124-T851 AL, T-L, 75F	AL 2024 T351 SHEET, LT TL, JET FUEL, 70F
2124-T851 AL, L-T, 350F	AL 2024 T3511 EXTRUSION, LT, LAB AIR, 70F
2124-T851 AL, S-T, 75F	AL 2024 T3511 EXTRUSION, LT, WET AIR, 70F
2124-T851 AL, T-L, -150 TO -200F	AL 2024 T3511 EXTRUSION, LT, SUMP TANK, 70F
2219-T62 AL, L-T &T-L, 75F	AL 2024 T3511 EXTRUSION, LT, 3.5% NaCl, 70F
2219-T62 AL, L-T &T-L, -320F	AL 7049 T73
2219-T62 AL, L-T &T-L, 350F	AL 7049 T7352, HAND
2219-T851 AL, L-T &T-L, 75F	AL 7049 T7352, DIE
2219-T87 AL, L-T, -320F	AL 7050 T651
2219-T87 AL, T-L, -320F	AL 7050 T7351
2219-T87 AL, L-T, 75F	AL 7050 T736
2219-T87 AL, L-T, 300 TO 350F	AL 7050 T76
2219-T87 AL, T-L, 300 TO 350F	AL 7075 T6
2219-T87 AL GTA WELD, AS WELDED, 75F	AL 7075 T7351
2219-T87 AL GTA WELD, AS WELDED, -320F	AL 7075 T7352
2219-T87 AL EB WELD, AS WELDED, 75F	AL 7075 T76
6016-6T AL, L-T & T-L, 75F	AL 7175
6061-T651 AL, L-T & T-L, 75F	AL 7178
6061-T651 AL, L-T, 300F	AL 7475 T6XXX
6061-T651 AL, T-L, 300F	AL 7474 T7XXX
7075-T6 AL, L-T, 75F	AL 357 T6, CHILLED, LT TL, 70F, LAB AIR
7075-T651 AL, L-T, 75F	AL 357 T6, CHILLED, LT TL, 70F, WET AIR
7075-T651 AL, S-T, 75F	AL 357 T6, CHILLED, LT TL, 70F, SUMP TANK
7075-T73 AL, L-T, LHA & HHA, 75F	AL 357 T6, CHILLED, LT TL, 70F, 3.5% NaCl
7075-T7351 AL, L-T,LHA & HHA, 75F	AL 357 T6, UNCHILLED, LT TL, 70F, LAB AIR
7075-T73 AL, T-L, LHA & HHA, 75F, HHA & LAB AIR	AL 357 T6, UNCHILLED, LT TL, 70F, 3.5% NaCl
7075-T7351 AL, T-L, LHA &HHA, 75F, HHA & LAB AIR	AL 357 T6, UNCHILLED, LT TL, 70F, WET AIR
7075-T7651 AL, T-L, 75F	AL 357 T6, UNCHILLED, LT TL, 70F, SUMP TANK
A356-T60 CAST AL, 75F	A-36, ROOM TEMP. (HENCE DENOTED AS RT), AIR
INCO 718 STA, L-T & T-L,75F	A-2128B OR A517F,RT,AIR
INCO 718 STA, L-T, 800F, <1HZ	A-2128B OR A517F, 500F, AIR
INCO 718 STA, L-T, 1000F, <1HZ	A-2128B OR A517F, 650F, AIR
INCO 718 GTA WELD, STA, 75F	A-2128B OR A517F, 800F, AIR
INCO 718 GTA WELD, STA, -320F	A-533B,LT LS TL, RT, AIR
INCO 718 EB WELD, STA, 75F	A-533B, ST, RT, AIR
INCO 718 EB WELD, STA, -320F	A-533B, SL, RT, AIR
AISI 301 SS , 1/2 HARD, 75F	A-533B, 550F, AIR
AISI 304 SS , ANN, 75F	X-65 PIPE STEEL, AIR
AISI 304 SS , SR, 75F	X-65 PIPE STEEL, SALT WATER, 10HZ
AISI 304 SS , ANN, 800F	X-65 PIPE STEEL, SALT WATER 1HZ

Table 2. Materials Included in Libraries

NASCRAC	F.M. & D.T.
AISI 304 SS , WELD SR, 800F	X-65 PIPE STEEL, SALT WATER 0.1HZ
AISI 316 SS , ANN, 75F	X-65 PIPE STEEL, SALT WATER 0.01HZ
AISI 316 SS , ANN, 800F	SS301, ANNEALED, RT
AISI 316 SS , WELD SR, 800F	SS301, 1/2 HARD, RT
4340 STEEL ,180-200 UTS, 75F	SS301, FULL HARD, -400F
D6AC STEEL, 220-240 UTS, HIGH K1C HT, 75F	SS304, ANNEALED, RT
300M STEEL, 280-300 UTS, 75F	SS304, ANNEALED, 1000F
HP9-4-0.20 STEEL, 200 UTS, 1525F 2HRS OQ,X, -65F LHA	SS310, ANNEALED, RT
HP9-4-0.20 STEEL, 200 UTS, 75F	SS310, ANNEALED, -400F
HP9-4-0.20 STEEL, 220-240 UTS, 75F	SS316, ANNEALED, RT
15-5PH STEEL, H1025, 75F	SS316, ANNEALED, 800F
17-4PH STEEL, H1025, 75F	SSPH 13-8Mo, H1000 BAR, LT, DRY AIR, RT
17-4PH STEEL, H900, 75F	SSPH 13-8Mo, H1000 BAR, LT, SUMP TANK, RT
PH13-8Mo STEEL, H1000, 75F	SSPH 13-8Mo, H1000 EXTR., LT, DRY AIR, RT
PH13-8Mo STEEL, H1000, 75F HHA, 1HZ	SSPH 15-5PH, H1025 BAR, LT, LAB AIR, RT
CUSTOM 455 STEEL, H1000, 75F	SSPH 13-8Mo, H1025 BAR, TL, SALT WATER, RT
A286 STEEL STA, 75F	AUSTENITIC STEEL, RT
A286 STEEL STA, 600F	FERRITIC STEEL, RT
A286 STEEL STA, 800F	MARTENSITIC STEEL, RT
A286 STEEL STA, 1000F	STEELS OF 95KSI STRENGTH, RT
TI-6AL-4V RA, L-T & T-L, 75F	STEELS OF 180KSI STRENGTH, RT
TI-6AL-4V RA, L-T & T-L, -100F	STEELS OF 200KSI STRENGTH, RT
TI-6AL-4V BA, L-T & T-L, 75F	LOW ALLOY WELD METAL, UPPER, RT
TI-6AL-4V STA, L-T & T-L, -320F	LOW ALLOY WELD METAL, AVE., RT
TI-6AL-4V STA, L-T & T-L, 75F	LOW ALLOY WELD METAL, LOWER, RT
TI-6AL-4V GTA WELD, SR, 75F	ST4340, TUS=200KSI, LAB AIR, 70F
	STD6AC, LAB AIR, 70F
	STD6AC PLATE, TUS=238KSI, JET FUEL, 70F
	ST 10Ni, TYS=180KSI, LT, LAB AIR, 70F
	ST 300M, TUS=280KSI, LABAIR, 70F
	ST 9-4-02 BAR, TYS=185KSI, LT, LAB AIR, 70F
	ST 9-4-02 BAR, TYS=189KSI, LT, DRY AIR, 70F
	ST 9-4-02 BAR, TYS=189KSI, LT, WET AIR, 70F
	ST 9-4-02 BILLET, TYS=161KSI, LT, LAB AIR, 70F
	ST 9-4-02 BILLET, TYS=178KSI, LT, LAB AIR, 70F
	ST 9-4-02 BILLET, TYS=186KSI, SUMP TANK, 70F
	ST 9-4-03 BAR, TYS=193KSI, LAB AIR, 70F
	ST 9-4-03 FORGING, TYS=198KSI, LAB AIR, 70F
	ST 9-4-03 FORGING, TYS=198KSI, SUMP TANK, 70F
	ST 9-4-02 PLATE, TYS=189KSI, LAB AIR, 70F
	ST AF1410, LAB AIR, 70F
	TI 6AL 4V, MILL ANNEALED, LAB AIR, 70F
	TI 6AL 4V, STA, LAB AIR, 70F
	TI 6AL 4V, RA, LAB AIR, 70F
	TI 6AL 4V, BETA ANNEALED, LAB AIR, 70F
	TI 6AL 6V2SN, MILL ANNEALED, LAB AIR, 70F
	INCONEL 718 BAR, HT F/C 1175F, TYS=160KSI, SL, AIR, RT
	INCONEL 718 BAR, HT F/C 1175F, TYS=160KSI, LT, AIR, RT
	INCONEL 718 BAR, HT F/C 1175F, TYS=160KSI, SL, 400F
	INCONEL 718 BAR, HT F/C 1175F, TYS=160KSI, LT, 400F

Table 2 (cont.). Materials Included in Libraries

C	$2.75*10^{-8}$
m	0
n	2.84
p	0.5
q	0.5
DK_o	2.5
K_c	54.9
C_o	1
d	1
K_{IC}	27

Table 3. Modified Forman Constants (from NASCRAC)

FUNCTION	F.M. & D.T.	pc-CRACK	PC-F.A.D.	NASCRAC
Number of geometries	12	9 or 19	15	33
LEFM	12	19	0	33
Creep	0	9	0	0
EPFM	12	9	0	33
Beta output	yes	no	no	no
Material properties	yes	no	no	yes
Number of materials				
total	85	0	0	76
types of materials	7	0	0	10
Residual strength				
LEFM	yes	no	no	no
EPFM	yes	no	no	no
Fatigue crack growth	yes	yes	no	yes
constant amplitude	yes	yes	no	yes
random amplitude	yes	yes	no	yes
semi -random amplitude	yes	yes	no	yes
with retardation	yes	no	no	yes
without retardation	yes	yes	no	yes
number of growth laws	5	7	0	6
Stress corrosion crack growth	yes	yes	no	no
constant stress	yes	yes	no	no
variable stress	yes	yes	no	no
Other features				
CREEP calculations	no	yes	no	no
Inspection intervals	yes	no	no	no
Instability (J-T analysis)	yes	yes	no	yes
Life after proof test	no	no	no	yes
a vs. K calculations	no	yes	no	yes
a vs. J calculations	no	yes	no	yes
C.O.A. calculations	no	no	no	yes
Critical crack size calculations	yes	yes	no	yes
Failure assesment diagram	no	no	yes	no
Safty Factor	no	no	yes	no

Table 4. Comparison of Software

FUNCTION	F.M. & D.T.	pc-CRACK	PC-F.A.D.	NASCRAC
Operation				
menu driven	yes	yes	yes	yes
printer support	dot	dot	dot	dot
plotter support	HP	HP	HP	HP
plot to printer	no	screen dump	screen dump	screen dump
CRT display of plots	no	yes	yes	yes
ability to save sessions	no	yes	yes	yes
help function	no	no	no	yes
mixed units	no	no	no	no
units available	SI, Imperial	SI, Imperial	SI, Imperial	SI, Imperial
error handling	poor	very good	very good	very good
file management	no	yes	no	no
ASCII data output	yes	yes	yes	yes
save plot files	yes	yes	yes	yes
Manual				
readablity	good	very good	good	very good
theory included	yes	yes	no	yes
example problems	yes	yes	no	yes
samples of output	yes	yes	yes	yes
agreement with program	good	very good	poor	very good

Table 4 (cont.). Comparison of Software

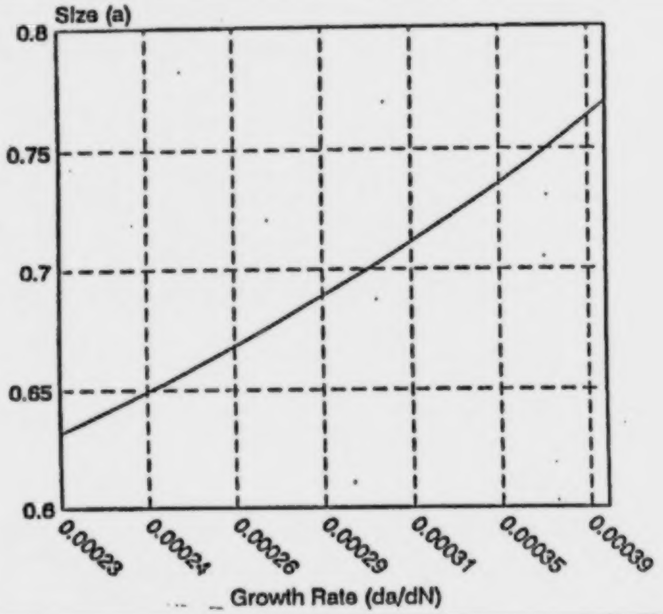

Figure 1. Crack Length vs Growth Rate for pc-CRACK

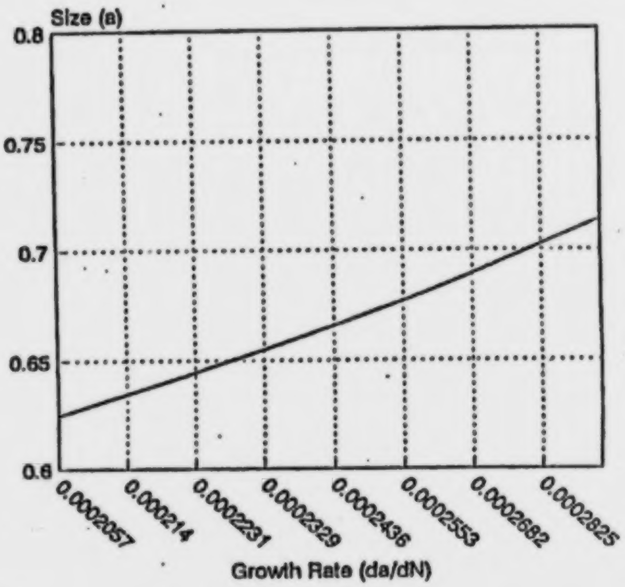

Figure 2. Crack Length vs Growth Rate for NASCRAC

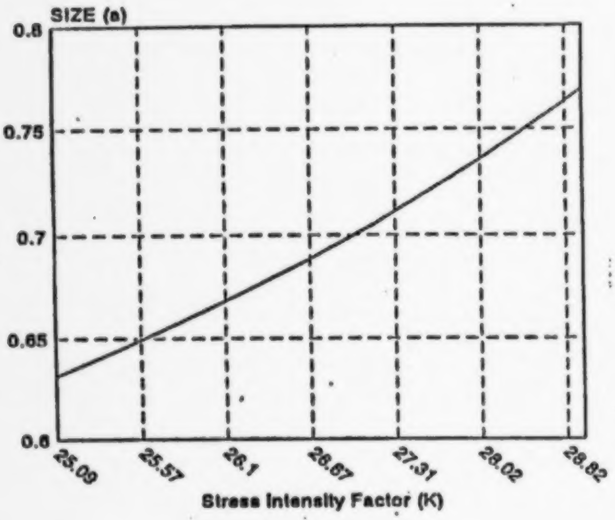

Figure 3. Crack Length vs K for pc-CRACK

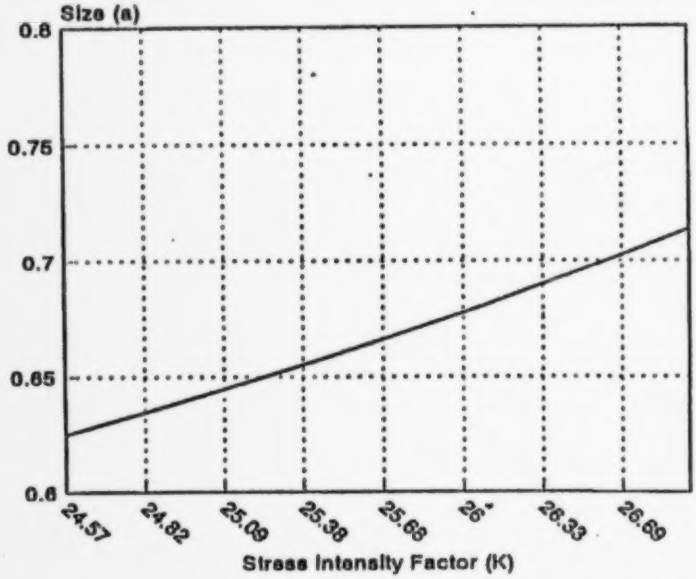

Figure 4. Crack Length vs K for NASCRAC

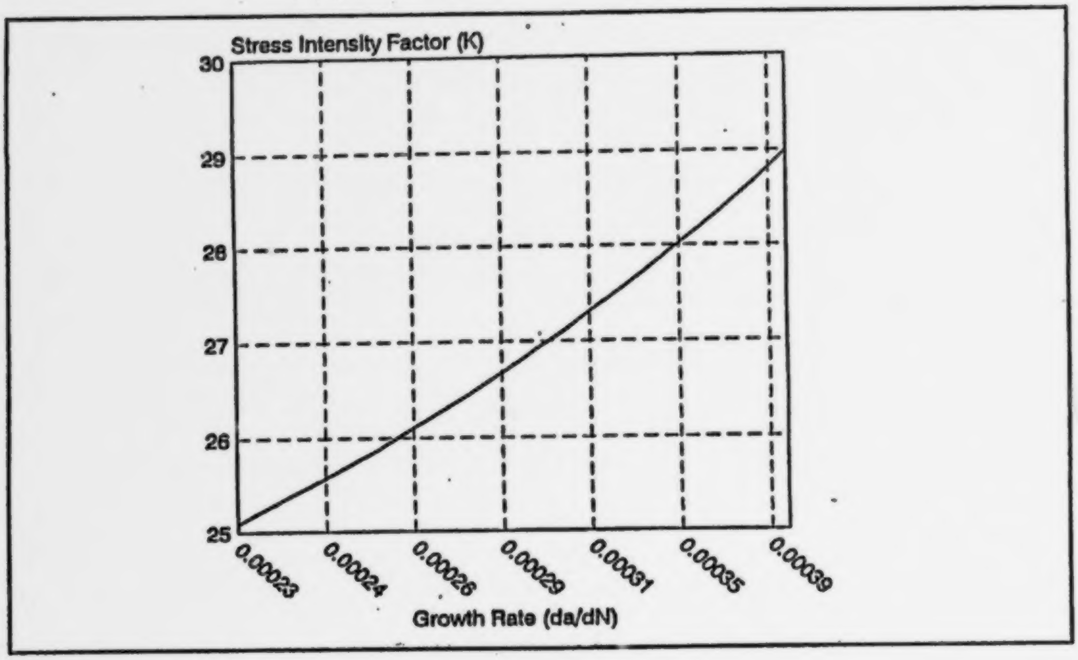

Figure 5. K vs Growth Rate for pc-CRACK

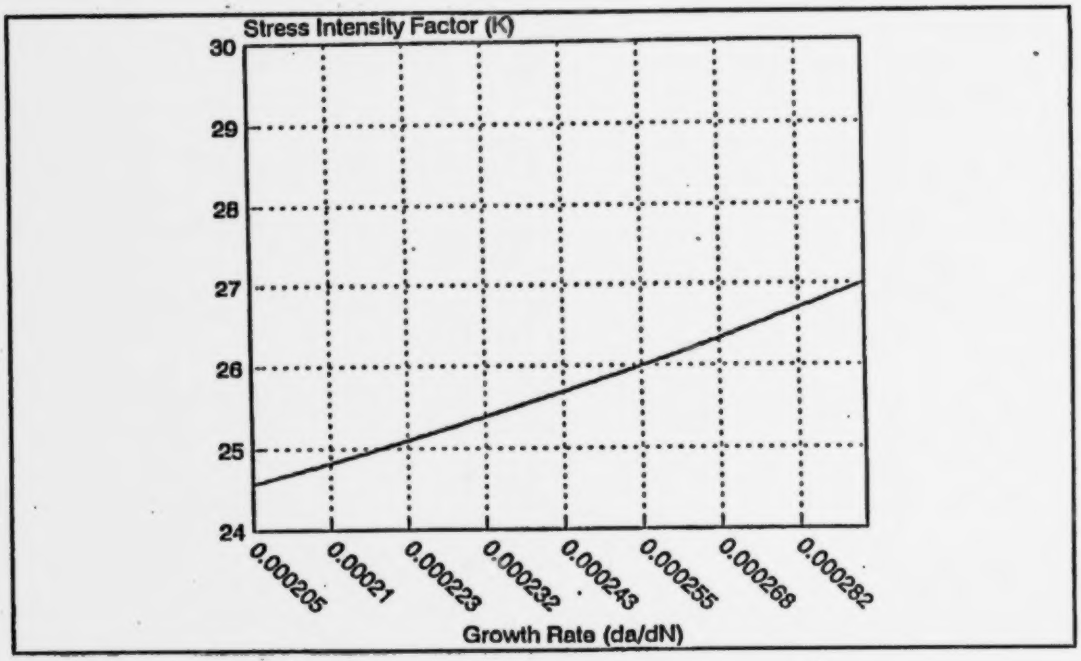

Figure 6. K vs Growth Rate for NASCRAC

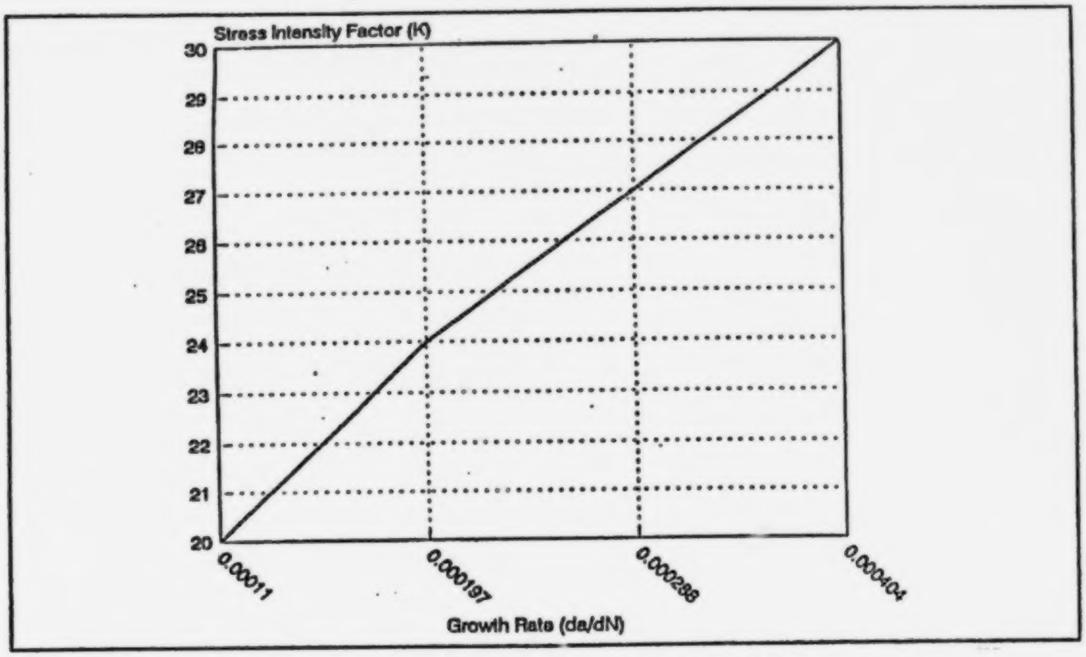

Figure 7. K vs Growth Rate for F.M. & D.T.

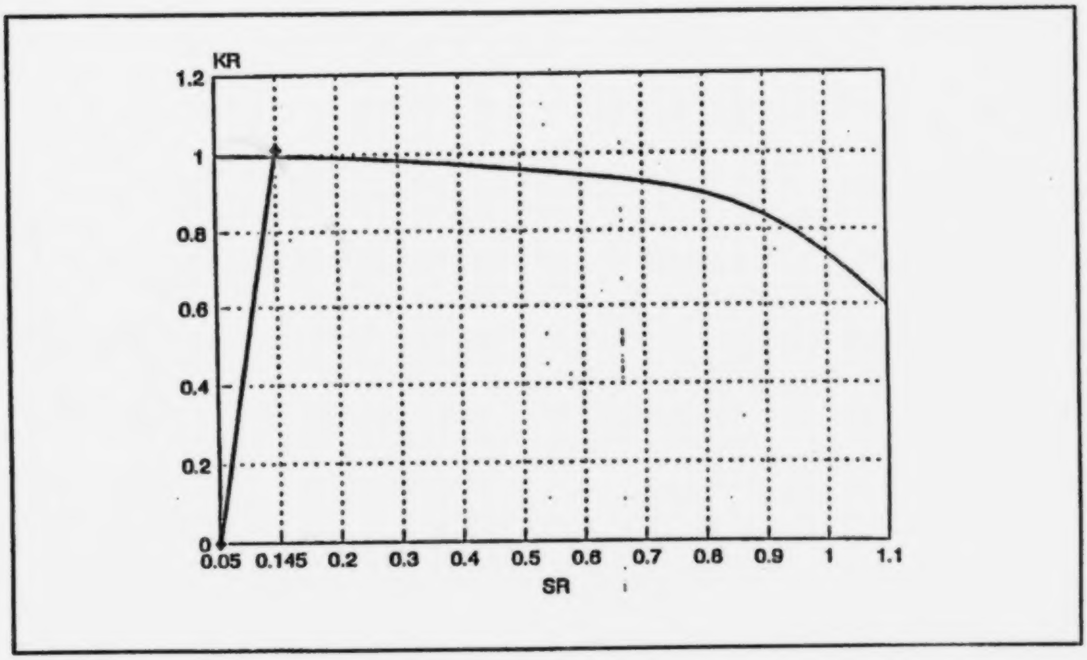

Figure 8. Failure Assessment Diagram from PC-FAD

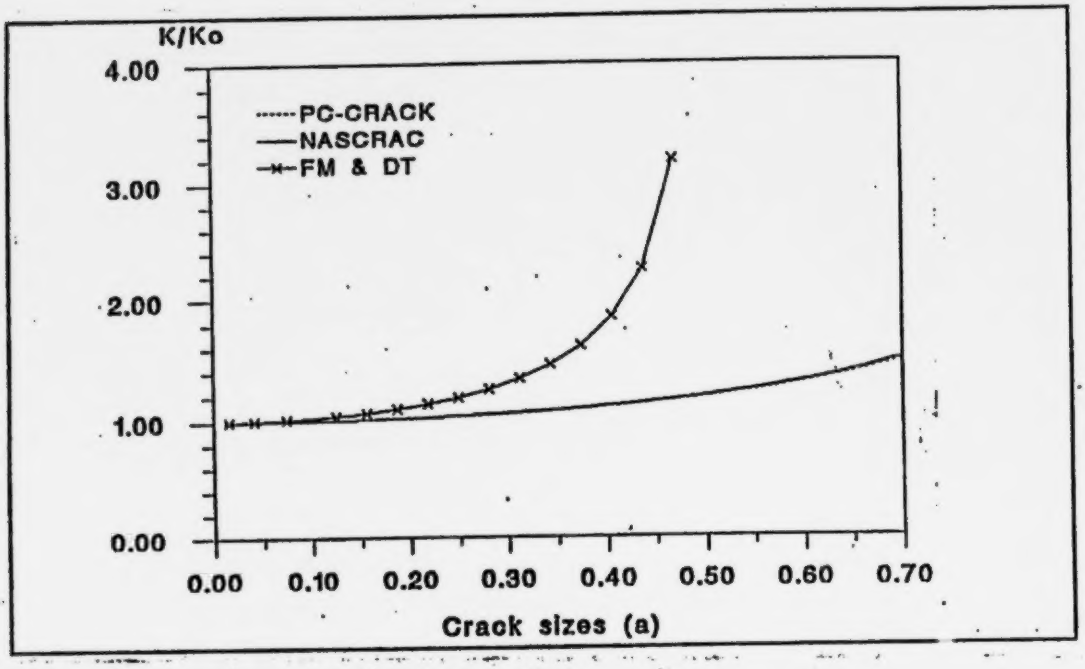

Figure 9. Comparison of K results, flat panel problem

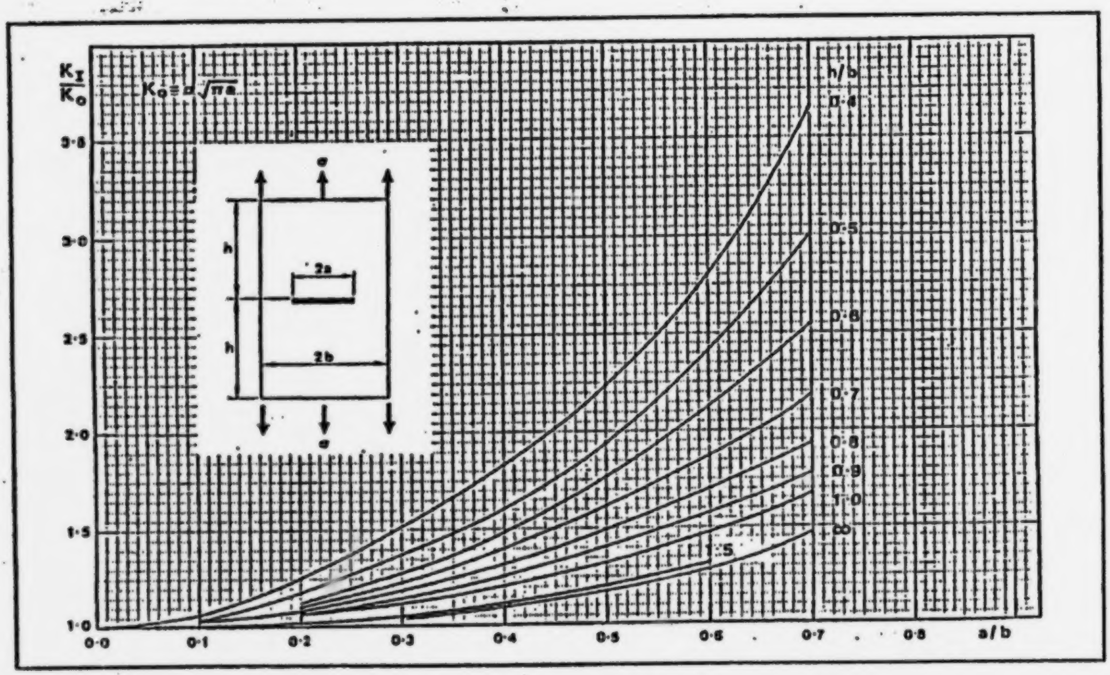

Figure 10. Handbook solution, flat panel problem [8]

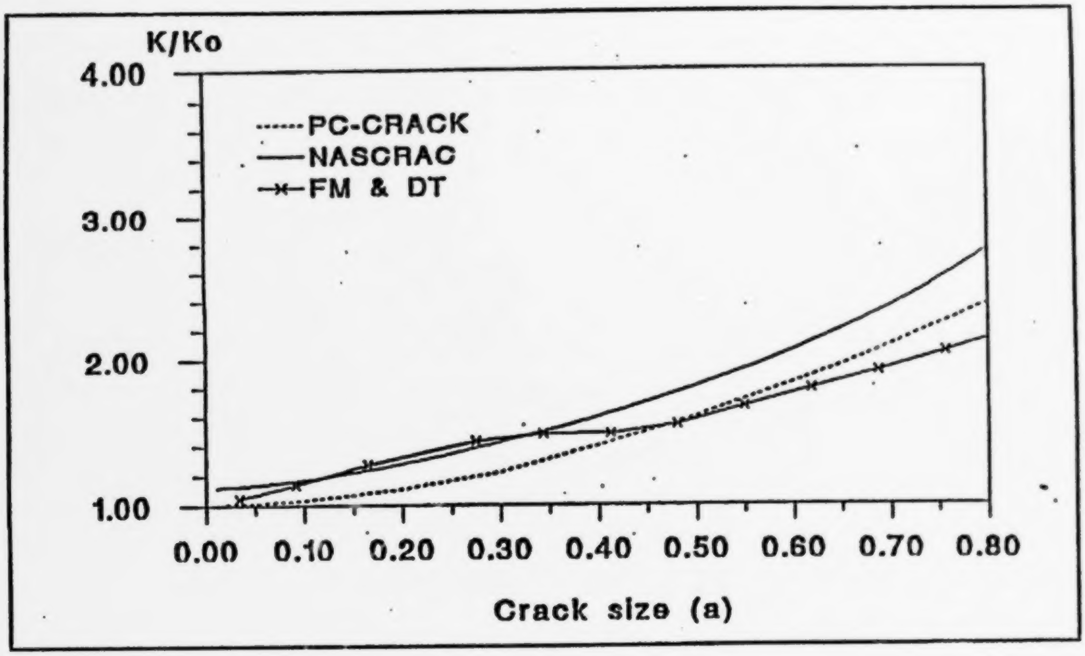

Figure 11. Comparison of K results for cylinder problem

APPENDIX

HARDWARE REQUIREMENTS

Fracture Mechanics & Damage Tolerance Analysis Software

-IBM-PC or compatible
-360K, 5", floppy drive
-DOS
-hard drive (optional)
-dot matrix printer (optional)
-HP plotter (optional)

NASCRAC

-IBM-PC or compatible
-640K
-360K, 5", floppy drive
-DOS 2.11 or better
-hard drive
-monitor (EGA optional)
-dot matrix printer (optional)
-HP plotter (optional)
-Math co-processor (optional)

pc-CRACK

-IBM-PC, XT, AT or compatible
-640K
-2 360K, 5", floppy drive
-1 360K, 5", floppy drive and hard drive (optional)
-DOS 2.0 or better
-CGA card and monitor or better
-dot matrix printer
-HP plotter (optional)

PC-FAD

-IBM-PC, XT, AT or compatible
-256K
-360K, 5", floppy drive
-hard drive (optional)
-DOS 2.10 or better
-CGA card and monitor
-dot matrix printer (optional)
-HP plotter (optional)

#510324

(15

A.P.H.I.U.S.

by G.R. Labbé, J.R. Matthews, D.R. Hay and J. Hélie

ADM(EM)/DGMEM/DSE
National Defence Headquarters
MGen George R. Pearkes Building
Ottawa, Ontario
K1A 0K2

*** ABSTRACT ***

Under the direction of DSE and the field supervision of DREA/DL, Tektrend International Inc. was awarded a contract for the development of a project entitled APHIUS which stand for Automated Pressure Hull Intelligent Ultrasonic System.

APHIUS is an ultrasonic inspection system whose hardware configuration and software capabilities are uniquely designed for submarine pressure hull inspection. However, future expansion will allow to meet a wide range of Canadian Forces naval vessel inspection requirements.

Inspection of submarine pressure hulls is a very complex and detailed task. If condemnation limits are to be based on the most serious defect type that the field inspector reports, the tasks of discrimination and the burden of the proof are dependent upon the inspectors' abilities. APHIUS provides assistance to the inspector by automating the interpretation process and providing advanced display capabilities. Handling of the information generated by the inspection for management decision-making is also addressed.

The benefits of automating the inspection of submarine pressure hulls is twofold; It will permit the revision of materials condemnation criteria of the pressure hull material based on defect identification, thereby raising the levels of the detectability, productivity, and reliability of the inspection and providing a consistent information system. The information system addresses the documentation aspect of maintaining the inspection result, presentation, interpretation, decision-making, and archiving of the data collected.

APHIUS addresses these issues by incorporating advanced inspection capabilities including state-of-the-art hardware and software, artificial intelligence methods to assist the operator during testing, and in post-test analysis to achieve the quality, productivity and reliability gains.

The system embodiment in terms of physical size and interface requirements specific to submarine will be described. Software capabilities specific to pressure hull steel and weldments will be presented.

DIRECTORATE
DSE
6
SHIP ENGINEERING

Metallic Materials

Metallic Materials

TEKTREND

APHIUS

AUTOMATED PRESSURE HULL INTELLIGENT ULTRASONIC SYSTEM

April 1993

Metallic Materials

TEKTREND

CONTENT

PART 1 ---------> INTRODUCTION

PART 2 ---------> HISTORY

PART 3 ---------> DEVELOPMENT PROJECT

PART 4 ---------> CONCLUSION

Metallic Materials

TEKTREND

REQUIREMENT

TO REDUCE THE AMOUNT OF REWORK ON SUBMARINE PRESSURE HULL WELDS DURING REPAIR AND/OR NEW CONSTRUCTION BY DEVELOPING AN IMPROVED ULTRASONIC INSPECTION SYSTEM.

Metallic Materials

TEKTREND

AIM

TO DEVELOP AN ADVANCED MODEL OF AN INDUSTRIAL QUALITY COMPUTER-AIDED ULTRASONIC INSPECTION SYSTEM, INCLUDING SOFTWARE AND HARDWARE FOR INSPECTION MAPPING, DEFECT CLASSIFICATION THROUGH ARTIFICIAL INTELLIGENCE, COMPLETE DATA RECORDING AND REPRODUCTION WITH EMPHASIS ON GRAPHICAL USER INTERFACES.

Metallic Materials

TEKTREND

SCOPE

TO DEVELOP AN INTELLIGENT ULTRASONIC SYSTEM FOR INSPECTION OF SUBMARINE PRESSURE HULLS INCLUDING PARENT PLATES AND WELDMENTS.

GENERATE NEW CRITERIA WHICH WILL PERMIT OVERHAULING THE OUDATED CONDEMNATION CRITERIA AND ELIMINATE WASTEFUL DEFECT REMOVAL.

Metallic Materials

TEKTREND

SCOPE (Cont'd)

IMPROVE PERFORMANCE OF THE ORIGINAL SYSTEM FOR FIELD APPLICATION

INCORPORATE FEATURES TO FACILITATE FIELD APPLICATION INCLUDING THE USER INTERFACE, DISPLAY AND REPORTS FORMATS, LOCATION TRANSDUCER ATTACHMENT, SCANNING MODE, PORTABILITY AND TRANSPORTABILITY.

Metallic Materials

TEKTREND

SCOPE (Cont'd)

PROVIDE A SIMPLE MEANS FOR TRANSDUCER CHARACTERIZATION IN THE FIELD.

PROVIDE EXTENDABILITY TO MEET NEEDS AND EVOLUTION OF CURRENT TECHNOLOGY.

RETAIN MAINTAINABILITY THROUGHOUT THE ORIGINAL MODULAR SYSTEM DESIGN.

Metallic Materials

TEKTREND

SCOPE (Cont'd)

PREPARE USERS MANUALS AND TRAINING MATERIALS.

Metallic Materials

MATRIX

SCIENTIFIC AUTHORITY -----> Mr. G.R. Labbé
DSE 6

TECHNICAL AUTHORITY -----> Dr. J.R. Matthews
DREA/DL

Mr. J.F. Boucher
DSE 6

Metallic Materials

TEKTREND

MATRIX (Cont'd)

PROJECT DIRECTOR -----> Dr. J.L. Kennedy
DRDM 8

PROCUREMENT MANAGER -----> Mr. B.T. Forster
DSS/SPO

PROCUREMENT OFFICER -----> Mr. Y. Laflèche
DPSupM 2

Metallic Materials

CONTRACTOR

TEKTREND INTERNATIONAL Inc.
2755 Pitfield
St-Laurent
Montréal, Québec
H4S 1T2

(514) 333-7371

Metallic Materials

TEKTREND

PHASING

PHASE	ITEM
I	DESIGN MAIN CONSOLE
II	DESIGN TRANSDUCER LOCATION SYSTEM
III	ASSEMBLE MAIN CONSOLE
IV	ASSEMBLE LOCATION SYSTEM
V	USER INTERFACE DEVELOPMENT
VI	DEVELOP AND IMPLEMENT REPORTING

Metallic Materials

TEKTREND

PHASING (Cont'd)

PHASE	ITEM
VII	IMPLEMENTATION OF CODE-BASED ACCEPTANCE CRITERIA
VIII	MANUALS AND TRAINING MATERIALS
IX	SERVICE AND UPGRADE PROGRAM
X	TRAINING

Metallic Materials

TEKTREND

MILESTONES

ITEM	ESTIMATED DATES
MAIN CONSOLE	Mar 93
LOCATION SYSTEM	Mar 93
USER INTERFACE	Aug 92
INTEGRATED HARDWARE AND SOFTWARE SYSTEM	Dec 92

Metallic Materials

MILESTONES

(Cont'd)

ITEM	ESTIMATED DATES
REPORTING SOFTWARE	Apr 93
KNOWLEDGE-BASED SYSTEM	Apr 93
MANUALS AND TRAINING MATERIALS	Jun 93
FINAL REPORT	Dec 93

Metallic Materials

TEKTREND

COST

DATA AS PER MAR 93 FORECAST

TOTAL ($000) -----> $609

FY	91/92	92/93	93/94	94/95
BY	75	275	220	39

#510325- (20)

Background Research Leading to the APHIUS Development Project

by

J. R. Matthews

Defence Research Establishment Atlantic
FMO Halifax, Halifax, Nova Scotia, B3K 2X0

Abstract

DREA Dockyard Laboratory began research in Pattern Recognition of weld defects in 1980. This research was aimed at producing signal processing that would allow the isolation of volumetric and crack like defects in weldments. With this ability a two level condemnation criteria, or weld reject criteria could be employed based on defect type with a projected savings in rework costs in the millions of dollars.

The work began with the generation of basic weld defects for the collection of ultrasonic data and production of software to extract features in the time, frequency, auto correlation, cross correlation and convolution domains. Features were evaluated by producing histograms from twenty signals. In this way we were able to isolate potentially useful features for determining the different defect types.

As soon as the research showed that pattern recognition would be successful, parallel work began with Tektrend to produce a system that would map defects and permit storage of rf waveforms for these defects. It was intended that data thus collected would be analysed in the lab and that defect maps would be produced with defect type determined by pattern recognition.

Three prototype inspection systems have been produced over the past twelve years with more and more power and capability being available to the inspector with real time defect classification and defect mapping now a reality.

This paper is a brief outline of the history of the research and development leading to the present APHIUS system.

Introduction

DREA Dockyard Laboratory began research in Pattern Recognition of weld defects in 1980. This work was part of a new research thrust in submarine materials technology which included welding research, high strain rate fracture research and NDE research. The Pattern recognition research was aimed at producing signal processing that would allow the isolation of volumetric and crack like defects in weldments. With this ability a two level condemnation criteria, or weld reject criteria could be employed based on defect type with a projected savings in rework costs in the millions of dollars.

The work began with the generation of basic weld defects for the collection of ultrasonic data [1]

1. crack like defects

2. geometric defects
3. incomplete fusion and penetration defects
4. slag inclusions
5. porosity

and production of software to extract features in the time, frequency, auto correlation, cross correlation and convolution domains. Features included for each domain included

1. maximum value (not considered in time domain since the waveforms are normalized to the maximum value)
2. minimum
3. area
4. max slope
5. location of max
6. location of min
7. duration
8. location of max slope
9. mean
10. rms
11. standard deviation
12. variance

Features were evaluated by producing histograms from twenty rf signals[1]. In this way we were able to isolate potentially useful features for determining the different defect types[2,3,4].

Pattern Recognition

The main goal of the pattern recognition research was to verify if features in UT signals and their transformations existed which could be used to classify defects according to type and therefore severity. Pattern recognition was conducted in three stages; first transformations were conducted on the rf waveforms, second features were extracted from each transformation and, third histograms were produced to evaluate individual features.

Histograms produced showed features to be either separated, touching or overlapping. In the earliest studies[1], cross correlation of an unknown waveform and reference waveform was the most useful for differentiating between fatigue cracking and slag whereas auto correlation was found to be more useful than convolution, time and frequency domains for separating fatigue cracks from holes. The mean value, RMS, standard deviation, and variance of the five waveforms were observed to be the best features for separating defects.

In later studies angled cracks were included in the library of defects being studied[3]. The RMS of the auto correlation, the standard deviation of the auto correlation, the variance of the time, the standard deviation of the time, and the standard deviation and RMS of the cross correlation, showed good separation in the numerical ranges for each type of defect and were consistent. Cross correlation values were slightly better than the time and auto correlation. The earliest study, which was conducted at a 20 MHz sampling rate, had suggested a wider improvement of cross correlation over the others, than identified in this study at 10 MHz sampling rate.

Many factors were evaluated as to their effect on the reproducibility of pattern recognition results. The most important factor turned out to be the impedance mismatch between the electronics and the transducers. A lot of work was conducted with the aim of developing techniques for the transportability of components, including transducers, while maintaining the same classifiers. It is now felt that this may be unachievable and that each set up, and transducer, will have to be trained separately. This would have been considered a disaster ten years ago but with the current APHIUS system complete training can be accomplished in less than an hour for a given set up and transducer.

Inspection Systems

As soon as the research showed that pattern recognition would be successful, parallel work began with Tektrend to produce a system that would map defects and permit storage of rf waveforms for these defects[5,6.]. It was intended that data thus collected would be analyzed in the lab and that defect maps would be produced with defect type determined by pattern recognition.

Several prototype inspection systems[7,8,9,10] have been produced over the past twelve years with more and more power and capability being available to the inspector with real time defect classification and defect mapping now a reality[11,12,13,14].

The early prototypes[7], of which there were several versions, were called SLAM(signal location and acquisition module). SLAM included a high speed 50 MHz digitizer with a 1024 data point buffer and an air-borne sonic location system. The system provided an easy and simple interface for an ultrasonic inspector to acquire data in the field with complete data record storage on magnetic cartridge tape that could be analyzed by an expert later in the laboratory. The recorded data included x,y coordinates and the complete rf waveform. The operators used a standard UT unit for the inspection and data was recorded when the operator depressed a button on the transducer. The rf signal was taken directly from the standard UT unit.

The later prototypes[11], designated APHIUS(Automated Pressure Hull Intelligent Ultrasonic System) were designed around IBM PC systems. These later prototypes combined a computer-based ultrasonic analysis work station with a computer-based ultrasonic field inspection capability. On-line, the systems performed complex signal processing including feature extraction and classification. The recognized defects were immediately available on a defect map. Off-line, the systems could be used as a signal examination machine and also used to train and develop classifiers. APHIUS was designed on the PC 80X86 open architecture to provide for expandability, growth and modification of the system as requirements and technology evolved. The ultrasonic capability was incorporated through a pulser/receiver on an expansion board as was data acquisition using an A/D conversion expansion board for complete waveform recording. Real time, on-line decision-making was made possible using the 80X87 numeric coprocessor chip and high-speed FFT and DSP expansion cards.

Conclusions

This paper has given a brief outline of the history of the research and development leading to the present APHIUS system.

References

1. J.P. Slade and J.R. Matthews, "Selection of Optimal Features for a Pattern Classifier to Identify Weld Defects," DREA RN/DL/82/3, September 1982.

2. J.R. Matthews and J.P. Slade, "Optimal Features for a Pattern Classifier to Identify Weld Defects in Submarine Pressure Hulls," Presented at 1983 ASNT Spring Conference, Orlando, Florida, 7-10 March 1983.

3. G.A. Sutherland and J.R. Matthews, "Effect of Crack Orientation on the Selection of Features for a Pattern Classifier to Identify Weld Defects Using Ultrasonic Techniques," DREA RN/DL/85/2, January 1985.

4. J.R. Matthews and G.A. Sutherland, "Selection of Features for a Pattern Classifier to Identify Weld Defects in HY 80 Weldments," Abstracts and Summaries of the CF/CRAD Meeting on Research in Fabrication and Inspection of Submarine Pressure Hulls, May 1985., May 1985.

5. J.R. Matthews, D.R. Hay, R.W.Y. Chan, "Automated Ultrasonic Inspection and Data Collection System," Presented at Ultrasonics International 83, Dalhousie University, Halifax, N.S., 12-14 July 1983.

6. D.R. Hay, "Automated Ultrasonic Inspection and Data Collection System", Tektrend International Inc., DREA Contractor Report, CR/85/413, August 1985.

7. R. Chan and D.R. Hay, "Automated Ultrasonic System for Submarine Pressure Hull Inspection", Tektrend Int., DREA CR/87/401, January 1987.

8. D.R. Hay, J.R. Matthews, and H.A. MacDonald, "Automated Ultrasonic System for Submarine Pressure Hull Inspection," in proceedings of the NATO Advanced Research Workshop on Signal Processing and Pattern Recognition in Nondestructive Evaluation of Materials, Quebec City, Canada, August 19 -22, 1987.

9. D.R. Hay, J.R. Matthews, and H.A. MacDonald, "Automated Ultrasonic System for Submarine Pressure Hull Inspection," Presented at the 2nd CF/CRAD Meeting on Research in Fabrication and Inspection of Submarine Pressure Hulls, Halifax, N.S., May 26-28, 1987.

10. J.R. Matthews, D.R. Hay and R.W.Y. Chan, "Computer Aided Ultrasonic Inspection of Submarine Pressure Hulls", in proceedings of Review in Progress in Quantitative NDE, Bowdoin College, Brunswick Maine, July 1989.

11. D.R. Hay and R.W.Y. Chan, "Automated Ultrasonic System and Pattern Recognition for Submarine Pressure Hull Inspection", Volume I: Main Report, prepared by Tektrend Inter. Inc., contractor report, DREA CR/90/409, Vol I, April, 1990.

12. R.W.Y. Chan, A. Pelletier and G. Borghi, "Automated Ultrasonic System and Pattern Recognition for Submarine Pressure Hull Inspection", Volume II: Aphius User's Manual, prepared by Tektrend Inter. Inc., contractor report, DREA CR/90/409, Vol II, April, 1990.

13. "Automated Ultrasonic System and Pattern Recognition for Submarine Pressure Hull Inspection", Volume III: Aphius Program Documentation, prepared by Tektrend Inter. Inc., contractor report, DREA CR/90/409, Vol III, April, 1990.

14. D.R. Hay, J.R. Hay and G. Borghi, "Automated Ultrasonic System and Pattern Recognition for Submarine Pressure Hull Inspection", Volume IV: Pattern Recognition Results, prepared by Tektrend Inter. Inc., contractor report, DREA CR/90/409, Vol IV, April, 1990.

#510326 (21)

ADVANCED FLAW SIZING IN PRACTICE

by

C.V. Sevenhoven, Royal Netherlands Navy, The Hague, The Netherlands
W.H. van Leeuwen, Röntgen Technische Dienst B.V., Rotterdam, The Netherlands

ABSTRACT

One of the activities of the Dutch Welding Institute (NIL) is to initiate and coordinate research projects, among which projects in the field of non-destructive testing (NDT). The most recent of these was the project "Advanced Flaw Sizing under Practical Conditions," which will be reported. The aim of this project was to evaluate the practical applicability of various non-destructive flaw sizing techniques on a series of weld samples with many different geometries, wall thicknesses and defect types. Apart from the accuracy of the sizing results, attention was paid to the ease and level of confidence of the signal interpretation, the necessity to use advanced systems under various conditions and the requirements with respect to the inspection personnel. An additional point of interest was to assess in which cases the TOFD (time-of-flight diffraction) technique would be useful for flaw detection as well as for sizing.

The flaw sizing techniques considered in this project were:

- the ultrasonic flaw tip reflection (FTR) technique,
- the ultrasonic time-of-flight diffraction (TOFD) technique,
- supersaft, which is an ultrasonic focused imaging technique,
- the alternating current potential drop (ACPD) technique, and
- the direct current potential drop (DCPD) technique.

The results and conclusions will be summarized.

Summary and Conclusions

One of the activities of the Dutch Welding Institute (NIL) is to initiate and coordinate research projects, among which projects in the field of non-destructive testing (NDT). The most recent of these was the project "Advanced Flaw Sizing under Practical Conditions", on which this document is the final report. The aim of this project was to evaluate the practical applicability of various non-destructive flaw sizing techniques on a series of weld samples with many different geometries, wall thicknesses and defect types. Apart from the accuracy of the sizing results, attention was paid to the ease and level of confidence of the signal interpretation, the necessity to use advanced systems under various conditions and the requirements with respect to the inspection personnel. An additional point of interest was to assess in which cases the TOFD (time-of-flight diffraction) technique would be useful for flaw detection as well as for sizing.

The flaw sizing techniques considered in this project were
- the ultrasonic flaw tip reflection (FTR) technique
- the ultrasonic time-of-flight diffraction (TOFD) technique [see fig 2 and fig 12]
- supersaft, which is an ultrasonic focussed imaging technique
- the alternating current potential drop (ACPD) technique
- the direct current potential drop (DCPD) technique.

Both ultrasonic tip diffraction based techniques (FTR and TOFD) were applied in several different ways. First, they were applied manually, i.e. with manual probe handling and conventional screen reading and data recording by the operator. Second, manual probe handling was combined with a simple go/no-go version of automatic data recording and B-scan display, using the Multiple Display Unit (MDU). Third, three different computerized systems involving mechanized scanning, advanced data handling and display were used. These three systems were:
- a system developed by RTD Rotterdam, based on existing laboratory instruments. This TOFD system was designed to be user friendly, applicable on a wide variety of inspection geometries and reasonably suitable for field applications.
- the Nerason system of Nucon IPS, Amsterdam. This is an existing advanced multi-purpose ultrasonic system, for which recently TOFD software has been developed. The Nerason system has proven its suitability to work under field conditions for many years. In this project it has been used in combination with an immersion scanning system.
- the Zipscan system of the british research institute AEA Harwell. Zipscan was the only system with which at the beginning of the project field experience in TOFD application existed. Since the system is not

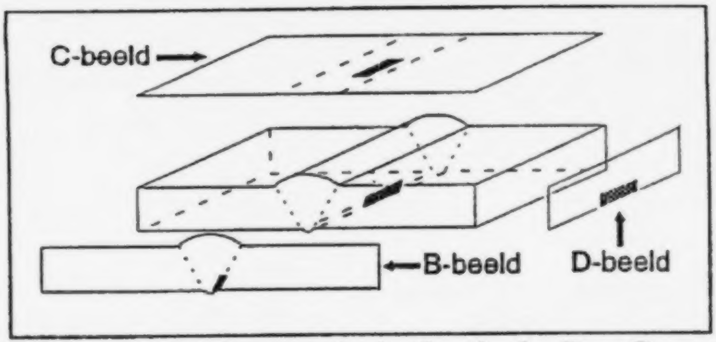
C-beeld
B-beeld
D-beeld

fig. 1: projectie van lasindicatie in B-, C- en D-beeld

[P.scan]

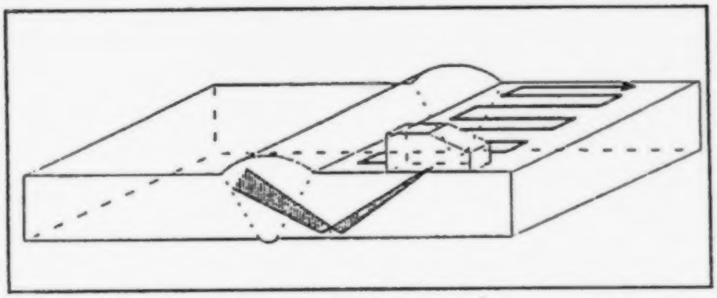

fig. 3: pulsecho meanderscanning

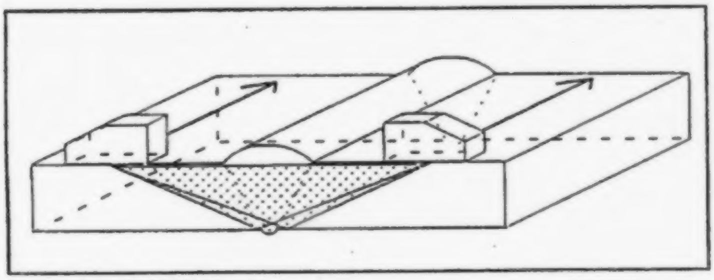

fig. 4: TOFD scanning

suitable to operate high frequency probes necessary for TOFD on small wall thickness samples, in addition a newer system called Flaw Monitoring System was applied.

The supersaft technique is developed by the Danish Welding Institute (now part of Force Institutes). It is a computer data processing routine to be applied on data collected with the P-scan system.

Test samples used in the project comprised (see figure 4.1):

- flat butt welded plates with wall thicknesses between 10 and 30 mm. The plates contained single side welded U- and V-welds with intentionally made weld defects of different kinds.
- T-shaped samples with K-welds containing fatigue cracks; wall thickness 38 mm.
- three tubular joint samples, two containing fatigue cracks and one containing a notch simulating a weld root defect. Tube diameters between 200 and 460 mm; wall thickness 8 to 16 mm.
- a split-tee type pipe repair sample containing notches in the weld toe. Wall thickness 9 mm (main pipe) and 27 mm (repair shell).

The ultrasonic measurements within the project were carried out by Röntgen Technische Dienst bv, Rotterdam and Nucon IPS, Amsterdam with contributions from AEA Harwell (England), the Danish Welding Institute and Shell/Billiton Research, Arnhem. The potential drop techniques were carried out by the Foundation for Advanced Metals Science (SGM), Hengelo.

The results and conclusions of the project can be summarized as follows:

1 - The apparently simple manually applied FTR technique frequently gives signals from other modes than tip diffraction. Signal interpretation requires theoretical knowledge and an analytical attitude. FTR application needs a case-by-case approach by a specialist. If the signals can be well interpreted as tip signals, the accuracy of the results is good: both in flaw hights and in depth positions of separate flaw tips a root-mean-square deviation from the actual values of 1 to 1.5 mm has been found.

2 - The TOFD technique is manually applicable when simple geometries are involved. Good level II ultrasonic operators can apply the technique after a few days training course.

3 - Use of the Multiple Display Unit with manual FTR and TOFD is possible, but in general hardly contributes to better signal interpretation or higher accuracy. Since the MDU is a heavy instrument without internal storage facilities, its use will not often be worthwhile in practice.

4 - Both manually applied TOFD and TOFD with advanced systems give accurate flaw sizing results. As with

the FTR technique, root mean square deviations are 1 to 1.5 mm, both for flaw hight data and flaw tip depth locations.

5 - Several good advanced TOFD systems exist. The accuracy of their results is similar, but they differ in practical applicability. The suitability of a system might be influenced by:

- * size and geometry of the inspected object (available manipulator types, contact or immersion technique, available software for special geometries)
- * smallest wall thickness that can be measured (sampling frequency)
- * scanning speed (in practice mainly important for flaw detection, much less so for sizing of already detected flaws).
- * vulnerability to weather conditions, shocks, etcetera; (lack of) portability.

6 - The RTD laboratory TOFD system is suitable for many different inspection geometries. It is easy to operate and portable, but rather vulnerable for shocks, dust and moisture. The measuring speed can be high.

7 - Nucon's Nerason system is transportable and can stand field conditions. At present only flat geometries can be inspected. The measuring speed is low. The immersion technique as applied with this system in general has the following disadvantages:

- * the immersion tank limits the size of the inspectable objects
- * variations in water path may complicate the data evaluation
- * if the immersion probes have fixed orientations, small irregularities in the object's shape have a strong influence on the beam angles and thus on signal strengths.

8 - The Harwell Zipscan and the Flaw Monitoring System are transportable and will stand field conditions. These systems are suitable for many different geometries and have a high measuring speed. The present Zipscan version is not suitable for wall thicknesses less than approx. 15 mm because the sampling frequency of 21 MHz is insufficient.

9 - Flaw detection with TOFD is only possible when advanced systems with TOFD B-scan presentation are used. On the flat plate samples used in this project, the detection rates were high, in particular with the systems using contact probes: 83% (RTD system), 90% (Zipscan/Flaw Monitoring System) and 66% (Nerason system). Apart from defects in the well known dead zone of the TOFD technique (the upper 3 to 4 mm), several shallow root defects were missed. Detection scores on root defects were 78% (RTD system), approx. 75% (Zipscan/FMS) and 44% (Nerason system). The necessity to perform only a longitudinal scan along the weld makes TOFD a potentially

fast technique.

10- An advantage of TOFD, which is particularly important in the case of flaw detection, is the fact that probe positioning and defect orientation are not critical.

11- Flaw sizing accuracy with manual TOFD of defects just under the dead zone was less accurate than elsewhere. This was not found for TOFD with advanced systems. The sizing accuracy near the back wall was the same as near the middle of the wall thickness.

12- On complex geometries like tubular joints, TOFD can be applied if suitable scanners and special data interpretation software are available; depending on the pipe diameters and the local geometry, a (slow) manual probe manipulation may be required. Data evaluation in this case requires special skill and experience.

13- Flaw sizing on complex geometries appears to be as accurate as on flat plates.

14- The sizing accuracy of supersaft is similar to that of FTR and TOFD, or slightly less.

15- As compared to TOFD, supersaft is much more time consuming and requires a higher skill and experience.

16- Supersaft gives more information on the defect type than TOFD.

17- Supersaft is not (yet) suitable for complex geometries in general. It may sometimes be applicable depending on the local geometry.

18- The DCPD technique as applied in this project is not suitable for defect sizing. Even its defect detection capability on the used test samples is still very limited.

19- The ACPD technique as applied in this project on welded plates with unworked surface condition, is not suitable for flaw hight measurement.

Enclosure 2 gives an overview of which techniques and systems have been used on which test samples, and on which of these measurements the various above conclusions are based. An impression of the applicability of the various techniques and systems is given in enclosure 3.

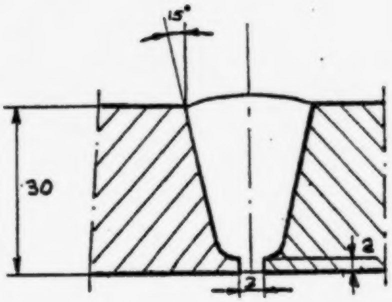

30 mm U-naad

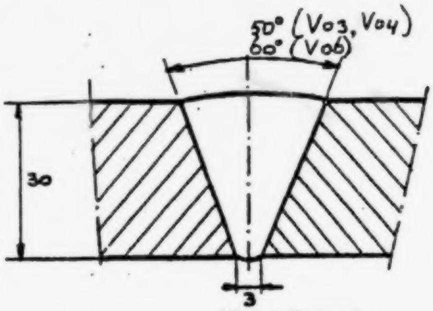
50° (V03, V04)
60° (V06)
30
3

30 mm V-naad

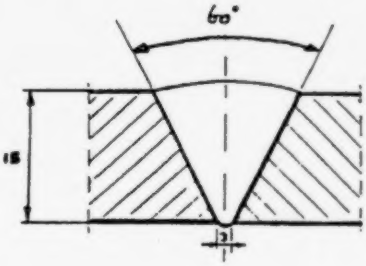

15 mm V-naad

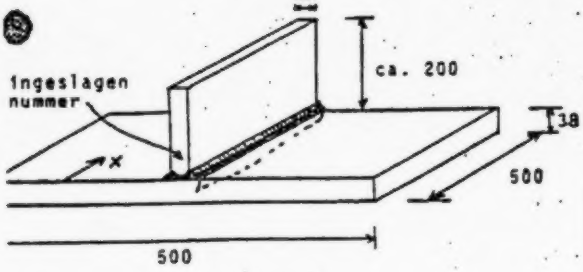
38
ca. 200
ingeslagen nummer
x
38
500
500

T-platen van de Koninklijke Marine

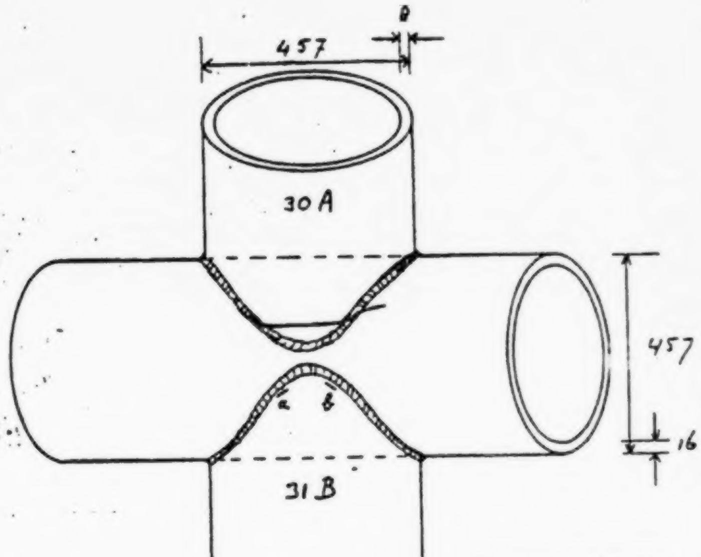
457
8
30 A
457
a
b
16
31 B

+ knooppunten van het Stevinlaborator

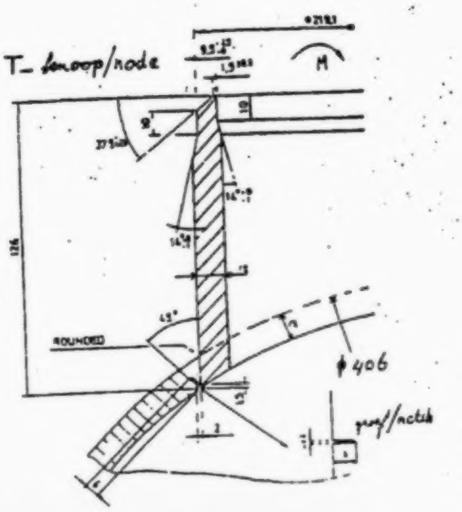
T- knoop/node
M
10
126
45°
ROUNDED
ϕ406
groef/notch

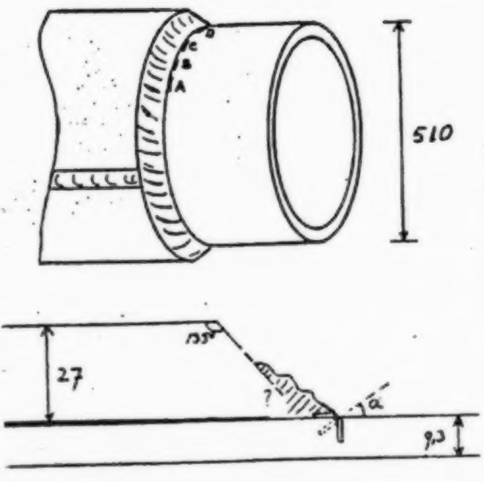
D
C
B
A
510
135°
27
α
9,3

Pijpreparatie type split-tee; Gasunie.

groef	lengte	diepte	α
A	15	2	0°
B	5	2	0°
C	5	1,5	0°
D	5	1,5	60°
E	5	3	60°
F	15	2	60°
G	15	2	90°
H	5	2	90°
I	5	2,5	90°

fig. 4.1.

TIME OF FLIGHT DIFFRACTION (TOFD)

TOFD - HIGHLIGHTS

- TOFD is a most accurate defect sizing technique
- high accuracy results from the use of diffraction waves from defect edges and the measurement of traveltime
- applicable on a wide range of geometries:
  - flat plates from about 10 mm wallthickness upto 300 mm and more
  - T-butt welds
  - tubular joints
  - nozzles
- probe positioning during scanning is not critical

PRINCIPLE

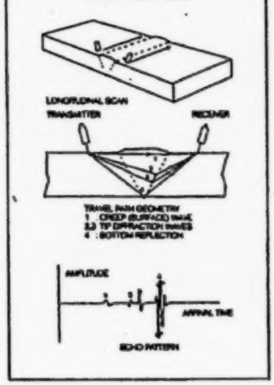
LONGITUDINAL SCAN
TRANSMITTER
RECEIVER
TRAVEL PATH GEOMETRY
1 : CREEP (SURFACE) WAVE
2,3 TIP DIFFRACTION WAVES
4 : BOTTOM REFLECTION
AMPLITUDE
ARRIVAL TIME
ECHO PATTERN

EXAMPLE OF LONGITUDINAL SCAN

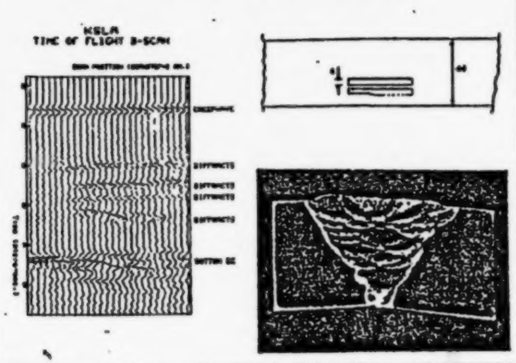

LOCUS CALCULATION AS A GENERAL APPROACH TO ANALYSIS OF TOFD DATA

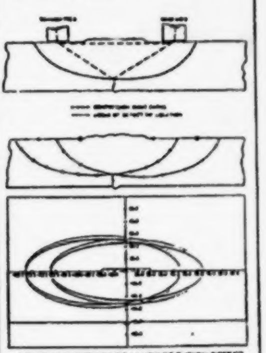

LOCATING THE EDGES OF A LACK OF FUSION DEFECT

SCHEME OF TOFD EQUIPMENT

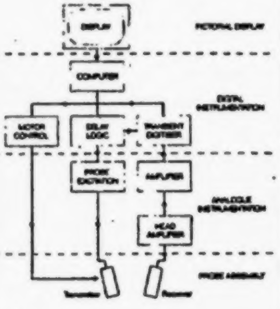
DISPLAY
PICTORIAL DISPLAY
COMPUTER
DIGITAL INSTRUMENTATION
MOTOR CONTROL
DELAY LOGIC
TRANSIENT DIGITISER
PROBE EXCITATION
AMPLIFIER
ANALOGUE INSTRUMENTATION
HEAD AMPLIFIER
PROBE ASSEMBLY
Transmitter
Receiver

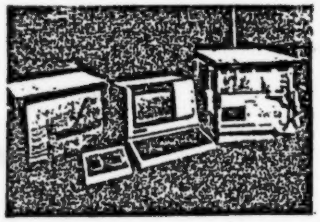

LONGITUDINAL SCANNING TOOL
(operated by diver underwater)

TOFD RESULTS ON A 90° T-NODE

TESTSAMPLE GEOMETRY

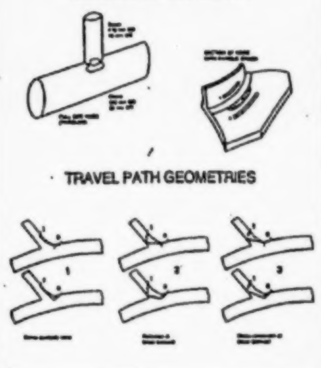

TRAVEL PATH GEOMETRIES

RESULTS

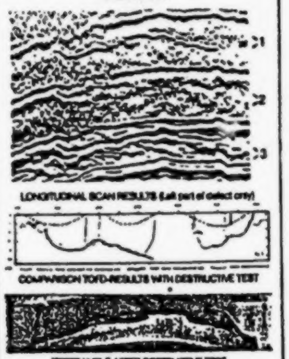

LONGITUDINAL SCAN RESULTS (Left part of defect only)

COMPARISON TOFD-RESULTS WITH DESTRUCTIVE TEST

TESTSAMPLE AFTER DESTRUCTIVE TEST

CONCLUSIONS

- TOFD is very suited for sizing but less suited for detection and characterization
- achievable sizing accuracy: 1 to 2 mm
- thickness of the near surface dead zone: 3 to 6 mm
- TOFD on simple (flat plate like) objects requires simple equipment with easy interpretation;
  TOFD on complex objects (e.g. nodes) or complex (multiple) defects requires dedicated equipment and skilled operators.
- Two validation test of TOFD with divers in a testtank and in 17 m. deep open water have demonstrated the applicability of the technique for use under practical circumstances.

Enclosure 1

MEETPROGRAMMA (planning)		proefstuksoort					
techniek	uitvoerder	vlak 15 & 30 mm	vlak 10 mm	T-platen	T-knoop	+ knoop	split-tee Gasunie
FTR/hand	RTD	4 x 4 (*)	1	1 (*)	1	1	1
TOFD/hand	RTD/Billiton	2 + 3 x 4	-	-	-	1 (-)	-
FTR/MDU	RTD	2	-	-	-	1 (-)	-
TOFD/MDU	RTD	2	-	-	-	1 (-)	-
Lab. app.	RTD	4	1 (2)	1	1	1 (2)	1
Nerason	Nucon	4	1 (2)	2	-	-	-
Zipscan	RTD/Harwell	3	1	-	-	1 (2)	1
Supersaft	RTD/SVC	2 (3)	-	- (2)	1	1 (-)	- (1)
ACPD/DCPD	SGM	4 (7)	- (2)	2	1 (-)	1 (2)	1

Tussen haakjes staat vermeld wat in werkelijkheid is uitgevoerd, indien dit afwijkt van de planning.
(*): Zie voor details tabel 6.1 in referentie 6.

Enclosure 2

REFERENCE TO CONCLUSION NO		proefstuksoort/sample type					
techniek technique	uitvoerder applied by	vlak/flat 15 & 30 mm	vlak/flat 10 mm	T-platen	T-node/knoop	+ nodes /knopen	split-tee Gasunie
FTR/man.	RTD	1	1	1	1	1	1
TOFD/man.	RTD/Billiton	2,4,11	-	-	-	-	-
FTR/MDU	RTD	3	-	-	-	-	-
TOFD/MDU	RTD	3	-	-	-	-	-
Lab. app.	RTD	4,5,6,9,11	4,5,6,9,11	4,5,6	4,5,6,13	6,12,(13)	4,5,6
Nerason	Nucon	4,5,7,9,11	4,5,7,9,11	4,5,7	-	-	-
Zipscan	RTD/Harwell	4,5,8,9,11	4,5,8,9,11	-	-	8,12,(13)	4,5,8
Supersaft	RTD/SVC	14,15,16	-	14-16	14,15,16	17	14,15,16
ACPD/DCPD	SGM	18,19	18,19	18,19	-	18,19	18,19

Enclosure 3
Toepasbaarheid van technieken en systemen voor fouthoogtebepaling; deze tabel geeft een snelle, maar **ongenuanceerde** impressie. Zie de conclusies voor meer details.
Applicability of techniques and systems for flaw hight measurement. This table is for quick reference only; see "Summary and Conclusions" for more details.

	proefstuksoort/sample type					
techniek technique	vlak/flat 15 & 30 mm	vlak/flat 10 mm	T-platen	T-node/knoop	+ nodes /knopen	split-tee Gasunie
FTR/man.	O	-	O	-	-	-
TOFD/man.	+	+/O	-	-	-	-
FTR/MDU	O	-	O	-	-	-
TOFD/MDU	-	-	-	-	-	-
Lab. app.	+	+	+	+	+	+/O
Nerason	+	+	(-)	-	-	-
Zipscan	+	-	+	+	(+)	-
Harw. FMS	+	+	+	+	+	+/O
Supersaft	+	+/O	+	(+)	-	+
ACPD/DCPD	-	-	-	-	-	-

+ goed toepasbaar / well applicable
O beperkt toepasbaar / limited applicability
- slecht of niet toepasbaar / not suitable

Noot: niet alle mogelijke proefstuk/techniek combinaties zijn binnen het project getest; een aantal beoordelingen in de tabel zijn vanuit de ervaringen met andere combinaties geëxtrapoleerd.
Note: not all possible combinations of test samples and techniques have been tested within the project. For combinations which were not tested, the table contains extrapolations from experiences with other combinations.

#510327

(23)

THE MEASUREMENT OF ELASTIC STRAIN FIELDS AND LINE-BROADENING NEAR CRACKS IN LOADED BARS OF HY-80 STEEL

by

T.M. Holden, J.H. Root and J.F. Mecke
AECL Research, Chalk River, Ontario Canada KOJ 1J0
and
J. Porter, Defence Research Establishment Atlantic, Halifax, N.S. B3K 2X0

ABSTRACT

The elastic strain fields in the neighbourhood of 6 mm and 20 mm deep cracks in bars loaded in three-point bending were measured by neutron diffraction. Calculations of the elastic strain field under the known loads included a stress-concentration contribution approximated by linear elastic fracture mechanics (LEFM). Close to the crack tip, the calculated load-induced strains with the LEFM contribution are in reasonable agreement with the measurements although the agreement is not good far from the crack. The diffraction linewidths can be related to the plastic deformation within the region of measurement. A 20% increase in linewidth occurred ahead of and behind the crack tip, and near the uncracked surface adjacent to the central support for the three-point bending. The radius of the enhanced linewidth region was about 5 mm near the crack tip.

1. INTRODUCTION

Recent engineering studies at the Defence Research Establishment Atlantic[1] (DREA) have established that plastic zone development around cracks takes on two distinct patterns depending on whether the crack is deep or whether it is shallow. For deep cracks the plastic zone first develops under load on or near the surface ahead of the crack, whereas for shallow cracks the pattern develops on the surface behind the crack. When the plastic pattern breaks to the top surface, the surface yields and two plastic hinges develop, one on either side of the crack. The surface plastic strains have been measured experimentally by the distortion of photo-etch patterns.

The purpose of the present experiments was twofold. First to measure the elastic strain fields near cracks under load by neutron diffraction and secondly to test whether it is feasible to identify the plastic zones near cracks at depth in the material by line-broadening of the diffraction lines. Two samples were studied with cracks penetrating 6 and 20 mm through the 40 mm thickness of the bar in order to characterize the differences between shallow and deep crack behaviour.

In order to have conventional measurement of the surface stress and in order to assess the applied loads, the samples were instrumented with strain gauges and a calibration experiment was carried out with known loads on an MTS-810 testing machine. Firstly the plastic load limit[2] was calculated for each sample, and then each sample was loaded in 3-point bending to 50% of this limit in the MTS-810 testing machine while monitoring the strain gauges.

Subsequently the sample were placed in a clamp-type three point bending rig supplied by DREA and mounted on the L3 spectrometer at the NRU reactor. Measurements were made at zero load, about half the calibrated load, and at the full calibrated load for each sample. Finally the shallow-crack sample was strained to 80% of the plastic load limit. Measurements of the axial strain response to the applied axial load in 3-point bending were made at the mid-width position as a function of through-thickness location and axial displacement from the crack on a 4mm grid. The diffraction line-broadening was obtained on the same grid.

The present paper summarizes and discusses the experimental findings and is organized as follows: the detailed description of the samples is given in Section 2, the neutron diffraction experiments are described in Section 3, the appropriate theory is reviewed in Section 4 and the results are presented, analyzed and discussed in Section 5.

2. SAMPLES

The samples of high strength low alloy steel were bars 254 mm long, 25.4 mm wide and 40.0 mm thick. The shallow crack, as seen at the surface, penetrated 6mm into the thickness, while the deep crack penetrated 20mm into the thickness. Each sample was instrumented with strain gauges as shown in the sketch of the 6 mm crack sample in Fig 1 which gives the position of each gauge.

The plastic load limit[2] P_L, the load at which the plastic zones from top and bottom surfaces first join, is given by

$$P_L = \frac{4}{3} b W^2_{RL} \frac{Y}{S} \qquad (1)$$

where b is the width of the test piece 24mm, W_{RL} is the thickness of the remaining ligament (34 and 20mm for the shallow and deep crack respectively), Y is the yield strength (80ksi,551.6MPa) and S is the span between supports in a 3-point bend test, 207mm. The plastic load limits were 36.1 kN for the deep crack and 104.3 kN for the shallow crack.

The samples were loaded to 50% of P_L in an MTS-810 testing machine in 5 kN steps for the 6mm crack and 2kN steps for the 20mm crack measuring the strains with strain gauges at each step. The samples were unloaded in the same steps and the strains remeasured to provide a calibration of the strain gauges. The load was ascertained in the neutron experiments by reading the calibrated strain gauges.

3. NEUTRON SCATTERING EXPERIMENTS

The neutron scattering experiments were carried out in the clamp-type 3-point bending rig which is shown mounted on the L3 spectrometer at the NRU reactor in Figure 2. The component of strain measured is along the length of the bar which corresponds to the elongation of the "fibres" of metal caused by the 3-point bending.

The wavelength of neutrons, 2.4824±0.0001Å, produced by reflection from the (113) planes of a Ge single crystal monochromator, was calibrated with Si powder from the National Institute for Standards and Technology. The (110) planes of the body-centred cubic structure of the steel give a diffraction peak near $2\theta=75°$. The instrumental angular width for this experiment has to be minimized in order to see line-broadening effectively and this setup represents a design compromise in the experiment between the angular width of the diffraction peak and the spatial resolution of the experiment. The minimum width observed was 0.44±0.01 deg. The region of intersection of the incident and scattered beams, the gauge volume, over which the strain and widths are averaged in the measurement, was defined by slits of width 2mm and height 2mm in absorbing cadmium placed in the incident and scattered beams.

The lattice spacing for the (110) planes, d_{110}, is related to the diffraction angle $2\theta_{110}$ and the known neutron wavelength, λ, by Bragg's law

$$\lambda = 2d_{110}\sin\theta_{110}. \tag{2}$$

The strain is calculated with respect to lattice spacings far from the crack under zero load, d^{o}_{110}, as follows:

$$\epsilon_{110} = (d_{110} - d^{o}_{110}) / d^{o}_{110}. \tag{3}$$

The values of the reference spacings for the 6mm crack and 20mm crack samples, are 2.0332(1) and 2.0331(1) Å respectively. The measured linewidths, Δ_m in degrees, of the diffraction peaks (FWHM) are determined from the fitted widths of the Gaussian lineshape. The linewidths far from the crack define the values of reference linewidths, Δ_r, which are principally due to the experimental resolution of the instrument with an intrinsic component from the manufacture of the crack. To determine an intrinsic width the reference linewidth is subtracted from the measured linewidth in quadrature as follows:

$$\Delta^2 = \Delta_m^2 - \Delta_r^2 \tag{4}$$

The root mean square strain is obtained by differentiating Bragg's law and is given in terms of the intrinsic FWHM, Δ, by

$$\left(\frac{\Delta d}{d}\right)_{rms} = \cot\theta \ \frac{.\pi\Delta}{720} \tag{5}$$

where the numerical factors convert from degrees at half maximum, to the standard deviation.

The measurements were made at zero load (with the 3-point bending rig just holding the sample) and two higher loads approximately 25 and 50% of P_L for each sample as determined by the gauge readings. In a final experiment the 6mm crack sample was taken to 80% of the plastic load limit, approximately 30% beyond the calibration in an attempt to generate more dramatic effects.

3.1 Linear Elastic Fracture Mechanics

The elastic stress field ahead of a sharp crack calculated within the theory of Linear Elastic Fracture mechanics is given by[3]

$$\sigma_x = \frac{K_I}{\sqrt{2\pi r}} \cos\frac{\theta}{2}\left\{1 - \sin\frac{\theta}{2} \cos\frac{3\theta}{2}\right\} \qquad (6)$$

$$\sigma_y = \frac{K_I}{\sqrt{2\pi r}} \cos\frac{\theta}{2}\left\{1 + \sin\frac{\theta}{2} \cos\frac{3\theta}{2}\right\} \qquad (7)$$

The coordinate axes are given in Figure 1, with the x-axis along the direction of the crack and the y-axis perpendicular to the crack. The distance from the tip is designated r and θ is the angle the position makes with the x-axis. In the approximation of plane stress, which would hold for thin sections or near the surface of the bars, σ_z is set equal to zero. In the interior of the bar, plane strain conditions would approximately hold, $\epsilon_z = 0$. In this case

$$\sigma_z = \nu(\sigma_x + \sigma_y) \qquad (8)$$

where ν is Poisson's Ratio.

The constant K_I is the stress intensity factor which depends on the geometry of the crack and the nature of the load, e.g. bending or uniaxial stress. For the case of 3-point bending, we may use the equation for K_I given by Broek[4]

$$K_I = \frac{PS}{bW^{3/2}}\left\{2.9\left(\frac{a}{W}\right)^{1/2} - 4.6\left(\frac{a}{W}\right)^{3/2} + 21.8\left(\frac{a}{W}\right)^{5/2} - 37.6\left(\frac{a}{W}\right)^{7/2} + 38.7\left(\frac{a}{W}\right)^{9/2}\right\} \qquad (9)$$

where P is the load (kN), S is the span between the supports, 0.207m, W is the beam thickness, a is the crack length and b is the width of the bar. K_I has the value 51.3MPa.$\sqrt{m}$ for a 50.2kN load on the 6mm crack sample and 48.5 MPa.$\sqrt{m}$

for a 17.8kN load on the 20mm crack sample. K_I scales with load for the same geometry.

The expression for the strain ϵ_y in the axial direction which is measured in the experiment is

$$\epsilon_y = \frac{1}{E} (-\nu\sigma_x + \sigma_y - \nu\sigma_z) \qquad (10)$$

For comparison with the strain gauges the bulk Young's modulus E and Poisson's Ratio ν are used. For comparison with the neutron results the diffraction elastic constants are used and both are given in Table 1.

To the strains generated by the stress enhancement under load at the crack tip must be added the applied strain ϵ_{app}, generated by the bending moment and this is given by

$$\epsilon_y^{app}(X,Y) = \frac{1}{E} \frac{3P}{bW^3} (S/2 - Y) \quad (2X - W) \qquad (11)$$

where Y is the axial offset from the crack position and X is the distance through the wall from the uncracked face.

Because of the divergence of the stress field near the crack tip, the value of the stress may exceed the yield point, σ_{ys}, for the material. The radius of the plastic zone, ahead of the crack may be deduced from Equation 7, setting θ=0. The size of the plastic zone is about $2r_y$. For the approximation of plane stress, i.e. near the surface

$$r_y = \frac{1}{2\pi} \left(\frac{K_I}{\sigma_{ys}}\right)^2 \qquad (12)$$

and in the approximation of plane strain i.e. at depth, it is a factor of 3 smaller[3]. For HY80 the yield stress is 80ksi (551.2 MPa). For the highest load applied to the 6mm crack, $P = 98.5$ kN, $r_y^{surface} = 3.8$mm and $r_y^{internal} = 1.3$mm. For the highest load applied to the 20mm crack, $P = 17.8$kN, $r_y^{surface} = 1.2$mm and $r_y^{internal} = 0.4$mm.

To find the macroscopic surface strains under load in a flawed bar, the bar is instrumented at zero load with strain gauges. The change in gauge reading is measured as a function of applied load. This effectively takes as zero reference state the residual strain state of the bar generated by producing the crack. In the case of measurements with neutrons, the residual stress/strain in the bar caused by generating the crack is measured with respect to a reference lattice spacing far from the crack. In order to find the strain generated by loading the bar the reference state is the residual strain state of the bar.

4. RESULTS AND DISCUSSIONS

4.1 Strain Gauge Results

For strain gauges well removed from the crack, for example gauges 10-13 which are 38.1mm from the crack, the effect of the crack is expected to be small, and the strain may be calculated from the applied load. For a load of 47 kN the strain at positions 10-13 calculated with the bulk elastic constants is 10.7×10^{-4}. This compares well with the average gauge readings of

$+11.4\pm0.4\times10^{-4}$ and $-11.3\pm0.3\times10^{-4}$. Likewise for the 20mm crack sample at the maximum load of 17kN, the calculated surface strain is 3.9×10^{-4}, and the average measured surface strains from gauges 10-13 are found to be 4.0 ± 0.1 and $-4.1\pm0.3\times10^{-4}$. This good agreement between the axial strain calculated and measured far from the crack in the calibration gives confidence in calculating the applied moments in the diffraction experiments. Closer to the defect, the effect of the crack is observed. For example at position #8, 10.2mm from the crack on the tensile face, the calculated strain for the 6mm sample at a load of 47kN is $+15.2\times10^{-4}$ whereas the measured strain is 7.1×10^{-4}. The effect of the crack is still important at position #9, 20.3mm from the crack, where the calculated strain is 13.5×10^{-4} and the measured strain is 12.1×10^{-4}.

Turning now to the strain gauge measurements made during the neutron scattering experiments, we use the strains measured on the gauges to calculate the surface stresses knowing the bulk Young's modulus. From the actual beam dimensions and the actual gauge locations, with no calibration factor, we may calculate the loads, P, from Equation 11. From the measured strains in the 3-point bending rig at positions 10-13, far from the crack, we have deduced that the applied loads were 23.5,50.2 and 83.4 kN for the 6mm crack sample and 8.6 and 17.8kN for the 20mm crack sample with an accuracy of ±3%. This accuracy was determined from the spread in strain gauge readings.

4.2 Strains Measured by Neutron Diffraction

The measured strains for the 6mm crack sample at loads of 0, 23.5, 50.2 and 83.4kN are shown as contour maps of strain as a function of position in Figure 3 for the 6mm crack sample and Figure 4 for the 20mm crack sample. Some measurements were made on both sides of the crack to check for symmetry and there was good agreement in these cases. However the data were mainly obtained on one side of the crack. The contour maps of strain are reflected about the line of the crack for ease of visualization.

Several features are noticeable immediately in Figure 3. Behind the crack the axial strain is compressive and independent of the load. A maximum of 4×10^{-4}in residual strain is noted 4mm ahead of the crack in the unloaded specimen. Under load the tensile strain ahead of the crack increases strongly, and at the same time a compressive strain develops on the opposite face. The maximum compressive strain was not found under the central support roller, but displaced 5-10mm to the side. The support roller is thus, in some sense, acting as a constraint in the development of the compressive strain. We believe that this feature would be absent in 4-point bending. The axial gradient of the strain is weak except close to the crack and near the support point.

The same general features are evident in the results for the 20mm crack; in Figure 4 the maximum in strain lies well ahead of the crack tip which comes at X=20mm. A compressive strain is observed behind the crack tip which is nearly independent of load. The behaviour near the support point at the compressive face is complex.

For detailed comparison with linear elastic fracture mechanics and with the strain gauge results we have subtracted off the residual elastic strain (Figure 5 and Figure 6) from the total strain under load. The results for the 6mm crack sample under loads of 50.2 and 83.4kN are shown in Figure 7 and the 20mm crack sample under a load of 17.8kN in Figure 8. The solid lines in each case are the calculated strain from the known loads applied in bending using the diffraction elastic constants for the (110) reflection. The short-dashed lines are the sum of the applied strain and the strains from the stress-enhancement, Equations 6 & 7, in the neighbourhood of the crack. At positions well removed from the crack i.e. 30, 50 mm, the applied strain gives an excellent description of the neutron results, and the dashed curve is in disagreement with the measured strains. We recall that the difference between the dashed and solid curves is the elastic stress field calculated within linear elastic fracture mechanics, Equations 6 and 7. This term is felt a long way from the crack tip because of the slow fall-off of the $1/\sqrt{r}$ term in Equations 6 and 7. This, therefore, appears to be a defect in the theory. It is interesting to note that the slope of the line at 50mm is less than at 30mm, since the moment is smaller in 3-point bending further away from the centre of the span.

Closer to the crack, at 8mm and 16mm, the calculated applied strain is less than the measured compressive strain near the compressive face, but is greater than the strain ahead of the crack. The applied strain line overestimates the strain behind the crack (shown dashed here) since the crack cannot support an axial stress. The deviations from the applied load behaviour are a maximum near the crack. The most dramatic effects are seen in the case of the largest applied load. The prediction of linear elastic fracture mechanics, shown dotted, overestimates the magnitude of the elastic strain. The strain gauge results of the total surface strain, elastic plus plastic, are included in Figures 7 & 8 and it is seen that there is good qualitative agreement between them and the elastic diffraction strains where they may be directly compared even though they are in different physical locations and even though strain gauges measure the total elastic plus plastic strain.

In retrospect it would have been a better procedure to measure the residual strain in the samples before loading the samples in the MTS-810 testing machine. This would have settled without any doubt that the residual strains originate in the fabrication of the fatigue crack. At present we have not proved that this is the cause of the residual strains although this remains likely to be correct.

4.3 Linewidths of the Diffraction Peaks

The intrinsic linewidths of diffraction peaks may have several causes, such as high dislocation density indicating plastic deformation or cold work, or a large variation of elastic strain within the set of correctly oriented grains fulfilling the diffraction condition. In a trivial way, a strong strain gradient within the gauge volume can also generate apparent widths although the gradients obtained in the present experiments are not large enough to give broadening. The diffraction linewidths have a magnitude between 0.4 and 0.5 deg. with a typical uncertainty of ±3%. The largest part of the linewidth originates in the instrumental resolution, and the intrinsic contributions add in quadrature. This uncertainty limits the information available from the linewidths. The results for the 6mm crack are plotted as a function of both position and load in Figure 9. The results far (20-50mm) from the crack show a significant through-thickness variation which is load independent and which presumably originates in the manufacture of the bar. The minimum linewidth is 0.445° and the scatter is statistically consistent with the estimated uncertainties. The curve drawn through the data for 20-50mm is reproduced for all the other distances as a base-line against which to measure crack or load induced effects. There are no additional contributions to the linewidth until the offset from the crack is 8mm or less. An intrinsic width is observed extending 12mm in from the compressive face at a load of 83.4kN. At a displacement of 4mm from the centreline an intrinsic width which appears to be load independent is observed at the crack tip. A load-dependent contribution is observed near the compressive face. On the centreline a 20% increase of linewidth occurs at the crack tip which is independent of load. The intrinsic linewidth corresponding to the maximum increase is 0.29±0.05°, and the rms strain is $(14.3\pm2.5)\times10^{-4}$. The width increase has disappeared 5mm from the location of the maximum. A load-dependent enhancement of the width is observed at the compressive face which extends 10mm into the material at a load of 83.4kN but only 2mm for the lower loads.

We conclude that the region of enhanced width with a radius of about 5mm is the plastic zone near the crack tip, since it is load independent.

Analogous results for the 20mm crack sample are shown in Figure 10. For this sample the through-wall variation far from the crack (20-50mm) is very slight, as indicated by the curve drawn through the points which serves as a baseline for the closer distances. In this case the region of enhancement of linewidth is restricted to the results on the centreline and it has disappeared 2mm ahead of the crack and 4mm laterally displaced. A region of enhanced width extends behind the tip of the crack to the tensile face of the bar and this effect is also visible 4mm to the side of the crack. The magnitude of the enhancement at the peak is 0.29±0.02 deg [rms strain = $(14.3\pm0.9)\times10^{-4}$] and behind the crack the intrinsic width is 0.15±0.07 deg [rms strain $(7.2\pm3.6)\times10^{-4}$]. The location of the peak in width is very close to the end of the crack and is offset from the peak in the strain field. The region of enhanced width 2mm around the crack tip is tentatively identified as the plastic zone. Measurements of the peak widths for specimens with known amounts of cold work should be made in order to correlate the effects in the cracked bars with plastic damage.

It would be valuable to compare the present strain results with finite element calculations of the elastic strain field within the 3-point bending geometry. This is because the existence of the support roller opposite the crack certainly acts in a constraining fashion with a strong perturbation of the expected stress enhancement field near the compressive face. It is possible to separate out the elastic and plastic parts of the strain field in the calculation and make the appropriate comparison. Linear elastic fracture mechanics does not seem to be capable of describing the results near the crack even though the calculated plastic zone sizes (Equation 12) are quite localized. It will be interesting to compare the predicted plastic zone size and shape with the regions of enhanced width seen in this experiment.

It would be very useful to make measurements on a photo-etched sample under load. In this way the plastic and elastic surface properties could be established and the plastic and elastic properties at depth could be found by neutron diffraction.

5.0 ACKNOWLEDGEMENTS

We wish to acknowledge the helpful advice of B.L. Wotton in making the strain gauge calibration and L.E. McEwan in preparing jigs to mount the bending rig on the spectrometer. R.H. Hosbons provided important guidance in the application of fracture mechanics.

6.0 REFERENCES

1. "A general discussion of short crack fracture", DREA discussion document, J.R. Matthews, J.F. Porter, C.V. Hyatt and K.J. Karis Allen. Proceedings of the Conference on shallow crack fracture mechanics, toughness tests and applications. Cambridge, England, 23-24 September 1992.

2. Standard Test Method for J_{ic}, a measure of fracture toughness. ASTM Standard E813-89.

3. "Fracture and Fatigue Control in Structures". S.T. Rolfe and J.M. Barsom (Prentice-Hall Inc.: New Jersey) 1977.

4. "Elementary Engineering Fracture Mechanics" D. Broek (Martinus-Nijhoof: Dordrecht) 1986.

5. D.J. Dever, J. Appl. Phys. 43, 2393 (1972.

6. E. Kröner, Z. Physik 151, 504 (1958)

TABLE 1

CALCULATED AND EXPERIMENTAL ELASTIC CONSTANTS FOR IRON

E bulk	(calc, a)	213 GPa
ν bulk	(calc)	0.288
E bulk	(experiment, b)	211 GPa
ν bulk	(experiment)	0.293
E_{110}	(calc, a)	225 GPa
ν_{110}	(calc)	0.276

a Calculated from the elastic constants for Fe[5] by the Kröner method[6]

b Smithells' Metals Reference Book, Sixth Edition, 15-5 Edited by E.A. Brandes (Butterworth and Co.)

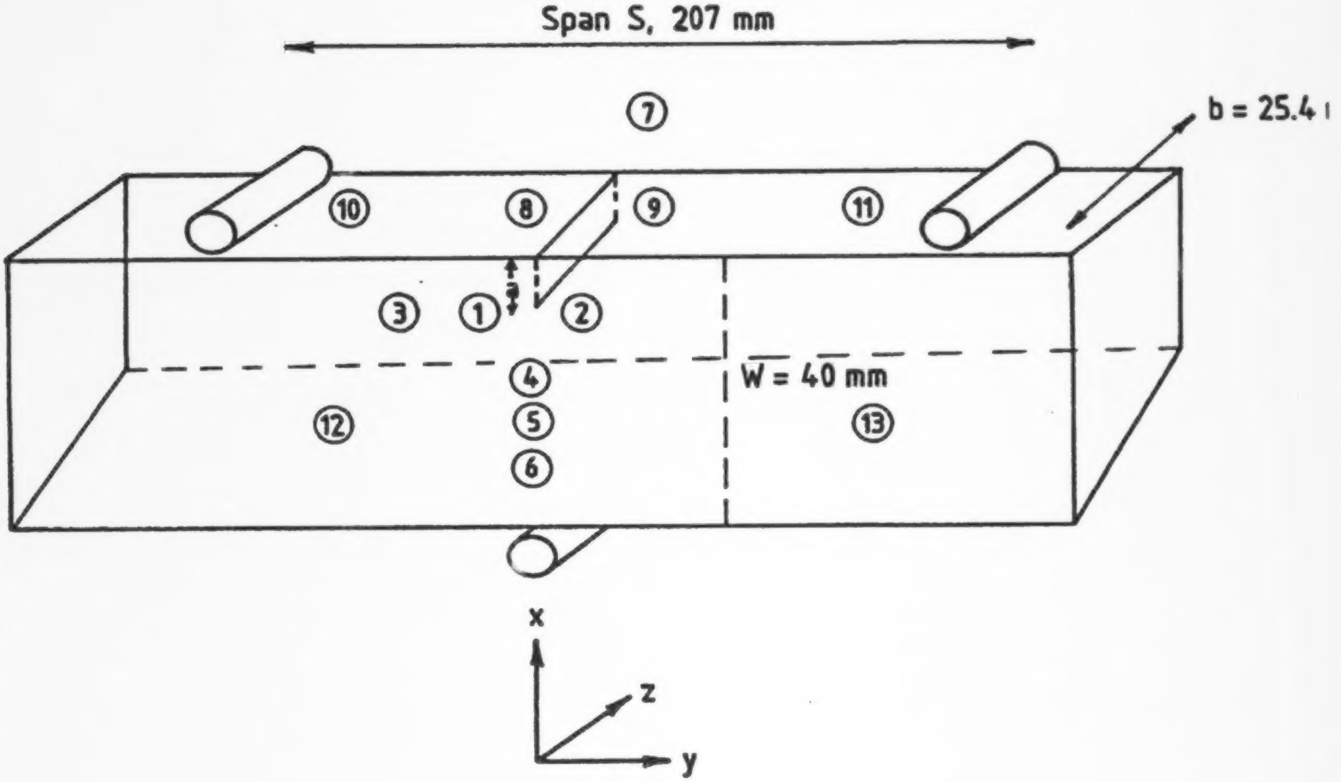

Fig. 1 Sketch of the bar, showing the location of gauges 1-13, three-point bending supports, dimensions and the coordinate scheme adopted. The strain gauges 4-6 are positioned the same distances from the crack tip for both 6mm and 20 mm crack samples. The crack is represented by a planar section penetrating into the bar and the shallow crack is shown here. The crack length, that is the penetration of the crack into the material is denoted by a.

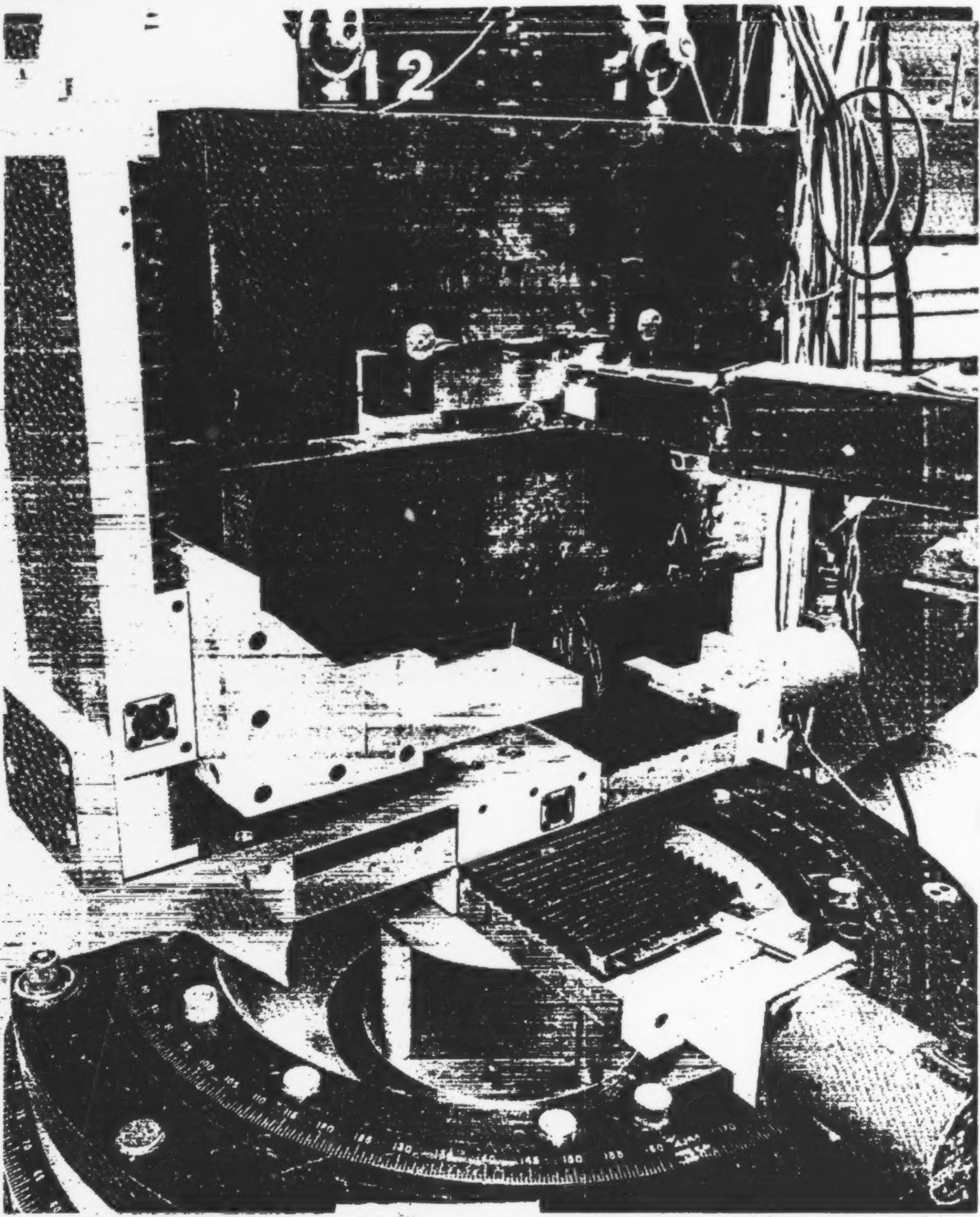

Fig. 2 Photograph of the 6 mm crack sample mounted in the 3-point bending rig on the L3 spectrometer at the NRU reactor. The X-Y-Z translator system is clearly seen supporting the rig. The snout holding the slit defining the scattered beam points at the sample from the right hand side.

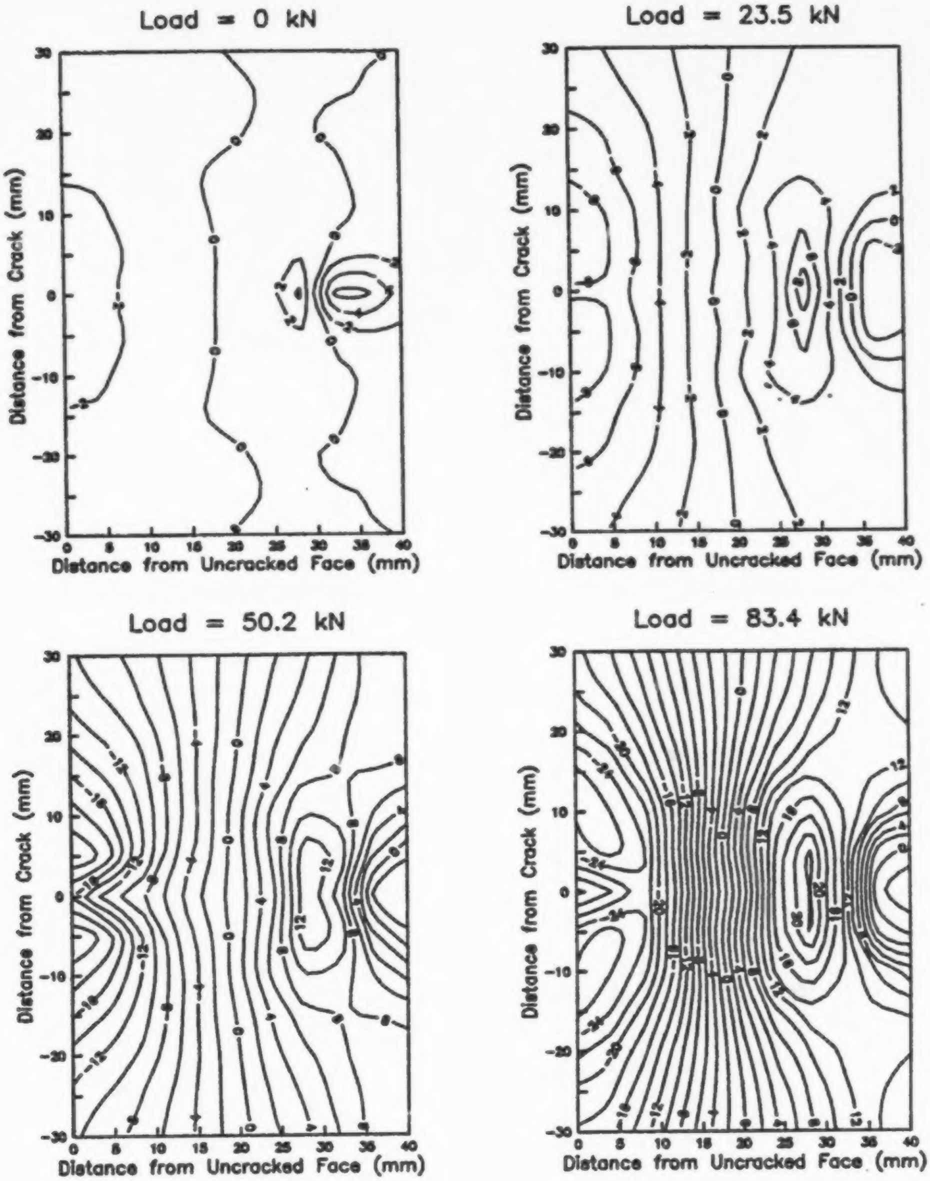

Fig. 3 Contour maps of strain as a function of distance from the uncracked face and lateral distance from the crack plane for the 6 mm crack sample at loads of 0, 23.5, 50.2 and 83.4 kN.

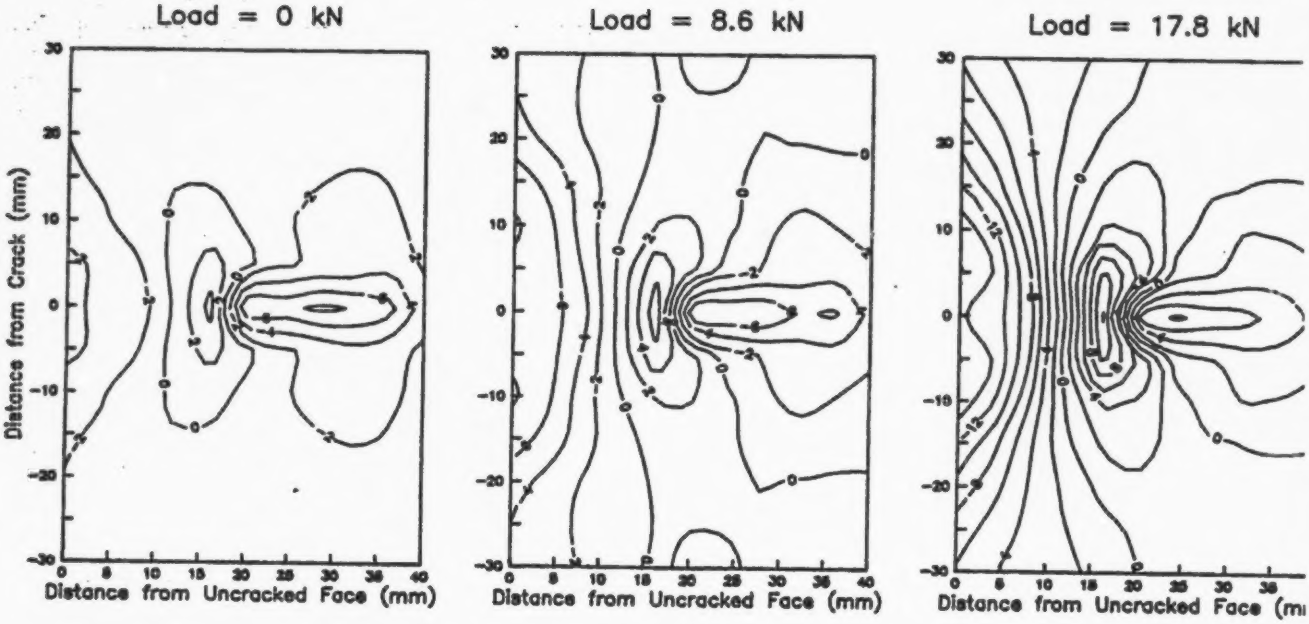
Load = 0 kN

Load = 8.6 kN

Load = 17.8 kN

Fig. 4 Contour maps of strain as a function of distance from the uncracked face and lateral distance from the crack plane for the 20 mm crack sample at loads of zero, 8.6 and 17.8 kN.

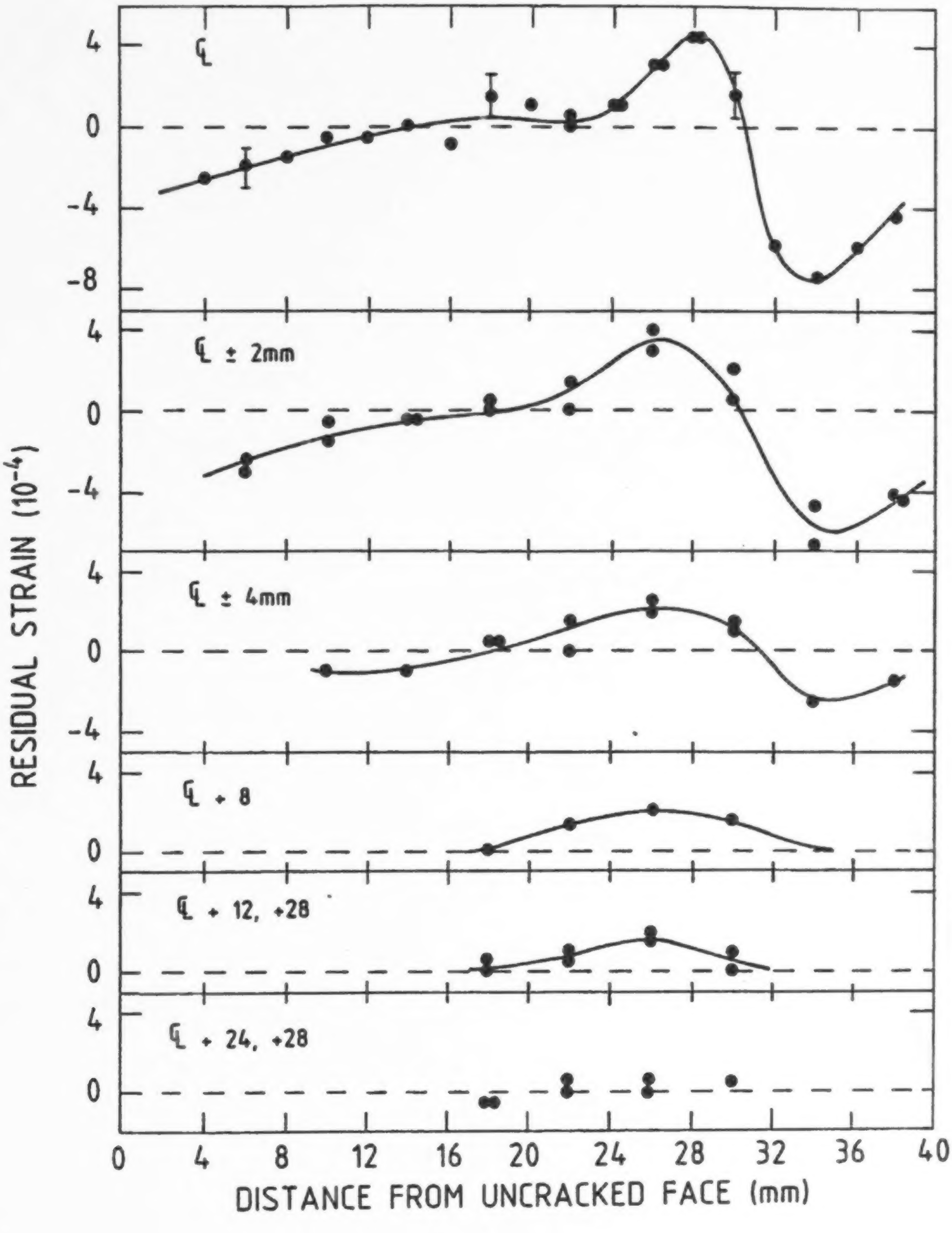

Fig. 5 Residual strains as a function of through-wall position at zero load for the 6 mm shallow crack sample. The different panels denote the results at different lateral displacements from the centreline, C_L, of the crack.

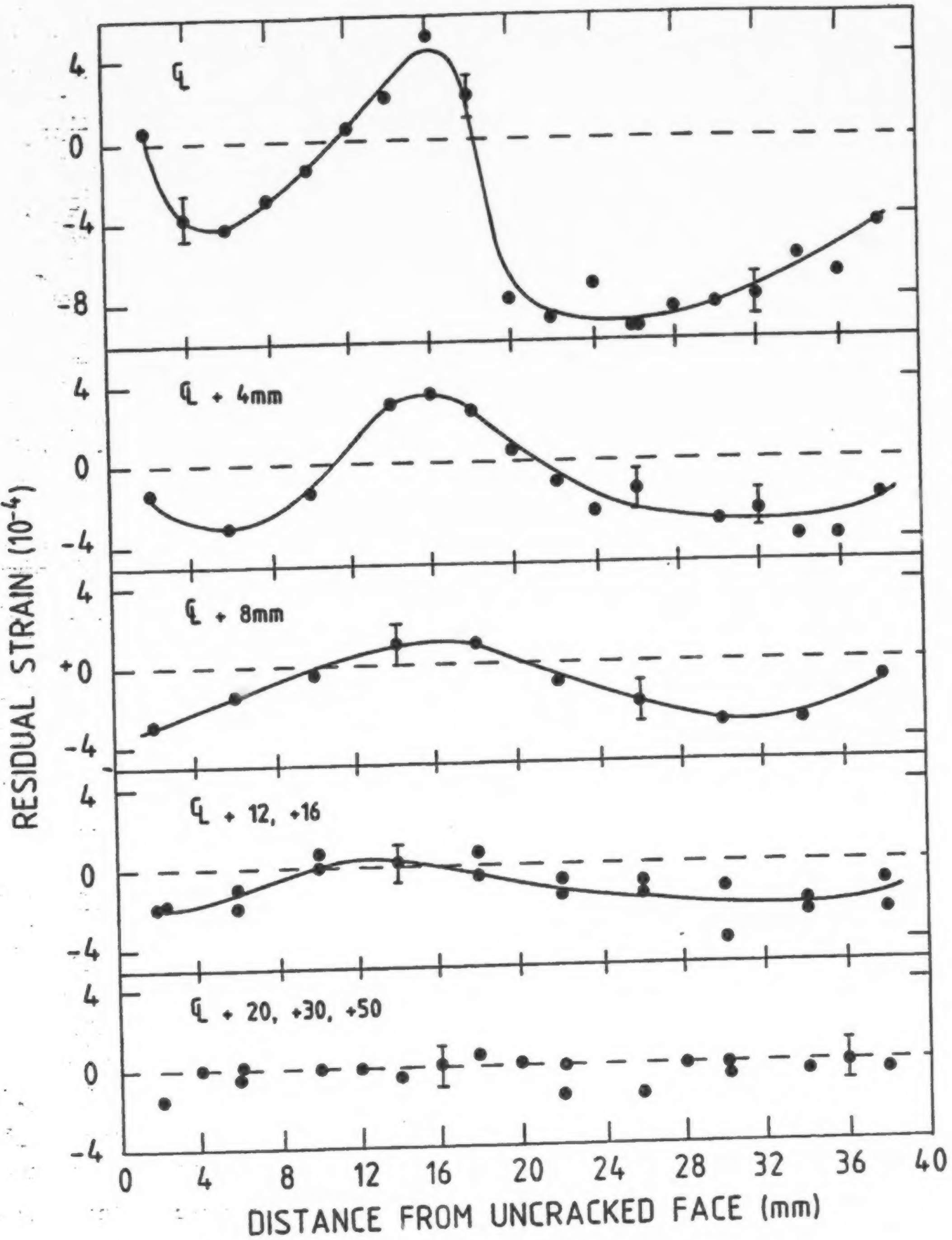

Fig. 6 Residual strains as a function of through-wall position at zero load for the 20 mm deep crack sample. The different panels denote the results at different lateral displacements from the centreline, C_L, of the crack.

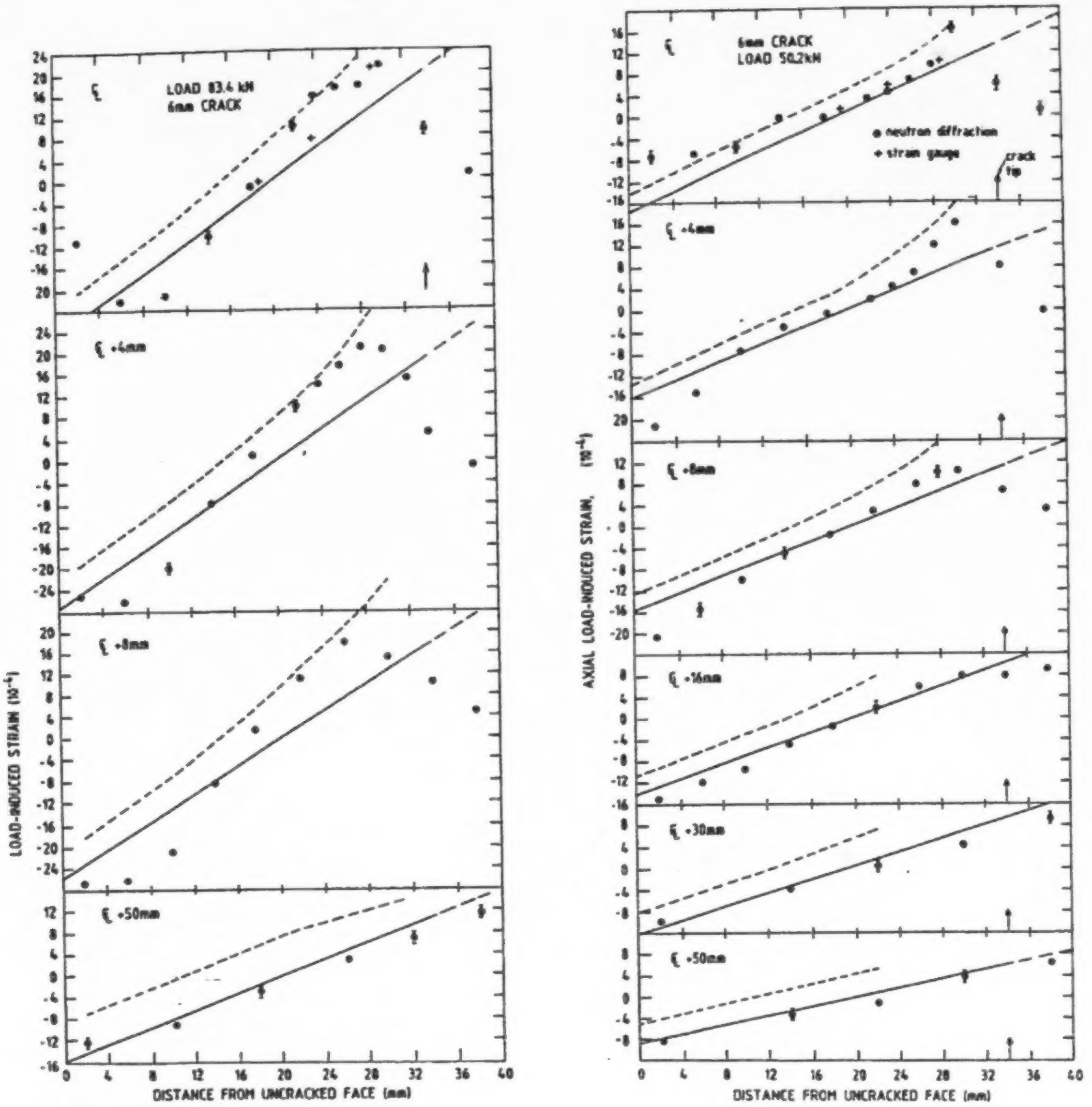

Fig. 7 Load-induced strain measured by neutron diffraction and by strain gauges as a function of position for the 6 mm shallow crack sample. Crosses denote surface strains. The solid curves are calculated from the known applied moment and are indicated by dashed lines at locations closer to the uncracked face than the penetration of the crack. Dash short dashed curves indicate the contribution to the strain from the stress enhancement calculated by linear elastic fracture mechanics.

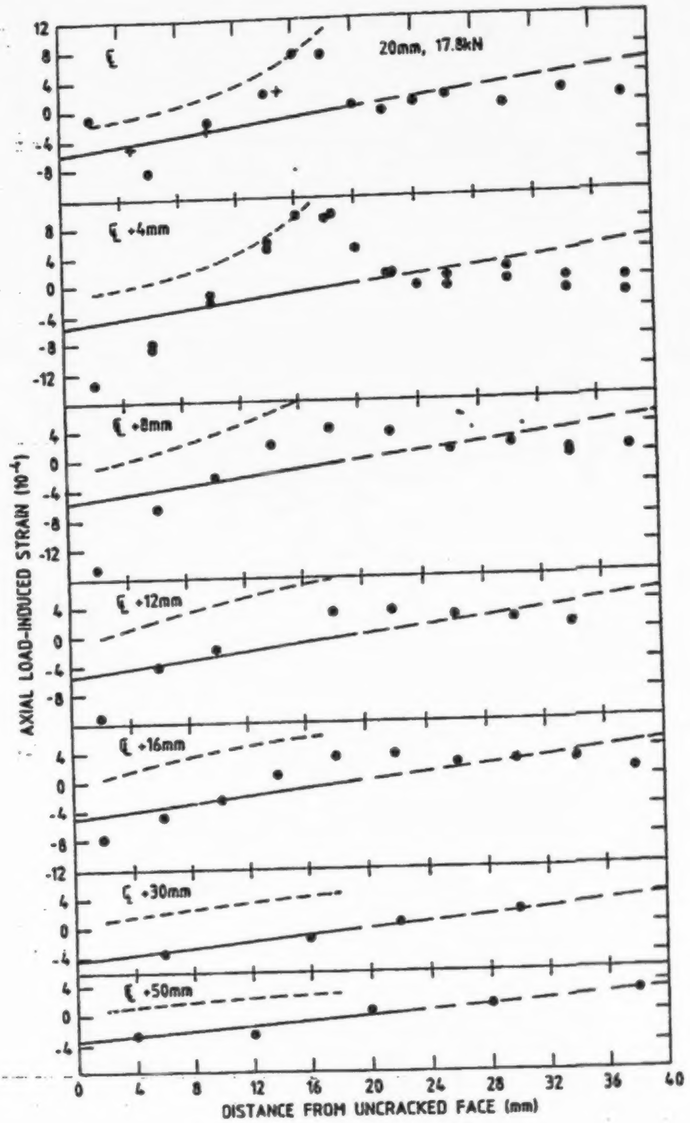

Fig. 8 Load-induced strain measured by neutron diffraction and by strain gauges as a function of position for the 20 mm deep crack sample. Crosses indicate surface strains. The solid curves are calculated from the known applied moment and are indicated by dashed lines at locations closer to the uncracked face than the penetration of the crack. Short dashed curves indicate the contribution to the strain from the stress enhancement calculated by linear elastic fracture mechanics.

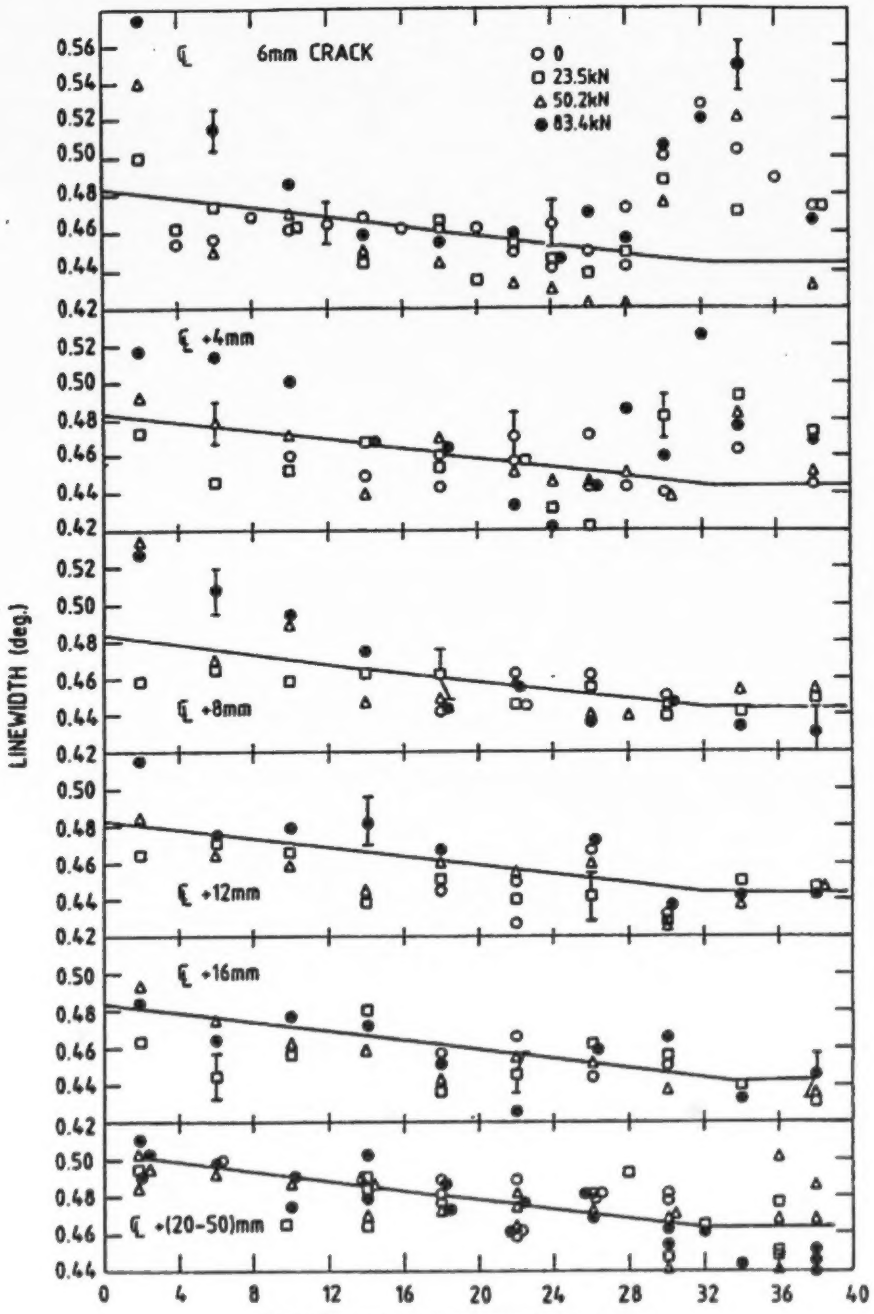

Fig. 9 Measured linewidths as a function of position for the 6 mm shallow crack sample. The solid curve through the data points is the best average width far from the crack which presumably originates in the history of plasticity of the bar. This result is reproduced in the other panels so as to indicate the widths associated with the crack. Enhanced linewidths are observed near the crack tip and opposite the tip on the compressive face.

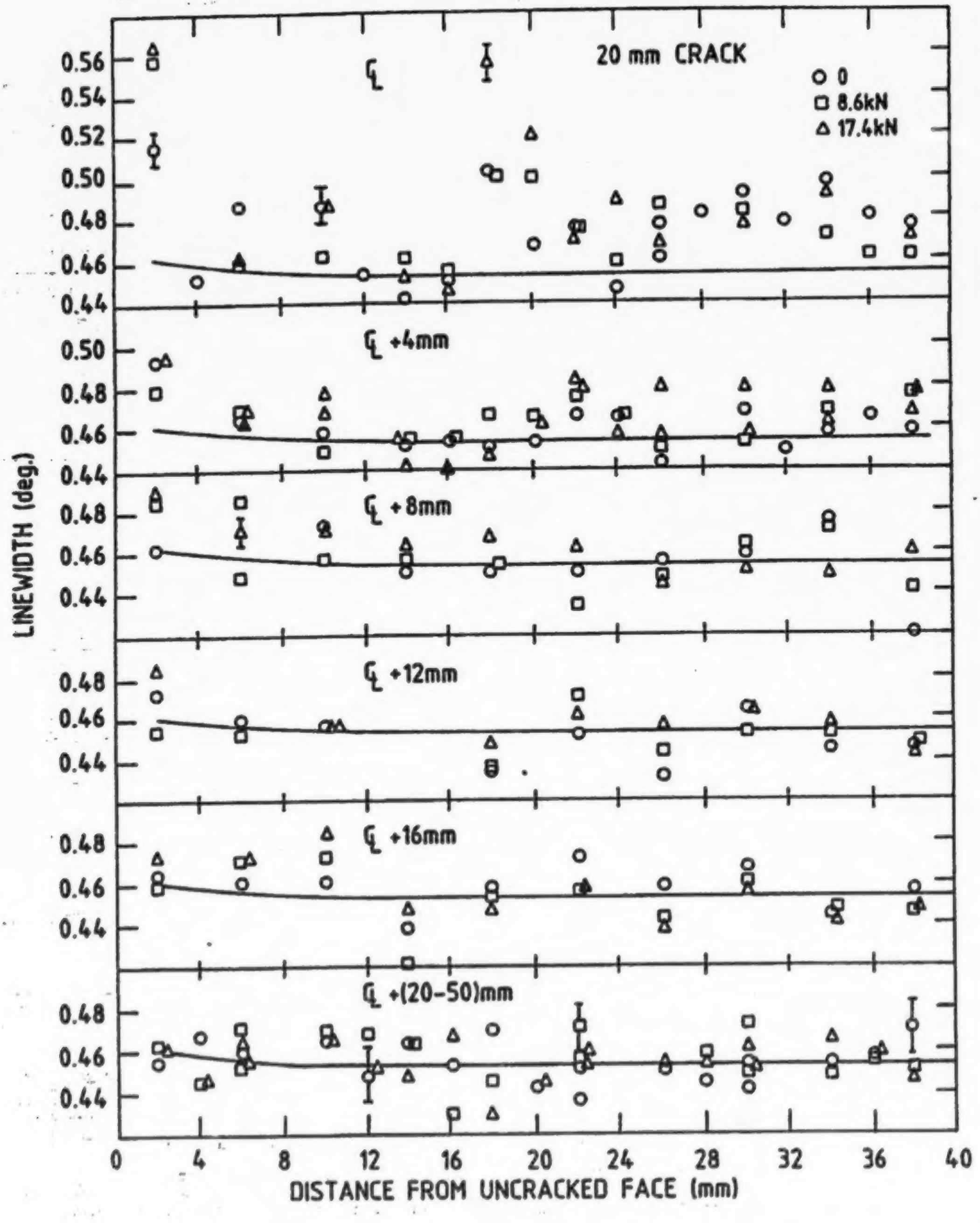

Fig. 10 Measured linewidths as a function of position for the 20 mm crack sample. The solid curve through the data points is the best average width far from the crack, which may originate in the plastic history of the bar. This result is reproduced in the other panels to indicate the widths specifically associated with the crack. Enhanced linewidths are observed near the crack tip and opposite the tip on the compressive face.

#510328 ②

DEVELOPMENT OF CAN/MIL HYW700QT STEEL

by G.R. Labbé, R. René, J.F. Porter and C.E. Billard

ADM(EM)/DGMEM/DSE
National Defence Headquarters
MGen George R. Pearkes Building
Ottawa, Ontario
K1A 0K2

*** ABSTRACT ***

As directed by the Scientific Authority, and contracted out to M.I.L. Davie Inc., Lévis, Quebec, the goal of this project was to develop a Canadian technology for the production of an high strength weldable steel, primarily for pressure hull application, as well as, for surface fleet and/or offshore application using a lower thickness process. A history of the first phase of the project will be covered, including the establishment of a consortium to produce quenched and tempered rolled plates, the mechanical properties of the steel, and the characterization of the steel with regards to welding cycles. The initial phase of Explosion Bulge Test will be discussed. A way ahead for the next phases, including filler material and weld evaluation will also be discussed as conclusion.

The consortium which is composed of SLATER STEEL as slab producer, IPSCO Inc. as roller, and ALGOMA STEEL as heat treater was established by the prime contractor. Approximately 31 metric tons of heat treated steel plates were acquired for evaluation. Promising mechanical properties were found such as yield strength (>118 ksi), charpy at -85°C (>37 ft-lb), and dynamic tear values at -40° (500 ft-lb). Also, nil ductility temperature was found below -100°C, which makes the steel ideal for low temperature applications. Explosion bulge tests performed in Dartmouth, Nova Scotia, with the Defence Research Establishment Atlantic (DREA) collaboration, demonstrated that the material can sustain high level of dynamic plastic deformation prior to rupture. Finally, over 1600 implants were welded and monitored for thermal fluctuations. The results were successfully collected and treated to draw the continuous cooling transformation diagrams and related abacuses.

DIRECTORATE
DSE
6
SHIP ENGINEERING

Metallic Materials

Metallic Materials

DEVELOPMENT OF CANADIAN STEEL AND WELDING PROCEDURES AND SPECIFICATION FOR SUBMARINE PRESSURE HULLS

April 1993

CONTENT

PART 1 ----------> OPENING REMARKS

PART 2 ----------> DEVELOPMENT PROJECT

PART 3 ----------> CONCLUSION

Metallic Materials

REQUIREMENT

TO DEVELOP PROCEDURES FOR THE WELDING OF HIGH STRENGTH, WELDABLE, QUENCHED AND TEMPERED STEEL OF THE HY100 TYPE WHICH WILL BE USED PRIMARILY IN THE FABRICATION AND/OR REPAIR OF SUBMARINE PRESSURE HULLS.

Metallic Materials

SCOPE

1.- NEED FOR ADVANCED WELDING TECHNIQUES.

2.- IMPROVE ADEQUACY OF WELDING TECHNIQUES.

3.- REDUCE HIGH COSTS OF WELD REWORK.

4.- OPTIMIZE THE WELDING PROCEDURES.

5.- OPEN ACCESS TO STEEL AVAILABILITY WITHIN CANADIAN BOUNDARIES.

SCOPE (Cont'd)

6.- PROVIDE MEANS TO WRITE STANDARDS FOR STEEL FABRICATION AND SPECIFICATIONS FOR THE WELDING OF THAT STEEL.

7. ENSURE THE APPLICATION OF DEPARTMENTAL POLICY TO ENCOURAGE INDUSTRIAL PARTICIPATION IN DEVELOPMENT, DESIGN AND FABRICATION OF MILITARY PROJECTS.

Metallic Materials

MATRIX

SCIENTIFIC AUTHORITY ----------> Mr. G.R. Labbé
DSE 6

PROJECT DIRECTOR ---------------> Dr. J.L. Kennedy
DRDM 8

PROCUREMENT MANAGER -----> Mr. T.W. Patrick
DSS/SPO

PROCUREMENT OFFICER --------> CPO2 S.M. Decary
DPSupM 2

Metallic Materials

CONTRACTOR

MIL DAVIE Inc.
22 George D. Davie
Lévis-Lauzon, Québec
G6V 6N7

(418) 837-5841

Metallic Materials

PHASING

PHASE	SERIES	ITEM
I	1000	Characterization of Canadian HYW700QT Steel
II	2000	Evaluation of Filler Materials
III	3000	Welding Procedures
IV	4000	Technical Specification Documentation

Metallic Materials

MILESTONES

PHASE	ESTIMATED DATES
I	21 May 93
II	15 Sep 93
III	29 Apr 94
IV	27 May 94

COST

DATA AS PER MAR 93 FORECAST

TOTAL ($000) -----> $5,341

FY	88/89	89/90	90/91	91/92	92/93	93/94	94/95	95/96	SUBYRS
BY	83	353	1,067	825	1,140	950	365	227	331

CRAD MEETING – HALIFAX, April 29, 1993

STRUCTURE OF THE CONFERENCE

PART 1: OPENING REMARKS AND CONTRACTUAL ASPECTS (DND)

SLIDE #	CONTENT	SUBJECT OF DISCUSSION	TIME
N/A	N/A		10 min.

Total: 3 OVERHEADS

PART 2: STEEL DEVELOPMENT PROJECT:

2a: INTRODUCTION (MIL)

SLIDE #	CONTENT	SUBJECT OF DISCUSSION	TIME
1	PROJECT TITLE	BUDGET, SCHEDULE	10 min.
2	PHASES	DESCRIPTION OF EACH PHASE	
3	GANTT CHART	STATUS OF THE PROJECT:	
4	LIST OF SUBJECTS	CONFERENCE PLAN:	

Total: 4 SLIDES

2b: HISTORICAL REVIEW OF STEEL ACQUISITION (METASOUDAGE)

SLIDE #	CONTENT	SUBJECT OF DISCUSSION	TIME
N/A	N/A		15 min.

Total: 12 SLIDES

2c: PRELIMINARY MECHANICAL PROPERTIES (MIL)

SLIDE #	CONTENT	SUBJECT OF DISCUSSION	TIME
5	SUB-PHASE TITLE	INTRODUCTION TO MECHANICAL TESTS	5 min.
6	MECHANICAL PROPERTIES	TENSION, CHARPY, CTOD, DW, DT, HARDNESS, ETC MELT I AND II + ANTICIPATED MELT II RESULTS	

Total: 2 SLIDES

2d: EXPLOSION BULGE TEST (DREA)

SLIDE #	CONTENT	SUBJECT OF DISCUSSION	TIME
N/A	N/A		15 min.

Total: 12 OVERHEADS

2e: STEEL CHARACTERIZATION WITH REGARDS TO THERMAL CYCLES (MIL)

SLIDE #	CONTENT	SUBJECT OF DISCUSSION	TIME
7	SUB-PHASE TITLE	INTRODUCTION TO STEEL CHARACTERIZATION USING THE IMPLANT METHOD	15 min.
8	PLAN OF THIS PART	LIST OF COVERED SUBJECTS	
9	LIST OF AVAILABLE METHODS	DESCRIPTION OF THE METHODS AND METHOD SELECTION	
10	SCKETCH OF AN IMPLANT	PRINCIPLE OF THE METHOD	
11	PHOTO OF AN IMPLANT	DESCRIPTION OF THE PHOTO, HARDNESS MEASUREMENTS	
12	CRUDE DATA POINTS	DESCRIPTION OF THE DATA POINTS AND CURVE ASPECT	
13	COOLING PART OF THE CRUDE DATA CURVE AND LINEAR REGRESSION CURVE	DESCRIPTION OF THE DADA ANALYSIS METHOD AND FINDING OF Tr8-5 AND Tr7-3	
14	RESULTING DATA POINTS ON CCT DIAGRAMS	DESCRIPTION OF DATA POINTS, NUMBER OF TEST PERFORMED COOLING TIME CRITERION	
15	RESULTING CCT DIAGRAM WITH HARDNESS CURVE	DESCRIPTION OF CCT DIAGRAM	
16	ABACUS OF ENERGY vs Tr	DESCRIPTION OF COOLING TIME ABACUS	
17	CCT AND ABACUS	USES OF CURVES AND ABACUSES	

Total: 11 SLIDES

2f: WAY AHEAD (MIL)

SLIDE #	CONTENT	SUBJECT OF DISCUSSION	TIME
18	LIST OF NEXT PHASES	DESCRIPTION OF PHASES TO COME	5 min.

Total: 1 SLIDE

PART 3: QUESTION PERIOD (DND)

SLIDE #	CONTENT	SUBJECT OF DISCUSSION	TIME
1	PROJECT TITLE	QUESTIONS	10 min.

Total: 1 SLIDE

TOTAL NUMBER OF SLIDES/OVERHEADS: 46 **TOTAL TIME: 1h25min.**

disk 20: d:\tableaux\CRADMEET.wk1

(24)

5 th CF/CRAD MEETING

DEVELOPMENT OF
CAN/MIL HYW700QT STEEL

MIL DAVIE INC.

DEVELOPMENT OF
CAN/MIL HYW700QT STEEL

Covered Subjects

- General Overview of the Project
- Historical Review of Steel Acquisition
- Mechanical Properties
- Steel Characterization - Implant Test
- Explosion Bulge Test Trials

MIL DAVIE INC.

DEVELOPMENT OF
CAN/MIL HYW700QT STEEL

● **General Overview of the Project**

○ Historical Review of Steel Acquisition

○ Mechanical Properties

○ Steel Characterization - Implant Test

○ Explosion Bulge Test Trials

MIL DAVIE INC.

General Overview

The four phases of the project

- Phase I : Steel Acquisition
- Phase II : Filler Material Evaluation
- Phase III: Development of Welding Procedures
- Phase IV: Writing of Reports and Specifications

MIL DAVIE INC.

DEVELOPMENT OF CAN/MIL HYW700QT STEEL
WORK PLANNING

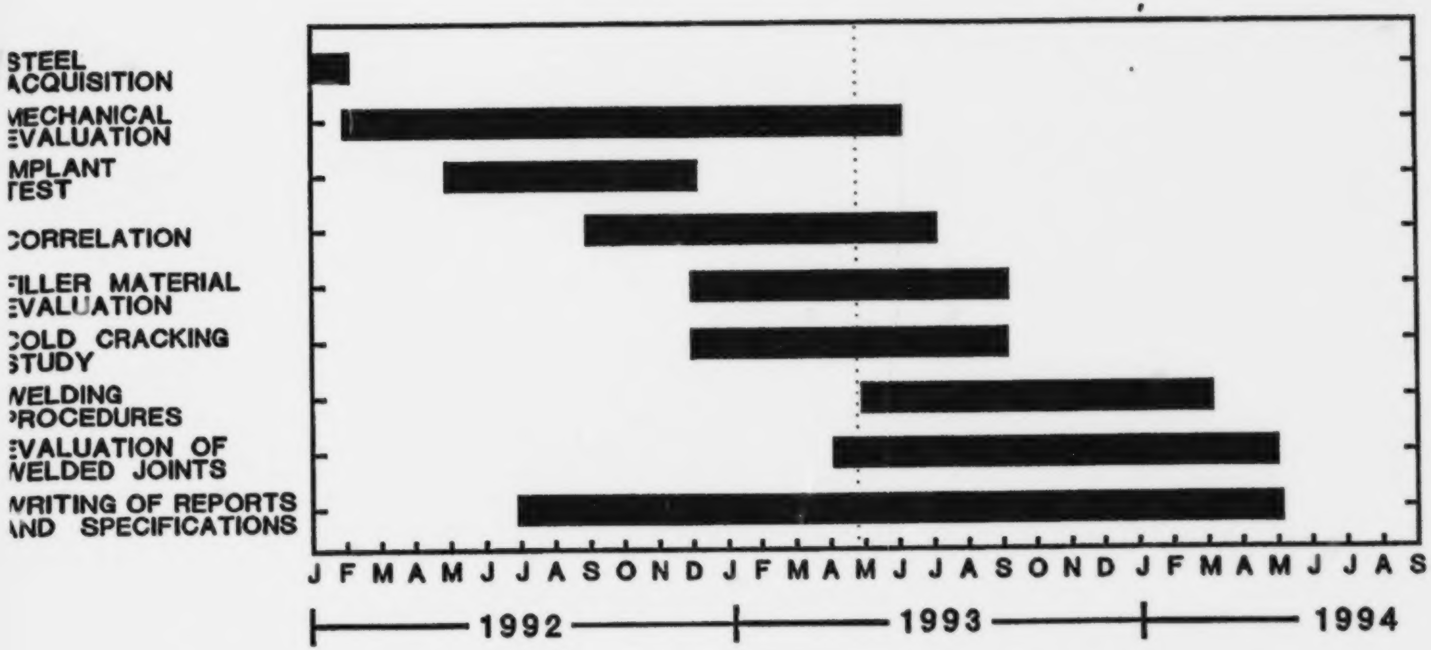

MIL DAVIE INC.

DEVELOPMENT OF
CAN/MIL HYW700QT STEEL

○ General Overview of the Project
● **Historical Review of Steel Acquisition**
○ Mechanical Properties
○ Steel Characterization - Implant Test
○ Explosion Bulge Test Trials

MIL DAVIE INC.

DEVELOPMENT OF
CAN/MIL HYW700QT STEEL

○ General Overview of the Project
○ Historical Review of Steel Acquisition
● **Mechanical Properties**
○ Steel Characterization - Implant Test
○ Explosion Bulge Test Trials

MIL DAVIE INC.

HYW700QT STEEL
MECHANICAL PROPERTIES

	HARDNESS	CVNT AT -85 °C	NDT	DTE AT -40 °C	TENSILE			
					YS	UTS	E	R
Melt I	26 HRc	37 ft-lb	-105 °C	500 ft-lb	118 ksi	130 ksi	21%	68%
Melt II	28 HRc	45 ft-lb	-105 °C	>500 ft-lb	120 ksi	135 ksi	20%	65%

MIL DAVIE INC.

DEVELOPMENT OF CAN/MIL HYW700QT STEEL

○ General Overview of the Project

○ Historical Review of Steel Acquisition

○ Mechanical Properties

● **Steel Characterization - Implant Test**

○ Explosion Bulge Test Trials

MIL DAVIE INC.

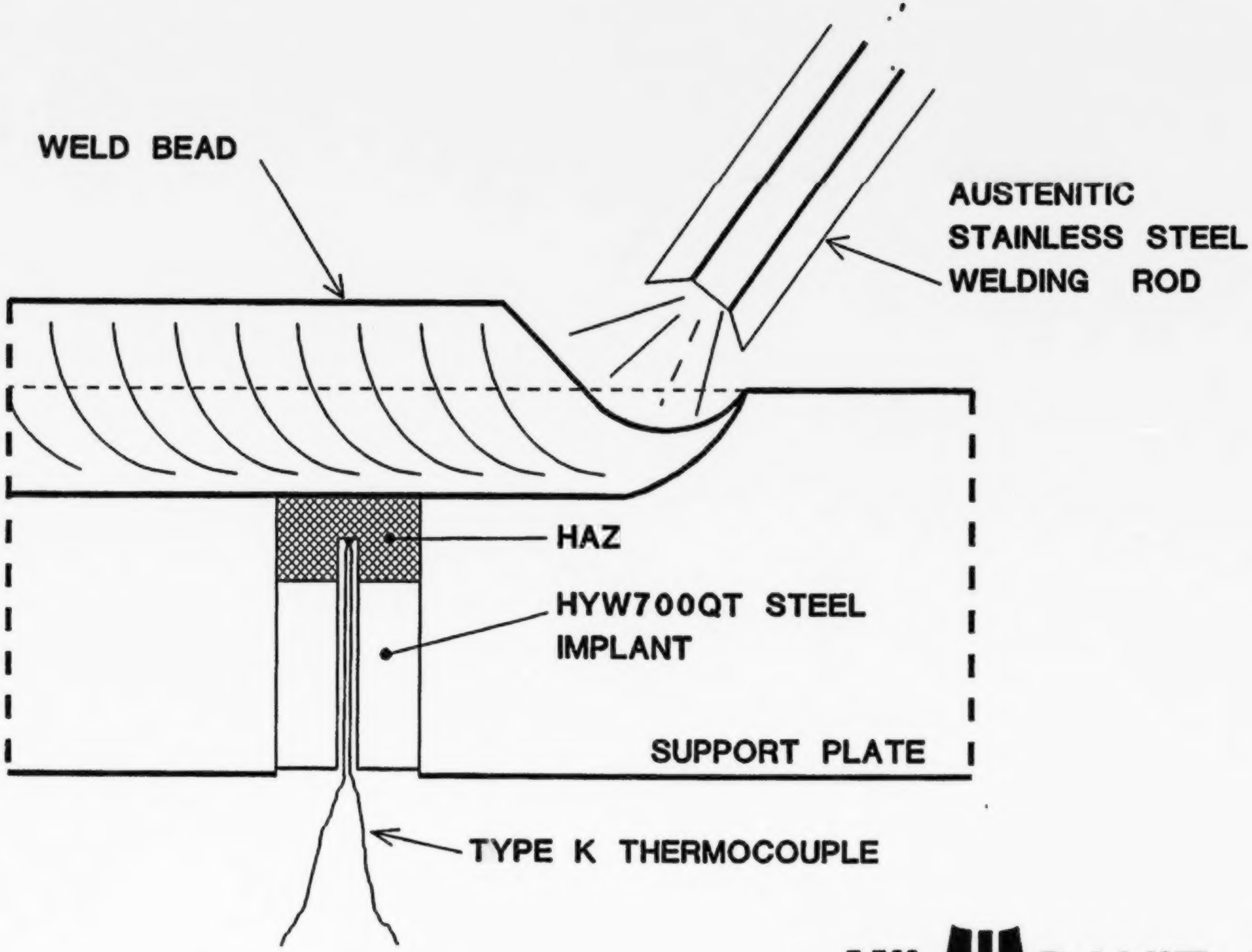
WELD BEAD
AUSTENITIC STAINLESS STEEL WELDING ROD
HAZ
HYW700QT STEEL IMPLANT
SUPPORT PLATE
TYPE K THERMOCOUPLE

MIL DAVIE INC.

IMPLANT TEST DATA CURVE

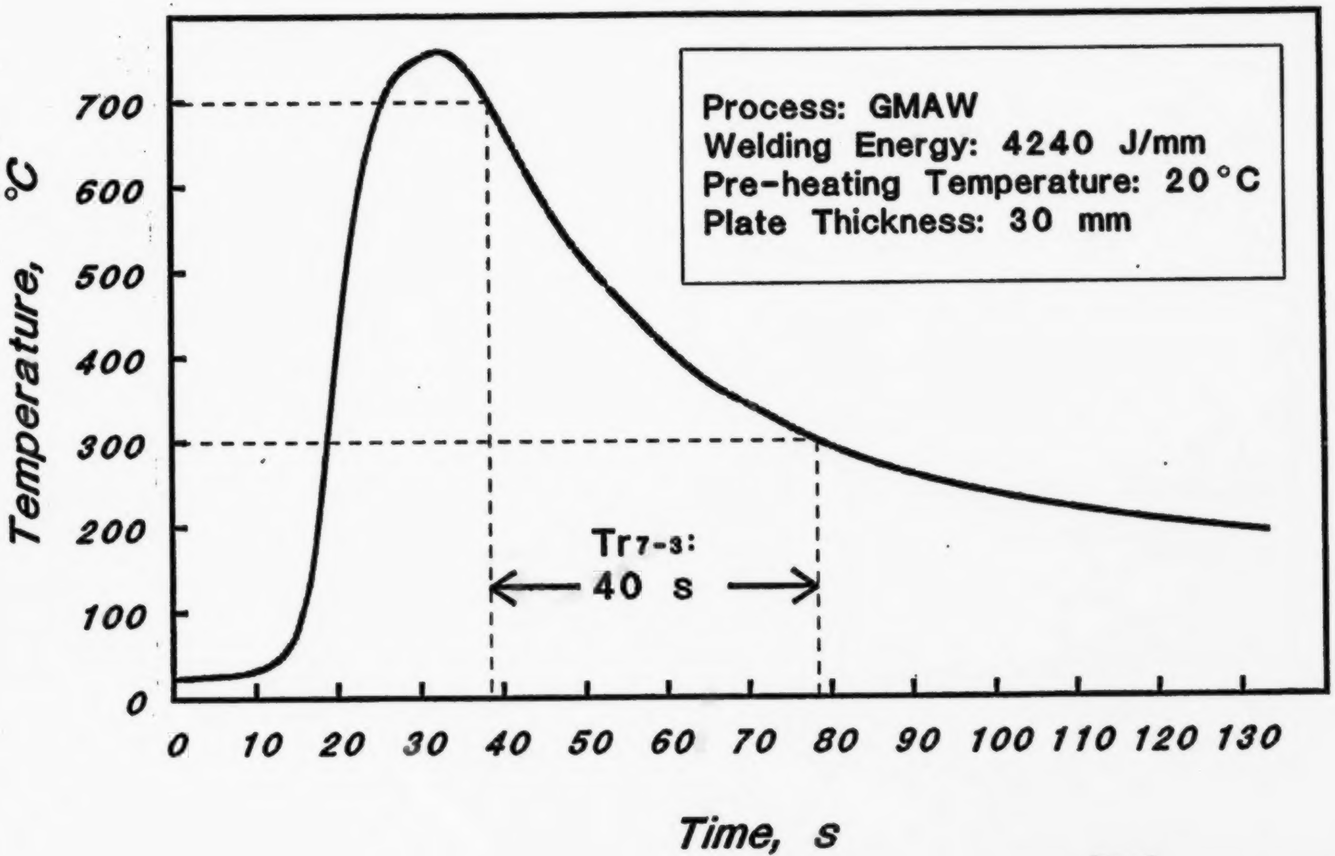

MIL DAVIE INC.

CAN/MIL HYW700QT STEEL

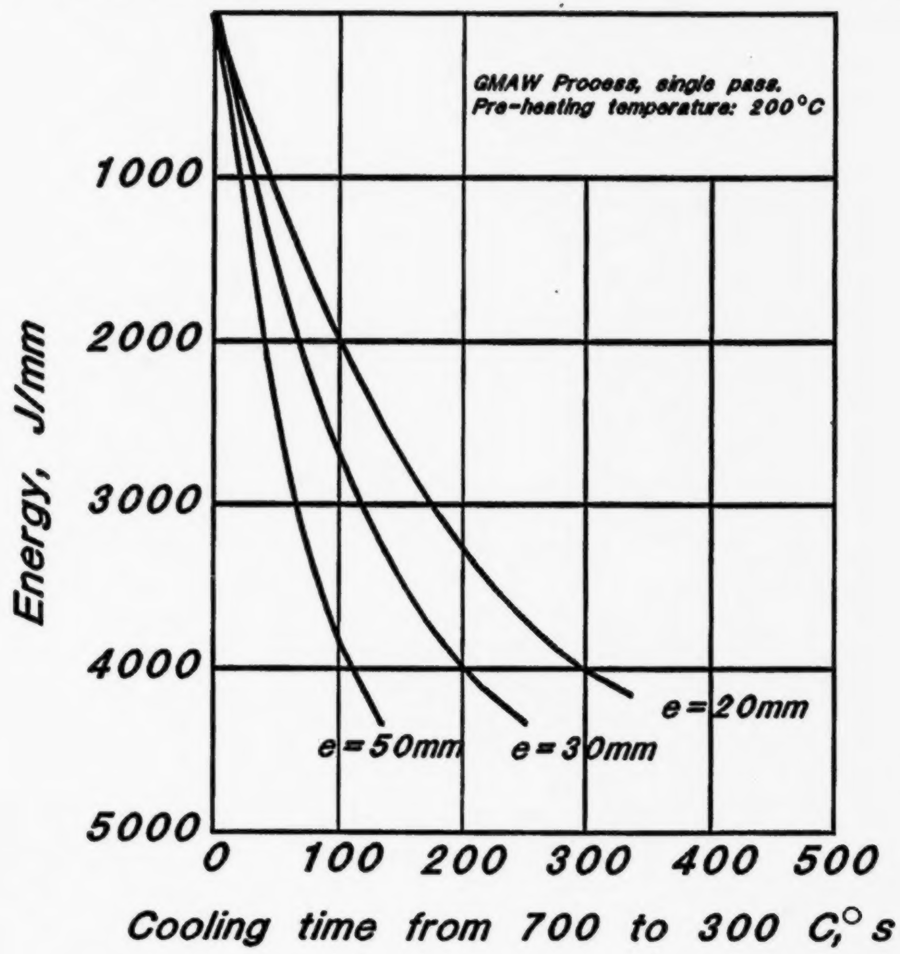

MIL DAVIE INC.

TRANSFORMATION TEMPERATURES

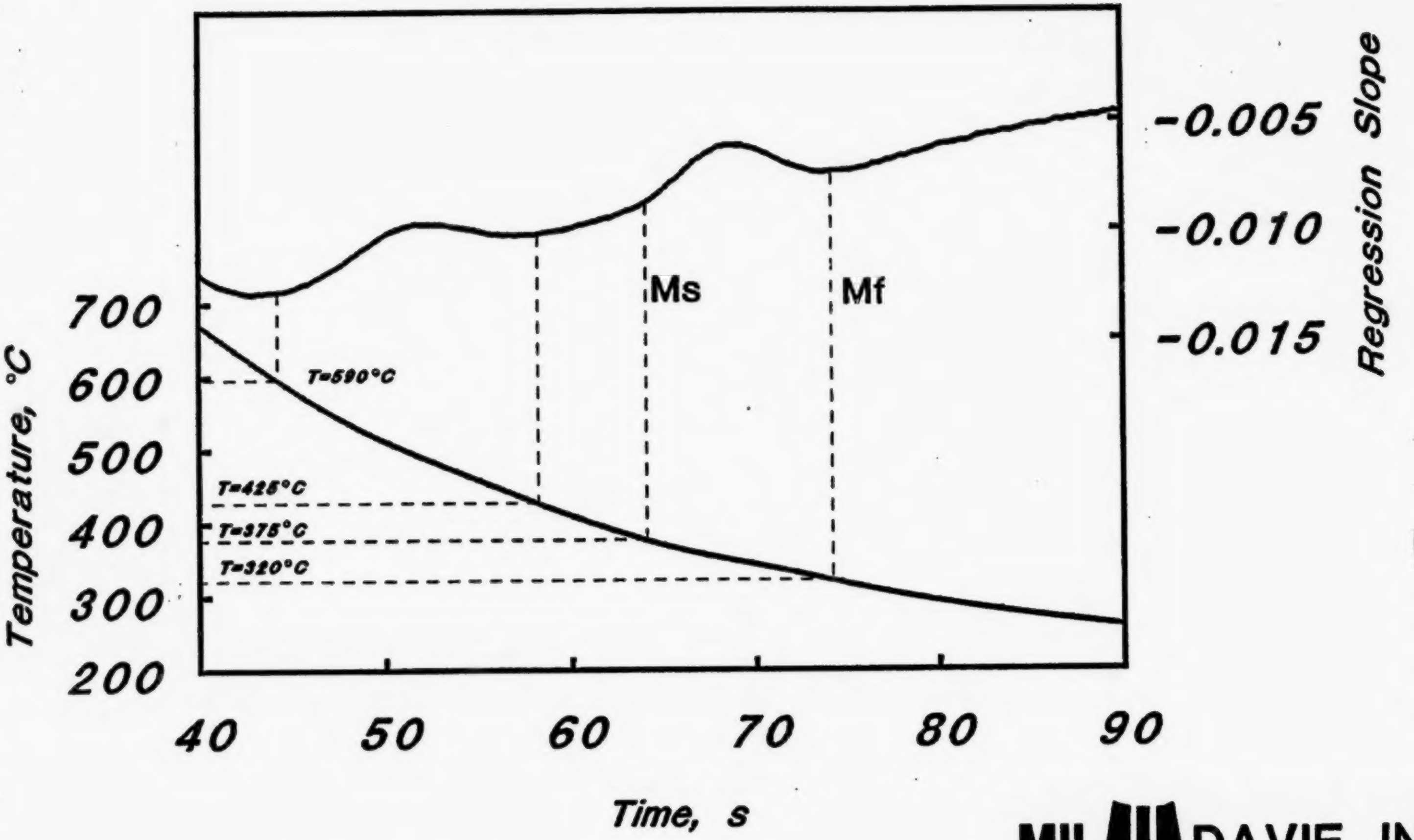

MIL DAVIE INC.

DATA POINTS

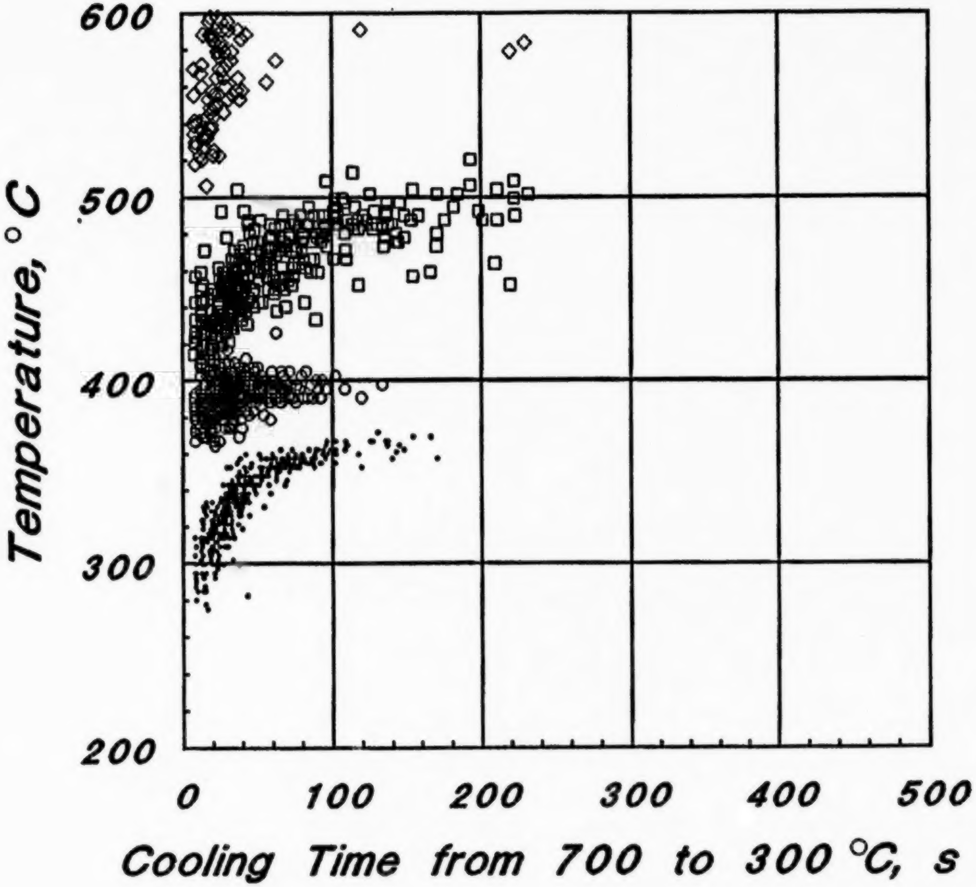
Temperature, °C
600
500
400
300
200
0
100
200
300
400
500
Cooling Time from 700 to 300 °C, s

CONTINUOUS COOLING TRANSFORMATION DIAGRAM FOR CAN/MIL HYW700QT STEEL

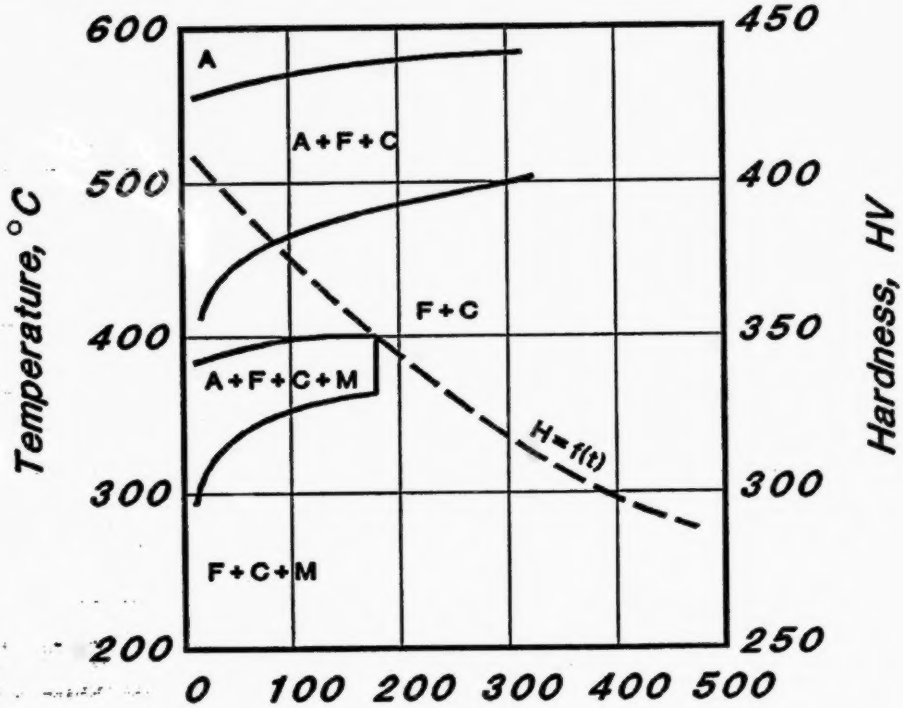

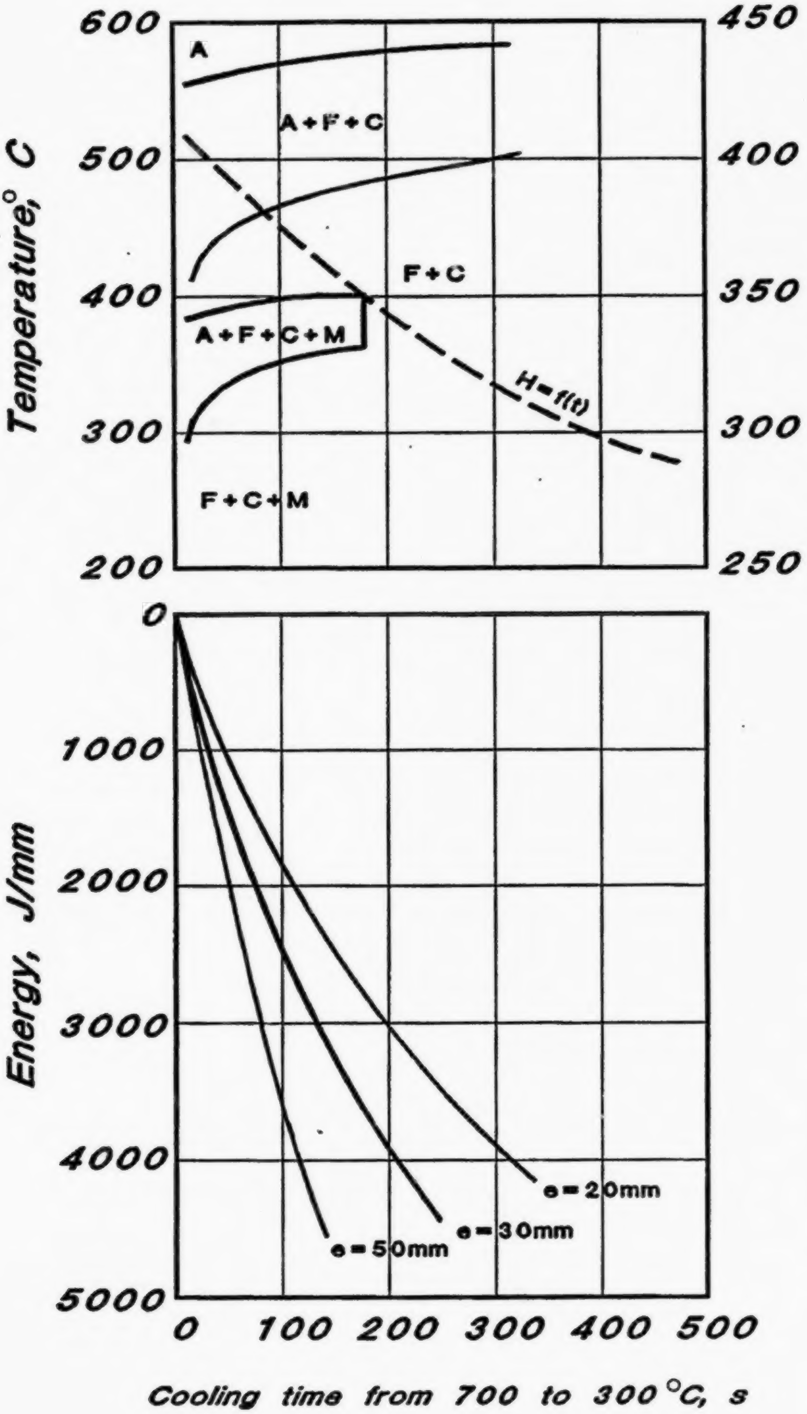

Cooling time from 700 to 300 °C, s

GMAW Process - Pre-heated at 200 °C

DEVELOPMENT OF CAN/MIL HYW700QT STEEL

○ General Overview of the Project
○ Historical Review of Steel Acquisition
○ Mechanical Properties
○ Steel Characterization – Implant Test
● **Explosion Bulge Test Trials**

MIL DAVIE INC.

DEVELOPMENT
OF
CANADIAN STEEL
AND
WELDING PROCEDURES
AND
SPECIFICATIONS

Contract Serial No W8477-7-PE01/01-SV
SSC File No 05SV.W8477-7-PE01

ONCE UPON A TIME . . .

DEPARTMENT OF NATIONAL DEFENCE

AND

MARINE INDUSTRIES LIMITED

HYW 700 QT

TO DEVELOP A

- Canadian Made
  - High Strength
    - High Toughness
      - Structural Steel

TO BE USED FOR THE

- Fabrication
  - Repair

of HMC Ships

MILESTONES

1984, December
*Request for Approval of Capital Project.

1986, November
* Request for Quotation.

1987, February
Submittal of the Proposal of the MIL Group.

1987, November
Signature of the Contract between DND/SSC and The MIL Group.

1988, June
Start of the Activities at MIL Tracy Plant, Tracy, Que.

1989, November
First melting.

1990, January
First rolling.

1990, October
Transfer of Welding R & D Laboratories to MIL Davie Inc Plant. in Lauzon, Que.

1991, April
Start of Testing Activities at MDI Plant.

Development
of
Canadian Steel and Welding
Procedures and Specidications

SSC File No. 05SV.W8477-7-PE01

SUMMARY

PHASE I CARACTERIZATION OF DEVELOPPED STEEL

- Draft of steel specification
- Steel Acquisition
    - *Melting
    - *Rolling
    - *Heat treating
- Mechanical Properties Evaluation
- Steel Response to Welding Thermal Cycles
- Toughness Evaluation

PHASE II CARACTERIZATION OF FILLER MATERIALS

- Humidity
- Potential Diffusible Hydrogen
- Storing and Handling Conditions
- SMAW, GMAW, FCAW, SAW.

PHASE III CARACTERIZATION OF WELDED JOINTS

- Susceptibility to Cold cracking
- Welding Procedure Qualification
- Weld Toughness Evaluation

PHASE IV SPECIFICATIONS & PROCEDURES

- Developped Steel
- Welding of Developped Steel

Development
of
Canadian Steel and Welding
Procedures and Specifications

SSC File No. 05sv.w8477-7-PE01

PARTICIPANTS

STEEL DRAFT SPECIFICATION by

The MIL GROUP
(MIL Davie Inc.)
Lauzon, Que.

STEEL MAKING by

SLATER STEEL
(Les Forges de Sorel)
Sorel, Que.

STEEL ROLLING by

IPSCO
Regina, Sask.

HEAT TREATING by

ALGOMA STEEL
Sault-Ste-Marie, Ont.

STEEL TESTING by

The MIL GROUP
(MIL Davie Inc.)
Lauzon, Que.

SUMMARY OF
DRAFT SPECIFICATION FOR
"CAN/MIL HYW700QT"

STEEL MAKING:

ELECTRIC ARC FURNACE; FULLY KILLED; VACUUM DEGASSED; FINE GRAIN PRACTICE.

DELIVERY CONDITION:

QUENCHED and TEMPERED.

TENSILE PROPERTIES:

Yield Strength:	700 - 800 MPa
Elongation (50mm):	18% min.
Reduction of Area:	45% min.

TOUGHNESS PROPERTIES:

Transverse CVN:	55 Joules
Explosion Bulge:	12% Red. of Thickness @ - 5°C

CHEMISTRY:

% C:	0.15 max.
% Mn:	0.50 max.
% Si:	0.25 max.
% Ni:	4.0 - 4.8
% Cr:	0.50 max.
% Mo:	0.40 max.
% V:	0.10 max
% S:	0.008 max.
% P:	0.015 max.

Development
of
Canadian Steel and Welding
Procedures and Specifications

CAN/MIL HYW 700 QT

TYPICAL RESULTS

CHEMISTRY

DRAFT SPECIFICATION REQUIREMENTS	MELT #1	MELT #2	
		LAB. A	LAB. B
% C : 0.15 max.	0.13	0.155	0.148
% Mn: 0.50 max.	0.36	0.29	0.27
% Si: 0.25 max	0.10	0.20	0.20
% Ni: 4.0 - 4.8	4.26	4.66	4.40
% Cr: 0.50 max.	0.39	0.41	0.40
% Mo: 0.40 max.	0.25	0.41	0.39
% V : 0.10 max	0.004	0.06	0.05
% Al: 0.015-0.050	0.018	0.016	0.025
% Cu: 0.25 max.	0.11	0.10	0.10
% Ti: 0.02 max.	0.001	0.000	0.002
% P : 0.015 max.	0.008	0.008	0.008
% S : 0.008 max.	0.004	0.010	0.008
% N_2: 0.015 max.	0.0070	0.0095	0.010

Development
of
Canadian Steel and Welding
Procedures and Specifications

SSC File No. 05SV.W8477-7-PE01

CAN/MIL HYW 700 QT

TYPICAL RESULTS

FOR MELT #1

HEAT TREATMENT:

*DOUBLE QUENCHING from 850°C,

*TEMPERING @ 600°C.

TENSILE PROPERTIES:

*YIELD STRENGTH:	763 MPa	747MPa
*TENSILE STRENGTH:	822 MPa	812MPa
*ELONGATION IN 50mm:	21.5%	22%
*REDUCTION OF AREA:	72.2%	69%

TOUGHNESS

*CVN @ -85°C	137J	104J

#510329 ㉔

MONOBLAST EXPLOSION BULGE EVALUATION OF HYW700QT SUBMARINE PRESSURE HULL STEEL

by

John F. Porter, Dan O. Morehouse and Glen Gorveatte

Defence Research Establishment Atlantic, Dockyard Laboratory
FMO Halifax, Halifax, Nova Scotia, B3K 2X0

ABSTRACT

In support of the development project to create a "made in Canada" submarine pressure hull steel and weldment, the DREA developed monoblast explosion bulge procedure was employed to evaluate the dynamic deformability of two inch thick HYW700QT steel plate and weldments. In explosion bulge evaluations, to qualify as a suitable material for submarine pressure hull applications, the test samples must attain a preset degree of plastic strain prior to the formation and extension of cracking. For HYW700QT the pass/fail strain level required was defined as 12 percent reduction in thickness at the bulge apex.

Six unwelded and two welded plates were prepared for evaluation. The first three unwelded plates were intended to define the relationship between charge weight employed and the strain level attained, while the remaining three unwelded plates were to be deformed to the qualification strain level. Following evaluation of the second plate, the strain levels attained became erratic, as a result of damage incurred by the anvil during the second explosive loading. Although in-situ repairs were attempted between shots, the anvil remained insufficiently rigid. Despite these difficulties, one plate surpassed the 12 percent qualification strain level while two other plates attained over 11 percent thinning. One of the two welded samples surpassed the 12 percent strain level while the other reached 10.5 percent, without the formation of cracking.

TABLE OF CONTENTS

Page No.

ABSTRACT

1.0 INTRODUCTION 1

2.0 EXPERIMENTAL PROCEDURE

- 2.1 Sample Preparation 2
- 2.2 Monoblast Procedure 2
- 2.3 Post Trial Examinations 4

3.0 RESULTS AND DISCUSSION

- 3.1 Response of Unwelded HYW700QT Plates 4
- 3.2 Response of HYW700QT Weldments 5

4.0 CONCLUSIONS 6

REFERENCES

TABLES

FIGURES

1.0 INTRODUCTION

An important consideration in the certification of a candidate submarine pressure hull steel and/or weldment is the material's ability to attain high levels of dynamic plastic deformation, prior to the formation and propagation of a crack. The explosion bulge procedure, originally proposed over 40 years ago [1] and currently defined by Mil STD 2149 [2] is a recognised qualification method to evaluate this ability in candidate pressure hull materials. The characterisation of weldment and steel performance under extreme loading conditions, employing a modified version of the explosion bulge procedure, has become an integral part of Defence Research Establishment Atlantic / Dockyard Laboratory's (DREA/DL) submarine materials technology program.

In an explosion bulge evaluation of a material, a full thickness sample is placed over an anvil which has a circular cut-out removed. An explosive charge is suspended over the center of the sample at a specified stand-off distance. When the test piece has attained the proper temperature, the charge is detonated and the pressure wave deforms the test plate material into the anvil opening, developing a balanced biaxial plastic set strain field in the bulge apex region of the test piece. In the original version of the procedure, the trials involved in-air detonation of the explosive charges. The charges were configured to produce a 3 percent reduction in thickness of the bulge apex per shot. As the level of thinning which must be attained to pass a sample may be as high as 16 percent (unwelded HY80), each individual panel underwent up to 5 or 6 individual loading events. The multishot approach was adopted as the very high weights of explosive required to generate the total deformation in one loading event were excessive. A very large explosive charge in close proximity could also cause metallurgical alterations to the test piece due to the extreme pressures and temperatures. The multishot procedure also permited the delineation of the failure strain level in those samples which do not attain the pass/fail thinning level. Unfortunately this procedure required extensive range facilities and was time consuming and costly. As a result considerable effort has been expended to identify or develop alternate testing methods which would characterise a steel or weldment's dynamic deformation performance with the same degree of confidence as the explosion bulge procedure.

A modified version of the explosion bulge procedure was developed at DREA for the evaluation of 2.54 cm (1 inch) and 5.08 cm (2 inch) thick plates [3,4]. This procedure involves submerging the test sample, anvil and charge in water. As water is an efficient energy transfer medium, the total level of plastic deformation required to qualify a sample can be achieved in a single loading event, employing a reasonable weight of explosive. The plate and anvil geometries remain unchanged from the original procedure, therefore the modes of deformation and the ability or inability of the sample to perform adequately are equally demonstrated in the in-air or monoblast approach.

This report describes the application of the monoblast explosion bulge procedure to the qualification of HYW700QT submarine pressure hull steel. A preliminary set of two HYW700QT weldments were also explosively deformed.

2.0 EXPERIMENTAL PROCEDURE

2.1 Sample Preparation

HYW700QT is an experimental quenched and tempered low carbon alloy steel, designed for a minimal yield strength of 700 MPa (95 ksi) with a high degree of toughness, suitable for submarine pressure hull construction. Two melts of HYW700QT were employed in these evaluations. Two welded samples were fabricated from material from the first melt, and six plain plates were cut from the second melt panels. The chemical compositions and mechanical properties for both melts are listed in Table 1.

Both welded samples were fabricated using a robotic gas metal arc welding (GMAW) procedure. A double V edge preparation was employed. A total of 26 weld passes, employing 1.2 mm (0.05 inch) diameter L-TEC 120 wire were required for each weldment. The shielding gas was 98% argon and 2% oxygen. Post welding mechanical testing established the weld metal yield and tensile strengths as 750 and 845 MPa (108 and 122 ksi) respectively. The weld reinforcements were ground flush to the parent metal to reflect Canadian submarine pressure hull fabrication practice.

The test plate dimensions were 76.2 by 76.2 by 5.1 cm (30 by 30 by 2 inches). Before delivering the test pieces to the field for evaluation, a 10.2 by 30.5 cm (4 by 12 inch) strip was lightly ground on the center sections on both surfaces of each panel. This grinding removed any primer, scale and oxides, producing a smooth mirror-like finish. Care was taken to ensure that the panel thickness was not significantly reduced as a result of this operation. A fine grid pattern of 0.305 cm (0.12 inch) diameter circles was electro-etched on these ground surfaces, traversing the bulge apex regions of the panels. Measurement of the degree of elongation of the circles following the evaluation permited calculation of the surface plastic set strain profiles attained. The electro-etched circular grid traversed the weldments and extended approximately 12.7 cm (5 inches) into the parent metal. Following the electro-etching, the surfaces were coated with a protective coating to inhibit oxidation.

2.2 Monoblast Experimental Procedure

The DREA version of the explosion bulge procedure for 5.08 cm (2 inch) thick samples involves submerging the test assembly and explosive charge underwater. The water between the explosive charge and the test piece acts as an efficient energy transfer medium, permitting the attainment of the total required deformation of the test sample in a single loading event. Figure 1 shows the experimental set-up just prior to submergence in approximately 3 metres (10 feet) of water. The critical dimensions of the anvil which control the modes of deformation conform to the standard in-air procedure.

A 12% reduction in thickness at the bulge apex, prior to the formation and propagation of a crack was defined as the pass/fail criterion for the HYW700QT plain and welded samples.

This criterion was arrived at after reviewing the standards for other similar steels and weldments. The test plate was considered to have failed if prior to attaining the 12% thinning, a crack had initiated and propagated into the hold down region of the sample, the crack had propagated through the plate thickness or if fragments had broken from the plate. Three samples of the material must satisfactorily attain or surpass the pass/fail strain level in order to qualify the material as suitable for submarine pressure hull applications from an explosion bulge perspective.

The explosive charges are fabricated from sheets of Detasheet C3 explosive cut into 25.4 cm (10 inch) squares and stacked to obtain the desired weight. The first three of the six unwelded HYW700QT plates were intended for use in determining the charge weight required to obtain the 12 % reduction in thickness in the bulge apex region in one loading event. Earlier evaluations of unwelded 50 cm (2 inch) thick HSLA100 plates showed that a charge weight of 13.6 kg (30 lbs) could achieve a 10 % thickness reduction. It was anticipated that the HYW700QT steel had a similar yield strength and as such, a charge weight of 16 kg (35 lbs) was estimated as sufficient to effect the desired thinning. As the charges are fabricated from stacked sheets of explosive, modifications to the charge weight could be easily accomplished in the field, should the previous loading have proven either too severe or insufficient. Following this phase of charge weight fine tuning, it was intended to employ charges of constant weight for all subsequent evaluations. Following the stacking of the Detasheet C sheets, a booster charge of 115 grams (0.25 lbs) of C4 plastic explosive was moulded into a plastic conical funnel. The end of a 15 m (50 feet) length of Det Cord was knotted and also pressed into the spout of the funnel. The funnel was then inverted and secured above the main charge. Once the test assembly had been submerged, an electrical detonator was pressed into the other end of the Det Cord, which had not been submerged.

The explosive support structure was constructed to ensure a stand-off distance (the distance between the bottom of the explosive charge and the top surface of the test plate) of 20.3 cm (8 inches). A larger stand-off distance would reduce dramatically the capability of the explosive charge to effect the panel deformation, whereas too small a stand-off distance could cause considerable damage to the anvil system and possibly induce microstructural alterations to the top surface of the panel due to the extreme pressures and adiabatic heating.

At the trial site, the plates were stored in a glycol chiller unit (Figure 2) and maintained at a temperature of approximately -25 degrees C (-13 degrees F). Each plate had one surface mounted and one interior mounted thermocouple, which continuously monitored the sample's temperature upon removal from the chiller. A plastic bag containing chipped styrofoam was placed into the anvil cavity prior to the placement of the test plate. This provided a compressible medium beneath the test plate facilitating the deformation. Once the plate was centered on the anvil and the explosive charge secured, the assembly was submerged underwater. When the plate interior reached -5 degrees C (23 degrees F), as indicated by the thermocouple, the explosive train was electrically detonated. This firing temperature corresponded to the lowest anticipated hull temperature in an operational submarine.

2.3 Post Trial Examinations

Following the explosive loadings, the test panels were retrieved and visually examined for cracking. Ultrasonic thickness measurements were taken in the bulge apex region of the deformed panels and the degree of thinning calculated. For welded panels, the thickness measurements were taken in the parent metal adjacent to the weldment at the bulge apex.

Upon return to the lab, the plates were degreased and the surface strain profiles measured with the DREA developed FAMOSS (Fibroscopic Apparatus for the Measurement of Surface Strain) system. The system employed a high resolution video camera which recorded the image of the deformed electro-etched grid at the point of interest on the panel. The video signal was transferred through a personal computer mounted frame grabber board, enlarged with the aid of the image enhancement program OPTIMAS and displayed on a monitor. A conically shaped plastic light guide, attached to the video camera illuminated the test plate surface and was used to ensure that the distance between the camera lense and the test piece surface was a fixed value. This eliminated the requirement to manually recalculate the image magnification factors of the video system between each frame. An OPTIMAS macro program led the operator through the commands to measure and record the dimensions of the deformed circles. The macro program automatically calculated the engineering plastic set strain (change in length / original length) for each point.

Metallographic and fractographic examinations were conducted on any samples which experienced cracking to ascertain the factors contributing to the inferior performance. In the case of evaluations on previously untested samples, metallographic examinations may also be conducted on samples which have passed in order to study the metallurgical factors contributing to the superior performance.

3.0 RESULTS AND DISCUSSION

3.1 Response of Unwelded HYW700QT Plates

Six unwelded plates were evaluated. As the charge weight required to effect the desired 12% plastic strain in a single shot for this material was unknown, the first three unwelded plates were to be employed to experimentally ascertain the relationship between the amount of explosive employed and the degree of deformation attainable. With this relationship established, the remaining three unwelded plates were to be deformed to the qualification strain level of 12%, employing a constant charge weight.

A summary of the plate responses with the corresponding weights of explosive employed is presented in Table 2. The lower than anticipated degree of thinning that occurred in the first plate with a 15.5 kg (34 lb) charge was the result of a significantly higher than expected yield strength of the material. In order to compensate for this, a larger charge was employed in the second plate evaluation. In this case the 18.2 kg (40 lb) charge deformed the plate to slightly below the targeted level. Figure 3 shows the bulged sample following this evaluation. The responses became erratic following the evaluation of the second plate due primarily to damage incurred by the anvil during the second explosive loading. The welds holding the ringed segments of the anvil failed and the retaining bolts stretched. Figure 4 shows the location of the six retaining bolts and the three rings which made up the anvil. In this photograph, the ring welds have failed. Although in-situ repairs were attempted between shots, the anvil remained insufficiently rigid, thereby absorbing significant amounts of the explosive energy, which would otherwise have contributed to the plate deformation. The originally flat top surface of the anvil experienced distortion as a result of the ring separation. The inner portion of the top ring deformed downward and thereby reduced the contact area of the hold down regions of the test samples. This would result in the absorption of some of the available explosive energy to deform the outer portions of the test pieces prior to deforming the central bulge section.

Despite these difficulties, one plate surpassed the 12 percent qualification strain level while two other plates attained over 11 percent. There was no occurrence of the surface cracking or tearing, which usually precedes failure, on the surfaces of any of the plates deformed. This suggests that the failure through thickness strain for these plates is well in excess of 12 percent.

The surface plastic set strain profiles for the convex and concave surfaces of each deformed plate are presented in Figures 5 to 10, in the order of their evaluation. The radial components of plastic strain are plotted versus the distance from the bulge apex. Each figure also includes the percentage through thickness reduction as a function of distance from the bulge apex. Examination of these plots revealed that the degree of tensile plastic strain on the convex surface of bulge remained essentially uniform over a radius of 10 cm (4 inches) from the bulge apex. The concave surface radial component of the plastic strains all remained close to zero. In all but one of the samples, these strains remained constant with distance or approached the zero strain level. The through thickness strain profiles consistently showed a maximum value at the bulge apex and reduced gradually with increased distance from the apex.

A midthickness section taken from the bulge region of one of the plates was polished and etched with picral and sodium metabisulfite to reveal the microstructure. Figure 11 displays a Bainitic microstructure with grain boundary ferrite and side plate ferrite constituents present.

3.2 Response of HYW700QT Weldments

The response of the two welded samples is given in Table 2. One weldment surpassed the 12 percent strain level while the other reached 10.5 percent, without the formation of cracking. These samples were evaluated following the damage to the anvil and the difference in responses, even though equivalent charge weights were employed is due to the varying degree of rigidity of the anvil system. The welding electrode yield strength was slightly lower than the yield strength of the base plate and both were significantly lower than the yield strength of the unwelded HYW700QT samples. As a result, even with a damaged anvil, a relatively low charge weight was capable of deforming the weldment samples to the degree observed.

Sample 700W1 was the only weldment with the circular grid electro-etched on its surfaces. Figure 12 summarises the convex and concave radial strain profiles as a function of distance from the weld centerline. The fusion line, at 3 cm (1.2 inches) from the centerline, was the location of the lowest strain on the convex surface. This is a result of the harder and less deformable heat affected zone material. Strain levels on either side of the fusion line were similar. Strain levels on the concave surface were uniform across the profile and slightly tensile.

4.0 CONCLUSIONS

The DREA developed monoblast explosion bulge procedure was employed to evaluate the dynamic deformability of the experimental submarine pressure hull steel HYW700QT. Due to damage incurred to the anvil system, only one sample attained the required 12% reduction in thickness at the bulge apex. Two other samples did surpass 11% thinning with no evidence of cracking or tearing on the plate surfaces. This suggests that the failure strain for this material is well in excess of the pass/fail criterion and that HYW700QT base plate meets the explosion bulge requirements. Two preliminary GMAW HYW700QT weldments were similarly explosively deformed and exhibited no evidence of cracking.

REFERENCES

1. C.E. Hartbower, W.S. Pellini, "Explosion Bulge Test Studies of the Deformation of Weldments", Welding Journal, Vol. 29, June 1951, pp. 307-318.

2. Mil-STD-2149 (SH), "Standard Procedure for Explosion Testing Ferrous and Non-Ferrous Metallic Materials and Weldments", November 1983.

3. J.F. Porter, J.R. Matthews, "The Role of Explosion Bulge Trials in Submarine Materials Research at DREA", Proceedings of a Workshop on Methods for Fracture Safety Assessment of Submarine Hull Materials, TTCP Technical Panel P1-Metallic Materials, May 1991.

4. J. F. Porter, D. O. Morehouse, "A Monoblast Explosion Bulge Procedure for Two Inch Thick Submarine Pressure Hull Materials", DREA/TC, March 1993.

Chemical Composition (% by wt.)	Melt 1	Melt 2
C	0.13	0.16
Mn	0.36	0.29
Ni	4.26	4.66
Cr	0.39	0.41
Mo	0.25	0.41
Cu	0.11	0.1
Si	0.1	0.2
Mechanical Properties	**Melt 1**	**Melt 2**
Yield Strength MPa (ksi)	807 (117)	924(134)
Ultimate Strength MPa (ksi)	896 (130)	958 (139)
% Elongation	21	20
Hardness (HRc)	26	34

Table 1: Chemical composition and mechanical properties of unwelded HYW700QT explosion bulge samples (supplied by MIL Davie Inc.)

Plate Identification	Charge Weight kg (lb)	Thinning (%)
70006X	15.5 (34.)	8.6
70016B	18.2 (40.)	11.6
70016X	20.0 (44.)	8.6
70012	21.8 (48.)	11.1
70010	25.0 (55.)	12.2
700W1*	18.6 (41.)	10.5
700W2**	17.7 (39.)	12.7
70015	24.5 (54.)	10.6

* - Welded plate with electro-etched grid
** - Welded plate without electro-etched grid

Table 2. Explosion bulge response of HYW700QT plates and weldments

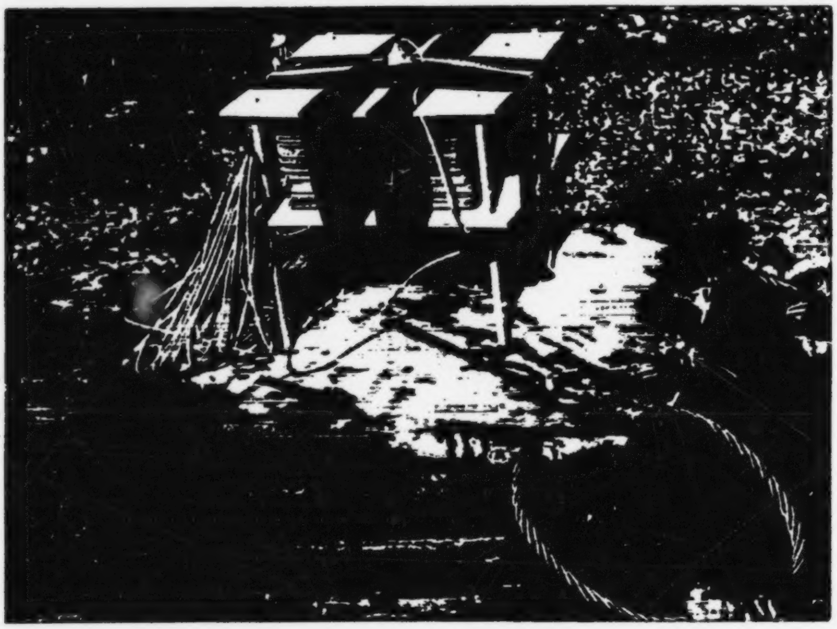

Figure 1: Experimental set-up for monoblast explosion bulge procedure.

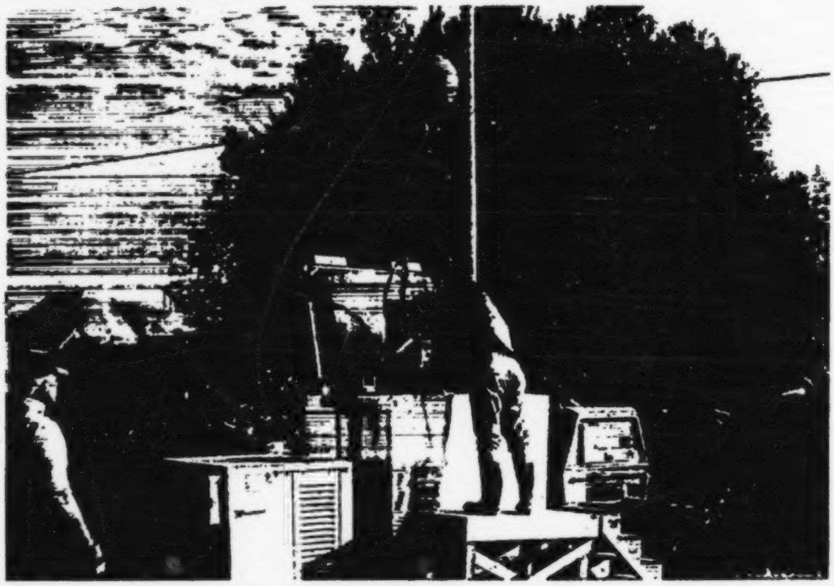

Figure 2: HYW700QT plate being retrieved from glycol chiller.

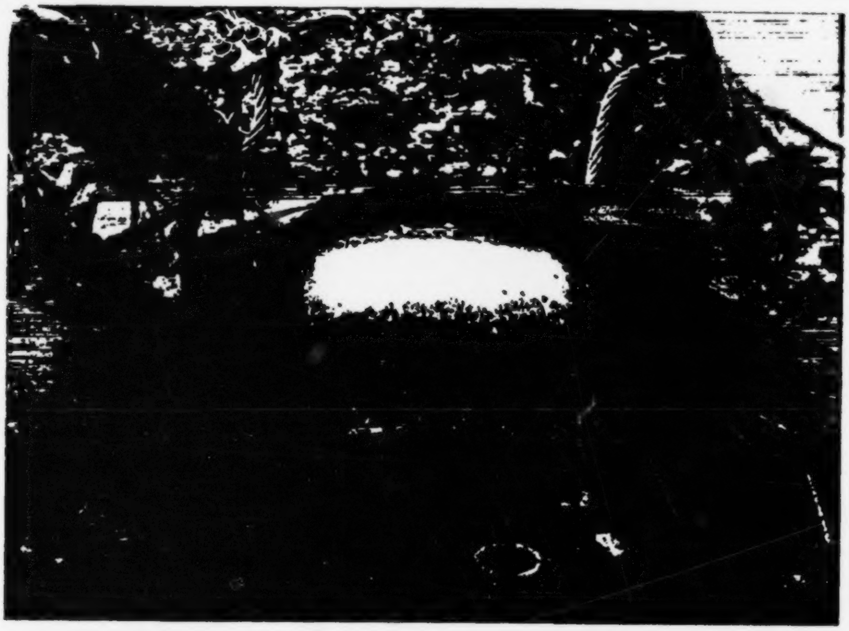

Figure 3: Plate 70016B following monoblast explosion bulge evaluation.

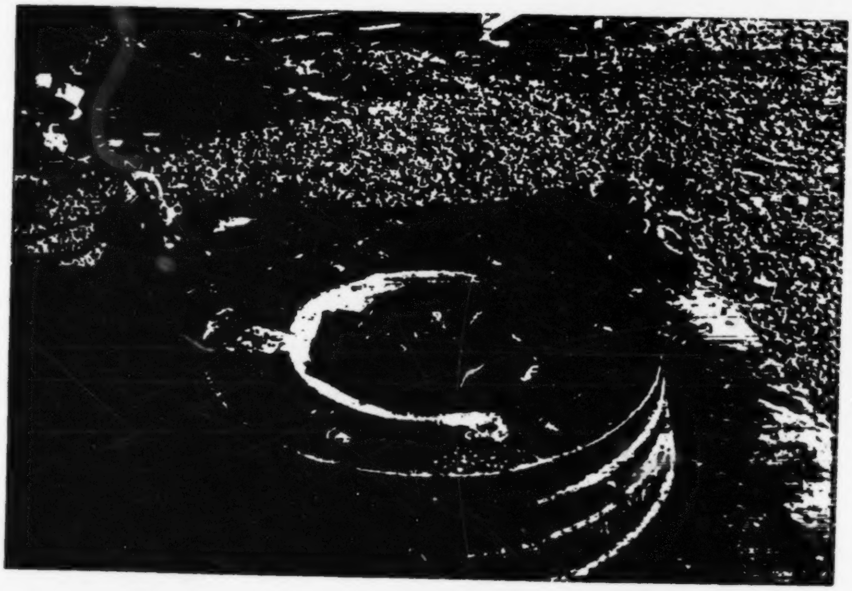

Figure 4: The explosion bulge anvil with stretched retaining bolts and failed ring welds.

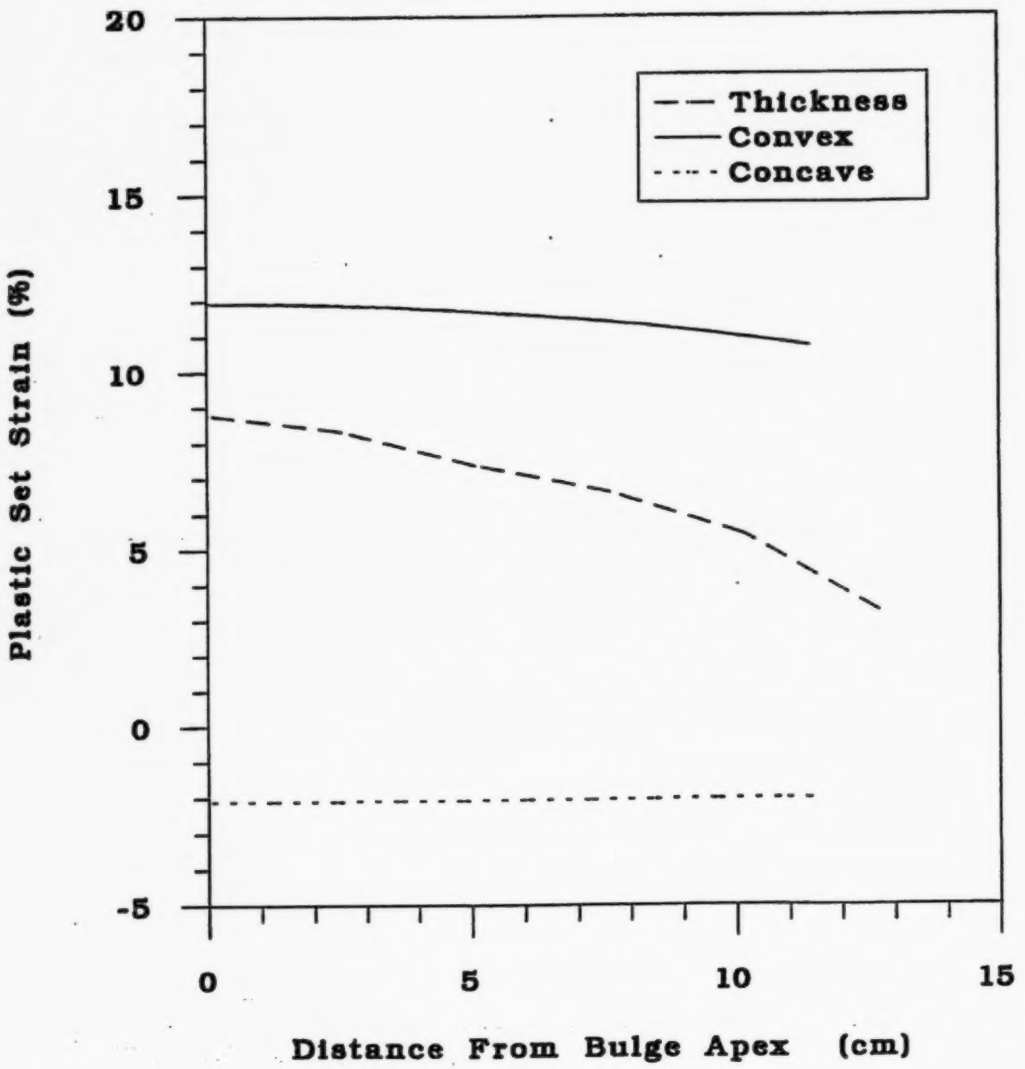

Figure 5: Plastic set strain profiles of unwelded HYW700QT following monoblast explosion bulge evaluation. (Plate # 70006X)

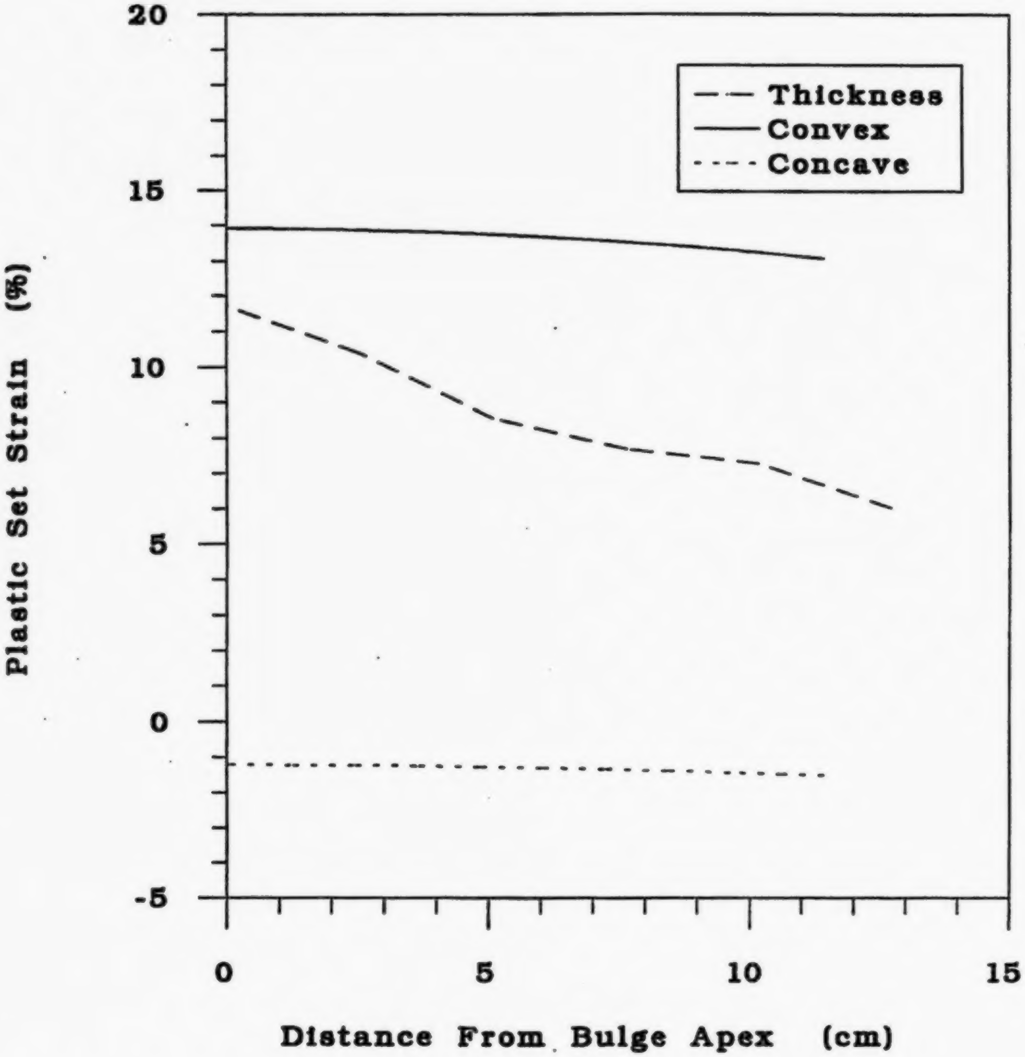

Figure 6: Plastic set strain profiles of unwelded HYW700QT following monoblast explosion bulge evaluation. (Plate # 70016B)

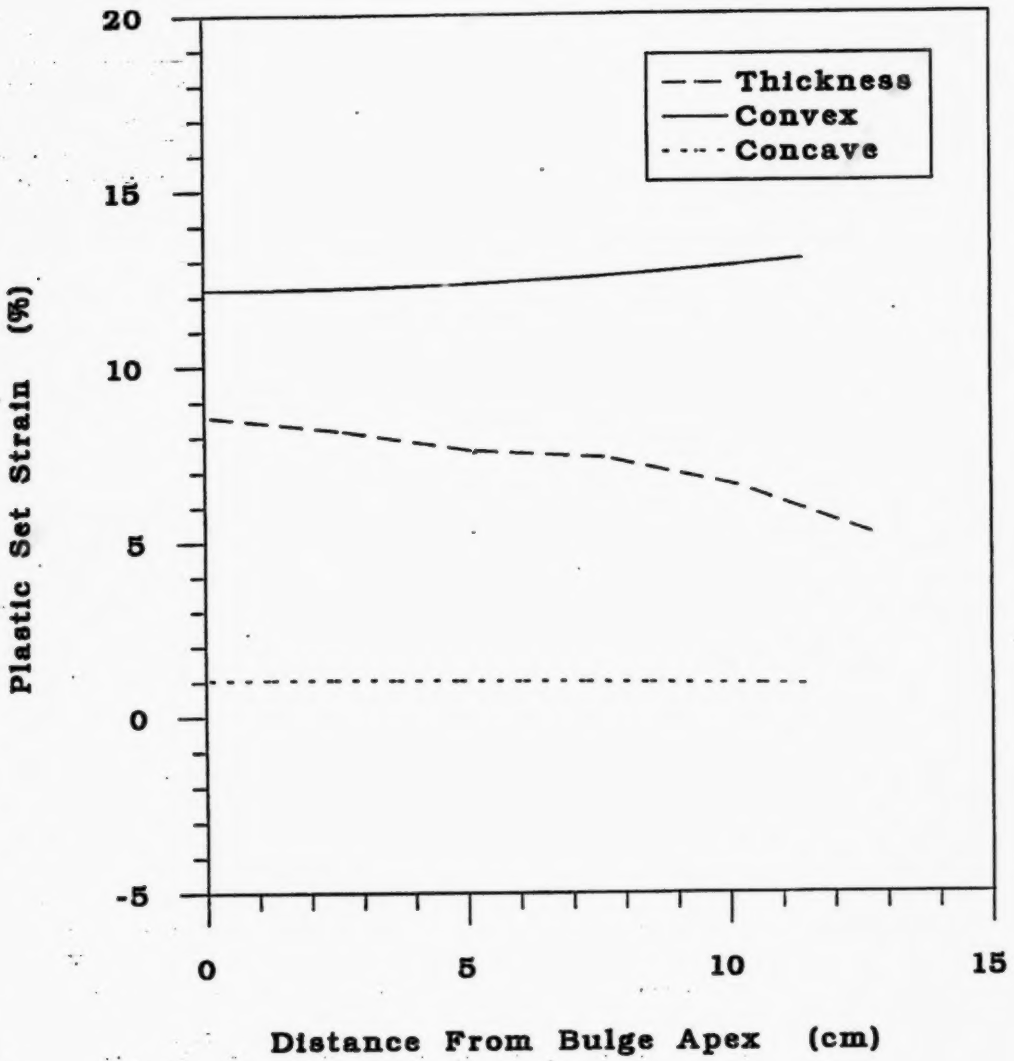

Figure 7: Plastic set strain profiles of unwelded HYW700QT following monoblast explosion bulge evaluation. (Plate # 70016X)

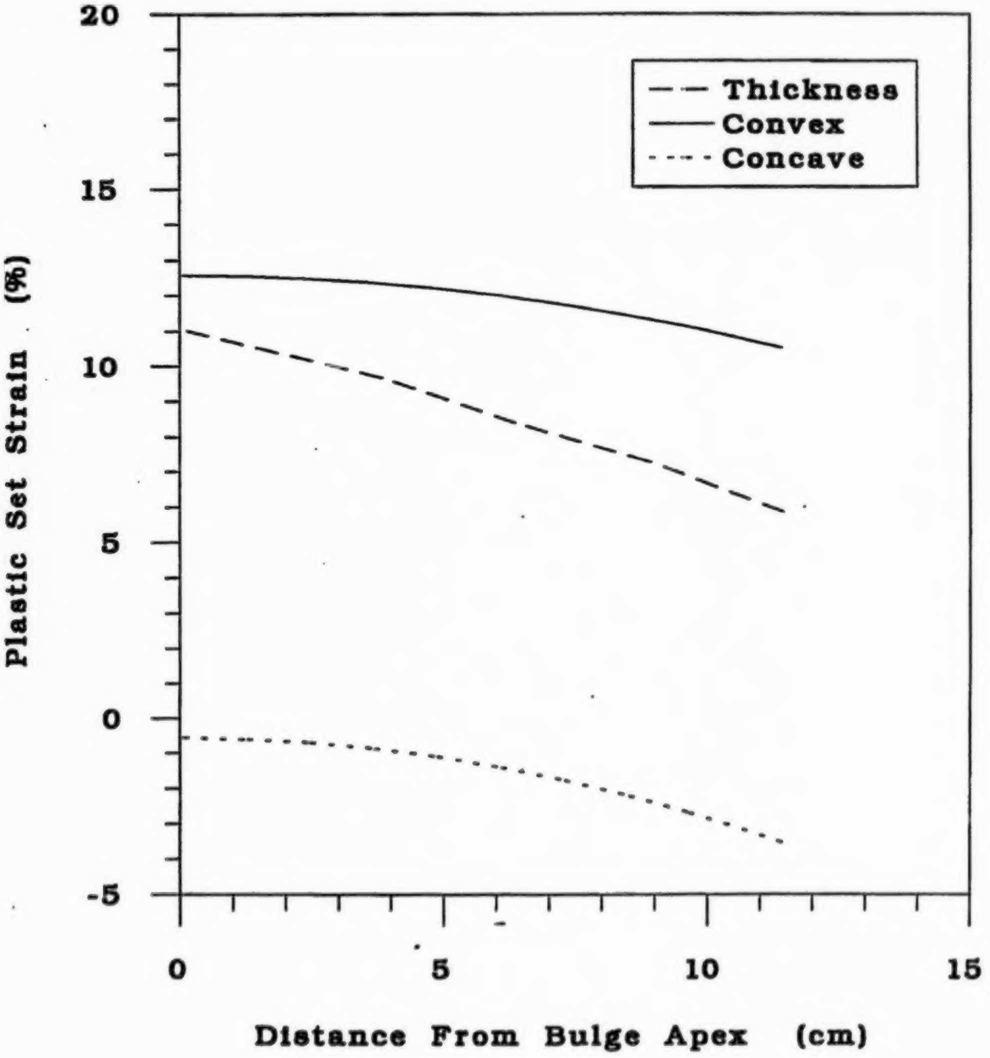

Figure 8: Plastic set strain profiles of unwelded HYW700QT following monoblast explosion bulge evaluation. (Plate # 70012)

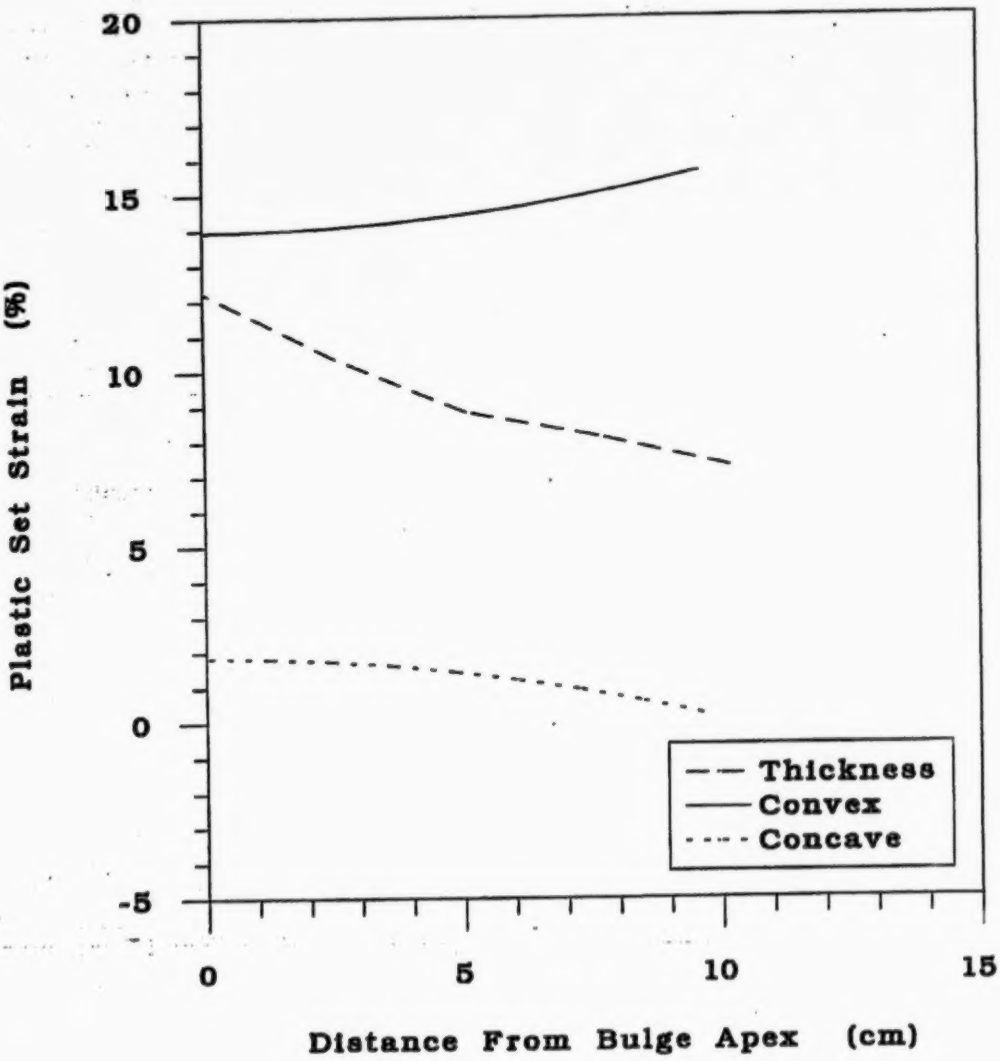

Figure 9: Plastic set strain profiles of unwelded HYW700QT following monoblast explosion bulge evaluation. (Plate # 70010)

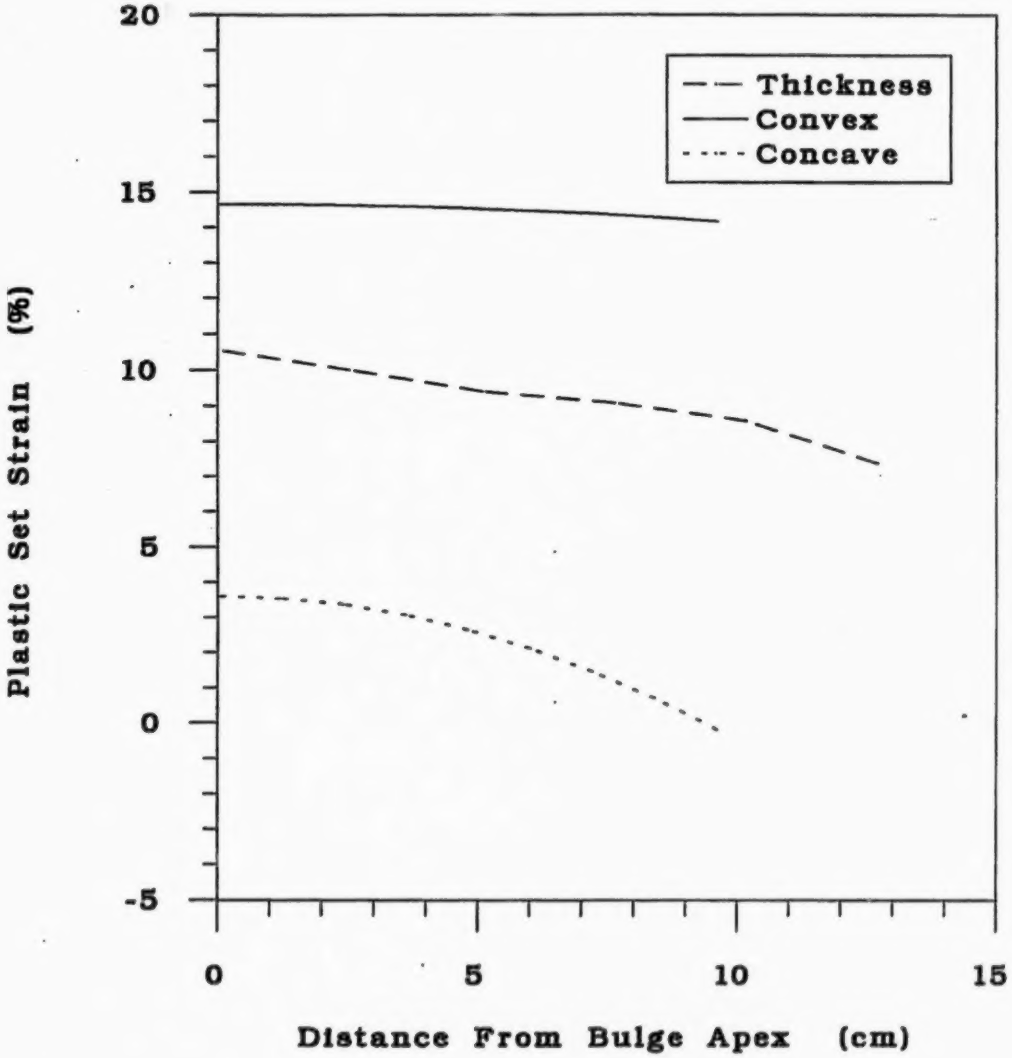

Figure 10: Plastic set strain profiles of unwelded HYW700QT following monoblast explosion bulge evaluation. (Plate # 70015)

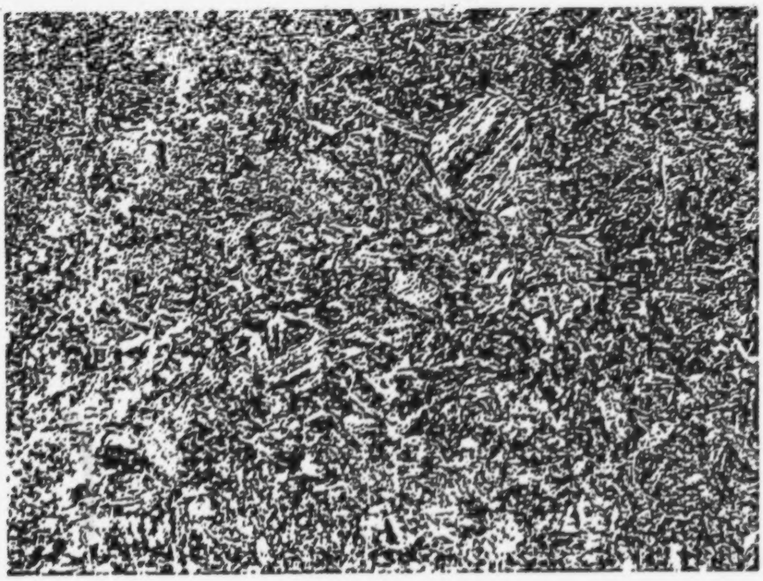

Figure 11: Midthickness microstructure of HYW700QT unwelded plate

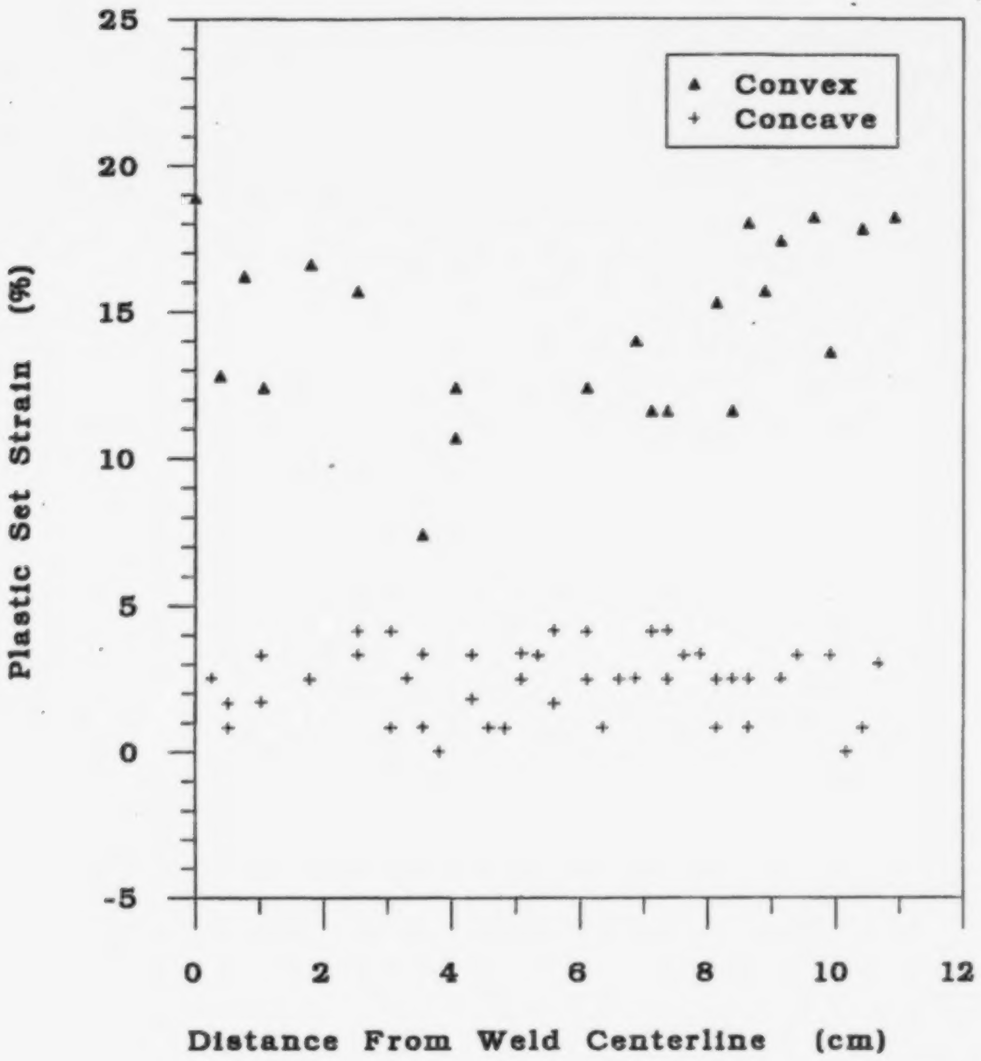

Figure 12: Plastic set strain profiles of welded HYW700QT following monoblast explosion bulge evaluation. (Plate # 700W1)

Mr. Paul Anstey
Defence Research Establishment Atlantic
P.O.Box 1012
Dartmouth, Nova Scotia B2Y 3Z7

Mr. Bob Armstrong
Defence Research Establishment Atlantic
FMO Halifax
Halifax N.S. B3K 2X0

Dr. M.N. Bassim
Dept. of Mechanical Engineering
University of Manitoba
Winnipeg, Manitoba R3T 2N2

(204) 474-8524
204-275-7507 fax

Ms. Teresia Betancourt
Nova Scotia Research Foundation Corpn.
100 Fenwick St. Box 790
Dartmouth, Nova Scotia B2Y 3Z7

424-8670
fax 424 4679

Mr. Charles Billard
MetaSoudage
c/o Centre R & D Metallurgie
MIL Davie Inc.
Case Postale 130
22 Geo D. Davie
Levis, Quebec, G6V 6N7

514 345 6500 ext 5441
514 899 1037fax

Mr. J.F. Boucher DGMEM/DSE 6
National Defence Headquarters
101 Colonel By Drive
Ottawa, Ontario K1A 0K2

819-994-8654
fax 819-997-2194

Mr. Mike Brauss
Proto Manufacturing Ltd.
2175 Solar Cr.
Oldcastle, Ontario N0R 1L0
(519) 737-6330

Mr. Lionel Burrell
Welding Foreman
SRUA
FMO Halifax
Halifax, Nova Scotia   B3K 2X0

Dr. M.K. Chernuka
Martec Ltd. Suite 400
1888 Brunswick St.
Halifax, Nova Scotia B3F 3F8

(902) 425 5101
421-1923

Mr. John Church
TIME Process Ltd.
7405 Kimbel St.
Mississauga, Ontario   L4T 3M6

(416) 677-7410

Ms. Joan Cunningham
Defence Research Establishment Atlantic
FMO Halifax
Halifax, Nova Scotia   B3K 2X0

Mr. Gary Dease
Defence Research Establishment Atlantic
FMO Halifax
Halifax N.S. B3K 2X0

Dr. Bernard Faucher
Metals Technology Labs
Energy Mines and Resources Canada
555 Booth St.
Ottawa, Ontario   K1A 0G1

Mr. Roy Gallant/
Mr. Duane Tuttle/
Mr. Duane Giffin/
Mr. Ralph Wallis/
Mr. Sean Bartlett
SRUA
FMO Halifax
Halifax, Nova Scotia   B3K 2X0

Mr. Jim Gianetto
Metals Technology Labs
Energy Mines and Resources Canada
555 Booth St.
Ottawa, Ontario   K1A 0G1

613-992-4425
613-992-8735 fax

LCdr. S. Garon
PMO TRUMP
National Defence Headquarters
101 Colonel By Drive
Ottawa, Ontario K1A 0K2

613 992-2003
fax 613 996-9440

Mr. Glen Gorveattte
Gorveatte Consulting
19 Oakwood Avenue
Dartmouth N.S.
B2W 3C8

Mr. Pat Griggs
Griggs Engineering
5 Benview Drive
Dartmouth N.S.
B2Y 1W4

Dr. Bob Hay
President
Tektrend International Ltd.
2755 Pitfield
Ville St. Laurent, Quebec H4S 1G3

(514) 333-7371

Mr. J. Helie
Tektrend International Ltd.
2755 Pitfield
Ville St. Laurent, Quebec H4S 1G3

(514) 333-7371

Lt(N) Brig Henry
PMO TRUMP
National Defence Headquarters
101 Colonel By Drive
Ottawa, Ontario K1A 0K2

Dr. T. Holden
Chalk River Nuclear Laboratories
Chalk River, Ontario K0J 1J0

(613) 584-3311

Dr. Roger S. Hollingshead
Defence Research Establishment Atlantic
FMO Halifax
Halifax, Nova Scotia B3K 2X0

Mr. Paul Holsberg
Annapolis Detachment
Caederock Division
Naval Surface Warefare Center
Code 2810
DTNSRDC
Annapolis, Maryland 21402

(410) 267-2841
410-267-4885 fax

Mr. Don Hussey
Donelad Ltd.
Suite 720 Sun Tower
1550 Bedford Highway
Bedford N.S. B4A 1E6

Dr. Calvin Hyatt
Defence Research Establishment Atlantic
FMO Halifax
Halifax N.S. B3K 2X0

Mr. Dave Jessop
Industrial Engineering
FMO Halifax B3K 2X0

Mr. Ken KarisAllen
Defence Research Establishment Atlantic
FMO Halifax
Halifax N.S. B3K 2X0

Dr. Jim Kennedy
CRAD/DRDM
National Defence Headquarters
101 Colonel By Dr
Ottawa, Ontario K1A 0K2

Mr. Donald Kerr
Saint John Shipbuilding Ltd.
Bayside Drive
P.O.Box 970
St John, New Brunswick E2L 4E5

(506) 632-6900
506-632-5915 fax

Dr. Mark Kirk
Edison Welding Institute
1100 Kinnear Road
Columbus Ohio 43212
614-486-9400
614-486-9528 fax

Mr. Gaetan Labbe DSE
National Defence Headquarters
101 Colonel By Drive
Ottawa, Ontario K1A 0K2

Mr. John Lavric
Saint John Shipbuilding Ltd.
Bayside Drive
P.O.Box 970
St John, New Brunswick E2L 4E5

Ms. Carol Lebowitz
David Taylor Research Center
Code 2815
Annapolis Maryland 21402-5067

(301) 267 3574/ (301) 267-2640 fax

Dr. G. Lee
Technical University of Nova Scotia
P.O.Box 1000
Halifax, Nova Scotia B3J 2X4

Lt(N) David Lloyd
PMO TRUMP
National Defence Headquarters
101 Colonel By Drive
Ottawa, Ontario K1A 0K2

Mr. Ken MacKay
Technical University of Nova Scotia
P.O.Box 1000
Halifax, Nova Scotia B3J 2X4

Dr. K.H. Magee
The Laser Institute
9924-45 Ave
Edmonton Alta T6E 5J1

403-436-9750
403-437-1240 fax

Dr. L. Malik
Materials Technology Centre
311 Legget Drive
Kanata, Ontario K2K 1Z8
(613) 592-2830

Mr. James Allen Manuel
Code 55YP2
NAVSEA
Washington, D.C. USA 20362
(703) 602 9400
(703) 602-1827

Mr. Ken Mason
Defence Research Establishment Atlantic
FMO Halifax
Halifax N.S. B3K 2X0

Dr. James R. Matthews
Defence Research Establishment Atlantic
FMO Halifax
Halifax, Nova Scotia B3K 2X0

(902) 427-3444
fax (902) 427-3435

Mr. K. McCormick
MIL Davie Inc.
Case Postale 130
22 Geo D. Davie
Levis, Quebec, G6V 6N7

418 837 5841
418 838 3809fax

Dr. Richard Morchat
National Defence Headquarters DRDM
101 Colonel By Dr
Ottawa Ontario

Mr. Dan Morehouse
Defence Research Establishment Atlantic
FMO Halifax
Halifax N.S. B3K 2X0

Dr. Jack Morrison
Defence Research Establishment Pacific
FMO Esquimalt
Victoria, B.C. V0S 1B0

Ms. Marjorie Ann E. Natishan
Annapolis Detachment
Caederock Division
Naval Surface Warefare Center
Code 2810
DTNSRDC
Annapolis, Maryland 21402

410-267-2264
410-267-4885fax

Dr. Irewole Orisamolu
Martec Ltd. Suite 400
1888 Brunswick St.
Halifax, Nova Scotia B3F 3F8

(902) 425 5101

Mr. James Pineault
Proto Manufacturing Ltd.
2175 Solar Cr.
Oldcastle, Ontario N0R 1L0
(519) 737-6330

Lt(N) P. James Pope D34
Naval Engineering Unit Atlantic
FMO Halifax
Halifax, Nova Scotia B3K 2X0

Mr. John Porter
Defence Research Establishment Atlantic
FMO Halifax
Halifax, Nova Scotia B3K 2X0

(902) 427-3423

Mr. Francois Racicot
Centre R & D Metallurgie
MIL Davie Inc.
Case Postale 130
22 Geo D. Davie
Levis, Quebec, G6V 6N7

Mr. Rajean Rene
Centre R & D Metallurgie
MIL Davie Inc.
Case Postale 130
22 Geo D. Davie
Levis, Quebec, G6V 6N7

Lt Cdr Jim Reath
Submarine Support Officer
FMO Halifax
Halifax Nova Scotia B3K 2X0

Mr. Etienne Robichaud
Defence Research Establishment Atlantic
FMO Halifax
Halifax N.S. B3K 2X0

Mr. Richard Robichaud
Donelad Ltd.
Suite 720 Sun Tower
1550 Bedford Highway
Bedford N.S. B4A 1E6

Mr. Dale Roushorn
Donelad Ltd.
Suite 720 Sun Tower
1550 Bedford Highway
Bedford N.S. B4A 1E6

Mr. R.T. Schmitke
Director Technology Division
Defence Research Establishment Atlantic
P.O.Box 1012
Dartmouth, Nova Scotia B2Y 3Z7

Mr. Bart Sickles
DTNSRDC
Code 1720.4
Bethesda, Maryland USA 20084

(202) 227-1601/1633

Mr. Frank Smith
German Marine
71 Ilsley Avenue
Dartmouth N.S.
B3B 1L5

902-468-1261
902-468-3855 fax

Lt(N) M. Smith, USN
DGMEM/DSE 5-5-3
National Defence Headquarters
101 Colonel By Drive
Ottawa, Ontario K1A 0K2

819-994-8829
fax 819-994-8873

Cdr R.W. Stillwell NAO
Naval Engineering Unit Atlantic
FMO Halifax
Halifax, Nova Scotia B3K 2X0

Lt(N) J. Turgeon D34
Naval Engineering Unit Atlantic
FMO Halifax
Halifax, Nova Scotia B3K 2X0

Mr. Cees Van Sevenhoven
Ministry of Defence
Royal Netherlands Navy
Ship Research and Development Division
Postbus 20702
2500ES s-Gravenhage, The Netherlands
fax 011 31 70 316 2751

Mr. Ron Verbeke
Naval Engineering Unit Atlantic
FMO Halifax
Halifax, Nova Scotia B3K 2X0

Mr. Tom West
SRUA
FMO Halifax
Halifax, Nova Scotia   B3K 2X0

Dr. N.G. Zamani
University of Windsor
Dept. of Mathematics and Statistics
Windsor, Ontario   N9B 3P4

(519) 253-4232 ext 3916